Experimental Investigation of the Topographic Modification of Earthquake Ground Motion

Jacob Dafni

A dissertation
submitted in partial fulfillment of the
requirements for the degree of

Doctor of Philosophy

University of Washington

2017

Reading Committee:

Joseph Wartman, Chair

Pedro Arduino

Steve Kramer

Program Authorized to Offer Degree:
Civil and Environmental Engineering

University of Washington

Abstract

Experimental Investigation of the Topographic Modification of Earthquake Ground Motion

Jacob Dafni

Chair of the Supervisory Committee:
Chair Joseph Wartman
Civil and Environmental Engineering

Topographic modification of earthquake ground motion can significantly impact ground motion amplitude and frequency content. While previous studies have investigated topographic modification of ground motion, also called *"topographic effect"*, there are discrepancies between the results of field and numerical investigations. A new experimental approach involving physical modeling in a geotechnical centrifuge was used to study topographic effects. The centrifuge captures the complexity of a physical process and shares many of the advantages of a numerical model (e.g., material properties, instrumentation location, and ground motions can be controlled). Experimental results show that *topographic amplification* can exceed amplification due to subsurface geology (i.e., *"site amplification"*). The results also indicate the main cause of topographic amplification is slope resonance, which leads to differential movement, and the development of shear planes between the slope and surrounding landmass. Slope resonant frequencies are within the range considered in engineering practice, which can impact the design of structures near slopes.

Findings from the centrifuge investigation were used to inform analyses of a ridge in the Port Hills suburb of Christchurch, New Zealand. Topographic effects were analyzed using data from a downhole array located adjacent to two cliff faces. A simplified procedure was adopted to establish a reference free field station. Results of the analyses were found to be in good agreement with the centrifuge investigation.

TABLE OF CONTENTS

LIST OF FIGURES

LIST OF TABLES

ACKNOWLEDGMENTS

There are many people to thank for their support in pulling this dissertation together. First and foremost, I would like to thank my advisor, Dr. Joseph Wartman. It's been a long journey and I really enjoyed working with you on this project. I especially thank you for your patience when I disappeared for a few a years to pursue work elsewhere. I would also like to thank my dissertation committee. I have had great experiences working with all of you, from time in the classroom, to working on my Master's thesis years ago. Thank you Dr. Pedro Arduino, Dr. Steven Kramer, Dr. Kenneth Creager and Dr. Jeffrey Berman. I look forward to seeing more of and working with all of you in the future.

I thank the National Science Foundation (NSF) for providing funding for this research project through the Network for Earthquake Engineering Simulation ($NEES$); award #0936543; NEESR-CR: Topographic Effects in Strong Ground Motion - From Physical and Numerical Modeling to Design. I would also like to thank the rest the research team who worked on this project. This includes the professors: Dr. Adrian Rodriguez-Marek, Dr. Dominic Assimaki, Dr. Brady Cox, and Dr. Miguel Pando; and my colleagues who beat me to the finish line; Dr. Manisha Rai, Dr. Seokho Jeong, and Dr. Clinton Wood, and Carlos Acosta.

I have numerous other friends and family to thank for all their support as I completed this project (you know who you are). It was a massive undertaking and I couldn't have done it without you. Thanks for the all the laughs along the way.

Chapter 1

INTRODUCTION

It is well established that significant alteration of ground motion amplitude, frequency content and duration may result from local geological subsurface conditions. Amplification and deamplification of propagating waves at different frequencies will occur due to resonances and interactions at soil layer boundaries, dependent upon the physical and mechanical material properties, and thickness of the substratum. These effects, deemed *site effects*, are typically considered in earthquake engineering via a simplified one-dimensional (1-D) analysis, where local geology is modeled by an idealized substratum with infinitely extending horizontal soil layers above an infinitely extending rock base. The frequency content and amplitude of ground motion, however, can also be significantly modified by surface topography, which requires the consideration of two-dimensional (2-D) or three-dimensional (3-D) topographic features.

Topographic modification of ground motion has been studied for almost 45 years with numerous investigations and literature emerging in the last couple decades. However, despite increased focus and research, these modifications, deemed *topographic effects*, are still not fully understood. As a result, these effects are typically not considered in seismic design, with the exception of some European codes, such as the EuroCode 8 (EC8) (Eur, 2004), which utilizes simplified modifications to the design spectrum. The complexities associated with 2-D and 3-D topographic features (i.e., slopes, ridges, hills, mountains, canyons and cliff-like topography) and their interaction with the geological substratum have led to quantitative discrepancies amongst previous research. Particularly, numerical investigations often do not quantitatively match field observations; although qualitative agreement has been achieved

(Bard and Riepl-Thomas, 2000; Geli et al., 1988). Field studies have typically been limited to aftershock recordings with sparse instrumentation, and often lack geological or geotechnical information, inhibiting the separation of site and topographic effects. Topographic studies performed numerically allow for parametric investigation, but typically suffer from simplifying assumptions, and may lack data for proper calibration.

The current research attempts to overcome some of the above limitations through physical modeling in a centrifuge. The centrifuge has the advantages of a numerical model in that material properties, instrumentation location, and the ground motions introduced can be controlled, but the complexity of a true physical process is maintained. Using dense arrays of accelerometers, topographic effects can be analyzed and more easily separated from site effects.

The findings from the centrifuge experiments are used to inform the analysis of a complex ridge-like structure at the Redcliffs site in the Port Hills suburb of Christchurch, New Zealand. Topographic effects are analyzed using data from a downhole array installed in close proximity to multiple cliff faces. To aid in the analysis, a simplified procedure was developed for establishing a reference free field station. Results from the case study analysis are compared to those from the centrifuge investigation.

1.1 Research Goals

The overarching goal of this research is to provide a better fundamental understanding of topographic effects. This includes knowledge of what the effects are and why these effects occur. By understanding the causes of these effects, the ability to predict topographic effects and topographic amplification is improved. For instance, numerical modelers will have a better understanding of the behavior that should be captured. This can impact the design of structures near slopes and methods used to analyze the stability of slopes subjected to transient earthquake loading.

Specific questions addressed are:

1. What is the main cause of topographic amplification?
2. What ground motion characteristics have the greatest influence on topographic effects?
3. How are the amplitude, frequency content and duration of ground motion affected by slopes?
4. What is the spatial extent of the effects on the above parameters?
5. What factors influence the spatial extent of topographic effects?
6. Do topographic effects lead to differential motion and how does this affect the ground response?
7. How does slope inclination affect the topographic modification of ground motion?
8. What geometric feature has the greatest influence: height or length of the slope?
9. Does the type of ground motion (i.e., broadband versus narrow band) influence topographic effects?
10. At the crest, do site effects or topographic effects dominate the ground response? Under what circumstances does one or the other control?
11. Can site effects be separated from topographic effects or do they influence each other?
12. Under what circumstances do topographic effects exist or not exist?
13. How does horizontal ground motion compare to vertical ground motion?
14. Can single station methods, such as H/V spectral analysis be used to analyze topographic effects?
15. For complex topographies, what influence does the polarization of ground motion have on topographic effects?

16. How useful is a centrifuge investigation for understanding topographic effects? How do findings from this investigation compare to a field case study? Can the same analysis methods be applied?
17. How do trends discovered in this study compare to past work?
18. How easily can topographic effects be predicted?
19. Do these effects occur within the frequency band of interest for engineering applications?
20. What impact could these effects have on the triggering of landslides?

1.2 Dissertation Outline

Motivation and goals for the research presented in this dissertation have been provided above. The remainder of this dissertation is organized as follows:

- Chapter 2 provides a brief literature review of the current understanding of topographic effects. Studies relevant to the goals of this research are highlighted.
- Chapter 3 presents an overview of the centrifuge investigation, including analysis of a flat ground configuration that served as an experimental baseline. Methods for analyzing topographic effects are provided. Results of a parametric analysis to identify trends in the ground response for three one-sided, step-like, soil slopes are presented. This is followed with discussion and conclusions sections that summarize the findings of the analysis.
- Chapter 4 shifts from a descriptive to causal understanding of topographic effects. The results from Chapter 3 were used to inform the selection of a suite of ground motions for time and time-frequency domain analysis. The analysis utilizes the dense arrays of accelerometers to study the causes and influences of topographic effects. This is again followed by discussion and conclusions sections that summarize the analysis findings.

- Chapter 5 presents a case study of the Redcliffs ridge located in Christchurch, New Zealand. Findings from the previous two chapters informed the analysis of data recorded in a downhole array for a geometrically complex ridge, composed mainly of weathered rock. A new simplified procedure is adopted to establish a reference free field station for the analysis of topographic effects. Findings are compared to those from the previous chapters, followed by discussion and conclusions sections.
- Chapter 6 summarizes findings from Chapters 2 through 5 and provides answers to the questions outlined above. This chapter concludes with a future work section.

Chapter 2

LITERATURE REVIEW

Previous research on topographic effects has mainly been carried out using macroseismic observations and instrumented field studies for earthquake events, or through numerical and analytical parametric investigations. Numerical and analytical studies have been performed by Ashford and Sitar (1997); Ashford et al. (1997); Assimaki et al. (2005a,b); Bouchon (1973); Bouckovalas and Papadimitriou (2005); Gao et al. (2012); Gazetas et al. (2002); Geli et al. (1988); Paolucci (2002); Papadimitriou (2011); Rizzitano et al. (2014); Sánchez-Sesma (1990); Sánchez-Sesma and Campillo (1993) and Tripe et al. (2013), among others. Field studies have also been performed by many researchers, including Barani et al. (2014); Buech et al. (2010); Burjánek et al. (2014); Celebi (1991); Davis and West (1973); Durante et al. (2017); Hailemikael et al. (2016); Hartzell et al. (1994); LeBrun et al. (1999); Marzorati et al. (2011); Massa et al. (2010, 2014); Pedersen et al. (1994); Pischiutta et al. (2010); Spudich et al. (1996); Stewart and Sholtis (2005); Stolte et al. (2017) and Wood and Cox (2015), among others. Numerical studies have tended to under-predict the magnitude of topographic amplification recorded in the field. However, more recent studies that incorporate more accurate stratigraphy or 3-D velocity structure have found better agreement between numerical models and field recordings (Assimaki and Jeong, 2013; Hailemikael et al., 2016; Hartzell et al., 2014, 2017; Pagliaroli et al., 2015). Comprehensive reviews of many of the studies performed can be found in Bard and Riepl-Thomas (2000), Geli et al. (1988) and more recently in Pagliaroli et al. (2011) and Massa et al. (2014), where tabulated and graphical information for both field and numerical studies is provided. This chapter will highlight important findings from these studies.

The effects of topography on ground motion determined by previous researchers are

qualitatively summarized below. Figure 2.1 illustrates features referenced in the following list.

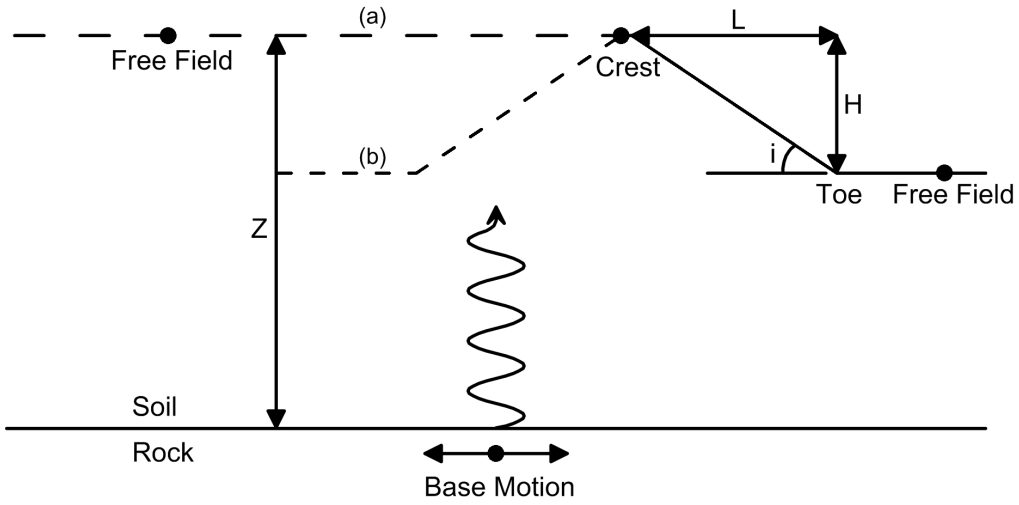

Figure 2.1: Important reference points and dimensions for an idealized (a) slope and (b) hill. The solid line to the right is shared by both diagrams.

- Ground motion is amplified near the crest of hills, ridges, and other concave topography (i.e., mountains and hill peaks), and deamplified near the toe or base of such features (convex topography), with differential response along the slope faces (Figure 2.1). This amplification it typically referred to as *topographic amplification*.

- Amplification near the crest increases as the slope inclination increases. For hill-like structures, amplification increases with shape ratio (Sánchez-Sesma, 1990), $SR = H/L$, where H and L are as shown in Figure 2.1.

- Amplification is greater for shear (S) waves than primary (P) compressional waves. Additionally, for slopes and ridges, amplification is greater for S waves with particle movement perpendicular to, rather than parallel to, the slope face (or ridge axis).

- Amplification is influenced by source-to-site direction and therefore is azimuth-dependent.
- Patterns of amplification and deamplification of ground motion are band-limited and frequency dependent such that:
  - for mountains and hills, peak amplifications typically occurs for propagating wavelengths comparable to the width (2L for line (b) in Figure 2.1) of the feature (Paolucci, 2002), and
  - for slopes, peak amplifications occur for propagating wavelengths equivalent to 5 times the slope height (Ashford et al., 1997).

  The associated frequencies are referred to as *topographic frequencies* and represent resonant frequencies for the topographic feature.
- If the incident wavelength is shorter than the characteristic dimension (i.e., L or H) described above, this can result in complex patterns of amplification and deamplification along the slope flanks. For wavelengths much greater than the characteristic dimension, topographic amplification is negligible.
- Topographic amplification varies with the seismic wave field and is greatest for vertically propagating waves.
- For idealized numerical studies with input motions consisting of vertically propagating pure shear waves, a "parasitic" vertical component of ground motion develops near the crest of slopes. At the crest, this vertical component is typically weaker than the horizontal component, but the crest vertical component may be greater than the horizontal component in the free field (Ashford and Sitar, 1997; Ashford et al., 1997; Assimaki et al., 2005a; Bouckovalas and Papadimitriou, 2005). The vertical component of motion is also typically amplified in field experiments, but less so than the horizontal component.

- A stratified subsurface typically leads to greater levels of amplification as compared to a homogeneous subsurface due to the interaction between the layered media (soil or rock) and topography. The interaction of other heterogeneities with topography (such as fracturing and weathering within a rock mass) can also affect the ground response.
- For field experiments, amplification patterns are typically similar in terms of frequency content (but not necessarily amplitude) for strong motion recordings and ambient noise measurements.

Although, there is agreement on the existence and general expected location of topographic amplification, factors that lead to greater levels of topographic amplification, and the magnitude of amplification remain poorly understood. Amplification values reported from field investigations range from 1 to 40 for maximum spectral ratios, and 1 to 10 for ratios of peak ground acceleration (PGA). Numerical investigations yield typical values between 1 and 3 for both spectral ratios and ratios of PGA (Bard and Riepl-Thomas, 2000; Massa et al., 2014; Pagliaroli et al., 2011).

This amplified motion can significantly impact engineering design. This is evidenced by the earthquakes listed in Table 2.1, for which major damage was concentrated on features susceptible to topographic amplification. In fact, two of the highest PGA values were recorded at the crest of topographic features; with values of 1.58g and 1.78g reported for the ridge of the Pacoima Dam and the crest of Tarzana Hill, respectively, during the 1994 Northridge earthquake (Sepúlveda et al., 2005b; Spudich et al., 1996). Therefore, it is important to understand why these discrepancies exist, so that more accurate modeling, and better prediction of topographic amplification can be achieved.

There are a number of explanations for the discrepancies between numerical and field studies, as well as the overall scatter of the field investigations. One explanation is that the definition of topographic amplification lacks consistency. Defining amplification requires the existence of a reference point. In field studies, a comparable reference site with similar geological conditions is not always readily available. Thus, either a recording at the base

Table 2.1: Earthquakes with Damage Attributed to Topographic Effects

Date	M_w	Location
1976	6.4	Friuli
1980	6.9	Irpinia
1985	7.8	Chile
1987	5.9	Whittier Narrows
1989	6.9	Loma Prieta
1994	6.9	Northridge
1995	6.2	Egion
1997	6.0	Umbria-Marche
1999	5.8	Athens
2001	7.7	El Salvador
2002	5.6	Molise
2009	6.3	L'Aquila
2010	7.0	Haiti

Table adopted and modified from Massa et al. (2010)

M_w = earthquake moment magnitude

of the topographic feature (which may experience deamplification, giving rise to greater perceived amplification) or some otherwise determined ideal location is used as a reference site for comparison to crest recordings. In other cases, horizontal to vertical (H/V) ratios (Cháves-García et al., 1997; Massa et al., 2010) or median site reference techniques (Maufroy et al., 2012) are employed when a sufficient reference site does not exist. Numerical and analytical studies for slopes, however, typically use the free field (1-D) response at some distance behind the crest as a reference location. Such simulations guarantee similar geologic conditions, enabling comparison of 1-D response to that of 2-D (or 3-D) response; something often not achievable in the field.

Another factor to consider is the intensity measures used to determine amplification. Many studies report ratios of PGA, which are directly comparable (aside from differing topographic and geologic conditions). Another commonly used intensity measure, however, is the spectral ratio, often reported in terms of Fourier amplitudes, but sometimes also given in terms of spectral accelerations. Aside from this complication, the Fourier spectrum may be either raw or smoothed depending upon the study. These differences in data filtering techniques can also lead to changes in perceived topographic amplification.

In line with the above, recent studies by Stolte et al. (2017) and Wood and Cox (2016) explored the use of various methods of spectral analysis for analyzing topographic effects. They compared the standard spectral ratio (SSR) to the H/V spectral ratio ($HVSR$), and median reference method (MRM), noted above (Maufroy et al., 2012). The SSR compares recordings along the surface to a single reference station. Ideally this station would be an equivalent free field site, but often it is located near the base of a feature or is chosen because it recorded the weakest ground motion. The $HVSR$ compares the H/V spectrum at each sensor location, and the MRM compares each recording along the array to the median spectrum for the array. The study by Stolte et al. (2017) found good agreement between the three methods, but found that amplification values were always lowest using the MRM. They also recommended that the $HVSR$ method not be used alone. The study by Wood and Cox (2016) found greater variation amongst the methods. In particular, the amplitudes varied and the $HVSR$ method showed amplification at frequency components that did not align with the other methods.

One last consideration is that numerical simulations incorporate many simplifying assumptions that may bias results towards lower topographic amplification values. In particular, many studies utilize a continuous half-space with a homogenous medium that has a constant shear wave velocity. Additionally, only specific seismic waveforms (i.e., P, SV or SH) are typically propagated through the models, which is unrealistic for field conditions.

In addition to qualitatively defining and quantifying the topographic modification of ground motion, previous researchers have also theorized causes and influences of topographic

effects. Previous studies have found agreement on some of the identified mechanisms. These have been summarized in Bard and Riepl-Thomas (2000) and Pagliaroli et al. (2011) and are provided below.

- The incidence angle of propagating waves relative to the sloping ground surface. In particular, surface motion can be particularly extreme for the case of critical incidence, cited as a contributing factor for the damage observed during the Whittier Narrows, California earthquake of 1987 (Bard and Riepl-Thomas, 2000; Kawase and Aki, 1990) (Bard and Riepl-Thomas, 2000).

- Focusing or de-focusing of seismic waves due to reflections off the surface of topographic features. This was demonstrated analytically for a wedge-shaped medium by Sánchez-Sesma (1990), however instrumental evidence of this effect does not currently exist (Bard and Riepl-Thomas, 2000).

- Diffraction of body and surface waves propagating downward and outwards from a feature, leading to interference patterns between the diffracted and direct waves. Diffracted surface waves generally are smaller in amplitude than direct body waves, and therefore contribute less energy. This was demonstrated by Pedersen et al. (1994) for a site in Greece, where the amplitude of outgoing waves was found to be roughly one-fifth of the incident wave (Bard and Riepl-Thomas, 2000).

- Resonance of the topographic feature. This phenomena was noted by Pagliaroli et al. (2011) and more extensively discussed in Paolucci (2002). Among others, it has been indicated as a controlling factor for the case of Tarzana Hill, California by Bouchon and Barker (1996) and Graizer (2009).

Typically the influence of topographic and site effects on the ground surface response have been considered separately. However, more recent studies, such as those by Assimaki and Jeong (2013); Assimaki et al. (2005a,b); Burjánek et al. (2014); Durante et al. (2017); Graizer (2009); Hailemikael et al. (2016); Marzorati et al. (2011); Rizzitano et al. (2014)

and Tripe et al. (2013), have indicated the two phenomena are coupled. In other words, topographic effects may be magnified or inhibited as a result of the subsurface stratigraphy, or other inherent heterogeneities. Softer soil (or rock) layers near the surface can aid in the resonance of a feature (Graizer, 2009), or lead to trapping of energy, resulting in additional amplification, or the generation of surface waves at the crest of a feature (Assimaki et al., 2005a). Soil non-linearity has also been shown (numerically) to impact topographic amplification (Assimaki et al., 2005a; Rizzitano et al., 2014). Additionally, lateral heterogeneities, such as fractures, faults, and weathering within a rock mass may influence topographic amplification (Burjánek et al., 2012, 2014; Durante et al., 2017; Imperatori and Mai, 2015; Marzorati et al., 2011; Pagliaroli et al., 2015; Takemura et al., 2015).

With an overall lack of consensus on the levels of topographic amplification expected for various features and site conditions, the effects of topography often aren't accounted for in engineering design. Design codes that do incorporate topographic effects, such as the EuroCode 8 (EC8) (Eur, 2004), usually apply simplifying factors that don't account for the frequency dependent nature of topographic amplification. Additionally, the vertical component of motion is often not considered. In order to mitigate this, recent studies by Rai et al. (2017) and Barani et al. (2014) have incorporated a topographic factor into ground motion prediction equations ($GMPEs$), which may then be used in engineering practice.

Despite the numerous studies outlined above, the topographic modification of ground motion is still not fully understood. The discrepancies between numerical and field studies have not been resolved. In order to bridge the gap between numerical and field studies, this study utilized physical modeling in a centrifuge. Smaller scale centrifuge experiments to investigate topographic effects have been performed (Brennan and Madabhushi, 2009; Ozkahriman et al., 2007; Yu et al., 2007). However, an extensive centrifuge investigation of topographic effects has not been previously conducted. Results from the analysis of the centrifuge investigation performed for this study are presented in the next two chapters. These results are then compared to a field case study, where a simplified approach for developing a reference free field station is explored.

CHAPTER 3 GLOSSARY OF TERMS & SYMBOLS

The figure below is provided for reference to make definitions in this glossary more clear. The figure consists of important reference points and dimensions for an idealized (a) slope and (b) hill. The solid line to the right is shared by both diagrams. Note that topographic factors reference the free field behind the crest, not that in front of the toe.

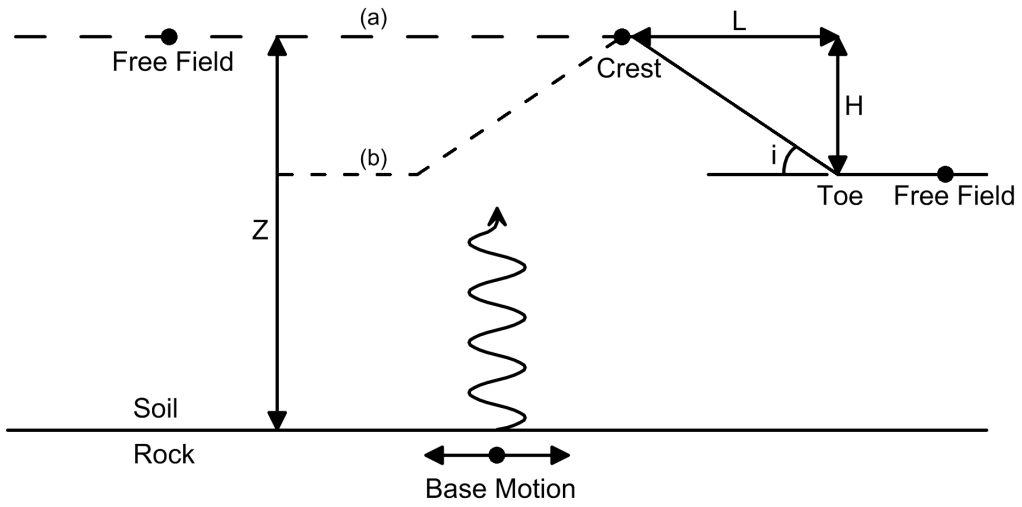

Apparent Amplification Ground motion amplification of the surface over the base input (or bedrock motion) with the contribution from the base motion removed. In the free field, apparent amplification represents site amplification (see below). It can be defined for any ground motion intensity measure (IM) such that $IM\ AA = (IM_s - IM_b)/IM_b$, where subscripts s and b represent any point on the surface and the base, respectively.

Banded Peak Spectral Acceleration Topographic Factor The banded peak (bp) Spectral Acceleration Topographic Factor ($SA\ TF$; see below) for a frequency band that spans from abou 0.6 to 1.1 times the topographic frequency (see below). The topographic factor is calculated using response spectra at different locations on the slope and free field. For the current study, the banded peak $SA\ TF$ is the peak $SA\ TF$ value for a frequency range of $2.5-5Hz$ and $5.0-7.5Hz$ for the 55g and 27.5g prototypes, respectively.

Site Amplification Ground motion amplification of the surface over the base input (or bedrock motion) resulting from propagation through the subsurface material.

Site Effects Modification of ground motion (i.e., amplitude, frequency content and duration) resulting from interaction with the subsurface material.

Site Frequency The frequency at which maximum site amplification is expected due to a tendency towards resonance of a subsurface soil layer. It is defined by $f_s = \bar{V}_s/4Z$ where $\bar{V}_s$ is the average shear wave velocity and Z is the soil layer thickness.

Slope Inclination The acute angle measured, in degrees, between the slope face and horizontal.

Strong Topographic Ratio Any topographic ratio (see below) between 0.7 and 1.3.

Topographic Amplification Ground motion amplification resulting from interaction with the surface topography only (i.e., excluding site amplification).

Topographic Effects Modification of ground motion (i.e., amplitude, frequency content and duration) resulting from interaction with the surface topography.

Topographic Factor A measurement of topographic effects through comparison of the surface response on a topographic feature to that of a flat ground free field surface, with the contribution of the free field removed. It can be defined for any intensity

measure (or other scalar parameter) such that $IM\ TF = (IM_s - IM_{ff})/IM_{ff}$, where subscripts s and ff represent any point on the surface and the free field, respectively.

Topographic Frequency The frequency at which maximum topographic amplification is expected to occur. It has been previously defined by $f_t = \bar{V}_s/5H$ for slopes and $f_t = f(\bar{V}_s/2L)$ for hill-like features, where $\bar{V}_s$ is the average shear wave velocity and H and L are the characteristic height and length of the topographic feature.

Topographic Ratio The ratio of mean square frequency to the topographic frequency (MSF/TR). A topographic ratio of one means the ground motion MSF is equal to the topographic frequency.

Topographic Zone of Influence The region or area where topographic effects exist (i.e., an area near a slope crest), bounded by locations where $TF = 0.2$ for spectral accelerations and $TF = 0.1$ for intensity measures.

Weak Topographic Ratio Any topographic ratio less than 0.7 or greater than 1.3.

AA	Apparent Amplification
AI	Arias intensity
f_s	Site frequency
f_t	Topographic frequency
H	Slope height
i	Slope inclination
L	Slope length
L_1	Distance from crest to end of topographic zone of influence towards the free field
L_2	Distance from crest to end of topographic zone of influence towards the slope toe
MSF	Mean square frequency
PGA	Peak ground acceleration
PSS	Peak ground shear strain
PGV	Peak ground velocity
SA	Spectral acceleration
STR	Strong topographic ratio
TF	Topographic Factor
TR	Topographic ratio
V_s	Shear wave velocity
$\bar{V}_s$	Average shear wave velocity
WTR	Weak topographic ratio
Z	Soil layer thickness
z_d	Depth measured below the ground surface

For any scalar ground motion measure above, a topographic factor or apparent amplification can be calculated and would be abbreviated by combining the acronym for the given measure and that of topographic factor or apparent amplification. For example, the Mean Square Frequency Topographic Factor would be written as $MSF\ TF$ and the Spectral Acceleration Apparent Amplification as $SA\ AA$.

Chapter 3

TOPOGRAPHIC EFFECTS: TRENDS DETERMINED THROUGH A CENTRIFUGE INVESTIGATION

The previous chapters have established that surface topography can significantly modify the frequency content and amplitude of seismic ground motion. Constructive interference of diffracted surface and body waves, wave focusing, and resonance can lead to ground motion amplification and more extensive damage near the crests of topographic features. A number of studies have been dedicated to this phenomenon, deemed *topographic effects*, for the case of hills, canyons, ridges, mountainous regions, slopes and cliff-type topography. Typically, these previous studies have been limited to numerical analysis or sparse recordings on specific geological features. Among these studies, often qualitative, but not quantitative agreement has been achieved. In particular, a discrepancy exists between numerical studies and field recordings (Bard and Riepl-Thomas, 2000; Geli et al., 1988), with numerical studies under-predicting the amplification levels found in field studies. Experimental field or case studies can be limited by a lack of instrumentation and/or geologic and geotechnical information, which inhibits the separation of effects due to the geologic substratum (i.e., *site effects*) and topographic effects. Numerical simulations allow for more controlled parametric analysis, but may lack data for proper calibration and incorporate simplifying assumptions that do not reflect true behavior observed in the field.

Physical modeling in a centrifuge provides an alternative approach to studying topographic effects in a fundamental manner. Controlling material properties, instrumentation location, and the ground motions introduced, allows pure topographic effects to be analyzed and more easily separated from site effects. This chapter presents analysis details and results of an extensive centrifuge experiment conducted to investigate and provide further

understanding of the topographic modification of ground motion (topographic effects). The experiment focuses on one-sided, step-like slopes (Figure 3.1 (c)) considering a number of factors, including ground motion type, amplitude, frequency content, duration, slope inclination and spatial influence. Comparisons to previous studies are included where appropriate.

3.1 Centrifuge Model and Testing

An overview of the centrifuge experiment including the model construction and the testing program is provided in this section. Additional details of the centrifuge experiment may be found on the NEESHub website (see Adrian Rodriguez-Marek, 2010). This includes the data collected, information on the testing equipment, and full diagrams for each of the ground configuration (inclusive of the model container and instrumentation).

Five model configurations consisting of dry, dense (relative density, $D_r \approx 100\%$) Nevada sand (Mikola and Sitar, 2013) were constructed and tested in a non-destructive manner at centrifugal accelerations of 55g and 27.5g (i.e., 55 and 27.5 times the acceleration of gravity) at the Center for Geotechnical Modeling at the University of California, Davis. The first testing configuration, a flat ground model simulating typical 1-D site response, served as an experimental baseline (Figure 3.1 (a) and (b)). The second, third and fourth configurations consisted of one-sided slopes of 30, 25, and 20 degrees, respectively, of which the 30 degree slope cross section is depicted in Figure 3.1 (c). The fifth was a dam-like configuration; however, it cannot be directly compared to the one-sided slopes and thus is not included in the discussion for the remainder of this chapter.

3.1.1 Model Construction and Instrumentation

The centrifuge model was constructed in an equivalent shear beam container with dimensions 1651 x 787 x 588 mm (length x width x height). The initial flat ground model was formed by air pluviating Nevada sand into the container in approximately 5.7 cm lifts to 90% relative density. After each lift, the model surface was hand vibrated to achieve a relative density near 100%. Loose surface sand disturbed by the vibrating process was then removed with

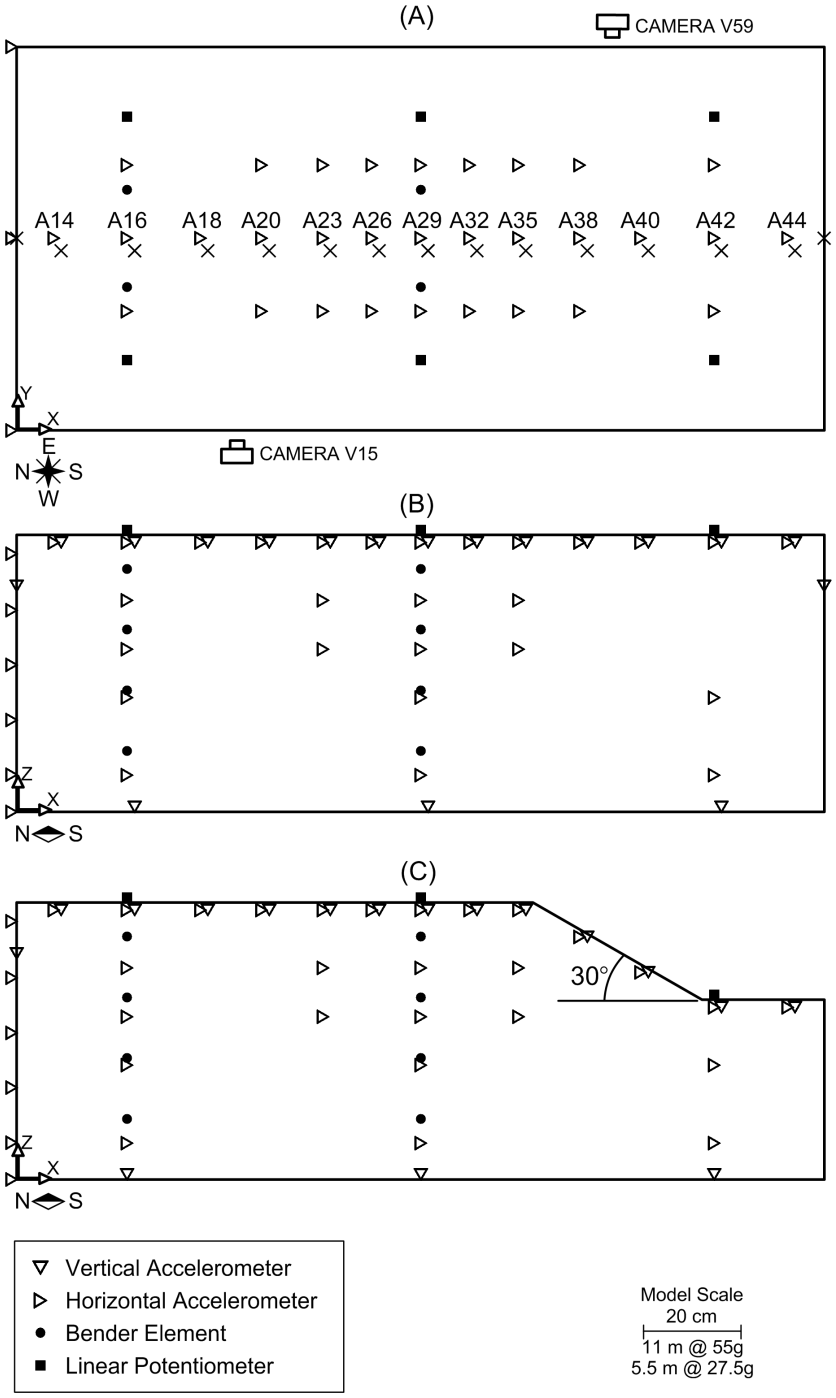

Figure 3.1: (A) Plan view of model and instrumentation. (B) Cross section of flat ground model and instrumentation. (C) Cross section of 30 degree slope configuration and instrumentation. Labeled sensors from (A) correspond to near surface sensors in (B) and (C).

a vacuum before the next lift was placed. Slopes were formed with the model container on the centrifuge arm using a vacuum with a guide that could be adjusted to different angles (Figure 3.2). For each of the slope configurations, the location of the slope toe remained unchanged, such that a change from a 30 degree slope to a 25 degree slope, for instance, would result in the crest of the slope shifting further north (Figure 3.1). In forming slopes, near surface instrumentation was moved (or removed) as necessary in the vertical (z) direction; x-y coordinates in plan view were maintained throughout the testing program (Figure 3.1). After each slope was formed a thin coarse sand layer was applied to the model surface and bonded with spray glue. This served to prevent surficial movement of sand particles and sensors. Photos of the centrifuge and model are given in Figure 3.2. Additional photos are provided on the NEESHub website (Adrian Rodriguez-Marek, 2010).

The model was instrumented with dense arrays of accelerometers, particularly near the surface, in order to capture topographic effects. Free floating arrays of bender elements were placed in the model to determine the shear wave velocity profile with depth. High speed cameras were utilized to monitor surface movement of the model. Additionally, a series of linear potentiometers was used to capture any surface settlement at selected locations. Instrument locations are given in Figure 3.1.

3.1.2 Testing Program

In conducting a geotechnical centrifuge test, the constructed model is spun up to g-levels much greater than the typical acceleration of gravity experienced on earth (i.e 1g). The centrifugal acceleration experienced by the model is determined by the rotational velocity and length of the centrifuge arm. The stresses developed within the model depend upon the centrifugal acceleration achieved. Through laws of similitude, the stresses developed can be related to an equivalent prototype of interest, which is representative of a larger site on the earth. For instance, if the depth of a soil layer at model scale is 0.6 meters and the centrifugal acceleration achieved is 55g, the equivalent height of the prototype soil column is 33 meters, or 55*0.6. Using this scale, the static vertical stresses of the prototype site can

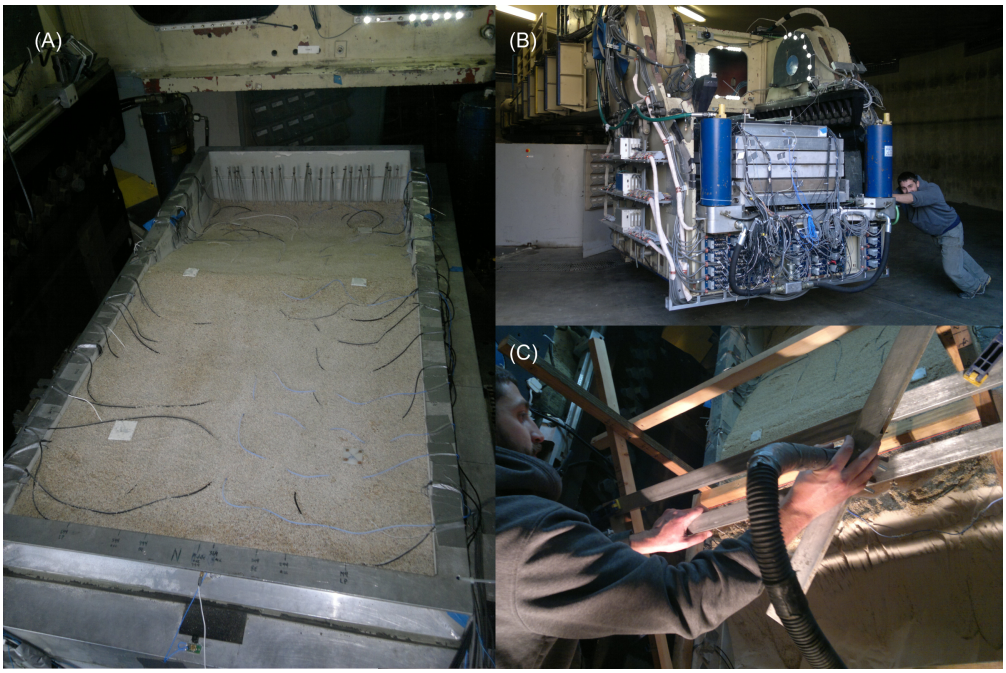

Figure 3.2: (A) The 20 degree slope from above inside the model container. (B) The author pushing the centrifuge bucket attached to the centrifuge arm above. The model container is in between the blue cylindrical compression chambers. (C) The author carving a second slope for the dam-like configuration using a vacuum and guide.

be calculated with depth in typical fashion (i.e., depth multiplied by material unit weight).

Once the appropriate g-level is achieved, ground motion can be introduced via an actuator (also known as a shaker) beneath the model container. In this case, a horizontal shaker that displaces in the north-south direction is utilized and the input (base) motion is directly measured by accelerometers on the east and west ends of the shaker (Figure 3.1). More information on centrifuge similitude and scaling laws can be found in Garnier et al. (2007), Leth et al. (2008), Springman (1997) and Taylor (1995).

For this testing program, four types of horizontal ground motion were introduced to all model configurations at both g-levels: Ricker wavelets (Ryan, 1994), sine wave packets, frequency sweeps and simulated earthquake motion. For a given g-level a similar suite of motions was introduced to each of the model configurations to allow for comparison between the different slopes and flat ground model. The typical target motions utilized during the

testing program are given below.

- Ricker wavelets with central frequencies of 1, 2, 4 & 6Hz at 55g and 1, 2, 4, 6, 8 & 12Hz at 27.5g.
- Sine wave packets consisting of 12 cycles of sine wave motion with central frequencies the same as above.
- Two frequency sweeps ranging from 0.13-6.05Hz and 0.5-7.0-0.5Hz at 55g, and ranging from 0.26-12.1Hz and 1.0-14.0-1.0Hz at 27.5g.
- Three earthquake motions: Chi Chi (TCU078E), Joshua Tree (JOS090) and Superstition Hills (BPTS315) at 55g; the same motions with the time step cut in half at 27.5g.

Frequencies are presented at the prototype scale. These motions were introduced at varying levels of amplitude ranging from 0.03-0.3g, and each motion was introduced at either two or three different amplitudes within this range for each model configuration. Sample input acceleration time histories of the ground motions are provided in Figure 3.3. For the remainder of this chapter, for consistency, it should be assumed that units are given at prototype scale unless otherwise stated.

For the four configurations considered in this chapter, a total of 141 ground motions were utilized, of which 54, 31, 28 and 28 motions were introduced for the flat ground, 30 degree slope, 25 degree slope and 20 degree slope configurations, respectively. In testing the model at two centrifugal g-levels, two prototypes were considered for each configuration. Of the two, the prototype associated with 55g was the main focus of the experiment, while the prototype associated with 27.5g played a complimentary role. As a result, more ground motions were introduced at 55g than 27.5g, such that 42 of 54, 20 of 31, 19 of 28 and 19 of 28 ground motions were used at 55g for the flat ground, 30 degree slope, 25 degree slope and 20 degree slope configurations, respectively. Of the number of motions listed above, 26 motions were common amongst the three sloped configurations.

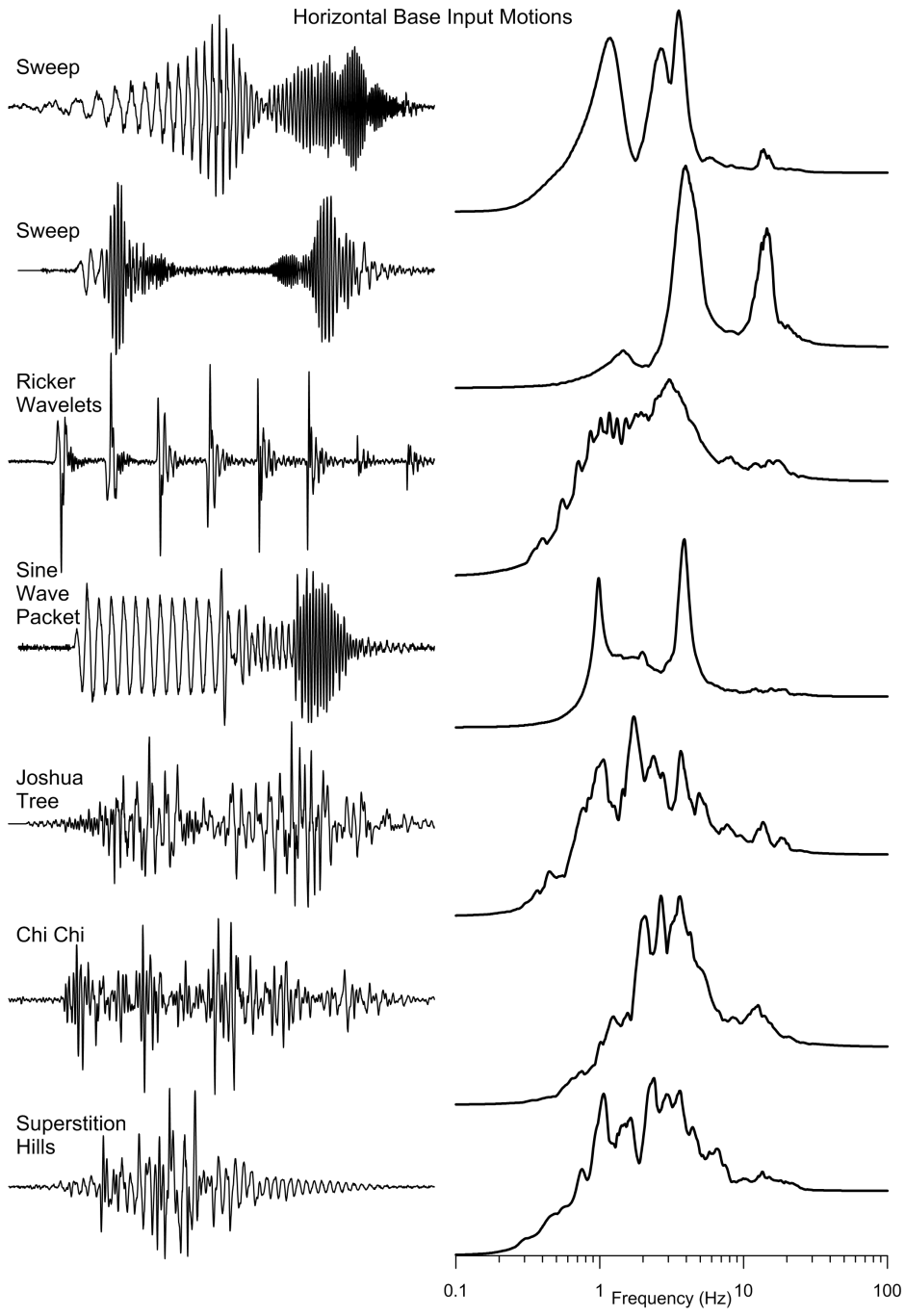

Figure 3.3: Sample recorded horizontal base motions introduced to the different centrifuge configurations. Time histories and response spectra with 5% damping are included.

The sine wave packets and Ricker wavelets introduced at different central frequencies were combined into one continuous motion in order to streamline the testing process. The intent, however, was to test the slope responses for a given sine wave or Ricker wavelet at a given central frequency. As a result, these motions were analyzed both as continuous motions and as individual motions by dividing the acceleration time histories according to the different associated central frequencies. Considering the motions individually, the motions common to the three slopes increases from 26 to 64, resulting in a total of 192 motions. However, the horizontal shaker had difficultly consistently producing the high frequency input motions. Consequently, the sine waves and Ricker wavelets with the highest target central frequencies (i.e., 6Hz and 12Hz for 55g and 27.5g, respectively) typically had a low signal to noise ratio and could not be included in the analysis. For this reason, 10 motions introduced to each slope were discarded, reducing the total number of motions analyzed for the three slopes to 162, with 54 per slope.

The testing program was designed to consider a wide range of ground conditions and ground motions as efficiently as possible, and consider the research questions outlined in Chapter 1. The flat ground model was used to calibrate ground motions and serve as a baseline for the experiment. Multiple iterations of the command ground motions were introduced until the achieved motions by the shaker more closely matched the desired ground motions to be introduced to the sloped configurations.

Idealized ground motions, such as the Ricker wavelets, sine wave packets and frequency sweeps, were designed to encompass estimates of the site and topographic frequencies. Estimates of these frequencies were made based on the g-level chosen, the well documented properties of Nevada sand (Mikola and Sitar, 2013) and the dimensions of the slopes. Earthquake motions that had already been calibrated to Nevada sand models (Mason et al., 2010) were chosen to test the ground behavior under more typical earthquake loading conditions. For each ground motion utilized in the investigation, a low, mid and high amplitude motion were introduced to test the effects of ground motion amplitude.

The model was designed and constructed to maximize the size of the slopes while mini-

mizing container boundary effects, and allowing for the existence of the free field behind the crest. This facilitated comparisons between the slope and free field behavior, typical of the study of topographic effects (see next section). Maximizing the slope size also allowed for a greater density of instrumentation within the slope. In this way, wave propagation and the spatial extent of topographic effects could be more easily tracked. Two g-levels were utilized so that two different slope prototypes could be analyzed for each slope configuration.

The tests were designed to be non-destructive (with the exception of the final configuration, not presented here) so that numerous ground motions could be introduced to any one configuration. To ensure similar ground conditions, the model was constructed with the aim of 100% relative density for the Nevada sand. This minimized additional densification during the experiment. The order in which the various slope configurations were constructed was also chosen to minimize impact to the existing ground surface. Likewise, ground motions were introduced moving from low to high amplitude to minimize any permanent displacements that may occur.

3.2 Analysis Methods

3.2.1 Background and Definitions

The previous chapter covered methods used in past studies to analyze topographic effects for different features. Some of the techniques are directly applicable to the one-sided step-like slopes studied in this investigation, and are briefly reviewed in this section. The steps needed to apply these techniques are also discussed.

A typical method for analyzing topographic effects is to compare the dynamic response of a slope at and around the crest to an equivalent 1-D free field response at some point behind the slope crest. This method of comparison can most easily be employed by establishing a *topographic factor* for different measures of ground motion intensity. Using *peak ground acceleration* (PGA) as an example, the topographic factor (TF), originally proposed by

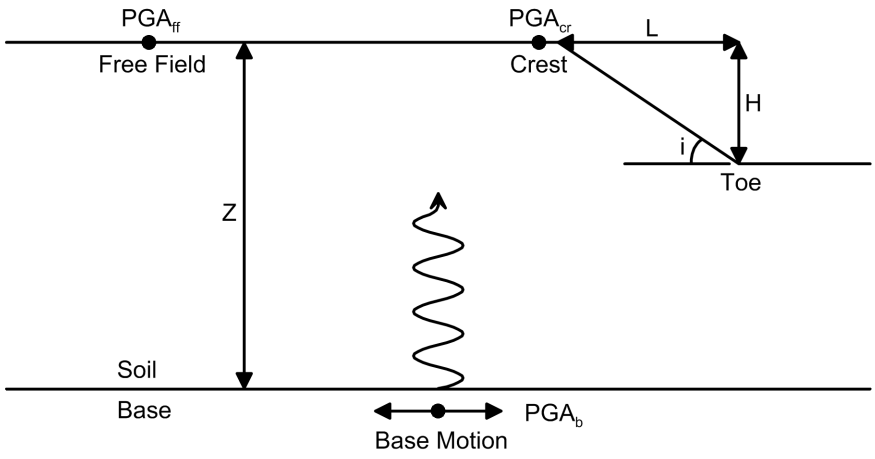

Figure 3.4: A schematic for a one-sided slope with properties of interest defined.

Ashford and Sitar (1997), can be written as follows:

$$PGA\ TF = \frac{PGA_s - PGA_{ff}}{PGA_{ff}} \tag{3.1}$$

where PGA_s is the PGA for any point on the slope (at the crest $PGA_s = PGA_{cr}$), and PGA_{ff} is the PGA under free field conditions. Defining the TF in this way allows site effects to be separated from the effects of topography. The TF represents a percent change (i.e., $0.3 = 30\%$) in ground motion amplitude, where a positive TF represents amplification, a negative TF represents deamplification and a value of zero represents no change as compared to the free field motion.

In order to gauge the relative contribution of site and topographic effects, *apparent amplification* (AA), also proposed by Ashford and Sitar (1997), but modified here, can be defined as:

$$PGA\ AA = \frac{PGA_s - PGA_b}{PGA_b} \tag{3.2}$$

where PGA_b is the PGA of the input motion, again using PGA as an example. By setting $PGA_s = PGA_{ff}$ in Equation (3.2), $PGA\ AA$ becomes a measure of *site amplification*. This can be compared to the case when $PGA_s = PGA_{cr}$, for which $PGA\ AA$ represents a

measure of combined site and *topographic amplification* (or deamplification). In the original definition given by Ashford and Sitar (1997), accelerations on the surface at and behind the crest were normalized by those determined in the free field in front of the slope toe. The input 'bedrock' motion used for normalization in Equation (3.2) was elected here as it provides an AA more representative of the true site amplification in the free field (and hence the combined topographic and site amplification near the slope) and because free field conditions in front of the slope toe were not captured in the experiment as a result of the proximity of the toe to the container boundary. A schematic illustrating the parameters defined in Equations (3.1) and (3.2) is provided in Figure 3.4.

The TF and AA are both measures of ground motion amplitude; however frequency content is also modified by topographic features. A 1-D column of soil (i.e., a soil layer with a flat ground surface) has a tendency to resonate at a certain frequency, f_s, defined by material properties and the height of the soil column, such that

$$f_s = \frac{\bar{V}_s}{4Z} \tag{3.3}$$

where $\bar{V}_s$ is the average shear wave velocity of the soil, Z is the thickness (height) of the soil column (Figure 3.4) and f_s is the *site frequency*. For a given soil layer, amplified ground motion would be expected to occur near the site frequency. Similarly, a *topographic frequency*, f_t, can be identified for a 2-D slope cross-section

$$f_t = \frac{\bar{V}_s}{5H} \tag{3.4}$$

where H is the slope height. The definition of topographic frequency given in Equation (3.4) was determined empirically by Ashford et al. (1997) in a numerical study of one-sided slopes subjected to shear waves. By normalizing the ground response at the slope crest by the free field behind the crest, Ashford et al. (1997) found the normalized response to consistently peaked at this frequency. The topographic frequency, then, is the ground motion frequency at which maximum topographic amplification is expected to occur.

Another definition of topographic frequency, originally suggested by Geli et al. (1988)

and later modified by Paolucci (2002), can be written as follows

$$f_t = f\frac{\bar{V}_s}{2L} \tag{3.5}$$

where L is the slope length, defined in Figure 3.4, and f is a factor ranging from $0.7 - 1.0$. Equation (3.5) is based upon analysis of a non-symmetric triangular-shaped hill and then is generalized to a symmetric hill shape. It is analytically derived using Rayleigh's method, assuming certain modal shapes and a Poisson's ratio of 0.25, to find the fundamental frequency of the hill for both in-plane and anti-plane shear waves. The original equation empirically proposed by Geli et al. (1988) is obtained by setting $f = 1.0$.

One definition for the topographic frequency is based on the length of the feature, while the other is based on the height. The definition based on height (Equation (3.4)) was developed while investigating one-sided slopes, while the other (Equation (3.5)) was related to hill-like features. Both were initially considered, however, Equation (3.4) proved to better align with the analysis results. Therefore, this definition was adopted and is simply referred to as the topographic frequency in the remainder of this chapter, unless otherwise stated. Input parameters and solutions to Equations (3.3) and (3.4) for the two prototypes tested (55g and 27.5g) are provided in Table 3.1.

Table 3.1: Summary of Important Parameters for Both Prototype Slopes

	Z(m)	H(m)	$\bar{V}_s$(m/s)	f_s(Hz)	f_t(Hz)
At 55g	31.4	11	250	2.0	4.5
At 27.5g	15.7	5.5	200	3.2	7.3

For comparative purposes, using Equation (3.5), the calculated frequencies would range from 4.6 to 6.6Hz, 3.7 to 5.3Hz and 2.9 to 4.1Hz for the 30, 25 and 20 degree slopes, respectively, at 55g. Calculated topographic frequencies would range from 7.4 to 10.5Hz, 5.9 to 8.5Hz, and 4.6 to 6.6 Hz for the 30, 25 and 20 degree slopes, respectively, at 27.5g.

The ranges for the three slopes overlap, but differ depending on the slope. The topographic frequency adopted in this chapter would fall within the range of that calculated for 25 degree slopes if Equation (3.5) is used.

3.2.2 Free Field Analysis

Analyzing topographic effects in the manner outlined requires knowledge of the free field response and shear wave velocity profile for the site. Free field conditions were first verified for the flat ground configuration before they were confirmed behind the crest of the slope configurations (Figure 3.4). A ProSHAKE (Edu, 1998-2017) analysis was conducted using the recorded base ground motions from the centrifuge experiment as inputs to the ProSHAKE model. The resulting ground motions produced at the base and surface of the ProSHAKE model were matched the recorded response at the base and the central near surface accelerometers for the flat ground configuration, where free field behavior was expected.

Because the shear wave velocity was relatively unknown, an iterative analysis was required to establish a satisfactory alignment between the ProSHAKE results and the centrifuge data. Shear wave velocity profiles determined in previous centrifuge studies with nearly identical conditions (i.e., the same material, centrifuge, and model container were used at similar g-levels) were used as guides for the iterative analysis (see Lai et al., 2004; Stevens et al., 1999), and a profile defined by $V_s = 132 * z_d^{0.27}$ was established; where z_d is depth below the ground surface. This result was confirmed through analysis by Liu (2012a) of the bender element data collected at different depths within the model. The average shear wave velocity values ($\bar{V}_s$) reported in Table 3.1 were calculated based on the soil layer thickness for the different g-levels (Z, as shown in Figure 3.4) and the defined velocity profile.

Once free field conditions were confirmed at the center of the flat ground model configuration, the extent of the free field conditions was determined by analyzing the boundary effects induced by the centrifuge model container. The response for the near surface central accelerometers was compared to that recorded at all other near surface sensors. Through this investigation, it was found that a central array of accelerometers running north-south from

sensor A20 through A38 (Figure 3.1 (a)) demonstrated free field behavior, such that these locations were not heavily influenced by container boundary effects. Thus, in determining an equivalent free field sensor for the slopes, only sensors in this array were considered.

To establish a reference free field sensor for the sloped configurations, the free field response of the flat ground model was compared to the surface response of sensors behind the crest of the three slopes at both g-levels. Comparisons were made between similar ground motions introduced to the different model configurations. However, due to changes in model mass the base input motion for the slopes was similar, but not identical to those introduced to the flat ground model. Consequently, amplitudes at the model surface had to first be normalized by the base input motion prior to comparison. For a given intensity measure (IM), a percent difference was determined for a given sensor as follows:

$$\%\ difference = \left(\frac{IM_{sl}/IM_{bsl}}{IM_{fl}/IM_{bfl}} - 1 \right) \times 100 \tag{3.6}$$

where the subscripts sl, bsl, fl and bfl represent the surface of a sloped configuration, base of a sloped configuration, surface of the flat ground model and base of the flat ground model, respectively. Using intensity measures of PGA, *peak ground velocity* PGV and *Arias intensity* AI, it was established that the average percent difference for sensor A20 (Figure 3.1 (a)) was near 10% or less for the three slope configurations tested at 55g. Additionally, the response spectrum was in qualitatively good agreement for the different ground motions investigated. Because sensor A20 is also free of container boundary effects, it was established as a reference free field sensor for analyzing the sloped configurations. By instituting a free field sensor, direct comparison of the free field response to the response in areas influenced by the surface topography (i.e., the slope crest) could be made without concern of bias resulting from differences in the base input motions. Comparisons between the surface response of the flat ground and slopes is provided in Section 3.3.3.

A free field sensor could not be established for the slope prototypes associated with testing at 27.5g. Because of the reduced size (half that of the 55g prototype) and stiffness of the prototype, none of the surface sensors were free of both topographic and boundary effects.

In comparing the response of the slopes to the flat ground, percent differences ranged from less than 10% up to 30% for the different intensity measures considered. However, to enable a more direct comparison in the results at both g-levels, analysis of the 27.5g prototype was still carried out in the same fashion as the 55g prototype, with the caveat that the magnitude of the TFs may typically be lower than the true magnitude. Despite this deficiency it was determined that overall qualitative trends in the data remained relatively unaffected, as is established by results presented in the next section.

3.3 Analysis Results

The aim of this section is to systematically present results of the analysis of the centrifuge data set outlined above. Analysis was performed to quantify and identify topographic effects for the three one-sided slopes. Figures with descriptions and highlights of the trends observed are introduced and briefly discussed. A summary of findings and more in depth discussion of these results, however, is reserved for the following section (Section 3.4).

The results presented are divided according to the manner in which the data was analyzed. To extract as much information as possible, the data was examined in three ways: *a*) data for each ground motion was analyzed individually; *b*) behavioral trends were determined for each slope inclination; and *c*) trends for the three slope inclinations were considered. As shown in Figure 3.1, most of the accelerometers were oriented to capture ground motion in the horizontal direction, with fewer accelerometers oriented in the vertical direction. Therefore, it should be assumed that results presented are for horizontal ground motion unless otherwise stated.

3.3.1 Observations for Single Ground Motions

Sinusoidal motion introduced to the centrifuge model in the form of the earlier described sine wave packets and frequency sweeps (Figure 3.3) provides a clear illustration of the fundamental effects of topography. Figure 3.5 presents a single sine wave packet introduced to the 30 degree slope at centrifugal acceleration 55g. The central frequencies for each of the 12 cycles of sine motion are ordered from lowest to highest for the time histories shown, with target values of 1, 2, 4, and 6Hz. Significant amplification of the base input ground motion at both the free field and slope crest locations is observed for motion with a central frequency near that of the site frequency (2Hz). However, at the slope crest, even greater amplification of the ground motion is observed for sinusoidal motion with a central frequency near the topographic frequency of the slope (4.5Hz); an amplification not seen in the free field. This effect is further illustrated by the response spectrum of the three motions, given at the bottom of Figure 3.5, which shows that the amplification due to the slope topography (topographic amplification) is clearly greater than site amplification.

Figure 3.6 provides another interpretation of a single ground motion, this time utilizing a frequency sweep that ranges from introduced to the 30 degree slope for the 55g prototype. The frequency sweep ranges from 0.5-7.0-0.5Hz and the base motion is shown in Figure 3.3. Figure 3.6 also introduces three new factors, the *spectral acceleration topographic factor* ($SA\,TF$), the *banded peak* (*bp*) $SA\,TF$ and the *mean square frequency* (MSF). The $SA\,TF$ is determined by substituting *spectral acceleration* (SA) values for PGA in Equation (3.1) for each discrete frequency at which the response spectrum is calculated. The *bp* $SA\,TF$ is then calculated by taking the peak $SA\,TF$ value for a chosen frequency band of interest. The spectrum was divided into frequency bands ranging from $0.5 - 2.5Hz$, $2.5 - 5.0Hz$, $5.0 - 7.5Hz$, $7.5 - 10.0Hz$, $10.0 - 12.5Hz$, and $12.5 - 15.0Hz$ for the analysis performed. For the 55g prototype the frequency band selected for analysis, and subsequently depicted in Figure 3.6, is from $2.5 - 5.0Hz$ being that it spans the topographic frequency, but is not influenced by the site frequency. For the same reasons the frequency band from $5.0 - 7.5Hz$

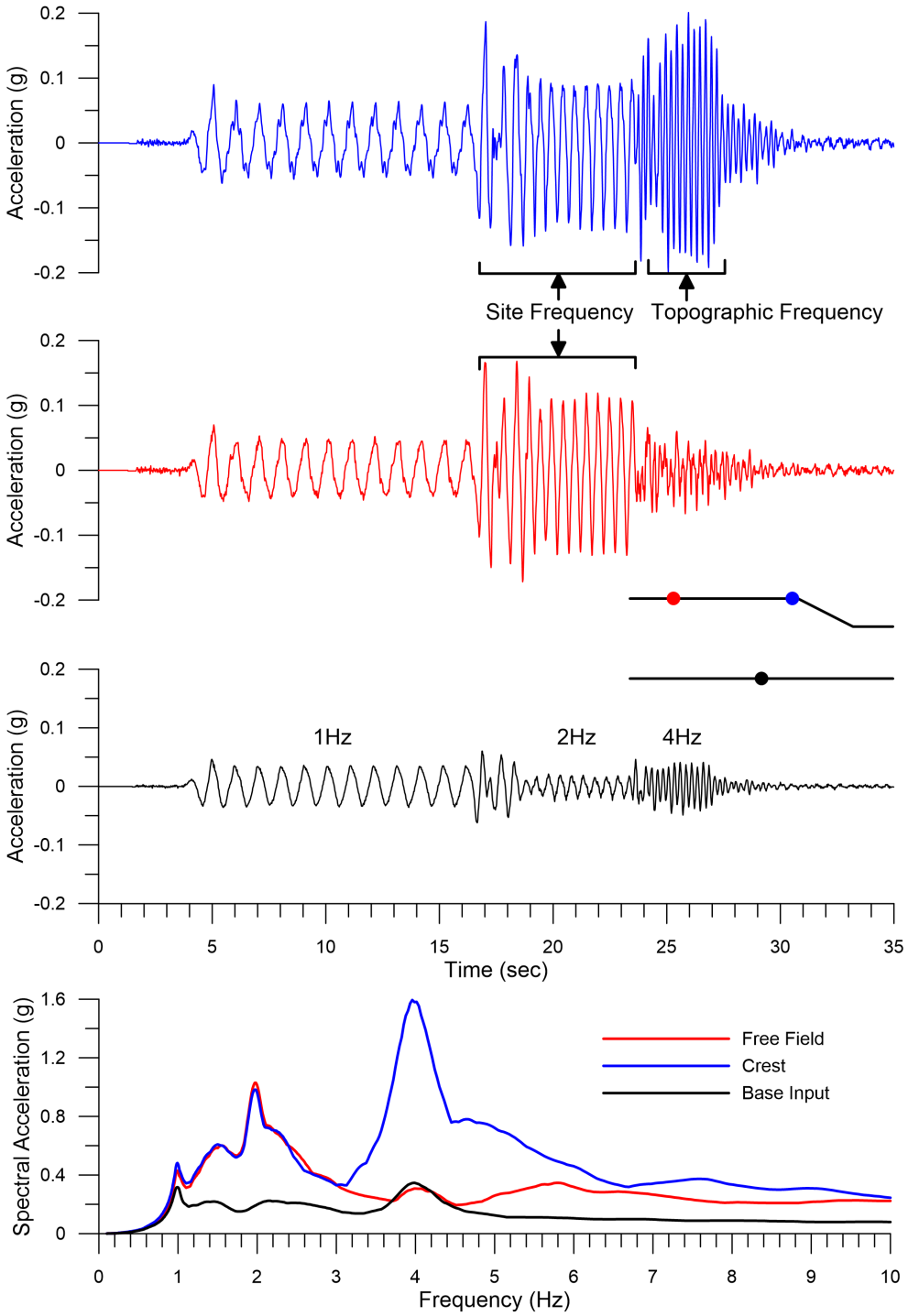

Figure 3.5: Acceleration time histories and response spectrum with 5% damping for a sine wave packet at the base, free field and crest of the 30 degree slope.

was used in analyzing the 27.5g prototype, to be depicted later in this section. Unless otherwise stated, it should be assumed these frequency bands are used whenever the *bp SA* is reported. The final factor introduced, MSF, provides a weighted frequency measure for a given ground motion. By rearranging the formula for mean square period defined by Rathje et al. (1998), the MSF can be calculated as follows:

$$MSF = \frac{\sum_i C_i^2 f_i}{\sum_i C_i^2} \qquad \text{for } 0.25 \leq f_i \leq 20Hz \tag{3.7}$$

where C_i is the Fourier amplitudes and f_i are the corresponding frequencies for i discrete points. The calculation is similar to that used to define a geometric centroid and thus, the MSF is a scalar representation of a centroid-like frequency for a given ground motion. That is, the spectral amplitudes below and above this frequency are balanced (within the frequency range).

The factors described above were contoured using the minimum curvature interpolation method, and the software Surfer 11 (Golden Software Inc., 2012). The minimum curvature interpolation method is designed to closely honor data while also generating the smoothest possible surface. The interpolation surface is similar to a thin, linear-elastic plate that passes through the defined data points while maintaining a minimum amount of curvature (Golden Software Inc., 2012; Smith and Wessel, 1990). More information about this interpolation method can be found in (Briggs, 1974; Golden Software Inc., 2012; Smith and Wessel, 1990).

By contouring the calculated factors described above, the spatial distribution and magnitude of topographic effects for a particular ground motion and slope configuration can be observed. For the frequency sweep in Figure 3.6, inspection of the top contour plot of the $SA\ TF$ (with axes of frequency versus distance across the surface of the model) reveals an amplified response at and around the slope crest with peak values occurring near the topographic frequency of the slope. The cross-sectional contour of the *bp* $SA\ TF$ (second plot) highlights the large areal extent of the slope affected within the frequency band of interest. A maximum *bp* $SA\ TF$ value of 4.7 (representing a 470% increase) is found at the slope crest. The final plot in Figure 3.6 shows differences in frequency content across the slope

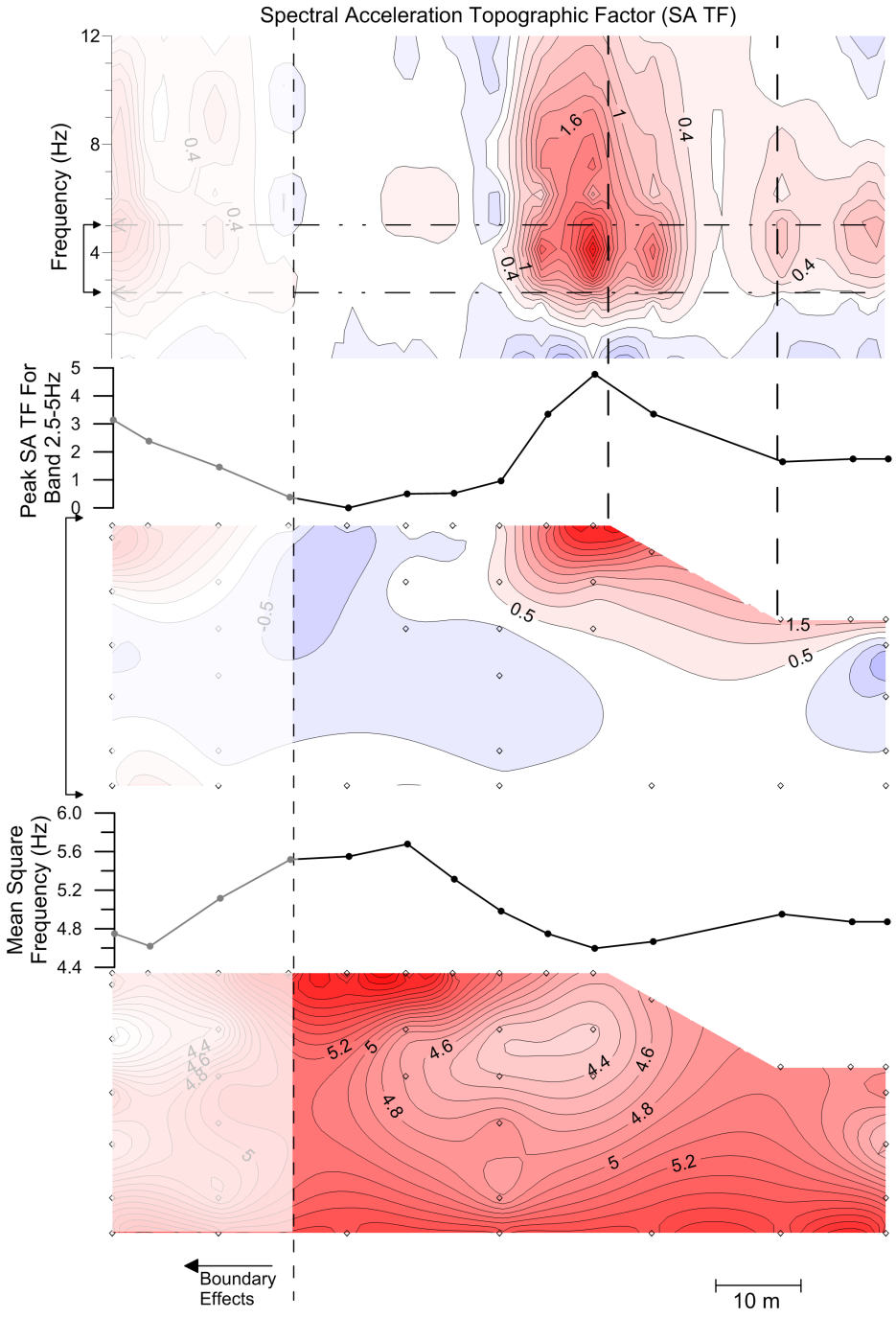

Figure 3.6: $SA\ TF$ contour with frequency versus distance; Band Limited $SA\ TF$ and MSF cross-sectional contours of a frequency sweep ranging from 0.5-7-0.5Hz for the 30 degree slope. Near surface values are given above the cross-sectional contours at instrument locations.

through a contoured cross-section of MSF. It can be observed that the MSF of the ground motion shifts towards the topographic frequency near the slope crest and again a large areal extent is affected. In the free field, the MSF is 5.6Hz, which is near the MSF of 5.4Hz for the input ground motion, while a value of 4.6Hz is calculated at the slope crest, near the topographic frequency of 4.5Hz. Parameter values calculated at the sensor locations are provided above both the cross-sectional contours. For all the plots, the lightened zones to the far left represent the area affected by the model container boundaries and should not be considered representative of the ground response for the slope.

Figure 3.7 is another example of contoured data using different methods of evaluating PGA for the same frequency sweep depicted in Figure 3.6. The PGA values, $PGA\ TF$, and $PGA\ AA$ are all provided in Figure 3.7. The three parameters exhibit similar trends, with an observed concentration of greater intensity that diminishes fairly quickly with distance behind the slope crest. However, different numerical values are associated with each of the three parameters. The raw PGA values provide scale for the ground motion considered, with a PGA of 0.20g and 0.57g found at the free field and crest locations, respectively. These values are representative of a moderate to high amplitude motion. The corresponding $PGA\ TF$ at the crest, which represents the maximum $PGA\ TF$, is approximately 1.9, equivalent to a 190% increase over the free field PGA. The $PGA\ AA$ indicates the level of amplification over the base input. For this motion, levels of amplification reached approximately 87% and 440% at the free field and crest, respectively. Thus, the contribution of amplification due to site effects is 87% and combined site and topographic effects at its maximum is 440%. Assuming the two effects can be decoupled, it can be inferred that, at the slope crest, 353% of the amplification for the PGA over the base motion resulted from the presence of topography. Thus, for the ground motion considered, the contribution of topographic amplification can be as much as 4 times greater than site amplification.

Other intensity measures, such as PGV and AI were also considered and can provide further insight into topographic effects. Figure 3.8 represents cross sectional contours of the TFs for PGA, PGV and AI for the same frequency sweep presented in Figures 3.6 and 3.7.

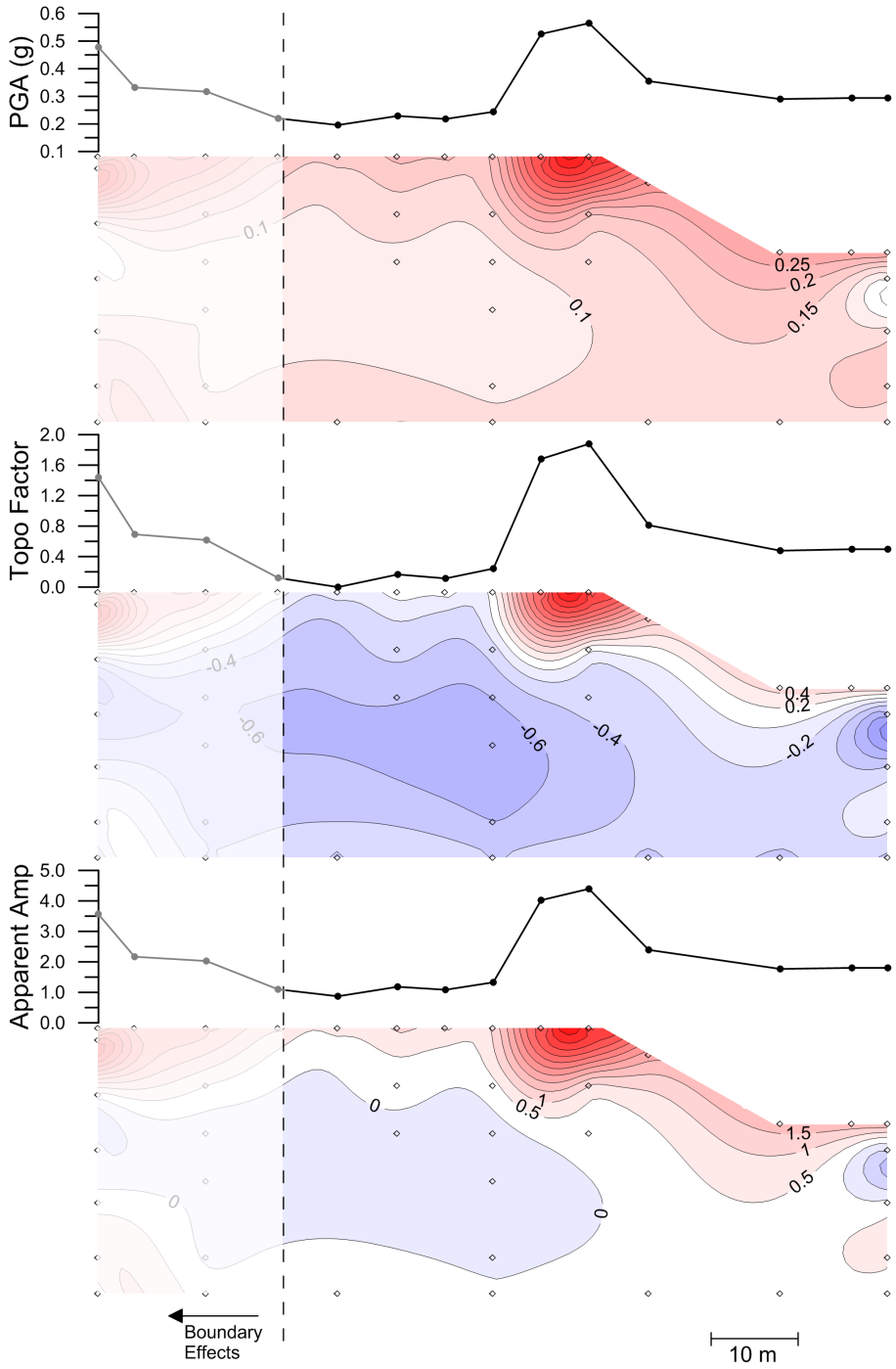

Figure 3.7: *PGA*, *PGA TF*, and *PGA AA* cross-sectional contours of a frequency sweep ranging from 0.5-7-0.5Hz for the 30 degree slope. Near surface values are given above the contours at instrument locations.

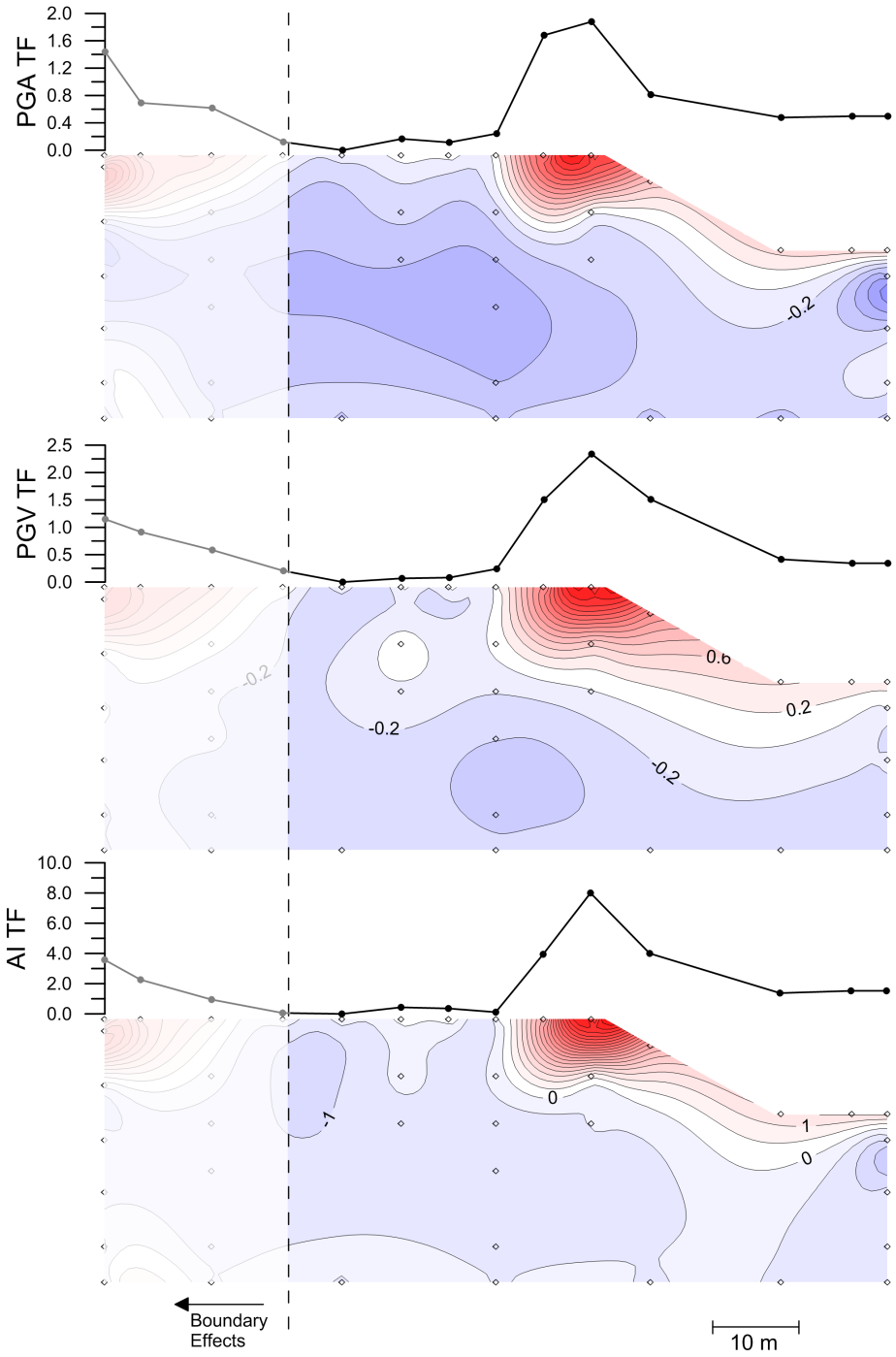

Figure 3.8: *PGA TF*, *PGV TF*, and *AI TF* cross-sectional contours of a frequency sweep ranging from 0.5-7-0.5Hz for the 30 degree slope. Near surface values are given above the contours at instrument locations.

For this motion, the patterns are fairly consistent with one another and the previous figures, in that concentrated amplification is captured near the slope crest. The TFs of 1.9, 2.3 and 8.0, for PGA, PGV and AI, respectively, are found at the slope crest, which coincides with the maximum overall response of the slope. The $AI\ TF$, which considers frequency content, amplitude, and duration of the entire ground motion, is notably greater than the $PGA\ TF$ and $PGV\ TF$, which consider one point within the ground motion. This difference in amplification then, is the result of amplification at multiple points throughout the time history. This is reflected in the high $bp\ SA\ TF$ value for this ground motion, which indicates a build-up of amplification, and thus amplification for multiple cycles of ground motion, at (and near) the topographic frequency. Although the numeric values of the TFs for the three intensity measures vary, the spatial variation and extent of topographic effects are consistent for the cross-sectional contours.

From the figures presented for a single ground motion and the given slope, a number of key observations can be made:

- An amplified response occurs at and around the slope crest compared to the free field response behind the crest. The magnitude of the amplification varies significantly depending upon the intensity measure considered, such that SAs near the topographic frequency and AI values can be significantly greater than PGA and PGV (Figures 3.6 and 3.8).

- The frequency content of the motion can be significantly altered by the presence of the slope such that the MSF of the ground motion shifts towards the topographic frequency at and around the slope crest (Figure 3.6).

- When decoupling the effects, topographic amplification is more substantial than site amplification at the slope crest (Figures 3.5 and 3.7). Additionally, the magnitude of amplification due to site effects (see amplification near the site frequency; Figure 3.5) is similar for both the crest and free field.

- The spatial extent of these effects can be significant, with topographic influence observed in areas both behind the slope crest and along the slope face (Figures 3.6, 3.7 and 3.8).
- Topographic effects are most significant within a limited frequency band concentrated near the topographic frequency, as defined by Ashford et al. (1997) (Figures 3.5 and 3.6).

3.3.2 Trends for Individual Slopes

The example presented above illustrates the wealth of information the can be acquired through analysis of a single ground motion. The featured ground motions accentuate the frequency dependent nature of topographic and site effects, allowing the responses in the free field and near the crest of slopes to be easily defined and separated. Comparisons of the observed behavior to that of other ground motions can be achieved by investigating all the ground motions introduced to a particular slope, thereby isolating individual nuances from observational trends. In this section analysis results for all motions introduced to each slope are presented, individually emphasizing the behavior of the 30, 25 and 20 degree slopes studied.

It should be noted that for each slope inclination, two prototype slopes were tested and analyzed as part of this study. Initially, each prototype was examined separately, however, the trends found were well aligned for a given slope inclination. In other words, once normalized, findings from the 27.5g prototype supported that of the 55g prototype, such that the results from the two prototypes could be combined (Dafni and Wartman, 2014). Therefore, results for each slope inclination presented in this section include two slope prototypes, but are presented singularly (i.e., referred to as the crest of the 30 degree slope, for example).

30 degree slopes

The parameters presented for the single ground motion evaluation are again utilized in the results presented here; namely, PGA, SA, *bp* SA and MSF. Figure 3.9 demonstrates the range of recorded input values and provides the correlated near surface free field and crest response for the PGA and *bp* SA of both 30 degree slope prototypes.

The data points are divided according to the type of ground motion they represent. The response at the crest is given by the color filled symbols, while the free field is represented by open symbols; both are plotted against the same input value. Sweep 1 refers to the frequency sweep previously described, ranging from 0.13-6.05Hz and 0.26-12.1Hz for the 55g

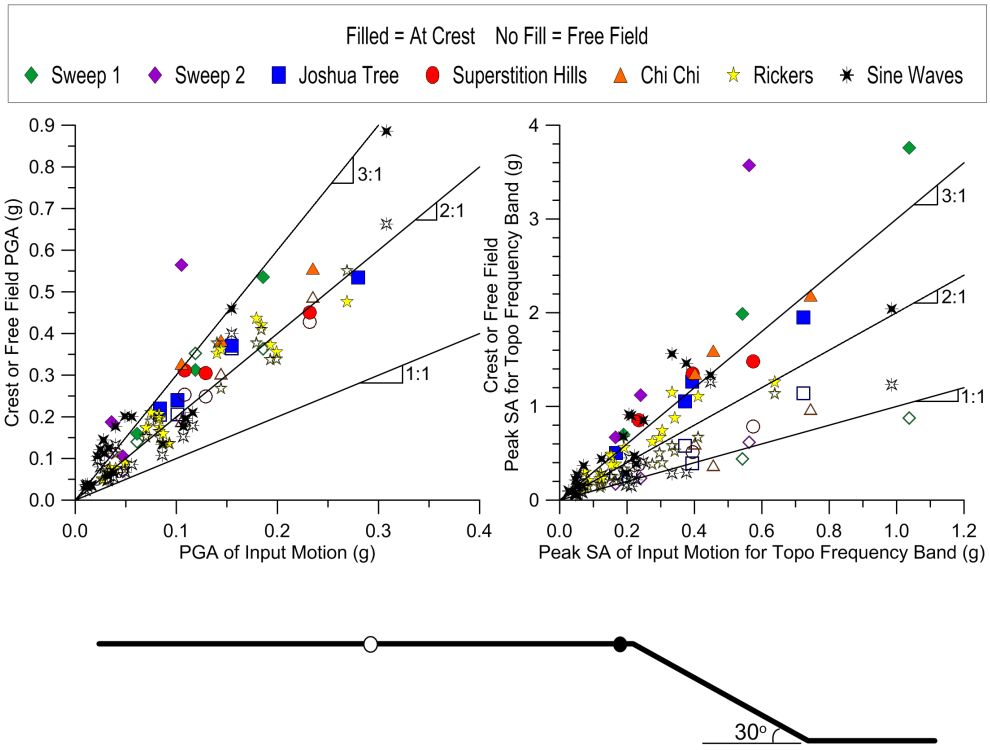

Figure 3.9: Free field and crest response versus input using PGA and $bp\ SA$ (using the frequency band inclusive of the topographic frequency) for both 30 degree slope prototypes (27.5 and 55g). The free field sensor (A20) is about 29 (14.5) meters from the crest sensor (A35), which is about 1.5 (0.75) meters behind the slope crest at 55g (at 27.5g).

and 27.5g prototypes respectively, while sweep 2 corresponds to frequency ranges of 0.5-7.0-0.5Hz at 55g and 1.0-14.0-1.0Hz at 27.5g. The sine waves and Ricker wavelets presented are those for which the time histories have been divided according to their central frequencies (described previously), as should be assumed for all remaining plots unless otherwise noted. No distinction is made between these motions according to the different central frequencies.

Inspection of the left plot in Figure 3.9 reveals that typical expected behavior is captured in the free field for the motions introduced. In particular, the recorded PGA values for the near surface free field are generally between 1 to 2 times greater than the input PGA values recorded at the stiff model base. For a 1-D undamped case, theory dictates that

the expected free field surface PGA should be twice that of the incident ground motion, but may lower in the presence of damping (Kramer, 1996). Of course, this doesn't account for changes in material stiffness that can also alter the surface response. Nevertheless, the recorded free field values are close to the theoretical values. The recorded PGA values at the crest location, however, vary considerably ranging from 2 to 5 times greater than the input PGA and are typically greater than the PGA values in the free field.

PGA can be influenced by high frequency components of the ground motion, and also doesn't carry information about the frequency content of the motion. The *bp* SA, however, provides insight into the ground response within the frequency band of interest. From Figure 3.9 it can be seen that peak SA values within the topographic frequency band, in the free field, range from less than 1 up to about 1.5 times that of the input values, indicating that little to no amplification typically occurred. However, at the crest, values range from 2 to almost 7 times greater than the input. Here, even though the variation in the crest response is similar, the trend is stronger than that found using PGA, with clear separation established between the free field and crest responses.

The left plot in Figure 3.10 breaks down the data in a manner similar to that described for Figure 3.9. However, in this case, the plot shows the MSF of the free field and crest versus the corresponding MSF of the input motion, normalized by the topographic frequency or site frequency. The purple diamonds, for both the free field and slope crest (farthest to the right in this plot), represent the frequency sweep featured in Figures 3.6, 3.7, and 3.8. It was observed in Figure 3.6 that the MSF shifted towards the topographic frequency at the slope crest, as is illustrated here in Figure 3.10. Further study of Figure 3.10 shows that this observation can be considered a trend for all the ground motions introduced to the 30 degree slopes. In the free field, the MSF is typically similar to the MSF of the input ground motion, with a handful that shifted to either higher or lower values. However, regardless of whether the free field MSF is greater than or less than the topographic frequency, the MSF nearly always shifts towards the topographic frequency of the slope. This shift can represent a significant difference in the ground motion frequency content between the free

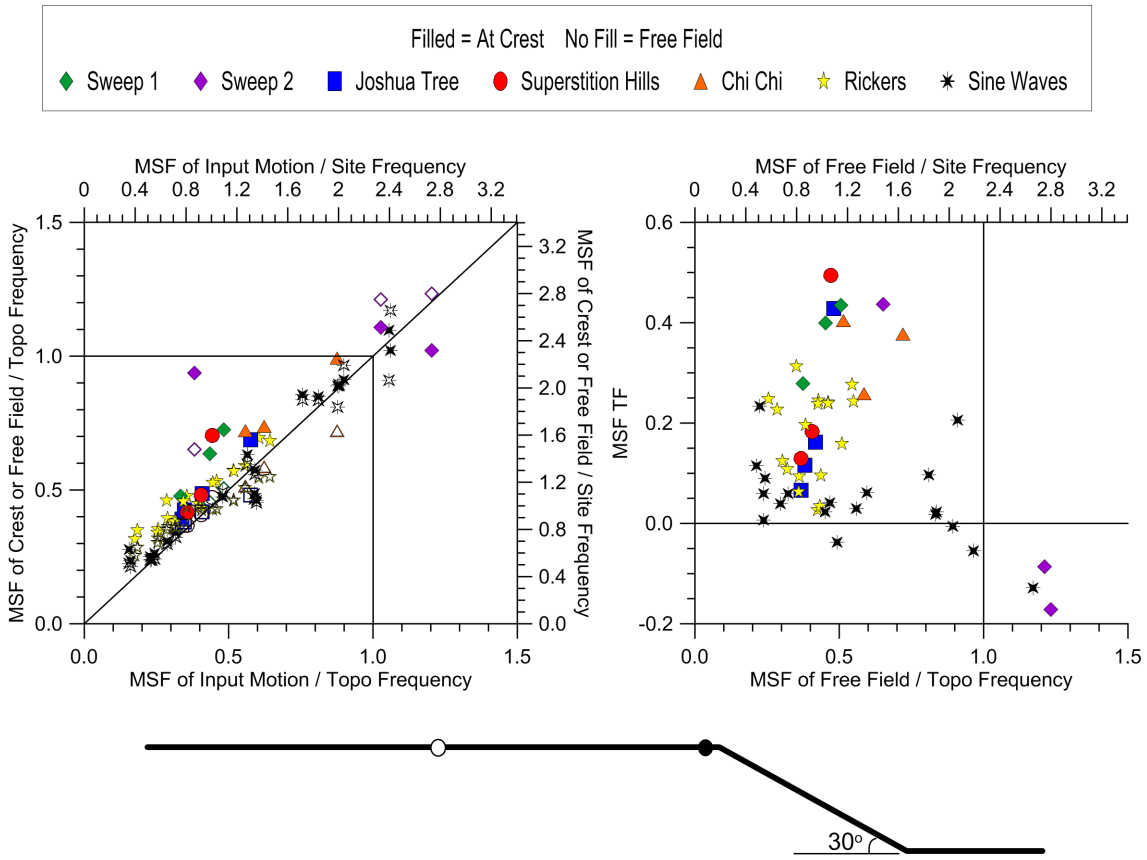

Figure 3.10: Free field and crest versus input MSF normalized by the topographic and site frequencies for both 30 degree slope prototypes. The free field sensor (A20) is about 29 (14.5) meters from the crest sensor (A35), which is about 1.5 (0.75) meters behind the slope crest at 55g (at 27.5g).

field and crest locations, a feature which is highlighted in the right plot of Figure 3.10.

The right plot in Figure 3.10 displays the $MSF\ TF$ at the slope crest versus the MSF of the free field ground motion normalized by both the topographic and site frequencies. The $MSF\ TF$ is calculated by substituting PGA with MSF in Equation (3.1), and as before, represents a percent change from the calculated free field value if the numeric value were converted to a percentage. From this plot a few key observations can be made. First, the shift towards the topographic frequency at the crest is confirmed (i.e., positive and negative $MSF\ TF$ values are calculated when the free field MSF is below and above the topographic frequency, respectively). Second, the shift in frequency content is typically greater (i.e., larger

$MSF\ TF$ values) when the difference between the MSF in the free field and the topographic frequency is greater. This appears to be true until the MSF in the free field is less than the site frequency, at which point the magnitude of the shift appears to decrease. And lastly, a significant change in ground motion frequency content can occur even if the MSF in the free field is not near the topographic frequency of the slope.

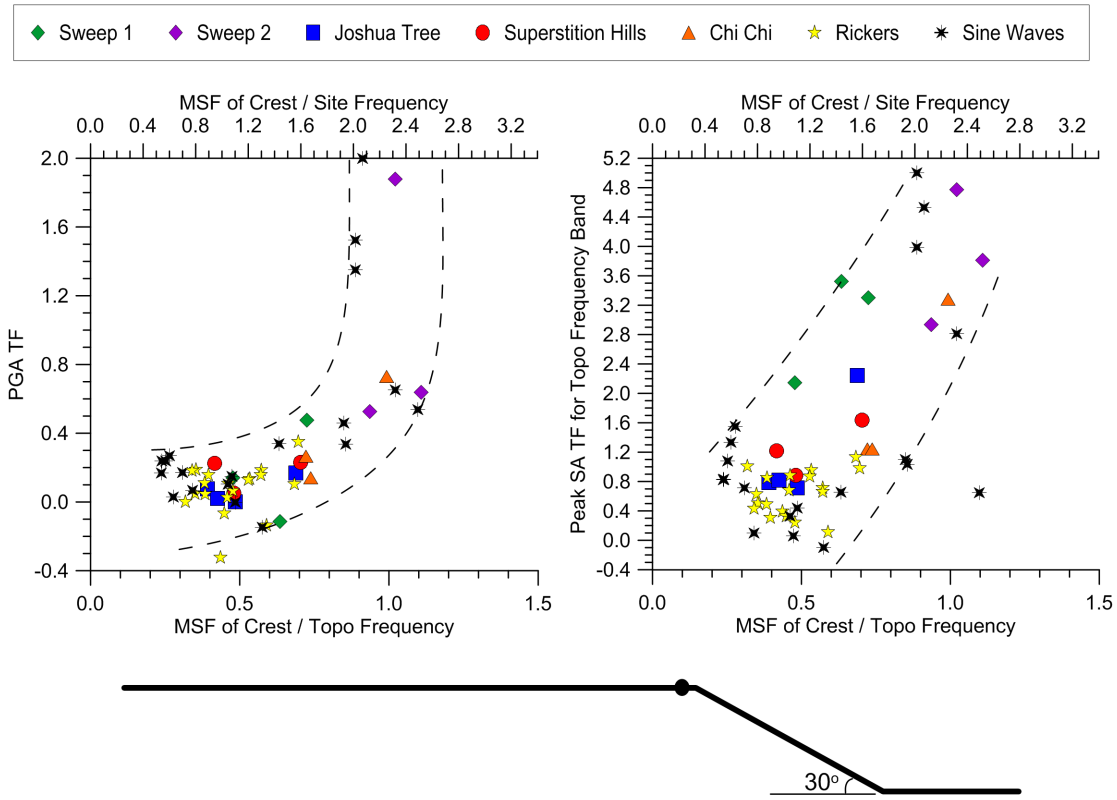

Figure 3.11: $PGA\ TF$ and $bp\ SA\ TF$ for the topographic frequency band versus MSF normalized by the topographic and site frequencies at the crest for both 30 degree slope prototypes.

Figures 3.9 and 3.10 illustrated the differences in ground motion amplitude and frequency content in the free field and at the slope crest, but how do these parameters relate to each other? Figure 3.11 provides plots of both the $PGA\ TF$ and $bp\ SA\ TF$ versus the MSF normalized by the topographic and site frequencies. The TFs are given for the crest location, where the maximum response is expected for the suite of ground motions considered.

Recalling that a positive TF indicates an amplified response over the free field, both these plots indicate a strong correlation between the MSF at the crest and the magnitude of amplification experienced. Namely, the amplification is greater (higher TF values) for ground motion with a MSF closer to the topographic frequency of the slope (a normalized value of 1 on the bottom x-axis), and less when the MSF is farther from the topographic frequency. In other words, at the slope crest a greater response can be expected when the energy balance point of the ground motion frequency content strongly coincides with the slope topographic frequency. This trend holds for both slope prototypes.

Figure 3.12 is an alternative way to observe the connection between the frequency content and amplitude of ground motion at the slope crest. While Figure 3.11 provides singular intensity measures versus MSF values for all the motions individually, Figure 3.12 provides the geometric mean of both the $SA\,TF$ and *spectral acceleration apparent amplification* (SA AA) for those motions across a spectrum of frequency values (normalized by the topographic frequency; actual frequency values for both prototypes are given on the top axis). Additionally, the influence of the MSF of the ground motion on the calculated $SA\,TF$ and $SA\,AA$ values is captured by grouping the different ground motions according to the proximity of the MSF to the topographic frequency of the slope (i.e., the geometric mean is given for all motions, motions that have a MSF within 30% of the topographic frequency, and those outside of that range).

In grouping the motions, MSF is used as a gauge for comparing the amount of amplification found at the slope crest. Specifically, the proximity of the motion MSF to the topographic frequency is considered. Due to natural variation in the ground response and in the motions utilized in this study, when grouping the motions it is logical to apply a range of MSF values centered around the topographic frequency. Although the most amplified motions have MSF within 20% of the topographic frequency, the cutoff of 30% (i.e., the normalized value of MSF/f_t ranges from $0.7 - 1.3$) was chosen to *a*) be inclusive of more motions in calculating the mean, thus reducing potential bias, and *b*) diversify the group of motions considered by including more earthquake motions (the 20% grouping is mainly

composed of sine waves and frequency sweeps; both idealized motions). It should be noted that for the 20 degree slopes, four of the motions included in this group actually fell outside of the 30% range. However, for consistency in comparing the results of the three slope inclinations, these motions were included in calculating the mean values depicted in subsection 3.3.2, where results for the 20 degree slopes are presented.

If the ratio of MSF to the topographic frequency is simply called the *topographic ratio* (TR), then a TR in the range of $0.7 - 1.3$ can be considered a *strong topographic ratio* (STR), and a ratio outside of that range can be deemed a *weak topographic ratio* (WTR). Using these descriptors, motions with a MSF within 30% of the topographic frequency can be described as STR motions and those with a MSF not within 30% of the topographic frequency can be referred to as WTR motions. For convenience, these abbreviations will be used for the remainder of this chapter.

Inspection of the top plot in Figure 3.12 reveals the concentrated frequency bandwidth for which the response at the crest is amplified most significantly over the free field. For the mean spectra presented, a peak response is found to encompass the topographic frequency, despite differences in raw frequency content of the motions for the two prototype slopes considered. The average peak response ranges from a TF of approximately 0.55 to 1.9 for WTR and STR motions, respectively. This significant difference further confirms the correlation between the motion frequency content and the level of measured amplification. Furthermore, considering the response at frequencies outside of the most amplified frequency band (from normalized frequencies of roughly 0.7–1.3), typically little to no amplification is found for WTR motions, STR motions have TFs as high as 0.9. The mean spectrum for all motions introduced to the 30 degree slopes is also included, but more closely reflects the response of the WTR motions. Of the 54 total motions, only 15 are STR motions, meaning the 39 WTR motions dominate the mean response when considering all motions. This is illustrated in Figure 3.12. For all cases, although the STR motions have a slightly more amplified response, generally little to no amplification is found around the site frequency (at a normalized frequency of approximately 0.44). Thus, on average site effects are expected

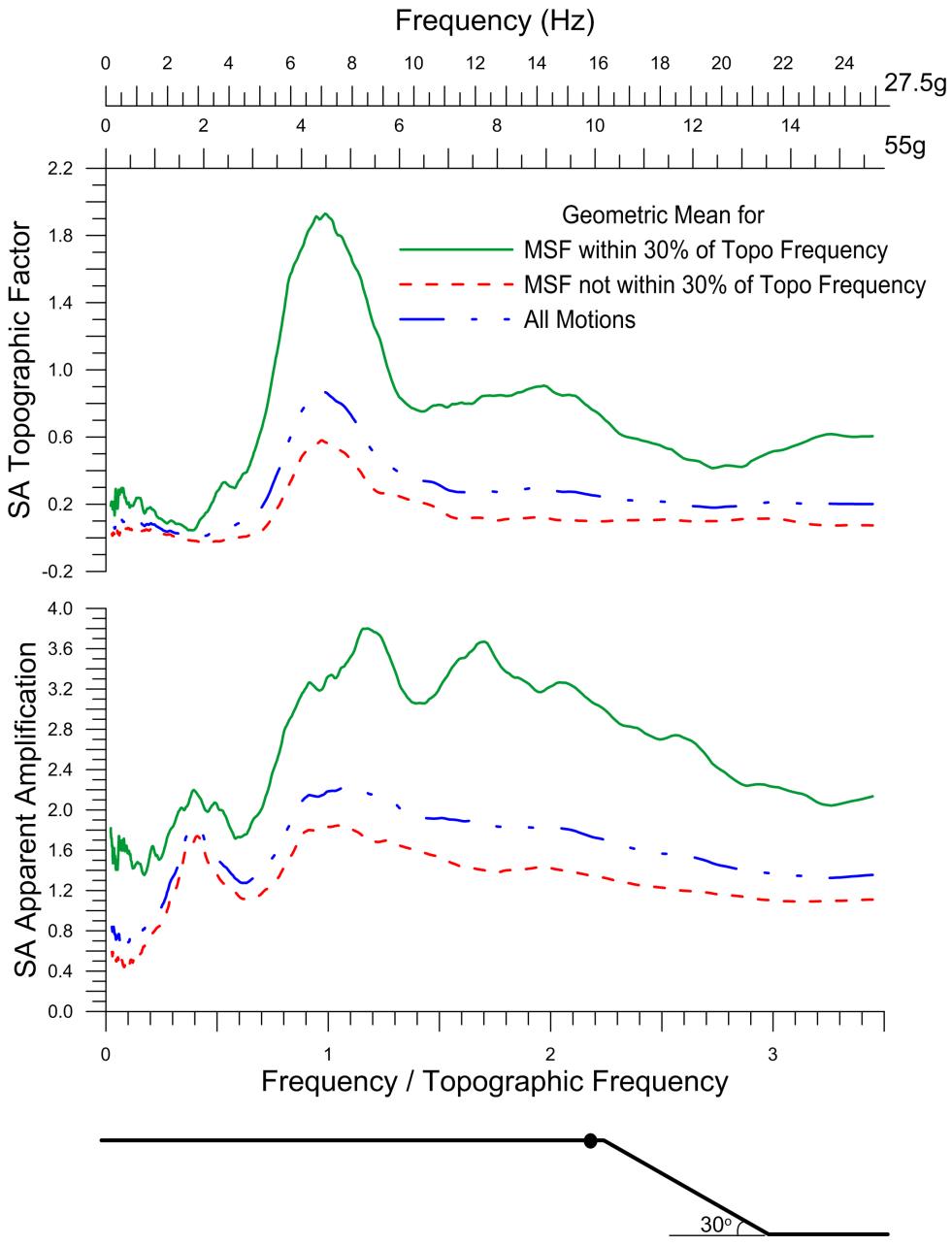

Figure 3.12: Geometric mean for the $SA\ TF$ and $SA\ AA$ spectra at the slope crest for both 30 degree slope prototypes grouped according to the MSF of the ground motion.

to be similar at the free field and crest locations, with a possible exception of some STR motions.

Through the $SA\ AA$, the bottom plot in Figure 3.12 compares the crest response to the input base motion. Again, the overall response is greater for the STR motions. The peak response is also found to be near the topographic frequency with an AA of 3.8 and 1.7 for STR and WTR motions, respectively. However, a concentrated bandwidth for amplification is not as well defined, and indeed more high frequency components beyond the topographic frequency are also significantly amplified. This result is a reflection of the inclusion of both site and topographic effects for the $SA\ AA$ spectrum. A secondary peak exists encompassing the site frequency, with peak values of 2.2 for STR motions and 1.8 for WTR motions. It is interesting to note that site effects are slightly greater for the STR motions. Although as shown STR motions are generally more amplified across all frequencies. A more important consideration, however, is the fact that on average, topographic effects can be significantly greater than site effects given the proper circumstances. That is, the STR motions are on average more amplified near the topographic frequency than they are at the site frequency. This is not the case for the WTR motions, which have roughly the same level of amplification at both frequencies. This significant finding will be touched upon more throughout this section and discussed more thoroughly in Section 3.4.

It should be noted here that the geometric mean was chosen to represent the data set instead of the typical arithmetic mean. The geometric mean is better suited in comparing observations over different ranges (i.e., the ground motions of varying intensity considered here) and working with percentages, applicable to both the TF and AA. Additionally, data outliers have less influence on the geometric mean than the arithmetic mean. However, for this data set the difference between the two means was found to be minimal.

Thus far, the figures presented in this subsection have focused on the response at the crest of the 30 degree slopes, with comparisons made to the free field and base through the use of the TF and AA, respectively. While the crest location typically exhibits the most extreme topographic effects, it is also important to know the relevant spatial extent of these

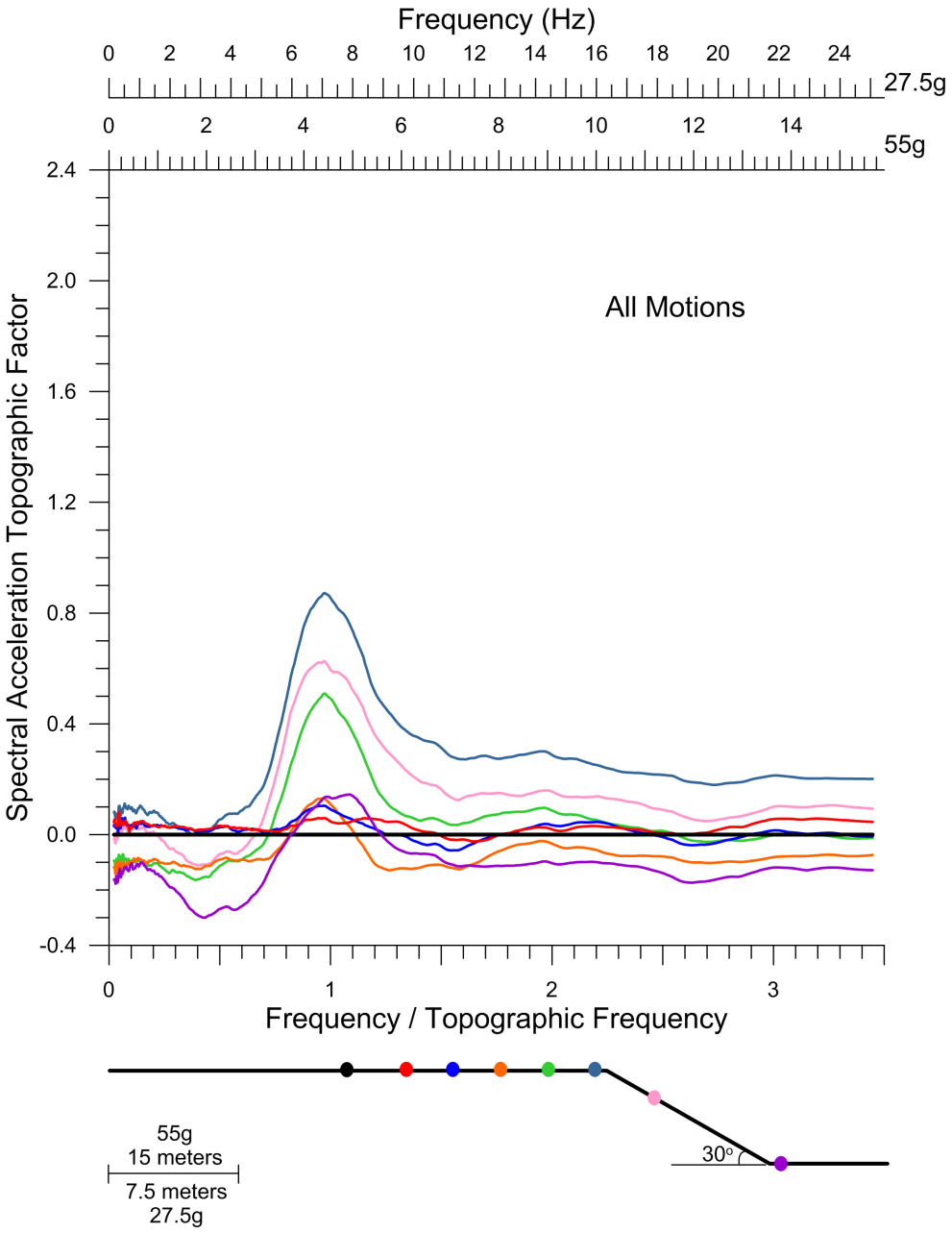

Figure 3.13: Geometric mean of the SA TF spectrum versus normalized frequency for all motions at different near surface sensor locations on the 30 degree slope. Spectra are color-coded to match sensor locations, which are provided at scale. The free field sensor is represented in black. Both prototypes are considered in calculating mean values.

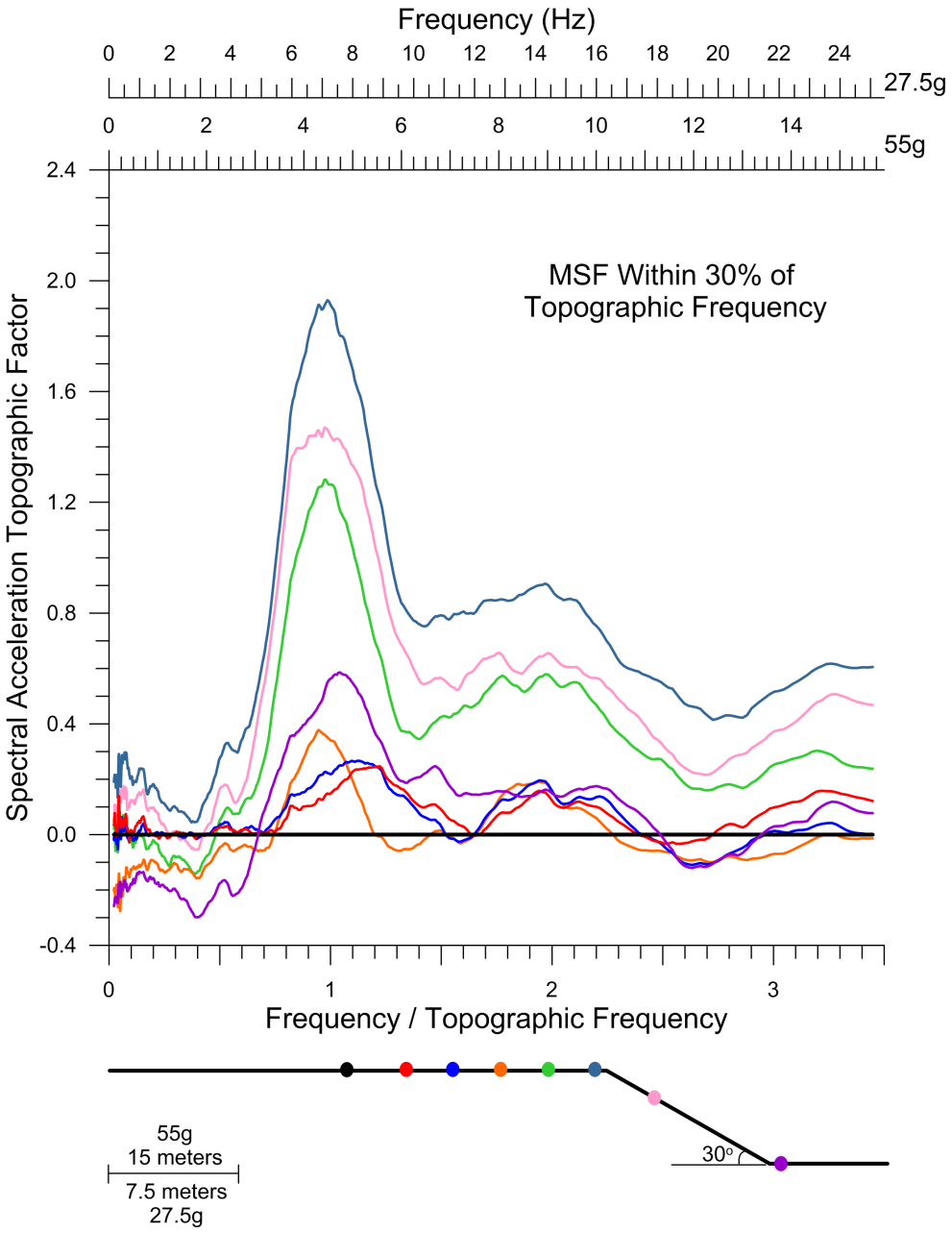

Figure 3.14: Geometric mean of the $SA\ TF$ spectrum versus normalized frequency for STR motions at different near surface sensor locations on the 30 degree slope. Spectra are color-coded to match sensor locations, which are provided at scale. The free field sensor is represented in black. Both prototypes are considered in calculating mean values.

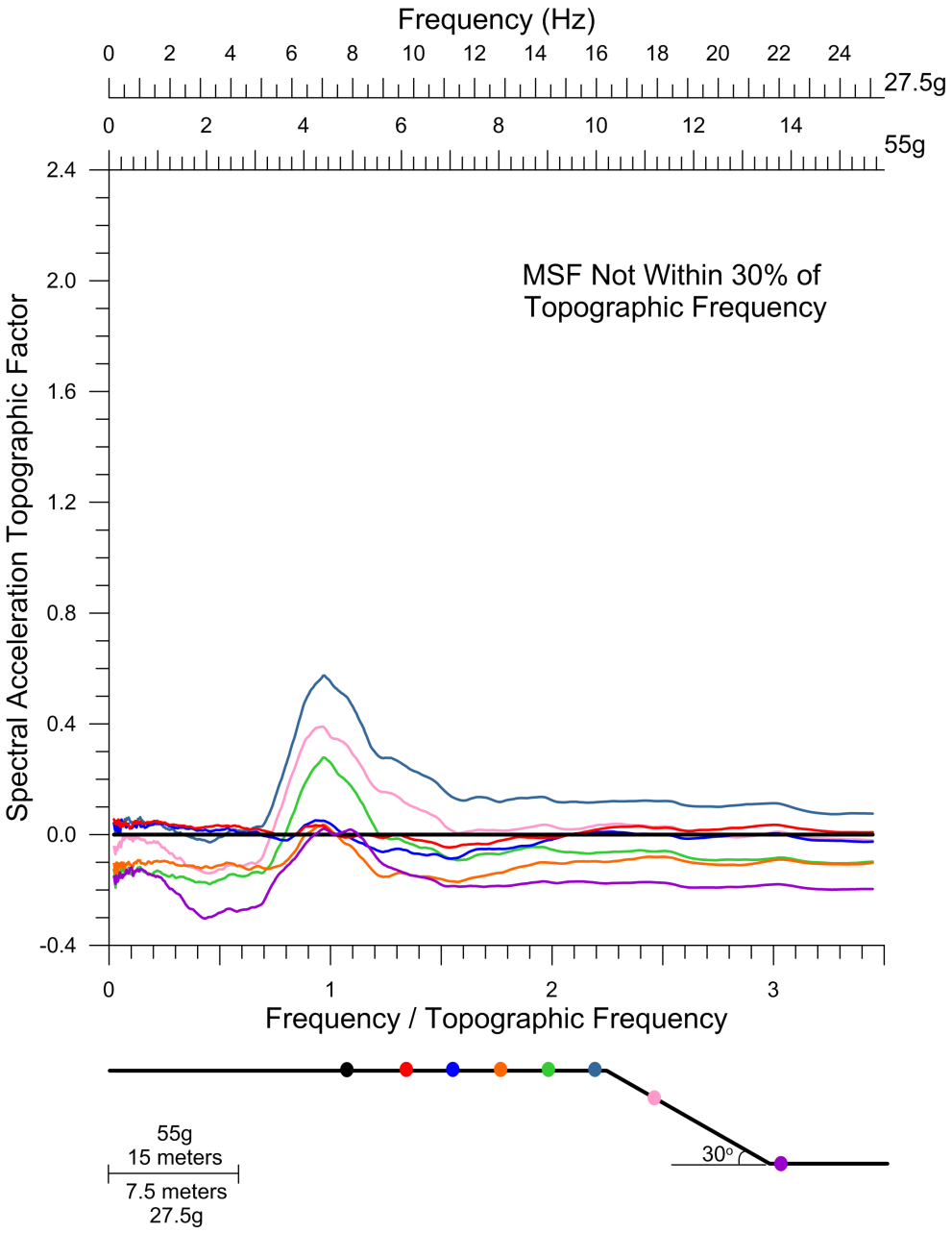

Figure 3.15: Geometric mean of the $SA\ TF$ spectrum versus normalized frequency for WTR motions at different near surface sensor locations on the 30 degree slope. Spectra are color-coded to match sensor locations, which are provided at scale. The free field sensor is represented in black. Both prototypes are considered in calculating mean values.

effects. Utilizing the same factors formerly presented, the next set of figures focus on the spatial distribution and variation in ground response over the surface of the 30 degree slopes.

Figures 3.13, 3.14 and 3.15 all present data in the same manner, but differ in their content. The ground motions are once again grouped according to MSF, with Figure 3.13 representing all motions, Figure 3.14 representing the STR motions and Figure 3.15 the WTR motions for both 30 degree slope prototypes. All three figures depict the geometric mean (for the stated group of motions) of the $SA\ TF$ versus normalized frequency for the near surface accelerometer locations presented. The spectrum and sensor plotted in black represent the free field location. The free field spectrum consists of a straight line with $SA\ TF = 0$ for all three figures, resulting from the calculation of the TF through normalization by the free field.

It is worth noting that the overall spatial variation across the slope does not significantly differ amongst the three figures, despite the grouping of the motions according to MSF. This indicates that the spatial pattern depicted is representative of typical behavior for the given slope conditions. In all cases, the average peak response occurs at the crest sensor location and diminishes with distance away from the slope crest in either direction (either behind the slope or down the face of the slope). Additionally, at each sensor location, the peak $SA\ TF$ value corresponds to a frequency band that encompasses the topographic frequency, even at the slope toe. The peak values tend to align with each other, with the exception of the slope toe, which is slightly shifted towards higher frequencies.

One factor that varies between the three figures is amplitude. As expected from study of the previously presented figures, at the crest, the STR motions exhibit greater levels of amplification over the free field response than WTR motions, and thus have higher TFs. With greater amplification at the crest comes greater amplification at other sensor locations, which consequently, results in an amplified response over a larger area of the slope. For the STR motions depicted in Figure 3.14, amplification occurs at all locations to the right of the free field sensor (including the slope toe), with a significant decrease in the amplification level beyond the sensors adjacent to the crest sensor. The affected area corresponds to a distance

of approximately 19 meters from slope crest to toe and 30.5 meters from the crest to the free field sensor for the 55g slope prototype, with half those distances (9.5 and 15.25 meters) for the 27.5g prototype. The WTR motions depicted in Figure 3.15, on the other hand, show negligible amplification beyond the sensors immediately adjacent to the crest sensor, with notable deamplification at the slope toe. For the 55g prototype, the sensors adjacent to the crest are approximately 5.5 meters towards the slope toe and 7.0 meters towards the free field sensor from the slope crest (and again half the distance for the 27.5g prototype).

Another important detail to note is the potential correlation between the size of the slope and the area influenced by topographic effects. As mentioned, two prototype slopes were used, but when plotted together the spatial variation at the sensor locations is found to be similar, even though the spacing of the 27.5g prototype sensors doubles in distance at 55g. Therefore, the spatial influence of topographic effects is not only a function of the level of amplification induced, but also appears to be a function of the size of the slope.

Figures 3.16, 3.17 and 3.18 are similar to the previous three figures, with the $SA\ AA$ spectrum plotted instead of the $SA\ TF$ spectrum. Although, a number of features highlighted in the previous three figures are also applicable here, (i.e., greater amplification for STR motions, breadth of spatial influence, etc.) new insight can be gained from these figures. Here, the normalized free field behavior can be relatively compared to other sensors across the slope, allowing amplifications near both the site frequency and topographic frequency to be spatially observed.

In the free field, maximum $SA\ AA$ values are expected to occur at the site frequency. For the case of a flat ground, the response at each of the sensor locations should be nearly identical (natural fluctuations aside). However, despite the presence of flat ground between the slope crest and free field, notable differences exist between the sensor spectra at the site frequency. The response at the crest is similar to (WTR motions) or slightly greater than (STR motions) the free field response. The next two sensors behind the crest, however, capture an on average weaker response. The final two sensors adjacent to the free field sensor match the free field response well. Therefore, there is a dip in the site response for the

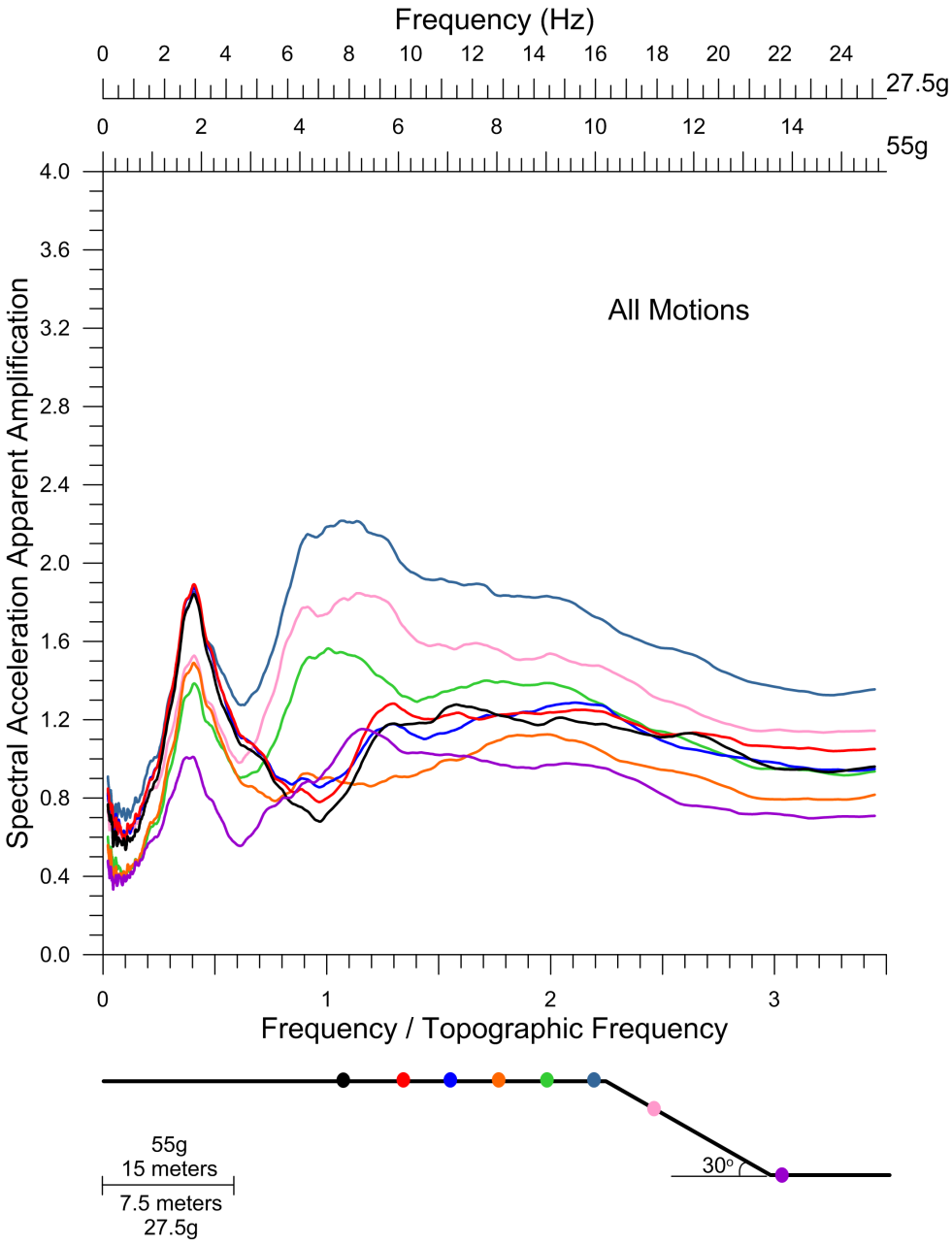

Figure 3.16: Geometric mean of the SA AA spectrum versus normalized frequency for all motions at different near surface sensor locations on the 30 degree slope. Spectra are color-coded to match sensor locations, which are provided at scale. The free field sensor is represented in black. Both prototypes are considered in calculating mean values.

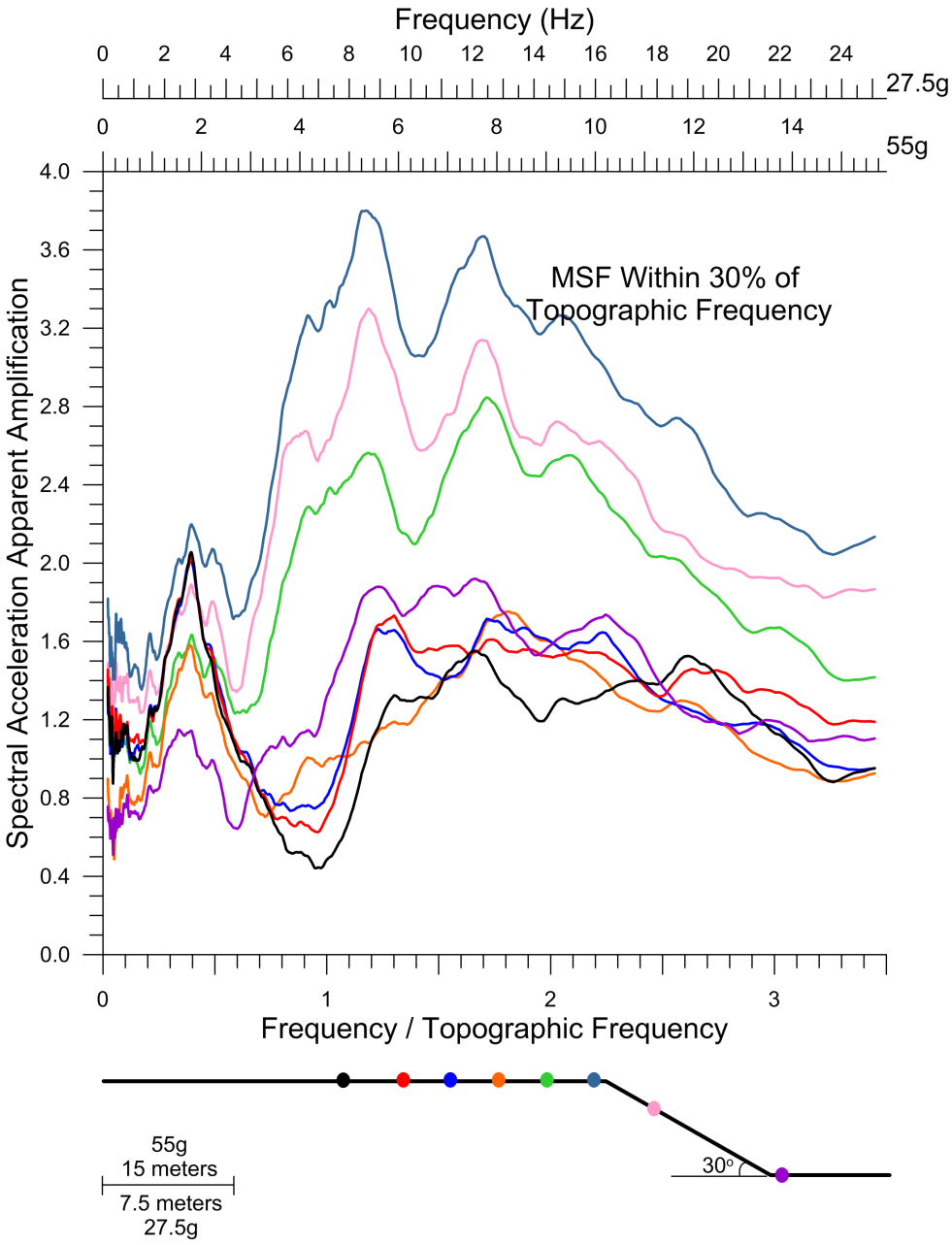

Figure 3.17: Geometric mean of the SA AA spectrum versus normalized frequency for STR motions at different near surface sensor locations on the 30 degree slope. Spectra are color-coded to match sensor locations, which are provided at scale. The free field sensor is represented in black. Both prototypes are considered in calculating mean values.

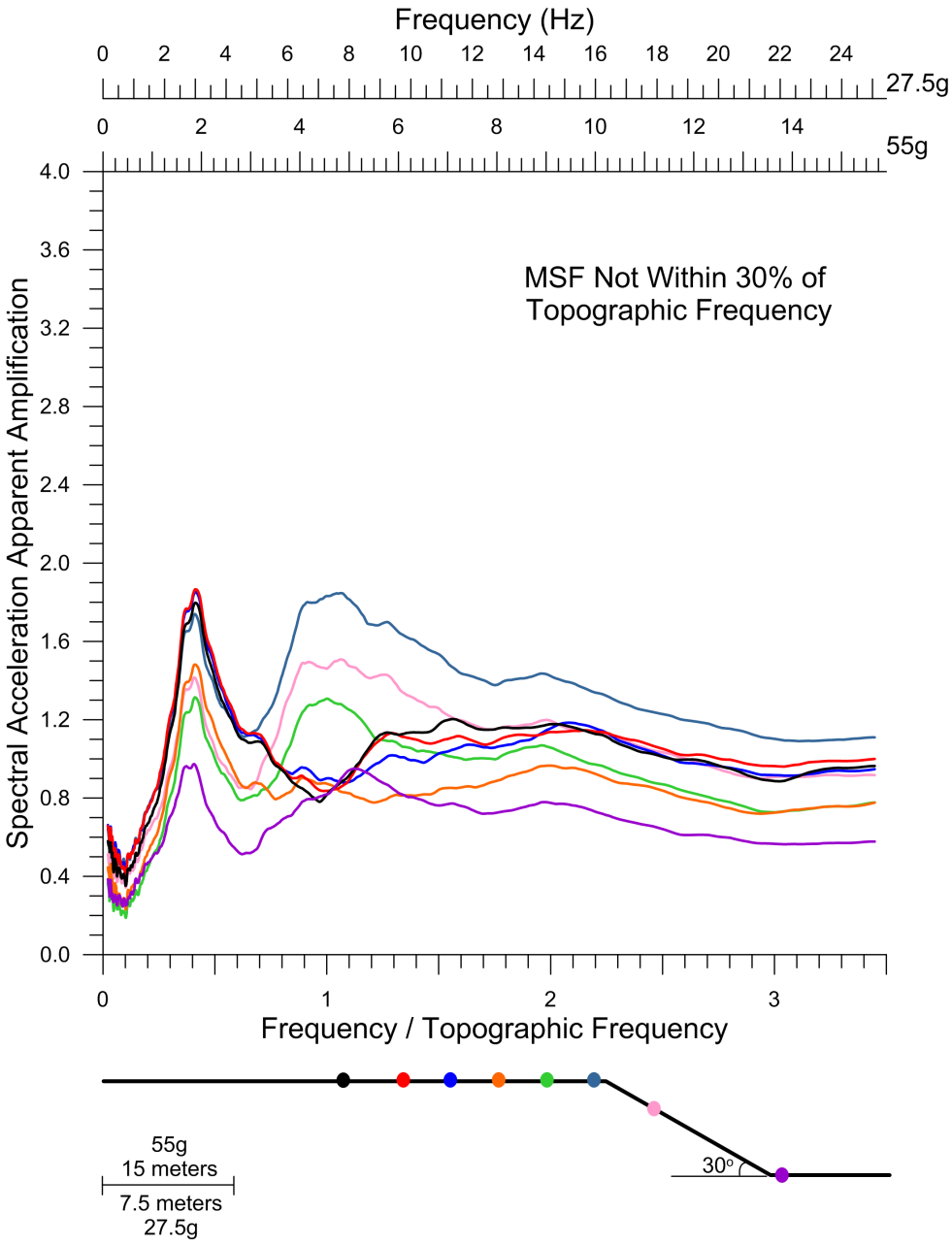

Figure 3.18: Geometric mean of the SA AA spectrum versus normalized frequency for WTR motions at different near surface sensor locations on the 30 degree slope. Spectra are color-coded to match sensor locations, which are provided at scale. The free field sensor is represented in black. Both prototypes are considered in calculating mean values.

sensors between the crest and free field sensors. Additionally, at the slope toe, the response is significantly weaker than other sensor locations. It should also be noted that the site frequency is shifted slightly due to a change in the height of the soil profile and subsequent change in the average shear wave velocity of the material below the toe.

At the topographic frequency, it is again evident that the influence of topography can be greater than site effects, most notably for the STR motions. Previously, either individual raw spectra (Figure 3.5) or the average crest response only (Figure 3.12) have been presented. Here the mean AA for both the free field and crest locations can be compared. From this, it can be inferred that, on average, little amplification over the base motion occurs at the topographic frequency in the free field (attributable to site effects), while at the crest it can be extreme. Thus, even though the combined site and topographic effects are considered in calculating AA, it is clear here that, given certain motions (i.e., STR motions), the influence of site effects at the topographic frequency contributes much less than the effects of topography to the overall amplification of the motion. Discounting the contribution of site effects at the topographic frequency and considering only the amplification resulting from topographic effects, for the STR motions, it can be established that the overall amplification due to topographic effects (near the topographic frequency) is on average greater than overall amplification due to site effects (using the peak response at the site frequency). This is not true for WTR motions where the contribution from site effects is comparable to the contribution of topographic effects at the topographic frequency.

Figure 3.19 provides another, perhaps more succinct, approach to studying the spatial extent of topographic effects, while still considering the frequency content of the ground motions. The geometric mean of the $PGA\ TF$ and $bp\ SA\ TF$ are plotted to scale across the slope with markers defining sensor locations. Again, the motions are grouped according to MSF, with all motions, STR motions and WTR motions depicted. For both intensity measures, TFs are significantly higher for the STR motions. The response peaks at the crest and diminishes with distance away from the crest in either direction. However, although the spatial pattern is similar for both intensity measures, there are notable differences in the

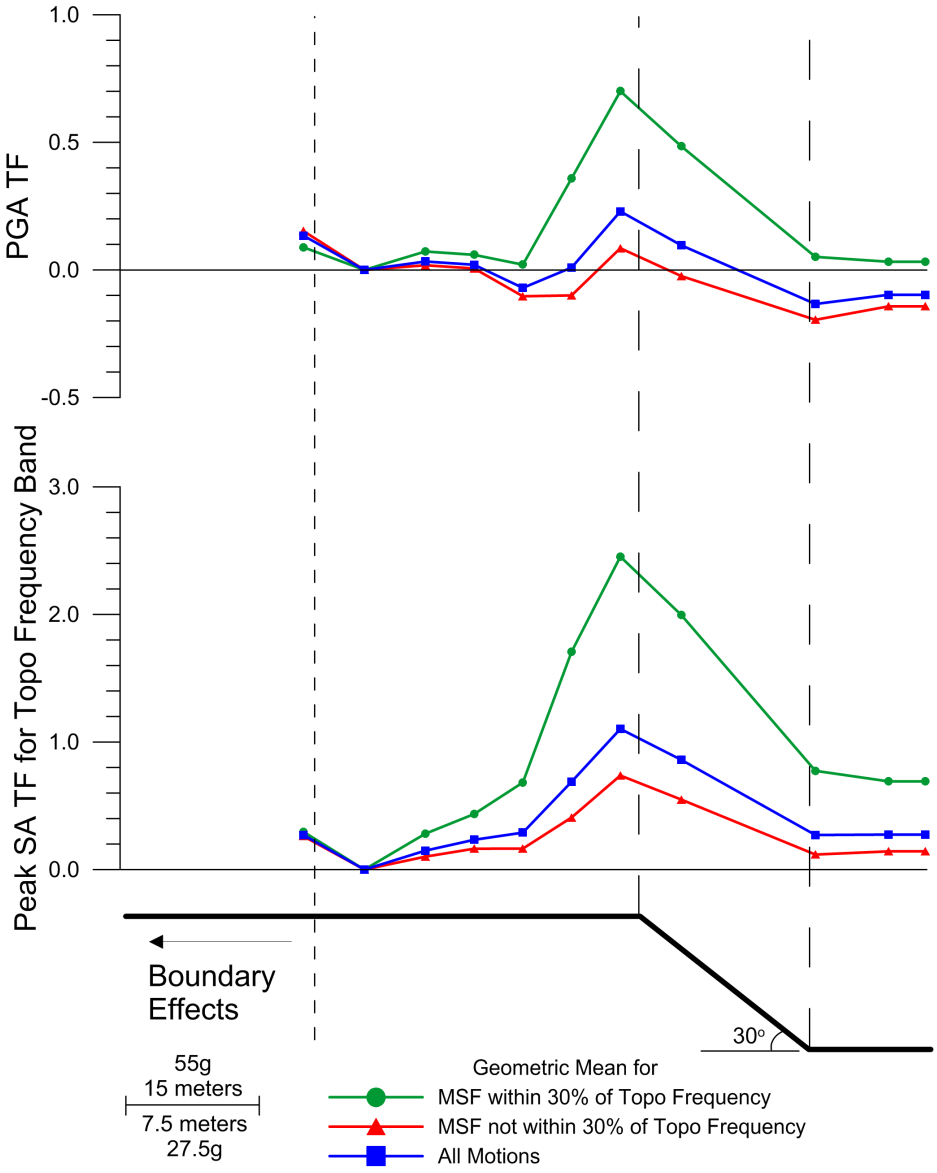

Figure 3.19: Geometric mean of $PGA\ TF$ and $bp\ SA\ TF$ for the topographic frequency band versus distance across the surface of the 30 degree slope for both prototypes, grouped according to the MSF of the ground motion.

amplitudes of the TFs.

The *bp* $SA\ TF$ plot follows a similar spatial pattern to the peak responses depicted in Figures 3.13, 3.14 and 3.15, as expected. However, the numeric values differ. For example, the *bp* $SA\ TF$ value for the STR motions at the crest is approximately 2.4, while the peak $SA\ TF$ spectrum value at the crest location is roughly 1.9. The reason for this difference is due to the manner in which the two are calculated. Looking at individual spectra, the peak value may shift to slightly higher or slightly lower frequencies in considering each motion. Averaging the spectra led to a defined peak that does not necessarily correspond to all the individual peaks considered. Therefore, a peak scalar value for one motion that would have been included in calculating the mean *bp* $SA\ TF$, may be offset by a non-peak value from another motion, which influences the calculation of the mean $SA\ TF$ spectrum. The peak in the mean $SA\ TF$ spectrum occurs where the combined contributions of the motions is greatest, while the *bp* $SA\ TF$ considers every peak of every motion before taking the mean.

In both plots, the STR motions sustain greater levels of amplification over a larger area of the slope. Peak values diminish from roughly 0.7 to the 0.35 to 0.5 range for the $PGA\ TF$ and from 2.4 to the 1.7 to 2.0 range for the *bp* $SA\ TF$ moving from the crest to adjacent sensors. At sensors located beyond that, the $PGA\ TF$ reaches negligible values. However, *bp* $SA\ TF$ values are still as high as roughly 0.7, beyond which the amplitude diminishes moving towards the free field and remains fairly constant moving towards the container boundary past the slope toe (possibly due to boundary effects). From this, it can be inferred that the area of the slope affected is greater for a frequency specific intensity measure (that includes the topographic frequency) than one which does not consider the motion frequency content. This is further supported by the WTR motions, which on average have a positive $PGA\ TF$ at the crest location only and suggest deamplification at the slope toe. For the mean *bp* $SA\ TF$ values, on the other hand, the amplified response remains significant for an area spanning from two sensors behind the crest sensor (12.5 (6.25) meters behind the crest at 55g (27.5g)) to the slope toe (although this amplified response at the toe may be influenced by the container boundary). Therefore, in determining the effects of topography,

it is important to consider the intensity measure chosen to represent the effects.

Figure 3.20 provides a final interpretation of the topographic spatial influence for the 30 degree slope. To create this figure, plots similar to those presented in Figure 3.19 were used with mean $PGA\ TF$ and *bp* $SA\ TF$ values replaced by values from each individual ground motion. For each ground motion, lengths L_1 and L_2 were measured in order to determine the *topographic zone of influence*, or the area of the slope in which ground motion is affected by the presence of topography. Both L_1 and L_2 are determined by measuring the distance from the crest to the point where either the $PGA\ TF$ or *bp* $SA\ TF$ reach a value of zero (at which point free field conditions have been reached), with L_1 measured behind the crest towards the free field, and L_2 measured towards the toe of the slope. These values were then normalized by the length of the slope, L, allowing the two slope prototypes to be considered in the same plot. It should be noted that L_2 was capped at the length of the slope, corresponding to a normalized value of 1. This cutoff for L_2 was chosen because beyond the toe (and possibly at the toe location) is likely influenced by container boundary effects, and thus may not represent naturally occurring behavior. A natural threshold for L_1 can be defined by the distance from the crest to the free field sensor, a normalized value of 1.6.

Inspection of the plots in Figure 3.20 reveals a trend that higher levels of amplification lead to a larger topographic zone of influence. That is, as the TFs increase, the measured normalized distances, L_1/L and L_2/L, also increase. For the *bp* $SA\ TF$, the L_2 threshold is consistently reached, meaning that in the topographic frequency range, SAs are almost always amplified over the entire face of the slope. The threshold is reached for all motions with a *bp* $SA\ TF$ greater than roughly 0.8. Behind the slope crest, however, the *bp* $SA\ TF$ values reach as high as 2.3 before L_1 values are equivalent to the distance from the slope crest to the free field. For the $PGA\ TF$, the L_2 threshold is also reached consistently once values are greater than 0.8. The L_1 threshold is consistently attained for $PGA\ TF$ values somewhere between 0.8 and 1.2 (a gap in the data exists here). This data represents ground motions introduced to both slope prototypes, and yet the numeric values and overall trends are consistent with one another, indicating once again that the topographic zone of influence

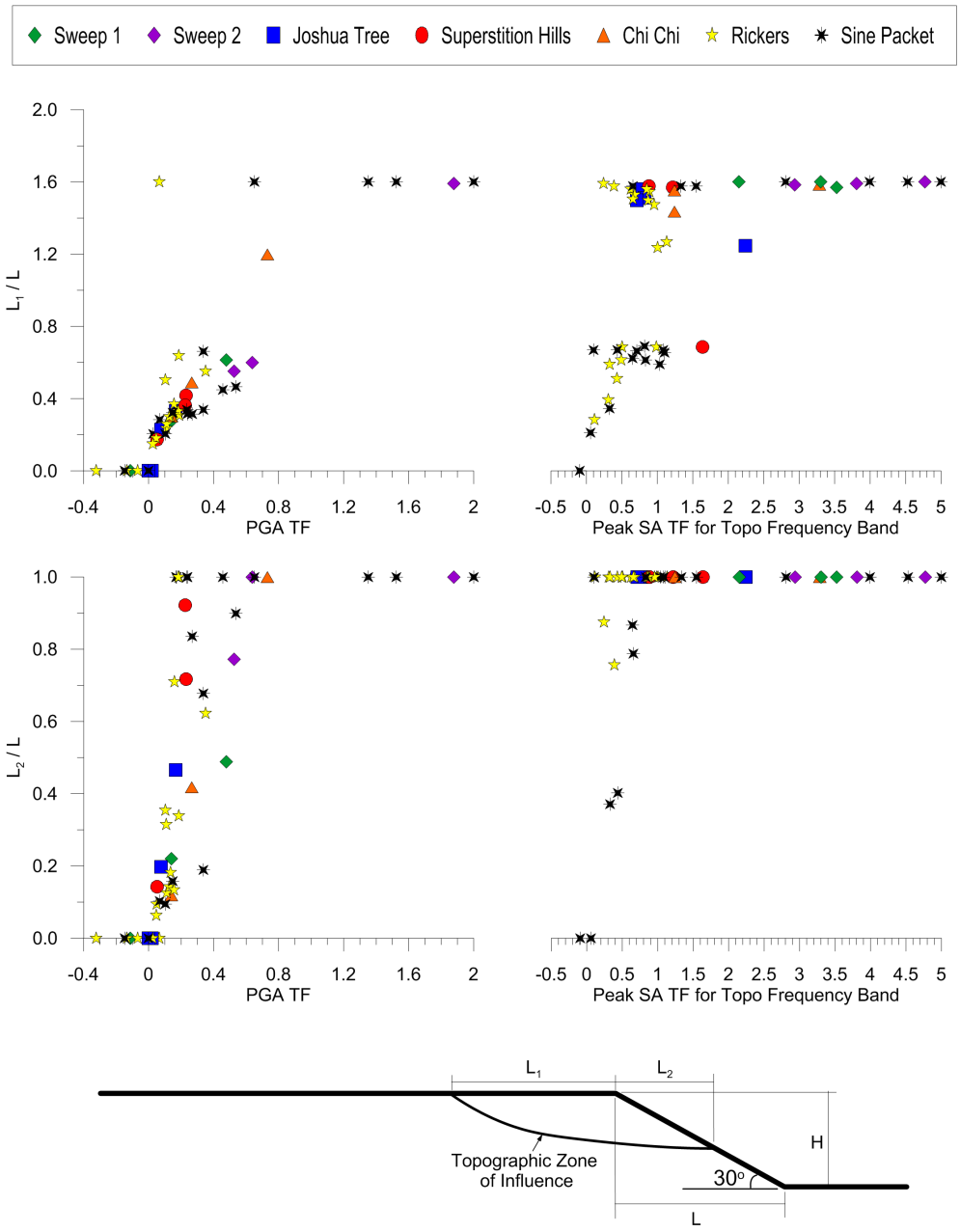

Figure 3.20: Normalized distance versus *PGA TF* and *bp SA TF* for the topographic frequency band at the slope crest for both 30 degree slope prototypes. Lengths L_1 and L_2 represent distances behind and in front of the crest, respectively, influenced by topography.

is not only impacted by the level of amplification, but the overall slope size as well.

A final note about this figure should be highlighted. As mentioned, distances L_1 and L_2 were based on the point at which the $PGA\ TF$ and the *bp* $SA\ TF$ reached values of zero. Because there is some natural fluctuation in the sensor measurements, (even for the flat ground) as discussed later in this chapter in Section 3.3.3, a cutoff value, below which a TF would be considered non significant could also have been used in determining the measured distances (i.e., 0.1 for $PGA\ TF$). Had this approach been used, it would have served to lower the size of the topographic zone of influence and resulted in a lower occurrence in the realization of the L_1 and L_2 thresholds. However, the overall trends would remain qualitatively unaffected.

To this point, the figures presented have focused on trends in the data that support correlations between certain ground motion parameters and topographic effects. The next two figures, Figure 3.21 and 3.22, emphasize parameters of interest that do not appear to be well correlated to topographic effects. Both figures contain three graphs, with the $PGA\ TF$ and the *bp* $SA\ TF$ plotted in Figure 3.21 and Figure 3.22 respectively, versus the *peak shear strain* (PSS), either PGA or *bp* SA of the base input ground motions, and the Trifunac duration at the slope crest. Trifunac duration can be defined as the elapsed time between points in an acceleration time history in which 5% and 95% of the total energy have been achieved (Kramer, 1996). The PSS was calculated by using the second order approximation developed by Zeghal et al. (1995) for analyzing downhole arrays to determine a shear strain time history. From the shear strain time history the maximum absolute value was taken as the PSS. This method was also applied to centrifuge data by Brennan et al. (2005). The shear strain time history can be calculated as follows:

$$\gamma(z_i) = \frac{1}{(z_{i+1} - z_{i-1})} \left[(u_{i+1} - u_i) \frac{(z_i - z_{i-1})}{(z_{i+1} - z_i)} + (u_i - u_{i-1}) \frac{(z_{i+1} - z_i)}{(z_i - z_{i-1})} \right] \tag{3.8}$$

where z is depth below the ground surface, u is displacement and subscripts i, $i-1$, and $i+1$ represent the sensor location and sensor locations above and below where the strain is calculated, respectively. To use this formulation, the recorded acceleration time histories

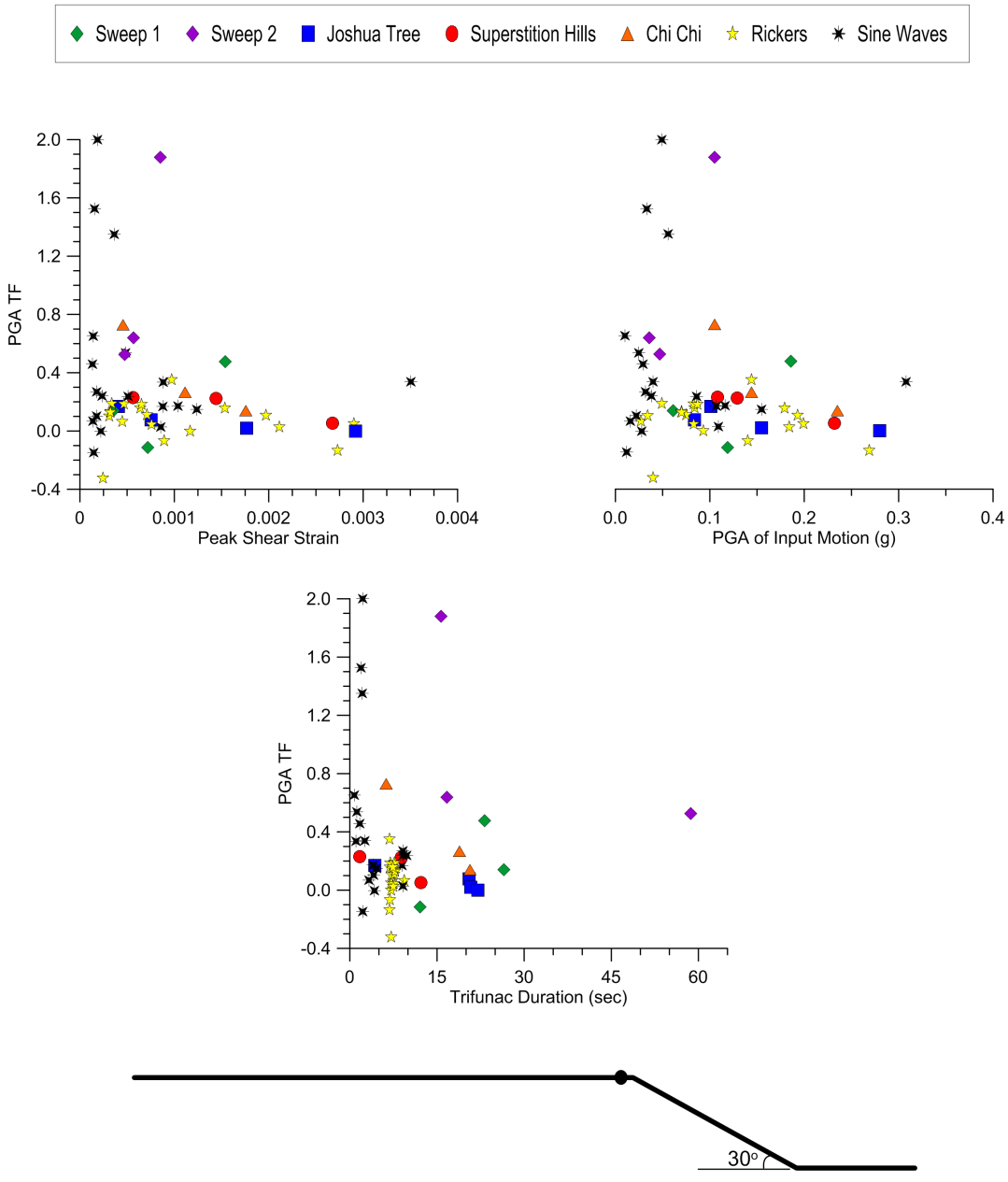

Figure 3.21: $PGA\,TF$ versus PSS, base input PGA and Trifunac duration at the 30 degree slope crest for both slope prototypes.

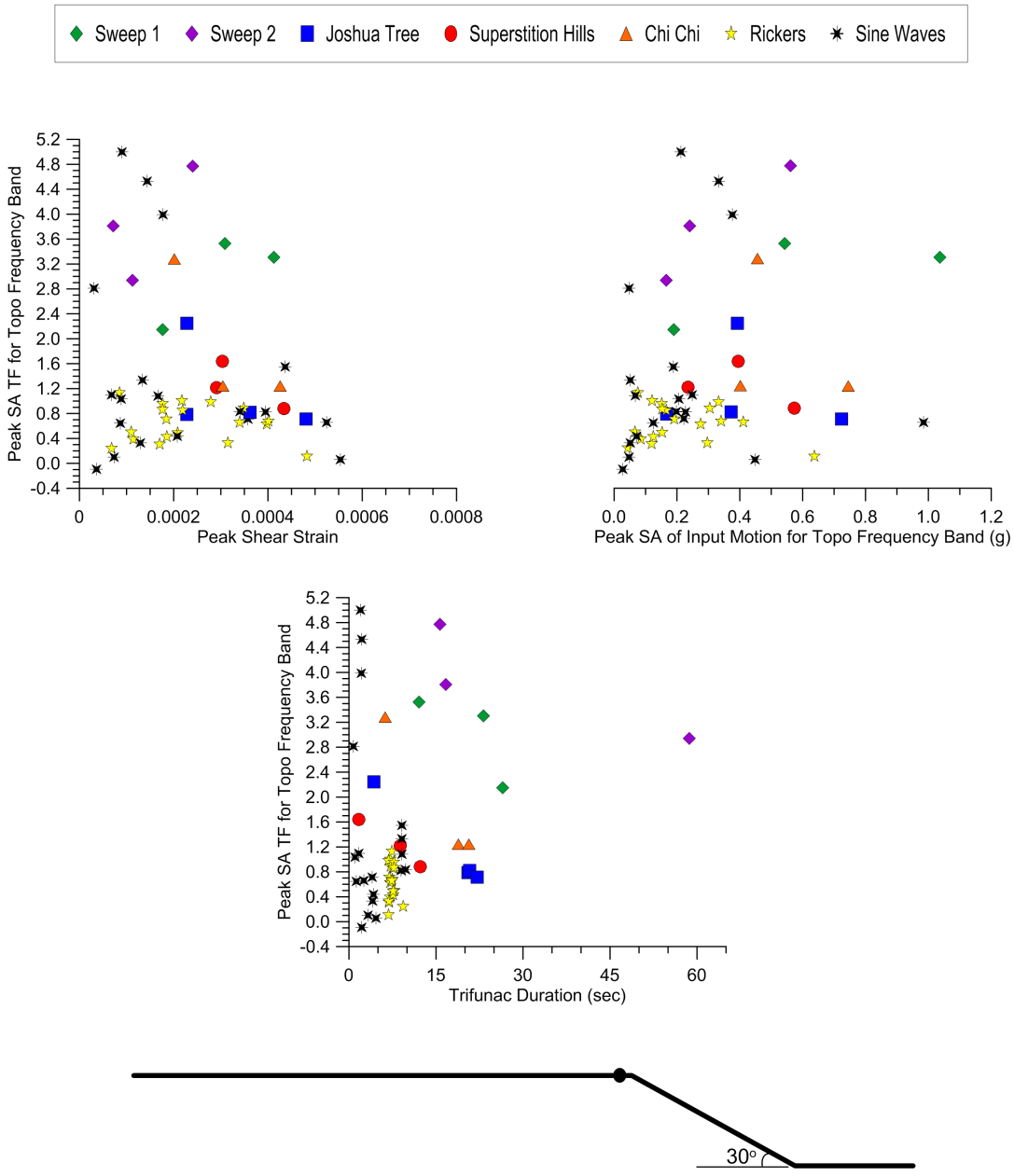

Figure 3.22: *bp SA TF* versus *PSS*, base input *bp SA* and Trifunac duration at the 30 degree slope crest for both slope prototypes.

were converted to displacement time histories through double integration and detrending. The PSS was also checked using another method developed by Ancheta et al. (2008), and although the results were similar, PSS values calculated using this method are not reported here.

From study of the two figures, it can be concluded that duration, PSS (which can be used to indicate effects of induced non-linearity) and the input amplitude of the ground motions do not impact the magnitude of topographic effects for the given slopes and ground motions. It can also be inferred that input PGA can serve as a good proxy to the amplitude of the PSS, in that the values correlate fairly well on an individual motion by motion basis. High input PGA values result in high PGS values and vice versa.

It should be mentioned here that the bracketed duration, defined by the time elapsed between the first and last exceedance of a chosen threshold amplitude (typically 0.05g, (Kramer, 1996)) of an acceleration time history, was also calculated and compared to the TFs. Again, no correlation was found. Lastly, changes in duration resulting from the presence of topography (i.e., at the slope crest) were also analyzed and found to be negligible.

The figures presented in this subsection have utilized PGA and different representations of SA to illustrate topographic effects. However, as mentioned in the previous subsection (3.3.1), changes in PGV and AI were also analyzed. Figure 3.23 compares the $PGV\ TF$ and $AI\ TF$ to the $PGA\ TF$ at the slope crest. The TFs for PGA and PGV are nearly identical, hovering around the 1:1 reference line. The $AI\ TF$, however, increases as the $PGA\ TF$ increases. This is likely a result of the way in which AI is calculated, which is as follows:

$$AI = \frac{\pi}{2g} \int_0^\infty \left[a(t)^2\right] dt \tag{3.9}$$

where g is the acceleration due to gravity, a is ground acceleration and t is time. Because all acceleration values are squared, increases in acceleration over the free field will be compounded resulting in even greater increases in AI. Additionally, while PGA considers a single point in the acceleration time history, AI considers all points in the time history. Thus, if multiple accelerations in the time history are amplified, this is reflected by an increase in the

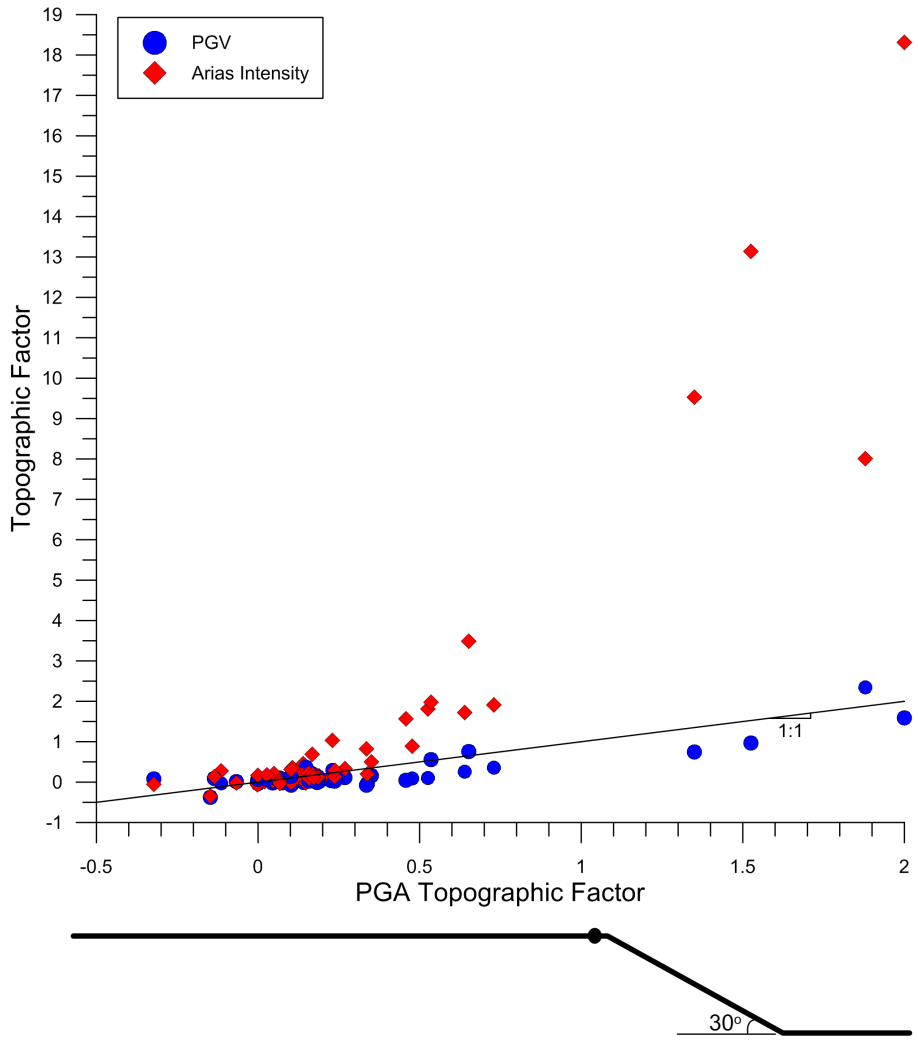

Figure 3.23: *PGV TF* and *AI TF* versus *PGA TF* at the 30 degree slope crest for both slope prototypes.

$AI\ TF$ and would not be accounted for with the $PGA\ TF$. Therefore, ground motions with topographic amplification throughout more of the ground motion will have greater $AI\ TF$ values. As shown these values can be significant for certain ground motions.

In this subsection, a number of significant trends were highlighted for the two 30 degree slope prototypes. Further discussion and a summary of the findings presented is reserved for Section 3.4 later in this chapter. However, one final note should be made here. As mentioned at the beginning of this section, many of the plots provided combined the ground responses of the two prototype slopes (both when motions were plotted individually or when mean values were given), even though one of the slopes is half the size of the other. This was accomplished by using normalized parameters, thereby negating the raw differences in the measures considered for frequency content, amplitude and size. However, prior to combining the results from the two prototypes, each was individually analyzed. After confirming the similarity in the data trends and overall amplitude of the normalized parameters, the figures presented here were created. The reality of the trends illustrated are significantly strengthened by the consistency in the results between the two prototype slopes.

25 degree slopes

The same group of figures provided for the two prototype 30 degree slopes in the previous subsection are utilized here for the two prototype 25 degree slopes and again for the two prototype 20 degree slopes in the following subsection. Because the content of the figures has already been explained in the previous subsection, the commentary surrounding the following figures will be reduced. Interpretation of the following figures will concentrate on comparison of the results for the 25 degree slope prototypes to the trends highlighted above for the 30 degree slope prototypes. For comparative purposes, graphs for all three slope inclinations are plotted to the same scale.

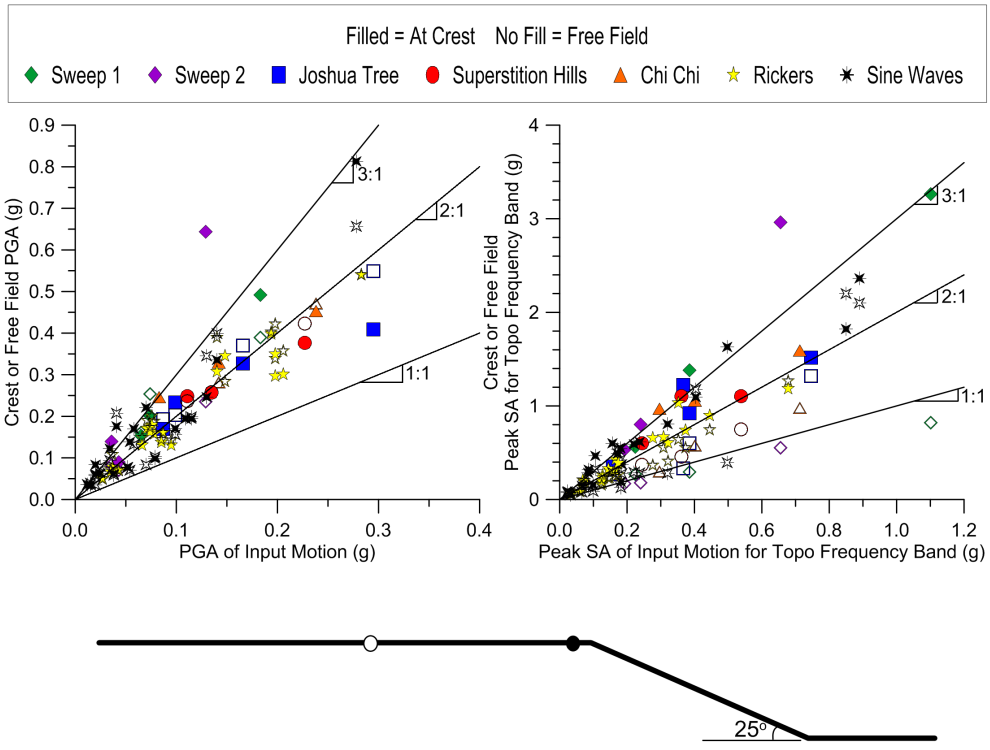

Figure 3.24: Free field and crest response versus input using PGA and $bp\ SA$ for the topographic frequency band for both 25 degree slope prototypes. The free field sensor (A20) is about 23.5 (11.75) meters from the crest sensor (A32), which is about 2.5 (1.25) meters behind the slope crest at 55g (at 27.5g).

Generally the results presented in Figure 3.24 are similar to those depicted in Figure 3.9 for the 30 degree slopes, with a few notable differences. The PGA and *bp* SA input and free field values are, aside from minor fluctuations, nearly identical to those recorded for the 30 degree slope prototypes, with the exception of a couple sine wave motions; one of which had both a greater input and free field *bp* SA value and one that only had a greater recorded value in the free field. The latter motion is likely an anomaly, but could have been caused by the closer proximity of the free field sensor to the slope crest. In other words, for that particular motion, the free field sensor may not have been clear of influence of topographic effects, leading to an amplified response. The other sine wave motion, where both the base and free field values shifted, resulted from the fact that the sine wave motion introduced to the 25 degree slope was inherently different than that of the 30 degree slope. This occurred due to a 'misfire' of sorts from the horizontal shaker used to produce the ground motions; although the same motion was used to command the shaker, a different motion was created.

The dissimilarities in sine wave motions are relatively minor to the overall discussion. A more significant difference in response between the 30 and 25 degree slopes, however, occurred at the slope crest. Although PGA values generally are in the same range as previously reported, from 1.5 to 5 times the input PGA, for a notably significant number of motions (earthquake motions in particular) the PGA at the crest was lower than that recorded in the free field. This was generally not true for the frequency specific *bp* SA values, however, the overall values did decrease in comparison to the 30 degree slope, from a range of 2 to 7 times, to a range of 2 to 4.5 times, greater than the input values. Both of these findings indicate a generally weaker response at the crest for the 25 degree slopes.

The noted contrast in relative ground motion amplitude between the 25 and 30 degree slopes is not found when interpreting ground motion frequency content. As illustrated by Figure 3.25, aside from minor variations in the calculated MSF values, the trends and patterns identified for the 30 degree slopes are also present here. Namely, in comparison to the free field, the MSF of the ground motion shifts towards the slope topographic frequency at the slope crest. Again, the shift in MSF is greater (larger $MSF\ TF$ values in the

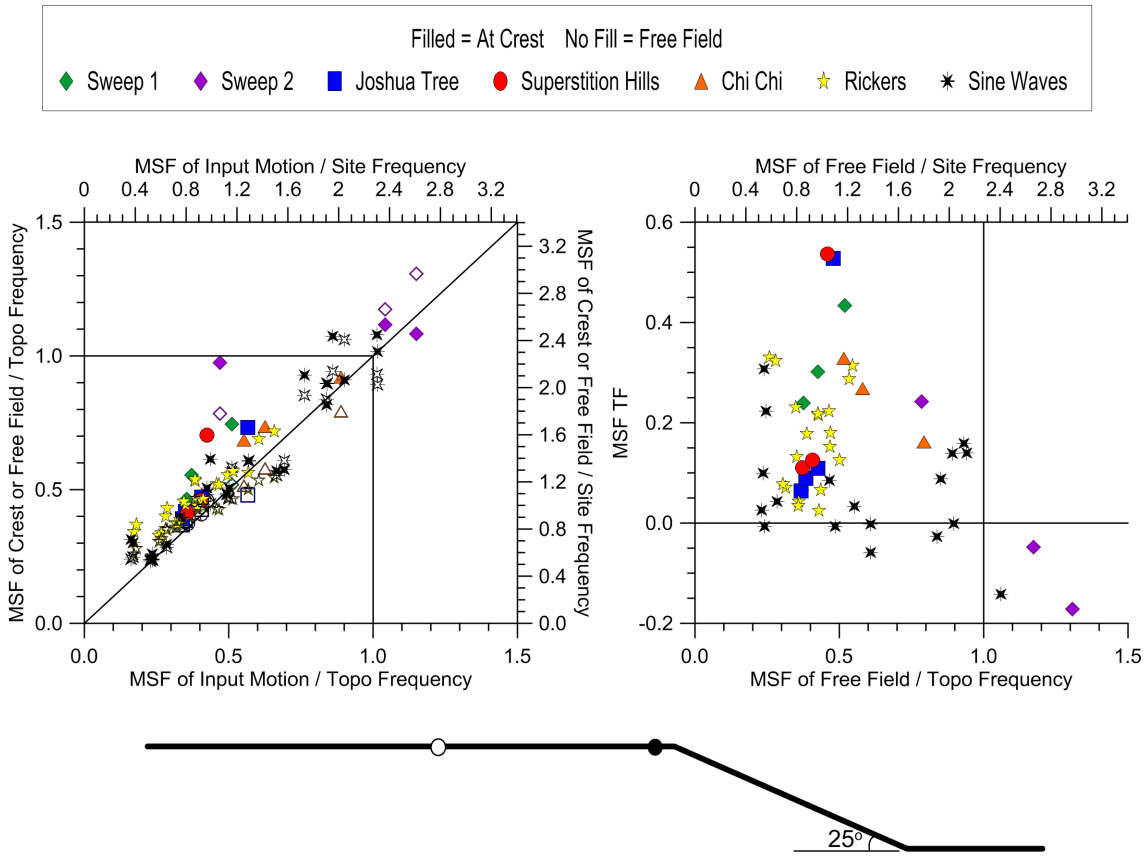

Figure 3.25: Free field and crest versus input MSF normalized by the topographic and site frequencies for both 25 degree slope prototypes. The free field sensor (A20) is about 23.5 (11.75) meters from the crest sensor (A32), which is about 2.5 (1.25) meters behind the slope crest at 55g (at 27.5g).

right plot of Figure 3.25) if the MSF of the ground motion is farther from the topographic frequency. This holds true until the MSF of the motion is less than or equal to the site frequency, at which point the magnitude of the shift in MSF declines. The overall magnitude of the shift (i.e., $MSF\ TF$ magnitude) for the 25 degree slopes is on par with that of the 30 degree slopes depicted in Figure 3.10 earlier.

The correlation between the ground motion MSF at the crest and the level of amplification of the crest over the free field response is also similar for the 30 and 25 degree slopes. As illustrated by Figure 3.26, the TFs for both PGA and $bp\ SA$ both generally increase as the MSF of the motion approaches the topographic frequency of the slope. At the site frequency

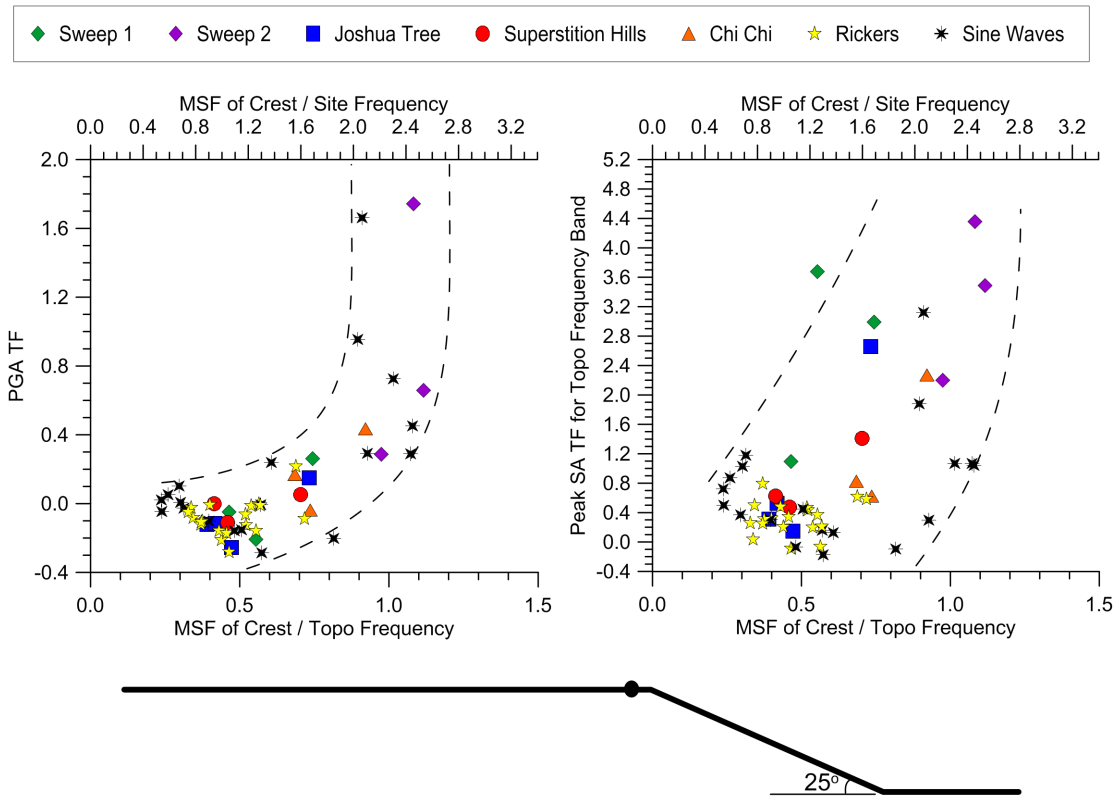

Figure 3.26: *PGA TF* and *bp SA TF* for the topographic frequency band versus *MSF* normalized by the topographic and site frequencies at the crest for both 25 degree slope prototypes.

($TR = 0.44$), typically little to no amplification and often deamplification occurs, however, below the site frequency a slight increase in the level of amplification is found. These patterns were also featured in Figure 3.11 for the 30 degree slopes. The main difference between the responses for the 25 and 30 degree slopes, however, is the overall magnitude of the TFs. More motions exhibited little to no amplification or even a degree of deamplification (i.e., small positive or negative TFs) at the 25 degree slope crest. And while the *PGA TF* and *bp SA TF* values reached as high as roughly 2.0 and 5.0 for the 30 degree slopes, respectively, maximum values of 1.75 and 4.4 were determined for the 25 degree slopes.

Figures 3.24, 3.25, 3.26 provide singular measures for each of the individually analyzed ground motions, with changes in frequency content and ground motion intensity tracked at

the free field, crest and soil layer base locations. Figure 3.27 allows the relationship between the crest and free field, as well as the crest and input base motions, to be interpreted in an average sense across a spectrum of frequencies, utilizing the $SA\ TF$ and $SA\ AA$, respectively; both determined at the slope crest. As before, in Figure 3.27, ground motions are grouped according to their MSF into categories of all motions, STR motions (those with a MSF within 30% of the topographic frequency) and WTR motions (those with a MSF not within 30% of the topographic frequency).

The trends of the results depicted in Figure 3.27 are practically indistinguishable from those given in Figure 3.12 for the 30 degree slopes, aside from the overall magnitude of the calculated spectra. As with the 30 degree slopes, peak $SA\ TF$ values are found near the topographic frequency of the slope, with the level of amplification declining moving towards both higher and lower frequencies. A decrease in the 30 degree slope peak values from 1.9 and 0.55, to 1.2 and 0.3 here for the STR and WTR motions, respectively, is observed. At higher frequencies, beyond the peak amplified frequency band (which encompasses the topographic frequency), STR motions can be amplified by as much as 40% ($TF = 0.4$), while WTR motions tend to be deamplified by as much as 10% compared to the free field. At frequencies lower than the topographic frequency band, for all cases, typically a slightly deamplified response is found. The same pattern is found here in grouping the ground motions according to the their MSF, in that on average greater levels of amplification are established for the STR motions, a fact that is also evidenced by the $SA\ AA$ spectrum.

For the $SA\ AA$ spectra, there are two noted peaks with one near (but typically higher than) the topographic frequency of the slope and the other near the site frequency associated with the substratum behind the slope crest. For the STR motions, the peak near the topographic frequency is greater than the peak at the site frequency, while for the WTR motions both peaks are numerically similar, as was the case for the 30 degree slopes. The peak $SA\ AA$ value for the STR motions is roughly 2.8, with the secondary peak reaching a value of 1.8, less than values of 3.8 and 2.2 determined for the 30 degree slopes. Although for the 25 degree slopes the difference between the responses at the site and topographic

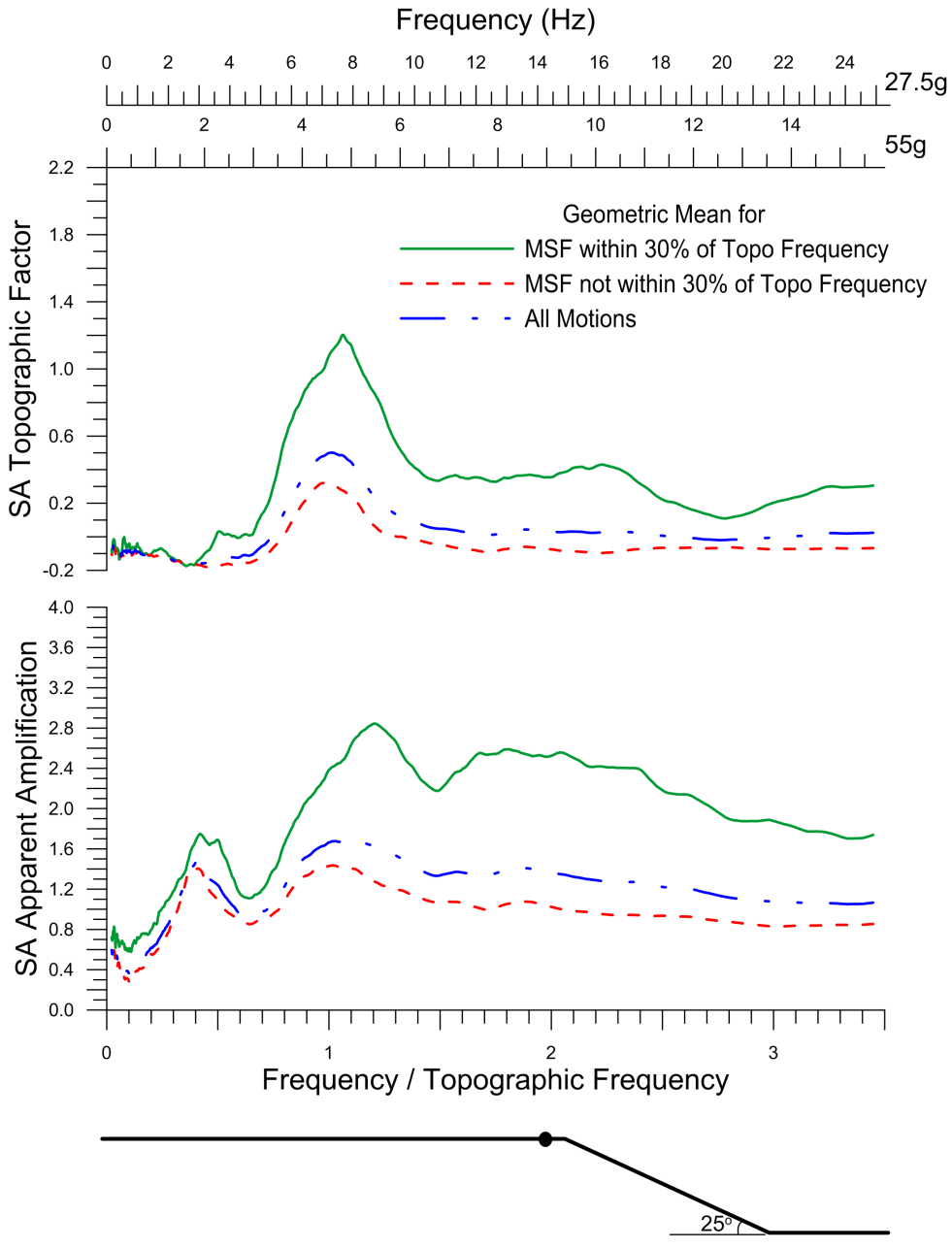

Figure 3.27: Geometric mean for the $SA\ TF$ and $SA\ AA$ spectra at the slope crest for both 25 degree slope prototypes grouped according to the MSF of the ground motion.

frequencies is minimized, this again shows that topographic effects can exceed site effects at the slope crest for certain cases. For the WTR motions, both peaks are at $SA\ AA$ values of roughly 1.4, compared to values of 1.7–1.8 for the 30 degree slopes. As seen previously, amplification at the site frequency, in comparison to the base input, is also greater for the case of STR motions, which are generally more amplified across all frequencies.

The emphasis of all the figures provided in this subsection thus far has been on the response at the slope crest in comparison to the base input and free field ground motion. The next group of figures focus on the ground response across the entire slope from the free field sensor behind the crest to the slope toe. The behavior observed for the crest has been, aside from amplitude, mostly similar to that of the 30 degree slopes. The following figures will demonstrate any spatial similarities and differences between the 25 and 30 degree slopes.

Figures 3.28, 3.29 and 3.30 present the mean spectrum for the $SA\ TF$ for all motions, STR motions, and WTR motions, respectively for the near surface sensor locations provided. Comparison of these plots to those for the 30 degree slopes in Figures 3.13, 3.14 and 3.15 reveals some fairly significant differences in the response across the slope, along with a few similarities.

The similarities in the responses of the 30 and 25 degree slopes include the general spectrum shape and overall spatial extent, with differences pertaining to the magnitude of amplification, and the locations of peak responses. The peak response for the marked sensor locations again occurs near the topographic frequency and diminishes moving towards both higher and lower frequencies. Also similar, is the fact that the amplification is greater for STR motions than WTR motions, resulting in notable topographic amplification over a larger spatial extent for those motions. The main difference, however, is the location of the peak ground response. For the 30 degree slopes, the peak response occurred slightly behind the crest and the response diminished moving away from the crest in either direction. There was a notable decrease at the adjacent sensors and a significant decrease beyond that. For the 25 degree slopes, the peak response occurs on the face of the slope slightly in front of the crest.

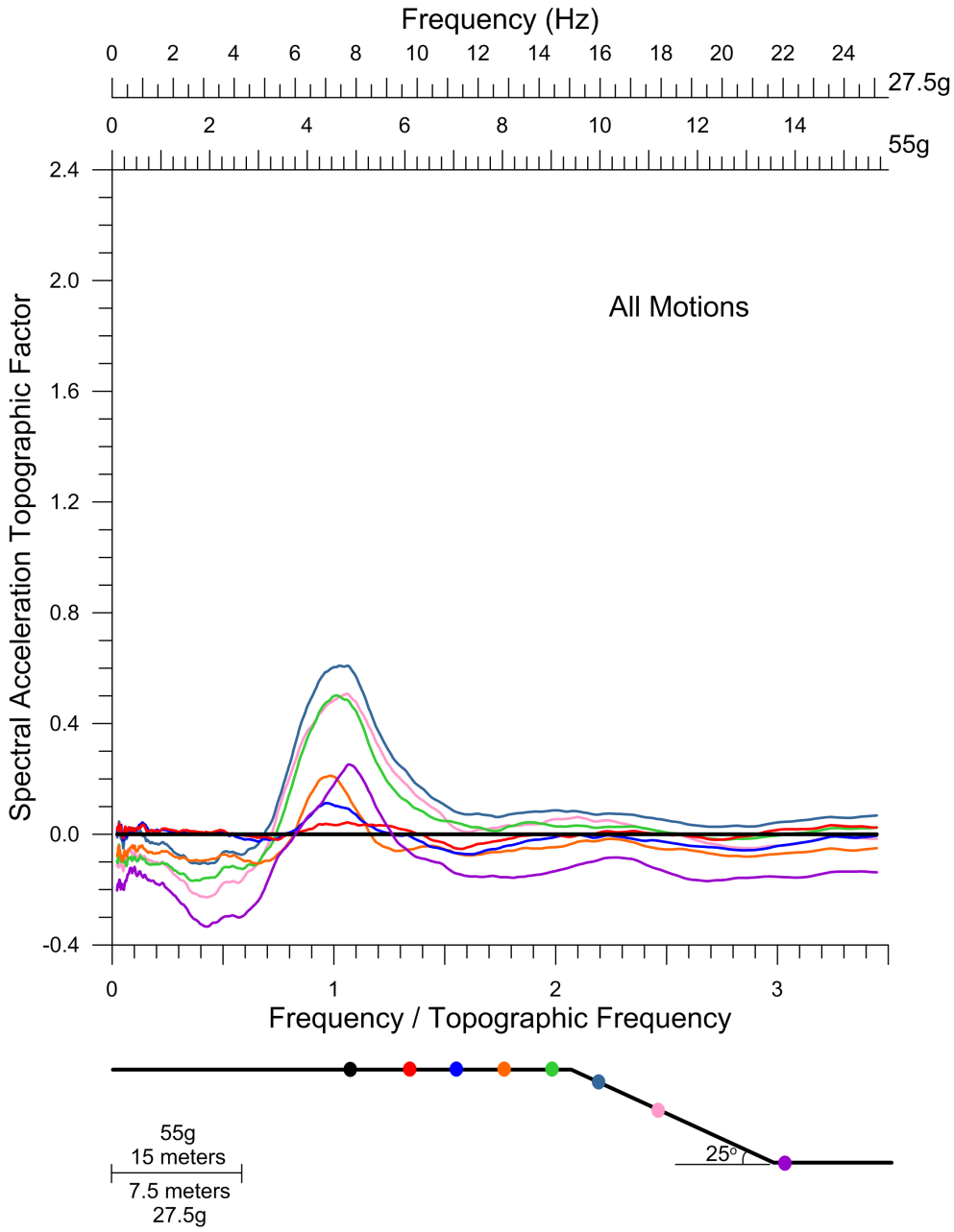

Figure 3.28: Geometric mean of the $SA\ TF$ spectrum versus normalized frequency for all motions at different near surface sensor locations on the 25 degree slope. Spectra are color-coded to match sensor locations, which are provided at scale. The free field sensor is represented in black. Both prototypes are considered in calculating mean values.

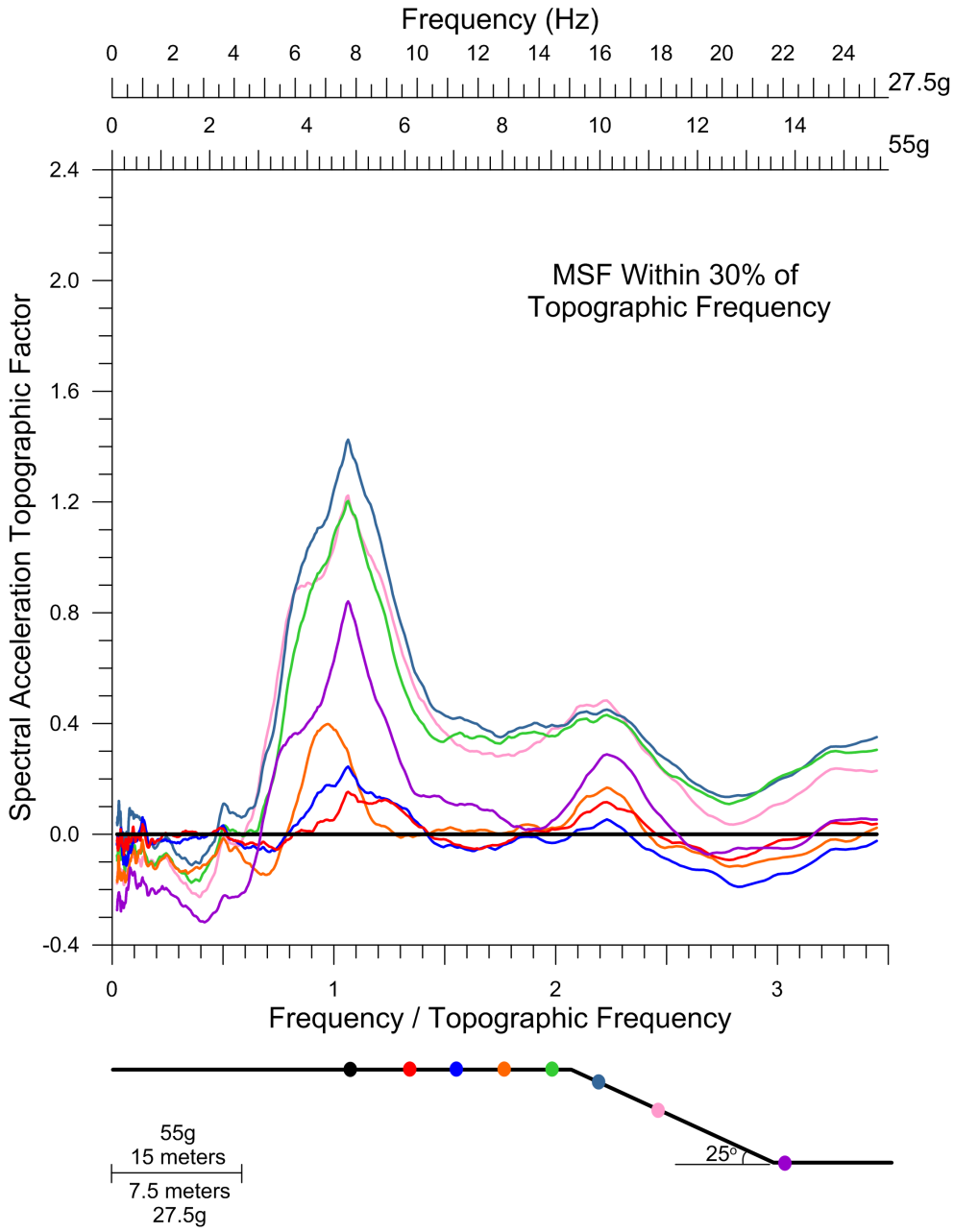

Figure 3.29: Geometric mean of the SA TF spectrum versus normalized frequency for STR motions at different near surface sensor locations on the 25 degree slope. Spectra are color-coded to match sensor locations, which are provided at scale. The free field sensor is represented in black. Both prototypes are considered in calculating mean values.

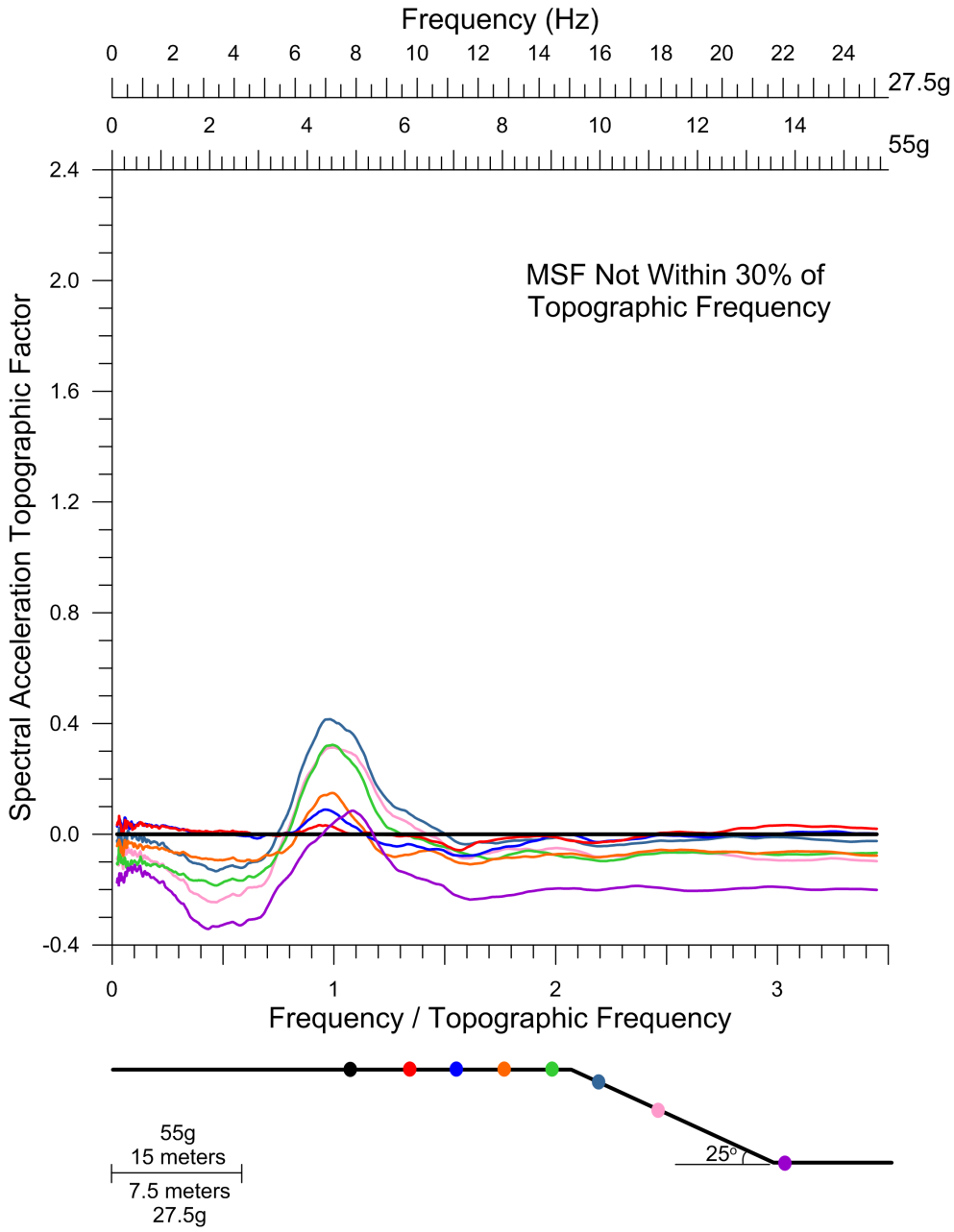

Figure 3.30: Geometric mean of the SA TF spectrum versus normalized frequency for WTR motions at different near surface sensor locations on the 25 degree slope. Spectra are color-coded to match sensor locations, which are provided at scale. The free field sensor is represented in black. Both prototypes are considered in calculating mean values.

The amplified response then decreases moving over and behind the crest as well as moving down the face of the slope towards the slope toe. A relatively minor decrease in amplitude occurs at the adjacent sensor locations prior to a larger decrease beyond. One exception, however, is the response at the slope toe for STR motions, where the decline in amplification magnitude is less significant than that found traveling an equivalent distance from the overall peak response in the opposite direction (i.e towards the free field sensor). These contrasts represent a shift in energy concentration, and subsequent spatial distribution, from behind the slope crest towards the face of the slope due to the change in slope inclination from 30 to 25 degrees.

In considering the different slope dimensions, and the shift in spatial distribution associated with the 25 degree slopes, it is important to have a concept of scale for determining the spatial extent of topographic effects. The face of the slope (measured horizontally from the slope crest to the slope toe) measures roughly 23.6 meters and 11.8 meters for the 55g and 27.5g prototypes, respectively. The distance from the slope crest to the free field sensor is 26.0 meters at 55g and 13.0 meters at 27.5g. As mentioned, the spatial influence of topographic effects for WTR motions is smaller than that of STR motions. The average peak response for both groups of motion occurs approximately 3.0 (1.5) meters in front of the slope crest for the 55g (27.5g) prototype. For the STR motions, the impact of topographic amplification is still substantial at the slope toe, 22.0 (11.0) meters from the peak response. For the WTR motions, however, amplification at the toe is fairly insignificant (with deamplification at most frequencies), and the influence of topographic effects diminishes somewhere between 7.0 (3.5) and 22 (11) meters from the peak response (i.e., somewhere between the sensor locations). Moving in the opposite direction, towards the free field sensor, the impact of topographic effects extends to distances of 16.5 (8.25) meters and 11 (5.5) meters behind the location of the peak response for the STR and WTR motions, respectively.

The spatial context provided in the previous paragraph can also be applied to the results depicted in Figures 3.31, 3.32 and 3.33, where the $SA\ AA$ is plotted in the same manner as $SA\ TF$ in the Figures 3.28, 3.29 and 3.30. The spatial extent of topographic effects

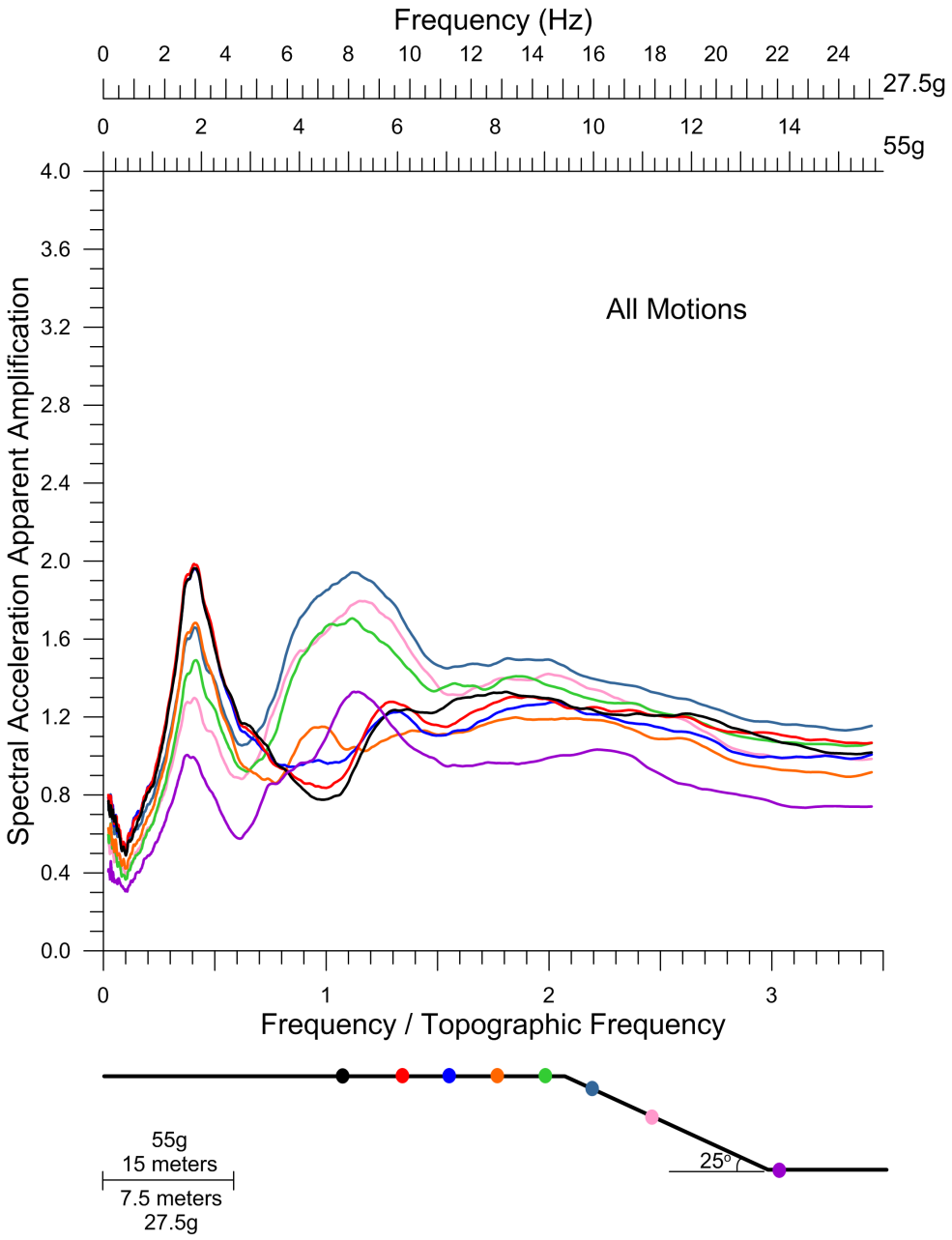

Figure 3.31: Geometric mean of the SA AA spectrum versus normalized frequency for all motions at different near surface sensor locations on the 25 degree slope. Spectra are color-coded to match sensor locations, which are provided at scale. The free field sensor is represented in black. Both prototypes are considered in calculating mean values.

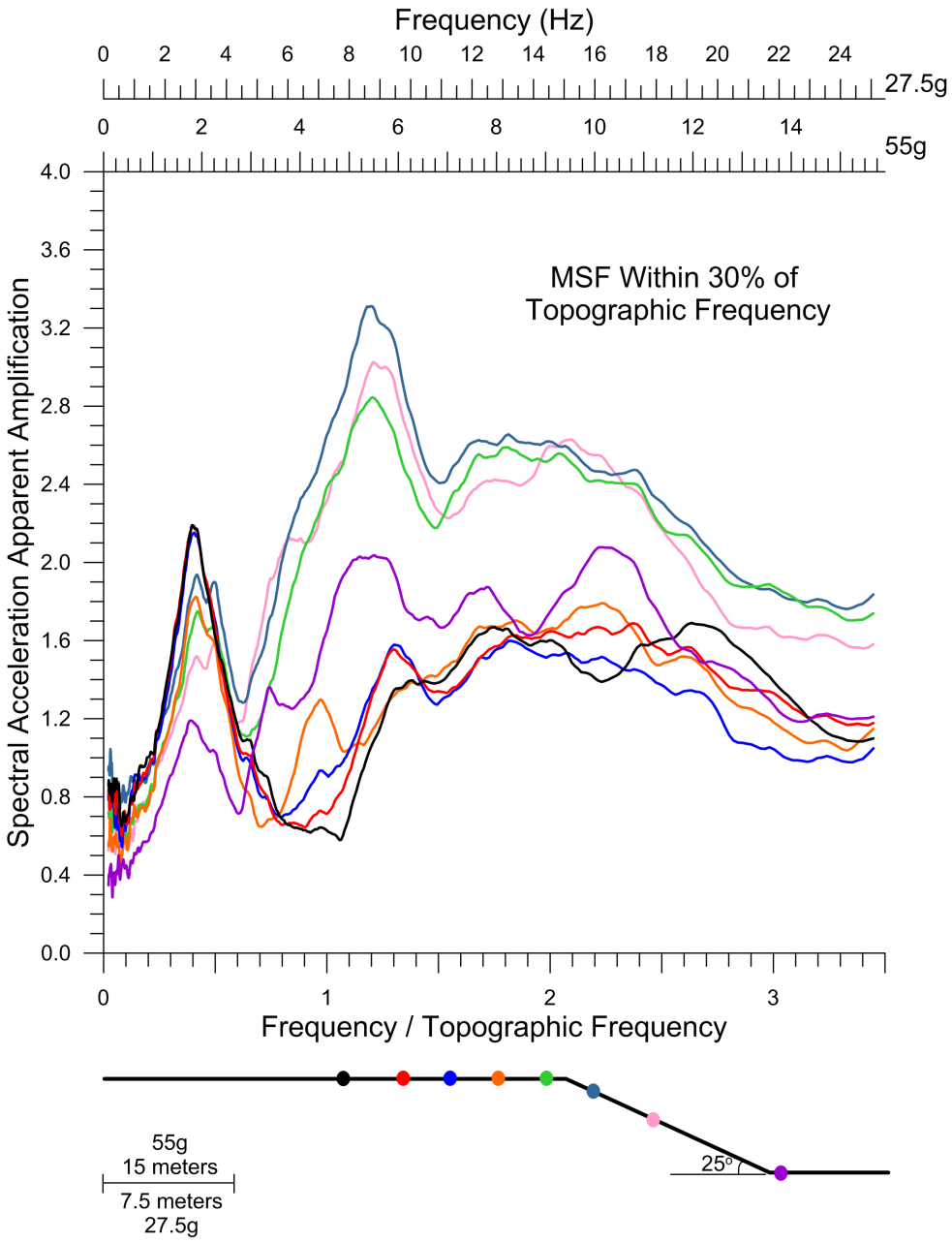

Figure 3.32: Geometric mean of the SA AA spectrum versus normalized frequency for STR motions at different near surface sensor locations on the 25 degree slope. Spectra are color-coded to match sensor locations, which are provided at scale. The free field sensor is represented in black. Both prototypes are considered in calculating mean values.

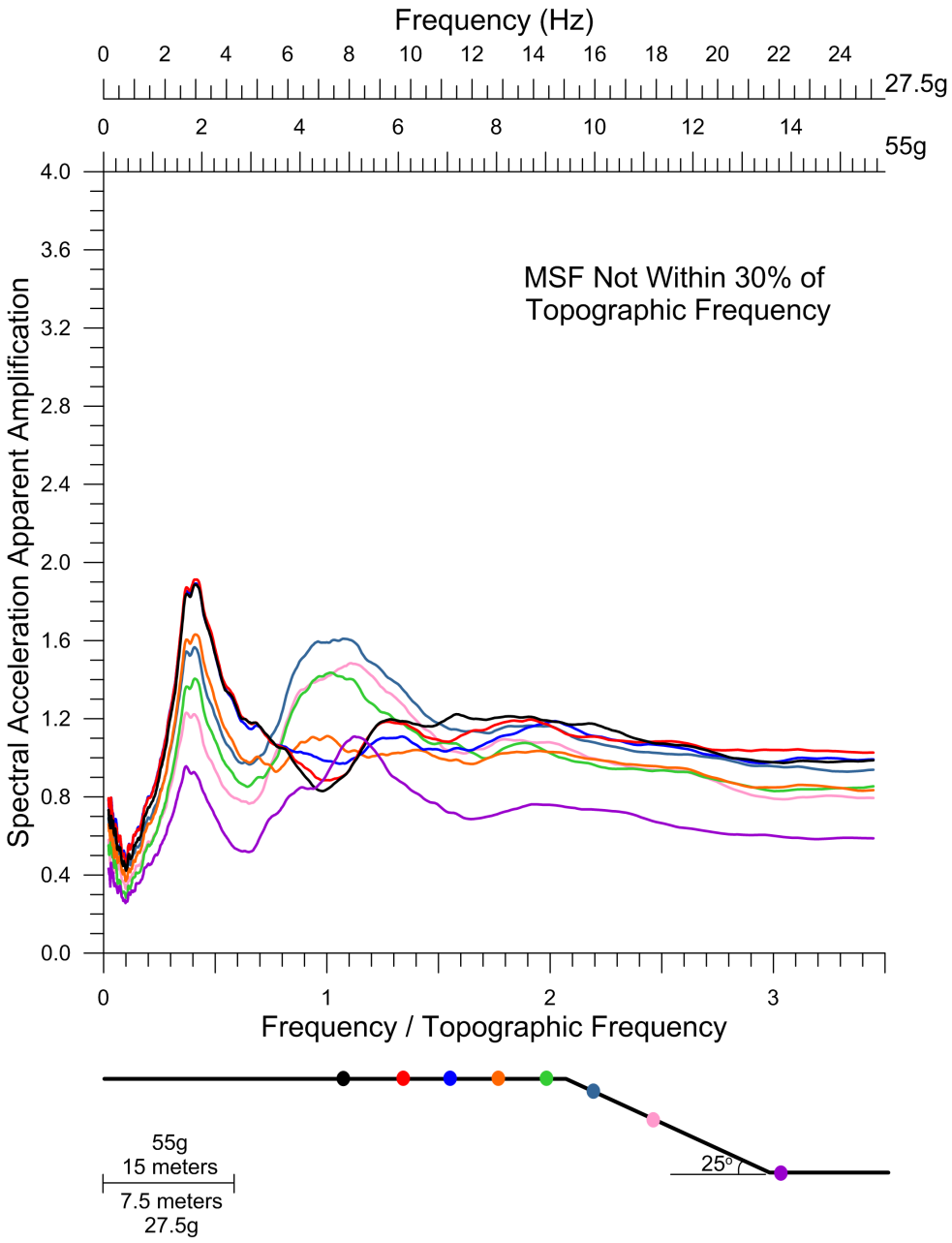

Figure 3.33: Geometric mean of the SA AA spectrum versus normalized frequency for WTR motions at different near surface sensor locations on the 25 degree slope. Spectra are color-coded to match sensor locations, which are provided at scale. The free field sensor is represented in black. Both prototypes are considered in calculating mean values.

and the differences between STR and WTR motions discussed above applies here as well. However, additional changes in spectral response are highlighted by the $SA\ AA$ spectrum. In particular, peaks both near the site frequency and topographic frequency are featured, allowing the spatial variation in amplification due to site effects and combined site and topographic effects to be examined.

The first peak in the spectrum (near a normalized frequency of 0.44) represents the response at the site frequency. As previously mentioned, the site frequency changes slightly for the different sensor locations on the face of the slope and at the slope toe, due to changes in the height of the soil column beneath these locations and a subsequent shift in the shear wave velocity. However, the change is minor, as both the height (Z) and average shear wave velocity ($\bar{V}_s$) are reduced. Thus, the changes in the two parameters effectively work towards offsetting one another as the site frequency is determined by $f_s = \bar{V}_s/4Z$. Nevertheless, there is a notable difference in the response at the site frequency for the different sensor locations. For all subsets of motions, the $SA\ AA$ values are nearly identical for the free field sensor and the next two adjacent sensors moving towards the slope crest (red and blue markers). Moving closer to the crest, the response at the next sensor (in orange) and first sensor on the slope face (in blue) experience a decrease in the $SA\ AA$, but are similar to one another. The sensor just behind the crest (in green), however, has an even weaker response despite being sandwiched between the blue and orange sensors. Finally, a even greater reduction in the $SA\ AA$ is seen moving down the slope face towards the toe, where the weakest response is measured. This differs from the 30 degree slopes, where the response slightly behind (at) the crest is comparable to that found in the free field.

The peak near the topographic frequency highlights the influence of topography on the ground response. Again, the greatest level of amplification (this time over the base input instead of the free field) occurs at the sensor slightly in front of the slope crest, with the adjacent sensors also exhibiting a reduced, but still significantly amplified response. The amplification at these sensors includes contributions from both site and topographic effects. To quantify topographic effects in this case, the spectrum for these sensors can be compared

to that in the free field, which is indicative of site effects only. For the STR motions, negating the contribution of site effects from the peak response, topographic effects would be responsible for an amplification comparable to that of the peak response for the free field sensor. In other words, the maximum contribution due to site effects in the free field, would be similar to the maximum contribution of topographic effects slightly in front of the crest. This differs from the 30 degree slopes, where the average maximum topographic effects were greater than the average maximum site effects. However, in considering the overall response at the individual sensors, it is apparent that amplification near the topographic frequency is greater than amplification at the site frequency for the three sensors surrounding the crest (green and blue) and on the slope face (pink). For the WTR motions, on the other hand, even the combined topographic and site effects near the topographic frequency do not exceed the site effects in the free field. Therefore, site effects are clearly more significant in this case.

Some of the spatial trends highlighted above for the 25 degree slopes are echoed utilizing different parameters in Figure 3.34. The peak response considering both the *bp* $SA\ TF$ and the $PGA\ TF$ is captured at the sensor slightly in front of the slope crest and a much more amplified average response is found for STR motions than for WTR motions. Consistent with the findings for the 30 degree slopes (Figure 3.19), the overall magnitude and areal extent for which significant amplification occurs is greater for the *bp* $SA\ TF$ than for the $PGA\ TF$. This distinction between the intensity measures used is particularly important in considering the WTR motions where an amplified response is captured when using the frequency specific *bp* $SA\ TF$, which opposes the mostly deamplified response portrayed when using $PGA\ TF$ as a measure of topographic amplification.

Contrasts between the two intensity measures found when considering the average response of the WTR motions, also exist when considering the average response of the STR motions. Differences in the measured response can be highlighted by considering three locations, the peak value and two sensors away from the peak value in either direction. Using PGA as an intensity measure, the average peak TF is roughly 0.5, representing a 50% increase over the PGA in the free field. Two sensors to the left or right (at the slope toe),

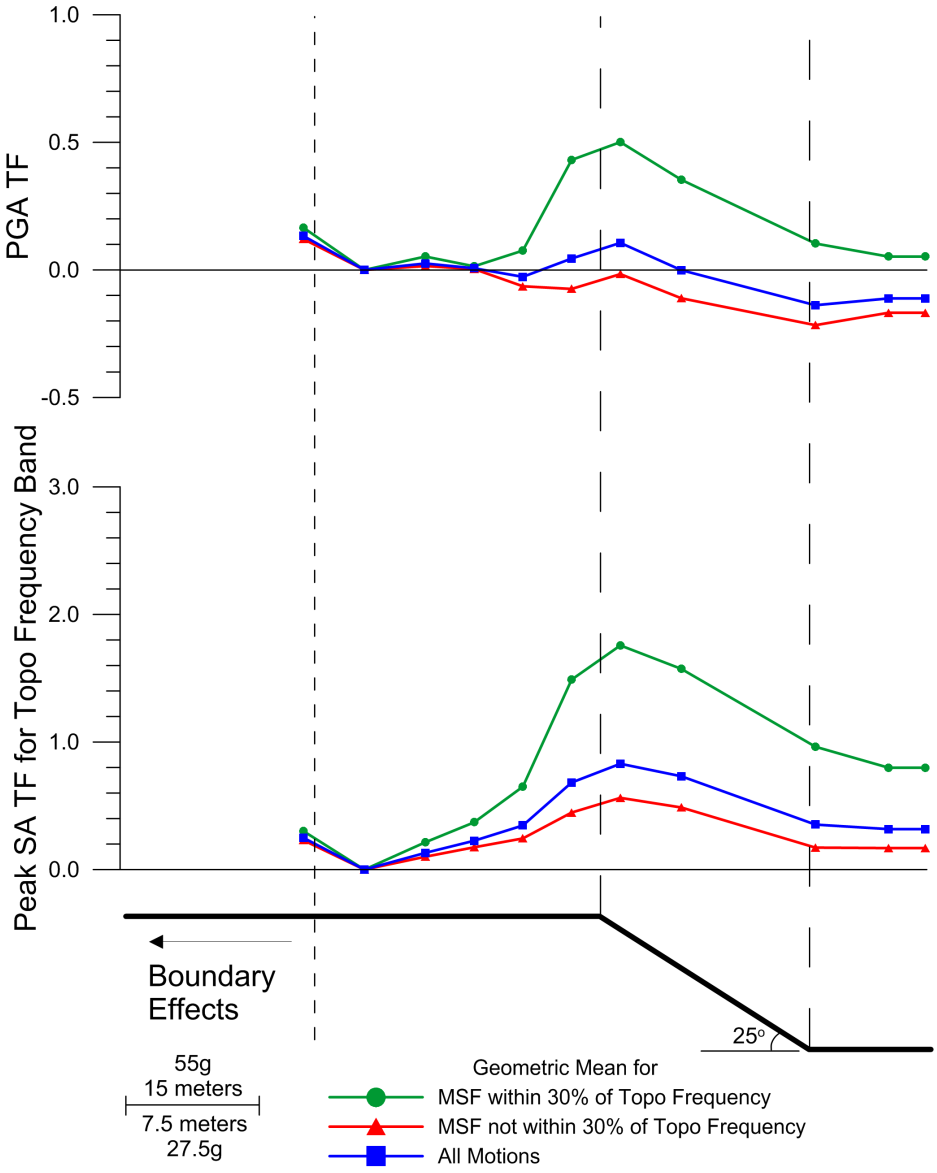

Figure 3.34: Geometric mean of $PGA\ TF$ and $bp\ SA\ TF$ for the topographic frequency band versus distance across the surface of the 25 degree slope for both prototypes, grouped according to the MSF of the ground motion.

the TF drops to roughly 0.1. The average *bp* SA TF on the other hand, peaks at roughly 1.7, with values of roughly 0.7 two sensors to the left and 1.0 two sensors to the right. This highlights not only differences in amplitude, but also spatial extent of topographic effects. Topographic amplification would be considered fairly insignificant two sensors from the peak using PGA TF, which is not the case using the *bp* SA TF. This emphasizes the impact of the chosen intensity measure on the perceived influence of topographic effects, a result of the frequency dependant nature of the phenomenon.

The results presented in Figure 3.35 confirm some of the spatial trends highlighted above, plotting the ground motions individually instead of using mean responses. As with the 30 degree slopes, the size of the area of the slope affected tends to increase as the level of amplification (measured through TFs) increases. Also similar to the 30 degree slopes, threshold values are reached for both intensity measures considering distances both in front of (L_2) and behind (L_1) the slope crest. The threshold values align with the slope toe, where $L_2 = 23.6$ (11.8) meters for the 55g (27.5g) prototype, and the free field sensor, where $L_1 = 26.0$ (13.0) meters at 55g (27.5g). What's interesting here is that despite the greater length of the slope face (compared to the 30 degree slopes, where $L = 19$ (9.5) meters at 55g (27.5g), the threshold value for L_2 is reached at lower levels of amplification than that determined for the 30 degree slopes. This is in tune with the shift in ground motion intensity towards the slope face mentioned earlier. The L_2 threshold is achieved consistently once the *bp* SA TF values are greater than 0.5 and the PGA TF values are greater than 0.35, as opposed to a value of 0.8 for both measures on the 30 degree slopes. The L_1 threshold, however, isn't achieved for all ground motions until a value above roughly 2.8 is reached for the *bp* SA TF, and is never consistently attained using the PGA TF. This compares to values of roughly 1.0 and 2.3 for PGA TF and *bp* SA TF, respectively, for the 30 degree slopes.

Thus far, spatial patterns for, and correlations with, topographic effects and different parameters have been presented in this subsection. Figures 3.36 and 3.37 represent parameters that are not well correlated with the effects of topography. The TFs of two intensity

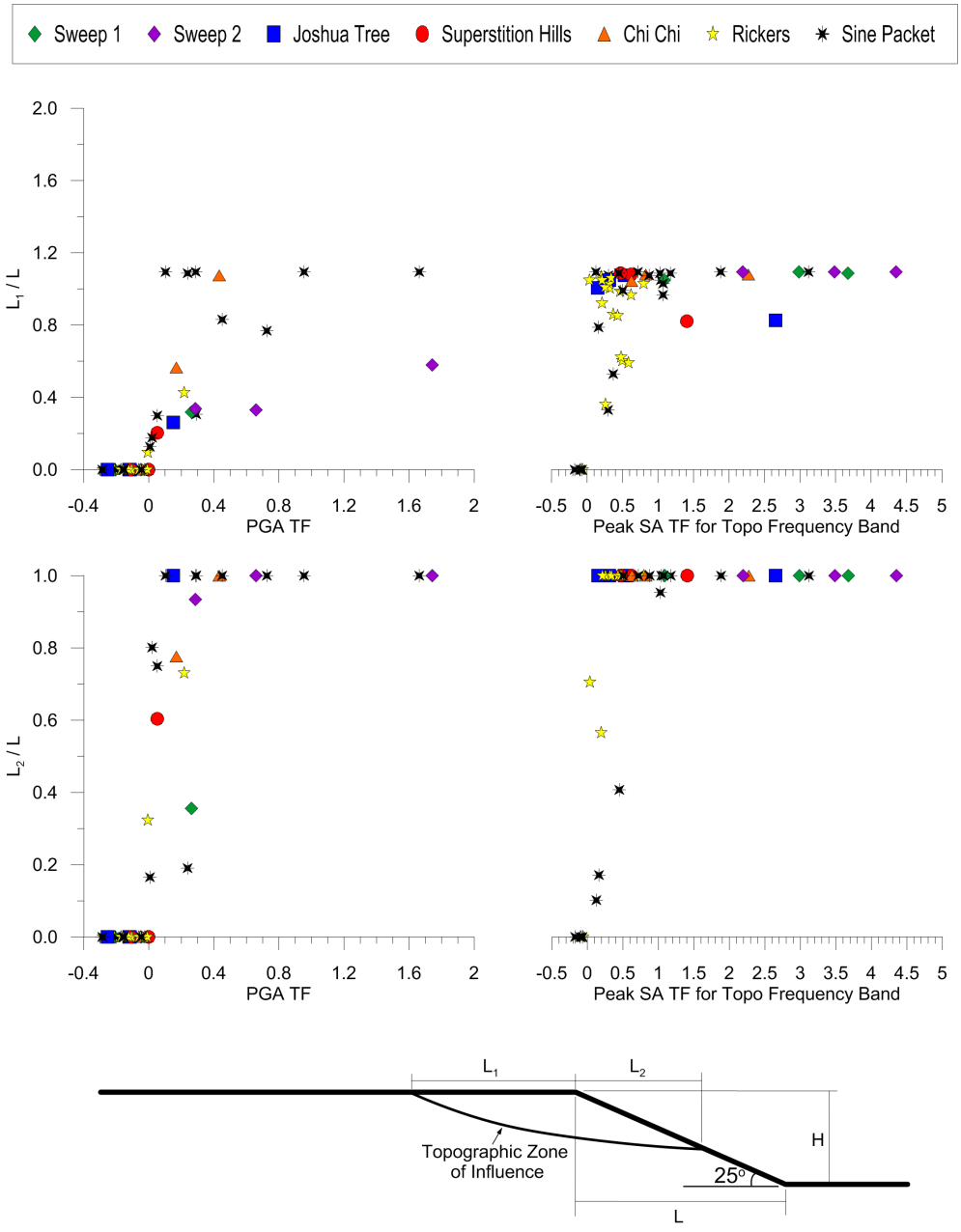

Figure 3.35: Normalized distance versus $PGA\ TF$ and $bp\ SA\ TF$ for the topographic frequency band at the slope crest for both 25 degree slope prototypes. Lengths L_1 and L_2 represent distances behind and in front of the crest, respectively, influenced by topography.

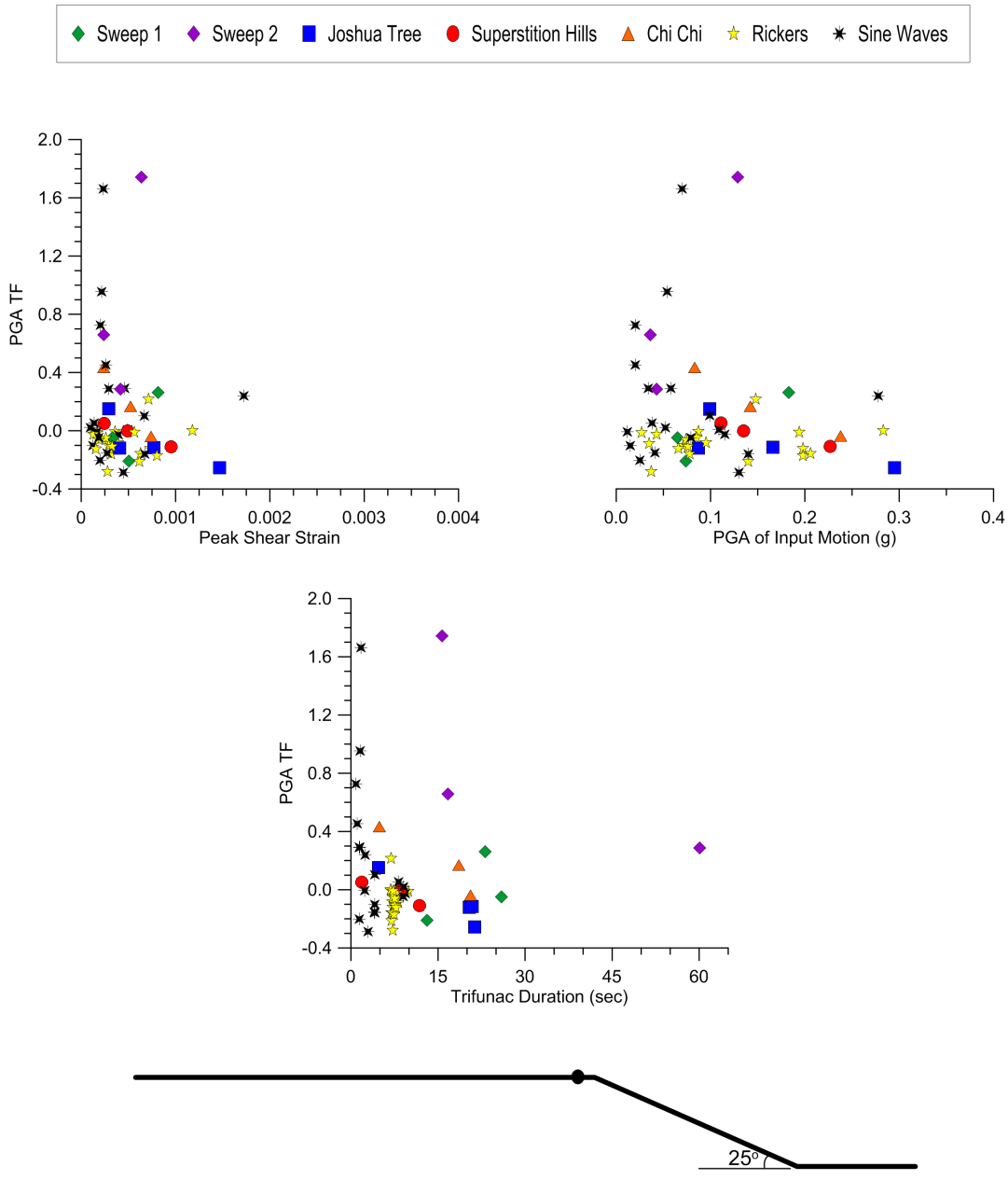

Figure 3.36: $PGA\,TF$ versus PSS, base input PGA and Trifunac duration at the 25 degree slope crest for both slope prototypes.

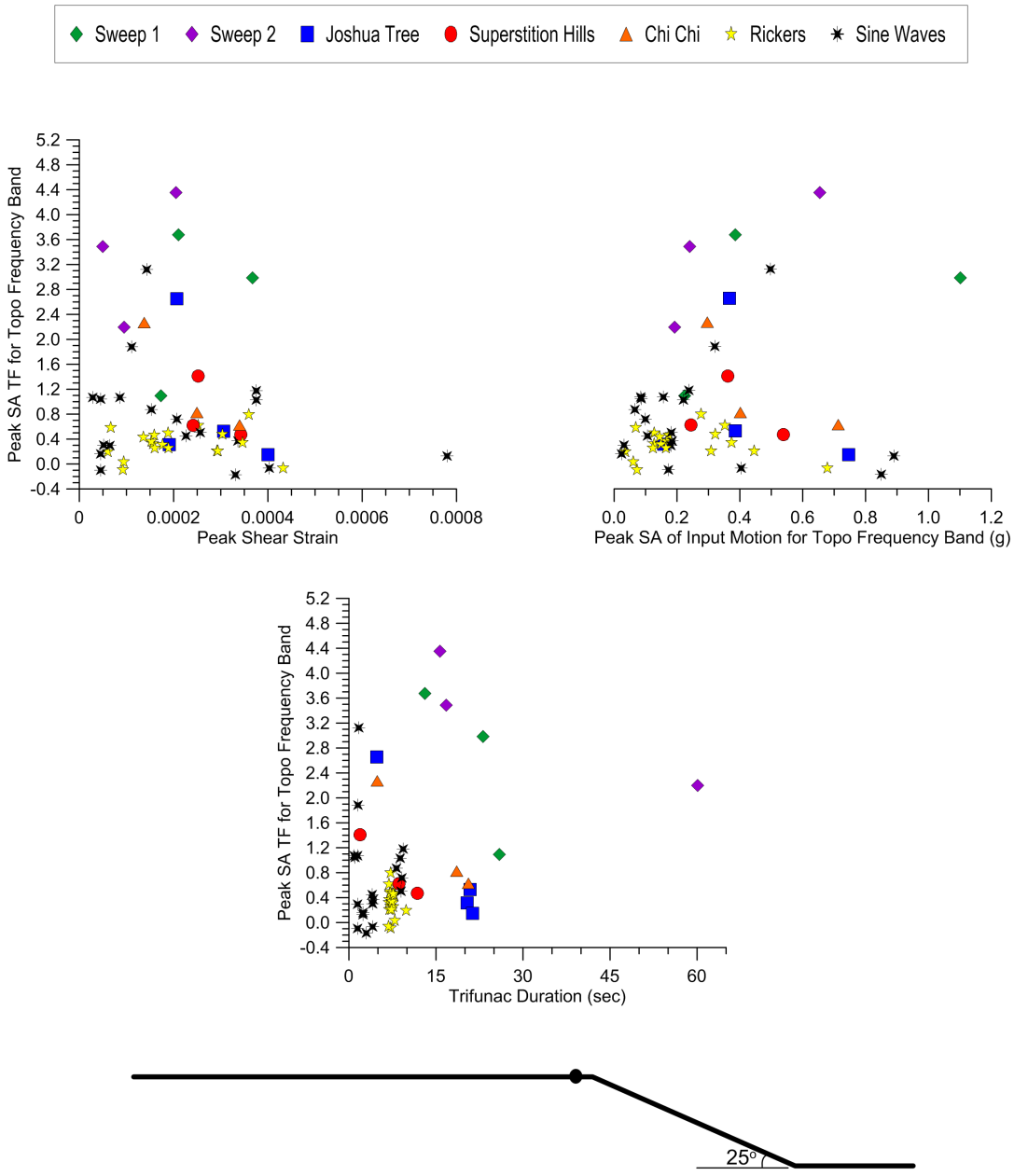

Figure 3.37: *bp SA TF* versus *PSS*, base input *bp SA* and Trifunac duration at the 25 degree slope crest for both slope prototypes.

measures, PGA and $bp\ SA$, are compared to the PSS (which relates to levels of induced non-linearity), the amplitude of base ground motion (which signifies the overall intensity of the motion — weak, strong etc.), and the motion duration. Here, as with the 30 degree slopes, there is no strong trend found between the levels of amplification (or deamplification) and these parameters, meaning their influence is, if not non-existent, negligible in comparison to other parameters.

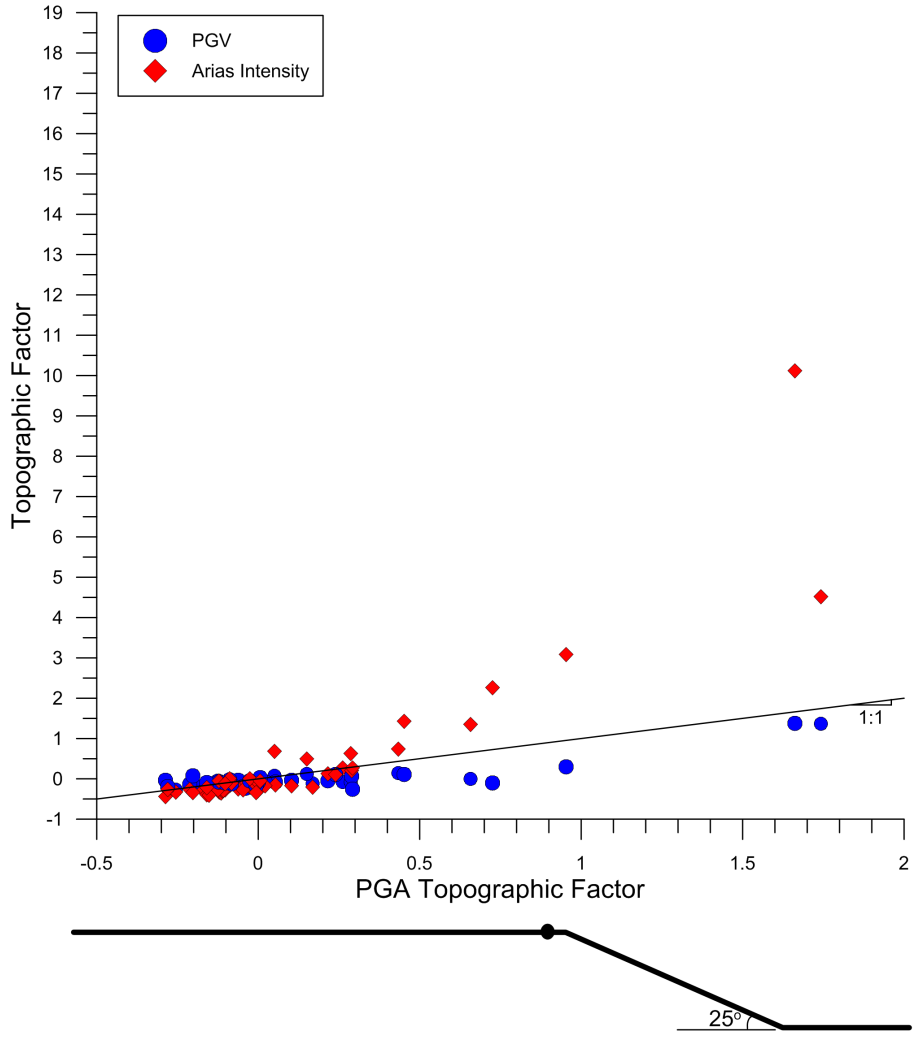

Figure 3.38: $PGV\ TF$ and $AI\ TF$ versus $PGA\ TF$ at the 25 degree slope crest for both slope prototypes.

The figures presented have used PGA and different measures of SA to highlight topographic effects. However, AI and PGV were intensity measures also utilized in the analysis. Figure 3.38 compares the $AI\ TF$ and the $PGV\ TF$ to the $PGA\ TF$ at the slope crest, as Figure 3.23 did for the 30 degree slopes. The pattern found here is similar to that of the 30 degree slopes, in that the $PGV\ TF$ tracks well with the $PGA\ TF$, whereas $AI\ TF$ tends to increase to values greater than the $PGA\ TF$ as the $PGA\ TF$ increases. Reasons for this increase in the $AI\ TF$ were discussed in the previous subsection and thus will not be repeated here.

It should again be emphasized that the results provided above are for two prototype 25 degree slopes. However, despite differences in size, the trends found on both slopes were well aligned with one another. This strengthens the findings presented and supports the normalization schemes utilized in analyzing the data. The similarities in the trends between the 30 and 25 degree slopes is also striking, especially when considering the consistency across four different slope prototypes. Some of the differences in the ground response that can be caused by a change in the slope inclination, however, were also highlighted in this subsection.

One final point that must be stressed is in regards to the topographic frequency. Modifying the topography from a slope angle of 30 degrees to 25 degrees resulted in changes in the slope shape and dimensions. However, the slope heights for the 30 and 25 degree slopes remained the same and thus, via Equation (3.4), the topographic frequencies were equivalent. Had Equation (3.5) been used, the topographic frequency would change due to the change in slope length. The results shown in the figures of this subsection supported the use of slope height to define the topographic frequency, in that topographic effects were found to be most significant for ground motion frequencies at or near the topographic frequency when defined this way.

20 degree slopes

The set of figures presented for the 25 and 30 degree slopes is provided in this subsection for the 20 degree slopes, the last of the three one-sided slopes analyzed. As in the previous subsection, similarities and differences between the results for this and the other slopes will be highlighted with more attention given to comparisons with the 25 degree slopes. The plots, trends, intensity measures and factors used in the previous subsections are again utilized in this subsection.

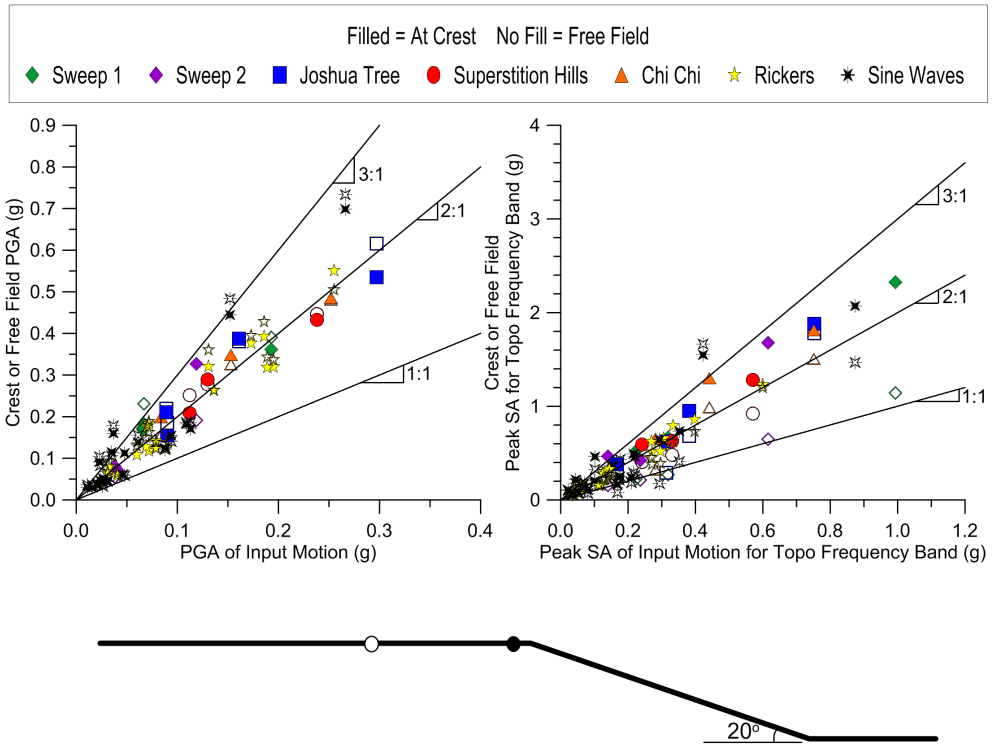

Figure 3.39: Free field and crest response versus input using PGA and $bp\ SA$ for the topographic frequency band for both 20 degree slope prototypes. The free field sensor (A20) is about 18.0 (9.0) meters from the crest sensor (A29), which is about 1.5 (0.75) meters behind the slope crest at 55g (at 27.5g).

The results presented in Figure 3.39 illustrate the relationship between the ground motion intensity at the substratum base, in the free field and at slope crest for the 20 degree slopes.

Aside from some minor variations, the PGA and $bp\ SA$ input and free field values are relatively similar to those for the 25 degree slopes. However, for a couple motions, a noted increase in the free field ground motion intensity is present. This may be a result of natural variation, or small differences in the ground motion introduced to the slopes. Although, this may also be a result of the now closer proximity of the free field sensor to the slope crest, meaning the free field sensor may exhibit some influence from the slope crest for those particular motions. This proves not to be the case, however, for most motions, which yielded similar results to the previous slopes.

Despite the similarities between the 30, 25 and 20 degree slopes at the base and in the free field, there is a marked difference in the response at the crest. Namely, for the 20 degree slopes, there is a significant reduction in the ground motion intensity. The PGA values at the crest range from 1.5 to 3 times the input, as opposed to up to 5 times found for the previous slopes. Furthermore, for a large number of ground motions, the PGA at the crest is less than that found in free field. This does not occur frequently when measuring intensity with the $bp\ SA$, however the range of values is again reduced from a range of 2 to 4.5 times for the 25 degree slopes to 2 to 3.5 times the input for the 20 degree slopes.

The relationship between the base, free field and crest ground motion frequency content is presented in Figure 3.40. The trend identified for the previous slopes is also found here for the 20 degree slopes, in that typically the MSF of the ground motion shifts towards the topographic frequency in moving from the free field to the crest. The magnitude of that shift, however, is reduced as evidenced by the right plot in Figure 3.40. The shift is, in general, greater if the MSF is farther from the slope topographic frequency, until MSF values in the free field drop below the site frequency. This was also true of the other slopes. However at it's maximum, the $MSF\ TF$ reaches a value of only 0.3, compared to a value of 0.55 for the 25 degree slopes representing a 25% decrease.

Similar overall data trends to those identified for the 25 and 30 degree slopes are revealed in Figures 3.39 and 3.40 for the 20 degree slopes. However, in both cases a reduction in the impact of topography is also established (i.e., lower amplitudes and smaller shifts in frequency

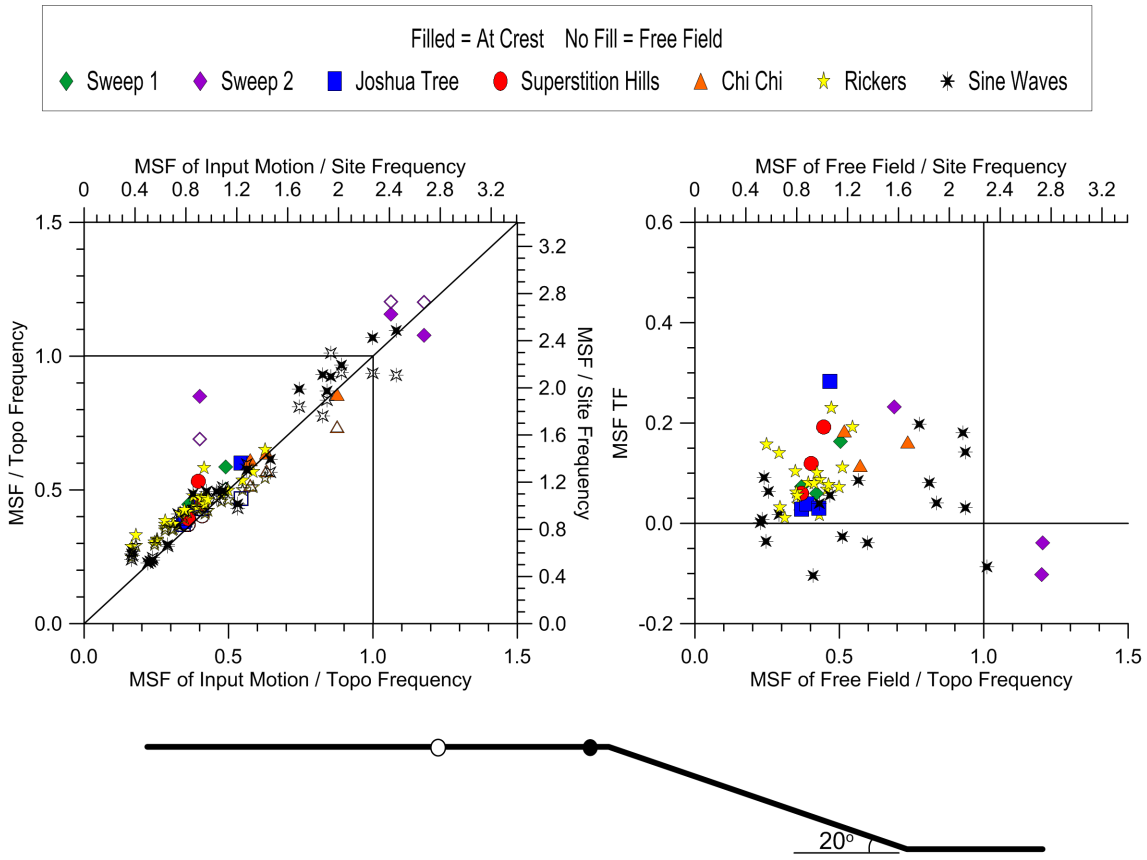

Figure 3.40: Free field and crest versus input MSF normalized by the topographic and site frequencies for both 20 degree slope prototypes. The free field sensor (A20) is about 18.0 (9.0) meters from the crest sensor (A29), which is about 1.5 (0.75) meters behind the slope crest at 55g (at 27.5g).

content). The same pattern is found in studying the correlation between the ground motion frequency content and levels of amplification at the slope crest, depicted in Figure 3.41. Here, as with the other slopes, there is a trend towards greater levels of amplification (higher TFs) as the MSF approaches the topographic frequency of the slope. However, the magnitude of the effects is considerably weaker. The TFs reach maximum values of roughly 0.9 and 2.8 for PGA and $bp\ SA$, respectively, compared to values of 1.75 and 4.4 for the 25 degree slopes. Additionally, there are a greater number of ground motions for which no amplification or even deamplification of the free field response occurred; true of both intensity measures.

The reduction in topographic effects measured at the slope crest is particularly apparent

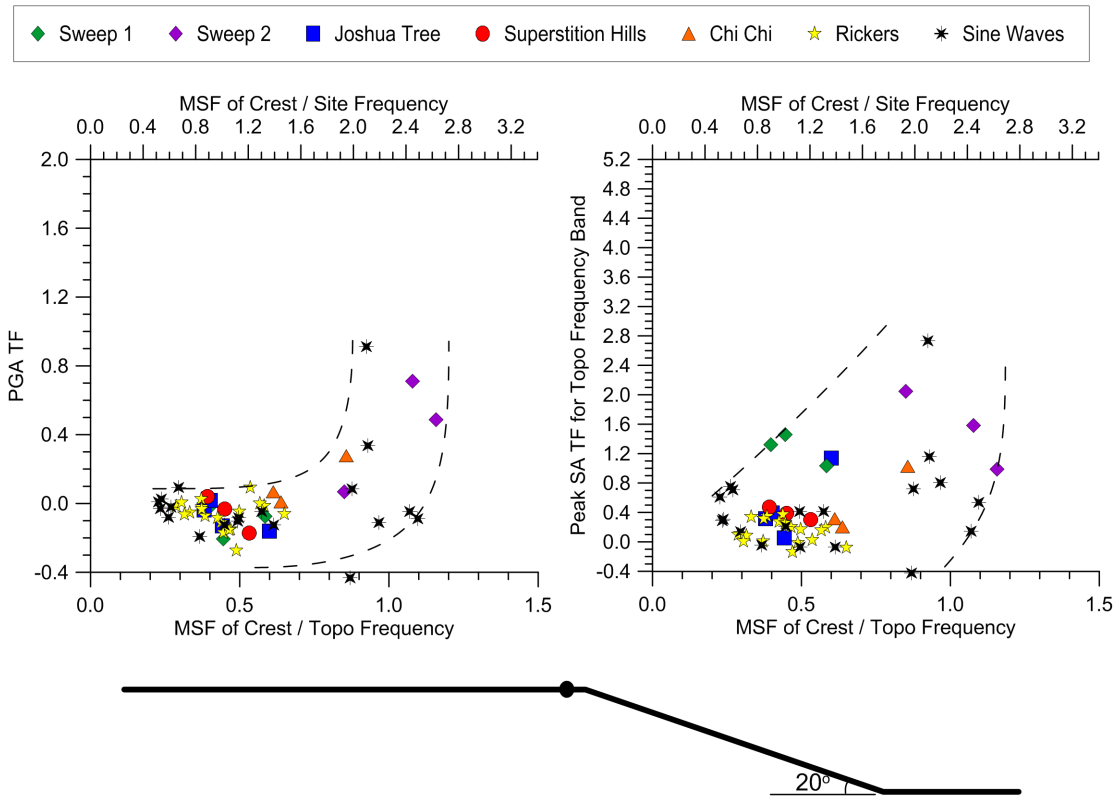

Figure 3.41: *PGA TF* and *bp SA TF* for the topographic frequency band versus *MSF* normalized by the topographic and site frequencies at the crest for both 20 degree slope prototypes.

when examining the mean *SA TF* and *SA AA* spectra plotted in Figure 3.42. For both plots, the *STR* motions again exhibit greater levels of amplification than the *WTR* motions across most frequencies, although the separation between the averages of these two subsets of motions is greatly reduced compared to the other slopes. Peak values for the *SA TF* spectrum are roughly 0.6 and 0.15 for the *STR* and *WTR* motions, respectively, whereas values of 1.2 and 0.3 were determined for the 25 degree slopes.

Despite a difference in amplitude, the overall shape of the *SA TF* spectrum is similar to the spectra for the other slopes. However, the *SA AA* spectrum is notably different. Before, a distinct, significantly amplified 'hump' could be identified near the topographic frequency with a peak value greater than (*STR* motions) or nearly equal to (*WTR* motions)

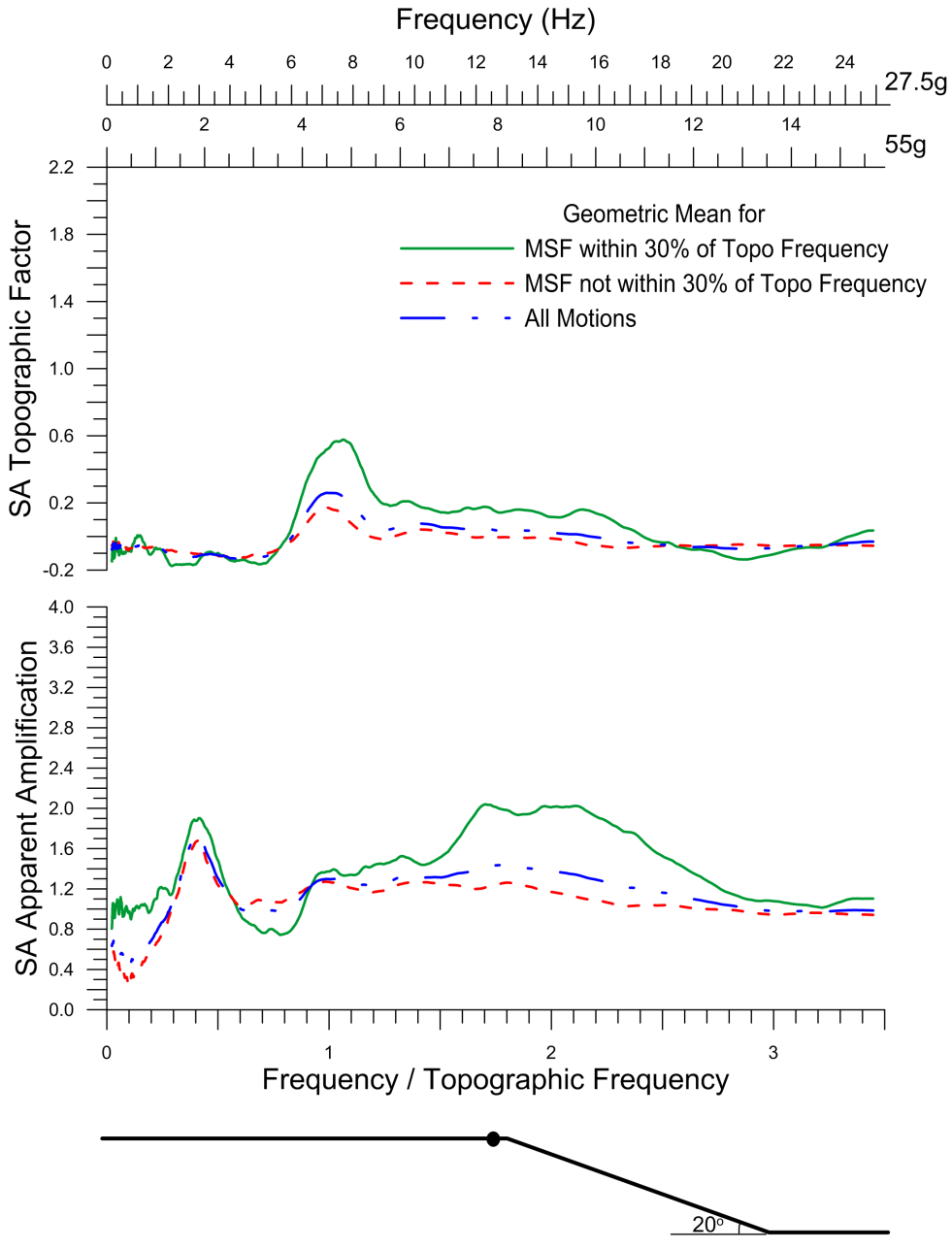

Figure 3.42: Geometric mean for the $SA\ TF$ and $SA\ AA$ spectra at the slope crest for both 20 degree slope prototypes, grouped according to the MSF of the ground motion.

the peak observed at the site frequency. Here, however, a peak value is non-existent at the topographic frequency, while naturally the peak value at the site frequency is maintained. These spectrum features clearly indicate a crest response dominated by site effects, with minimal contribution from topographic effects, for the 20 degree slopes.

While Figure 3.42 provided a glimpse of topographic effects for all motions, STR motions and WTR motions at the slope crest, Figures 3.43, 3.44 and 3.45 allow the effects of the three motion subsets to be viewed across the entire slope. Each figure contains the $SA\,TF$ spectrum for one of the three motion groupings. All three figures exhibit a similar spatial pattern (i.e., peak and weaker responses occur at the same sensor locations). However, as previously mentioned, the mean representing all motions is more similar to the behavior of the WTR motions because the WTR motions represent a larger percentage of the total motions analyzed. Consequently, the discussion is concentrated on the differences between the responses of the WTR and STR motions, and comparison of these motion subsets to the other slopes.

The geometric mean of the STR motions for each of the marked sensor locations is given in Figure 3.44. From this plot, it's evident that topographic effects can still be quite prevalent, even though they are not as significant at the crest (Figure 3.42). In this case, the peak response is captured near the middle of the slope face (marked by the pink and blue sensors), with a peak mean $SA\,TF$ value of roughly 1.4. While this is less than peak values found for the 30 degree slopes, it is similar to that of the 25 degree slopes and is significant, representing a 140% increase over the free field. Once again, amplification is greatest near the slope topographic frequency and declines moving to higher and lower (to the point of deamplification) frequencies. The sensors associated with the peak response are roughly 9.5 (4.75) meters and 16.5 (8.25) meters, measured horizontally, in front of the slope crest for the 55g (27.5g) prototype. Moving away from the two peak sensors in either direction results in a decline in the level of amplification, with, on average, a larger response captured at the slope toe, 30.3 (15.15) meters from the slope crest at 55g (27.5g). The response continues to diminish moving over and behind the slope crest to the free field sensor, which is 19.5 (9.75)

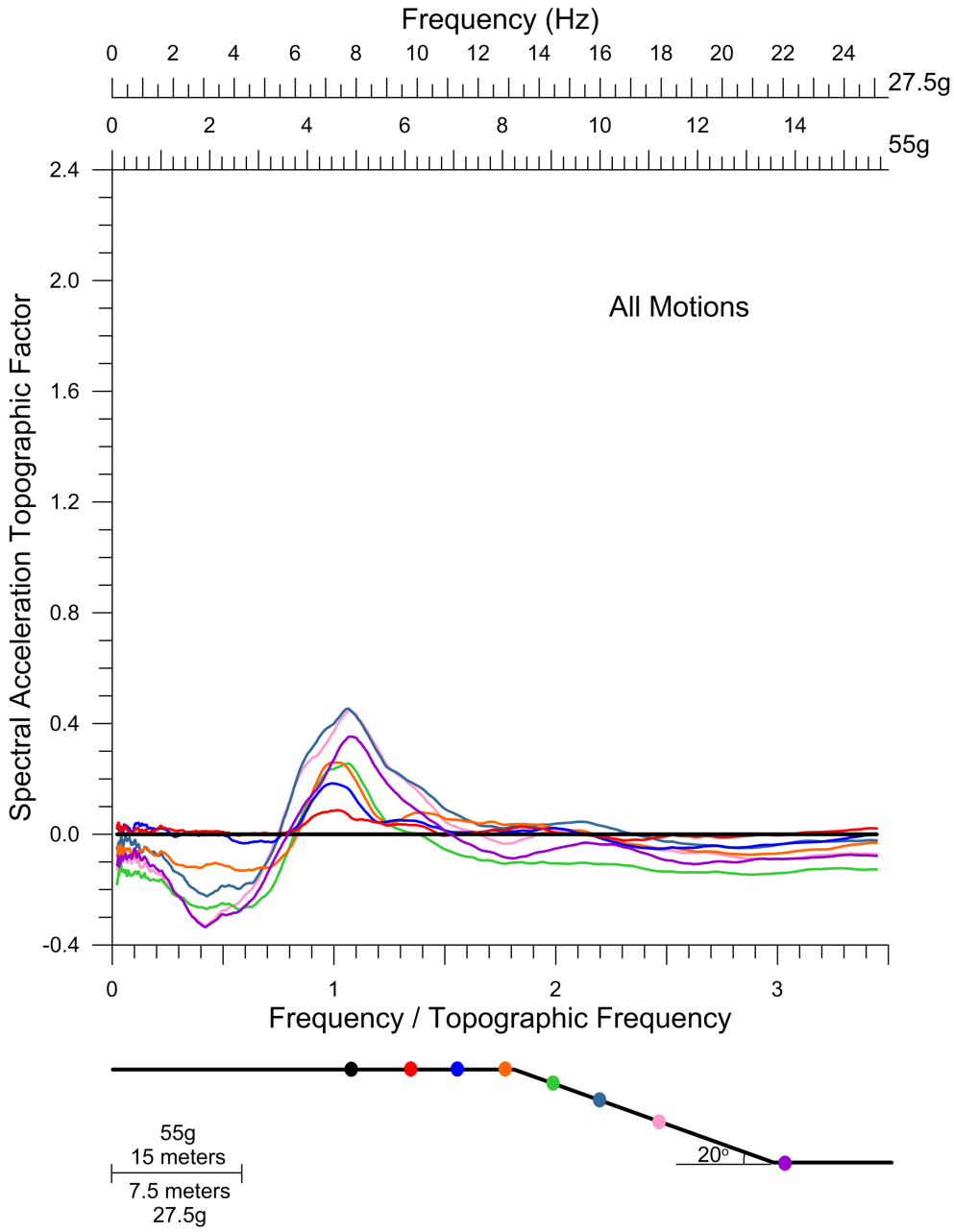

Figure 3.43: Geometric mean of the $SA\ TF$ spectrum versus normalized frequency for all motions at different near surface sensor locations on the 20 degree slope. Spectra are color-coded to match sensor locations, which are provided at scale. The free field sensor is represented in black. Both prototypes are considered in calculating mean values.

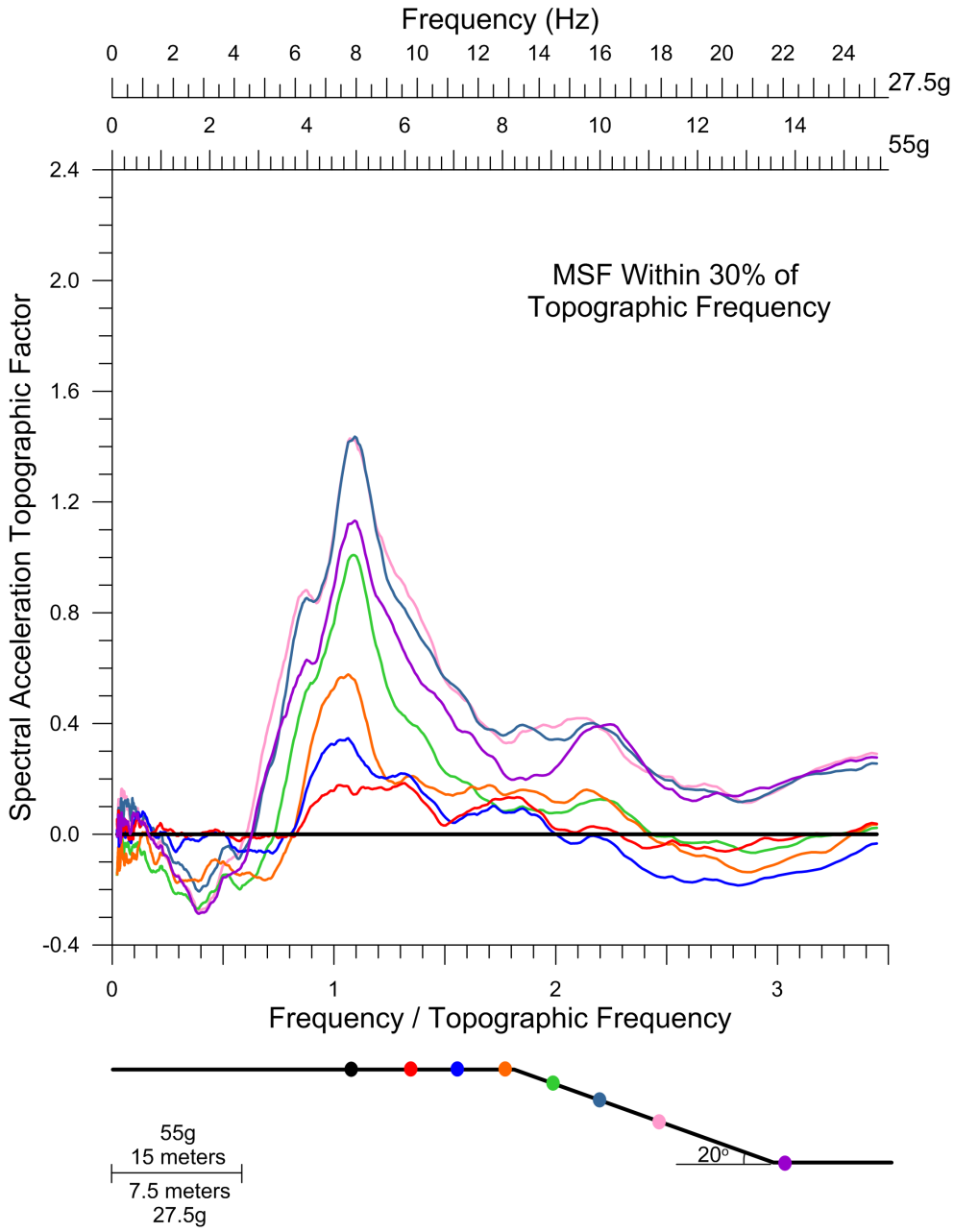

Figure 3.44: Geometric mean of the SA TF spectrum versus normalized frequency for STR motions at different near surface sensor locations on the 20 degree slope. Spectra are color-coded to match sensor locations, which are provided at scale. The free field sensor is represented in black. Both prototypes are considered in calculating mean values.

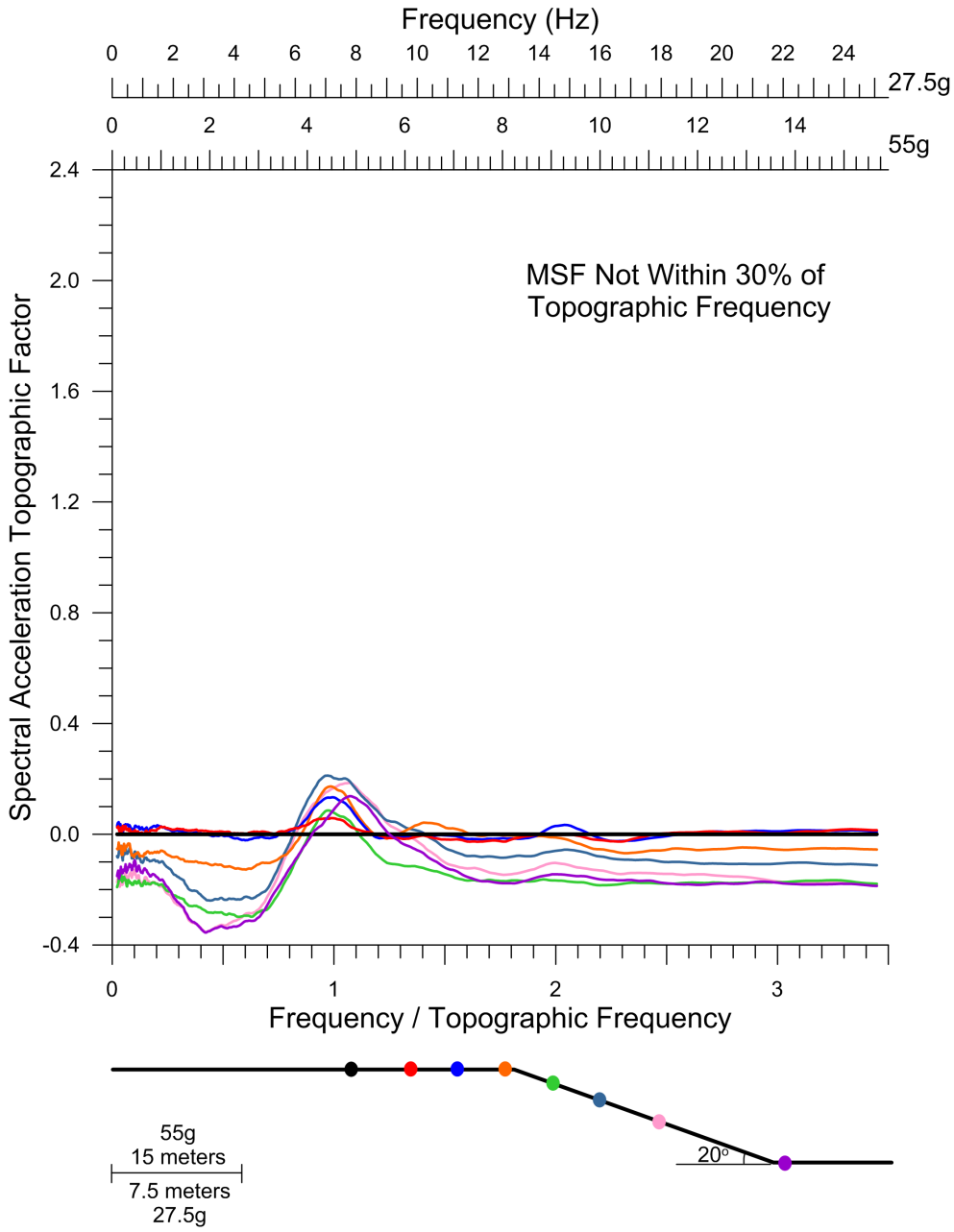

Figure 3.45: Geometric mean of the SA TF spectrum versus normalized frequency for WTR motions at different near surface sensor locations on the 20 degree slope. Spectra are color-coded to match sensor locations, which are provided at scale. The free field sensor is represented in black. Both prototypes are considered in calculating mean values.

meters from the crest at 55g (27.5g). In comparing the 20 degree to the 25 degree slopes, a shift in the peak response, and subsequent spatial area influenced by topographic effects, further down the slope face (towards the toe) is found here. This is similar to the behavioral change witnessed when comparing the 30 and 25 degree slopes.

The spatial variation of the WTR motions, depicted in Figure 3.45 differs from that of the STR motions. Peak values are found in the same locations as the STR motions, however, at other locations the pattern changes. The next tier in amplification level below the peak values includes the sensor at the toe, at the crest, and just behind the crest (purple, orange and blue markers). An even weaker response is recorded for the sensor just in front of the crest (in green) and adjacent to the free field sensor (in red). The reason, however, for this variation is likely less to do with topographic effects and more to do with natural variation in the substratum and sensor recordings. The peaks at all of these locations are within roughly 10% of one another and the maximum represents an amplification of only 20% over the free field. Across most frequencies in the spectra, the response is either comparable to that of the free field or deamplified. From these observations, it is evident that for the WTR motions, the effect of topography on the ground motion amplitude is minimal for the 20 degree slopes.

The spatial distribution for the subset of motions highlighted above is similar to that depicted in Figure 3.46, 3.47 and 3.48. In these figures, however, the $SA\ AA$ spectrum is provided, which through normalization by the base, allows both site and topographic effects to be observed. The amplification of ground motion due to site effects is best represented by the free field sensor, depicted in black. The more similar the response at other sensors is to that of the free field sensor, the more likely the ground motion is dominated by site effects. As mentioned previously, however, site effects will vary as the depth of the soil profile changes. This contributes to the different levels of amplification exhibited by the sensors along the slope face and at the toe near their respective site frequencies (which are similar to the site frequency of the free field sensor), as illustrated by the $SA\ AA$ spectra depicted.

At the site frequency, represented by the first peak in the $SA\ AA$ spectrum, the amplification pattern is similar for both the STR and WTR motions. The response of the free

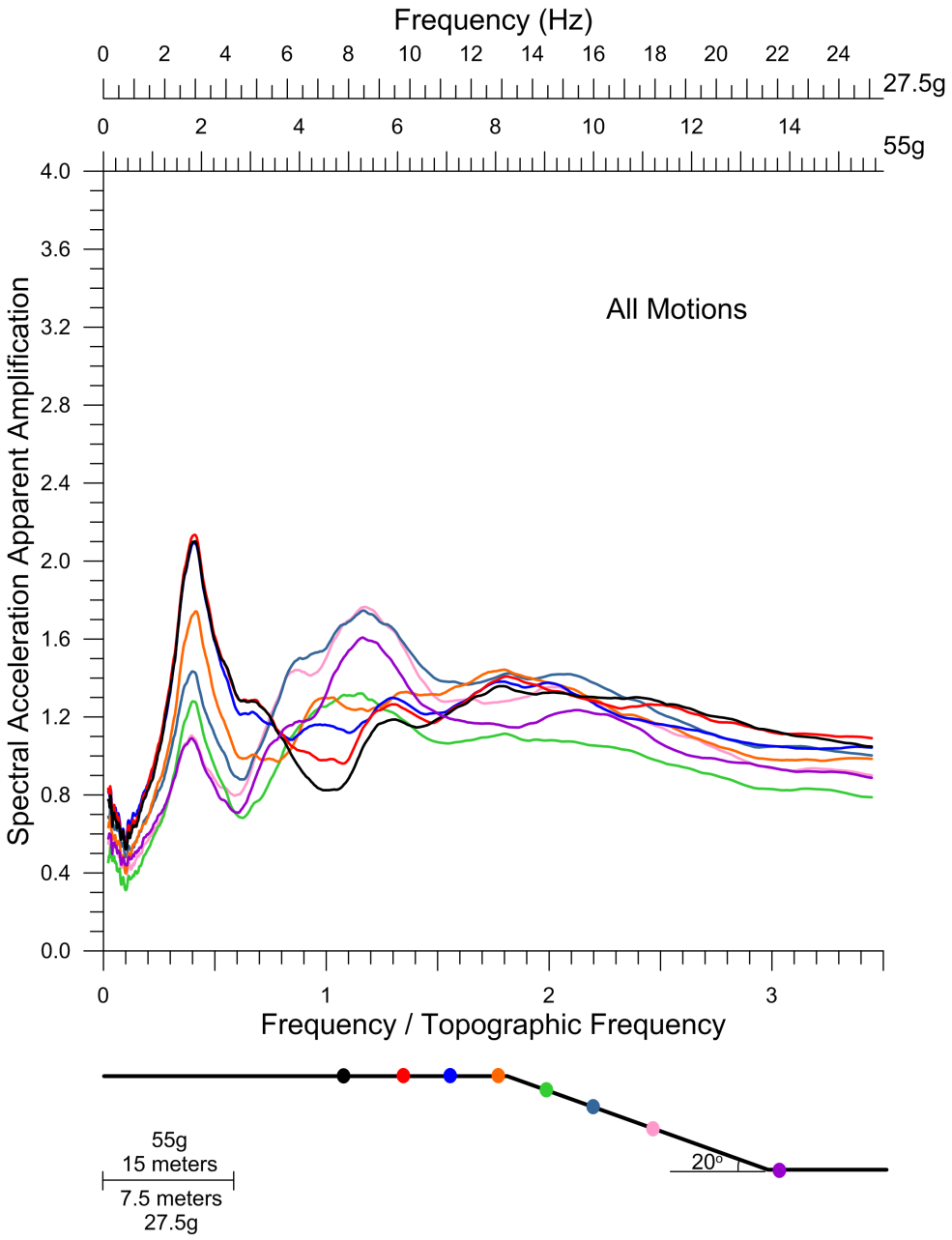

Figure 3.46: Geometric mean of the SA AA spectrum versus normalized frequency for all motions at different near surface sensor locations on the 20 degree slope. Spectra are color-coded to match sensor locations, which are provided at scale. The free field sensor is represented in black. Both prototypes are considered in calculating mean values.

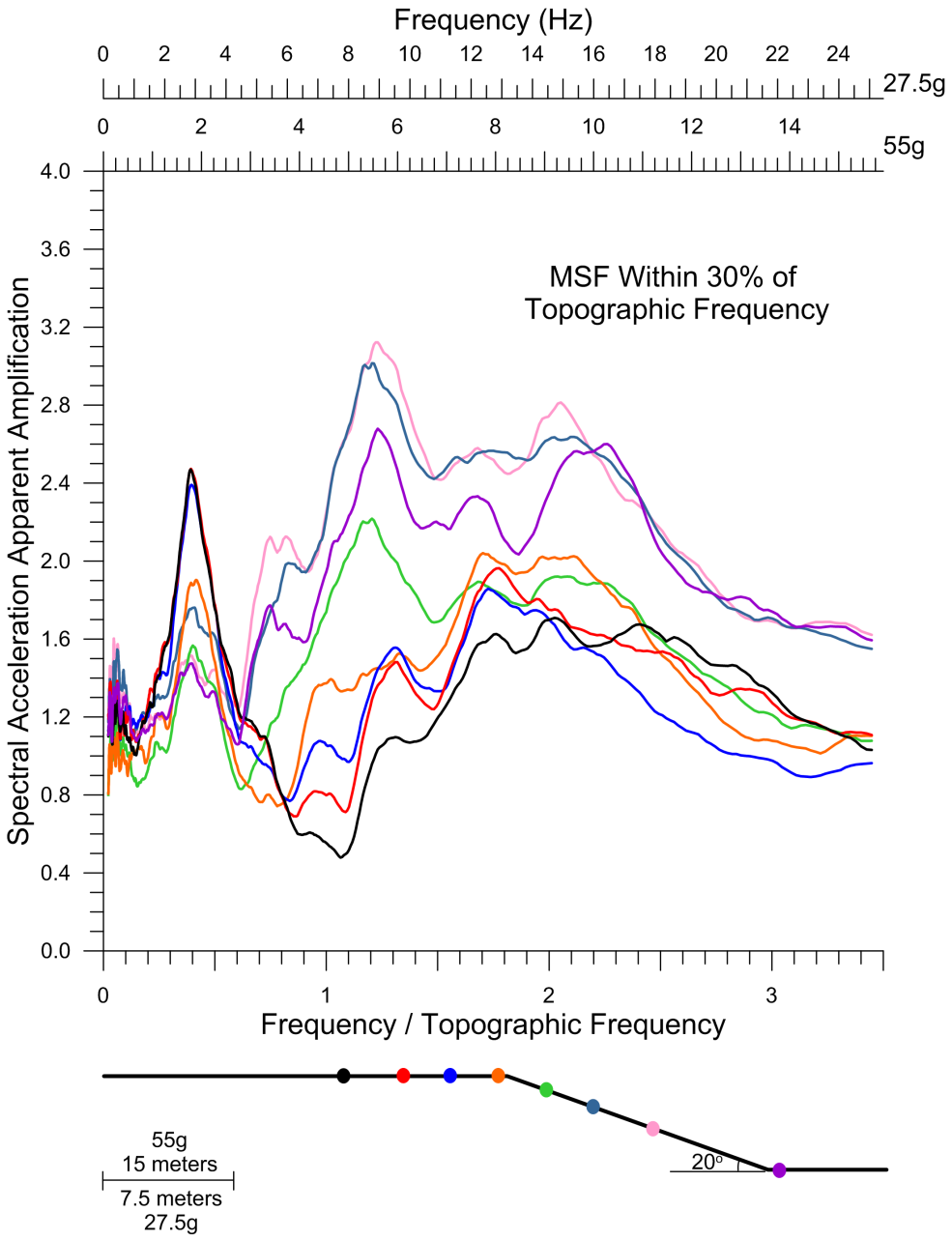

Figure 3.47: Geometric mean of the SA AA spectrum versus normalized frequency for STR motions at different near surface sensor locations on the 20 degree slope. Spectra are color-coded to match sensor locations, which are provided at scale. The free field sensor is represented in black. Both prototypes are considered in calculating mean values.

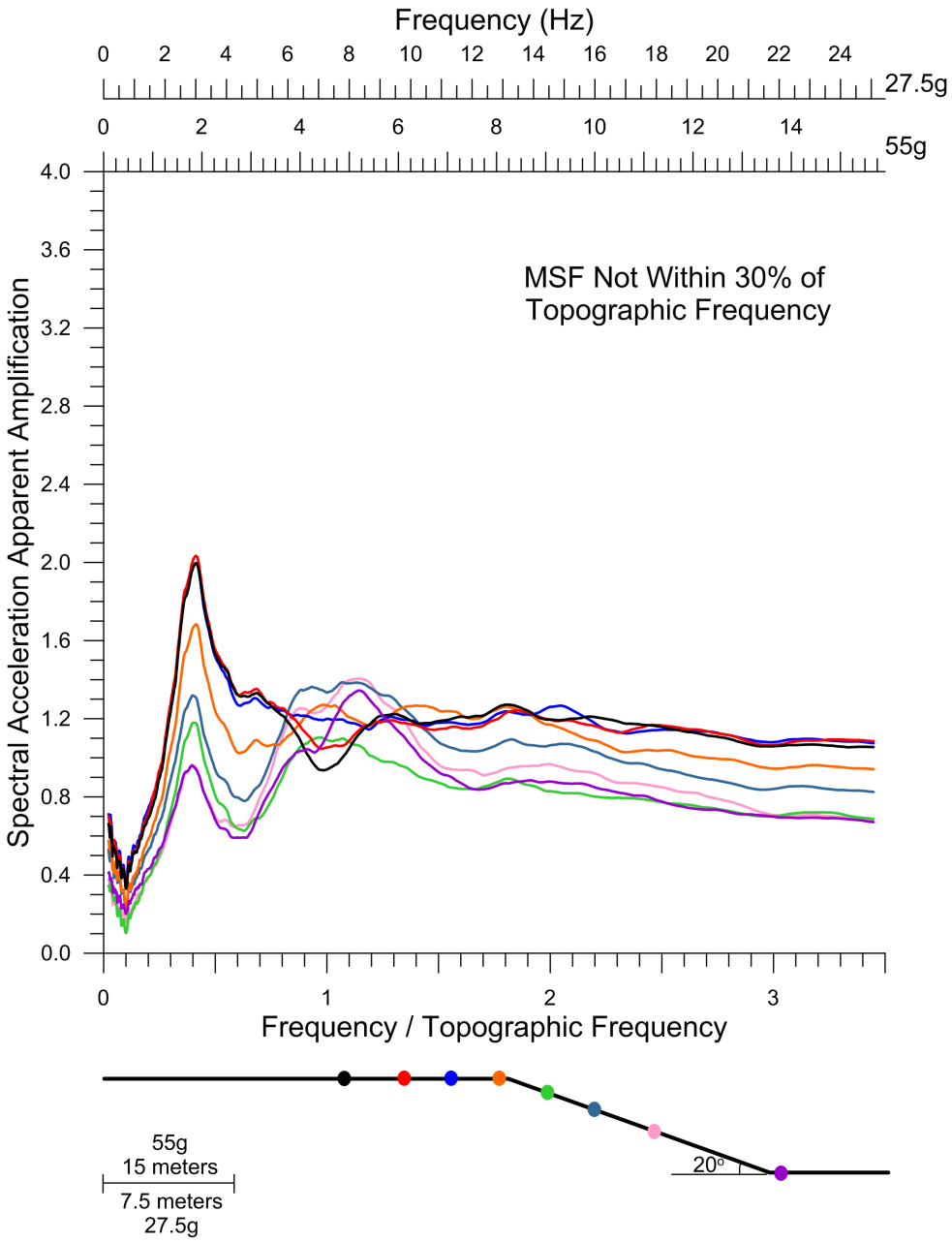

Figure 3.48: Geometric mean of the SA AA spectrum versus normalized frequency for WTR motions at different near surface sensor locations on the 20 degree slope. Spectra are color-coded to match sensor locations, which are provided at scale. The free field sensor is represented in black. Both prototypes are considered in calculating mean values.

field sensor (in black) is indistinguishable from that of the next two adjacent sensors (in red and blue). Moving to the right, the level of amplification is reduced at the slope crest (in orange), before diminishing further on the slope face, with slightly weaker intensity for the sensor nearer to the crest (in green) than the sensor towards the middle of the slope (in blue). Amplification levels are smallest further down the slope face (in pink) and at the slope toe (in purple). Thus, generally speaking, the level of site amplification decreases moving from higher to lower elevation (i.e., moving from the full slope height down to the slope toe).

Near the slope topographic frequency, there is a stark difference between the responses of the STR and WTR motions, and the spatial pattern is more similar to that found for the $SA\,TF$ spectrum, as expected. As with the $SA\,TF$ spectrum, the mean peak intensity occurs at the sensor locations near the middle of the slope (in pink and blue). For the STR motions, the level of amplification diminishes moving in either direction, with a stronger response captured at the slope toe. Moving to the left, the intensity continues to decline moving over the crest back to the free field sensor. As with the other slopes, levels of amplification found near the topographic frequency are greater than those occurring at the site frequency, for the STR motions. However, this amplification results from a combination of site and topographic effects. Excluding the contribution of site effects at the topographic frequency, the contribution from topographic effects alone would not be greater than the average peak site amplification measured near the site frequency. This differs from the findings for the other slopes. For the WTR motions, the response is almost completely dominated by site effects. Amplification levels at most sensors are comparable to or less than those found for the free field sensor and topographic effects are minimal.

The spatial variation in ground motion intensity described above is confirmed for two intensity measures in Figure 3.49. The plots consist of TFs for both the PGA and the *bp* SA, calculated at the near surface sensors across the 20 degree slopes. Both plots reveal similar observations to those already highlighted for the 20 degree slopes and those previously discussed for the other slopes. Namely, for WTR motions, ground motion intensity is weaker than STR motions, and deamplification, or minimal amplification is found at nearly all

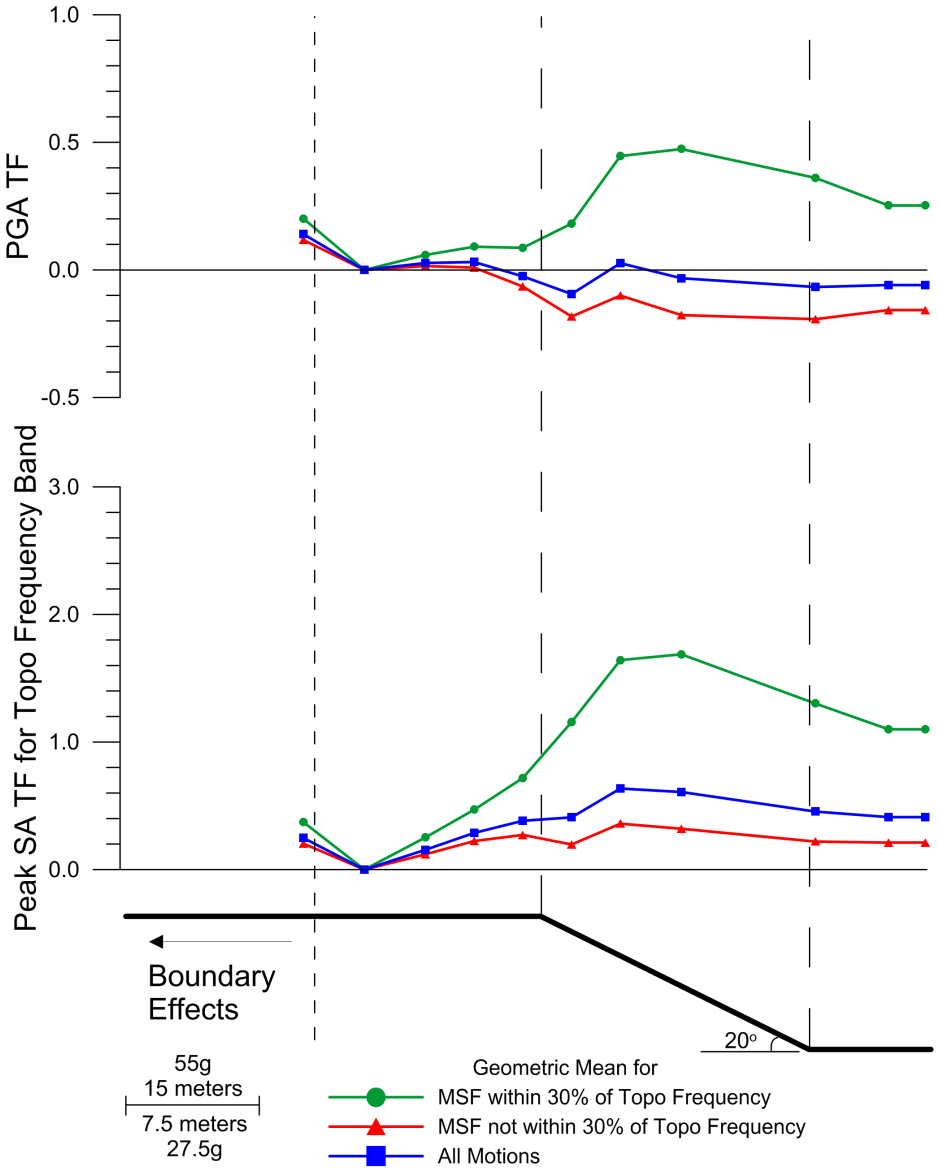

Figure 3.49: Geometric mean of $PGA\ TF$ and $bp\ SA\ TF$ for the topographic frequency band versus distance across the surface of the 20 degree slope for both prototypes grouped according to the MSF of the ground motion.

sensors considering the $PGA\ TF$ and the $bp\ SA\ TF$, respectively. Also, amplification determined using the $bp\ SA\ TF$ is greater, and subsequently, the perceived spatial extent of topographic amplification is also greater. This is a result of the frequency specific nature of the topographic modification of ground motion. In using a frequency specific intensity measure, the full impact of topographic effects is captured. Regardless of the intensity measure used, however, the spatial variations in intensity remains the same for the STR motions, in that peak levels of amplification occur near the middle of the slope and decrease moving in either direction, with greater values at the slope toe than in the free field behind the crest.

While the previous plots highlighting the spatial variation of topographic effects and ground motion intensity used mean values for different subsets of ground motions, Figure 3.50 provides spatial information for each ground motion individually. The trend here is the same as that discovered for the other slopes, in that generally an increase in topographic amplification results in an increase in the spatial area that is amplified. Although, for the 20 degree slopes, little to no amplification, and often deamplification was found for a large number of motions, particularly when considering the $PGA\ TF$. Naturally, the spatial influence is non-existent for these motions, resulting in L_1 and L_2 values equal to zero. Thus, less motions are available to confirm a trend, as illustrated by the left two plots in Figure 3.50. Regardless, the trend of the motions that do exhibit topographic effects is similar, with both the L_1 and L_2 threshold values reached for both TFs. The threshold values for the 20 degree slopes are 19.5 (9.75) and 30.3 (15.15) for the 55g (27.5g) prototype for L_1 and L_2, respectively. The L_1 threshold is consistently reached by all motions with $PGA\ TF$ values above 0.3 and $bp\ SA\ TF$ values greater than 1.3. The L_2 threshold is attained consistently for motions with $PGA\ TF$ values greater than 0.1 and $bp\ SA\ TF$ values greater than 0.9. This is consistent with the concentration of energy on the slope face depicted earlier, in that the L_2 threshold is achieved at lower levels of intensity than the L_1 threshold despite a threshold length 10.8 (5.4) meters greater at 55g (27.5g).

Trends and correlations between different ground motion parameters and topographic

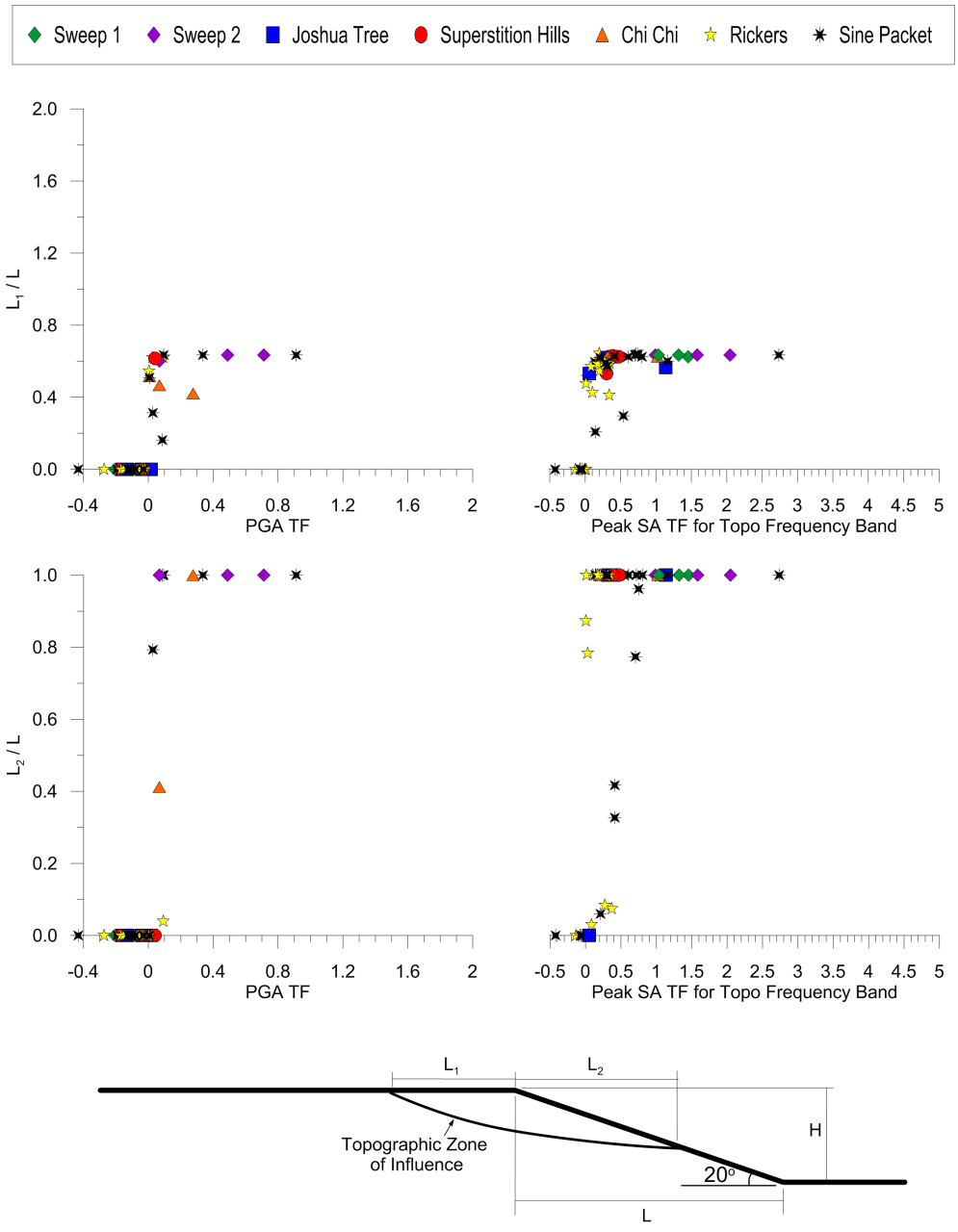

Figure 3.50: Normalized distance versus $PGA\ TF$ and $bp\ SA\ TF$ for the topographic frequency band at the slope crest for both 20 degree slope prototypes. Lengths L_1 and L_2 represent distances behind and in front of the crest, respectively, influenced by topography.

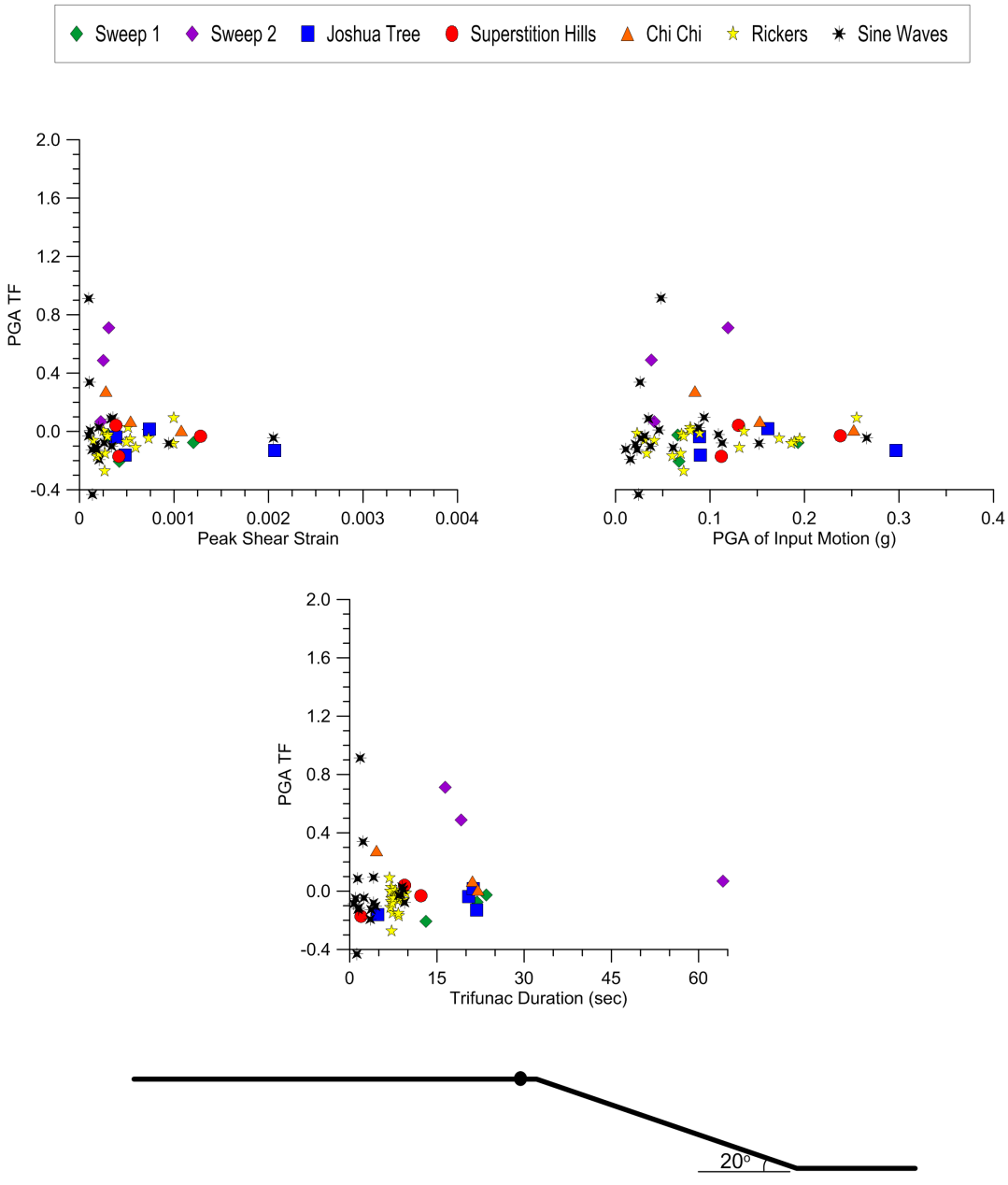

Figure 3.51: $PGA\,TF$ versus PSS, base input PGA and Trifunac duration at the 20 degree slope crest for both slope prototypes.

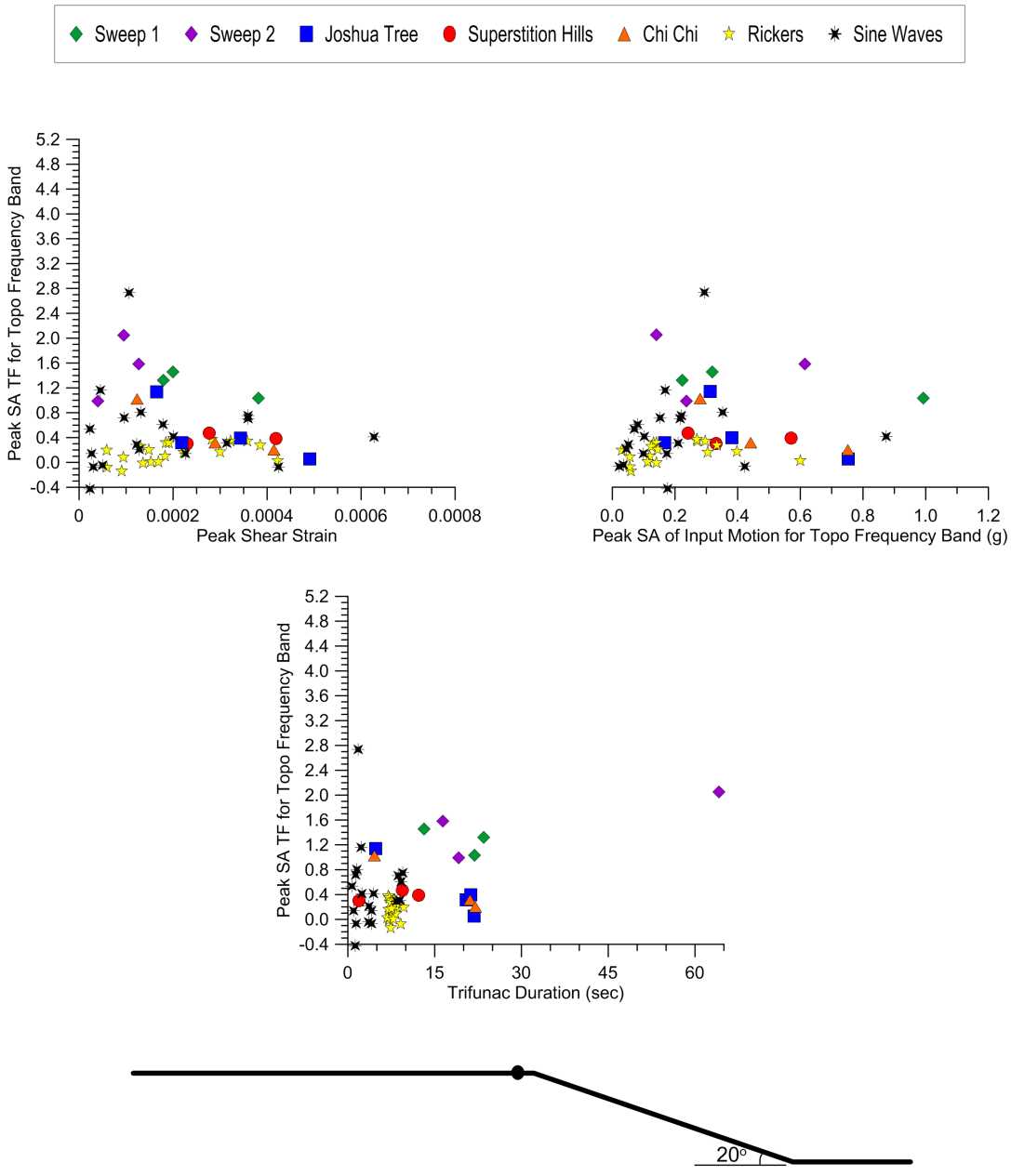

Figure 3.52: *bp SA TF* versus *PSS*, base input *bp SA* and Trifunac duration at the 20 degree slope crest for both slope prototypes.

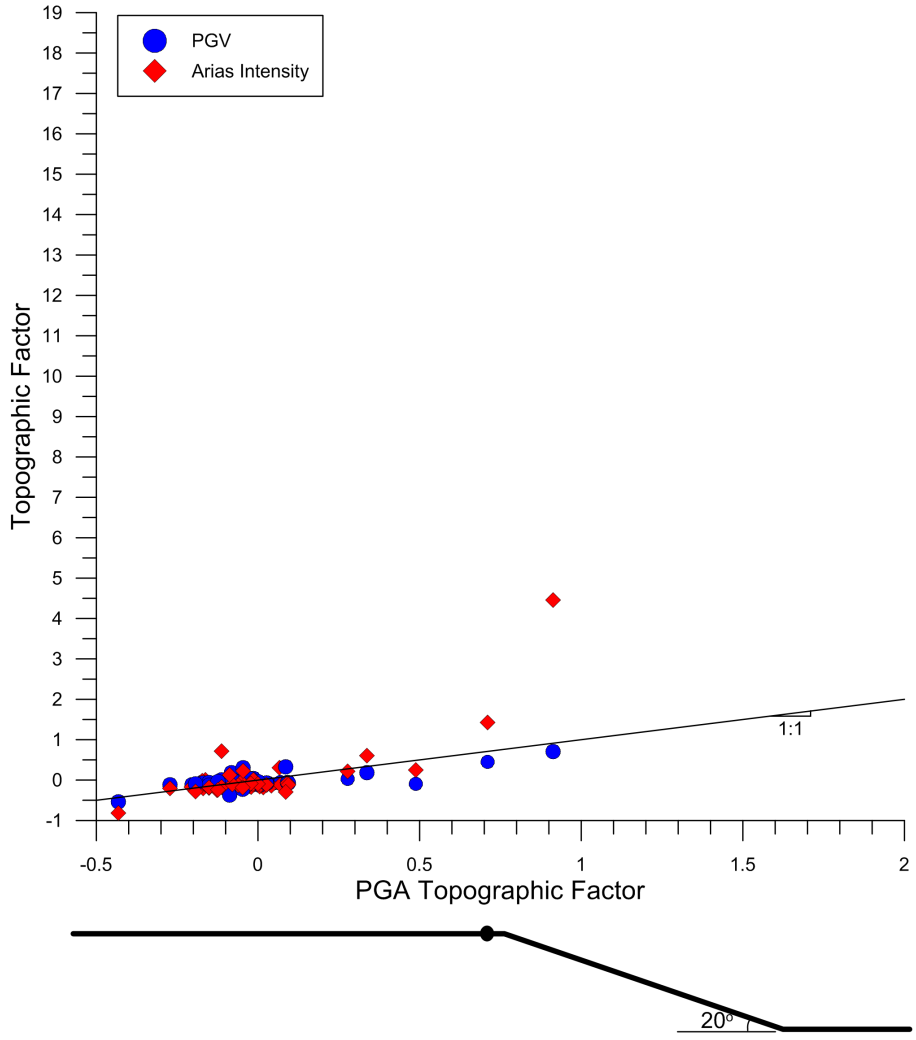

Figure 3.53: *PGV TF* and *AI TF* versus *PGA TF* at the 20 degree slope crest for both slope prototypes.

effects have been highlighted in this subsection for 20 degree slopes. These have shared similarities with the trends identified for the other slopes considered. Figures 3.51 and 3.52 provide results that are also consistent with the findings for the other slopes. Both the $PGA\ TF$ and the *bp* $SA\ TF$ are compared to the PSS, Trifunac duration and base input amplitude for each individual ground motion at the slope crest. Again however, the three parameters appear unrelated to the influence of topography on ground motion.

The final plot of this subsection compares the TFs for PGA, which has been used extensively throughout the previous plots, to those determined for PGV and AI at the slope crest. The $PGV\ TF$ values are mostly similar to $PGA\ TF$ values, tracking along the 1:1 reference line. The $AI\ TF$ values tend to increase to values greater than the $PGA\ TF$ as levels of topographic amplification increase (i.e., as the TFs increase). Despite lower overall magnitudes of the TFs, these patterns are consistent with those found for the other two slopes and have already been discussed.

3.3.3 Trends for the Three Slope Inclinations

The results of analysis for a single ground motion and for all the ground motions introduced to the 30, 25 and 20 degree slopes have been given. The figures presented have revealed a number of significant characteristics and relationships between different ground motion parameters and their influence on topographic and site effects. While similarities and differences between the individual interpretations of the results for each of the slope geometries were outlined above, direct comparison of the ground response of the different slopes has not been provided.

This section presents results for all common ground motions introduced to the three slope configurations. The same ground motion parameters introduced above are utilized in the analysis results given here. Additionally, comparison of the behavior of the slopes and the flat ground response is also provided. Axis scales used in the previous plots are maintained in the figures in this subsection where appropriate.

Figures 3.54, 3.55 and 3.56 depict the $SA\ TF$ and $SA\ AA$ spectra for all ground motions, STR motions and WTR motions. The spectra are plotted against frequency normalized by

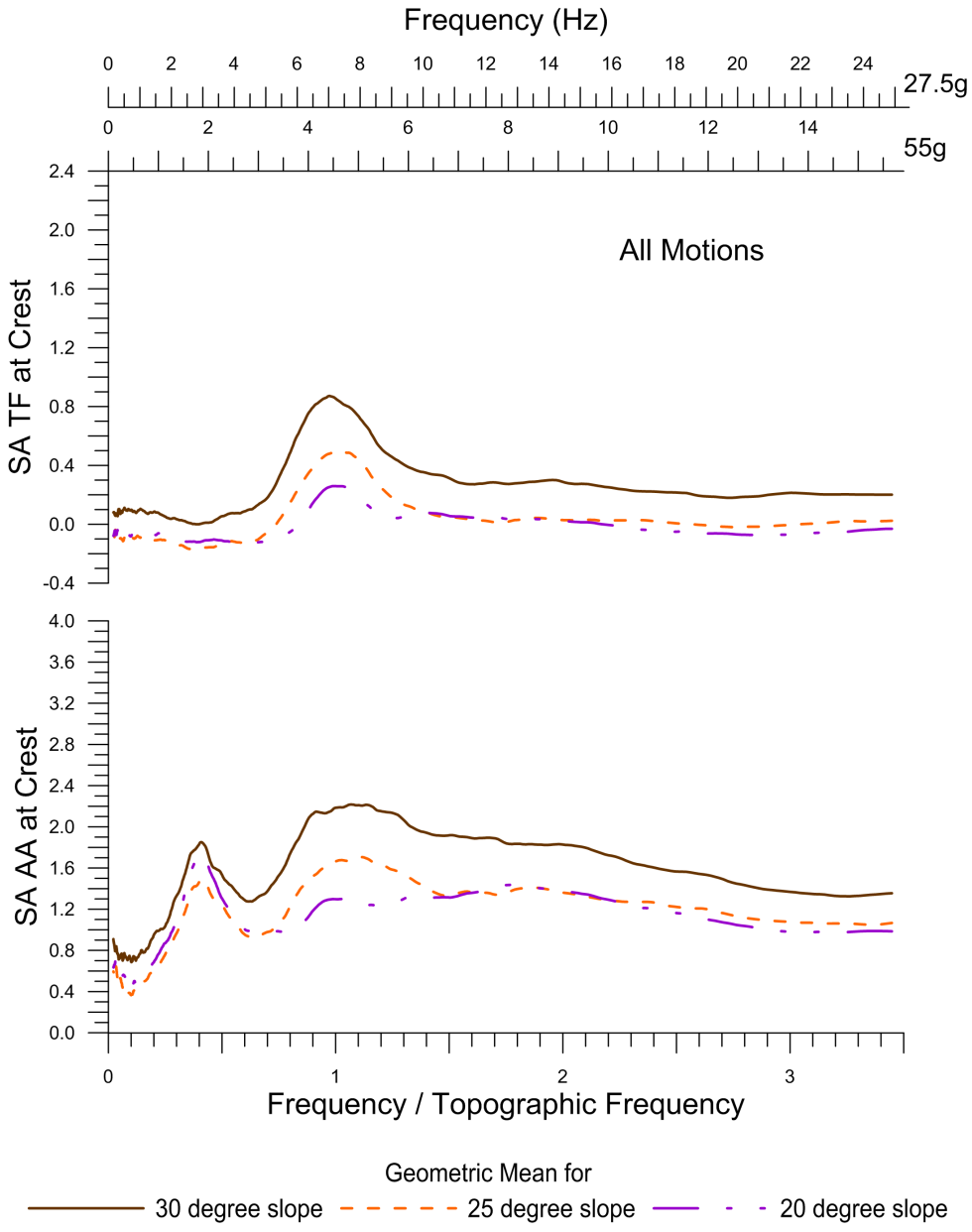

Figure 3.54: Geometric mean for the $SA\ TF$ and $SA\ AA$ spectra versus normalized frequency for all ground motions at the slope crest of the 30, 25 and 20 degree slopes. Data from both prototypes is included in calculating the mean for each slope inclination.

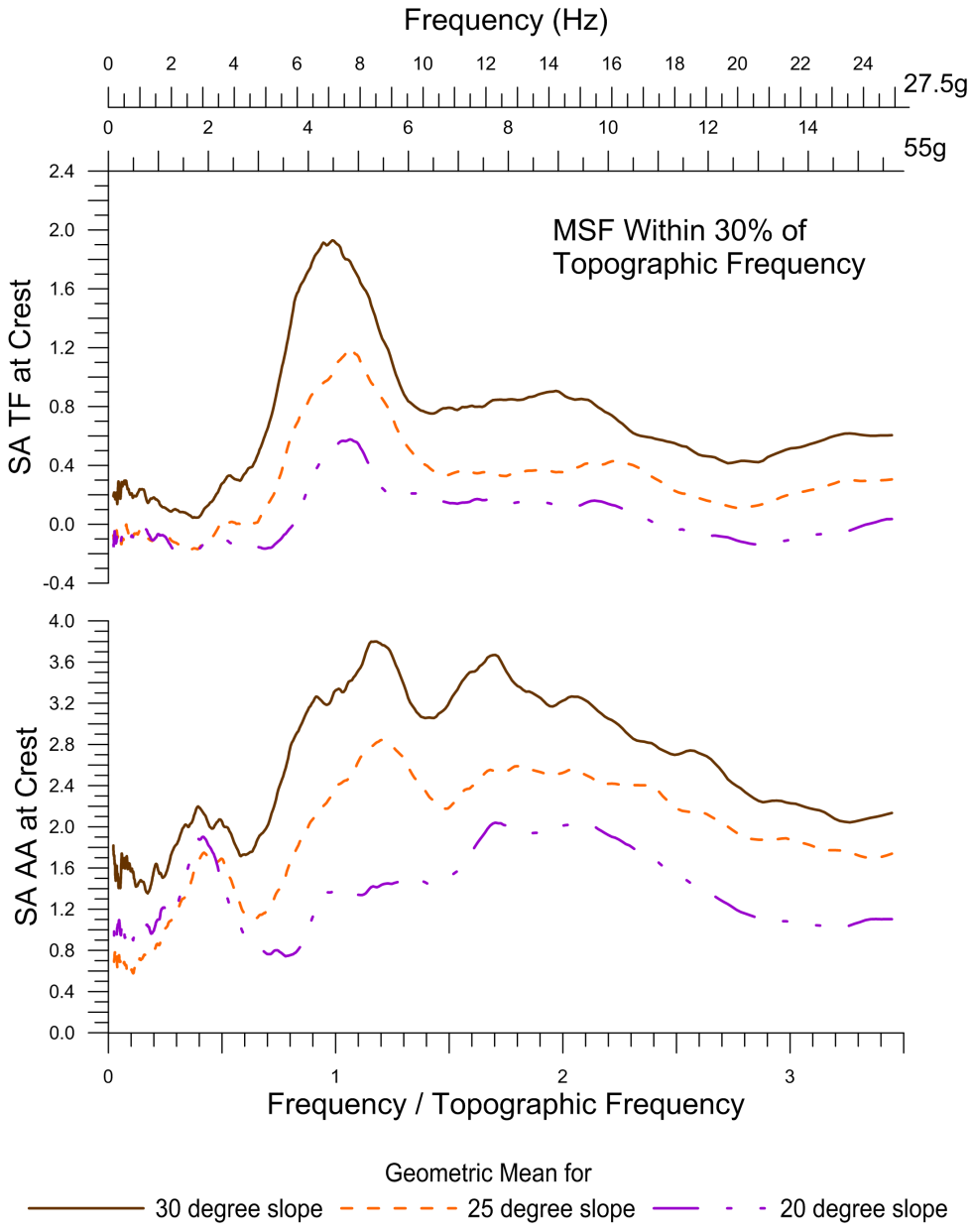

Figure 3.55: Geometric mean for the $SA\ TF$ and $SA\ AA$ spectra versus normalized frequency for the STR ground motions at the slope crest of the 30, 25 and 20 degree slopes. Data from both prototypes is included in calculating the mean for each slope inclination.

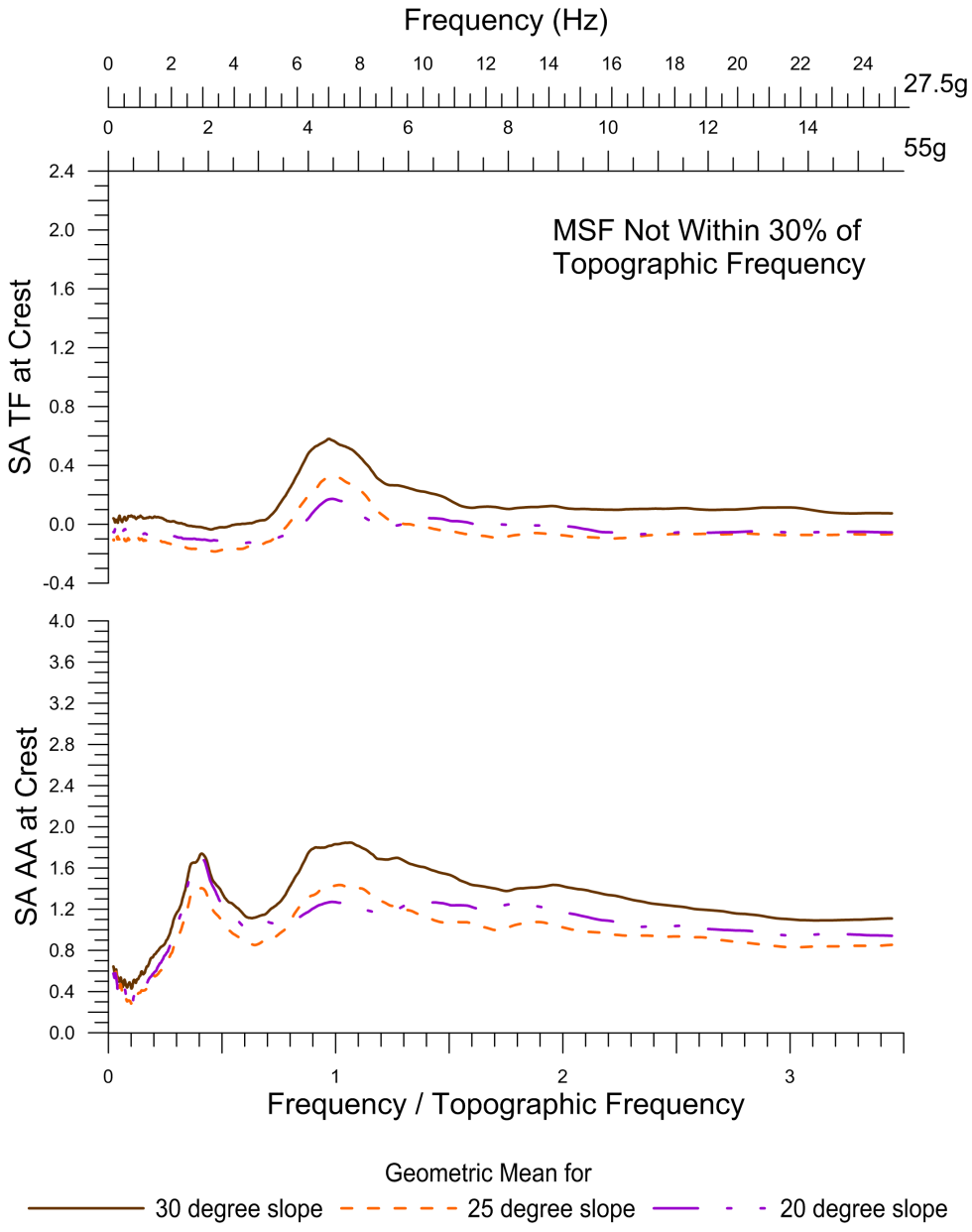

Figure 3.56: Geometric mean for the $SA\ TF$ and $SA\ AA$ spectra versus normalized frequency for the WTR ground motions at the slope crest of the 30, 25 and 20 degree slopes. Data from both prototypes is included in calculating the mean for each slope inclination.

the topographic frequency for the 30, 25 and 20 degree slopes and represent the mean response at the slope crest. The motions are grouped in the same manner for the different slopes, with 'all motions' representing the common set of ground motions introduced to each of the slope geometries. The figures are similar to Figures 3.12, 3.27 and 3.42 previously presented. However, instead of plotting the three ground motion subsets (all, STR and WTR) together for one slope geometry, the response for all three slope configurations is plotted together for each subset.

The mean spectra depicted in Figure 3.54 for all motions can be calculated by using a weighted average of the spectra for the STR and WTR motions. Because the WTR motions represent nearly three quarters of the ground motions included, the measured response for all motions is more likely to be numerically similar to that of the WTR motions. For this reason, it is more informative to focus on the spectrum plots for the STR and WTR motions. The spectra for all motions is included, however, for completeness and to show that the overall qualitative response portrayed by the spectra is not significantly altered by grouping the motions. That is, the trends relative to the different slope geometries are similar in considering all motions, STR motions or WTR motions, despite quantitative differences.

For both the STR and WTR motions, the response captured at the crest of the different slopes considered is qualitatively similar, but quantitatively different. As the slope angle decreases from 30 down to 20 degrees, the ground motion intensity weakens and topographic effects are diminished. The magnitude of this reduction, however, depends upon the characteristics of the ground motion, evidenced by the difference in mean responses for the STR and WTR motions.

The shape of the $SA\ TF$ spectra is the same as depicted in previous subsections for both subsets of motions, with peak values near the topographic frequency that decrease moving to higher and lower frequencies on the spectrum. For the STR motions, average peak values of roughly 1.9, 1.2 and 0.6 are determined for the 30, 25, and 20 degree slopes, respectively, while average peak values of 0.55, 0.3 and 0.15 are found for the WTR motions. Thus, levels of topographic amplification (amplification over the free field) decrease by 70% (from 190

to 120) and 60% (from 120 to 60) as the slope inclination is lowered from 30 to 25 to 20 degrees for the STR motions. For the WTR motions, decreases of 25% and 15% occur as the slope inclination decreases from 30 to 25 degrees and 25 to 20 degrees, respectively. Because WTR motions are less influenced by the presence of topography, it is logical that the impact of changing the slope geometry would be smaller on these motions than it would for STR motions, which are heavily influenced by topography.

The $SA\ AA$ spectra at the slope crest also have the same defining features discussed in previous subsections. Notably, the spectra have an initial peak near the site frequency of the sand layer beneath the slope crest and another broader peak near the topographic frequency for the slopes. For the 30, 25 and 20 degree slopes, average peak values of 2.2, 1.8 and 1.9 are found near the site frequency, with peak values of 3.8, 2.8 and 1.4 (this last number is not truly associated with a peak as one does not exist) near the topographic frequency, for the STR motions. For the WTR motions, average peak values are 1.7, 1.4 and 1.7 near the site frequency and 1.7, 1.4 and 1.3 near the topographic frequencies. The fluctuations in the peak response near the site frequency is likely due to natural variation in the recordings for the different accelerometers (the crest sensor is different for each slope geometry), although the response is typically slightly higher for STR motions than for WTR motions. Near the topographic frequency, the mean peak amplification decreases 100% and 140% as the slope inclination changes from 30 to 25 degrees and 25 to 20 degrees, respectively, for STR motions while only declining by 30% and 10% for the WTR motions.

The decreases in the peak response near the topographic frequency that occur from decreasing the slope inclination have significant implications for the overall ground response at the slope crest. In comparing the two peaks, the peak near the topographic frequency is 160% greater than the peak near the site frequency (using AAs of 3.8 and 2.2) for the 30 degree slope STR motions; dropping to 100% greater and then 50% less for the 25, and 20 degree slopes, respectively. This indicates that for the STR motions, the effects of topography have a greater impact on the ground motion amplitude than site effects for the 30 degree slopes. This impact lessens and is then weaker than site effects moving to the

25 and 20 degree slopes, respectively. Therefore, a decrease in slope inclination not only minimizes the influence of topographic effects, but can also impact the balance between the components of ground motion controlling the ground response.

In the above paragraphs and in the previous sections of this chapter, there has been mention of variation in the accelerometer recordings across the surface of the model configurations that is not influenced by changes in topography. These fluctuations can occur for a number of reasons, including small differences in sensor alignment (i.e., the sensors may be rotated 1 or 2 degrees from one another), heterogeneity of the sand substratum (the aim was for a homogeneous medium, but this is nearly impossible to achieve) and fluctuations in the electronics themselves (i.e., tendencies of the accelerometers). As a result, even for a flat ground surface, the recordings at the different near surface sensor locations vary. Using PGA as a ground motion intensity measure, the average coefficient of variation for the suite of ground motions introduced to the flat ground model was roughly 9% for the near surface accelerometers. This is not insignificant considering that the values should be roughly equivalent. Natural variation in the recorded response can have implications for what can or should be deemed a significant level of amplification (or deamplification) when considering topographic effects through normalization by a free field or base sensors. By comparing the ground surface response of the flat ground model to the relevant responses of the different slopes, the effects of sensor variation can be investigated, as is illustrated by Figures 3.57 and 3.58.

Figure 3.57 depicts the geometric mean of the $SA\ AA$ spectrum for the sensor locations highlighted on the flat ground model. For comparison, the mean $SA\ AA$ spectrum for the free field sensor of the 30, 25 and 20 degree slopes is provided. The number of ground motions included in calculating the mean is reduced from 54 (used in all figures for the different slopes) to 46, which is the number of common motions introduced to both the flat ground and slope configurations. The spectra calculated for the free field sensor are in black, with a solid line representing the mean flat ground response, and various dashed lines representing the three slope geometries.

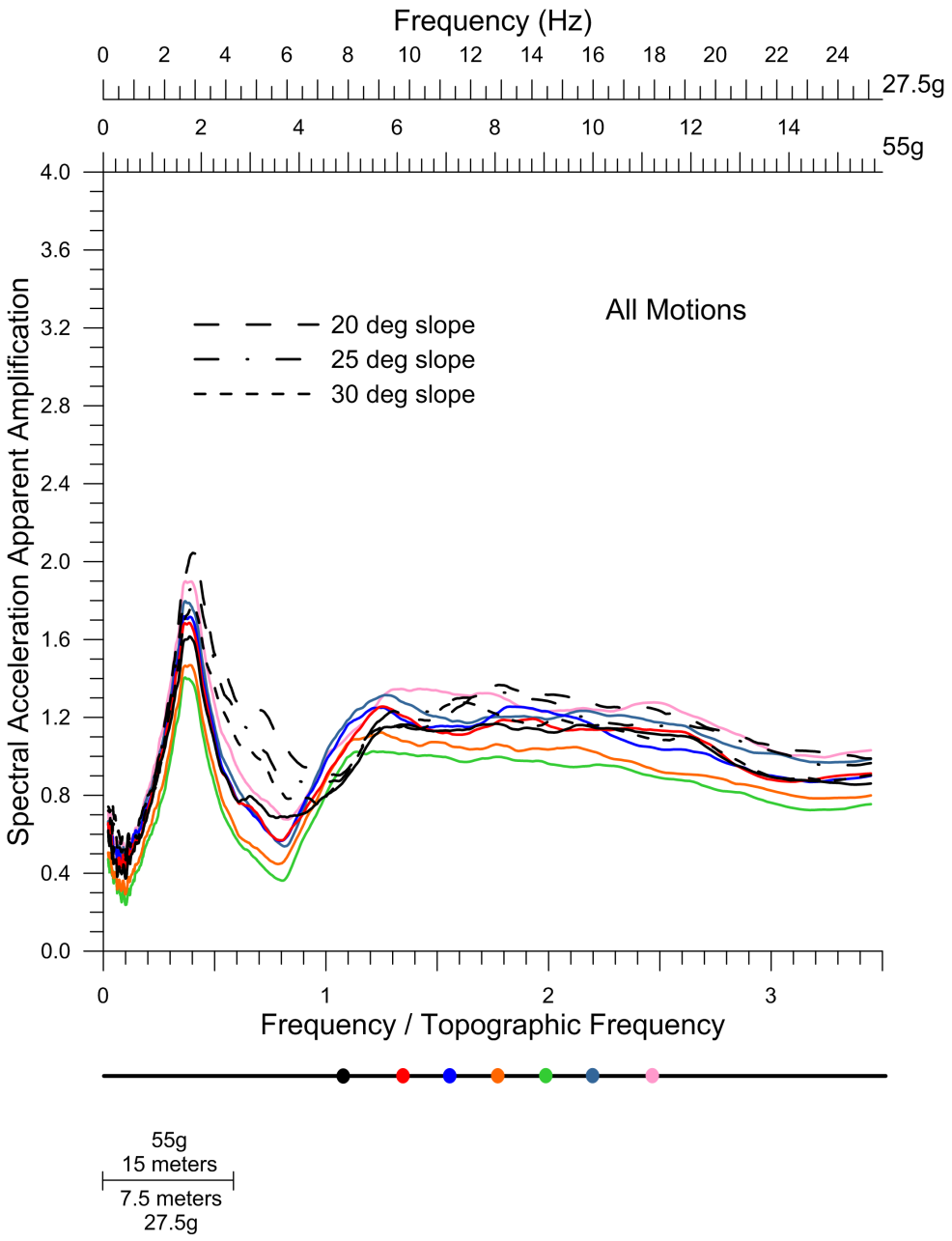

Figure 3.57: Geometric mean of the $SA\ AA$ spectrum versus normalized frequency for all motions at different near surface sensor locations for the flat ground model configuration compared to the free field sensor spectra for the 30, 25 and 20 degree slopes. Spectra are color-coded to match sensor locations, which are provided at scale. The free field sensor is represented in black. Both prototypes are considered in calculating mean values.

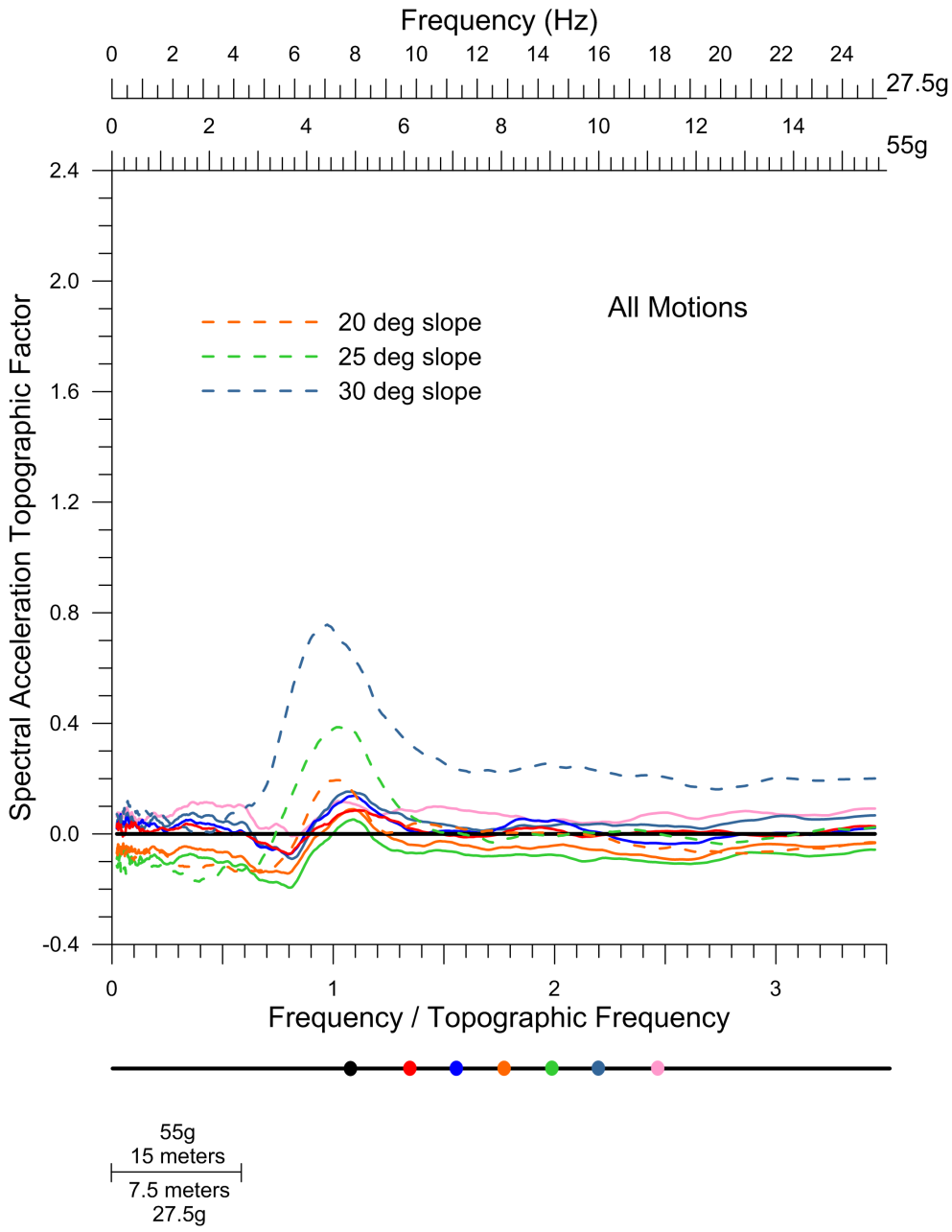

Figure 3.58: Geometric mean of the $SA\ TF$ spectrum versus normalized frequency for all motions at different near surface sensor locations for the flat ground model configuration compared to the spectra of the crest sensors for the 30, 25 and 20 degree slopes. Spectra are color-coded to match sensor locations, which are provided at scale. The free field sensor is represented in black. Both prototypes are considered in calculating mean values.

Peak values (near the site frequency) are 1.75, 1.85 and 2.05 for the 30, 25 and 20 degree slopes, respectively, compared to a peak value of 1.6 for the same sensor near the flat ground surface. The increase in the peak response is likely a result of closer proximity of the slope crest to the free field sensor. In changing the slope geometry from 30 to 25 to 20 degrees, the free field sensor location did not change, but the crest moved closer to the free field sensor each time. Thus the average response may be slightly influenced by topographic amplification at the slope crest. This may also help explain the increased response at frequencies between the site and topographic frequencies (between normalized values of 0.44 and 1.0 on the x-axis) for the different slopes. However, despite this possibility, the range in peak $SA\ AA$ values for the free field sensor (from 1.6 to 2.05) is no greater than the natural variation of the sensors across the flat ground model, whose peak values range from 1.4 to 1.9. Additionally, with the exception of the 20 degree slope, the peak values observed for the slopes fall within the range of peak values found for the flat ground model (i.e., 1.4 to 1.9) and for all cases the spectra are similar at higher and lower frequencies. Therefore, the overall fit between the $SA\ AA$ spectra of the flat ground model and slope free field sensors is acceptable. The differences in the spectra, however, should be considered in interpreting the analysis results.

Figure 3.57 suggests that topographic effects on ground motion amplitude would be slightly minimized at frequencies between the site and topographic frequency. Figure 3.58, on the other hand, demonstrates that topographic effects would be slightly amplified for a small range of frequencies slightly greater than the topographic frequency. Figure 3.58 provides the mean $SA\ TF$ spectra for the marked sensor locations across the flat ground model, using the same free field sensor for normalization as previously stated (in black). For reference, the $SA\ TF$ spectra for the 30, 25 and 20 degree slope crests are also given (in blue, green and orange). In this case, normalization by the free field results in less variation across the flat ground surface than normalization by the base did in the previous figure. Including all frequencies, mean $SA\ TF$ values range from roughly -0.2 to 0.15, which is close to the mean peak value of 0.2 determined at the crest of the 20 degree slope. Therefore, 75% of the perceived average amplification at the 20 degree slope crest could be considered insignificant.

This indicates that a threshold value for amplification (or deamplification) should be applied when interpreting topographic effects for this data set. Considering mean SAs, a cutoff of 20% in either direction (0.2 or -0.2) is appropriate for the set of ground motions analyzed. On average then, considering all ground motions, topographic amplification at the crest of the 20 degree slopes would be almost negligible and would be reduced for the other slope inclinations. The impact of this threshold on the perceived spatial influence of topographic effects will be illustrated in the next group of figures.

Comparison of the spatial variation in the ground response across the surface of the different slopes is provided in Figures 3.59, 3.60 and 3.61 for all, STR and WTR motions, respectively. For each motion subset, the geometric mean $PGA\ TF$ and $bp\ SA\ TF$ is provided at the near surface sensors for the 30, 25 and 20 degree slopes. Crest locations for each of the slope geometries are marked by dashed lines extending above the idealized slope cross sections located below the plots. The same trend highlighted earlier is once again demonstrated here, in that the ground motion intensity generally increases with increasing slope inclination (with the exception of peak values found for STR motions of the 25 and 20 degree slopes). The magnitude of and distribution of the amplified ground response, however, depend on the ground motion characteristics, illustrated by the differences in the responses for the STR and WTR motions.

For the STR motions depicted in Figure 3.60, peak amplification is captured 1.5 (0.75) meters behind, 3.0 (1.5) meters in front of and 16.5 (8.25) meters in front of the crest for the 30, 25 and 20 degree slope 55g (27.5g) prototypes. The change in location of the peak response marks a significant shift in the concentration of energy from the slope crest to the face of the slope as the slope inclination decreases from 30 to 20 degrees. This is particularly apparent at the slope toe, where the ground motion intensity is most amplified for the 20 degree slopes. Another distinction between the behavior of the slopes is the distribution of energy across the slope surfaces. Even though peak values are greatest for the 30 degree slope, the level of amplification isn't sustained at nearby sensor locations. In contrast, an amplified response is maintained over a larger area for the 25 and 20 degree slopes with little decline

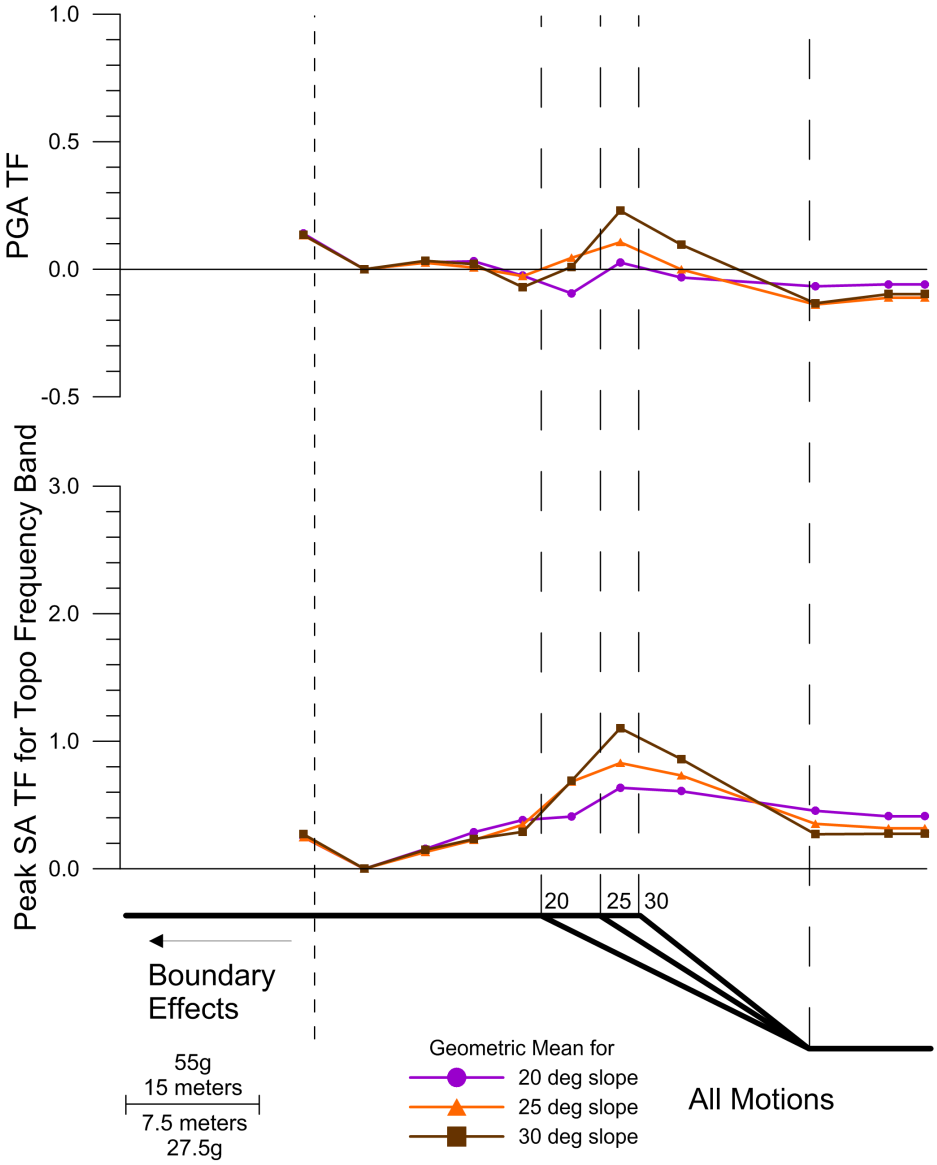

Figure 3.59: Geometric mean of *PGA TF* and *bp SA TF* for the topographic frequency band, for all motions, versus distance across the surface of the 30, 25 and 20 degree slopes. Data from both prototypes is included in calculating the mean for each slope inclination.

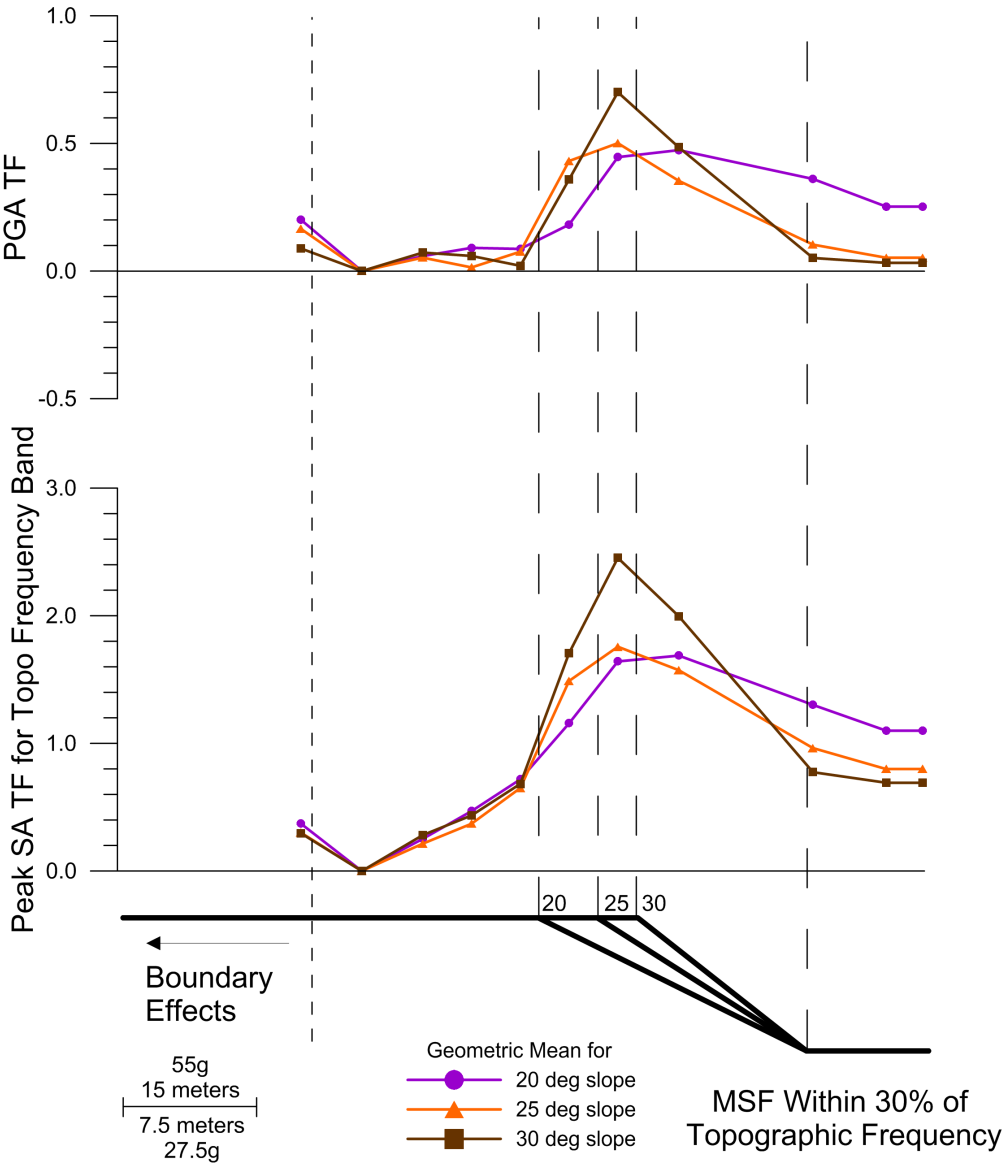

Figure 3.60: Geometric mean of $PGA\ TF$ and $bp\ SA\ TF$ for the topographic frequency band, for STR motions, versus distance across the surface of the 30, 25 and 20 degree slopes. Data from both prototypes is included in calculating the mean for each slope inclination.

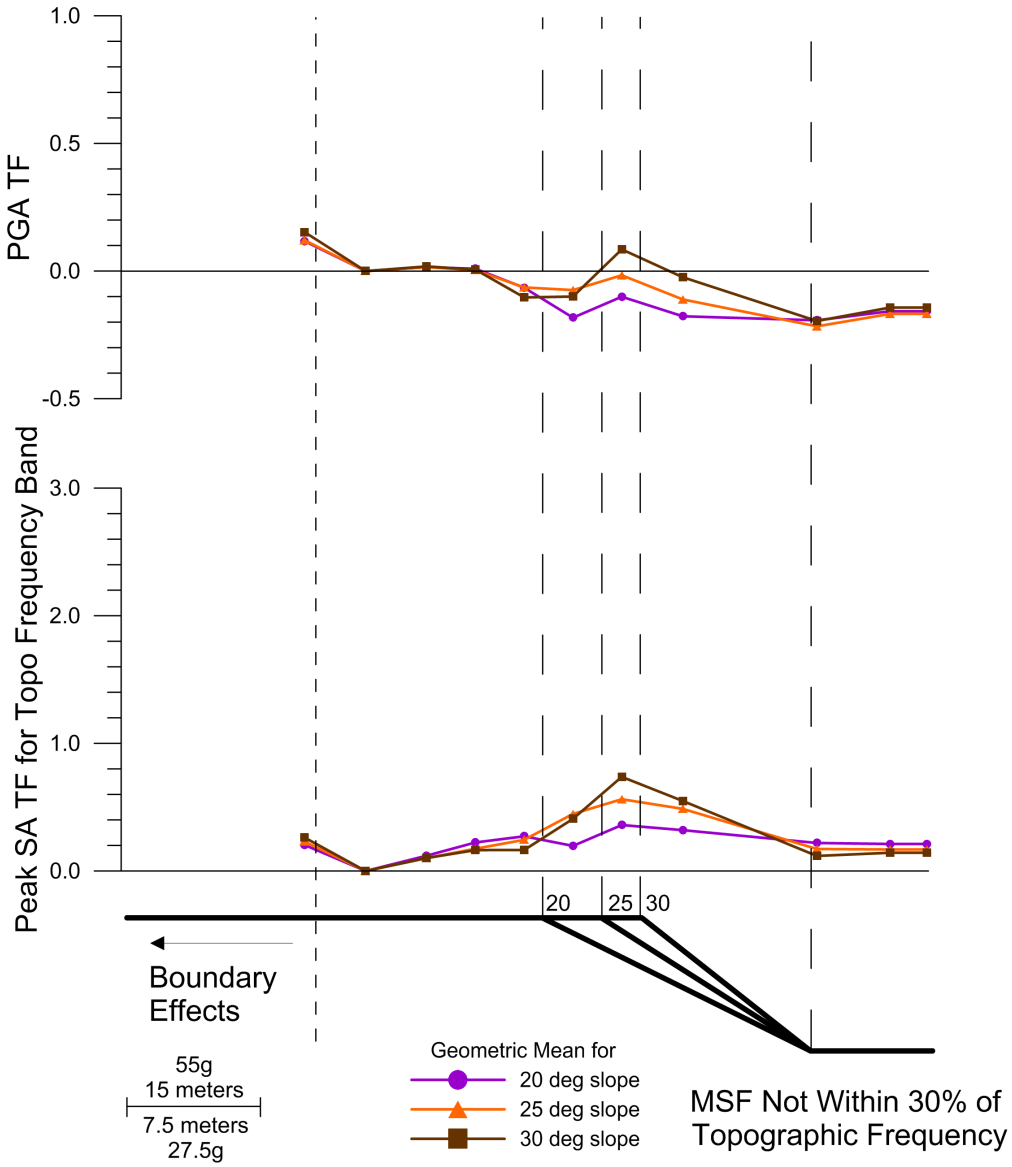

Figure 3.61: Geometric mean of $PGA\ TF$ and $bp\ SA\ TF$ for the topographic frequency band, for WTR motions, versus distance across the surface of the 30, 25 and 20 degree slopes. Data from both prototypes is included in calculating the mean for each slope inclination.

from the peak value for most adjacent sensor locations. The reduction in amplification is less extreme, thus energy is more evenly distributed over the slope surface.

Figure 3.61 demonstrates that differences in the ground response across the surface of the three slope geometries are less pronounced for WTR motions. For the WTR motions, peak amplification occurs in the same locations as the STR motions, although for the 20 degree slopes, the mid-slope sensor closer to the crest now represents the peak by a small margin over the mid-slope sensor closer to the toe (the opposite was true for the STR motions). The gap between the peak values for the 30 and 25 degree slopes is less extreme in comparison to the STR motions, while it has slightly widened in comparing the 25 and 20 degree slopes. Additionally, the overall spatial distribution is similar for the three slopes even though the geometry changes. This is a logical outcome since the WTR motions are not as heavily influenced by topography and thus changes in topography do not result in significant relative differences in the overall ground response and energy distribution.

Figures 3.59, 3.60 and 3.61 reveal the spatial extent and magnitude of topographic amplification across the slope surfaces, but when can this amplification be considered significant and how does that affect the perceived spatial extent of topographic effects? Figure 3.62 helps answer this question by comparing the mean response for all common motions introduced to the flat ground model to that of the slope configurations. Beginning at the free field sensor and moving (to the right) towards the slope crests, it is clear that the TFs determined for the flat ground don't begin to diverge from that of the slopes until roughly halfway between the second and third sensor, approximately 15 (7.5) meters from the free field sensor for the 55g (27.5g) prototype. This is true of both the PGA and the $bp\ SA\ TFs$. On the other end of the slopes, container boundary effects are found to begin influencing the ground response on the slope face and increase moving towards and beyond the slope toe to the container boundary. This is evidenced by the perpetual increase in the TFs determined for the flat ground surface in that area.

In comparing the container boundary effects found for the flat ground and slopes, it is important to recognize that the ground conditions have changed and thus a direct comparison

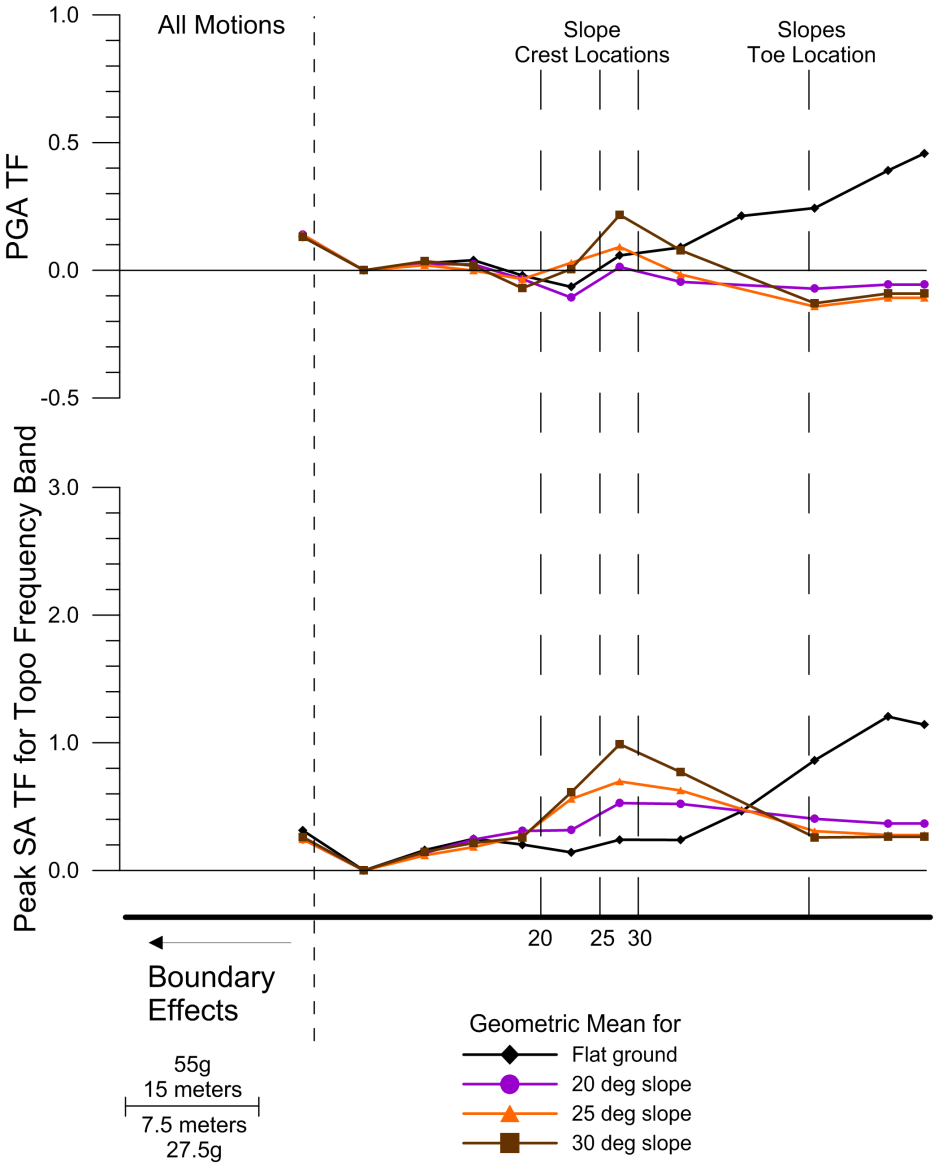

Figure 3.62: Geometric mean of *PGA TF* and *bp SA TF* for the topographic frequency band, for all motions, versus distance across the surface of the 30, 25 and 20 degree slopes as well as the flat ground model. Data from both prototypes is included in calculating the mean for each slope inclination.

may not be appropriate. That is, the quantity to which the container boundary affects the ground motion amplitude for the flat ground cannot necessarily be applied directly to the slope toe. This is evidenced by the difference in the measured response in the area beyond the toe. For the flat ground case, the amplitude generally increases to the right of the equivalent location for the slope toe, while for the slopes, the amplitude remains relatively constant. Because the ground surface has changed in both elevation and shape, it is difficult to separate inherent differences in the ground response resulting from those changes (i.e., topographic effects) from container boundary effects near the slope toe. However, the findings from the flat ground model can be applied qualitatively by recognizing that the response at the toe is likely influenced by container boundary effects, and as a result, the amplitude would probably be lower without the presence of the container. This may also be true of locations on the lower half of the slope face.

In considering sensor locations not affected by the container boundary, TFs reach as high as 0.2 and 0.1 for the *bp* SA and PGA, respectively, on the flat ground surface. For an idealized flat ground surface, however, these factors would all be equal to zero and thus these peaks are a result of natural variation in the measured response. These peak values are also found in the free field region where the ground response of the slopes and flat ground diverge (Figure 3.62) indicating that the response for the slopes in this region is also a result of natural variation and thus not related to topographic effects. Therefore, for the typical mean response of the suite of ground motions utilized in this study, these levels of amplification can be deemed insignificant. Using the same free field region as a marker for divergent behavior, threshold values for significant amplification can also be applied to the mean response of the STR and WTR motions. Values of roughly 0.5 and 0.1 for the STR motions and 0.2 and 0.0 for the WTR motions can be applied for the *bp* $SA\,TF$ and $PGA\,TF$, respectively.

Implementing the thresholds determined above would serve to effectively reduce the perceived magnitude and spatial extent of topographic amplification. For the STR motions, average peak values would be reduced to roughly 1.9, 1.2, and 1.2 for the *bp* $SA\,TF$ (which

are coincidentally roughly equivalent to the peak $SA\ TF$ values determined for the mean spectra) and 0.6, 0.4 and 0.4 for the $PGA\ TF$ for the 30, 25 and 20 degree slopes respectively. For the WTR motions, average $PGA\ TF$ values for all slopes would generally indicate no change or a deamplified response, while average peak values for the *bp* $SA\ TF$ would be 0.6, 0.4 and 0.2 for the 30, 25 and 20 degree slopes.

The resulting change in effective spatial extent influenced by topographic effects can be examined using nomenclature defined in the previous section, whereby distances L_1 measures from the crest location back towards the free field and L_2 measures from the slope crest towards the toe (horizontally). Because mean values are used in the motion subsets, distances L_1 and L_2 determined here should be thought of as average lengths. The L_2 values are essentially equivalent to the length of the slope for all cases, thus being equal to 19 (9.5), 23.6 (11.8), and 30.3 (15.15) meters for the 30, 25, and 20 degree slopes for the 55g (27.5g) prototype. The L_1 values vary some for the different intensity measures, but generally fall within the same range. For all intensity measures and subsets considered, that range is from 12.5 to 18.0 (6.25 to 9.0) meters, 8.0 to 13.5 (4.0 to 6.75) meters and 1.5 to 7.0 (0.75 to 3.5) meters for the 55g (27.5g) prototype of the 30, 25 and 20 degree slopes, respectively.

The influence of slope inclination is again highlighted in Figures 3.63, 3.64 and 3.65 for the case of all, STR and WTR motions. However, in this case, instead of using mean values, box and whisker plots are utilized, which, for each subset of motions, provide the full range of TFs for both PGA and the *bp* SA at the slope crest. A key for interpreting the box and whisker plots is provided in each of the three figures. It is clear from all three figures that the range of values generally increases as the slope inclination is increased and that the ranges for the three slope geometries overlap. It is also obvious that the frequency specific *bp* $SA\ TF$ reaches greater maximum values, but also encompasses a larger range of values than those found using $PGA\ TF$. Although PGA values are more consistent, this indicates that the PGA is not necessarily as sensitive to topographic effects as a frequency specific intensity measure.

In comparing the three figures, the importance of separating the motions according to

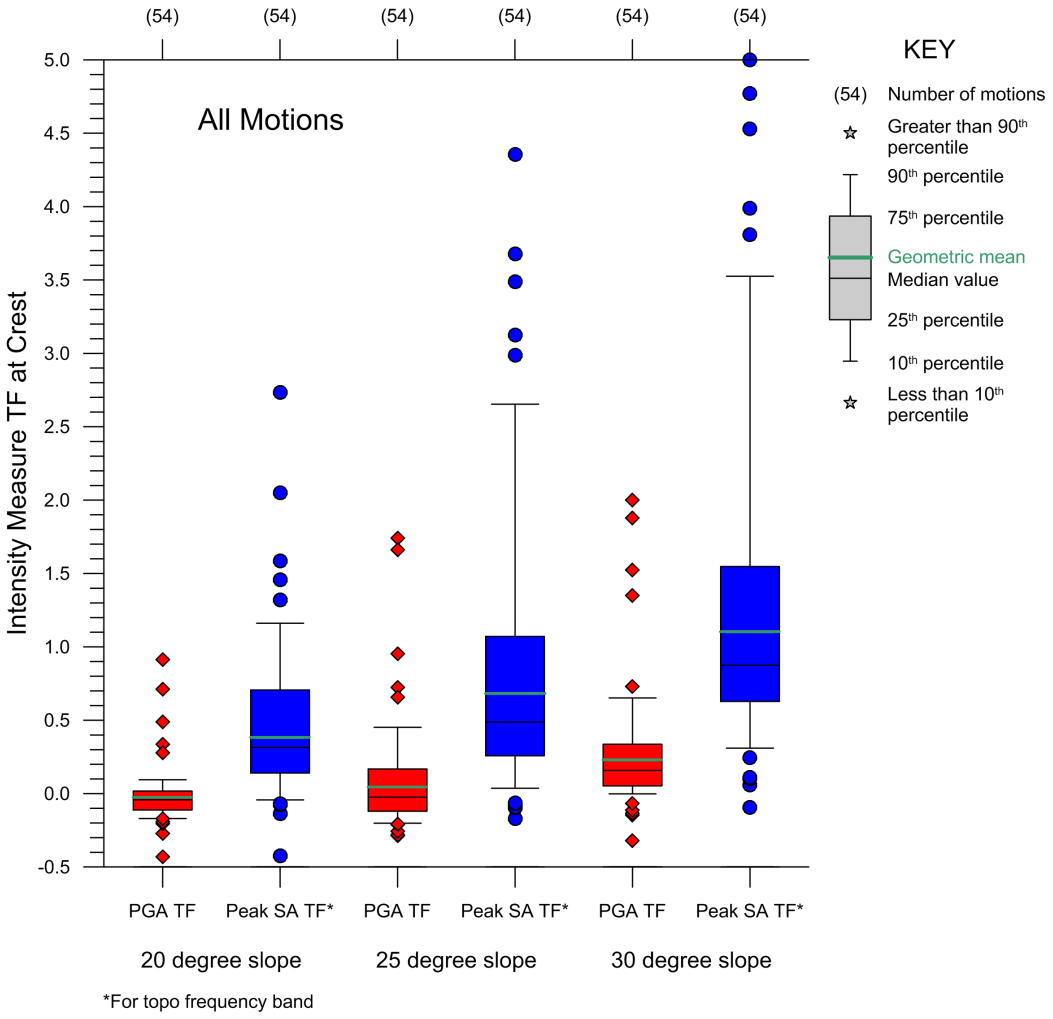

Figure 3.63: Box and Whisker plot for all motions at the crest of the 30, 25 and 20 degree slopes, showing the range of values for the $PGA\ TF$ and banded $SA\ TF$ for the topographic frequency band. Data from both prototypes is included for each slope inclination. A interpretive key for the box-whisker plot is provided.

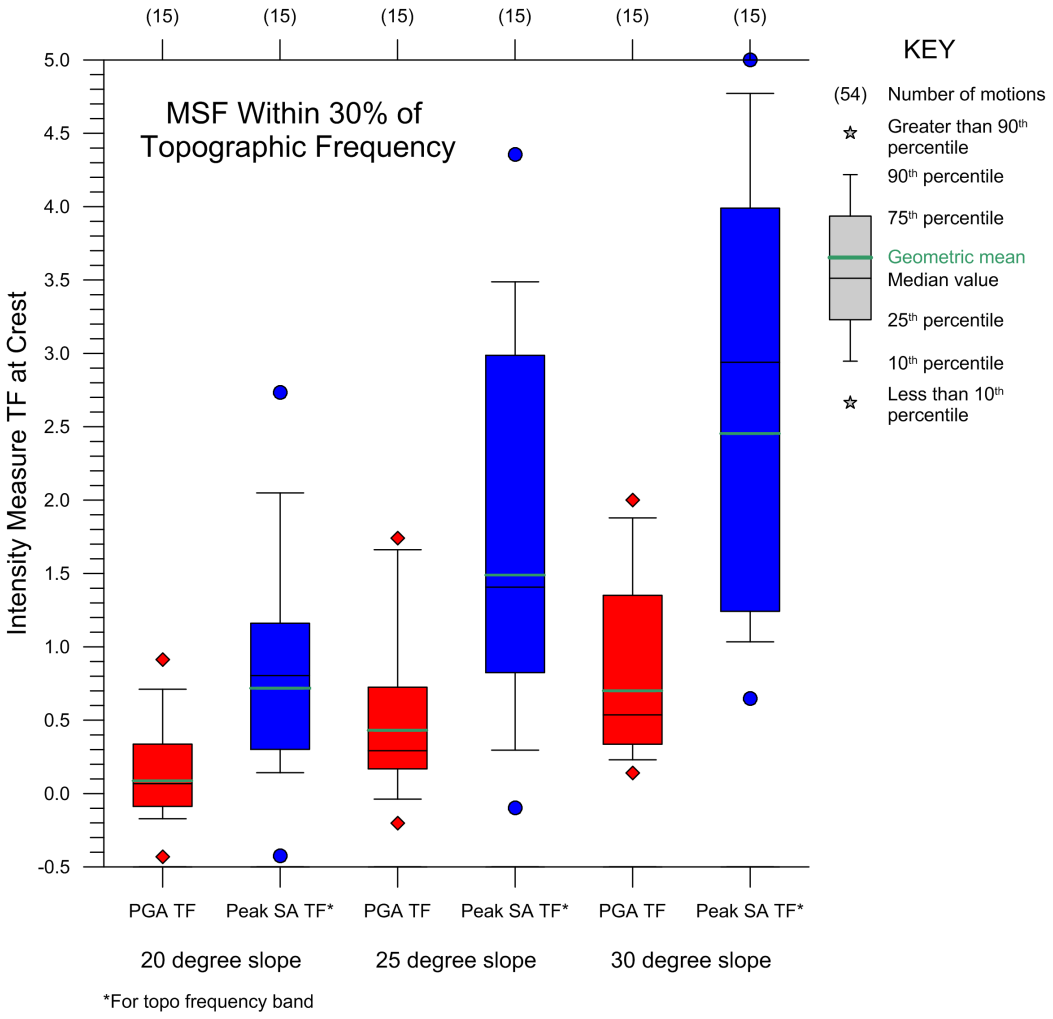

Figure 3.64: Box and Whisker plot for STR motions at the crest of the 30, 25 and 20 degree slopes, showing the range of values for the $PGA\ TF$ and banded $SA\ TF$ for the topographic frequency band. Data from both prototypes is included for each slope inclination. A interpretive key for the box-whisker plot is provided.

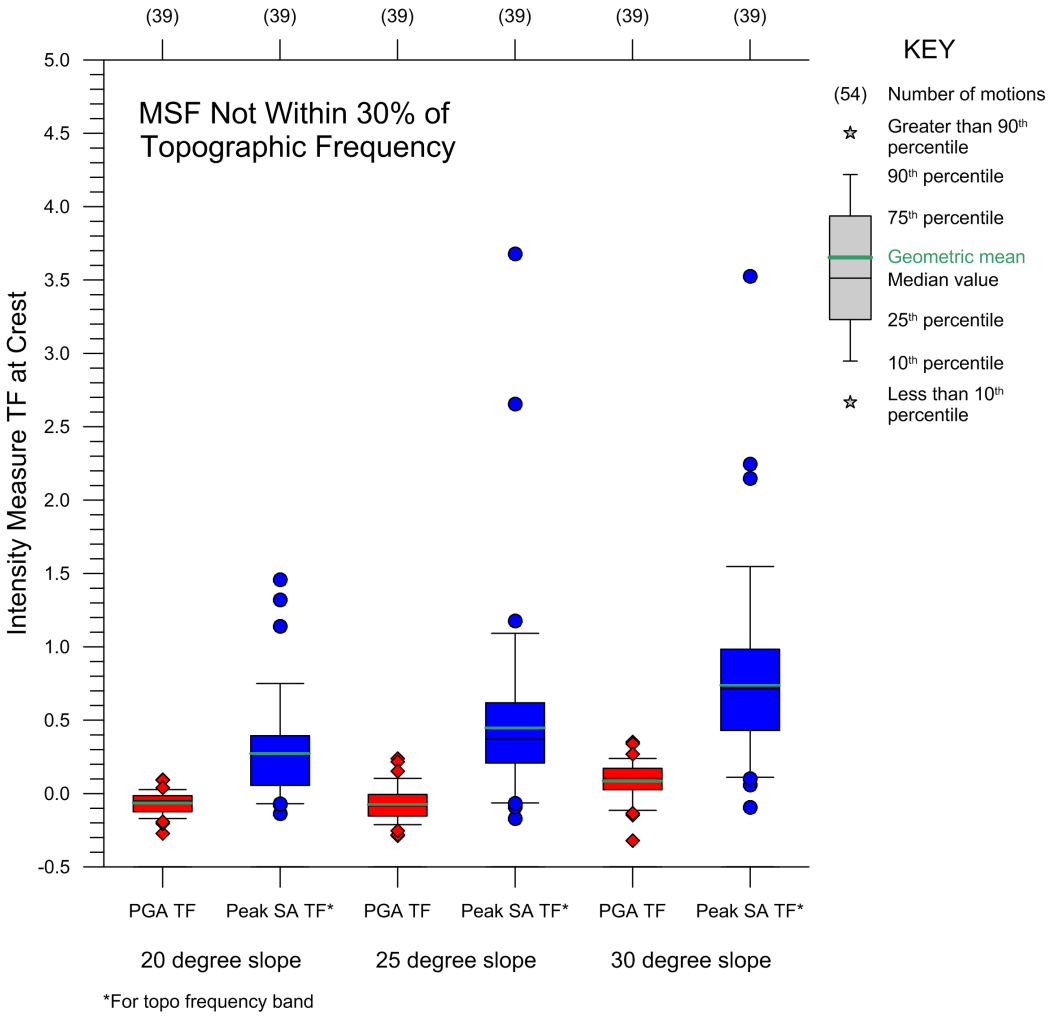

Figure 3.65: Box and Whisker plot for WTR motions at the crest of the 30, 25 and 20 degree slopes, showing the range of values for the $PGA\,TF$ and banded $SA\,TF$ for the topographic frequency band. Data from both prototypes is included for each slope inclination. A interpretive key for the box-whisker plot is provided.

frequency content is apparent. In Figure 3.63, representing all ground motions, the top whisker, which represents TFs between the 75th and 90th percentile for the set of ground motions, constitutes a large range of the greatest values, particularly for the *bp SA* TF. Additionally, a number of motions exhibiting the highest levels of amplification are placed above the 90th percentile mark. This indicates that it would be uncommon to achieve such high levels of amplification. It would be incorrect, however, to assume this is true of a typical group of ground motions. By grouping the ground motions according to frequency content, the outlook is changed. For the STR motions, depicted in Figure 3.64, the TFs that appeared less likely to be achieved when considering all motions (i.e., in the upper 25th percentile), are now presented as more typical for the group of motions considered. This can be attributed to the fact that STR motions achieve greater levels of topographic amplification. The same idea can be applied to the lower end of the spectrum for WTR motions, for which topographic effects are less significant. This is illustrated in Figure 3.65 where the typical range of values for the TFs are relatively low and the differences between the slope geometries is less pronounced.

The TFs for PGA and the *bp* SA are again utilized in Figures 3.66 and 3.67 for all ground motions. The response at the slope crest is plotted individually for each of the common ground motions introduced to the three different slope geometries. Similar to figures presented in the previous subsections for the individual slopes, the TFs are plotted against the MSF normalized by the topographic frequencies of 4.5Hz and 7.3Hz for the 55g and 27.5g prototypes, respectively. The trend depicted in the two figures is the same as before, in that ground motions with a MSF closer to the topographic frequency exhibit greater levels of amplification (i.e., larger TFs). However, the deterioration of that trend as the slope inclination is decreased is illustrated here. For both intensity measures, the level of amplification is consistently greater for the steepest of the three slope geometries. This is true at all frequencies, but is particularly pronounced as the MSF approaches the topographic frequency. As the slope inclination decreases, ground motion intensity decreases and no amplification or deamplification (compared to the free field) is more common. This once

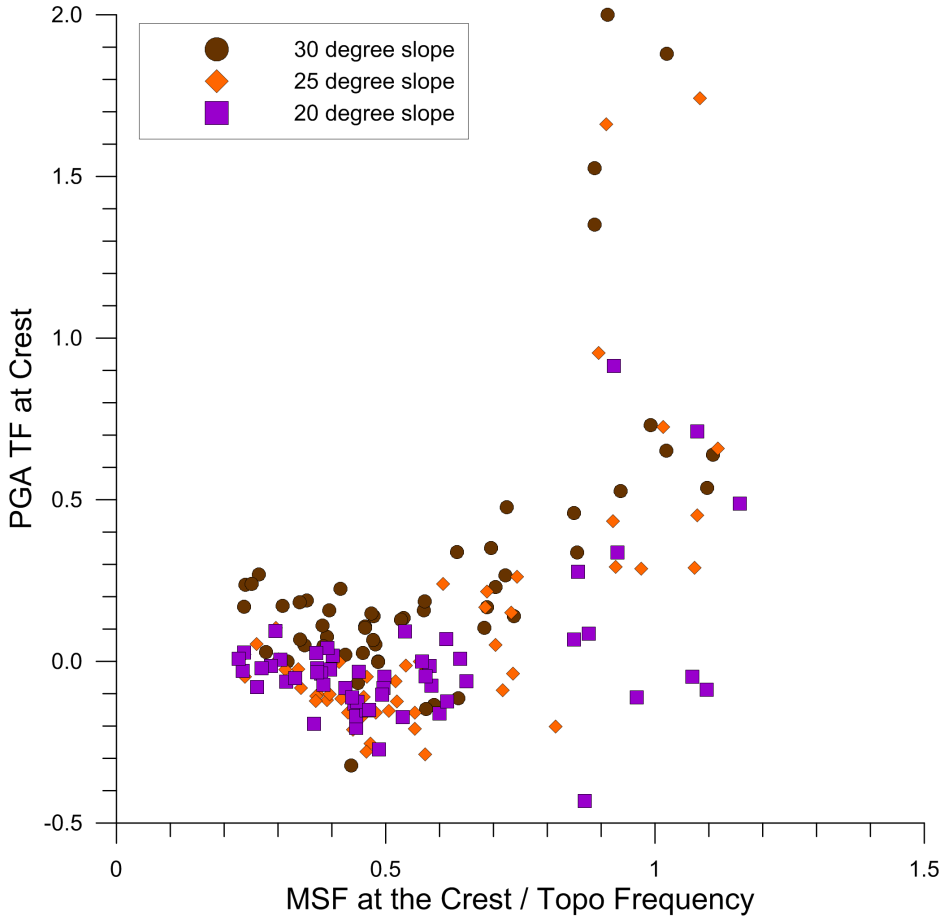

Figure 3.66: $PGA\ TF$ versus MSF normalized by the topographic frequency at the slope crest for the 30, 25 and 20 degree slopes. Data from both prototypes is included for each slope inclination.

again highlights the influence of slope inclination on ground motion amplitude at the crest of slopes.

Thus far, analysis results of data collected through physical modeling in a centrifuge have been presented for a single ground motion, for each slope geometry individually and comparatively for all three slope geometries. Each slope geometry is inclusive of two prototype slopes, which differ in size but are otherwise topographically similar. Ground motion data for both slope prototypes were typically combined in the analysis which was used to produce the figures presented. Slope dimensions and other pertinent information, such as average shear

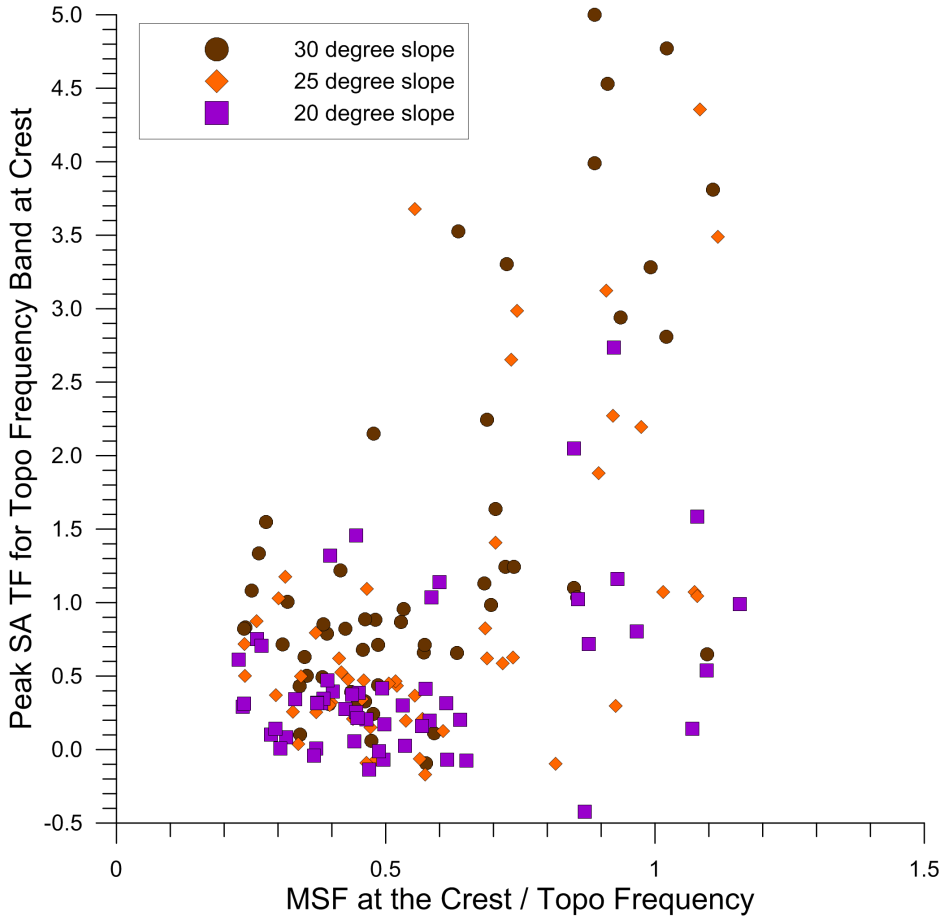

Figure 3.67: *bp SA TF* for the topographic frequency band versus *MSF* normalized by the topographic frequency at the slope crest for the 30, 25 and 20 degree slopes. Data from both prototypes is included for each slope inclination.

wave velocity, were provided in Table 3.1 and throughout the commentary above. However, more information about the different slopes, sensors, ground motions used, and other details relevant to the centrifuge experiment are provided on the NEESHub website (Adrian Rodriguez-Marek, 2010).

All the results presented to this point have been for horizontal ground motions, which constitute the main focus of the centrifuge experiment and subsequent analysis. However, vertical ground motion was also recorded across the surface of the different slopes and at the base of the model (see Figure 3.1). The next subsection presents the analysis results for the

vertical ground motions using similar visualization techniques to those utilized above.

3.3.4 Vertical Ground Motion

Vertical ground motions were recorded near the surface across the model as well as in three locations at the base of the model container. The near surface accelerometers were placed in close proximity to horizontally oriented sensors in a central array aligned in the north-south direction (see Figure 3.1). While horizontal base (input) accelerations were recorded on the horizontal shaker just beneath the container, the vertical base accelerations were captured at the bottom of the sand deposit and were attached to the model container. Because the model container is rigidly attached to the shaker, however, accelerations recorded at the shaker should be similar to those recorded at the base of the model container. It should be noted that the shaker is designed to only introduce ground motion in the horizontal direction, but that vertical ground motion is introduced as the result of container rocking, and the interaction of the centrifuge bucket-shaker-container system. Sample time histories and response spectra of vertical base motions recorded are given in Figure 3.68. These motions correspond to the time histories and response spectra provided earlier for the horizontal base motions in Figure 3.3.

Aside from the central array of vertically oriented accelerometers near the ground surface and the sensors at the base, no other vertical sensors were employed in the model. Consequently, cross-sectional contour plots of different intensity measures, such as those depicted in Section 3.3.1, could not be created using vertical ground motion intensity measures. Analysis of the data was further limited by electronic failure or malfunction of a number of the sensors throughout the testing program, both near the surface and at the base of the model. As a result, useful data was not recorded for near surface sensors located at the crests of the 30 and 20 degree slopes. This, coupled with other malfunctioning sensors at locations of importance, made analysis of topographic effects unfeasible for those slope geometries. Consequently, topographic effects could only be analyzed for the 25 degree slopes, the results of which are presented in this subsection.

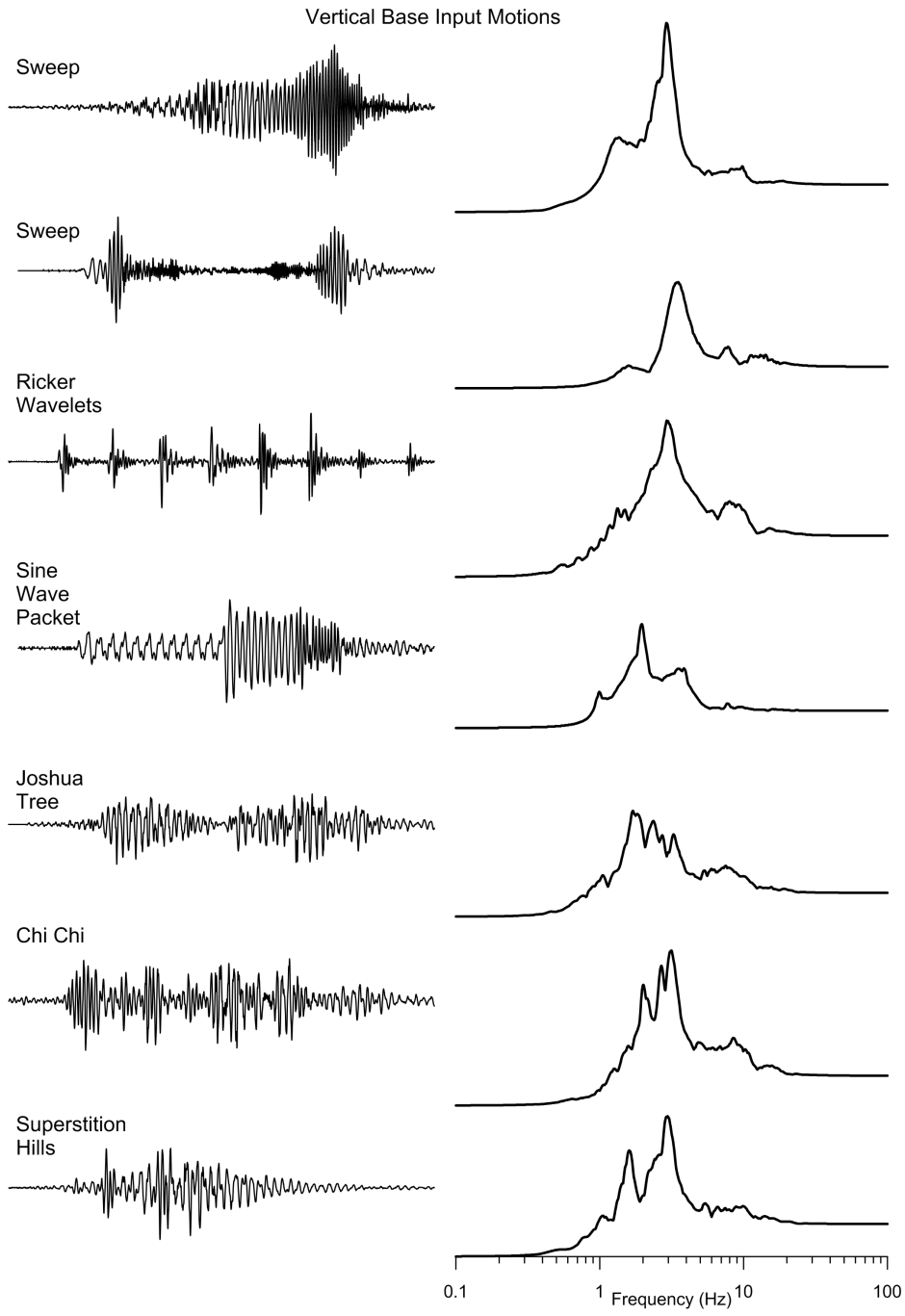

Figure 3.68: Sample vertical motions recorded at the base of the model container for the different centrifuge configurations. Time histories and response spectra with 5% damping are included.

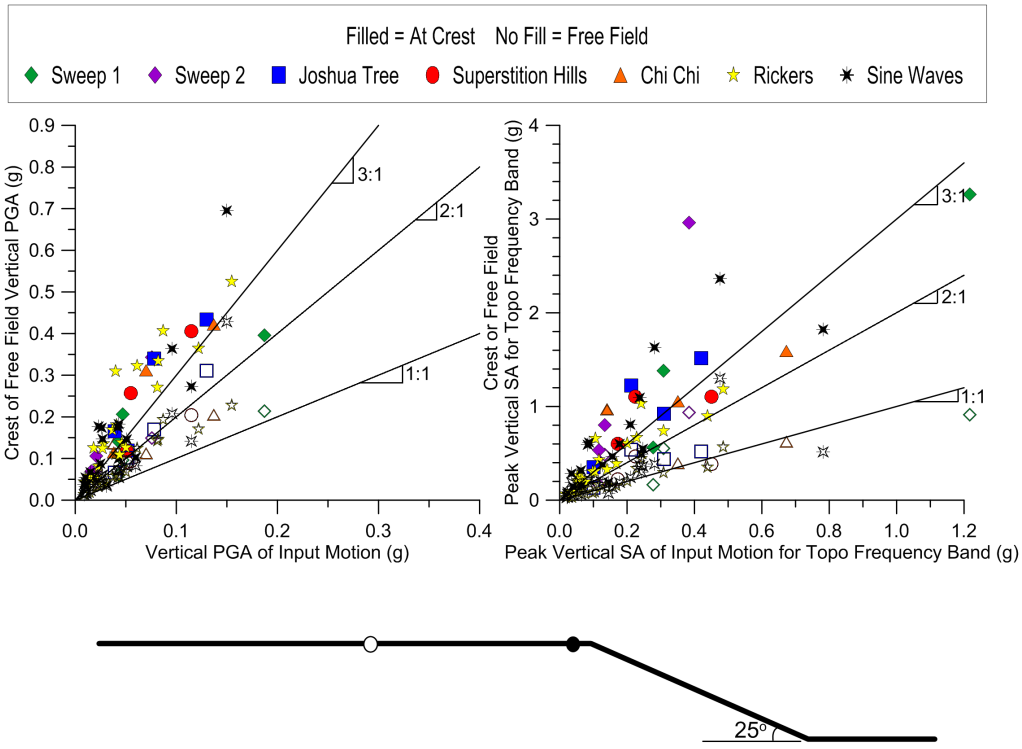

Figure 3.69: Vertical free field and crest response versus input using PGA and $bp\ SA$ for the topographic frequency band for both 25 degree slope prototypes. The free field sensor (A20) is about 23.5 (11.75) meters from the crest sensor (A32), which is about 2.5 (1.25) meters behind the slope crest at 55g (at 27.5g).

For the 25 degree slope, useful data was recorded at important locations of interest, such as the slope crest, the base of the sand substratum, and the free field behind the crest, for both slope prototypes. Figure 3.69 compares the PGA and $bp\ SA$ for the topographic frequency band at these three locations. The topographic frequency mentioned here and used throughout this subsection is based on horizontal accelerations and thus the topographic frequency bands are consistent with those previously used in interpreting the horizontal ground motion.

The pattern depicted in Figure 3.69 is, in general, similar to that exhibited by the horizontal ground motions. The PGA measured in the free field is typically 1 to 2 times that

of the input PGA and the $bp\ SA$ are mostly similar to the input values, evidenced by the number of motions that plot on the 1:1 reference line. However, for a few motions, the $bp\ SA$ are as much as 2.5 times the input. In contrast, at the crest, PGA ranges from 2 to 4.5 times the input values, exceeding 3 times the input for most ground motions. For the $bp\ SA$, values at the crest range from 2 up to 7 times those of the input ground motions.

Although the relationship between the free field, crest and base amplitudes for the vertical and horizontal ground motions are alike, the true amplitudes at each of these locations can differ. This is demonstrated in Figure 3.70, where vertical PGA in the free field, at the crest and at the base are plotted against horizontal PGA at the same locations. The vertical base PGA ranges from roughly 0.2 to 1 times the horizontal PGA values. In the free field, however, the range of values is narrowed and for nearly all ground motions PGA in the vertical direction is about half that of the horizontal direction. At the slope crest, vertical PGA range from 0.5 to 1 times the horizontal PGA, however, most ground motions plot along the 1:1 reference line. This establishes that ground motion intensity in the vertical and horizontal directions if often equivalent at the slope crest for the given circumstances. This observation coupled with the fact that vertical ground motion intensity in the free field and at the base is significantly less than that in the horizontal direction, indicates that topography can significantly impact ground motion amplitude in the vertical direction.

The vertical ground motion frequency content is also influenced by topography, as illustrated by Figure 3.71, which compares the MSF at the crest, free field and base locations. Unlike the ground motion amplitude, however, the trends found here for vertical motions do not coincide with those of the horizontal motions. In particular, the MSF in the free field is typically greater than that of the base motion and the MSF at the crest is typically less than the free field and does not necessarily shift towards the slope topographic frequency. In comparing the free field to the crest, a shift towards the topographic frequency, however, does occur once the TR in the free field is greater than roughly 0.8, evidenced by the right plot in Figure 3.71. For motions with a TR greater than 0.8, the shift towards the topographic frequency is more significant the farther the MSF is from the topographic frequency. This

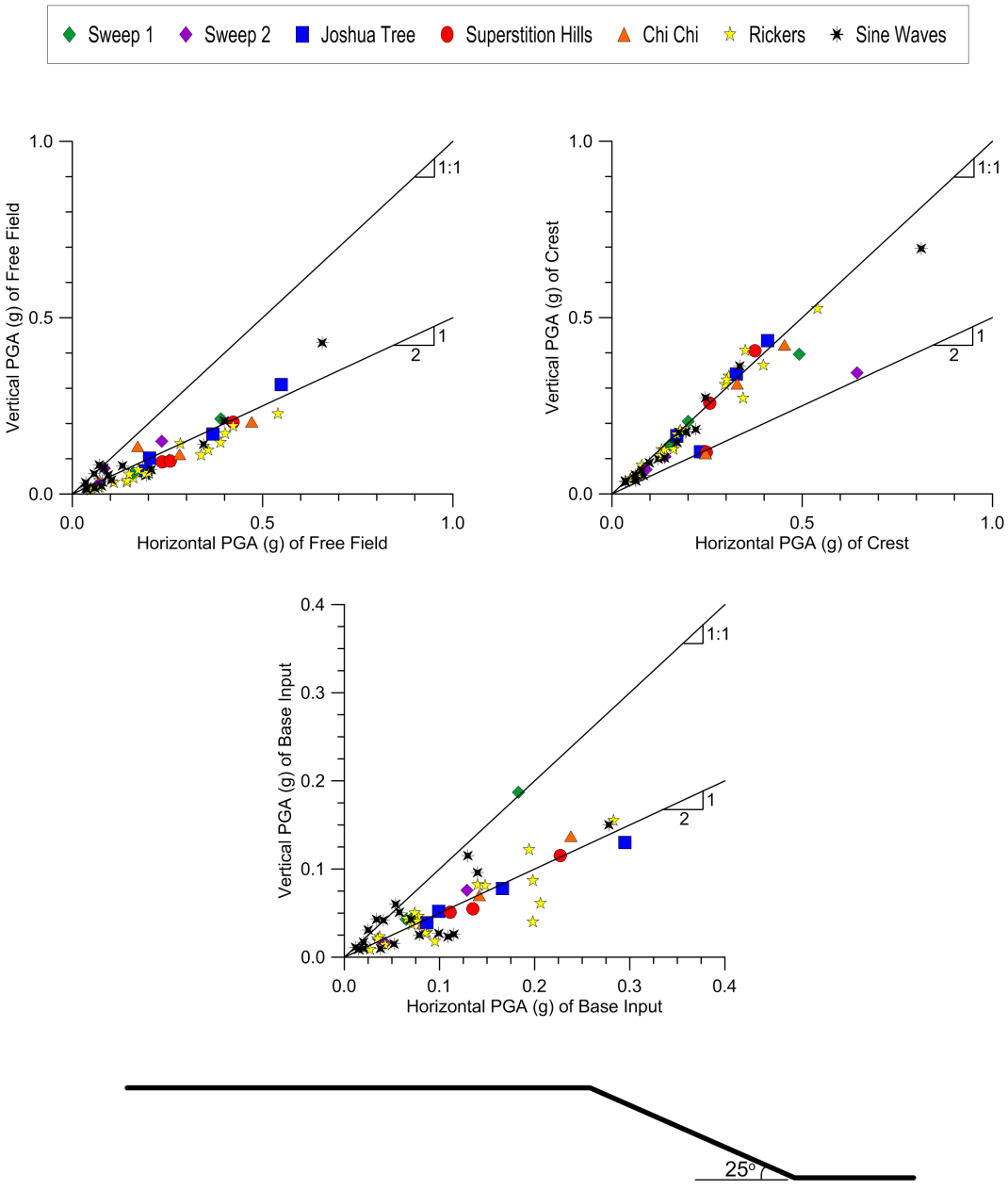

Figure 3.70: Vertical PGA versus horizontal PGA for the crest, free field and base input of both 25 degree slope prototypes.

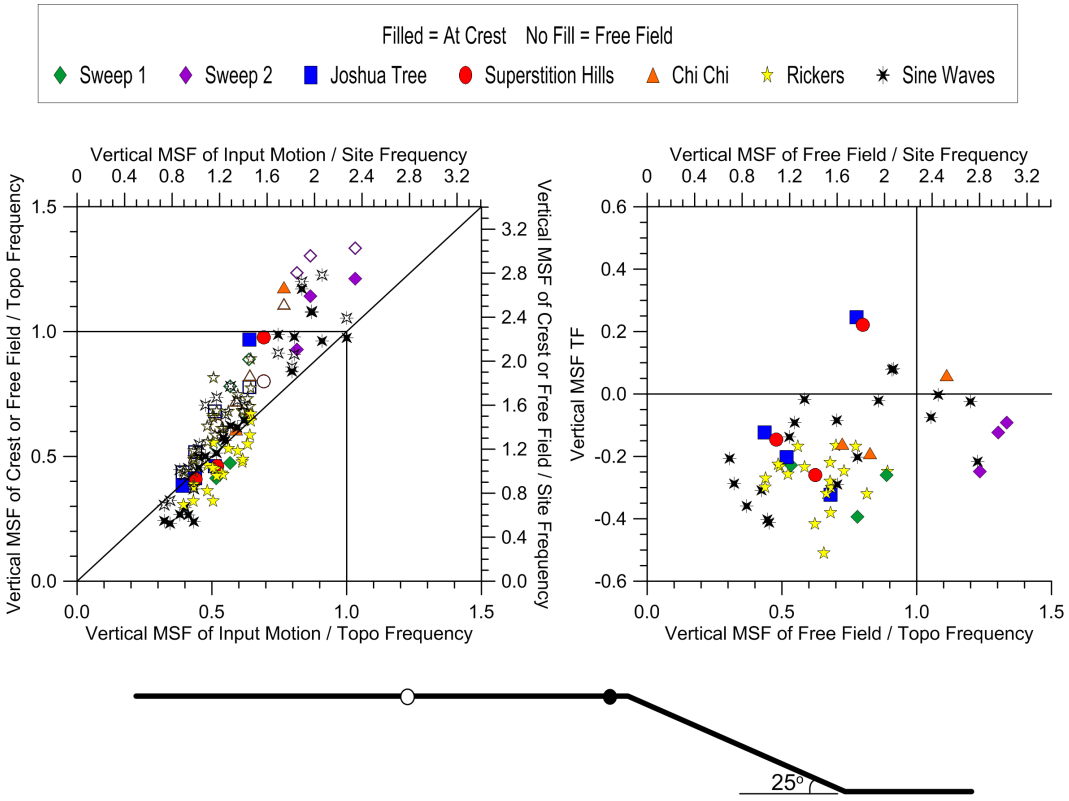

Figure 3.71: Vertical free field and crest versus input MSF normalized by the topographic and site frequencies for both 25 degree slope prototypes.

behavior is more aligned with that found for the horizontal ground motions.

To visualize how the vertical ground motion frequency content compares to that of the horizontal ground motions directly, Figure 3.72 plots the vertical versus horizontal normalized MSF for the free field, crest and base. For the input ground motions, the MSF is seen to be higher in the vertical direction below a normalized frequency of 0.8 and lower for normalized frequencies above 0.8. This suggests that for vertical ground motions, low frequency components are relatively weaker (or high frequency components are relatively stronger) than horizontal motions with energy concentrated at lower frequencies, while the opposite is true for horizontal ground motions with energy concentrated at higher frequencies. In the free field, the MSF for all vertical motions is either the same or greater than

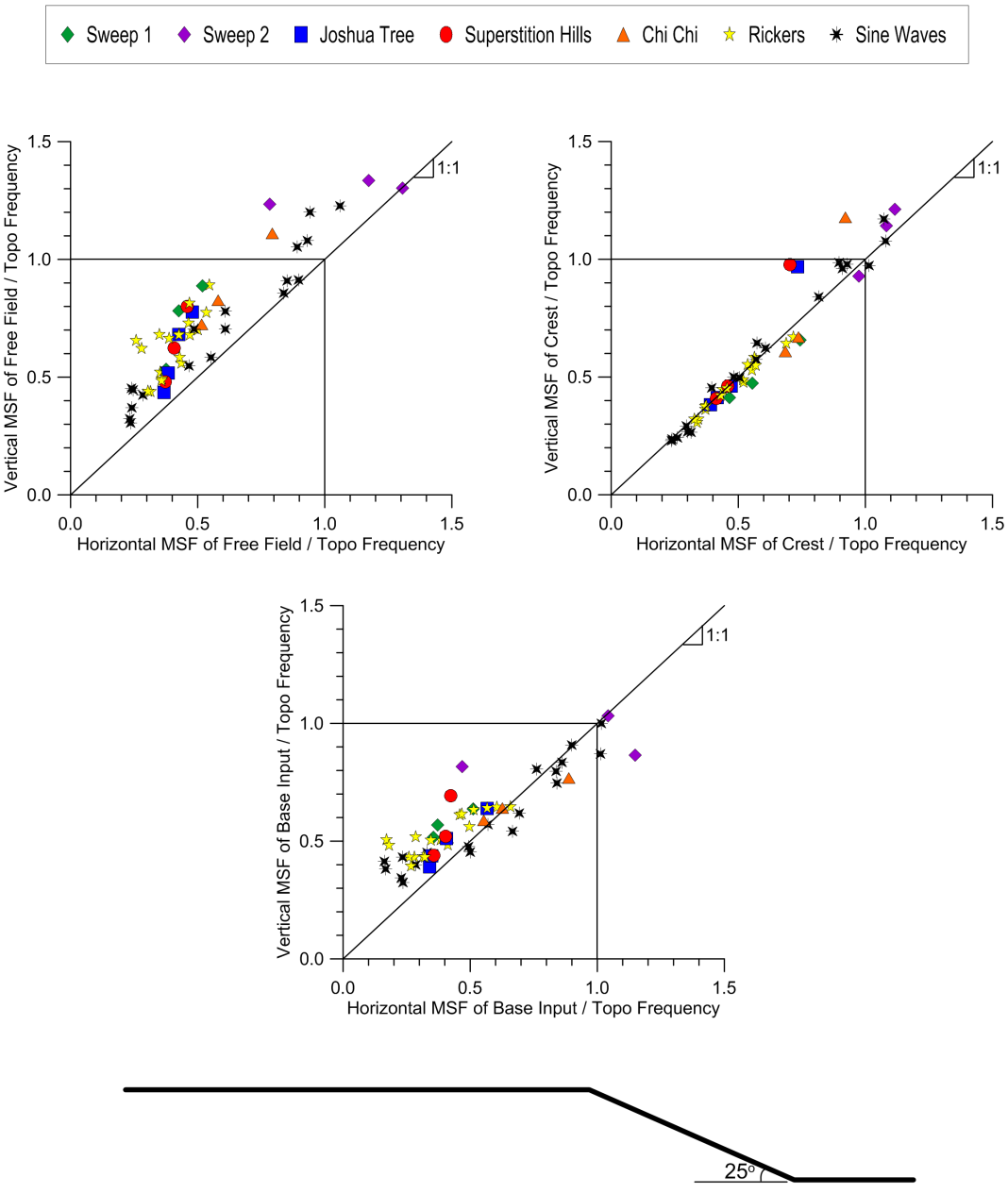

Figure 3.72: Vertical MSF versus horizontal MSF, both normalized by the topographic frequency, for the crest, free field and input of both 25 degree slope prototypes.

the horizontally oriented motion. At the crest, however, the frequency content is nearly identical in most cases. This was also true of PGA (Figure 3.70), suggesting the horizontal and vertical ground motions at the crest are similar.

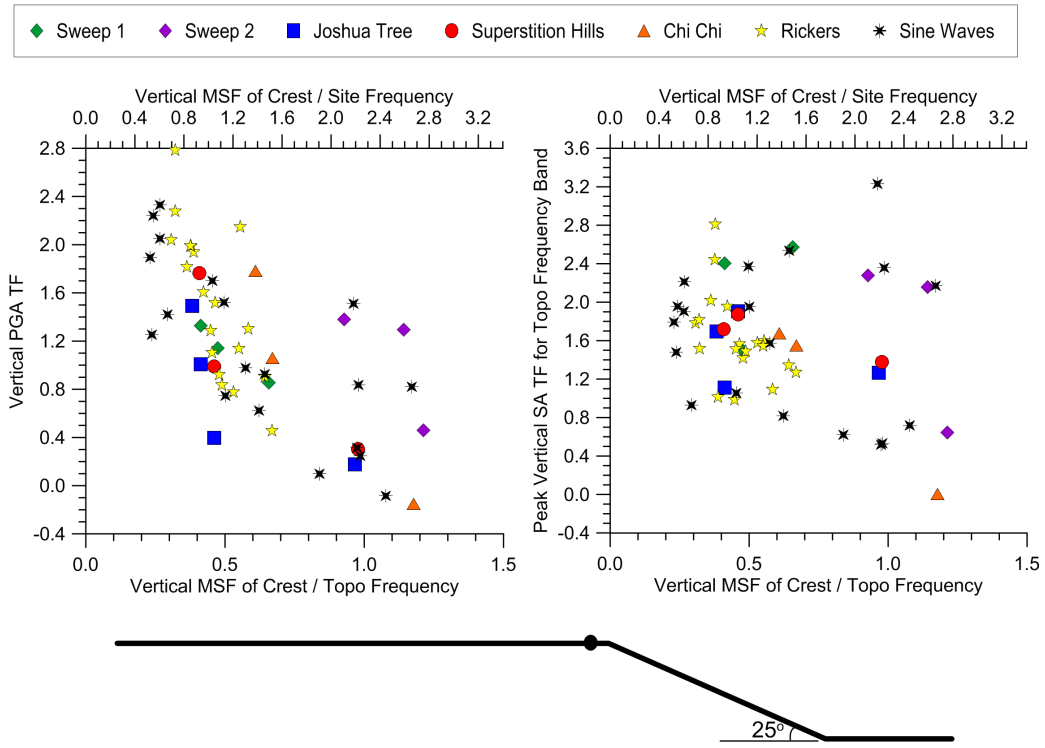

Figure 3.73: Vertical $PGA\ TF$ and $bp\ SA\ TF$ for the topographic frequency band versus MSF normalized by the topographic and site frequencies at the crest for both 25 degree slope prototypes.

Figure 3.73 shows the relationship between the ground motion amplitude and frequency content in the vertical direction. Plots of both the vertical $PGA\ TF$ and vertical $bp\ SA\ TF$ versus normalized MSF at the slope crest are given for both 25 degree slope prototypes. The TFs are determined in the same manner as for the horizontal ground motions, only considering vertical ground motion in this case. That is, the vertical amplitude at the crest is normalized by the vertical free field amplitude and the field free component is negated. The result is that any value above zero represents amplification over the free field and any

below zero represents deamplification. The factors can be converted to percent change by multiplying by 100. For nearly all ground motions, both intensity measures indicate an amplified response at the crest. The relationship between the amount of amplification and the ground motion frequency content is similar for both plots. Namely, amplification is typically greater for motions with lower $MSFs$. A handful of motions, however, do exhibit significant levels of amplification near the topographic frequency, particularly considering the *bp* $SA\ TF$, where the greatest value (roughly 3.2) was determined for a ground motion with a normalized frequency near 1. Additionally, amplification of roughly 150% for the PGA is found for a ground motion with a MSF near the topographic frequency, although this is still 130% less than the maximum amplification of 280% achieved. In general, the influence of the proximity of the MSF to the topographic frequency is not exceptional, and the relationship between MSF and ground motion amplitude is nearly opposite that of the horizontal ground motions; particularly for ground motions with a TR below 0.8.

The relationship between ground motion frequency content and amplitude for the vertical ground motions is further highlighted in Figure 3.74. The geometric mean, including data at the crest of both 25 degree slope prototypes, is given for the vertical $SA\ TF$ and vertical $SA\ AA$ spectra. Mean spectra are provided for all motions, STR motions and WTR motions, with the STR and WTR subsets consisting of the same group of motions used for the horizontal ground motions. It is apparent that the effect of grouping of the motions according to frequency content is not as pronounced as that found for the horizontal motions; particularly at higher frequencies of the $SA\ AA$ spectrum, where the response for each subset is comparable. However, there are notable differences for frequencies at the lower end of the spectrum and at higher frequencies of the $SA\ TF$ spectrum. Specifically, the STR motions are on average weaker than the WTR motions, a result that is in contrast with the horizontal ground motions.

In all cases, the peak mean response occurs at low frequencies, dips at a normalized frequency of roughly 0.7, reaches another smaller peak ($SA\ TF$) or plateau ($SA\ AA$) near the topographic frequency and then generally levels out at higher frequencies. It should be

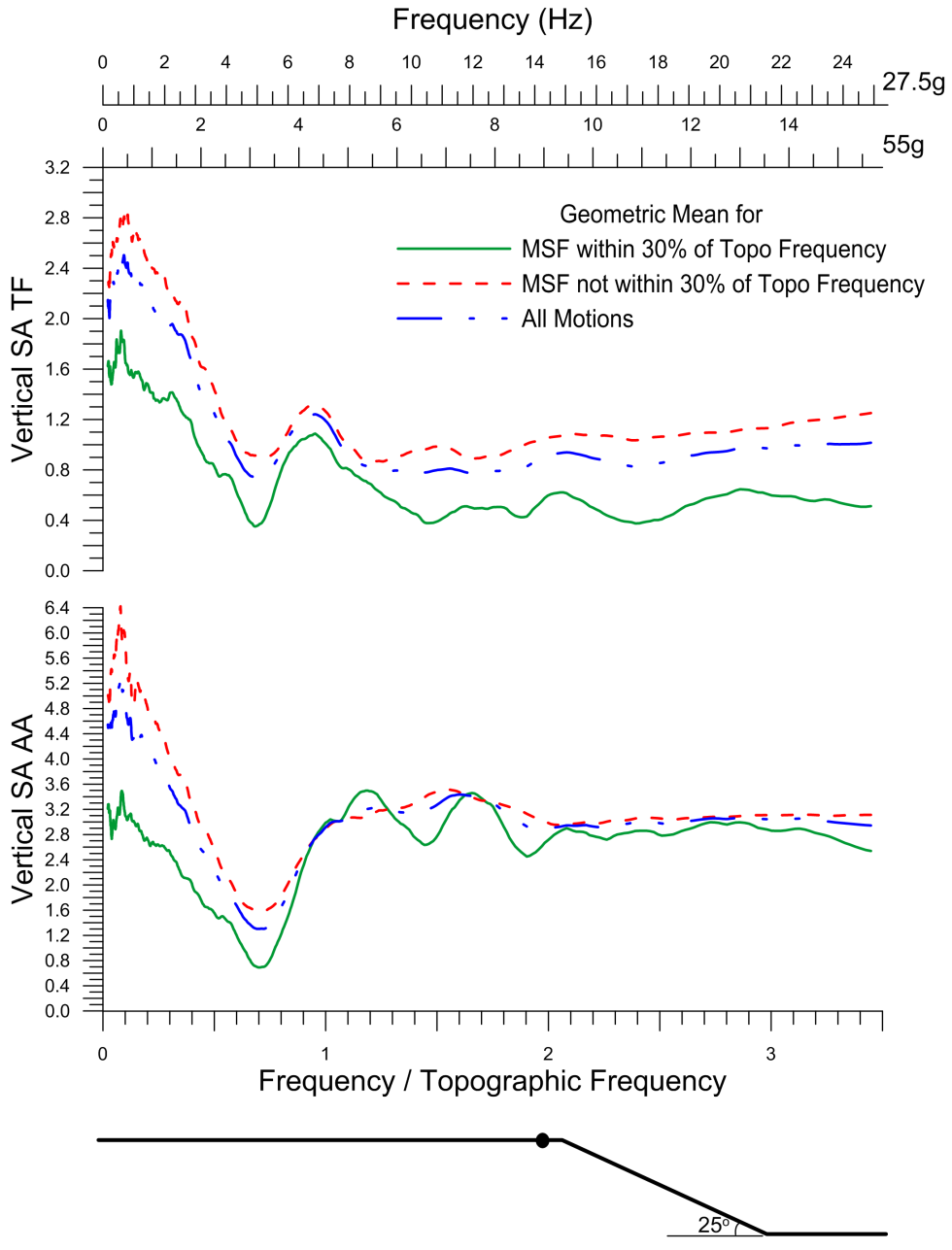

Figure 3.74: Geometric mean for the vertical $SA\ TF$ and $SA\ AA$ spectra at the slope crest for both 25 degree slope prototypes grouped according to the MSF of the ground motion.

noted that every frequency on the $SA\,TF$ spectrum is amplified by at least 40%, indicating that, on average, the intensity of the entire ground motion (not just at specific frequencies) at the crest is amplified compared to the free field. This finding also differs from horizontal ground motions where the amplitude at lower frequencies were typically similar to the free field.

The spectra in Figure 3.74 show the relative mean ground response of the crest to the free field and base of the sand substratum in the vertical direction. These spectra can be compared to those depicted for horizontal ground motion in Figure 3.27 to highlight differences in the response. However, in order to gain a better understanding of how the response in the vertical and horizontal direction differ across a range of frequencies, it's easiest to compare the spectra directly. In Figure 3.75, this comparison is achieved by normalizing the vertical spectrum by the horizontal spectrum for the free field, crest and base. After normalization, much like the TFs, the spectrum is zeroed by subtracting 1 from each SA ratio. Thus, a value greater than zero represents a vertical SA greater than the corresponding horizontal SA at that frequency. Both the geometric mean and standard deviation are provided for all ground motions.

The scales are different for each of the three plots in order to better visualize the changes in the normalized spectra. For the base motion, at the lowest frequencies, vertical SAs are approximately 80% less than horizontal SAs on average, or conversely, the vertical SAs are 20% of the horizontal. This percentage then steeply rises to 70% for SAs near the site frequency and peaks at 80% near a normalized frequency of 0.7. The percentage then drops and levels out at roughly 55% at higher frequencies. The pattern in the free field differs, but is similar to that of the base. At low frequencies, mean vertical SAs are roughly 25% of the horizontal SAs. This percentage gradually rises, this time peaking at approximately 60% near the topographic frequency, before declining to roughly 55% at higher frequencies. At the crest, however, the normalized average response across all frequencies is more consistent. Furthermore, the SAs of the vertical and horizontal ground motion are more comparable. The vertical SAs fluctuate between 80 and 90% of the horizontal SAs for frequencies less than

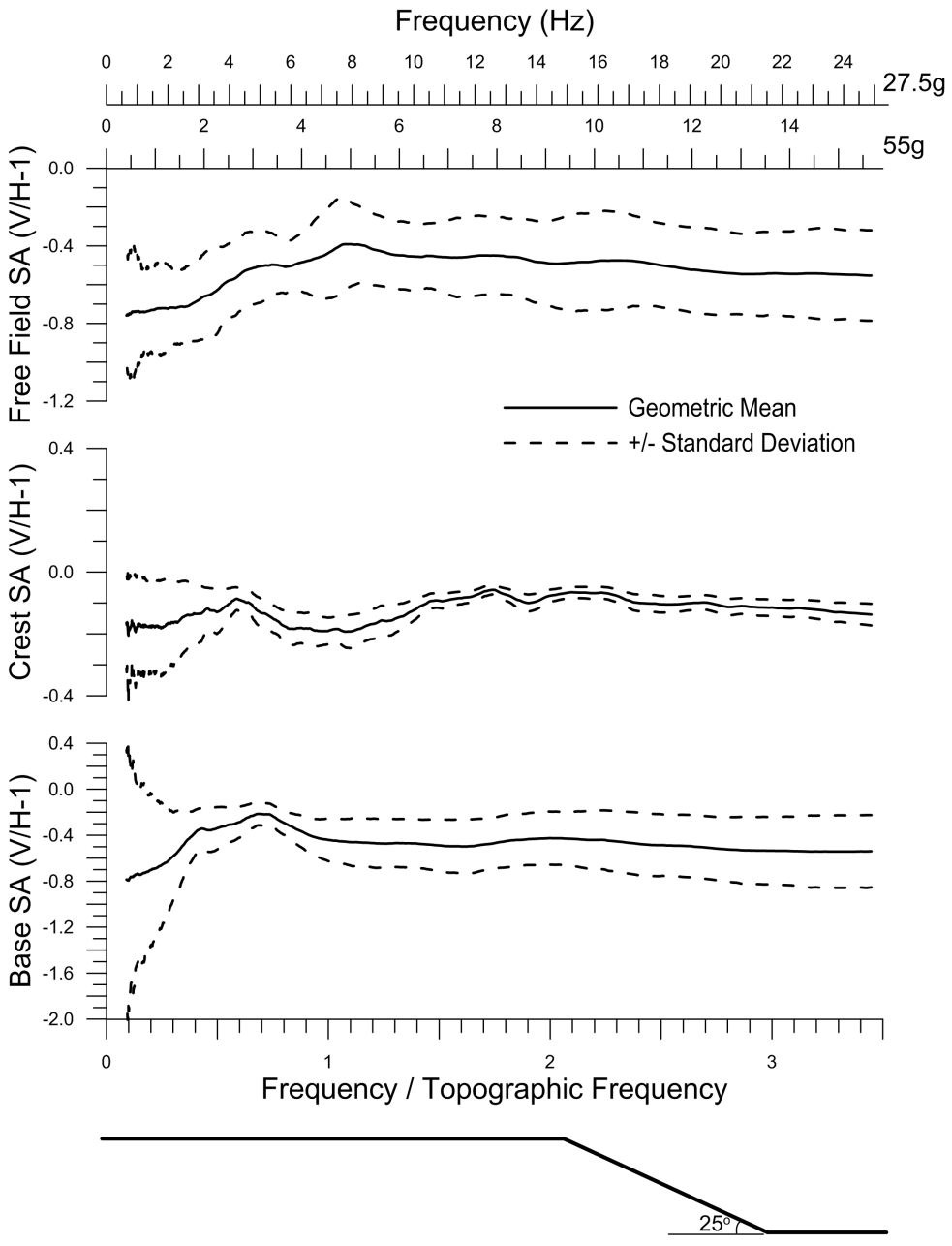

Figure 3.75: Geometric mean of vertical response spectrum normalized by the horizontal response spectrum for the free field, slope crest and base of both 25 degree slope prototypes. The normalized spectra are zeroed, similar to the TFs.

or equal to the topographic frequency, before leveling off around 90% at higher frequencies.

The notable lack of energy at lower frequencies for vertical motions at the base and in the free field does not exist at the slope crest. For this reason, the spectra depicted in Figure 3.74 exhibit significant amplification at low frequencies that overshadows amplification at other frequencies. Subsequently, the spectra also significantly differ in shape from those determined for the horizontal ground motions. A more familiar shape is achieved, however, if instead, the vertical response at the crest is normalized by the horizontal ground response in the free field (i.e., in past studies, for example by Ashford and Sitar (1997); Assimaki et al. (2005a); Bouckovalas and Papadimitriou (2005)) and at the base, illustrated by Figure 3.76.

The vertical to horizontal $SA\,TF$ and $SA\,AA$ spectra given in Figure 3.76 are similar in shape to those for the horizontal ground motions provided in Figure 3.27 for the 25 degree slopes. For both spectra, the response is greater near the topographic frequency for STR motions than for WTR motions. Amplification peaks near the topographic frequency for the $SA\,TF$ spectrum and a peak is found at the site frequency for the $SA\,AA$ spectrum before dipping and then plateauing near the slope topographic frequency. The peak mean $SA\,TF$ value of roughly 0.5 is significant, but by comparison weaker than the value of roughly 1.2 achieved for the horizontal $SA\,TF$.

The results presented for vertical ground motions have mainly focused on the response at the crest in comparison to the free field and base thus far. Figure 3.77 provides results for other locations along the slopes, allowing the spatial extent of topographic effects to be observed. The mean vertical $PGA\ TF$ and mean vertical $bp\ SA\ TF$ are plotted for all motions, STR motions and WTR motions at the locations where data was successfully recorded. As mentioned previously, a number of sensors did not function properly during the testing program. As a result, there are gaps in the spatial data that were not present in analyzing the horizontal ground motions.

Despite gaps in the spatial data, enough information is available to make useful observations. For both intensity measures, amplification peaks at the slope crest and typically diminishes to insignificant quantities at adjacent sensor locations in either direction. This

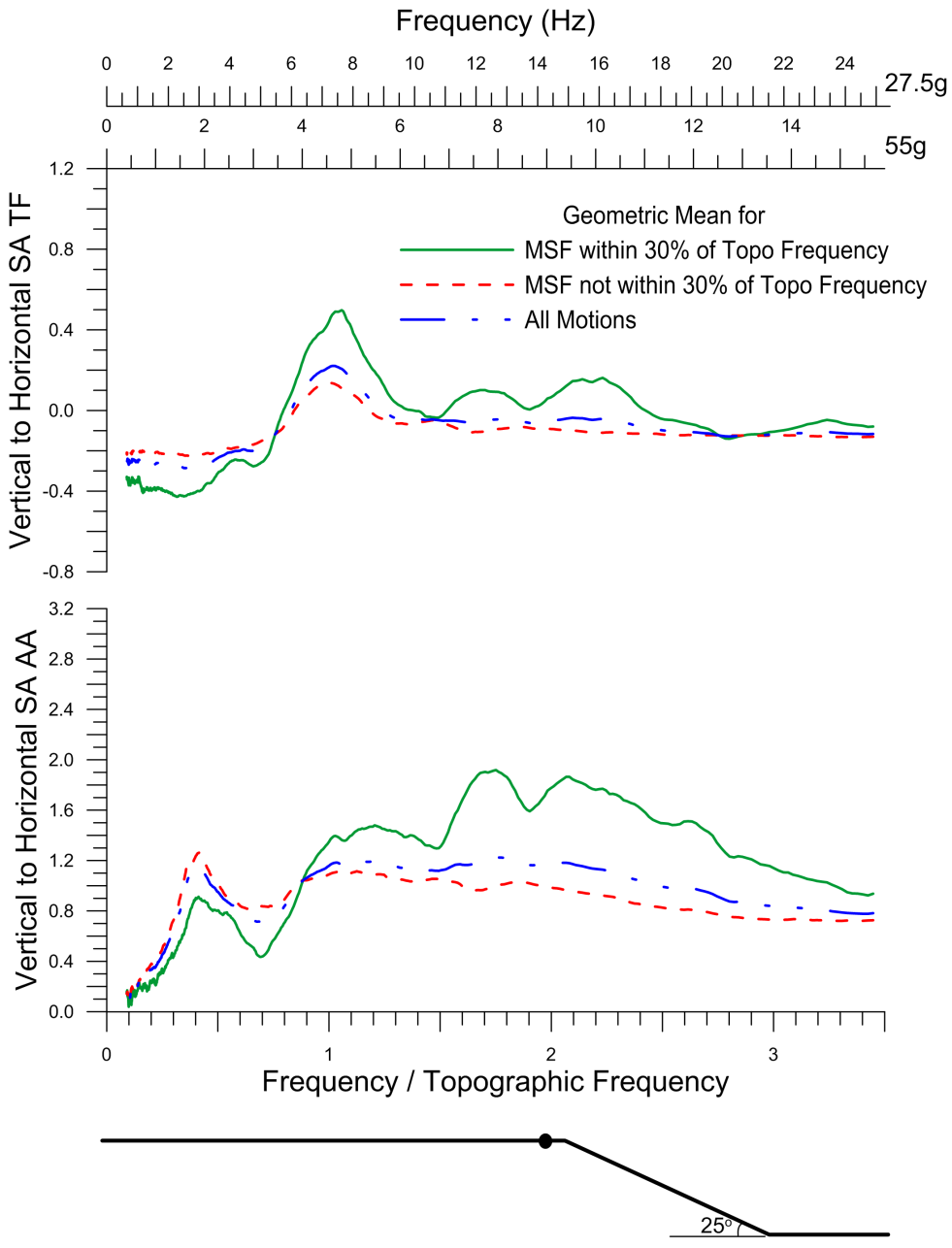

Figure 3.76: Geometric mean for the vertical to horizontal $SA\ TF$ and $SA\ AA$ spectra at the slope crest for both 25 degree slope prototypes grouped according to the MSF of the ground motion.

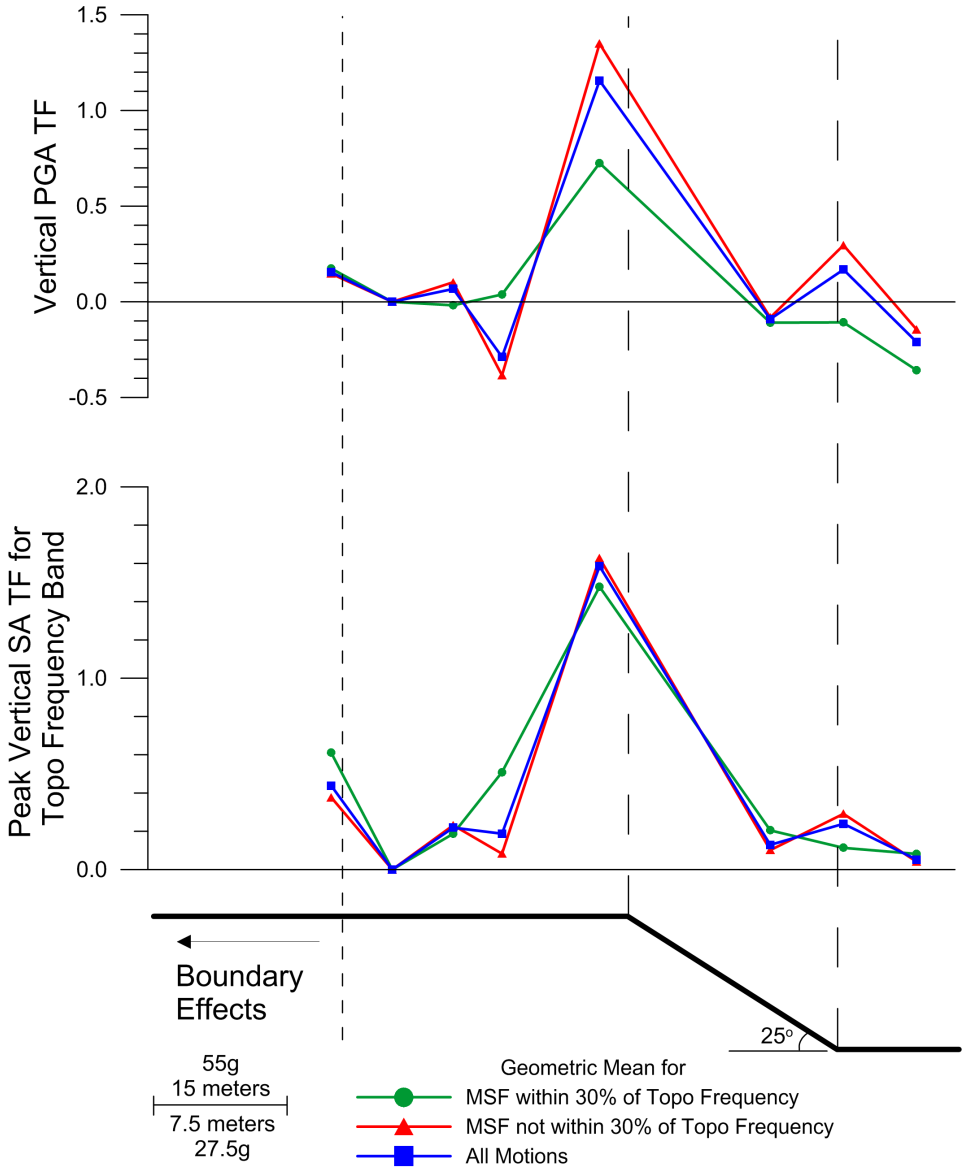

Figure 3.77: Geometric mean of the vertical $PGA\ TF$ and $bp\ SA\ TF$ for the topographic frequency band versus distance across the surface of the 25 degree slope for both prototypes grouped according to the MSF of the ground motion.

indicates that, on average, the vertical response is amplified for distances up to 16.7 (8.35) meters in front of the crest and 13.5 (6.75) meters behind the crest for the 55g (27.5g) prototype in comparison to the free field response. Of course, these distances may be exaggerated as a result of the lack of data between the crest and the sensor locations depicted. However, the distances observed here are comparable to those found for the horizontal ground motions.

Similar to Figure 3.74, the difference in mean values for the ground motion subsets are minimal near the topographic frequency, as is reflected here for the *bp* $SA\ TF$. At the crest, where maximum levels of amplification are observed, the mean *bp* $SA\ TF$ reaches 1.5 and 1.6 for the STR and WTR motions, respectively. A significant difference in the mean TFs determined for the STR and WTR motions is found, however, using PGA as an intensity measure, with maximum values of roughly 0.7 and 1.35 for the STR and WTR motions, respectively. As with the horizontal motions, due to relative differences in amplification for different frequencies, there is a noted difference in the perceived level of topographic amplification depending upon which ground motion intensity measure is used.

Thus far, relationships between different ground motion parameters and topographic effects for vertical ground motion have been introduced. Figures 3.78 and 3.79 present ground motion parameters that don't appear correlated to topographic effects by plotting the vertical $PGA\ TF$ and *bp* $SA\ TF$ at the slope crest against the Trifunac duration, PSS and base motion intensity. It is evident from these plots that none of these parameters influence the level of topographic amplification. The only possible exception is the input PGA, in that greater $PGA\ TFs$ are found for lower input PGA values. However, there are a number of ground motions with low input PGA values for which amplification was minimal or non-existent. Therefore, further study is required to confirm this potential trend.

The PGA and different measures of SA have been utilized in comparing ground motion intensity across the two prototype 25 degree slopes throughout this subsection. Other intensity measures, however, were also used in the ground motion analysis, such as the PGV and AI. Figure 3.80 compares the vertical $PGA\ TF$ to vertical TFs for PGV and AI at the slope crest. The $PGV\ TF$ values are generally similar to the $PGA\ TF$, plotting near

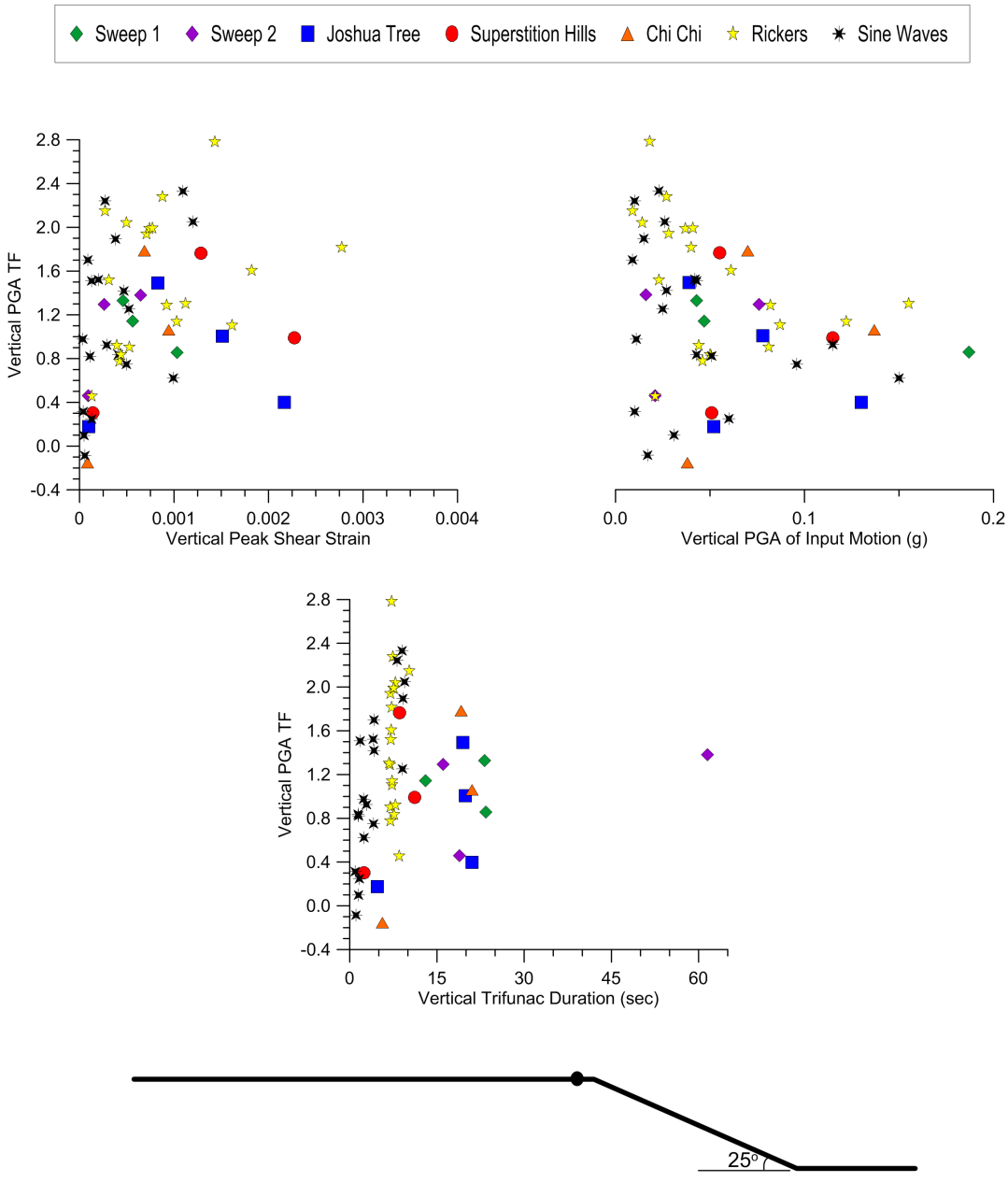

Figure 3.78: Vertical $PGA\ TF$ versus PSS, base input PGA and Trifunac duration at the 25 degree slope crest for both slope prototypes.

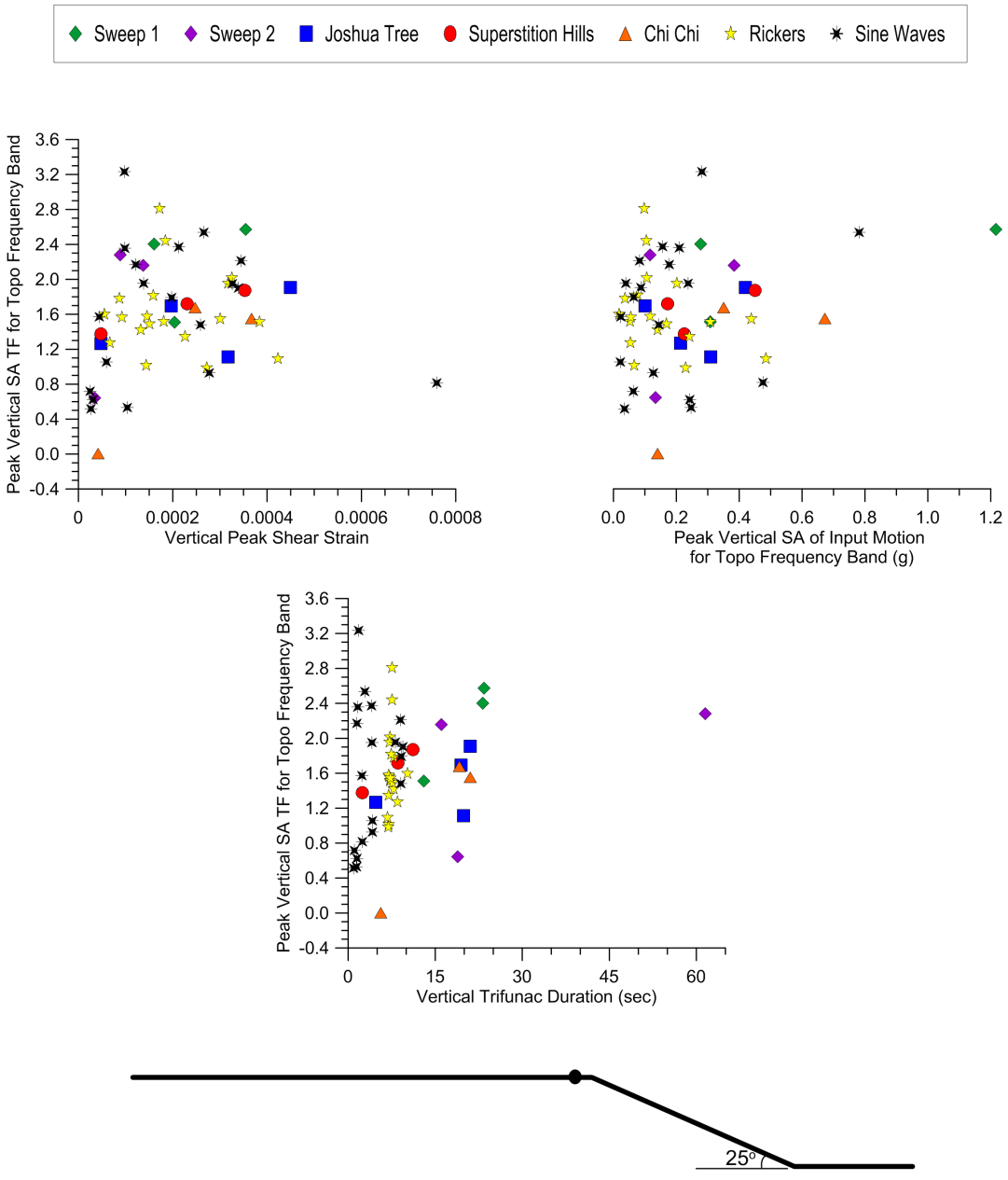

Figure 3.79: Vertical *bp SA TF* versus *PSS*, base input peak vertical *SA* and Trifunac duration at the 25 degree slope crest for both slope prototypes.

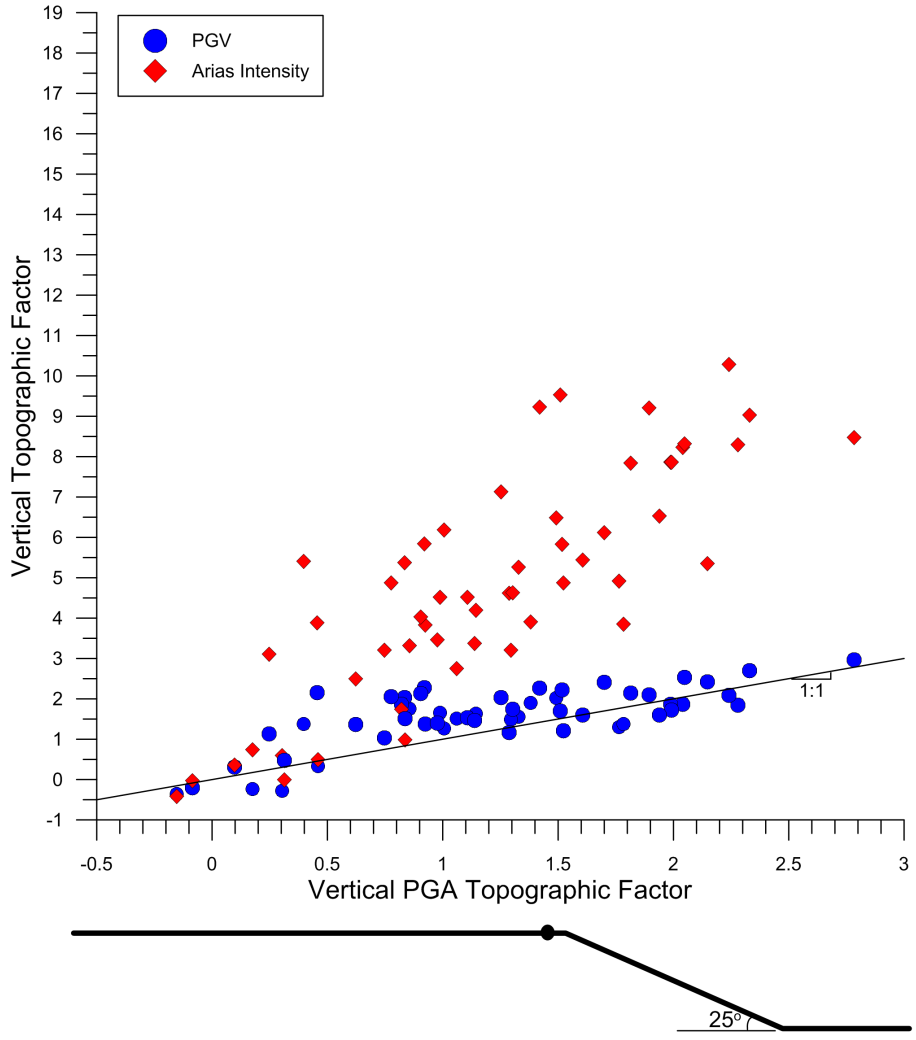

Figure 3.80: Vertical $PGV\ TF$ and $AI\ TF$ versus $PGA\ TF$ at the 25 degree slope crest for both slope prototypes.

the 1:1 reference line. The $AI\ TF$ values, however, are typically greater than $PGA\ TF$ for nearly all ground motions in the data set. The AI considers the build-up of energy for the entire ground motion, while the PGA or PGV consider a single point in time. Thus, greater $AI\ TF$ values signify change (from the free field) across a larger portion of the ground motion (and ground potentially ground motion frequencies) that may not be captured by PGA. This is in agreement with the $SA\ TF$ spectra presented earlier, which exhibited an amplified response across all frequencies of the ground motion.

It should be noted that the calculation of the response spectrum is based upon horizontally oscillating single degree of freedom systems. Thus, SAs determined this way are not typically used to quantify vertical accelerations. However, the normalized spectra presented in this subsection were based on the typical response spectrum calculations in order to allow for direct comparison to the horizontal ground motions presented in the previous subsections.

Finally, caution is warranted in interpreting the results presented in this subsection for vertical ground motion recorded during the centrifuge testing program. For pure horizontal shaking, there should not be a vertical component of ground motion present at the base of the soil substratum or in the free field. Indeed, for most numerical studies, the free field vertical component of motion does not exist, and thus vertical motion at the crest (deemed a parasitic vertical motion by Assimaki et al. (2005a)), is often normalized by the horizontal component of motion in the free field. However, for earthquakes recorded in the field, a vertical component of motion almost always exists. In the centrifuge, a vertical input motion is created as a result of 2-D and 3-D interactions of the shaker, container system, as well as due to rocking of the container and bucket attached to the centrifuge arm (Ilankatharan, 2008; Lai et al., 2002; Wilson et al., 1997).

The effects of container rocking are more extreme further from the center of the model, and therefore are most pronounced at the container boundaries. Of the three accelerometers at the base of the model, only one produced reliable data and it was located towards the north end of the container (see Figure 3.1), and thus was susceptible to container rocking. Additionally, although the free field sensor is free of boundary effects from the container, it

too is likely influenced by rocking. The sensor at the crest of the 25 degree slopes, however, is closer to the center of the model and thus the effects of rocking should be minimized. Normalization schemes adopted to interpret topographic effects are used throughout this subsection whereby vertical motion at the crest was normalized by the base and free field motion. The sensors used in these schemes are affected in different ways by container rocking, and consequently, the results determined in this way may be skewed. However, differences in observed behavior can still provide insight into topographic effects, as it is clear that vertical ground motions are significantly impacted at the slope crest in terms of both frequency content and amplitude. Furthermore, topographic effects interpreted by normalizing the vertical ground motions at the crest by horizontal motions at the base and free field, are minimally influenced by rocking, and thus useful for quantifying the impact of topography on vertical ground motion.

3.4 Discussion

Results from the analysis of topographic modifications of ground motion from a comprehensive centrifuge investigation of 3 one-sided slope geometries have been presented. The data collected included two slope prototypes (differing in size) for each of the slope inclinations of 30, 25 and 20 degrees. For each slope geometry, 54 common ground motions were introduced at the base of a thick sand layer using a horizontal shaker. Trends in the data were highlighted using a number of ground motion measures to analyze differences in the ground response across the surface of the slopes. This section serves to summarize and discuss the observations from the previous section in the context of topographic effects on ground motion for one-sided slopes.

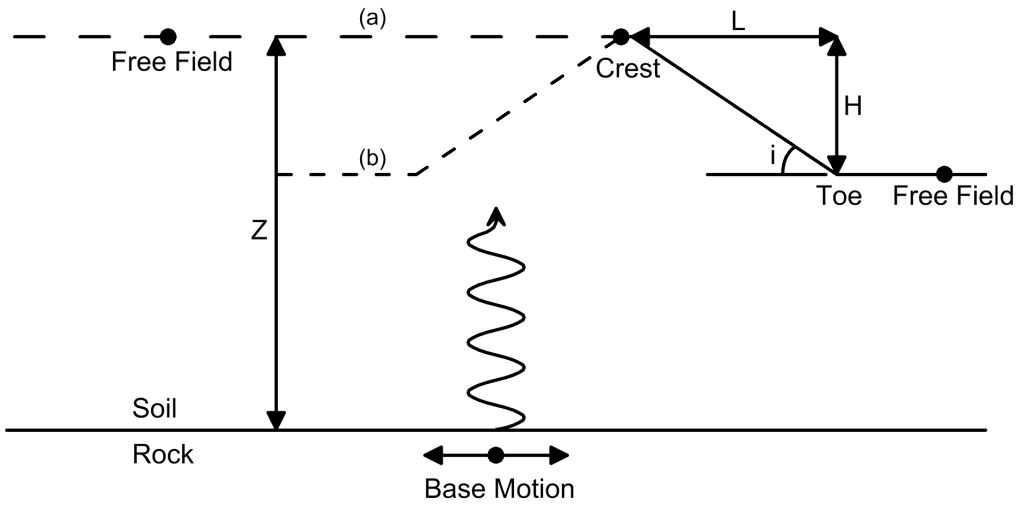

Figure 3.81: Important reference points and dimensions for an idealized (a) slope and (b) hill. The solid line to the right is shared by both diagrams.

An example of an idealized slope cross-section similar to those investigated is given in Figure 3.81 (line a). Important reference parameters, such as soil layer thickness (Z), slope height and length (H and L), slope inclination (i) and locations of interest, such as the slope

crest, are labeled in the diagram. In this case, the 'rock' half space at the base of the soil layer is mimicked by the metal model container rigidly attached to the actuators (shaker) below. Shear waves initiated by horizontal shaking of the actuators, propagate through the soil layer and interact with the geometry on the ground surface.

Using the average shear wave velocity and dimensions of the slope (or hill) depicted in Figure 3.81, a topographic frequency for the feature can be defined, at which peak topographic amplification is expected to occur. Two such frequencies were defined earlier in Section 3.2, with $f_t = \bar{V}_s/5H$ (Equation (3.4)) and $f_t = f(\bar{V}_s/2L)$ (Equation (3.5)) where f is a factor ranging from $0.7 - 1.0$, $\bar{V}_s$ is the average shear wave velocity, and H and L are the characteristic height and length of the slope (or hill). The former was determined empirically for slopes (line a in Figure 3.81) by Ashford et al. (1997), while the latter was semi-empirically arrived at for hill-like features (i.e., following line b in Figure 3.81), with the most recent iteration proposed by Paolucci (2002). One definition for the topographic frequency is based on the length of the feature, while the other is based on the height.

This investigation included six different slopes with three different slope inclinations. The slope height remained constant at 11 meters for the 55g prototype and 5.5 meters for the 27.5g prototype, while the slope inclination changed in both cases, resulting in different slope lengths. Despite changes in slope length, peak mean topographic amplification was observed at the same frequency for each of the prototype sizes and was found to be consistent with the definition proposed by Ashford et al. (1997). Accordingly, this definition of topographic frequency has been used exclusively in the analysis results presented, with $f_t = 4.5Hz$ and $f_t = 7.3Hz$, determined for the 55g and 27.5g prototype slopes, respectively. Equation (3.4) may be suitable for other hill-like topographic features not considered in this study, however, Equation (3.5) is proven to be more appropriate for the case of one-sided slopes.

The slope height and shear wave velocity are controlling parameters for the determination of the topographic frequency, which in turn influences topographic effects. Thus, the slope height and shear wave velocity can be considered indirect influences on the topographic modification of ground motion. Through the current investigation, a number of other pa-

rameters have been identified, and presented in Section 3.3, that directly impact if and to what extent ground motions are modified by slope topography. These parameters, along with their impact, will be highlighted in the following discussion with a subsection dedicated to each parameter. It should be noted that, as with Section 3.3, the discussion first focuses on horizontal ground motion, with a separate subsection devoted to vertical ground motion. A followup discussion, where findings from this investigation are compared to those of previous studies is also included.

3.4.1 Frequency Content

Ground motion frequency content is found to be one of the most influential parameters that can significantly impact the magnitude of topographic effects. The degree to which both the ground motion amplitude and frequency content at the crest and other locations on the slope are affected is dependant upon the frequency content of the incident motion. In particular, the relationship between the frequency content and the site and topographic frequencies is found to be of importance.

In this study, the MSF was utilized as a measuring stick for the relative ground motion frequency content at different sensor locations in and along the slopes considered. The MSF is a centroid-like frequency based on the Fourier amplitudes of a ground motion. Thus, energy contributions at frequencies above and below the MSF are relatively similar for the range of frequencies considered. A shift in MSF towards a higher value implies that more energy exists at frequencies higher than the original MSF value, while a shift in energy towards lower frequencies is marked by a lower MSF value.

For the ground motions considered, MSF values determined for the free field were typically similar to those of the base motion or shifted slightly towards the site frequency of the sand layer. At the slope crest, however, the MSF tended to shift towards the topographic frequency, a result of increased energy at that frequency. The magnitude of this shift was dependent upon the frequency content of the motion. In comparing MSF in the free field to that at the crest, it was found that motions with a MSF greater than the site frequency, but

farther from the topographic frequency experienced a greater shift towards the topographic frequency (shifting by as much as 55%) than those with a MSF already near the topographic frequency. If the MSF in the free field was less than the site frequency, however, the magnitude of the shift was reduced, or sometimes did not occur, indicating that topographic effects were less pronounced and site effects likely dominated the response for those motions. These effects were more pronounced for broadband motions, such as the frequency sweeps and earthquakes (see Figures 3.10, 3.25 and 3.40).

For a number of motions, the MSF at the slope crest moved closer to the slope topographic frequency as a result of the shift in the frequency content described above. This change in frequency content, could subsequently be related to the amplitude of the ground motion at the slope crest. The closer the ground motion MSF was to the topographic frequency, the more amplified the response was compared to the typical response in the free field. Ground motions with a MSF farther from the topographic frequency, and particularly those closer to the site frequency, generally exhibited little to no amplification (see Figures 3.11, 3.26 and 3.41). As an example, at the crest of the 30 degree slope, compared to the free field response, ground motions with a MSF similar to the topographic frequency were amplified by as much as 200% using PGA and roughly 500% using the $bp\ SA$ as a ground motion intensity measure, respectively. For the same slope conditions, no amplification or even deamplification of 20 to 30% was found for motions with a MSF near the site frequency.

This finding is significant because it implies that topographic amplification is influenced by the ground motion frequency content and highlights the importance of the site and topographic frequencies. Specifically, topographic amplification need not be considered in all cases, such as for ground motions with more energy near the site frequency, but can be extreme for ground motions with energy concentrated near the topographic frequency. This is true for ground motions recorded at the crest. Because of shifts in frequency content discussed above, however, incident motions with $MSFs$ near, but greater than the site frequency must also be considered. Although, it should be noted that motions with $MSFs$ already near the topographic frequency tended to be more amplified than those undergoing

larger shifts in frequency content.

Shifts in the ground motion frequency content and amplitude can be attributed to the frequency specific nature of topographic effects. Amplification of the ground motion was typically concentrated in a specific bandwidth that encompassed the topographic frequency, with less pronounced amplification sometimes present at other frequencies. Because components of the motion near the topographic frequency are more amplified, greater levels of amplification occur for motions with energy concentrated at those frequencies. This is supported by numerous figures in the previous section, such as Figures 3.12, 3.27 and 3.42. Furthermore, the amplification of the frequency components associated with the topographic frequency induces a shift in the ground motion frequency content, discussed above.

3.4.2 Amplitude

No connection between the amplitude of the incident ground motion and the level of topographic amplification was observed. Amplification at the crest was greater for some of the lower amplitude motions for the range of motions considered (input PGA values ranged from 0.03 and 0.3g). However, a large percentage of the lower amplitude motions were amplified no more than those with higher base amplitudes in considering both PGA and the $bp\ SA$ (See Figures 3.21, 3.22, 3.36, 3.37, 3.51 and 3.52). Therefore, it is possibly coincidence that some of the lower amplitude motions (according to PGA) were the most amplified motions at the slope crest.

The most greatly amplified motions at the slope crest, however, were found to correlate to the spatial extent of topographic effects, or the topographic zone of influence. Motions that exhibited greater topographic amplification typically affected a larger area of the slope. The magnitude of amplification declined with distance from the location on the slope where peak amplification (i.e., at the slope crest for the 30 degree slopes) was recorded. The distance required for the response to attenuate back to typical 1-D behavior was greater for the more amplified motions (See Figures 3.20, 3.35 and 3.50 and for example, compare Figures 3.14 and 3.15).

3.4.3 Slope Inclination

Modifications of the amplitude and frequency content across the surface of the slopes was influenced by the frequency content of the incident motion, and the modified amplitude in turn impacted the spatial distribution of topographic effects. The slope inclination affects all three of these elements. The relationship between frequency content and amplitude, or amplitude and spatial extent aren't necessarily changed by altering the slope angle. However, the magnitude of these effects is limited as the slope inclination decreases.

Ground motions with a MSF near the topographic frequency are typically the most amplified whether the slope angle is 20 or 30 degrees, however, the level of amplification is decreased for the 20 degree slopes. Similarly, the magnitude of the shift in frequency content towards the slope topographic frequency is reduced as the slope inclination decreases and generally the trend is not as strong for the 20 degree slopes as it is for slopes with an inclination of 30 degrees (particularly at the slope crest). Additionally, the number of motions for which no discernable topographic effects were found increased as the slope inclination decreased (See Figures 3.66 and 3.67). These results conform to the current understanding, in that topographic effects are greater for steeper slopes (Bard and Riepl-Thomas, 2000). An interesting consequence of changing the slope inclination was the alteration of the spatial distribution of topographic effects across the slopes.

For the 30 degree slopes the maximum ground motion intensity was recorded slightly behind the slope crest. For the 25 degree slopes, the peak response was located slightly in front of the slope crest, but for the 20 degree slopes it was found in the middle of the slope face. Therefore, decreasing the slope angle led to a shift in the location of the maximum recorded response on the slope. Despite this shift, however, the overall spatial extent of topographic effects was similar for the three slope geometries for motions in which topographic amplification was found. On average, significant topographic amplification extended 11 (5.5) meters behind (towards the free field behind the slope crest) and 22 (11) meters in front (towards the slope toe) of the location where the peak amplification was recorded

on the slope of the 55g (27.5g) prototype. Thus, the average size of the area on the slope affected was not altered, but the location of the affected area and distribution of energy was shifted as the slope inclination changed (See Figures 3.60, 3.61 and 3.62).

It should be highlighted that the size of the topographic zone of influence differed for the two prototype slope dimensions. The three slope inclinations tested at 27.5g were half the height and length of those tested at 55g and as a result, the topographic zone of influence at 27.5g was on average half that of the 55g slopes. Therefore the size of the topographic zone of influence was found to scale with the size of the slope considered. Normalizing by the slope height, the topographic zone of influence, on average, extends to distances of H meters behind and $2H$ meters in front of the location of peak topographic amplification. The distance in front of the peak response (i.e., $2H$) should be cautiously interpreted. A natural cutoff of the slope toe was used to analyze the extent of topographic effects and this number reflects that cutoff point. However, container boundary effects likely influenced the ground response leading to greater amplitudes at the slope toe. Therefore, the value of $2H$ could be viewed as an upper limit to the extent of topographic effects in that direction.

Another important consideration is the depth below the slope crest that was influenced by topographic effects. Typically a curved surface could be drawn connecting surface locations at the edge of the topographic zone of influence in either direction from the peak response (i.e., points H behind and $2H$ in front). This is evidenced by the cross-sectional contours provided in Figures 3.6 and 3.8. While this method for determining the depth affected is not precise, it provides a reasonable estimate of the depth for which topographic effects must be considered. A diagram of the topographic zone of influence is provided at the bottom of Figures 3.20, 3.35 and 3.50.

3.4.4 Type of Ground Motion

Four types of ground motions were utilized in this study with variations in frequency content and amplitude. The Ricker wavelets and sine wave motions were narrow-banded in that they were associated with a specific central frequency. The frequency sweeps and earthquake

motions were rich in frequency content and thus could be considered broadband motions.

The type of ground motion did not appear to influence the magnitude of topographic effects captured in this study. Both broadband and narrow-band motions exhibited changes in frequency content and amplitude and typically followed the same trends. Because frequency content has a significant impact on topographic effects, in general, a broadband motion would presumably be more susceptible to topographic modifications, as the likelihood of the motion containing frequencies that would be amplified as a result of the topography is greater. The amplification of these components of motion would also, subsequently, have a more profound effect on the ground motion MSF. However, a narrow-banded motion with energy concentrated at a frequency compatible with the topographic feature can still be significantly modified. Differences in the behavior of these types of motions is analyzed further in the time domain in the next chapter.

3.4.5 Duration

The ground motion duration was not found to impact topographic effects, nor was it modified by topography. Only overall ground motion duration was analyzed in this study. The influence of duration of motion at particular frequencies was not explored. Although, even motions with a number of cycles at the same frequency, such as sine wave motions, did not appear to be affected. The impact of cycles of motion at particular frequencies will, however, be investigated further in the next chapter.

3.4.6 Induced Non-Linearity

The PSS was used as a measure of induced non-linearity resulting from higher intensity shaking. Non-linear soil behavior has been thought to either increase topographic amplification due to energy trapping in the softened layers near the surface (Assimaki et al., 2005b) or possibly decrease it due to the damping of energy that results from the reduction in stiffness (Bard and Riepl-Thomas, 2000). However, using PSS as a proxy for non-linear behavior, no correlation between topographic amplification and non-linear behavior was found.

3.4.7 Vertical Motions

Analysis of the vertical component of ground motion was limited due to malfunctioning accelerometers across the slope configurations. Only the 25 degree slopes could be properly analyzed as it was the only configuration for which the crest sensor was functioning properly. As with the horizontal motions, vertical motions at the crest, free field and base were analyzed and the responses were compared.

It should be reiterated here that vertical ground motion recorded in the centrifuge is influenced by container rocking and that the base vertical motions recorded are a result of this rocking, as well as 2-D and 3-D interaction of the centrifuge bucket-shaker-container system. However, these effects are minimized at the slope crest, where topographic effects were found to be significant.

In considering vertical ground motion at the crest normalized by that in the free field, or at the base, amplifications were found to be greatest at low frequencies and were amplified by as much as 280%. Both the free field and base ground motions typically lacked low frequency components of motion that were present at the slope crest, which tended to mimic the response of the horizontal component of motion (but was typically slightly weaker). Although the low frequency components of ground motion at the crest exhibited the greatest levels of amplification, SAs typically were amplified across all frequencies in comparison to the free field. Additionally, unlike horizontal ground motions, the level of amplification was not tied to the proximity of the MSF of the motion to the topographic frequency of the slope. In fact, motions with low $MSFs$ at the crest were typically the most amplified. This result is due to the lack of energy found at lower frequencies in the free field (see Figure 3.74).

Other qualitative aspects of the vertical motions were found to be similar to those of horizontal ground motions. Namely, ground motion duration, induced non-linearity and the amplitude of the incident vertical ground motion did not appear to influence the magnitude of topographic effects (see Figures 3.78 and 3.79). Additionally, the spatial extent of topo-

graphic effects was roughly equivalent to that found for horizontal motions (see Figure 3.77). However, as mentioned previously, data at sensor locations adjacent to the crest sensor was not captured. Consequently, it was assumed that topographic effects were prevalent at these locations when determining the topographic zone of influence.

As the vertical accelerometer at the crest is the least susceptible to container rocking effects, insight into topographic effects can also be gained by normalizing vertical ground motion at the crest to horizontal motion at different points of interest (i.e., the free field and base). In comparing vertical and horizontal motion at the crest, it was found that PGA values and MSF values were typically similar (see Figures 3.72 and 3.70). However, SAs were on average slightly weaker at all frequencies (see Figure 3.75). This indicates that although weaker, at the crest, the ground motion in both the vertical and horizontal directions is generally similar. As a result, the vertical to horizontal $SA\ TF$ spectrum produced by normalizing the response in the vertical direction at the crest by the horizontal response in the free field was similar to that produced for the horizontal ground motions (see Figure 3.76). In particular, topographic amplification was found to peak within a concentrated bandwidth encompassing the topographic frequency and indeed the measured vertical response at the crest was greater than that of the horizontal free field by roughly 50%. Either no amplification, or deamplification, was observed at all other frequencies outside of the bandwidth encompassing the topographic frequency.

3.4.8 Additional Discussion and Comparison to Past Studies

In order to perform non-destructive tests, the slope inclinations considered in this study were limited by the ground material used (dry Nevada sand). As a result the slope inclination was limited to 30 degrees. This was compared to the response of shallower slopes with inclinations of 25 and 20 degrees. However, despite the limited range of slope inclinations investigated, the observed effects of slope steepness were consistent with previous studies. That is, at or near the crest, where the peak response is typically detected, topographic amplification was greater for steeper slopes (Ashford et al., 1997; Bard and Riepl-Thomas, 2000; Bouckovalas

and Papadimitriou, 2005; Tripe et al., 2013). Additionally, changes in frequency content associated with topographic effects were also more significant at higher slope inclinations. One noticeable difference in the observed behavior, however, was the location where peak topographic amplification was observed.

Greater amplification was observed near the crest for the 30 and 25 degree slopes. However, the peak response for the 20 degree slopes was found in the middle of the slope face. Past studies of similar slope conditions have not typically considered slopes with inclinations less than 30 degrees, with the exception of one study performed by Bouckovalas and Papadimitriou (2005); although for this study, results along the slope face were not reported. Without a basis for comparison, it is unclear if the outcome for the 20 degree slopes is unique to the testing conditions of this study. It's possible that for longer, shallower slopes the differential motion between the slope toe and crest is more extreme, leading to a more amplified response on the slope face; something that may not occur on steeper, shorter slopes. It should be noted that regardless of location, however, peak values of topographic amplification did generally decline with slope inclination, with the exception of STR motions, for which peak mean values on the 25 and 20 degree slopes were found to be comparable (although in different locations). To better understand this occurrence for STR motions and the cause of this shift in the location where peak amplification is observed, further investigation is required.

From these findings, it is clear that topographic effects should be considered with slopes as shallow as 20 degrees, even though the effects are minimized. Because slopes shallower than 20 degrees were not considered in the current study, a threshold slope inclination, below which topographic effects need not be considered, was not found. The relevance of topographic effects at 20 degrees, however, is consistent with the findings of Bouckovalas and Papadimitriou (2005), and the Eurocode (Eur, 2004) which recommend a cutoff slope inclination of 17 and 15 degrees, respectively.

For a given slope inclination, ground motion frequency content was found to be the highly influential. Highlighted earlier, observed changes in the ground motion frequency content and amplitude were found to be related to the frequency content of the incident motion

with notable differences between the free field and crest responses observed. Additionally, topographic amplification peaked within a concentrated bandwidth that encompassed the topographic frequency; illustrated by the spectra of the $SA\ TF$ presented in the previous section. This band-concentrated response is consistent with the findings of previous studies (Bard and Riepl-Thomas, 2000; Geli et al., 1988). The connection between topographic amplification and the frequency content of the incident motion has also formerly been qualitatively observed by (Bouckovalas and Papadimitriou, 2005; Brennan and Madabhushi, 2009; Tripe et al., 2013). The quantitative link between amplification and the MSF of the motion relative to the site and topographic frequencies is new to this study.

Of the studies referenced above, those performed by Bouckovalas and Papadimitriou (2005) and Tripe et al. (2013) were numerical, while that by Brennan and Madabhushi (2009) was a physical model in a centrifuge. The centrifuge study by Brennan and Madabhushi (2009) pointed out the significance of the incident ground motion frequency content and found that frequencies above the site frequency were amplified at the crest, similar to the current investigation. This study, however, was limited in scope with conclusions mainly drawn from one ground motion, inhibiting the ability to expand this idea further. For the numerical simulations, wavelet pulses and harmonic motions were deployed at differing central frequencies and the relative peak amplifications observed for these different ground motions were compared. Motions with central frequencies near the topographic frequency were typically found to exhibit greater amplification. This too is similar to the current investigation when considering the Ricker wavelets and sine motions, for which the MSF would typically align with the central frequency of the motion. Using MSF, however, enabled the connection between frequency content and topographic amplification to be quantified and importantly can be applied to real ground motions.

Due to its correlation to ground motion frequency content relative to the site conditions, topographic amplification is difficult to quantify such that it would be applicable to a wide variety of conditions. This may explain, in part, the discrepancies in reported amplification values from previous studies. For numerical and analytical investigations, amplification val-

ues between 1 and 3 (corresponding to TFs of 0 and 2 in this study) have been reported considering both spectral amplitudes and PGA. For field studies amplification ranges of 1 to 5 and 1 to 30 have been reported for PGA and spectral amplitudes, respectively (Bard and Riepl-Thomas, 2000; Geli et al., 1988; Pagliaroli et al., 2011). Typically, Fourier amplitudes, rather than SAs from a response spectrum, have been used in determining spectral amplification, although both have been considered.

For the current investigation, TFs ranged from -0.4 to 2.0 (ratios of 0.6 to 3.0) for PGA and -0.2 to 5.0 (ratios of 0.8 to 6.0) for peak SAs near the topographic frequency. These ranges overlap with and exceed numerical studies, and are comparable to the lower levels of amplification found in the field investigations. Field investigations typically lack a proper reference sensor and, consequently, amplification at the crest of a feature is often quantified by comparing the response to the toe. This can lead to increases in perceived amplification due to deamplification at the toe of the topographic feature (Geli et al., 1988). Changes in geology and lack of geotechnical information can also lead to differences in amplification levels found in the field. Additionally, many of the features studied have been mountains or hills, for which the crests are more susceptible (than slopes) to constructive interference of diffracted propagating waves, possibly leading to greater amplification.

Although numerical investigations have typically been found to underestimate topographic amplification in the field, as mentioned, the amplification range found in this study does overlap with those found numerically. In making this comparison, however, it should be considered that a number of these investigations have been for slopes steeper than those investigated here and, as discussed earlier, greater amplification is typically achieved for steeper slopes. Investigations that have considered 30 degree slopes have found amplifications at the crest to correspond to TFs of roughly 0.2 (Ashford et al., 1997), 0.2 (Bouckovalas and Papadimitriou, 2005) and 0.8 (Tripe et al., 2013), considering peak SA at the topographic frequency, which is significantly lower than those found in the current study. This discrepancy may result from differing site conditions, such as differing shear wave velocities and slope heights. However, it could be the product of simplifying assumptions used to model

topographic behavior (i.e., using a constant shear wave velocity with depth).

The most recent study, by Tripe et al. (2013), suggested that the proximity of an underlying rock base (or stiffer material, creating a large impedance contrast) beneath the soil layer which the slope consists of, influences topographic amplification. It was found that the amplification increased as the depth to bedrock decreased. This was also noted by Ashford et al. (1997) where transfer functions of the response at the slope crest over the base input at both the topographic and site frequencies were found to increase with decreasing depth to bedrock. And indeed, the studies by (Ashford et al., 1997) and (Bouckovalas and Papadimitriou, 2005), where the soil was modeled as a half space continuum, did find lower amplification values. Thus, this explanation could apply to differences in the observed behavior of the former studies and the results of the current investigation. In the Tripe et al. (2013) study, the shallowest depth to bedrock considered was 125 meters. For this study, the depth to the base of the container was 31.4 meters (15.7 meters) for the 55g (27.5g) prototype. This may account for the increased amplification found in this investigation. It should be noted, however, that no appreciable difference in topographic amplification was found between the two prototypes, despite changes in the depth of the soil layer. Although, the slope height, which differs for the two prototypes, remained constant in the study performed by Tripe et al. (2013) while only the depth to bedrock was altered.

Both the study by Tripe et al. (2013) and Ashford et al. (1997) indicated that site amplification dominated the response at the slope crest, making topographic amplification a secondary contributor to the ground motion amplitude. This investigation contrasts with those findings. For the 30 degree slopes, on average, topographic amplification was found to be greater than site amplification for motions that had a MSF within 30% of the topographic frequency. This is illustrated by Figure 3.17 in the previous section, where the combined effects of site and topographic amplification at the topographic frequency are greater than site amplification at the site frequency. Discounting the contribution of site effects at the crest, the amplification at the topographic frequency would still be greater, on average, than site amplification at the site frequency in the free field (where the peak response occurs). This

new finding has important implications for the consideration of topographic amplification, as it can no longer be thought of as secondary to site amplification for all cases.

Comparisons between the results of this and previous studies have been provided for horizontal ground motion. However, the vertical ground response can also be compared to the featured former studies. The studies performed by Ashford et al. (1997), Bouckovalas and Papadimitriou (2005) and Tripe et al. (2013) analyzed vertical amplification by normalizing the vertical response at the crest by the horizontal response in the free field, and found ratios of roughly 0.2, 0.2 and 1.6, respectively for 30 degree slopes. This compares to a mean ratio of 1.5 for motions that have a MSF within 30% of the topographic frequency for the 25 degree slopes analyzed in this investigation. The results reported by Tripe et al. (2013) are, again, more similar to those from this study, potentially influenced by the presence of a strong impedance contrast beneath the soil substratum.

3.5 Conclusions

The results of an extensive centrifuge experiment to investigate topographic modification of ground motion have provided useful insights into the trends associated with the phenomenon for the case of one-sided slopes. A number of qualitative findings from previous studies have been confirmed and others have been discovered. The effects of topography were quantified for the site conditions investigated, and comparisons to relevant previous studies were provided.

In order to quantify topographic effects, it was found that both slope inclination and ground motion frequency content, in relation to the site and topographic frequencies, must be examined. Therefore, some knowledge of the site conditions is required, such as the shear wave velocity profile and soil layer depths. The frequency ranges for which topographic effects must be considered were well within the typical range of frequencies of concern for engineering practice. Frequencies of importance will vary, however, given different slope conditions and therefore cases may exist where topographic effects need not be considered. Indeed, even for the site conditions analyzed in this study, it was found that ground motions

with a MSF below that of the site frequency didn't typically exhibit significant topographic effects. Other effects and significant findings from the analysis presented in this chapter are highlighted below. The reader is referred to Section 3.2 and the Chapter 3 Glossary for a reminder of the various factors and parameters introduced during this chapter.

- Both frequency content and amplitude are affected by topography, such that at the slope crest:
  - PGA ranged from 50% less than to 200% greater than the free field;
  - for STR motions, at locations of peak amplification, mean PGA values are roughly 60%, 40%, and 40% greater (adjusted for natural fluctuations) than the free field for the 30, 25, and 20 degree slopes, respectively;
  - peak SA near the topographic frequency ranged from 50% less than to 500% greater than the free field;
  - for STR motions, at locations of peak amplification, mean peak SA are roughly 190%, 120–140% and 120–140% greater (adjusted for natural fluctuations) than the free field for the 30, 25, and 20 degree slopes, respectively (the peak amplitude listed for the 20 degree slopes is reflective of the peak response, which occurred on the slope face — at the crest, the mean peak values are roughly 60%);
  - ground motion MSF shifts by as much as 55% for the 30 and 25 degree slopes and 30% for the 20 degree slopes in comparison to the free field;
  - vertical SAs are on average 50% greater than that of the horizontal free field motion for STR motions for the 25 degree slopes.
- The topographic amplification ranges given above overlap with and exceed previous numerical investigations and span the lower range of field studies.
- The most significant levels of topographic amplification are concentrated to a frequency band encompassing the topographic frequency; consistent with previous studies.

- The topographic frequency defined by Ashford et al. (1997) is appropriate for the slopes considered.
- Peak topographic effects occur at the crest of steeper slopes (also consistent with previous studies), but can migrate to the face of shallower slopes (further investigation is required to confirm this finding for other slope conditions).
- Greater topographic amplification leads to a larger topographic zone of influence.
- The topographic zone of influence on average spans a horizontal distance of the slope height, H, behind (towards the free field) and $2H$ in front of (towards the slope toe) the location where peak amplification occurs.
- In terms of SAs, topographic amplification can be greater than site amplification for certain conditions (i.e., for given frequency content and slope steepness).
- Vertical ground motion is similar in amplitude and frequency content to horizontal ground motion at the slope crest.

Physical modeling in the centrifuge, despite limitations, has proven to be a powerful tool for collecting data to be used in analyzing topographic effects in a systematic, practical manner. Boundary effects were carefully examined and considered in the data analysis, although they could not be completely avoided. The spatial extent of topographic effects was particularly difficult to quantify due to the possible presence of container boundary effects near the slope toe, and on the lower face of the slope. However, an area between the free field sensor and the face of the slopes (towards the toe) was free of these effects. The centrifuge data is interpreted further in the next chapter, which continues to explore the topographic modification of ground motion, and investigates the mechanisms leading to topographic effects, by carrying out analysis in the localized time domain.

Chapter 4

TOPOGRAPHIC EFFECTS: TIME DOMAIN ANALYSIS OF CENTRIFUGE DATA

Evidence of topographic effects identified through the analysis of data from an extensive centrifuge investigation of one-sided slopes was provided in the previous chapter. Qualitative trends and quantitative results were presented for a large volume of ground motions, using various intensity measures. The response at numerous near surface slope locations were highlighted, with emphasis on the crest, and the free field behind the crest. The surface response was also compared to the input (base) motion.

The aim of this chapter is to shift from a descriptive to causal understanding of topographic effects. The previous chapter focused on *what* occurred; topographic effects were identified and quantified. This chapter focuses on the fundamental reasons *why* topographic effects occur. By understanding the causes and influences of topographic effects, the ability to predict topographic effects and topographic amplification is improved. For instance, numerical modelers will have a better understanding of the behavior that should be captured. This can impact the design of structures near slopes and methods used to analyze the stability of slopes during transient earthquake loading.

The effects of topography have been studied numerically, analytically and experimentally for a number of topographic features. This has naturally led to the exploration and development of numerous theories about what causes and influences topographic effects. Previous studies have found qualitative agreement on some of the identified mechanisms. These have been summarized in Bard and Riepl-Thomas (2000) and Pagliaroli et al. (2011), and were presented in Chapter 2. Some of the mechanisms thought to influence and/or cause topographic effects are:

- The incidence angle of propagating waves relative to the sloping ground surface. In particular, surface motion can be particularly extreme for the case of critical incidence, cited as a contributing factor for the damage observed during the Whittier Narrows, California earthquake of 1987 (Bard and Riepl-Thomas, 2000; Kawase and Aki, 1990).

- Focusing or de-focusing of seismic waves due to reflections off the surface of topographic features. This was demonstrated analytically for a wedge-shaped medium by Sánchez-Sesma (1990), however instrumental evidence of this effect does not currently exist (Bard and Riepl-Thomas, 2000).

- Diffraction of body and surface waves propagating downward and outwards from a feature, leading to interference patterns between the diffracted and direct waves. Diffracted surface waves generally are smaller in amplitude than direct body waves, and therefore contribute less energy. This was demonstrated by Pedersen et al. (1994) for a site in Greece, where the amplitude of outgoing waves was found to be roughly one-fifth of the incident wave (Bard and Riepl-Thomas, 2000).

- Resonance of the topographic feature. This phenomena was noted by Pagliaroli et al. (2011) and more extensively discussed in Paolucci (2002). Among others, it has been indicated as a controlling factor for the case of Tarzana Hill, California by Bouchon and Barker (1996) and Graizer (2009).

Typically the influence of topographic and site effects on the ground surface response have been considered separately. However, recent studies, such as those by Assimaki et al. (2005a); Graizer (2009); Tripe et al. (2013), have indicated the two phenomena are coupled. In other words, topographic effects may be magnified or inhibited as a result of the subsurface stratigraphy. Softer soil (or rock) layers near the surface can aid in the resonance of a feature (Graizer, 2009), or lead to trapping of energy, resulting in additional amplification, or the generation of surface waves at the crest of a feature (Assimaki et al., 2005a). Additionally, surface waves generated by resonance of the free field in front of toe of the slope could

propagate up the slope face, resulting in greater amplification at the crest (Assimaki et al., 2005a).

Each of the hypothesized causes identified above are addressed for the analyses presented in this chapter. The mechanisms that influence topographic effects are explored utilizing data from the dense arrays of accelerometers, at depth and near the surface of the slopes considered. The conditions that lead to, and characteristics of, these modifications are demonstrated through analysis in the localized time and time-frequency domains using a representative suite of ground motions.

The mechanisms presented are directly applicable to the site conditions explored, and therefore cannot necessarily be applied across a broad range of topographic features. This is particularly true if site and topographic effects are indeed coupled. However, the results from the centrifuge experiments provide further insight into the mechanisms that lead to topographic effects; complimenting and expanding upon previous work using other methods. Use of the centrifuge allowed for significantly greater data resolution and better site characterization than can be accomplished in a field experiment, while still maintaining the complexity of a true physical process. Suites of ground motions were introduced allowing the influence of various ground motion characteristics to be examined.

The structure of this chapter is similar to that of the previous chapter, in that results are first presented for horizontal ground motions, followed by discussion of the vertical ground motions recorded mainly near the ground surface. The combined motion of the horizontal and vertical components is also explored as a means of identifying the potential presence of Rayleigh waves; allowing the overall displacement shape of the slope to be visualized.

4.1 Analysis Approach

4.1.1 Ground Motions

Time and time-frequency domain analyses were performed for a select group of ground motions based on the characteristics of those motions and the results presented in the previous

chapter. The selected suite of motions ranged from those exhibiting significant topographic effects to those for which the effects were minimal, allowing differences in behavior to be observed. Additionally, at least one of each type of motion (i.e., frequency sweeps, sine waves, Ricker wavelets and earthquakes) introduced during the centrifuge investigation was included in the analysis. Typically, the slope response was considered for multiple iterations of each motion type to ensure that similar behavioral patterns could be identified. However, for brevity only select representative motions will be presented here.

The representative motions can be easily divided into two main categories — idealized motions and earthquake, or non-idealized, motions. Acceleration time histories of the idealized motions recorded at the base (i.e., input motions) are depicted in Figure 4.1, comprised of a series of Ricker wavelets, a packet of sine waves and two frequency sweeps. The selected earthquake base motions are presented in Figure 4.2 and include Joshua Tree (JOS090), Superstition Hills (BPTS315), Chi Chi (TCU078E) and Chi Chi with the time step cut in half ($^1/_2\Delta t$).

As described in the previous chapter, series of Ricker wavelets and sine waves (with 12 cycles) at different target central frequencies were strung together in time as a measure of efficiency during the centrifuge investigation. As a result, the motions were introduced to the different slopes as they are depicted in the top two plots in Figure 4.1. However, the intention was to examine the response of the slopes to 12 cycles of sine wave motion, or Ricker wavelet pulses, at specific central frequencies. Thus, these motions were divided in time and assessed as separate ground motions for portions of this analysis.

For the Ricker wavelets, the pulses were introduced such that at each central frequency, there was a displacement pulse in both the positive (towards the slope face) and negative (away from the slope face) direction for the one-sided slopes. Thus, in dividing the wavelets in time, two Ricker wavelets were included for each divided time history. The representative pair of wavelets to be presented in this chapter is depicted in the top plot of Figure 4.1, between the two vertical gray lines. The target frequency for these wavelets was 4Hz, however, the achieved central frequency was closer to 2Hz.

For the wavelets, after each pulse, ground motion ceased before the next pulse was introduced, making the division of the time history fairly straightforward. For the sine wave motion, on the other hand, erratic ground motion was typical during the transition from one central frequency to another. In order to concentrate on steady-state sine wave motion, the transient portion of the motion was eliminated when dividing the time histories. Consequently, instead of 12 cycles of sine wave motion, typically 8-10 cycles of sine wave motion was preserved for each central frequency. For the representative motion used, the time cutoff points for sine wave motion with target frequencies of 1Hz, 2Hz and 4Hz are depicted in the second plot of Figure 4.1, between the blue, green and red lines, respectively. For both the wavelets and sine wave motions, the beginning and end of the time histories were subsequently padded with zeros after they were divided in time.

Ground motion parameters for each of the motions depicted in Figures 4.1 and 4.2 are given in Tables 4.1 and 4.2, respectively, for the base, crest and free field locations. It should be noted, that in the tabulated values for the Ricker wavelets and sine wave motions are representative of the divided time histories outlined above. Next to each ground motion, a letter, or letter-number designation is provided as a reference for the particular ground motion. Due to the large volume of motions introduced throughout the testing program and due to the fact that each ground motion type was introduced at multiple amplitudes, each unique command motion (i.e., motion commanded to the shaker) was given a letter representation for ease in data analysis. This was particularly useful in comparing the response from the same command motion for different slopes or model configurations. For example, the frequency sweep designated (c) was introduced to all six model configurations. The actual recorded base motion naturally differed, due to changes in model mass and inherent variation in the motion produced by the shaker, but the command motion remained the same. The divided motions also received a number designation, which simply refers to the order in which a pair of wavelets or 12 cycles of sine motion appear for the different central frequencies. Thus, the designation (l3) refers to the third pair of wavelets for the ground motion (l) (depicted in the top plot of Figure 4.1).

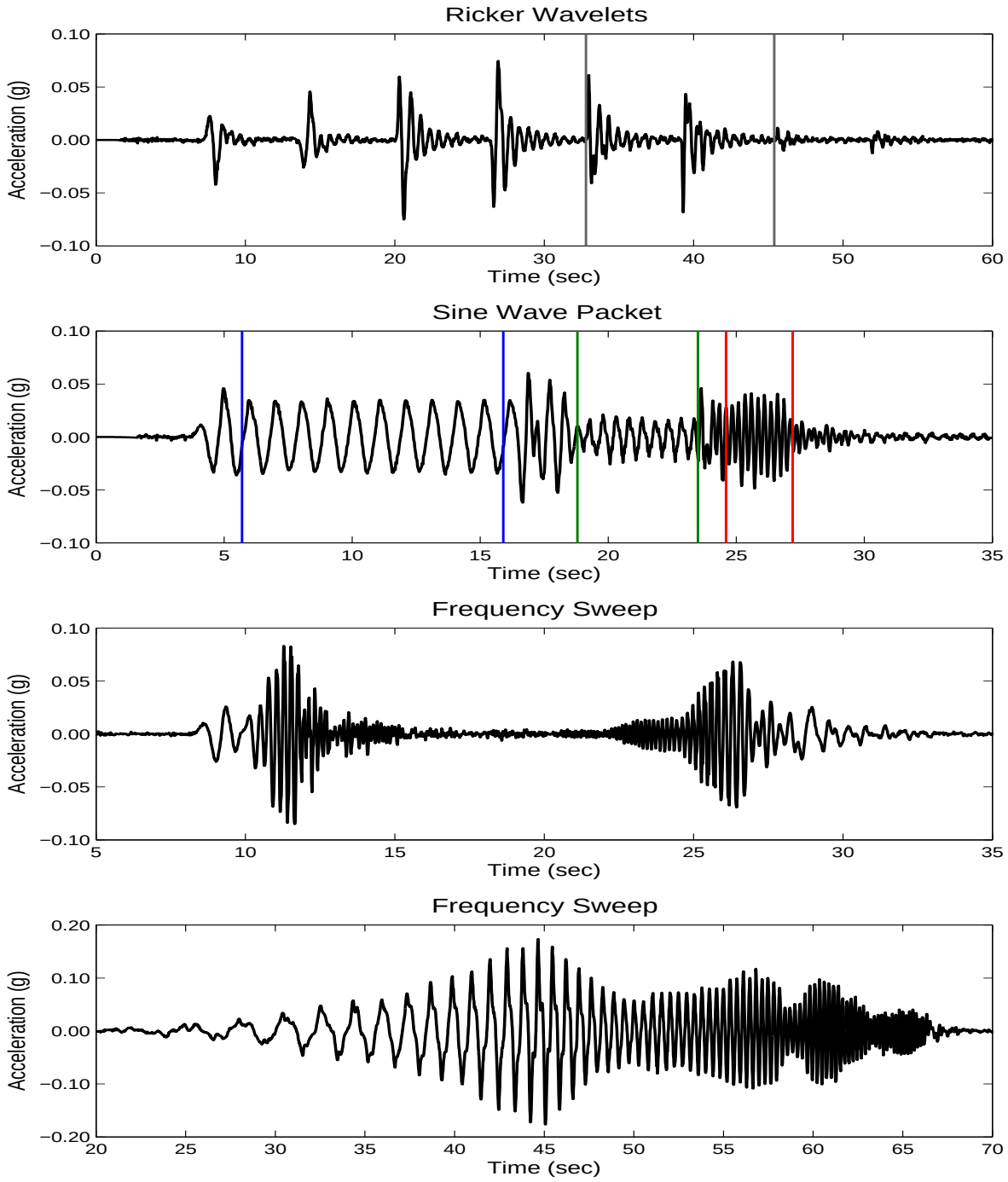

Figure 4.1: Group of idealized base motions introduced to the 30 degree slope at 55g used in the localized time and time-frequency domain analysis. Vertical lines in the top two plots represent breakpoints where the motions were split according to central frequency, and were subsequently analyzed separately.

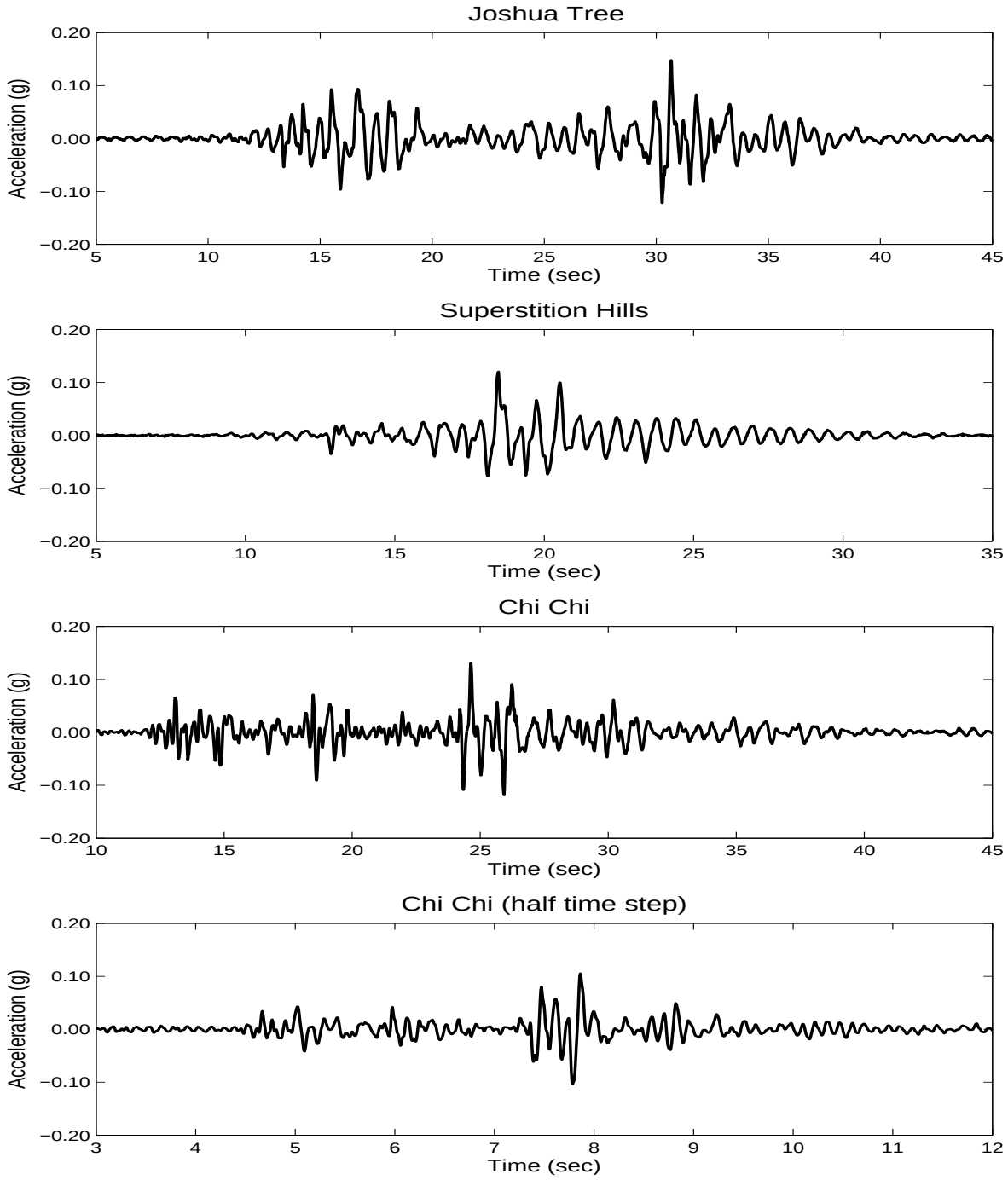

Figure 4.2: Group of earthquake base motions introduced to the 30 degree slope at 55g, with the exception of the half time step Chi Chi motion (bottom plot), which was introduced at 27.5g, used in the localized time and time-frequency domain analysis.

The parameters provided in the two tables are as previously defined in Chapter 3, and consist of the mean square frequency (MSF), peak ground acceleration (PGA), peak ground velocity (PGV), Arias intensity (AI), and banded peak spectral acceleration ($bp\ SA$). These parameters are provided for the base (input), free field, and crest motions. Therefore, differences in frequency content and amplitude (i.e., for the free field and crest) can be identified through inspection of these parameters, revealing motions for which topographic effects (in particular topographic amplification) are greatest. Although each motion listed will be covered in detail, information in these tables can be used as a general characterization reference for the different ground motions at locations of interest.

With the aim of examining ground motions for which topographic effects are most pronounced, the representative motions selected are recordings from the 30 degree slopes. As demonstrated in the previous chapter, topographic effects are found to be greater for steeper slopes. Initially, analysis was performed for the 55g prototype only, as more ground motions were introduced at this g-level (i.e., it was the main focus of the centrifuge investigation with the testing at 27.5g playing a complimentary role). However, for the earthquake motions, topographic effects typically were not as pronounced at 55g. In order to demonstrate that the effects could be more prominent for a transient motion, the Chi Chi motion (with $^1/_2\Delta t$) introduced at 27.5g (which did exhibit more significant effects) was also included in the time and time-frequency domain analysis.

For vertical ground motion, amplification is significantly greater at the slope crest. Due to malfunctioning sensors, the response in the vertical direction at the crest, however, was only captured for the 25 degree slopes. Therefore, motions from the 25 degree slope prototypes were considered in analyzing vertical ground motion. Subsequently, horizontal ground motion from the 25 degree slopes was also interpreted to allow for ample comparisons between the horizontal and vertical components of motion.

In order to better understand some of the nuances of different sensors and the boundary effects induced by the centrifuge container, comparisons between the slope response and flat ground configuration were also made as needed. A sample comparison is provided in

Table 4.1: Ground motion parameters for the idealized ground motions (Figure 4.1)

		$MSF(Hz)$	$PGA(g)$	$PGV(m/s)$	$AI(m/s)$	$bp\ SA(g)$
Wavelets (l3)	B	2.064	0.070	0.068	0.032	0.152
	FF	1.928	0.152	0.129	0.195	0.249
	C	2.400	0.172	0.152	0.231	0.487
Sine Wave (q1)	B	1.030	0.038	0.098	0.084	0.068
	FF	1.069	0.053	0.131	0.135	0.074
	C	1.132	0.066	0.143	0.174	0.155
Sine Wave (q2)	B	2.652	0.028	0.022	0.013	0.071
	FF	2.101	0.144	0.182	0.378	0.255
	C	2.187	0.144	0.182	0.375	0.366
Sine Wave (q3)	B	4.044	0.049	0.028	0.024	0.333
	FF	4.343	0.067	0.047	0.026	0.283
	C	4.105	0.201	0.122	0.510	1.562
Freq Sweep (c)	B	5.416	0.105	0.039	0.156	0.562
	FF	5.550	0.196	0.064	0.518	0.619
	C	4.597	0.565	0.214	4.660	3.573
Freq Sweep (d)	B	2.176	0.186	0.167	1.866	1.037
	FF	2.273	0.363	0.370	7.700	0.874
	C	3.261	0.536	0.403	15.250	3.760

B = base (input); FF = free field; C = crest

*Letter-number designations in parenthesis (i.e., l3) are used for identification of specific ground motions used in the testing program.

Table 4.2: Ground motion parameters for the earthquake motions (Figure 4.2)

		$MSF(Hz)$	$PGA(g)$	$PGV(m/s)$	$AI(m/s)$	*b.p.* $SA(g)$
Joshua Tree (w)	B	1.559	0.155	0.172	0.430	0.372
	FF	1.714	0.364	0.319	3.792	0.578
	C	1.912	0.371	0.344	3.834	1.052
Sup Hills (g)	B	1.608	0.129	0.141	0.170	0.235
	FF	1.658	0.249	0.261	1.090	0.383
	C	1.872	0.305	0.266	1.206	0.850
Chi Chi (h)	B	2.509	0.144	0.166	0.256	0.402
	FF	2.314	0.303	0.244	1.952	0.601
	C	3.249	0.384	0.280	2.534	1.349
Chi Chi (za)	B	6.397	0.105	0.043	0.040	0.456
	FF	5.261	0.190	0.081	0.180	0.372
	C	7.244	0.328	0.110	0.523	1.593

B = base (input); FF = free field; C = crest

*Letter-number designations in parenthesis (i.e., l3) are used for identification of specific ground motions used in the testing program.

Section 4.4 for the combined horizontal and vertical components of motion. It should be noted that the same command ground motions (according to the letter and letter-number designations described above) were used in making comparisons between the slopes and flat ground, however, the true ground motion introduced may differ slightly between the flat ground and slopes as a result of the change in soil mass. Units are given at prototype scale throughout the chapter unless otherwise stated.

4.1.2 Analysis Methods

The goal of the analyses performed was to determine potential mechanisms that lead to topographic effects and characterize the ground response at times when pronounced topographic effects occurred. To accomplish this, changes in ground motion were monitored using data from the dense arrays of accelerometers both near the surface and at depth for the slopes investigated. A cross-section for both the 30 and 25 degree slopes, with sensor locations marked and the horizontal surface sensors labeled, is provided in Figure 4.3.

Changes in ground motion were investigated in both the time and the time-frequency domain. This required the ability to visualize the recorded data, or different components of the data, at multiple sensor locations. By adopting multiple visualization techniques, the dominant behaviors associated with topographic effects were identified. The methods utilized in this analysis are described below.

Time Histories

One of the easiest methods for visualizing changes in ground motions in time is to study time histories of those ground motions. Data was recorded in volts, but were linearly converted to acceleration readings in 'g' via a conversion factor. These acceleration time histories were then integrated in time to obtain velocity time histories, which were integrated in time to acquire displacement time histories.

Even with filtering of signal noise, it is typical that low period drift is exacerbated by the integration process and can heavily affect the displacement time histories in particular. Consequently, the signal must be detrended, or baseline corrected, with the assumption that no permanent deformation has occurred (i.e., the displacement time history begins and ends with a zero reading). While necessary, applying a baseline correction in this manner is essentially the same as applying a high-pass filter with an unknown corner frequency (Boore and Bommer, 2005).

Displacement time histories used in the analysis did indeed require detrending. This

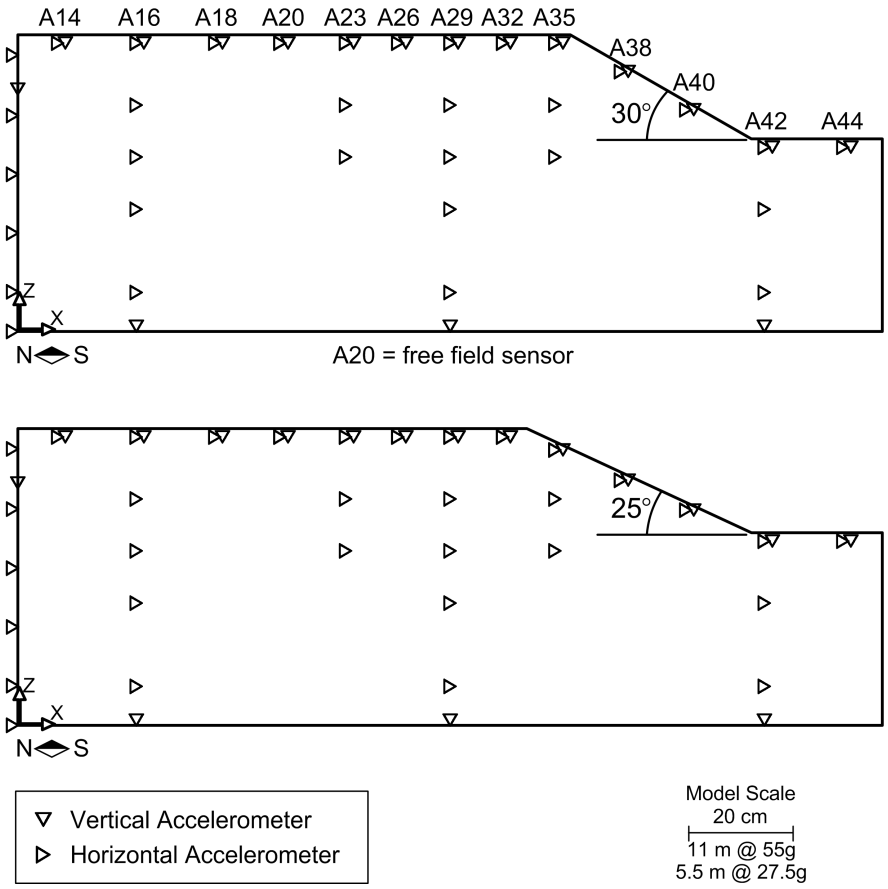

Figure 4.3: Cross-Sections for the 30 degree (top) and 25 degree (bottom) slopes. Both horizontally and vertically oriented accelerometer locations are marked. Labels for the horizontal surface accelerometers are provided for the near surface sensors.

was accomplished with the built-in detrend function in MATLAB (2011), using the option whereby a linear best fit line is removed from the data at discrete locations in time. For the motions that were divided in time (i.e., the wavelets and sine waves), the original motion was used for determining velocity and displacement time histories first, before dividing these histories into the same time spans used for the acceleration time histories. This helped limit the influence of detrending, and ensured all divided motions were detrended in the same manner.

Acceleration, velocity and displacement time histories were plotted and compared at key locations, allowing differences in behavior to be observed. Both full time histories, and portions of these time histories will be presented and used for illustration throughout the chapter.

Husid and Cumulative AI Plots

The cumulative AI is a plot of the increase in AI intensity in time. At the beginning of a time history, the cumulative AI parameter equals zero and at the end is equivalent to the Arias intensity for the motion. The Husid parameter (Husid, 1969) is the cumulative AI plotted in time, normalized by the total AI and therefore begins at 0 and ends at 1. The AI is a measure of ground motion energy, and thus the cumulative AI and Husid plot allows the build-up of energy to be detected in time for a given ground motion. Comparing differences in the cumulative AI plots at locations of interest allowed deviations in the ground motion energy to be quantified in time.

Stockwell Spectrum

The Stockwell spectrum, or spectrum created using the S transform, provides a time-frequency representation of spectral amplitude. In other words, the relative amplitude at different frequency components of a ground motion can be tracked in time. The Stockwell spectrum extends the theory of the continuous wavelet transform, whereby the phase of the motion remains intact. Additionally, the Stockwell spectrum relates to the well known

Fourier spectrum such that the average of the local Stockwell spectra in time is equal to the Fourier spectrum. For more details, refer to Stockwell et al. (1996).

Due to the frequency dependent nature of topographic effects, the Stockwell spectrum proved to be a highly productive method for investigation of these effects in time. The amplitude was contoured against axes of frequency versus time and differences in the spectra were compared. The Stockwell spectrum was determined using time history values of acceleration, velocity, and displacement; for which a comparison is provided for one ground motion in Section 4.2. The spectra for the remaining motions are determined based on velocity.

Stockwell Mean Square Frequency

Using the Stockwell spectrum, the mean square frequency was calculated for each discrete time step, thus providing a measure of mean square frequency in time, based on the Stockwell instead of Fourier amplitude. The Stockwell mean square frequency is not a standard measure, in that, to the author's knowledge, it has not been previously published. However, it was found to be useful in providing a singular measure of a centroid-like frequency at different instances in time. Because the Stockwell transform was found to highlight high frequency noise, however, an upper cutoff frequency of 12Hz, instead of 20Hz (used for the Fourier transform) was used in determining the mean square frequency. Again, comparison between acceleration, velocity and displacement based Stockwell MSF is provided for one motion, with that calculated using velocity presented for other ground motions.

Hilbert Transform

The Hilbert transform finds a function $y(t)$ for some signal $x(t)$ such that $z(t) = x(t) + iy(t)$. It can be calculated by taking the fast Fourier transform (fft) of a signal, zeroing values at negative frequencies and then taking the inverse fft. The result is such that $y(t)$ represents a negative 90 degree time shift from the original signal. The absolute value of $z(t)$ essentially provides an upper envelope to the original signal. Additionally, the instantaneous frequency

can be determined by taking the time derivative of the ground motion phase, which is equal to $tan^{-1}\left({}^{y}/_{x}\right)$. More information on the Hilbert transform can be found in (Liu, 2012b).

For the current investigation, the Hilbert transform was utilized for determining the phase of the different signals in time. In particular, it was important to be able to determine and quantify the difference in phase between ground motion at or near the slope crest and in the free field. The effect of differential motion at these locations could then be observed. As with the Stockwell parameters, comparison between acceleration, velocity and displacement based phase differences is provided for one motion, with that calculated using velocity presented for other ground motions.

Stress-Strain Time Histories

The impact of non-linear behavior on topographic effects was investigated in time by studying the cyclic shear stress-strain time histories. Sensors at ground elevations equivalent to the mid-point and base of the slopes were considered at three different locations ranging from below the crest back towards the free field. However, only the locations below the crest are presented in this chapter. The three locations are circled in red in Figure 4.4. Note that the"free fiel" location is actually just in front of the typical reference free field sensor in this figure.

The cyclic shear strain and shear stress were evaluated using the downhole array method developed by Zeghal et al. (1995) and later applied to centrifuge data by Brennan et al. (2005). To determine the shear strain time history at a given location, i, the following equation can be applied

$$\gamma(z_i) = \frac{1}{(z_{i+1} - z_{i-1})}\left[(u_{i+1} - u_i)\frac{(z_i - z_{i-1})}{(z_{i+1} - z_i)} + (u_i - u_{i-1})\frac{(z_{i+1} - z_i)}{(z_i - z_{i-1})}\right] \tag{4.1}$$

where γ is the shear strain, z is depth below the ground surface, u is horizontal displacement (determined through double integration of the acceleration time histories) and subscripts i, $i-1$, and $i+1$ represent the sensor location and sensor locations above and below where the strain is calculated, respectively. The shear stress time history at a given location, i, can be

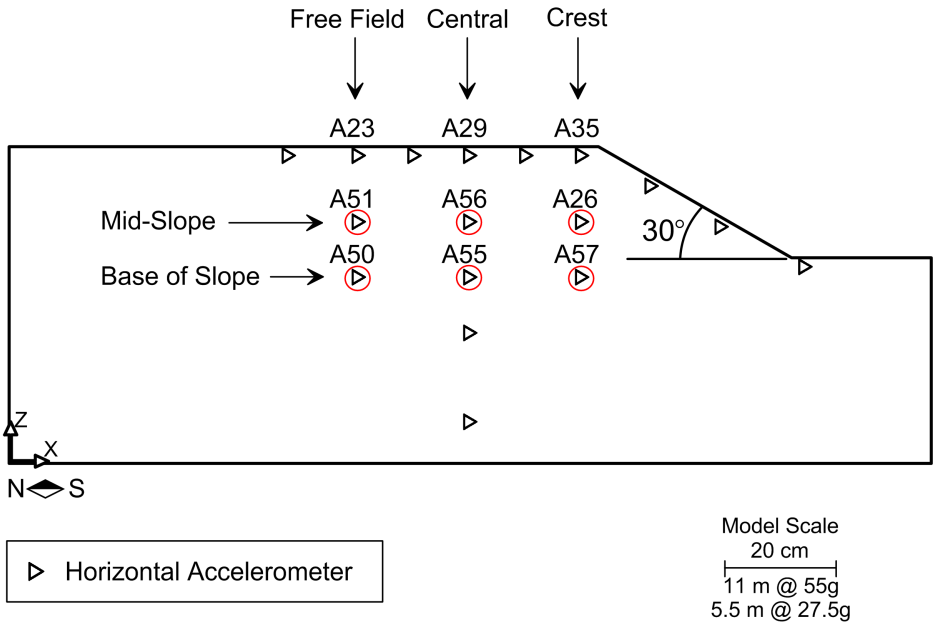

Figure 4.4: Cross-Section for the 30 degree slope with central horizontal accelerometer locations marked. Near surface sensors span from the free field to the slope toe. Stress-strain histories were calculated at the locations circled in red.

calculated as follows

$$\tau(z_i) = \frac{1}{2}\rho z_i \left(\ddot{u}(0) + \ddot{u}(z_i)\right) \tag{4.2}$$

where τ is the shear stress, $\ddot{u}$ is the horizontal acceleration and $\ddot{u}(0)$ represents the surface acceleration, which can be obtained through extrapolation using near surface accelerometers by

$$\ddot{u}(0) = \ddot{u}_1 + z_1 \frac{\ddot{u}_2 - \ddot{u}_1}{z_2 - z_1} \tag{4.3}$$

Vector Videos

To aid in the visualization of the data both across the surface of the slopes, and at depth, a series of videos were made for the different ground motions that tracked acceleration, velocity and displacement at the different sensor locations in time. The videos proved to be instrumental in understanding and observing the response of the slopes and differences in the ground response at times when topographic effects were or were not observed. One type of video produced is deemed vector videos.

Vector videos could be created using acceleration, velocity or displacement amplitude, but were typically created using either velocity or displacement. Vectors were produced at all sensor locations in a scaled cross-section of the 30 and 25 degree slope and flat ground models. These vectors shift in time according to amplitude and orientation of the data time histories, using the sensor location as the vector origin. Vectors were confined to horizontal (moving left or right) or vertical (moving up or down) movement to represent the axes of measurement utilized in the investigation. However, the vectors were also combined to analyze the resultant ground motion. Because velocity and displacement amplitudes were relatively small compared to the overall scale of the slope, the amplitudes were typically magnified by a scaling factor.

The vector videos proved to be particularly useful for the identification of the wavelengths of the propagating shear waves, particularly for idealized sinusoidal motions. The relative amplitude both near the surface and at depth in the free field could then be compared to that of the area encompassing the slope crest for the different wavelengths.

Mesh Videos

Meshes of the 25 and 30 degree slope and flat ground model cross-sections were also created by interpolating the acceleration, velocity and displacement amplitudes from the different sensor locations. The MATLAB 'v4' interpolation scheme was used, which produces a smoothed surface and also extrapolates beyond the data (i.e., from the near surface sensors to the surface). The accuracy of the 'v4' interpolation scheme was checked by plotting the vector data beneath the mesh to ensure that no unexpected erratic movement occurred. Often the vector and mesh videos were combined to better visualize overall movement in concert with the recorded movement at specific sensor locations. These combined videos are presented in this chapter.

For the mesh videos, a gridded mesh of amplitude was produced at each discrete time step and stitched together. The meshes move relative to the previous time step depending upon the amplitude (i.e., with the movement vectors). Thus, the meshes allow total slope

movement to be directly visualized, while also capturing relative movement within the slope. Typically velocity or displacement time histories were used in making these videos.

Movement in both the vertical and horizontal directions could be considered both individually and simultaneously. However, it is recognized that due to the lack of vertically oriented sensors, the meshes are not as well constrained in the vertical direction. Thus, while it is useful to observe both vertical and combined movement, when vertical motion is included, the overall mesh response should be interpreted with caution.

Contour Videos

Contour videos were created by interpolating acceleration, velocity or displacement amplitudes at the different sensor locations for a scaled cross-section of the 30 or 25 degree slopes. As with the contoured cross-sections presented in the previous chapter, the minimum curvature method was used as an interpolation scheme, with gridding and contouring performed in Surfer 11 (Golden Software Inc., 2012). Contours of amplitude were produced for each discrete time step and then subsequently stitched together in time. There were not enough sensors oriented in the vertical direction to contour the data. Therefore, only horizontal ground response was considered in the contour videos. Combined motion was also not considered using the contour videos.

Vertical to Horizontal Videos and Plots

In order to better understand and capture total combined movement as well as the relative contribution of the vertical and horizontal components of motion, plots of the vertical to horizontal velocity and displacement were created at locations where both components were recorded. Vertical amplitude was plotted against horizontal amplitude at each discrete instance in time and stitched together to create a video. Additionally, plots of the entire time histories were produced for key locations, such as the slope toe, slope crest, the free field and the base of the soil profile. The time histories were plotted in polar coordinates so that the direction of movement could be quantified by measuring the angle from the horizontal.

A few different iterations of videos were produced. Videos of the vertical to horizontal amplitude (displacement and velocity) were created individually at locations of interest and were also plotted together overlaying a cross-section of the slopes using all near surface sensors for which both components of motion were recorded. By linearly connecting these locations, the overall surface motion could be observed. These plots are combined with the vector and mesh videos and presented in this chapter

The videos produced were crucial to understanding the slope response localized in time, however, it is impossible to present videos in this document. Therefore, select snapshots at different time frames will be used to illustrate identified trends in the behavior of the slopes. The implications of this behavior in relation to topographic effects will be discussed. Strings of snapshots are also presented when appropriate.

4.2 Idealized Motions

Idealized ground motions allow the effects of certain ground motion characteristics to be more easily identified because the complexity typical of a true earthquake motion is reduced. Each idealized motion could represent one component of a typical earthquake motion, which may have different components appearing in tandem or simultaneously in time. Through study of idealized motions, mechanisms associated with topographic effects can be related to specific ground motion components. The relationships identified can then be used to guide analysis of more transient earthquake motions. Analysis results and observations for the idealized ground motions utilized in the centrifuge investigation are presented in the following subsections. Results and observations for the earthquake motions are presented in Section 4.3.

4.2.1 Sine Waves

Idealized ground motion that was particularly useful for analyzing the causes of topographic effects was sine wave motion at different central frequencies. Analysis and results for the (q) sine wave packet introduced to the 55g, 30 degree slope model are presented in this section.

The sine wave packet consists of 12 cycles of sine wave motion at target central frequencies of 1, 2, 4 and 6Hz, which transition from low to high frequencies. These frequencies span both the site frequency (2Hz) and topographic frequency (4.5Hz) for the slope. It should be noted that the shaker used to introduce ground motions had difficulty producing sine wave motion at 6Hz; therefore, discussion and results are focused on sine wave motion at 1, 2 and 4Hz.

Comparison of Acceleration, Velocity and Displacement

Analysis results and figures in the remainder of the chapter are mainly presented using velocity, rather than acceleration or displacement, as an amplitude parameter. Acceleration is commonly used for engineering purposes for which spectral accelerations and acceleration based intensity measures, such as PGA, are utilized. Most of the parameters used in the parametric analysis presented in the previous chapter were derived from acceleration time histories. However, velocity proved to be favorable for understanding and demonstrating the causes of topographic effects. Differences between acceleration, velocity, and displacement for some of the analysis methods used are illustrated in Figures 4.5 through 4.10, and discussed below.

As described in Section 4.1.2, velocity was obtained by integrating the acceleration time history data and displacement was obtained by integrating the velocity time histories. The displacement time histories were then detrended to remove drift. The resulting acceleration, velocity and displacement time histories at the crest, free field and base (blue, green and red lines) for the (q) sine wave packet are presented in Figure 4.5. The crest, free field and base locations are the same as those referenced in the previous chapter. Namely, data at the crest is that recorded at sensor A35 for the 30 degree slope (about 1.5 meters behind the crest), data for the free field is that recorded at sensor A20 (about 30.5 meters behind the crest) and data at the base is that recorded at the shaker and represents the input ground motion.

The integration process has a smoothing effect that tends to filter higher frequencies, thereby reducing the amplitude at those frequencies. This effect can be observed by compar-

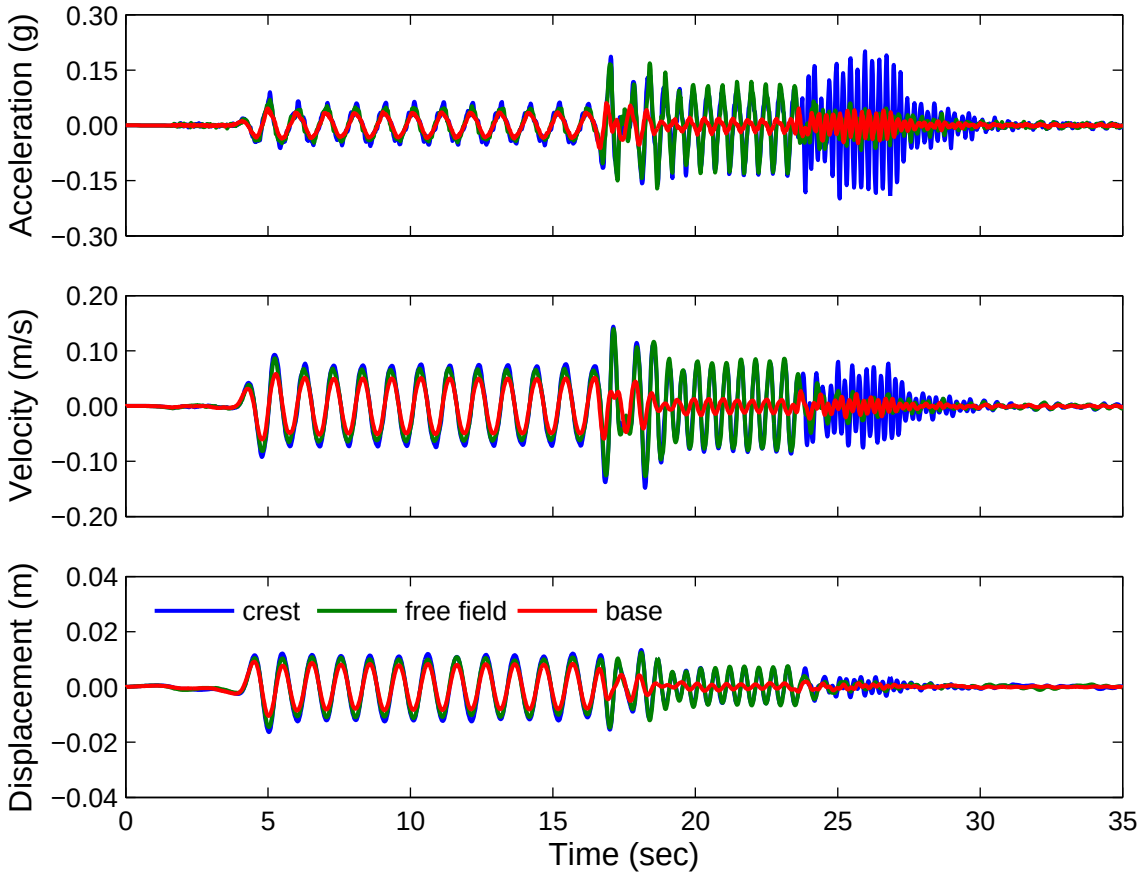

Figure 4.5: Acceleration, velocity, and displacement time histories at the crest, free field and base locations for the (q) sine wave packet of the 55g, 30 degree slope model.

ing the amplitude of sine wave motion at different frequencies for the acceleration, velocity and displacement time histories shown in Figure 4.5. The motion consists of 1Hz sine wave motion between about 4 and 16 seconds, 2Hz sine wave motion between about 19 and 23.5 seconds and 4Hz sine wave motion between about 24.5 and 27.5 seconds (6Hz sine wave motion was attempted between about 28 and 30 seconds) with transitions between. The relative amplitude of motion at these frequencies differs depending on the amplitude parameter used (see Table 4.3).

Table 4.3: Relative amplitude versus frequency content for (q) sine wave packet

Location	Relative Amplitude	Central Frequency		
		Acceleration	Velocity	Displacement
Crest	high	4Hz	2Hz*	1Hz
	mid	2Hz	4Hz*	2Hz
	low	1Hz	1Hz*	4Hz
Free Field	high	2Hz	2Hz*	1Hz
	mid	4Hz*	1Hz*	2Hz
	low	1Hz*	4Hz	4Hz
Base	high	4Hz*	1Hz	1Hz
	mid	1Hz*	4Hz*	2Hz*
	low	2Hz	2Hz*	4Hz*

*Amplitudes are similar for the given location and amplitude parameter (i.e., at crest for velocity time history).

Ground motion at 1Hz is emphasized and ground motion at 4Hz is deemphasized by integrating from acceleration to displacement at the crest, free field and base. At the base and crest, ground motion at 4Hz shifts from having the greatest to least amplitude (although, at the crest, the amplitude of velocity is similar for ground motion at 1, 2 and 4Hz). In the

free field, the amplitude is greatest at 2Hz for acceleration and velocity, but at 1Hz for displacement.

Ground motion at or near the site frequency (2Hz) and topographic frequency (4.5Hz) is amplified at the crest, and ground motion near the site frequency is amplified in the free field. Because ground motion at 4Hz, and to a lesser degree at 2Hz, is deemphasized by integrating from acceleration to velocity, observed site and topographic amplification may be less pronounced when using velocity, rather than acceleration, as an amplitude parameter. Differences in site and topographic amplification between acceleration, velocity and displacement based Stockwell spectra are shown in figures 4.6 through 4.8, and discussed below.

Figures 4.6 through 4.8 show normalized Stockwell spectra using acceleration, velocity and displacement as an input to the S transform (see Section 4.1.2). For Figure 4.6 the spectral amplitude at the base was subtracted from the spectral amplitude in the free field, and these values were normalized by the maximum difference between the spectral amplitudes. The same process was followed for Figures 4.7 and 4.8, taking differences between the crest and base, and crest and free field, respectively. These normalized amplitudes vary between -1 and 1, where negative values represent deamplification (from 0 to -1, moving from white to blue) and positive values (from 0 to 1, moving from white to red) represent amplification. A value of 1 then, would represent maximum amplification. Note that in this context, amplification and deamplification is based on differences in spectral amplitude rather than a traditional multiplicative factor or ratio (such as would be determined by dividing the crest by base spectral amplitude, for instance). The normalized amplitudes were contoured and plotted against frequency (y-axis) and time (x-axis), allowing amplification and deamplification of different frequencies to be observed throughout the time history. Frequencies are normalized by the topographic and site frequencies on the left and right y-axes, respectively. Dashed lines are plotted where frequency is equal to the site and topographic frequency.

Normalized spectral amplification of the free field over the base (Figure 4.6) is similar whether using acceleration, velocity or displacement to determine spectral amplitudes. There

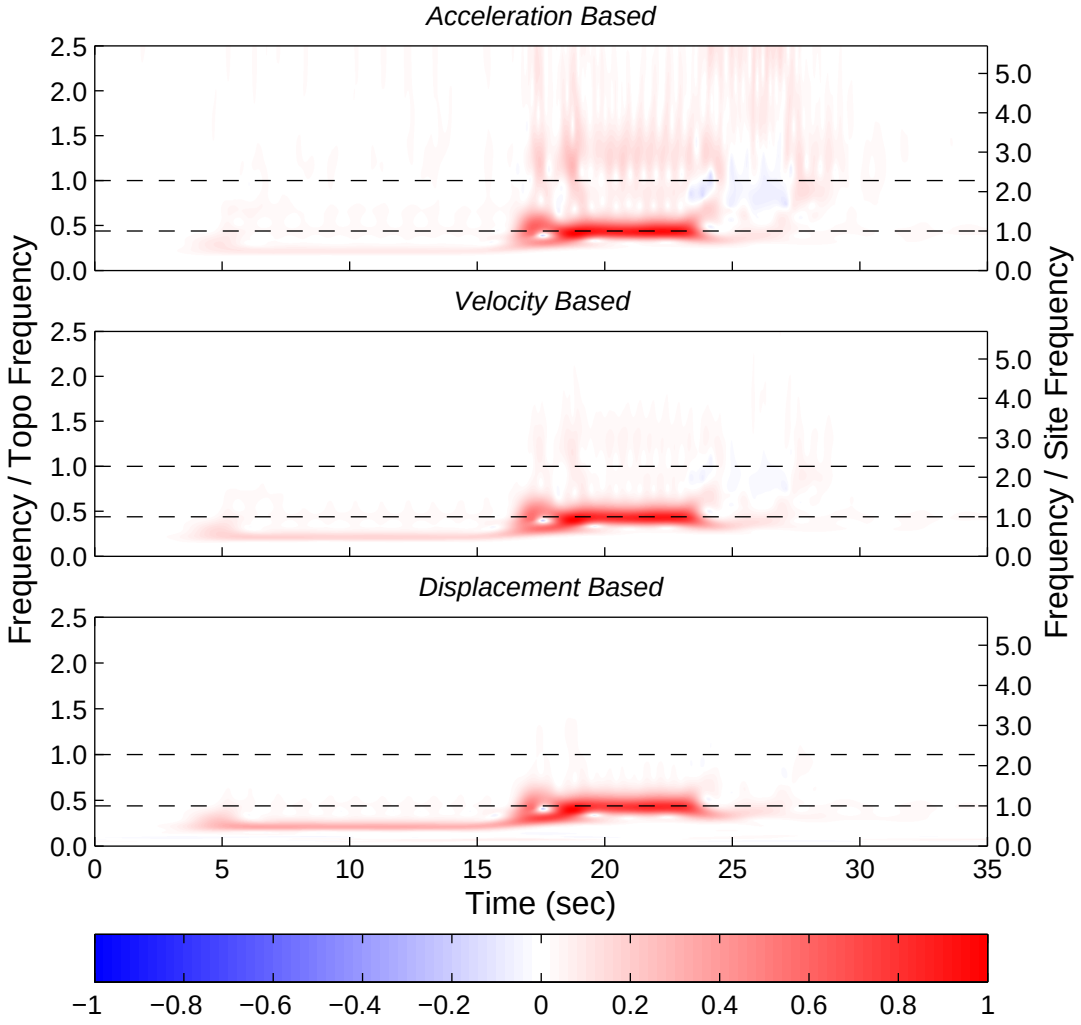

Figure 4.6: Difference between the free field and base Stockwell amplitude, normalized by the maximum difference, using acceleration, velocity, and displacement time histories for the (q) sine wave packet of the 55g, 30 degree slope model.

is slightly less relative amplification at 2Hz, and slightly more relative amplification at 1Hz (1.0 and 0.5 times the site frequency) in progressing from acceleration to displacement. There are higher frequency components (above the topographic frequency) amplified for the acceleration based spectrum, that are reduced for the velocity based spectrum, and are not seen for the displacement based spectrum. At 4Hz, there is either slight deamplification or no amplification. Note that because values are normalized, values of amplification are not directly compared for the acceleration, velocity and displacement spectra; rather relative amplification at different frequencies within the ground motion are compared.

More significant differences are observed when considering normalized spectral amplification of the crest over the base (Figure 4.7). For the acceleration based spectrum, amplification is greatest at 4Hz, followed by 2Hz and then 1Hz. For the velocity based spectrum, amplification is greatest at 2Hz, followed by 4Hz and then 1Hz. For the displacement based spectrum, amplification is greatest at 2Hz, followed by 1Hz and then 4Hz. This indicates that at the crest, site amplification may appear to be greater than topographic amplification (over the base motion) when using velocity based, instead of acceleration based, spectral amplitudes. As with Figure 4.6, higher frequencies are muted in progressing from acceleration to displacement.

As presented in the previous chapter, one method for measuring topographic amplification is to compare the response at the crest to that in the free field. When comparing the normalized Stockwell spectra of the crest to the free field, the behavioral patterns are similar whether using acceleration, velocity, or displacement based spectra (Figure 4.8). For all cases, relative amplification is greatest near the topographic frequency, at 4Hz. There is also either no, or a slight deamplification at the site frequency, 2Hz. Deamplification is slightly more pronounced for the displacement based spectrum when compared to the other two. The most notable differences include an increase in relative amplification at 1Hz, and the muting of higher frequencies, in progressing from acceleration to displacement based spectra.

The previous figures compared amplitude and relative amplification using acceleration, velocity and displacement as an amplitude parameter. Figure 4.9 compares the frequency

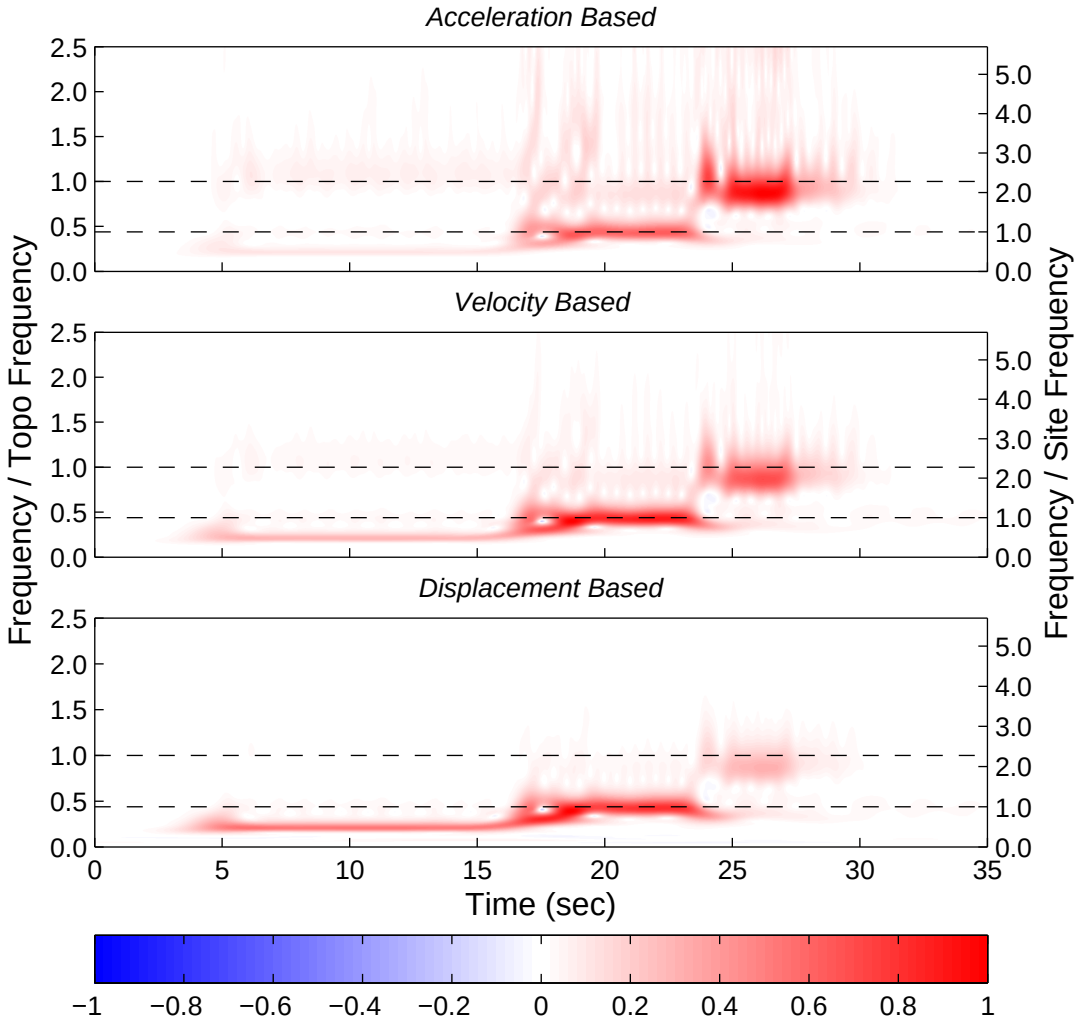

Figure 4.7: Difference between the crest and base Stockwell amplitude, normalized by the maximum difference, using acceleration, velocity, and displacement time histories for the (q) sine wave packet of the 55g, 30 degree slope model.

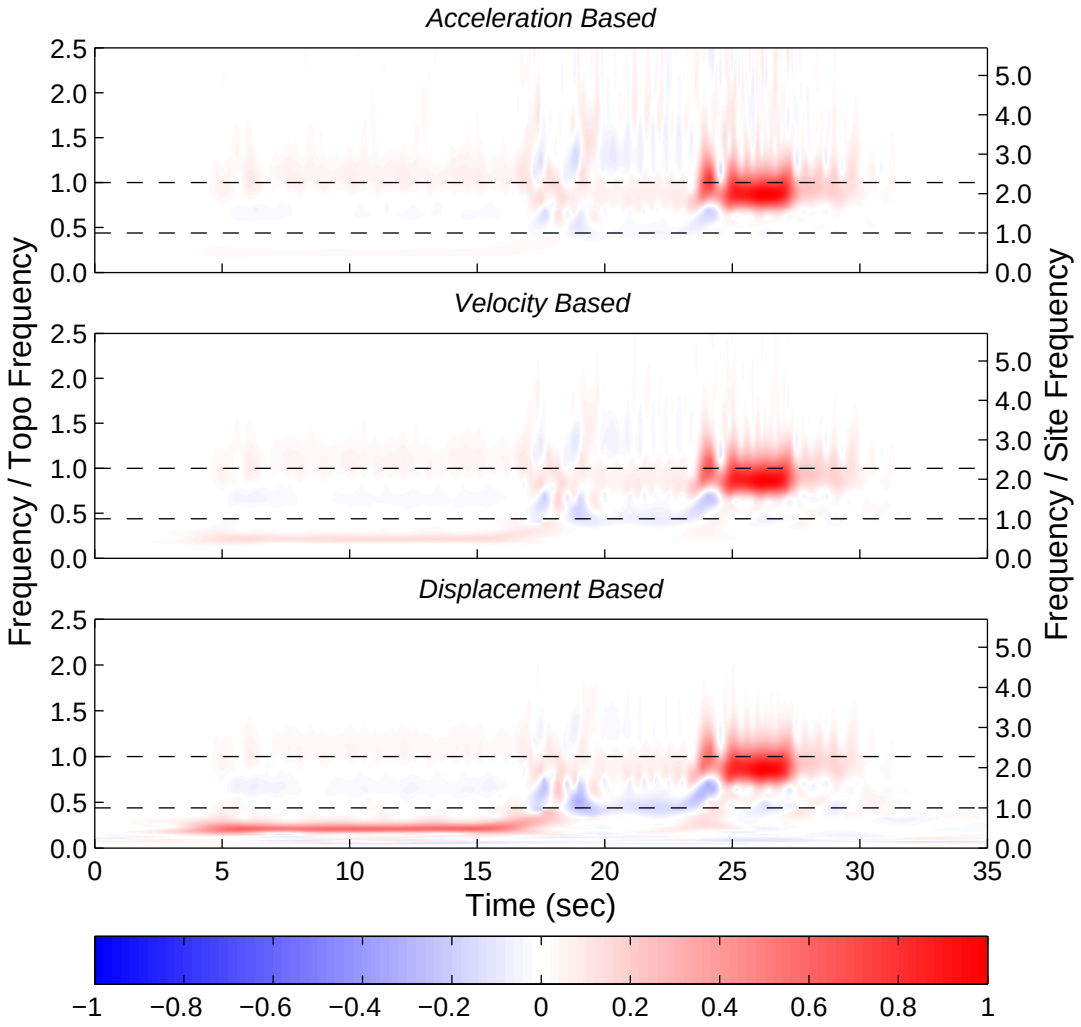

Figure 4.8: Difference between the crest and free field Stockwell amplitude, normalized by the maximum difference, using acceleration, velocity, and displacement time histories for the (q) sine wave packet of the 55g, 30 degree slope model.

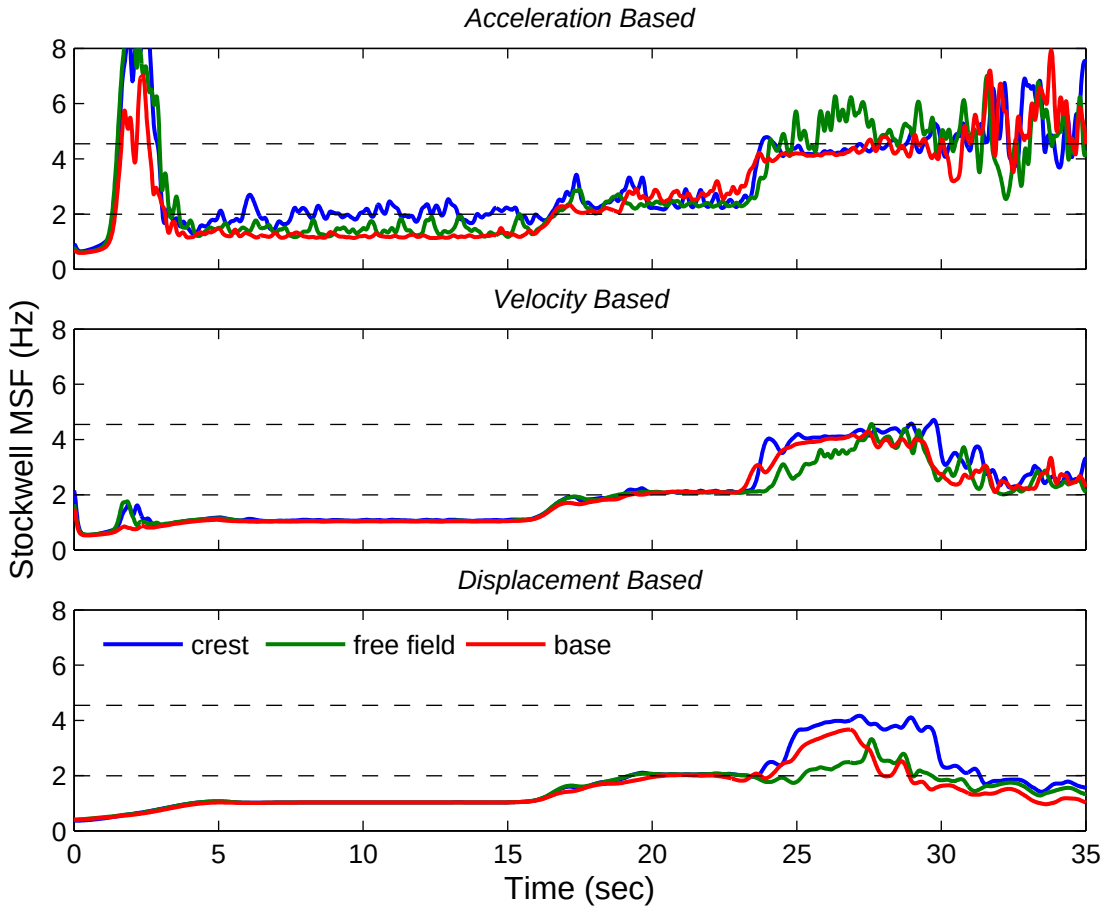

Figure 4.9: Crest, free field and base Stockwell MSF with time, using acceleration, velocity, and displacement time histories for the (q) sine wave packet of the 55g, 30 degree slope model. Dashed lines correspond to the site (2Hz) and topographic (4.5Hz) frequencies.

content for these amplitude parameters at the crest, free field and base. Figure 4.9 is a plot of the Stockwell MSF in time. At each time step, the MSF was calculated based on the Stockwell spectrum, using Equation (3.7) presented in the previous chapter. However, the upper frequency was limited to 12Hz instead of 20Hz for this calculation. The dashed horizontal lines represent the topographic frequency (4.5Hz) and site frequency (2Hz).

The smoothing effect of integration is clear for the Stockwell MSF, particularly at the crest and free field. The influence of higher frequency components, or noise, can be seen in the acceleration based plot. For the 1Hz motion, the MSF differs by almost 1Hz at the crest, and for motion at 4Hz, the free field MSF is on average above the input and crest MSF as a result of a low signal-to-noise ratio. For comparison, the influence of high frequency ambient noise can be seen between about 0 and 3 seconds (prior to the start of ground motion) where the MSF is greatest for all ground motions. For the velocity based plot, the crest and free field follow the input MSF at 1 and 2Hz. At 4Hz, the free field transitions more slowly from 2Hz to 4Hz than the base and crest. This behavior is discussed in more detail later in this section. For the displacement plot, the crest and free field also follow the input MSF at 1 and 2Hz, but the ground motion at 4Hz is more muted. The free field MSF remains right around 2Hz and the base motion never reaches a MSF of 4Hz.

A final comparison of acceleration, velocity and displacement based parameters is presented in Figure 4.10, which highlights ground motion phasing. The phase angle in time was calculated using the Hilbert transform (see Section 4.1.2) at the crest, free field and base. The difference between the crest and base (red) and the crest and free field (green) was smoothed using ten passes of a boxcar filter with width three. Note that a phase difference of 180 degrees means the ground motion is completely out of phase and that a phase difference of 0 degrees means the motions are in phase.

The overall phasing patterns are similar regardless of which amplitude parameter is used. Namely, the crest and free field are in phase at 1 and 2Hz and move in and out of phase at 4Hz; the crest and base are in phase at 1Hz, about 90 degrees out of phase at 2Hz and are generally out of phase at 4Hz. Although the patterns are similar, however, the movement

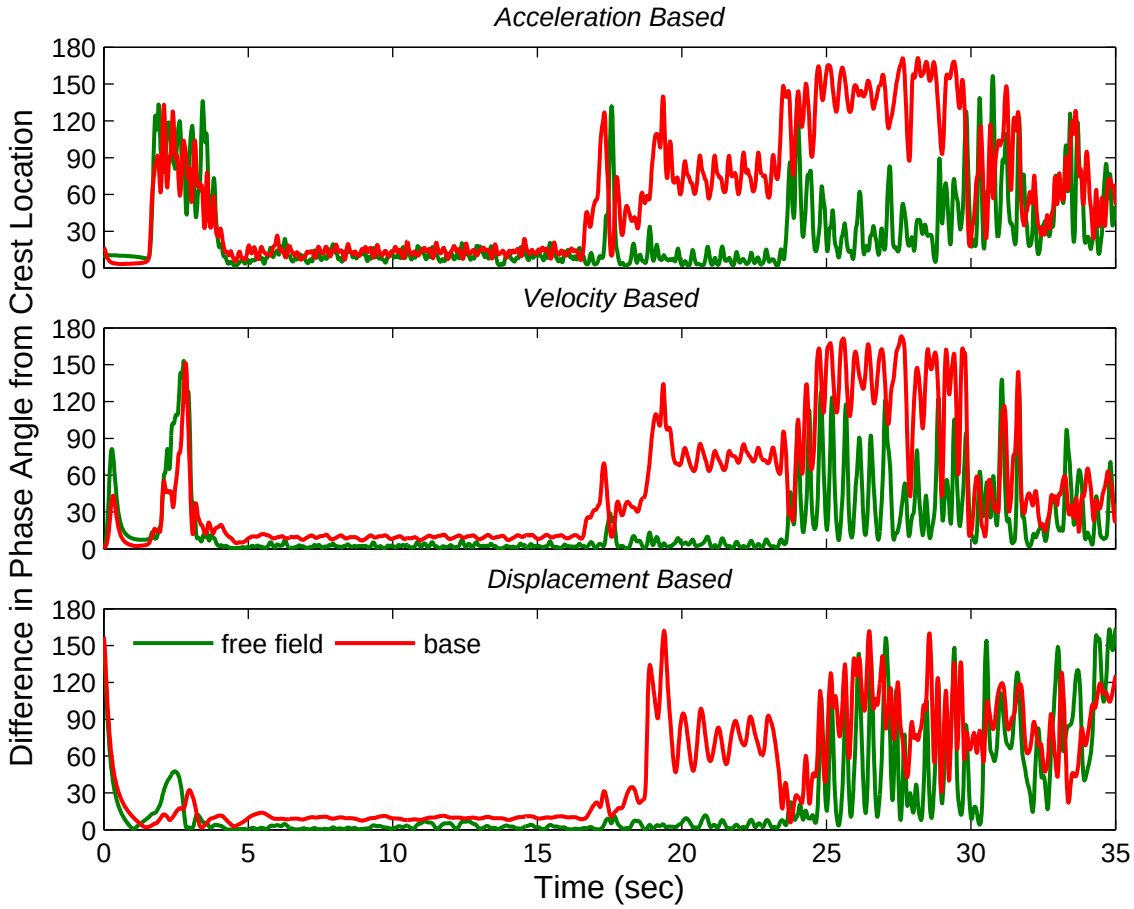

Figure 4.10: Difference in phase angle between the crest and free field, and the crest and base using acceleration, velocity, and displacement time histories for the (q) sine wave packet of the 55g, 30 degree slope model.

in and out of phase at 4Hz is more clearly defined for the velocity and displacement based phase differences. This behavior is discussed in the context of topographic effects later in this section.

Based on the features and differences highlighted above, velocity was chosen as an amplitude parameter for presentation in the remainder of this chapter. In general, similar trends could be observed for each of the parameters. However, the effects of phasing and changes in frequency content can be more clearly observed with velocity, compared to acceleration, by reducing some of the higher frequency components and noise. Velocity can also be related to ground strain and is closer to actual slope movement than acceleration, which is helpful in interpreting the vector, mesh and contour videos (see Section 4.1.2) used to understand wave propagation. The velocity time histories also maintain some of the higher frequency components that are important to understanding topographic effects, but are heavily muted in the displacement time histories; which have more uncertainty due to the detrending process required after integrating the data a second time. However, despite the advantages listed above, it should be noted that the magnitude of topographic amplification (particularly over the base motion) may be less pronounced using velocity instead of acceleration.

Analysis of Topographic Effects

The figures and discussion above highlighted the differences between acceleration, velocity and displacement for the (q) sine wave packet. The velocity based plots are reintroduced, along with additional plots in Figures 4.11 through 4.18 below. The discussion, however, will shift in focus to the causes and mechanisms behind the featured topographic effects.

The causes of topographic effects can be understood by studying the wave propagation near the topographic feature. They can also be understood by relating the input ground motion to the response of the topographic feature and comparing that response to the free field response. Four parameters that illustrate ground motion behavior in time at the crest, free field and base are provided in Figure 4.11 for the (q) sine wave packet.

Three of the four plots in Figure 4.11 have been previously presented — the velocity time

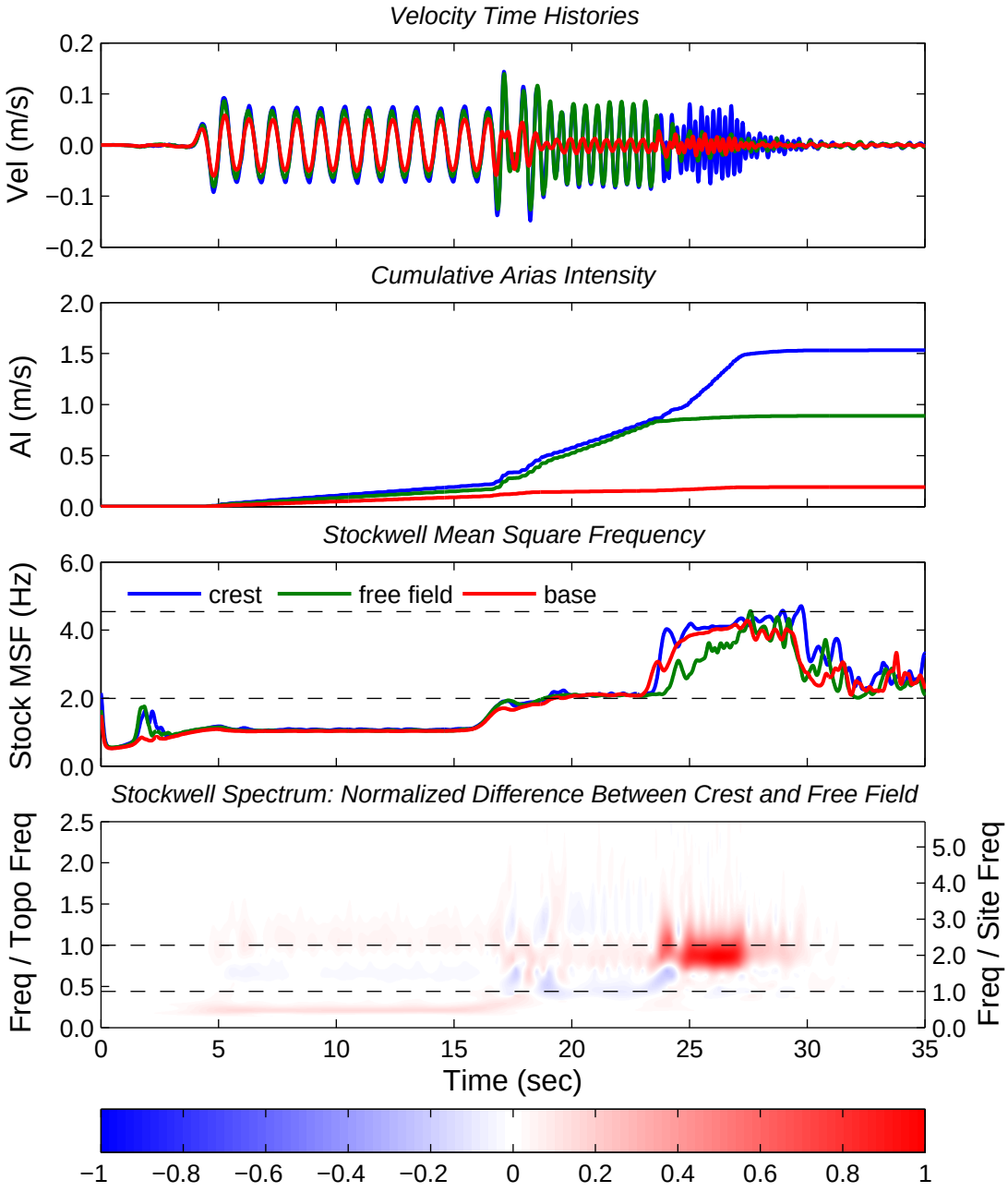

Figure 4.11: Velocity time history, cumulative Arias Intensity, and Stockwell MSF plots for the base, crest and free field; and the difference between the crest and free field Stockwell amplitude, normalized by the maximum difference, for the (q) sine wave packet of the 55g, 30 degree slope model.

history, Stockwell MSF, and the normalized difference of the Stockwell spectrum between the crest and free field — and therefore will not be described again here. The additional plot consists of the build-up AI in time, or the cumulative AI. The cumulative AI ranges from zero, prior to the ground motion, to the total AI, at the end of the motion and is given in meters per second. This is similar to a Husid plot (Husid, 1969), except that the values are not normalized by the total AI, for which the plot would range from 0 to 1 and be unitless. It should be noted that the cumulative AI is, like the velocity time histories, based on integration of the acceleration time histories and has units of velocity (meters per second). However, acceleration values are squared prior to integration and then multiplied by a constant ($\pi/2g$).

Because the frequency content of the sine wave packet is essentially divided in time, deviations in ground motion behavior at specific frequencies are well illustrated. The central frequencies of the base motion (1, 2 and 4Hz) are well defined in the Stockwell MSF plot in Figure 4.11. At 1 and 2Hz, and the transition between, the MSF of the free field and crest track well with the base motion. That is, the frequency of the sine wave motion at the crest and free field matches the forcing frequency. As the forcing frequency transitions to 4Hz, the frequency content at the three locations begins to deviate. The MSF at the crest quickly moves to 4Hz and then trends upwards towards the topographic frequency (4.5Hz), even after the base (which transitions more slowly and then maintains a MSF of 4Hz) MSF begins to decrease. This decrease in MSF at the base begins around 27.5 seconds and coincides with the transition towards an attempt at 6Hz sine wave motion (which could not be achieved). In the free field, the MSF transitions upward from 2Hz (the site frequency) more slowly and doesn't match the base MSF until it peaks and beings to drop off.

Inspection of the cumulative AI plot reveals similar patterns when considering the build-up of ground motion energy at the different central frequencies. That is, the behavior of the free field and crest is similar at 1 and 2Hz, but deviates at 4Hz. Energy at the base builds up gradually with time across all frequencies. At 1Hz, energy builds up slightly faster than the base at the crest and free field. The rate of energy build-up then increases at the crest

and free field for 2Hz motion. At 4Hz, the energy at the crest continues to build at an even faster rate, while the energy build-up in the free field levels out. The crest and base motion then both start leveling out where 6Hz motion was attempted. Similar amplitude patterns can also be seen in the velocity time history plot.

The frequency and amplitude patterns of the crest and free field, relative to each other, is illustrated in the normalized Stockwell plot in Figure 4.11. This plot reveals that the spectral amplitude at the crest is slightly amplified at 1Hz (0.5 times the site frequency), is either slightly deamplified or not amplified at 2Hz (site frequency), and reaches maximum amplification at 4Hz (near the topographic frequency of 4.5Hz), when compared to the free field. Note that the ground motion continues to be amplified near the topographic frequency (which corresponds with the Stockwell MSF in this time frame) where 6Hz ground motion was attempted between about 27.5 and 30 seconds.

Insight into the causes of topographic effects can be gained by breaking down the behavior described above. In the free field, significant amplification of the base motion is expected at the site frequency of 2Hz. This results from a tendency towards resonance of the soil layer, based on the soil layer thickness and shear wave velocity. Because the soil beneath the crest represents a soil column of the same height and shear wave velocity as that of the free field, there is also a tendency towards resonance at the site frequency at this location. As shown in Figure 4.11, the response at the crest and free field is similar for ground motion at 2Hz, with significant amplification occurring at both locations. This indicates that topographic effects at the crest are minimal, if not negligible, and the resonant mode of the site dominates the response at the site frequency.

The behavior at the crest and free field deviates as ground motion shifts to 4Hz, which is near the topographic frequency of 4.5Hz. The response in the free field lags behind the transition to 4Hz ground motion at the base. This is likely a residual effect of the tendency towards resonance at the site frequency, and the low amplitude motion at 4Hz, which wasn't amplified in the free field. In other words, it took time for energy at the site frequency to dampen and the competing energy at 4Hz was minimal, which delayed the shift in MSF to

4Hz.

At the crest, however, the transition towards the topographic frequency occurred simultaneously with the shift in the base motion, despite similar resonant conditions at the site frequency. Any residual effects from the resonant mode at the site frequency were suppressed by excitation near the topographic frequency, resulting in ground motion amplitude similar to that observed at 2Hz. And, as was seen in the free field, it took time for the energy near the topographic frequency to dampen at the crest as the base motion transitioned from 4Hz ground motion to the attempted 6Hz motion. This indicates that the topographic frequency, which is based on the slope height and shear wave velocity of the soil, is similar to the site frequency, in that it represents a mode of (tendency towards) resonance, specific to the slope geometry. This also indicates that the mode that dominates is dependent upon the frequency content of the propagating shear waves.

The ground motion at 1Hz is below both the topographic and site frequencies. The response at the crest and free field is similar, with slightly greater amplitude at the crest. The difference in amplitude is small enough, however, that it could be due to natural fluctuations in ground motion across the surface of the model or bias of the recording sensors, rather than topographic effects.

The frequency and amplification patterns described above are further illustrated in Figure 4.12. Figure 4.12 shows three variations of the velocity based normalized Stockwell plots, with velocity time histories at the crest, free field and base for reference (top plot). The Stockwell plots include the base Stockwell specturm normalized by the maximum value at the base, the difference between the crest and base spectral amplitudes normalized by the maximum difference, and the difference between the free field and base spectral amplitudes normalized by the maximum difference. From these plots the relative amplitude at different frequencies and locations can be more readily observed.

Inspection of the base motion reveals that the spectral amplitude is greatest at 1Hz, and is comparable, but lower (about 30% of that at 1Hz) at 2Hz and 4Hz. Despite the input amplitude, spectral amplification at the crest and free field is lowest at 1Hz. Rather, the

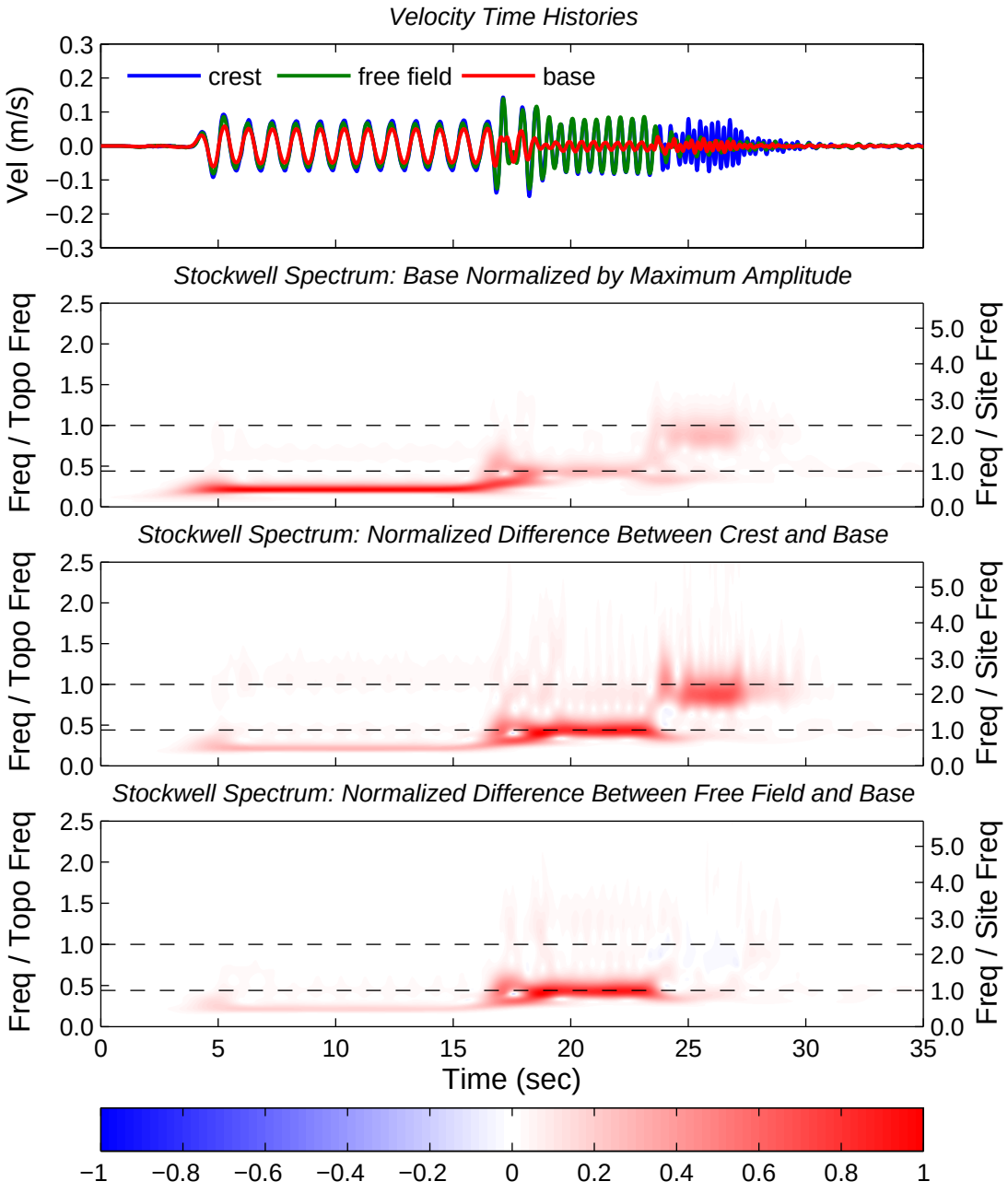

Figure 4.12: Velocity time histories, and normalized Stockwell plots of the base ground motion, the difference between the crest and base, and the difference between the free field and base, for the (q) sine wave packet of the 55g, 30 degree slope model.

greatest spectral amplification over the base occurs at the site frequency for the crest and free field, with comparable amplification near the topographic frequency at the crest. Although the spectral amplitude of the base motion is similar at 2Hz and 4Hz, the amplification at the crest is slightly higher at the site frequency (2Hz). This may be the result of: *a*) higher frequency components of motion being damped more quickly than lower frequency components; *b*) a difference of 0.5Hz between the incident motion and the topographic frequency, which does not exist for the site frequency; or *c*) amplification at the site frequency being greater than amplification at the topographic frequency with all else being equal. It should be noted, however, that the cumulative AI, indicated a quicker increase in energy near the topographic frequency, than at the site frequency at the crest. This is highlighted in Figure 4.13, and aligns with the normalized Stockwell plot for acceleration provided in Figure 4.7.

Generally, energy is concentrated at the ground motion central frequencies, however, there is some underlying energy near the site frequency as the ground motion shifts to 4Hz. This component of the motion is slightly amplified at the crest and free field. Because there is little to no amplification for the 4Hz motion in the free field, this component of motion dominates the response in the free field (hence the slow transition in Stockwell MSF during this transition).

Low amplitude ground motion is also introduced beyond the 4Hz motion at slightly lower frequencies, but still near the topographic frequency (where 6Hz motion was attempted). This motion is amplified at the crest, with amplification levels similar to that for 1Hz motion. This indicates that the incident amplitude at the topographic frequency may influence the resulting level of amplification at the ground surface.

The amplification patterns described above are illustrated and quantified using cumulative AI in Figure 4.13. Again, the velocity time histories are given for reference in the top plot. The Husid plot for the base ground motion (cumulative AI normalized by the total AI) is provided below the time histories. The difference between the cumulative AI for the crest/free field and the base cumulative AI is provided in the third plot, and the difference between the cumulative AI of the crest and free field is provided in the bottom plot.

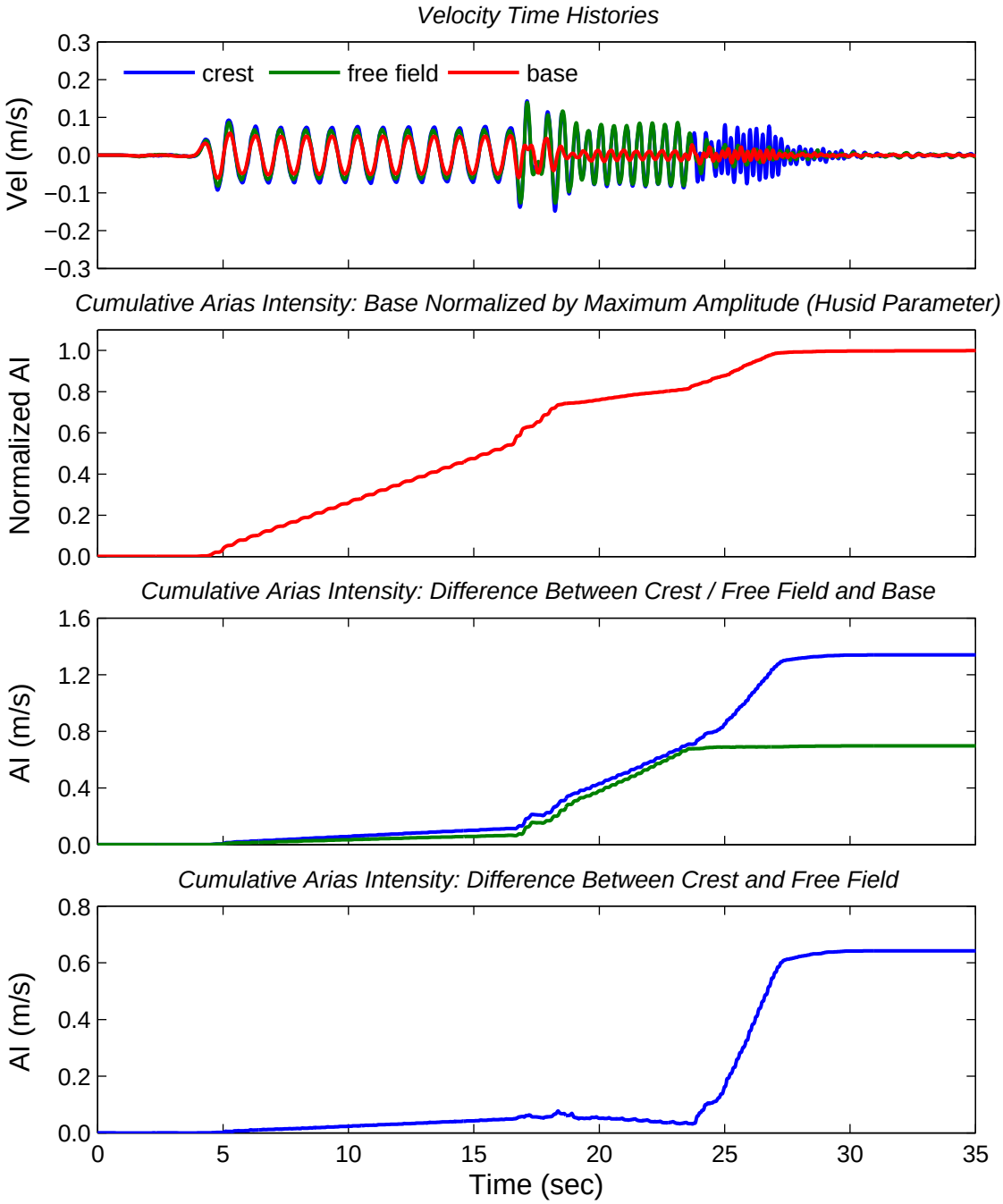

Figure 4.13: Velocity time histories, and cumulative Arias Intensity plots of the base ground normalized by the maximum, the crest and free field normalized by the base, and the crest normalized by the free field, for the (q) sine wave packet of the 55g, 30 degree slope model.

For the base motion, the rate of energy build-up is similar for the 1Hz and 4Hz motion, and is lower for the 2Hz motion. As seen previously, amplification of the crest and free field at 1Hz is small compared to that at the site and topographic frequencies; with differences of 0.07 and 0.11 between the crest and base, and free field and base, respectively over an 11.9 second time frame (an increase of about 0.01 per second). At the site frequency, amplification at the crest and free field increases to a rate of about 0.08 per second and 0.09 per second, respectively. Transitioning towards the topographic frequency, amplification continues to increase at the crest, at a rate faster than that at the site frequency, to a cumulative AI difference of about 0.48 (an increase of about 0.19 per second). Thus, at the crest, quicker increases in energy for the base (input) motion resulted in quicker increases in amplification for the site and topographic frequencies. This means the level of amplification may be tied to the incident wave amplitude at those frequencies. For the free field, amplification drops to zero near the topographic frequency, meaning no amplification of the base motion occurs. In line with the patterns described above, amplification of the crest over the free field is negligible at 1 and 2Hz, but increases at a rate of 0.19 per second near the topographic frequency.

Using the cumulative AI, the relative amplification patterns differ slightly from those illustrated by the normalized Stockwell plots. The most obvious reason for these differences is that the parameters are different, and therefore may preserve or highlight different components of ground motion. Amplification is determined through subtraction for both, but the cumulative AI is an aggregate parameter, while the Stockwell spectrum is based on discrete instances in time. Amplification for the cumulative AI is based on the rate at which the build up of energy changes at the locations of interest. Amplification for the Stockwell spectrum is based on spectral amplitudes at specific instances. Lastly, the cumulative AI is not independent of ground motion frequency content, and therefore accounts for all ground motion frequency components, while the Stockwell spectrum considers discrete frequencies. Because the (q) sine wave packet has energy concentrated at specific central frequencies in time, this factor is less influential in the case. However, this factor becomes important when

considering earthquake motions.

Thus far, the discussion has been focused on ground motion at the crest, free field and base. How this relates to the ground motion at depth is highlighted in Figures 4.14 and 4.15. These figures show snapshots in time of the model cross section. The (q) sine wave packet has been divided according to frequency content into the motion at 1Hz (q1), 2Hz (q2) and 4Hz (q3), with snapshots of each provided. Note that the snapshots are taken at times when the velocity amplitude has peaked at both the crest and free field.

Figure 4.14 uses vectors to show velocity amplitude at the instrument locations. The vectors are red when positive, moving towards the slope face, and blue when negative, moving from the slope face. The cross section (outlined in black) and vectors are overlaid with a mesh that moves with the vectors and interpolates values in between sensor locations. Additionally, the velocity time history at the crest, free field and base is provided, centered at those locations, with a red circle marking the time instance shown. The reference free field sensor is the fourth from the left near the surface, about 27.5 meters from the left edge, and 30.5 meters from the slope crest. A time stamp is given in the lower right corner and a magnification factor is provided in the lower left corner of each plot.

Figure 4.15 shows contoured velocity amplitude at the same snapshots in time, again using data at sensor locations and interpolating in between. A time stamp is provided below the contoured section. The base velocity time history is also provided with a red dot marking the time instance shown.

Although displacement vectors would allow the true movement of the slope to be observed, the velocity vectors and mesh in Figure 4.14 still demonstrate the mode shapes and wavelengths associated with the various ground motion frequencies. The ground motion wavelength is defined as the material shear wave velocity divided by the ground motion frequency ($\lambda = V_s/f$). The mode shapes are the deformed shape at a specific frequency, and are usually related to natural frequencies of the soil (such as the site frequency, which represents the first mode of vibration).

At the site frequency, the mode shape is such that the entire soil layer is in phase (i.e.,

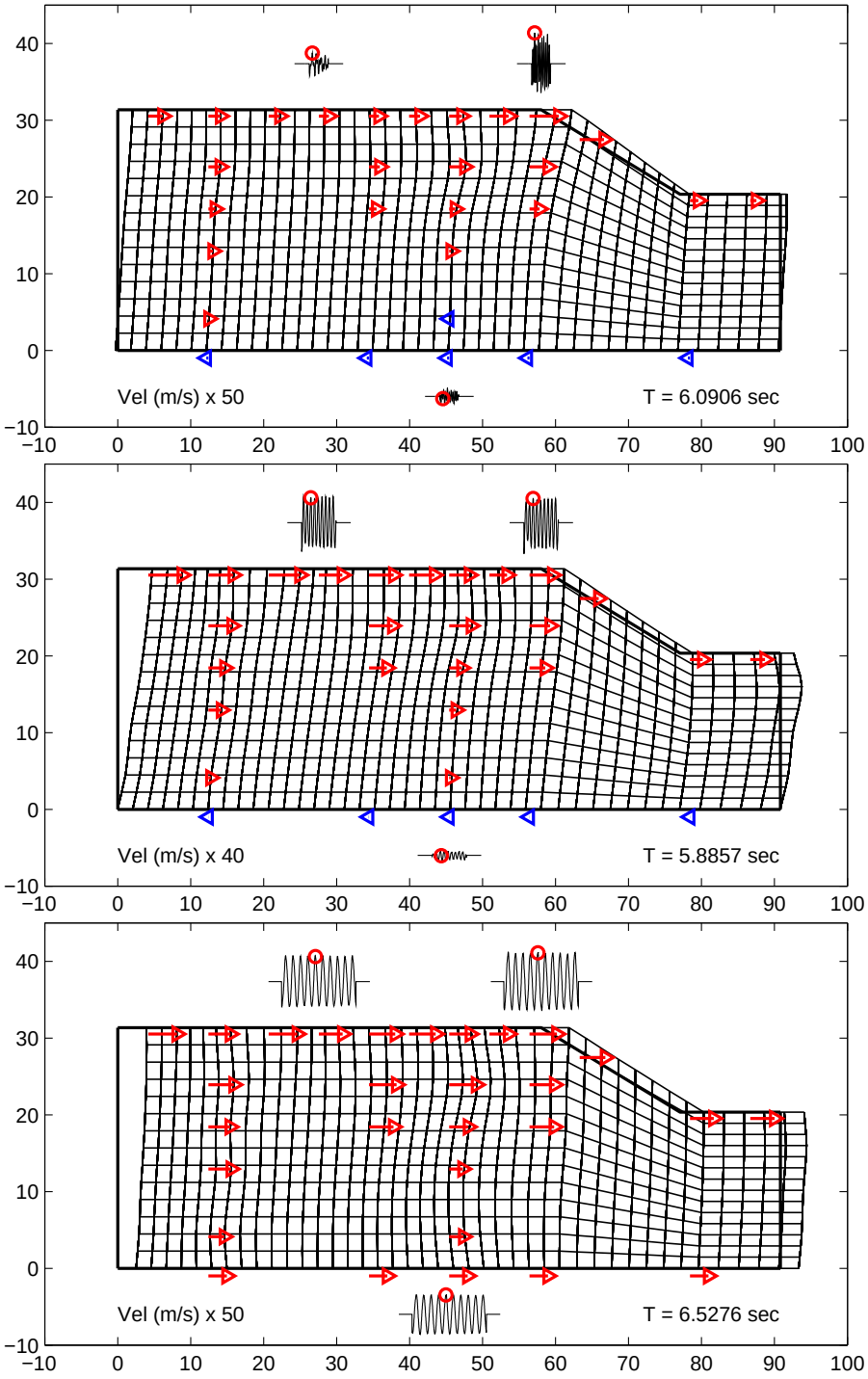

Figure 4.14: Velocity vectors and mesh of the 55g, 30 degree slope model, with crest, free field and base velocity time histories for sine wave motion with central frequencies of 4Hz (q3), 2Hz (q2), and 1Hz (q1) in the top, middle and bottom plots, respectively. Velocity is scaled by the factor in the lower left corner of each plot. Distances on axes are in meters.

moving together in the same direction) with depth. For a harmonic wave, the amplitude of movement decreases with depth such that it is zero at the base of the soil layer and at a maximum at the surface of the soil layer. This shape represents one quarter wavelength of the propagating wave.

The mode shape associated with the site frequency can be identified through inspection of the middle plot in Figure 4.14. The base, just below the soil layer, is just beginning to move in a direction opposite that of the soil layer above, and the velocity increases as you move from the base towards the ground surface. The average shear wave velocity of the soil is 250 meters per second. Thus, for the 2Hz ground motion depicted, the wavelength is 125 meters. The soil layer is 31.4 meters, which is about one quarter of 125 meters. Therefore, the expected behavior is established for 2Hz motion for the given site conditions. In this case, the behavior of the wedge shaped mass of soil, which constitutes the slope, follows that of the soil mass behind the slope crest (i.e., site effects control the response).

At the topographic frequency, the relationship of the mode shape to the slope geometry is similar to that of the mode shape at the site frequency and the site geometry. At a frequency of 4.5Hz, the wavelength is 55.6 meters. The height of the slope is 11 meters, which is about one fifth (rather than one quarter) of the 55.6 meters. In this case, the amplitude of movement is at a maximum at the crest and decreases to zero a few meters below the toe of the slope.

The slope can be viewed as a reduction in mass and stiffness as compared to the flat ground site behind the slope crest. This reduction in mass, or lack of confinement on the slope face, and stiffness allows the slope to move more freely. At the site frequency where the entire landmass moves in phase and the ground motion wavelength is large compared to the slope, the effect of the slope is minimized. However, as the topographic frequency is approached, the mode shape is such that the entire slope is encouraged to move together, while the ground below moves in the opposite direction. This leads to excitation of the slope and landmass extending behind the slope crest. As the landmass in front of the crest is reduced, less force is required for the slope to move. This may explain why greater

topographic amplification is observed for steeper slopes.

A mode shape similar to that described above is depicted in the top plot of Figure 4.14. For 4Hz ground motion, the wavelength is longer than that at the topographic frequency (62.5 meters), meaning about half the wavelength is shown. Note that the mode shape is not symmetrical, particularly beneath the slope crest, due to ground motion amplification.

For ground motion at 1Hz, which is not near the topographic or site frequencies, the wavelength is about 250 meters. This wavelength is 8 times the soil thickness and about 23 times the height of the slope. The site is small in comparison to the ground motion wavelength. As a result, the variation in amplitude between the base and surface is also small and the site and base move in phase (see the bottom plot in Figure 4.14). Likewise, because the size of the slope is insignificant compared to the ground motion wavelength, the effects of the slope are minimized.

While Figure 4.14 was useful for depicting mode shapes, variations in amplitude at the different sine wave packet frequencies is more easily observed in Figure 4.15. For ground motion at 1 and 2Hz (bottom and middle plots) amplitudes are similar at given elevations across the model, meaning topographic effects are minimal at these frequencies. That is, site effects control the ground response. As was discussed previously, the difference in amplitude between the ground surface and base is greater at 2Hz than at 1Hz.

One observation worth noting at these frequencies is the fluctuation in amplitude observed near the ground surface. The amplitude fluctuates from high to low moving from the crest in both directions. Higher amplitudes at the container boundaries may be a result of boundary effects. Fluctuations at other locations are likely partially due to natural variations in the near surface soil and small biases in the sensor recordings. Indeed some fluctuation was observed along the ground surface for the flat ground model configuration as well. The lower amplitude near the slope toe may be due to the reduced soil layer thickness at this location, resulting in lower amplification. It is possible, however, that some of the fluctuation may result from the presence of the 30 degree slope. In particular, it could be due to the presence of Rayleigh waves produced at the crest that propagate along the ground surface. This idea

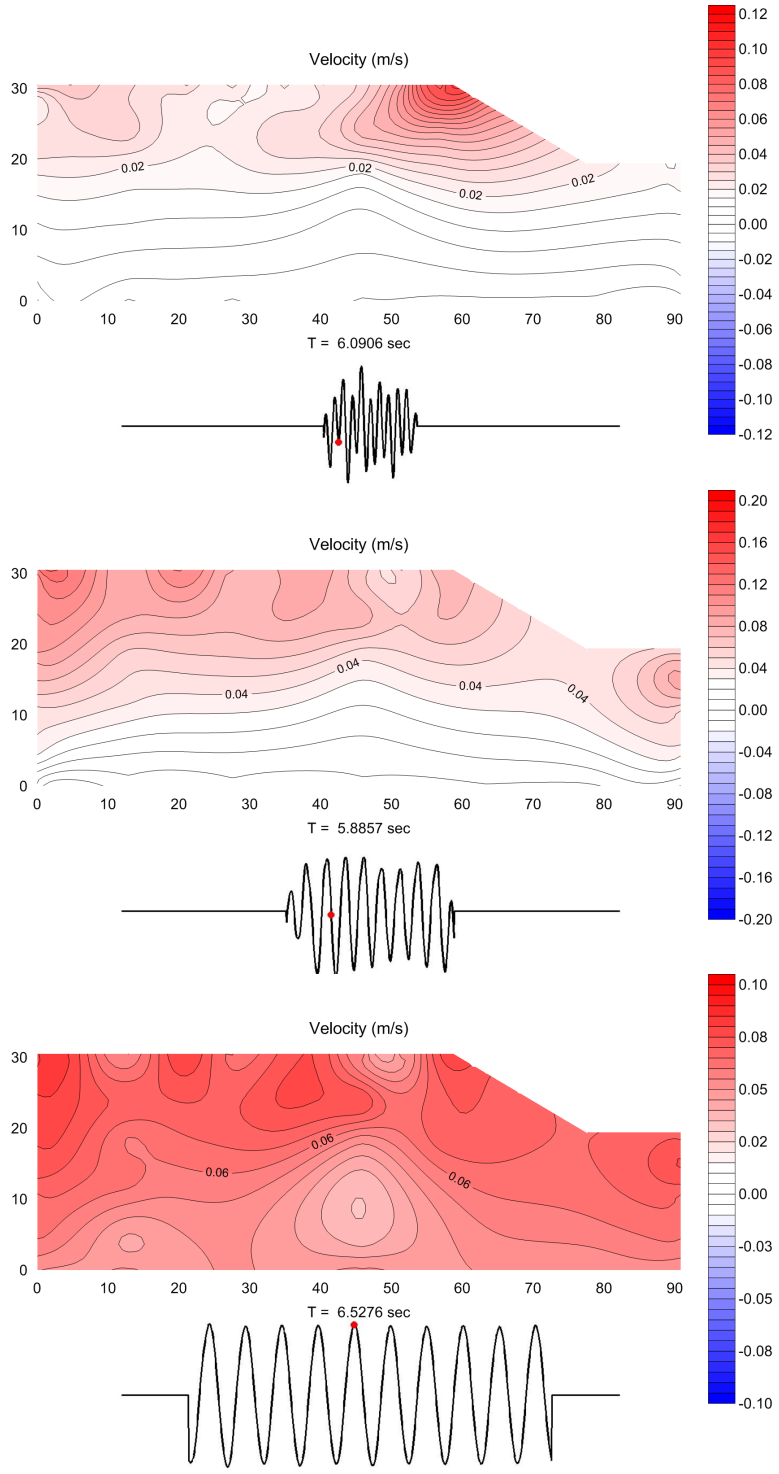

Figure 4.15: Velocity contours of the 55g, 30 degree slope model, with base velocity time histories, and time stamps for sine wave motion with central frequencies of 4Hz (q3), 2Hz (q2), and 1Hz (q1) in the top, middle and bottom plots, respectively. Distances on axes are in meters.

is discussed further in Section 4.4.

The breadth and depth of topographic effects near the topographic frequency are well illustrated by the contour plot of 4Hz ground motion (top plot of Figure 4.15. An amplified response (compared to the free field area, about 27.5 meters from the left edge) encompasses the entire slope and extends at least about 15 meters behind the slope crest. This indicates a separation in behavior between the landmass excited near the topographic frequency (which is similar in shape to a deep seated landslide mass) and the landmass behind it, which is subjected to typical site effects. These landmasses will interact with each other and at different frequencies will move in and out of phase with each other, as shown in Figure 4.16.

Figure 4.16 shows plots of differences in phase between the crest and other locations. The middle plot illustrates differences in phase between the crest and free field as well as the crest and base. The bottom plot shows differences between the crest (sensor A35) and other near surface sensor locations behind the crest, including the free field (sensor A20). The sensor locations are depicted in Figure 4.3, and are generally 5.5 meters apart; the exception being that sensors A20 and A23 are about 7 meters apart. The top plot shows the velocity time histories for the crest, free field and base for reference.

Differences in phase between the base and the crest were touched upon previously in the discussion of wavelengths. At 1Hz, the base and crest move in phase with each other (phase difference is near 0). At 2Hz, the phase difference fluctuates some, but generally the base and crest are around 90 degrees out of phase with each other, which is in line with the mode shape described. At 4Hz, the phase difference between the crest and base also fluctuates, but generally the two locations are out of phase with each other, which is also in line with the mode shape.

For ground motion at 1 and 2Hz, the free field and other near surface sensors are shown to be in phase with the crest. However, at 4Hz, the free field moves in and out of phase with the crest. The separation between the behavior at the crest and the behavior in the free field can be gauged by the behavior at other near surface sensors. Sensors adjacent to the crest

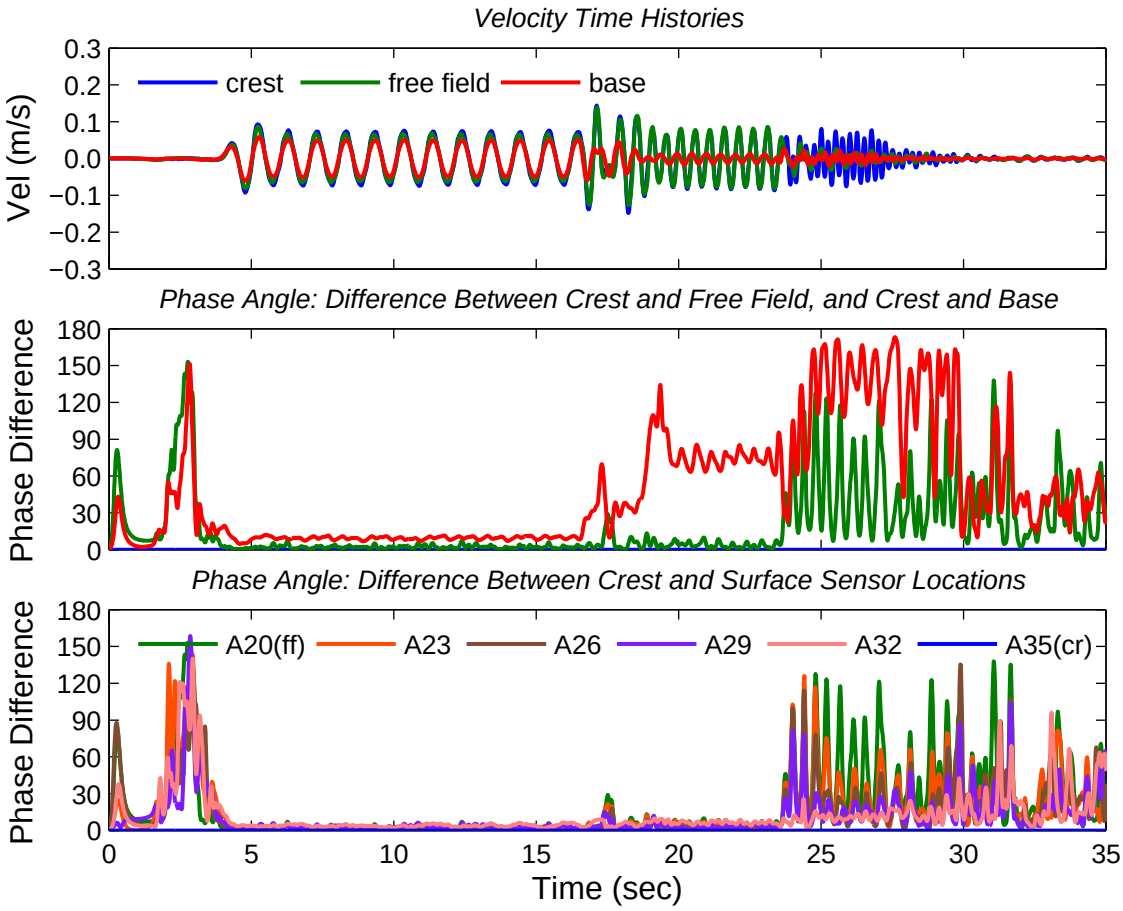

Figure 4.16: Velocity time histories, and plots of the difference in phase angle between the base, free field, other surface locations and the crest, for the (q) sine wave packet of the 55g, 30 degree slope model. In the bottom plot, legend designations represent near surface sensor locations ranging from the free field (A20) to the crest (A35).

remain in phase, but the behavior shifts towards that of the free field as the distance from the crest increases.

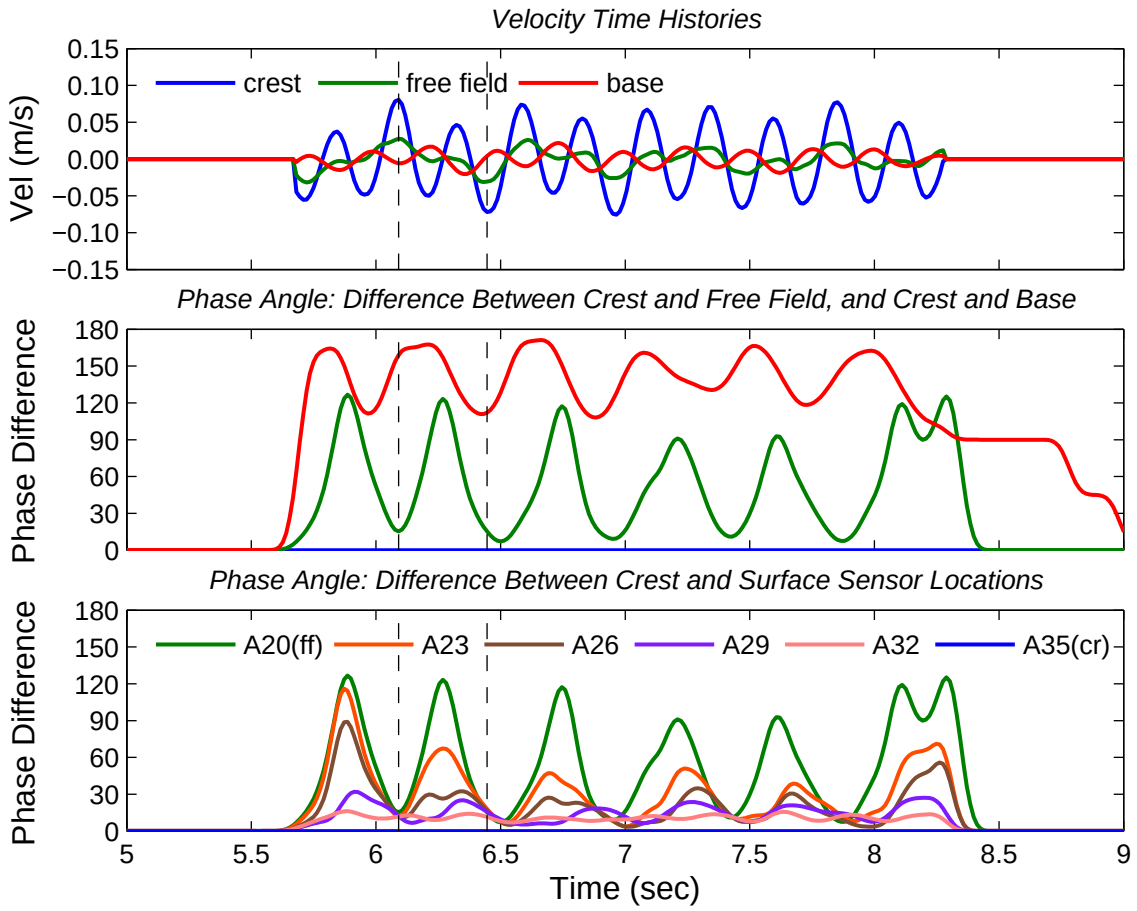

Figure 4.17: Velocity time histories, and plots of the difference in phase angle between the base, free field, other surface locations and the crest, for the (q3) sine wave motion (central frequency of 4Hz) of the 55g, 30 degree slope model. In the bottom plot, legend designations represent near surface sensor locations ranging from the free field (A20) to the crest (A35). Vertical dashed lines mark the time frame for which snapshots are presented in Figure 4.18.

Phase differences for ground motion near the topographic frequency is better illustrated in Figure 4.17 which focuses on the ground motion at 4Hz. The underlying ground motion at 2Hz, particularly in the free field, of the (q3) motion, can be identified in the velocity time histories in the top plot. This, along with the amplified motion near the crest are responsible for the phase differences highlighted in the middle plot. Both areas gravitate towards their respective natural frequencies. In between the crest and free field, some soil

takes on the behavior of the free field and some more closely mimics the behavior of the crest. The transition location between these two behaviors can be identified in the bottom plot of Figure 4.17. At the beginning and end of the motion, sensor A26 matches the phase of the free field more closely, but matches that of the crest in between. So, for this motion, the transition between the free field response and that of crest area is likely somewhere between sensors A26 and A29 or about 12.5 to 18 meters behind the crest.

The phase differences described above influence the ground motion amplitude at the crest. When the crest and free field move in phase, the amplitude at the crest tends to be greater than when the two locations are out of phase. This behavior is illustrated in Figure 4.18 which shows snapshots of cross sections in time starting at the first dashed vertical line and ending at the second dashed vertical line in Figure 4.17. Over this time frame, the crest and free field start in phase, move out of phase and then move back in phase.

The plots in Figure 4.18 consist of contoured velocity, and velocity vectors and mesh cross sections, side by side at the same moments in time. The first snapshots (top plots) are the same as those depicted in Figures 4.14 and 4.15 for the 4Hz sine wave motion. These first snapshots were discussed previously, but are a good reference point for the behavior that follows. At this point in time, the free field and crest are in phase and reaching a point of local maximum velocity towards the slope face.

The next snapshot shows the free field and crest moving out of phase with each other. The area around the crest is gaining velocity towards the free field, while the free field is decreasing in velocity, but still moving towards the slope face. The effect of this phase difference on the amplitude around the crest is shown in the next snapshot. At this point, the movement of the free field still has not changed direction, but the crest area has reached a local maximum velocity away from the slope. The resistance of the soil mass in the free field has slowed the soil mass around the crest, so that the maximum amplitude is less than that of the first snapshot.

For the next two snapshots, the area around the crest and the free field remain out of phase. At this point in time, the area around the crest and the free field are gaining velocity

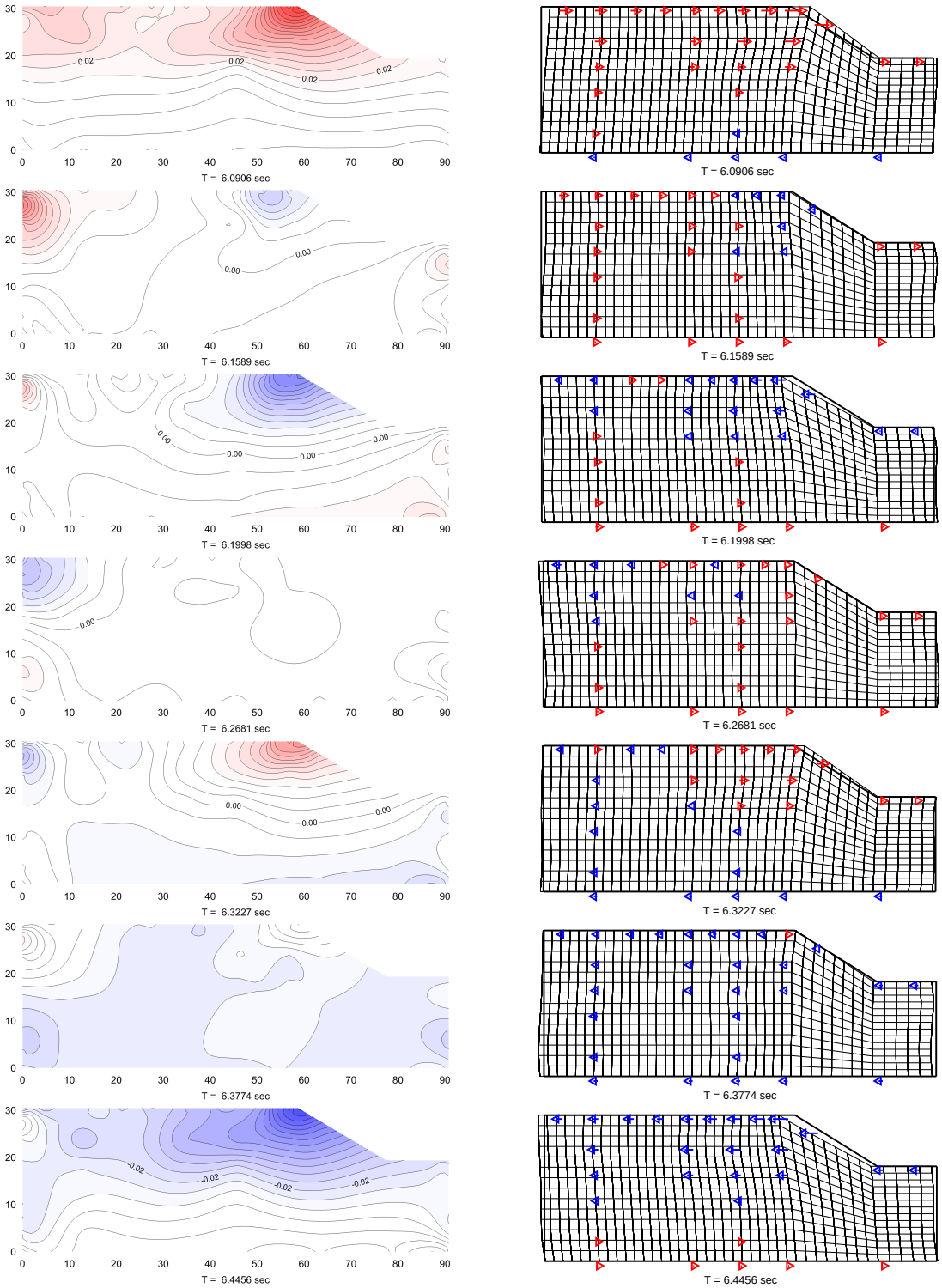

Figure 4.18: Time series of velocity contours (left plots) and velocity vectors and mesh (right side) for the (q3) sine wave motion (central frequency of 4Hz) of the 55g, 30 degree slope model. The time series spans the vertical dashed lines shown in Figure 4.17.

in opposite directions; the free field away from the slope face and the crest area towards the slope face. The area around the crest has not gained momentum lost in the previous cycle and without support of the free field soil mass (i.e., if the free field moved with the crest area), the amplitude around the crest is again lower than that of the first snapshot.

For the final two snapshots, the crest and free field move back into phase, gaining velocity away from the slope face. The crest area has regained momentum and is not impeded by the free field soil mass. The result is an amplitude near the crest that is comparable to that of the first snapshot.

Close inspection of Figure 4.17 reveals that the pattern described above continues throughout the 4Hz sine wave motion. Thus, phasing differences between the free field and crest should be considered when analyzing topographic effects and topographic amplification. The influence of phasing, however, should be considered a secondary effect on the ground motion amplitude near the slope. The tendency towards resonance near the topographic frequency has a more significant impact on the slope response.

4.2.2 Frequency Sweeps

Using the sine wave packet introduced in the previous section, some of the mechanisms and influences of topographic effects were identified. The same patterns as well as additional mechanisms are presented in this section using frequency sweeps. Frequency sweeps are still idealized in that they represent sinusoidal motion, but they cover a larger range of frequencies in a smaller amount of time and are closer to transient, or real-life earthquake motion.

Two sweeps (d and c) used in the centrifuge experiment, and introduced to the 30 degree slope at 55g, are introduced in this section. The (d) sweep was designed to move from low to high frequency (about 0.1 to 6.0Hz) with the same number of cycles and same amplitude at each frequency. The (c) sweep was designed to move from low to high and then from high to low frequency (0.5 to 7 to 0.5Hz), at a consistent amplitude, with the number of cycles increasing with frequency. As is shown in the figures that follow, the achieved base motions did not follow design. Namely, constant amplitude across all frequencies could not

be accomplished, and notable amplitude at higher frequencies (i.e., above about 5.5Hz) could not be produced.

Frequency Sweep (d)

Fluctuations in ground motion amplitude at the various frequencies of the (d) sweep are illustrated for the crest, free field and base in Figures 4.19 through 4.21. These figures are the same as those introduced for the (q) sine wave packet in Figures 4.11 through 4.13. Velocity time histories are included in each figure. Additionally, Figure 4.19 provides plots of cumulative AI, the Stockwell MSF and the normalized difference in Stockwell amplitude between the crest and free field. Figure 4.20 provides normalized Stockwell plots of the base; and the difference between the crest and base, and the free field and base. Figure 4.21 provides the base Husid plot, and cumulative AI plots of the amplification of the crest and free field over the base, and amplification of the crest over the free field. The time frame in which topographic amplification occurs (between 57 and 66 seconds) is bounded by solid vertical black lines. Solid vertical gray lines mark changes in the response measured at the crest (and other locations) during this time frame (at 60.6, 62.2 and 63.7 seconds).

Topographic effects can be defined by notable differences in the response of the crest and free field locations. An amplified response at the crest compared to the free field, or topographic amplification, is clearly illustrated by the velocity time histories, cumulative AI plot, and normalized Stockwell plot in Figure 4.19. Topographic amplification occurs for Stockwell MSF values ranging from 3.1 to 5.6 Hz, or about 0.7 to 1.3 times the topographic frequency. At frequencies below 3.1Hz (which includes the site frequency at 2Hz), differences in the response at the crest and free field are minor by comparison. It should be noted that central frequencies between about 0.4 and 5.3Hz were achieved for the base motion, but that frequencies at the crest and free field reached about 5.6Hz. This is likely a result of energy build-up as the second mode of resonance for the site is approached (which occurs at a frequency of 6Hz).

Changes in the behavior at the crest can be observed during the time frame when topo-

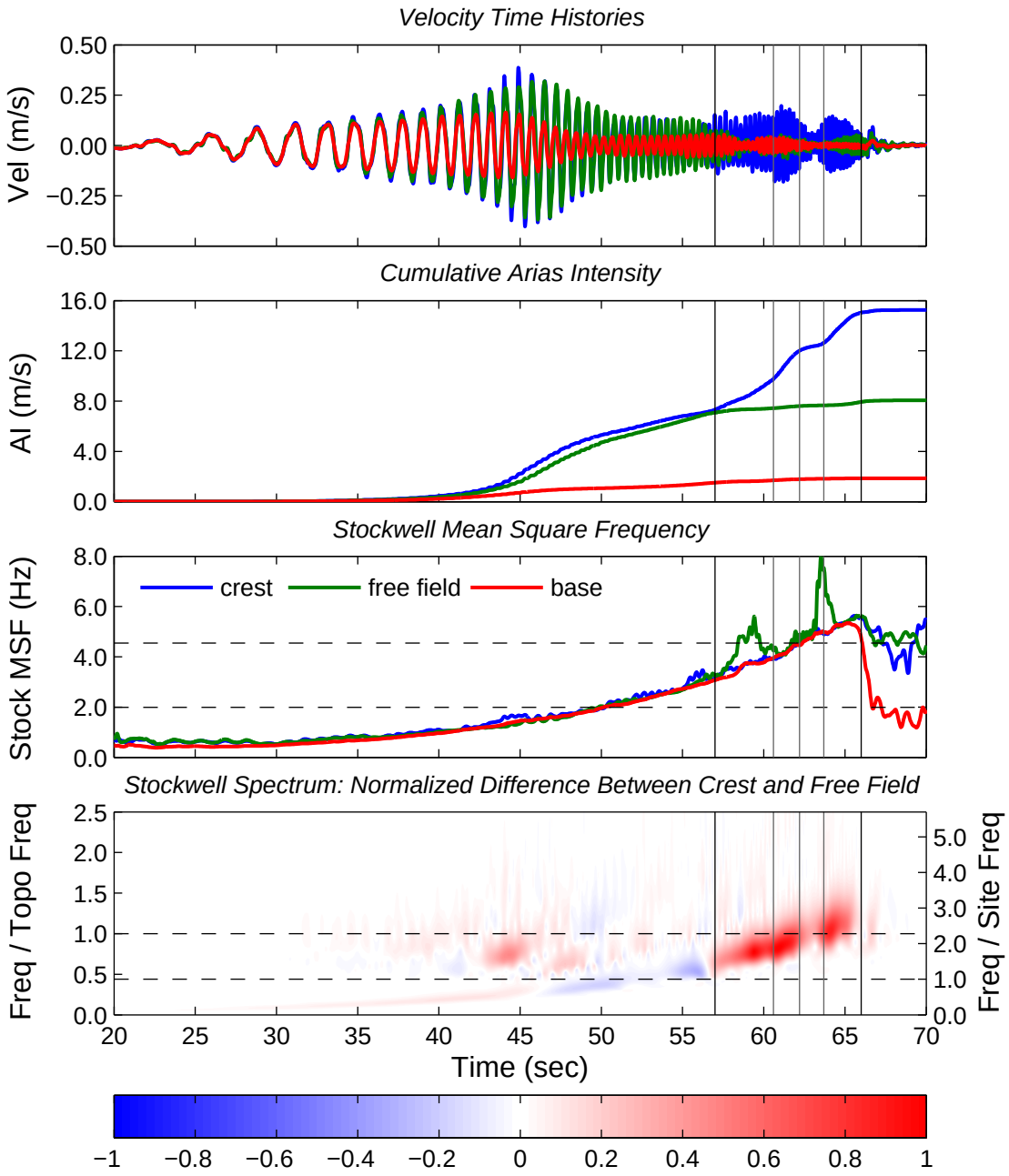

Figure 4.19: Velocity time history, cumulative Arias Intensity, and Stockwell MSF plots for the base, crest and free field; and the difference between the crest and free field Stockwell amplitude, normalized by the maximum difference, for the (d) frequency sweep of the 55g, 30 degree slope model. Vertical gray lines mark changes in the response at the crest while topographic amplification occurs (bounded by the vertical black lines).

graphic amplification occurs. These changes are evidenced by contrasts in the slope of the cumulative AI plots and fluctuations in the level of amplification, both in comparison to the free field, and to the base. There are a number of factors contributing to these differences in behavior. One such factor is the amplitude of the incident (base) ground motion.

Inspection of the velocity time histories and normalized Stockwell plots in Figure 4.20 reveals a pattern of slow increases, followed by sharper decreases in the base motion amplitude. The amplitude increases from the beginning of the motion before decreasing near the site frequency. The amplitude again increases before dropping off just after topographic amplification begins. The amplitude again builds and then drops off just after reaching the topographic frequency, and then increases slightly and levels out until the end of the motion. With each successive drop in amplitude, the overall amplitude of the base motion decreases (i.e., the amplitude prior to the drop is not achieved again). This pattern is also illustrated by changes in the slope of the base motion Husid plot in Figure 4.21.

It is possible that these drops in amplitude are a result of the limitations of the shaker used to produce the motion. As previously mentioned, the shaker had difficulty producing higher amplitudes at higher frequencies. Some of the drops in amplitude, however, may also result from the interaction of the soil mass and shaker, as the drops tend to occur at points in time where excitation of the entire soil mass, or excitation of the slope occur. Thus, it's also possible this excitation temporarily overwhelms the shaker, causing it to lose momentum.

These drops in the input (base) amplitude also correspond with instances of lower amplification. Amplification of the base motion at the crest and free field is greatest near the site frequency when the amplitude of the base motion is greatest. The amplification then decreases after the first drop in the base motion amplitude. This is highlighted by the Stockwell plots in Figure 4.20 and cumulative AI plots in Figure 4.21, where amplification increases by 2.90 from about 44 to 49 seconds (a rate of 0.58 per second), but then only increases by 1.62 between 49 and 55 seconds (a rate of 0.27 per second).

The next two drops in the base amplitude coincide with the occurrence of topographic amplification. The level of amplification in the free field barely increases through most of this

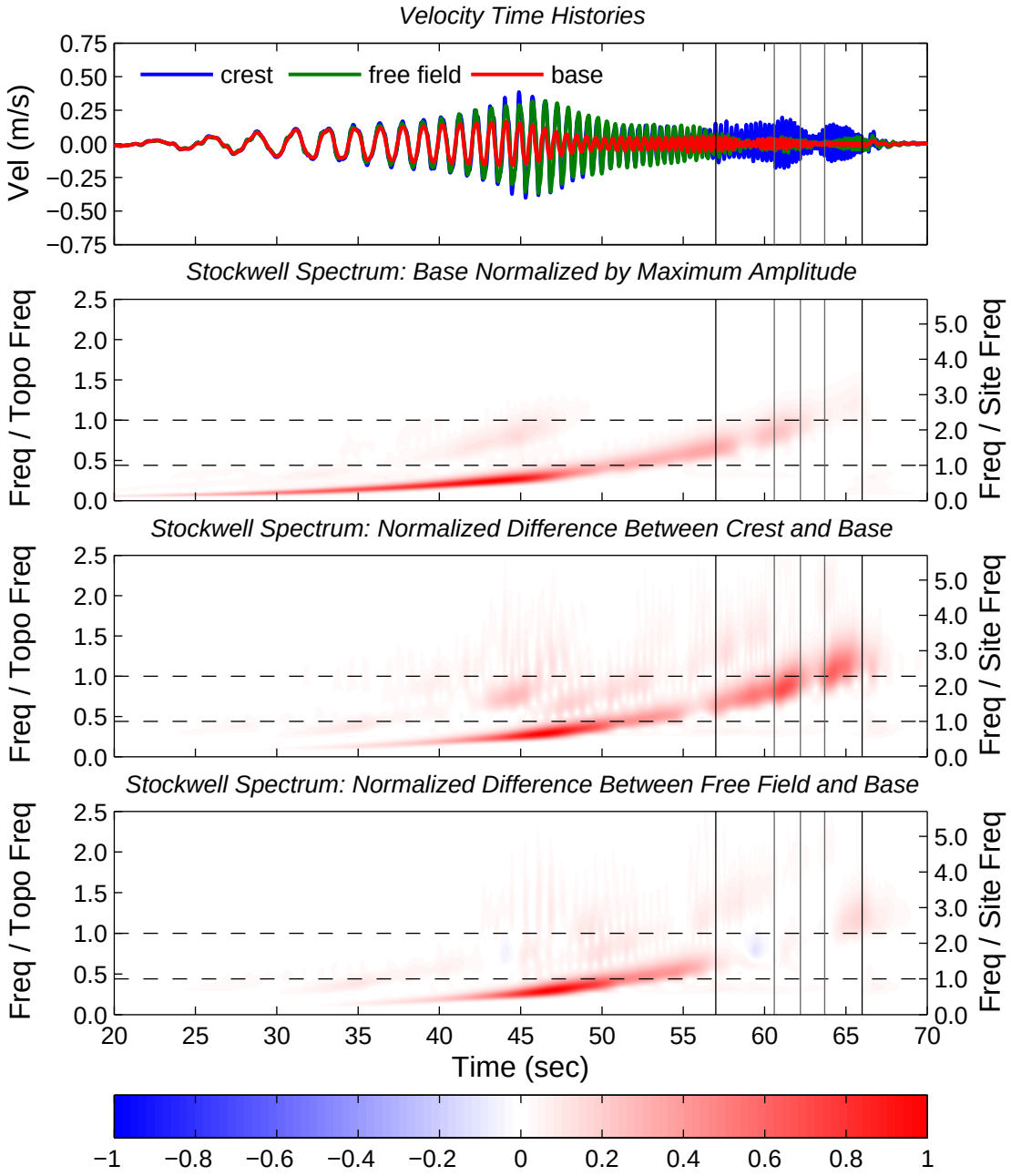

Figure 4.20: Velocity time histories, and normalized Stockwell plots of the base ground motion, the difference between the crest and base, and the difference between the free field and base, for the (d) frequency sweep of the 55g, 30 degree slope model. Vertical gray lines mark changes in the response at the crest while topographic amplification occurs (bounded by the vertical black lines).

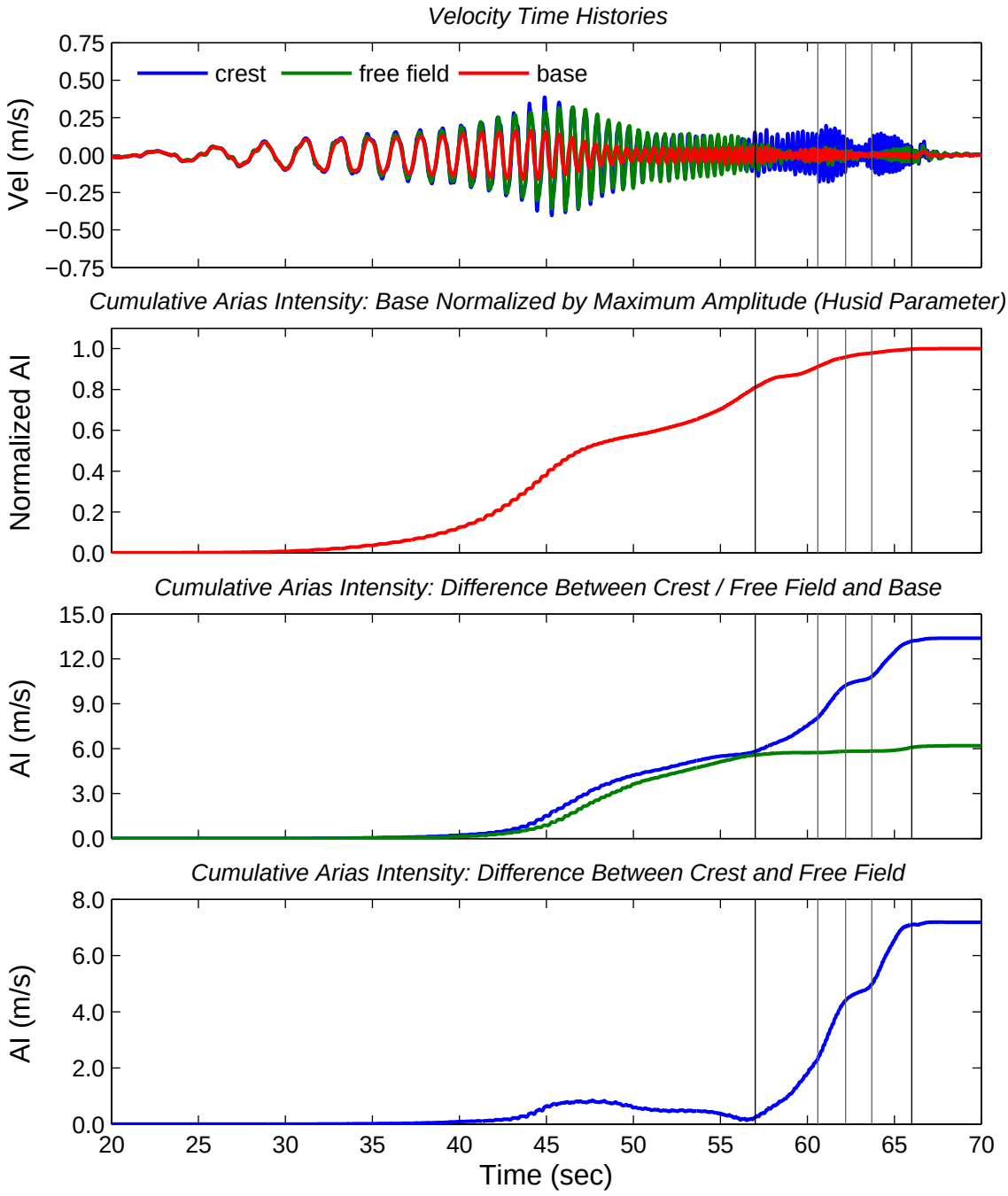

Figure 4.21: Velocity time histories, and cumulative Arias Intensity plots of the base ground normalized by the maximum, the crest and free field normalized by the base, and the crest normalized by the free field, for the (d) frequency sweep of the 55g, 30 degree slope model. Vertical gray lines mark changes in the response at the crest while topographic amplification occurs (bounded by the vertical black lines).

time frame, with a slightly greater increase as the second mode of resonance is approached; starting and ending at an AI amplification of 5.74 and 6.07, respectively. It should be noted that because the amplitude is low in the free field during this time frame, the motion is dominated by high frequency noise when the base amplitude drops, evidenced by an increase in the Stockwell MSF (Figure 4.19). At the crest, amplification over the base increases through the first drop in the base amplitude, and then levels out some at the second drop in the base amplitude. In between these amplitude drops, and after the second drop has occurred, increases in amplification are similar (2.17 in 1.6 seconds, and 2.37 in 1.7 seconds) and occur more rapidly. A similar pattern is observed when considering topographic amplification over the free field, which maximizes at 7.19 for the cumulative AI.

For convenience, the time frames discussed above will be referred as time frames (tfs) 1 through 4 for the remainder of this discussion. That is, $tf1$ is from the first vertical black line to the first vertical gray line (from 57 to 60.6 seconds); $tf2$ is from the first to second vertical gray line (60.6 to 62.2 seconds); $tf3$ is from the second to the third vertical gray line (62.2 to 63.7 seconds); and $tf4$ is from the third vertical gray line to the last (second) vertical black line (63.7 to 66 seconds). The first and second drops in base amplitude described above correspond with $tf1$ and $tf3$, respectively.

The behavior at the crest, described above, indicates that the amplitude of the incident wave affects the level of topographic amplification. However, the level of amplification is similar before and after the last drop in amplitude (during $tf2$ and $tf4$), despite the fact that the overall base amplitude was lower in $tf4$. This indicates that other factors are contributing to the level of amplification. Proximity of the ground motion frequency to the topographic frequency is likely a contributing factor, and may contribute to the lower level of amplification observed during $tf1$. However, the frequency content of the ground motion is closer to the topographic frequency in $tf2$ than $tf4$, and again, similar levels of amplification are observed for these time frames. One factor that can be linked to this behavior is ground softening within, and at the base of the slope, as demonstrated in Figure 4.22.

Figure 4.22 provides velocity time history plots, one which highlights time frames 1

through 4 (left plot), and one that compares the overall time frame in which topographic amplification occurs to the time frame just before (right plot). Below each time history plot are stress-strain plots at the mid-slope and base of the slope locations below the crest (see Figure 4.4 in Section 4.1.2). Vertical colored lines in the time history plots mark the beginning of, and match the color of, the time frames plotted in stress-strain plots. The time at which the stress-strain plots end is marked by a vertical gray line.

Based on the plots in Figure 4.22, it appears that softening at the base of the slope impedes some of the energy from propagating farther up the slope, a case of potential base isolation. Softening at the base of the slope is more extreme prior to, rather than during the time frame in which topographic amplification occurs. However, the softening at the base of the slope reduces, despite increases in the base amplitude, as $tf1$ is approached (plots on the right). The decrease in softening combined with the increase in base amplitude could lead to greater amplification (which in turn could lead to more softening). However, the level of amplification remains fairly constant between the site frequency and the beginning of $tf1$. This results from the shift away from frequencies which tend towards a more amplified response; in this case the site frequency. The increase in base amplitude, and reduction in softening, is offset by the shift in frequency content.

During $tf1$, the response at the crest is amplified and the base amplitude, along with the response at the base of the slope, fluctuates. The base amplitude is greatest during the beginning of $tf1$, however, due to softening at the base of the slope, amplification is the lowest during this time frame. The base amplitude then decreases, resulting in a stiffer response, and subsequently, greater amplification. The base amplitude then increases again, softening at the base of the slope occurs, and the level of amplification is reduced.

Note that the raw amplitude at the crest (see the velocity time histories) is similar despite the changes in the base amplitude during $tf1$. This is true except just after the drop in base amplitude, during the transition towards a stiffer response at the base of the slope. During that transition, the input amplitude is minimal and energy is still impeded from propagating up the slope.

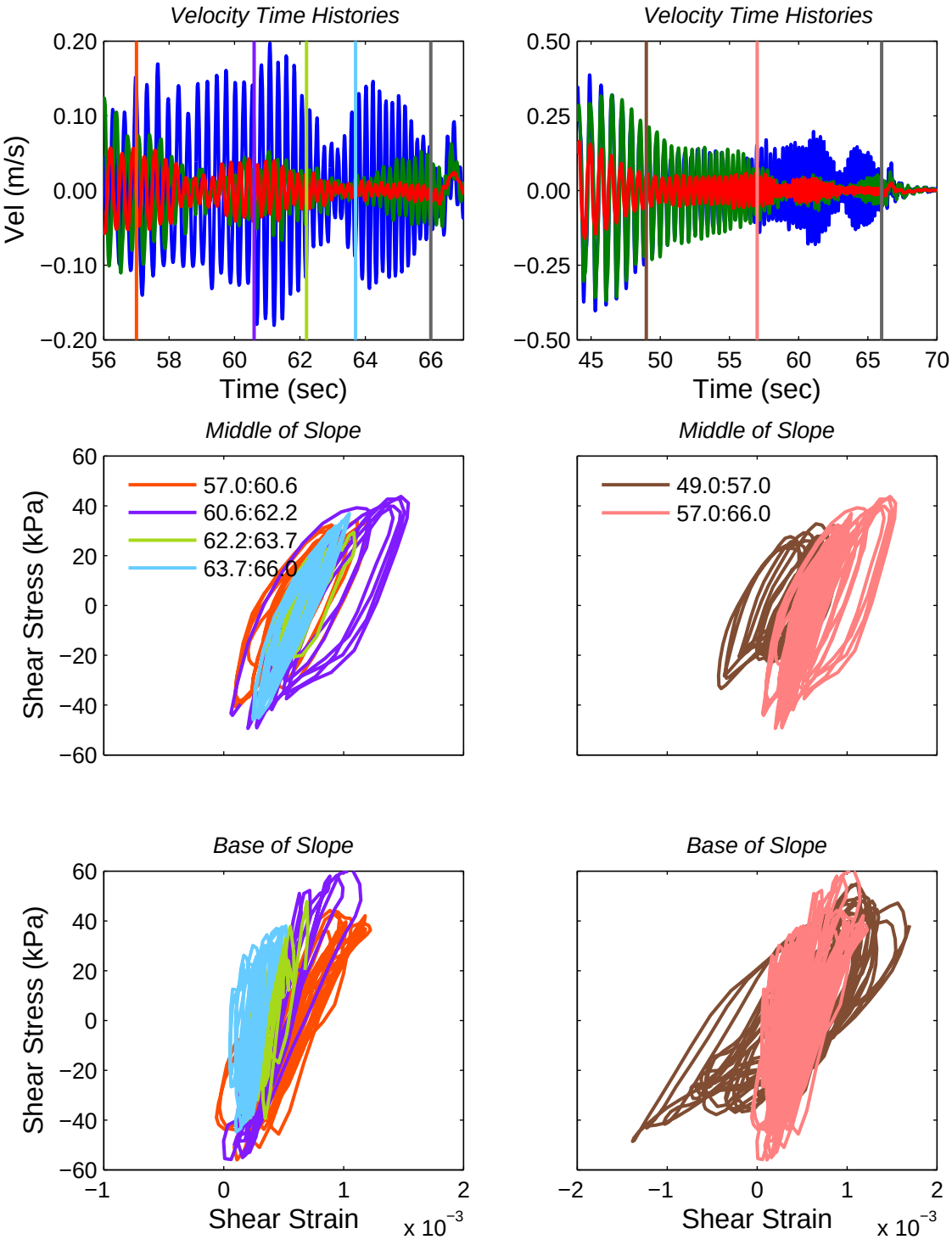

Figure 4.22: Velocity time histories, and stress-strain plots at the mid-slope and base of slope elevations below the crest, for the (d) frequency sweep of the 55g, 30 degree slope model. Colored vertical lines in the velocity time histories match the colors used in the stress-strain plots, marking the beginning of the time frame for that color.

The base amplitude peaks entering and then reduces throughout $tf2$. The stiffness at the base of the slope increases, and amplification, as well as raw amplitude, at the crest also increase. The increase in excitation of the slope leads to softening, and damping of energy within the slope, through the increased movement.

During $tf3$ the base amplitude and amplitude at the crest both drop significantly. This results in a stiffer response at the base of the slope, but with little input energy to amplify, amplification at the crest decreases. As the base amplitude increases again, the amplitude at the crest also increases towards the end of $tf3$. Thus, $tf3$ can be viewed as a transition period. Energy in the system is damped, and little new energy enters the system; momentum is temporarily lost. As new energy is introduced, momentum increases again, as seen in $tf4$.

During $tf4$ the response at the base of the slope is roughly linear elastic (no softening), and amplification levels are similar to that of $tf2$, despite the base amplitude being roughly one third of that in $tf2$, and despite ground motion frequencies farther from the topographic frequency. The raw amplitude is similar to that achieved during $tf1$, again, despite lower base amplitudes; and it should be noted the ratio of raw amplitude (between the crest and base) in $tf4$ is greater than that during $tf2$. The level of amplification (and raw amplitude) does decrease approaching the end of $tf4$. However, this is likely a result of shifting farther from the topographic frequency or phasing with the free field (see discussion below).

Softening at the base of the slope can result from increases in the input (base) motion amplitude and excitation of the slope near the topographic frequency. Ground motion associated with topographic amplification leads to differential motion, and could lead to the development of a slip plane, near the base of the slope. This softening impedes energy from reaching the slope and crest. Therefore, softening at the base of the slope may essentially place a cap on the level of amplification that can occur for a particular site.

Given other influences discussed, the effects of phasing on the ground response are less clear for the (d) frequency sweep. For the (q) sine wave motion, phasing could be isolated considering that the ground motion frequency and stiffness remained fairly constant. However, the potential influence of phase differences illustrated in Figure 4.23 should be

considered.

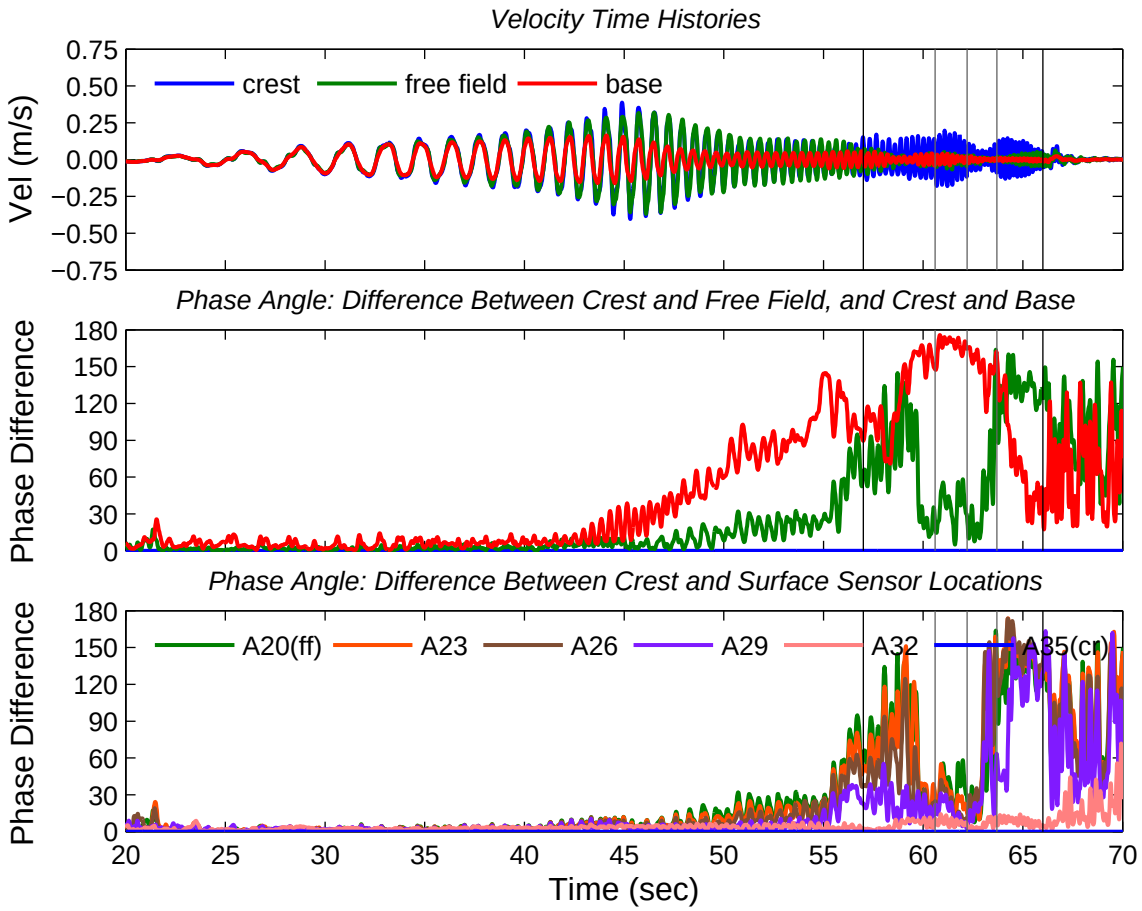

Figure 4.23: Velocity time histories, and plots of the difference in phase angle between the base, free field, other surface locations and the crest, for the (d) frequency sweep of the 55g, 30 degree slope model. In the bottom plot, legend designations represent near surface sensor locations ranging from the free field (A20) to the crest (A35). Vertical gray lines mark changes in the response at the crest while topographic amplification occurs (bounded by the vertical black lines).

While topographic amplification is occurring, the impact of phasing is likely proportional to the relative ground motion amplitude between the free field and crest. During $tf4$, when the two locations are out of phase, the amplitude at the crest decreases as the amplitude in the free field increases. This could be partially influenced by phasing. If the free and crest were in phase during $tf4$, the raw amplitude at the crest may be greater, and therefore, the perceived amplification would also be greater. This would mean amplification during $tf4$

would be greater than during $tf2$ (when the free field and crest are in phase). This would also indicate that the impact of non-linear behavior, or ground softening, is greater than that highlighted in the discussion above.

Phase differences between the crest and base are as expected. The two areas move towards being out of phase as the topographic frequency is approached. They then move towards being back in phase as the second mode of resonance for the site is approached.

Phasing with areas between the crest and free field varies depending on the ground motion frequency content. At lower frequencies (below the topographic frequency) separation in behavior between the free field landmass and slope is likely somewhere between sensors A26 and A29 (between 12.5 and 18 meters from the crest). At higher frequencies (above the topographic frequency), however, the separation in behavior is likely somewhere between sensors A29 and A32 (between 7 and 12.5 meters from the crest); as the behavior at A29 tends to match the free field. This indicates that the area subjected to topographic effects is dependent upon the ground motion frequency content. This concept is illustrated in Figure 4.24.

Figure 4.24 provides eight cross section snapshots of velocity contours for the (d) sweep motion. The snapshots span the time frame bounded by dashed vertical black lines (between 60.0 and 65.4 seconds) in the velocity time history (top plot) and Stockwell MSF (second plot) plots for the crest, free field and base. The topographic frequency (4.5Hz) and site frequency (2Hz) are marked by dashed horizontal black lines in the Stockwell MSF plot. The snapshots encompass the topographic frequency, with the Stockwell MSF ranging from 3.9 to 5.3Hz (about 0.85 to 1.15 times the topographic frequency). Time stamps are provided below each snap shot; they are ordered from top to bottom and then left to right.

As illustrated by the snap shots, the depth and breadth of topographic amplification vary with frequency content. That is, at lower frequencies, a larger area of the slope is amplified compared to higher frequencies. This likely can be tied to the ground motion wavelength (which is greater at lower frequencies) relative to the slope. At lower frequencies, the whole slope will tend to move together, whereas at higher frequencies, portions of the slope will

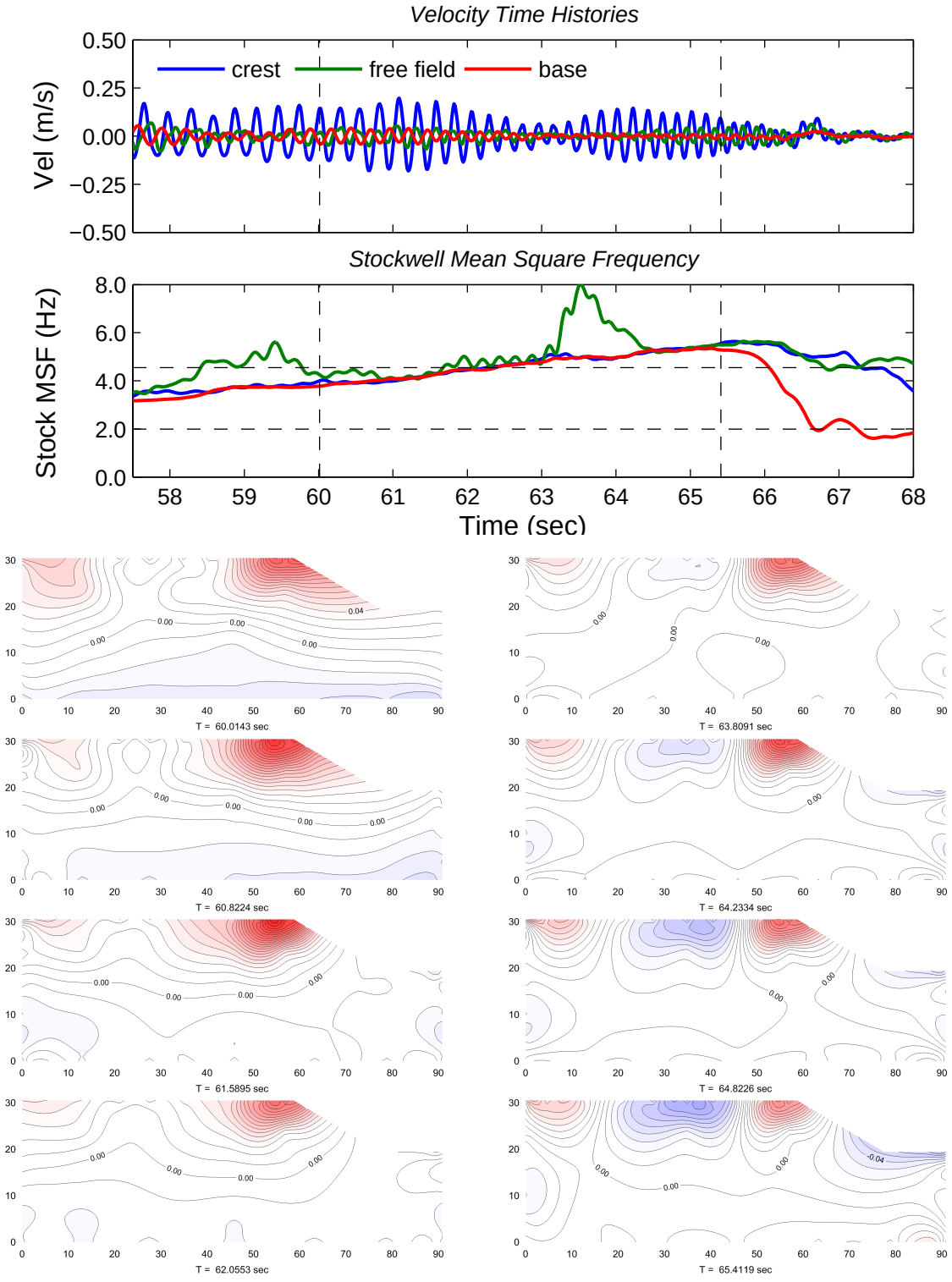

Figure 4.24: Time series of velocity contours for the (d) frequency sweep of the 55g, 30 degree slope model. The time series spans the vertical dashed lines shown in the velocity time history (top plot) and Stockwell MSF (second plot) plots.

move in opposing directions. Note that the ground motion amplitude varies for the snap shots presented, but has little effect on the size of the area amplified.

Frequency Sweep (c)

Inspection of Figures 4.25 through 4.30 presented in this section for the (c) sweep reveal similar patterns to those described in Figures 4.19 through 4.24 for the (d) sweep. Topographic amplification is observed for a band of frequencies near the topographic frequency, and amplification is influenced by non-linear behavior, the input amplitude, and phasing with the free field. Differences in the ground motions, however, cause these mechanisms to manifest in different ways, and provide additional insight into the mechanisms that contribute to topographic effects.

The influence of ground motion frequency content and the duration of ground motion at various frequencies is well illustrated by the (c) sweep. The sweep is designed such that the duration of motion increases as the frequency increases (hence the long 'dead zone' in the center of the motion at frequencies where the shaker could not produce any discernable amplitude). This means more energy is concentrated at higher frequencies, such as near the topographic frequency, and less is concentrated at lower frequencies, such as the site frequency. The result is that most of the motion (outside of the 'dead zone') is prone to topographic amplification, as shown in Figure 4.25. As with the previous section, the time frame in which topographic amplification occurs is bounded by vertical black lines, and changes in behavior are marked by vertical gray lines.

Topographic amplification occurs between crest Stockwell MSF values of 3.6 and 5.2Hz in moving from low to high frequencies (between 10.9 and 13.1 seconds) and 5.2 to 4.3Hz moving from high to low frequencies (between 25.2 and 27.5 seconds). These correspond to base Stockwell MSF values of 3.8 and 4.8Hz (although shortly after, this value increases) in moving from low to high frequencies and 5.2 to 3.2Hz in moving from high to low frequencies. It should be noted that, although the base motion was designed to sweep from 0.5 to 7 to 0.5Hz, outside of the 'dead zone', the frequencies ranged from 0.8 to 5.2Hz, and then 5.2

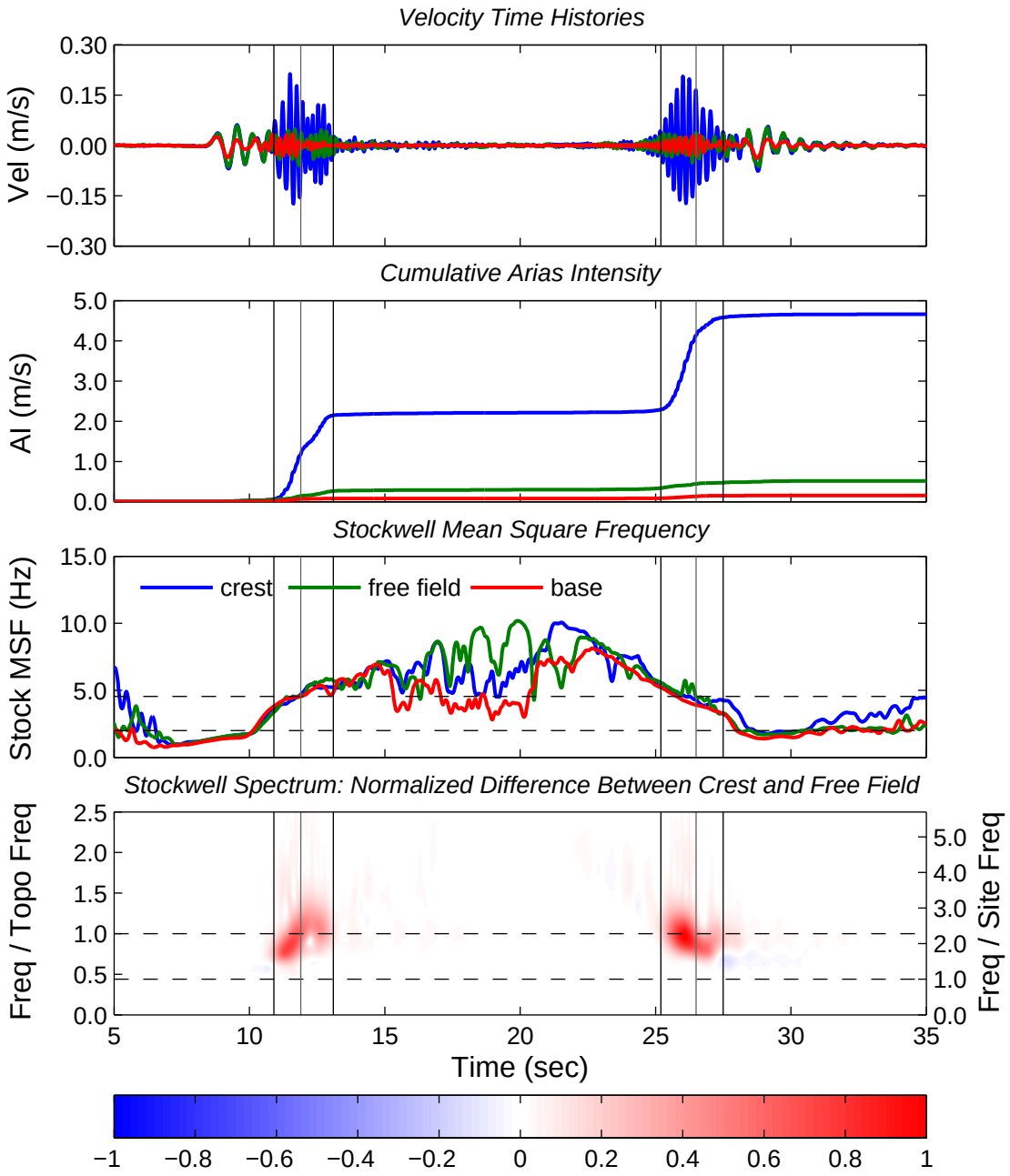

Figure 4.25: Velocity time history, cumulative Arias Intensity, and Stockwell MSF plots for the base, crest and free field; and the difference between the crest and free field Stockwell amplitude, normalized by the maximum difference, for the (c) frequency sweep of the 55g, 30 degree slope model. Vertical gray lines mark changes in the response at the crest while topographic amplification occurs (bounded by the vertical black lines).

to 1.4Hz. Based on the smoothness of the base Stockwell MSF, it appears the shaker did attempt to produce ground motion up to 7Hz while ramping up and starting around 8Hz ramping down.

The range of frequencies over which topographic amplification occurs is about 0.8 to 1.2 times the topographic freqeuncy, which is less than that for the (d) sweep (where it was 0.7 to 1.3). The (d) sweep had a larger number of cycles at each frequency, meaning more energy entered the system at any given frequency. This suggests that the duration of motion at relevant frequencies may affect the frequency range over which topographic effects occur. Additionally, the Stockwell MSF at the crest closely follows that of the forcing, or base, Stockwell MSF when moving from lower to higher frequencies, but then hovers around the topographic frequency when moving from higher to lower frequencies. This suggests that the ordering of the ground motion frequency components may influence topographic effects.

Focusing on the first part of the (c) sweep, after the ramping up portion of the motion (between 8 and 10 seconds), the base motion quickly moves past the site frequency and then increases in amplitude, building energy while approaching the topographic frequency. This is illustrated in the velocity time histories, but also in the normalized base Stockwell plot and base Husid plots in Figures 4.26 and 4.27. At about 11.9 seconds, near the topographic frequency, the base amplitude sharply drops. This is similar to the response observed in the (d) sweep. The base amplitude then increases again slightly before fading around 13 seconds.

Again for convenience, the four time frames highlighted in the figures in this section will be labeled time frames 1 through 4. The first, $tf1$ is from the first vertical black line to the first vertical gray line (from 10.9 to 11.9 seconds); $tf2$ is from the first vertical gray line to second vertical black line (11.9 to 13.1 seconds); $tf3$ is from the third vertical black line to the second vertical gray line (25.2 to 26.5 seconds); and $tf4$ is from the last (second) vertical gray line to the last (fourth) vertical black line (26.5 to 27.5 seconds).

Because the ground motion is rich with frequency content near the topographic frequency, energy at the crest builds quickly. The difference in cumulative AI between the crest and

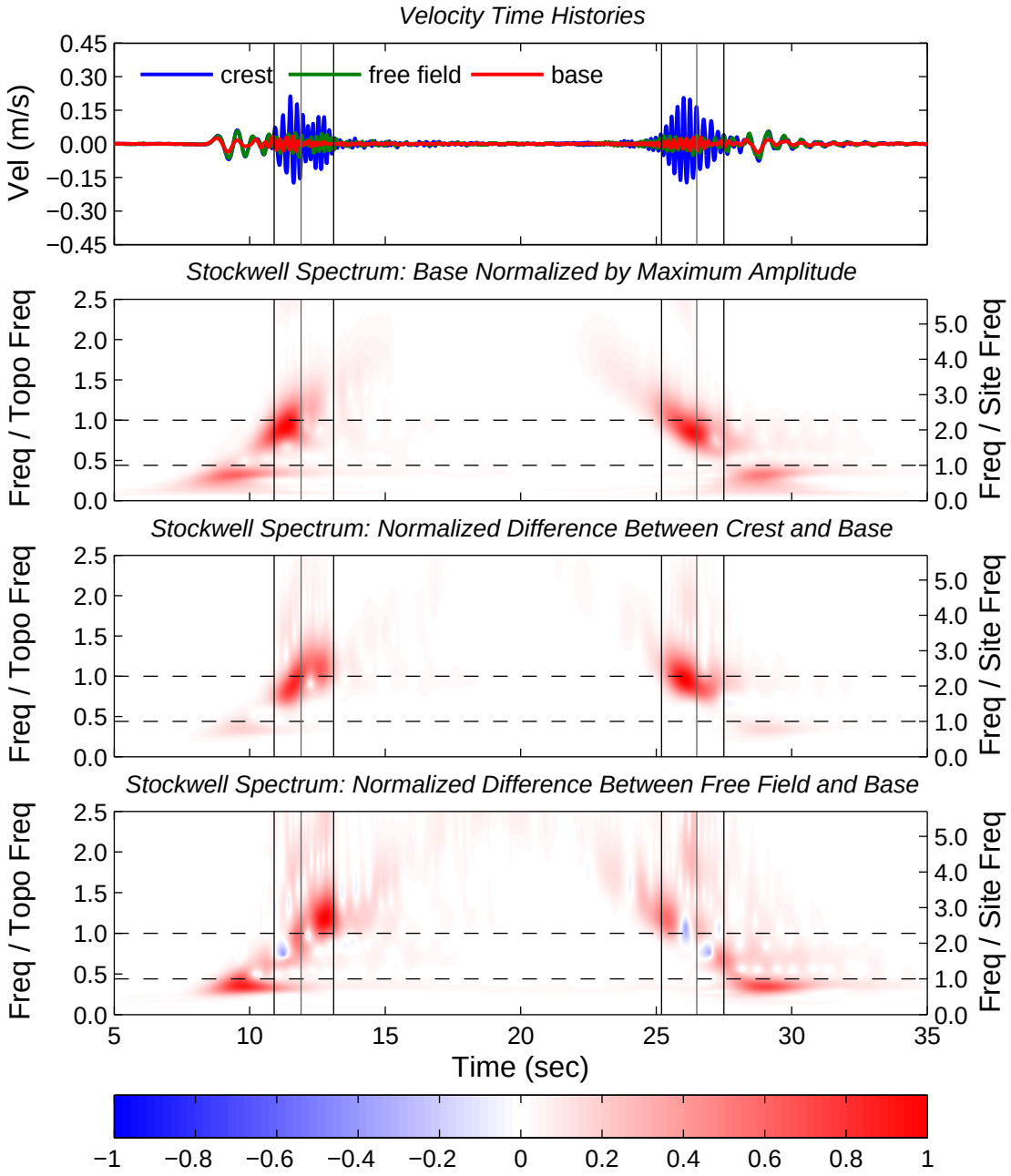

Figure 4.26: Velocity time histories, and normalized Stockwell plots of the base ground motion, the difference between the crest and base, and the difference between the free field and base, for the (c) frequency sweep of the 55g, 30 degree slope model. Vertical gray lines mark changes in the response at the crest while topographic amplification occurs (bounded by the vertical black lines).

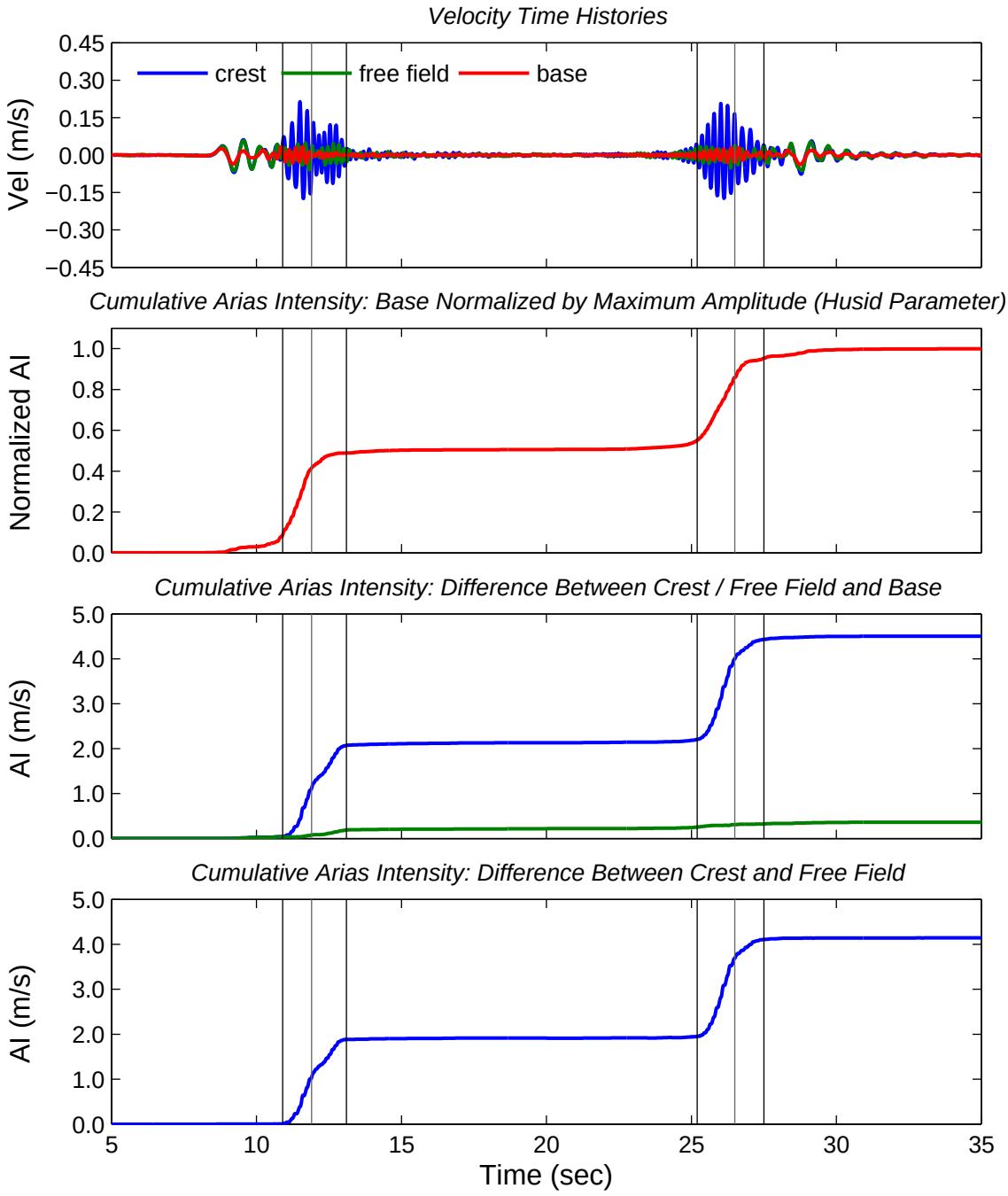

Figure 4.27: Velocity time histories, and cumulative Arias Intensity plots of the base ground normalized by the maximum, the crest and free field normalized by the base, and the crest normalized by the free field, for the (c) frequency sweep of the 55g, 30 degree slope model. Vertical gray lines mark changes in the response at the crest while topographic amplification occurs (bounded by the vertical black lines).

base increases from 0.05 to 1.15 (an increase of 1.1) in one second (during $tf1$). For most of this time period the ground at the base of the slope behaves in a linear elastic manner and energy is not impeded from propagating farther up slope. Towards the end of this time frame, softening occurs at the base of the slope, and the amplitude at the crest decreases (see Figure 4.28). The behavior at the base of the slope becomes linear elastic during $tf2$, and the amplitude at the crest increases again. However, because the base amplitude is lower, the overall amplitude and level of amplification are lower than $tf1$. The difference in cumulative AI increases from 1.15 to 2.08 (an increase of 0.93) in 1.2 seconds (an increase of 0.78 per second).

Phasing with the free field may also influence the reduction in amplitude during $tf2$. Inspection of Figure 4.29 shows that the difference in phase between the free field and crest increases moving from $tf1$ to $tf2$. The shift toward moving out of phase also coincides with an increase in amplification of the free field over the base as the second mode of resonance for the site is approached. As a result, amplification of the crest over the free field is also lower in $tf2$ than during $tf1$. The difference in cumulative AI between the crest and free field reduces from a rate of 1.05 to 0.69 per second.

When ramping up from low to high frequencies, amplification of the free field near the second mode of resonance for the site (3 times the site frequency, or 6Hz) is comparable to that at the first mode of resonance (see Figure 4.26). When ramping down from high to low frequencies, amplification of the free field for these two modes is also comparable (although greater at the site frequency, near the first mode), but is generally lower than observed while ramping up. At the site frequency (first mode), this is likely a result of reduced input (base) amplitude. Near the second mode, however, this is likely caused by a reduction in the duration of motion near that frequency. This is evidenced by the Stockwell MSF in Figure 4.25. While ramping up, the Stockwell MSF of the base motion begins to level out, staying near a frequency of 6Hz. While ramping down, however, the Stockwell MSF decreases at a constant rate.

During $tf3$, (while ramping down) the base amplitude steadily increases. Amplitude at

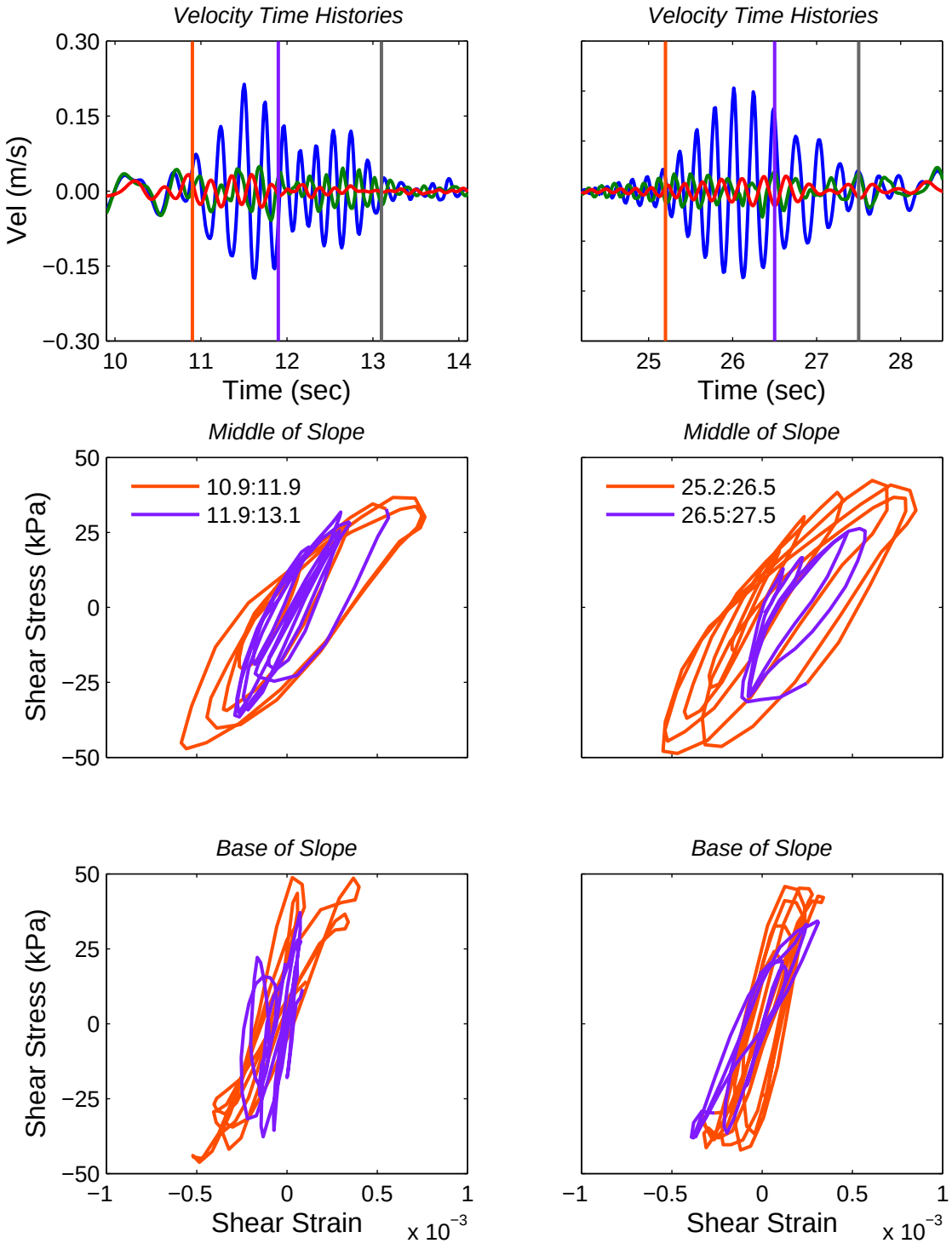

Figure 4.28: Velocity time histories, and stress-strain plots at the mid-slope and base of slope elevations below the crest, for the (c) frequency sweep of the 55g, 30 degree slope model. Colored vertical lines in the velocity time histories match the colors used in the stress-strain plots, marking the beginning of the time frame for that color.

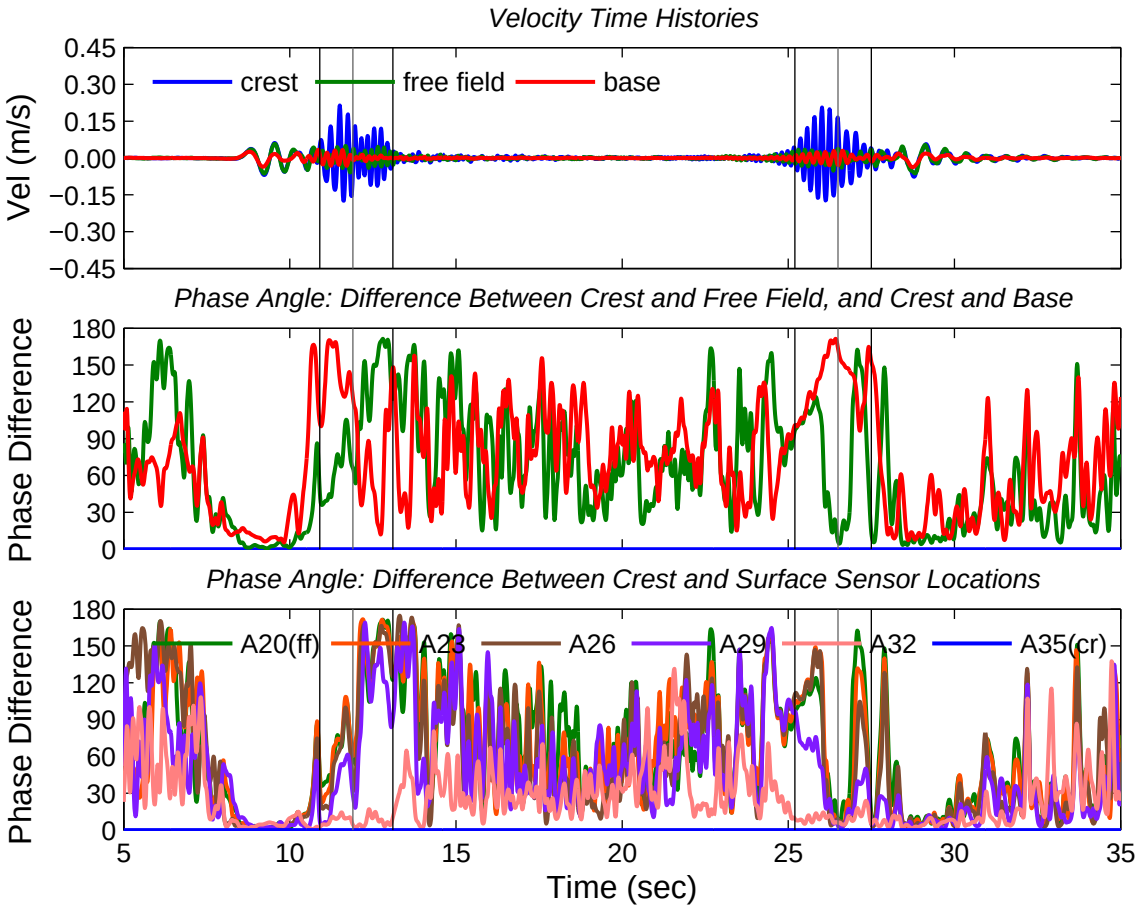

Figure 4.29: Velocity time histories, and plots of the difference in phase angle between the base, free field, other surface locations and the crest, for the (c) frequency sweep of the 55g, 30 degree slope model. In the bottom plot, legend designations represent near surface sensor locations ranging from the free field (A20) to the crest (A35). Vertical gray lines mark changes in the response at the crest while topographic amplification occurs (bounded by the vertical black lines).

the crest also steadily increases, peaking at the topographic frequency, and the maximum amplification for the ground motion is reached (see Figure 4.26). The difference between the crest and base cumulative AI is 1.79 over 1.3 seconds (an increase of 1.38 per second) and the difference between the crest and free field is 1.74 (an increase of 1.34 per second) during $tf3$ (see Figure 4.27). Note that the similarity in these two numbers indicates there is little amplification of the free field over the base during this time frame (an increase of 0.05 occurs).

As the amplitude at the crest increases, softening at the base of the slope increases, as does softening and damping of energy at the mid-slope location. The amplitude (and amplification) at the crest decrease entering $tf4$ as a result, even though the base amplitude continues to increase. The base amplitude then drops before increasing again slightly at the end of $tf4$.

This behavior leads to lower overall amplification at the crest compared to $tf3$ (the difference in cumulative AI between the crest and base increases by 0.42 per second). Softening at the base and mid-slope locations also subside as a result (see Figure 4.28). Because of the reduction in damping during $tf4$, however, it is likely that energy built up at the topographic frequency takes longer to damp out, even though the input amplitude drops. This is evidenced by the Stockwell MSF at the crest, which remains near the topographic frequency as the forcing frequency drops through $tf4$ (see Figure 4.25).

Again, with the influence of other contributing factors, it is unclear the extent to which phasing between the crest and free field influence of the overall response. However, during the ramping down phase, time periods of greater amplitude at the crest can again be tied to differences in phasing (see Figure 4.29). Through $tf3$, the crest and free field move from out of phase to in phase as the amplitude (and amplification) at the crest peak. Through $tf4$ the crest and free field move back out of phase after the drop in base amplitude and the amplitude at the crest decreases. Perhaps the most independent check on the influence of phasing occurs near and past the end of $tf4$. The crest and free field temporarily move back in phase (before moving out of phase again) and the result is an increase in amplitude at the

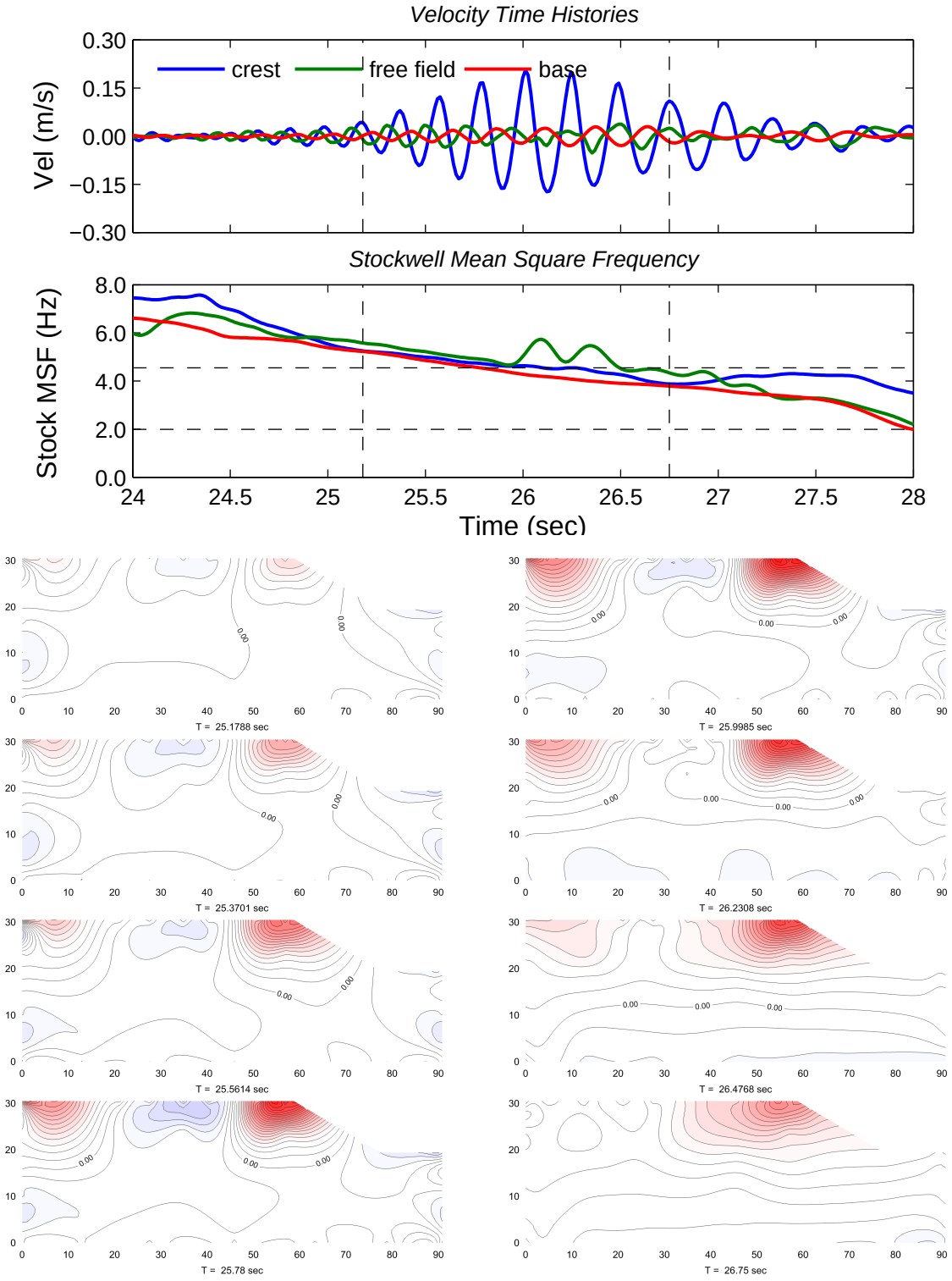

Figure 4.30: Time series of velocity contours for the (c) frequency sweep of the 55g, 30 degree slope model. The time series spans the vertical dashed lines shown in the velocity time history (top plot) and Stockwell MSF (second plot) plots.

crest (and free field) compared to the moments just before and after.

From the figures in this section, it is clear that topographic amplification occurs above and below the topographic frequency. Based on Figures 4.23 and 4.24 for the (d) sweep, it appeared that the size of the amplified area is proportional to the wavelength of the ground motion. This is reinforced by phasing differences highlighted in Figure 4.29, where the separation of behavior between the free field landmass and the slope varies with frequency. At lower frequencies, the separation occurs somewhere between sensors A26 and A29, whereas at higher frequencies the separation occurs between A29 and A32. This pattern is the same as that observed for the (d) sweep.

This pattern is also confirmed for the (c) sweep in Figure 4.30. The snapshots presented are for the ramping down portion of the ground motion between 25.2 and 26.7 seconds; moving between Stockwell MSF frequencies of 5.5 and 4.0Hz. For higher frequencies, the concentration of amplitude is close to the slope crest. As the wavelength of motion increases (the frequency decreases), it is observed that the are subjected to topographic amplification increases. This pattern holds despite larger differences in amplitude than was presented for the (d) sweep; and despite moving from high to low, instead of low to high frequencies.

4.2.3 Ricker Wavelets

One final idealized motion used in this study to provide insight into the causes of topographic effects is Ricker wavelets. As with sine wave motion, the intention was to introduce Ricker wavelets at four central frequencies: 1, 2, 4 and 6Hz. In this case, the aim was to observe propagation of and the subsequent surface response for a single pulse in each direction (towards and away from the slope face) at each of these frequencies. The shaker had difficulty producing Ricker wavelets at higher central frequencies, and thus no wavelets with a central frequency close to the topographic frequency were produced. Therefore, a pulse for which topographic effects would be maximized cannot be presented. The closest pair of wavelets (one in each direction) that was produced had a central frequency near the site frequency. This pair of wavelets for the (l) motion, deemed (l3) is presented in this section.

Energy is mainly concentrated near the site frequency for the (l3) Ricker wavelets. However, some higher frequency components were introduced, particularly near the beginning of each pulse. This is illustrated by the Stockwell MSF plot in Figure 4.31 and the normalized Stockwell plot for the base motion in Figure 4.32. During the initial portion of each pulse, the base MSF reaches a value around 3.6Hz before decreasing to about 2Hz (the site frequency) for the remainder of the motion. The Stockwell plot shows that at the beginning of the motion, the higher frequency component of motion is similar in intensity to the underlying low frequency motion. However, the high frequency component dissipates as the motion continues.

Note that for this motion, acceleration time histories (and acceleration based parameters) are presented, rather than velocity. Because the motion is relatively simple, and mainly consists of low frequency motion, the ground response is not obscured by higher frequency components. Instead, by preserving the high frequency components of motion, differences in the behavior at the crest and free field are better illustrated.

At the crest, components of motion near the site frequency and topographic frequencies are amplified. The level of amplification matches the intensity of the base motion, in that it is similar at each frequency. Amplification is greater for the second wavelet than the first. This again matches the base motion, for which the amplitude of the second wavelet is also greater than the first (see Figure 4.32). This behavior indicates that excitation can occur at both the site and topographic frequencies simultaneously, leading to an increase in overall amplitude. This is particularly notable for the second wavelet, where the cumulative AI plots of the crest and free field deviate.

The higher frequency components of motion are not amplified in the free field. Because the amplitude of the high frequency components at the crest is greater for the second wavelet, this leads to greater levels of topographic amplification for that wavelet (see bottom plot of Figure 4.31). Hence the larger deviation in the cumulative AI between the crest and free field for this wavelet. In the free field, amplification mainly occurs for the components of motion near the site frequency. The free field amplitude at the site frequency is similar to

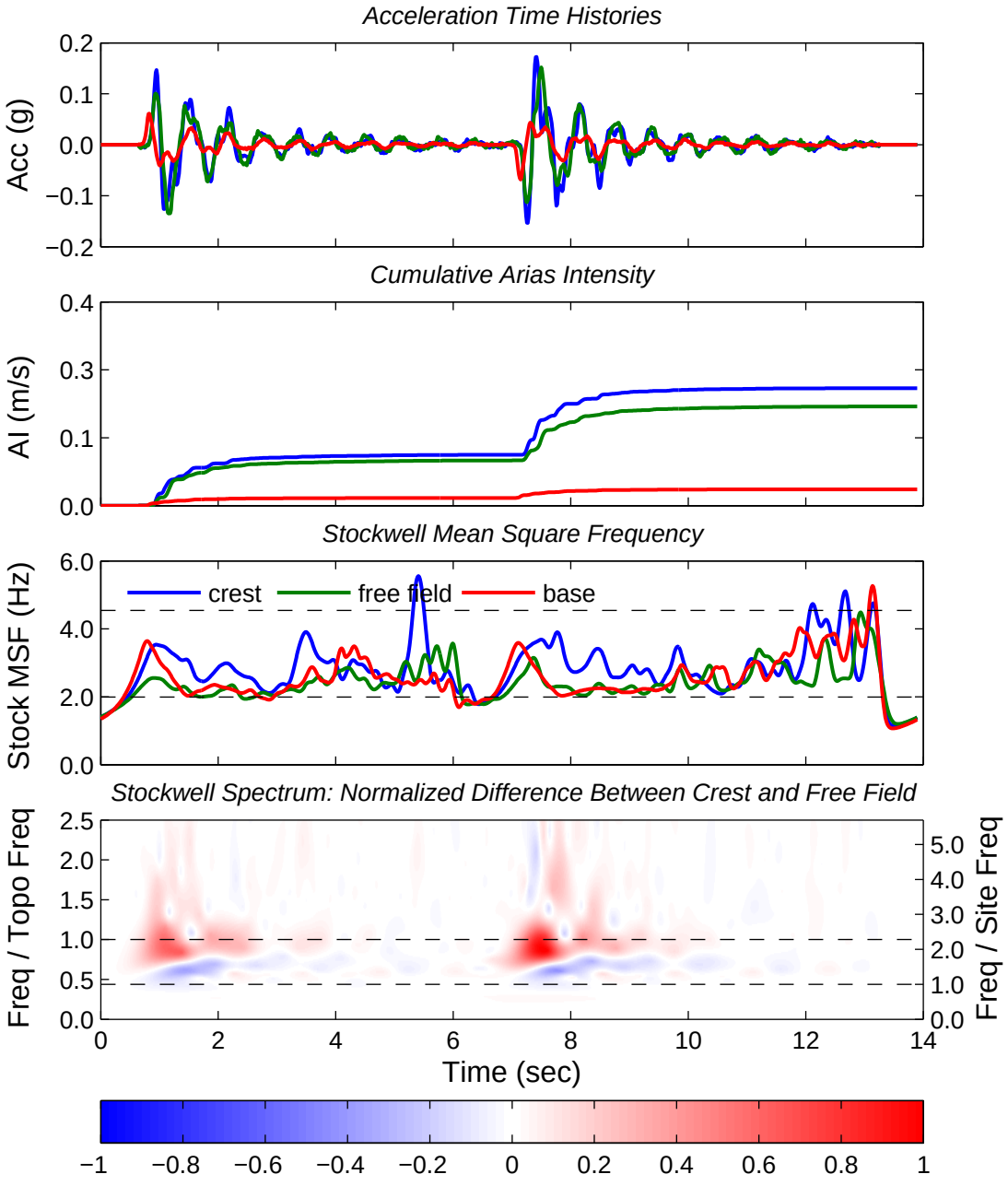

Figure 4.31: Acceleration time history, cumulative Arias Intensity, and Stockwell MSF plots for the base, crest and free field; and the difference between the crest and free field Stockwell amplitude, normalized by the maximum difference, for the (l3) Ricker wavelets of the 55g, 30 degree slope model.

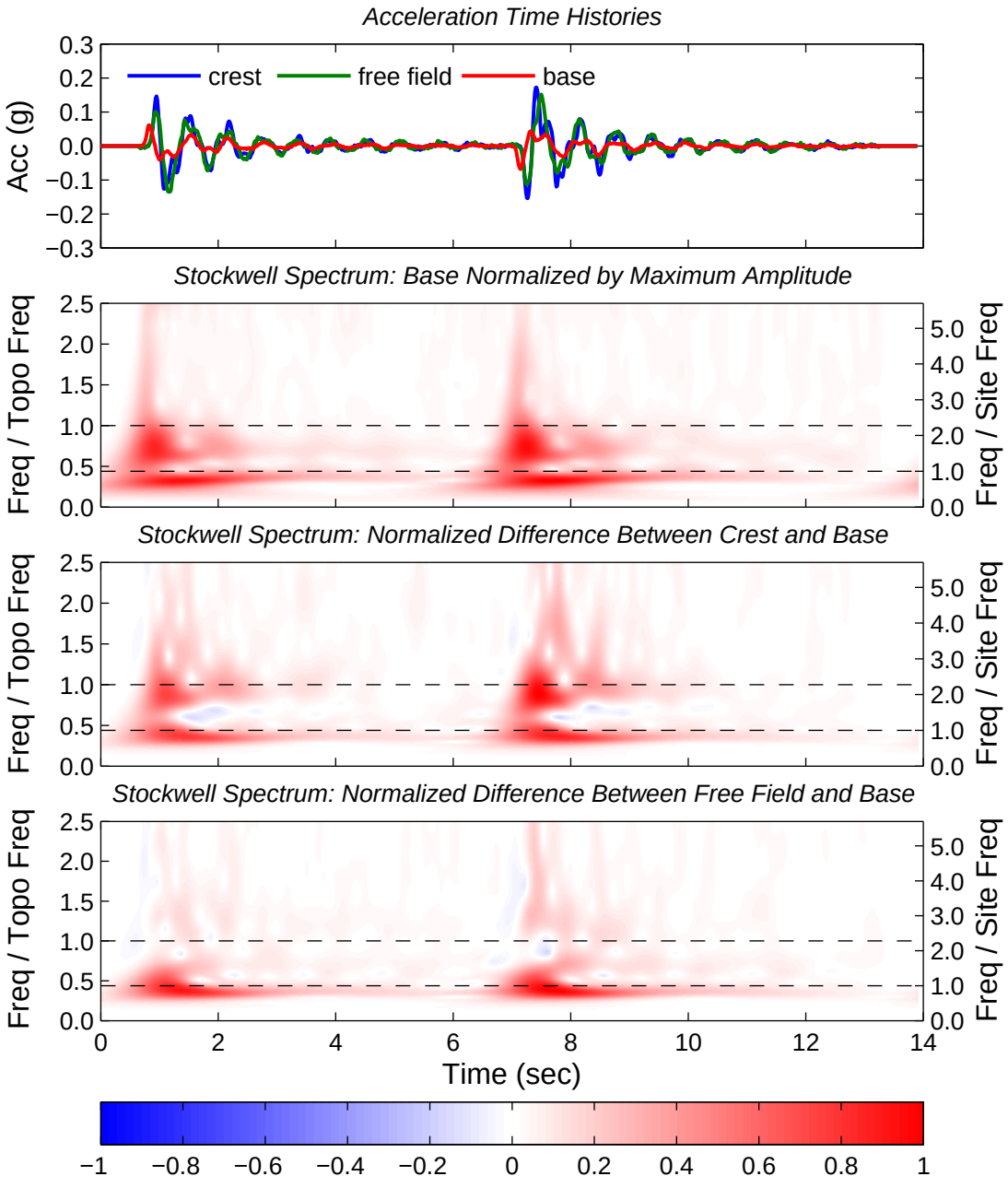

Figure 4.32: Acceleration time histories, and normalized Stockwell plots of the base ground motion, the difference between the crest and base, and the difference between the free field and base, for the (l3) Ricker wavelets of the 55g, 30 degree slope model.

that at the crest.

One final observation that will be discussed is shifts in ground motion frequency content. The base motion introduces energy *below* both the site and topographic frequencies. However, at the crest, amplification is greatest *at* the site and topographic frequencies. And in the free field amplification is greatest *at* the site frequency, as illustrated in Figure 4.32. This is also highlighted in Figure 4.31 where the Stockwell MSF at the crest remains high after the base motion has returned to the site frequency and the Stockwell MSF in the free field gravitates toward the site frequency when the base motion introduces the higher frequency components of motion. The tendency towards excitation at the topographic and site frequencies, therefore, leads to shifts in the ground motion frequency content (i.e., ground motion intensifies at these frequencies). Because this shift does not occur for the higher frequency components in the free field, ground motion at frequencies between the site and topographic frequency appear deamplified at the crest compared to the free field (see Figure 4.31).

4.3 Earthquake Motions

The idealized motions presented in the previous section were useful for understanding the basic mechanisms and causes of topographic effects and topographic amplification. The mechanisms could typically be isolated for specific frequencies at specific instances in time. The understanding gained from the idealized motions is applied to more complicated, transient earthquake motions in this section. Four earthquake motions are considered, including (g) Superstition Hills, (w) Joshua Tree, (h) Chi Chi, and (za) Chi Chi with the time step cut in half.

4.3.1 Chi Chi

Chi Chi (h)

Figure 4.33 presents velocity time histories, cumulative AI, and the Stockwell MSF for the (h) Chi Chi earthquake motion. The normalized difference in the Stockwell spectrum of the crest and free field is also provided. The patterns highlighted in these plots are similar to those identified for the idealized motions in the previous section:

- Topographic amplification occurs at frequencies between 0.7 and 1.3 times the topographic frequency;
- The spectral amplitude at the site frequency is nearly equivalent at the crest and free field;
- Frequencies between the site and topographic frequencies are deamplified at the crest compared to the free field; and
- The Stockwell MSF gravitates towards the topographic frequency at the crest and towards the site frequency in the free field.

The level of amplification and deamplification at various frequency components varies throughout the motion, with topographic amplification mainly concentrated in the first half

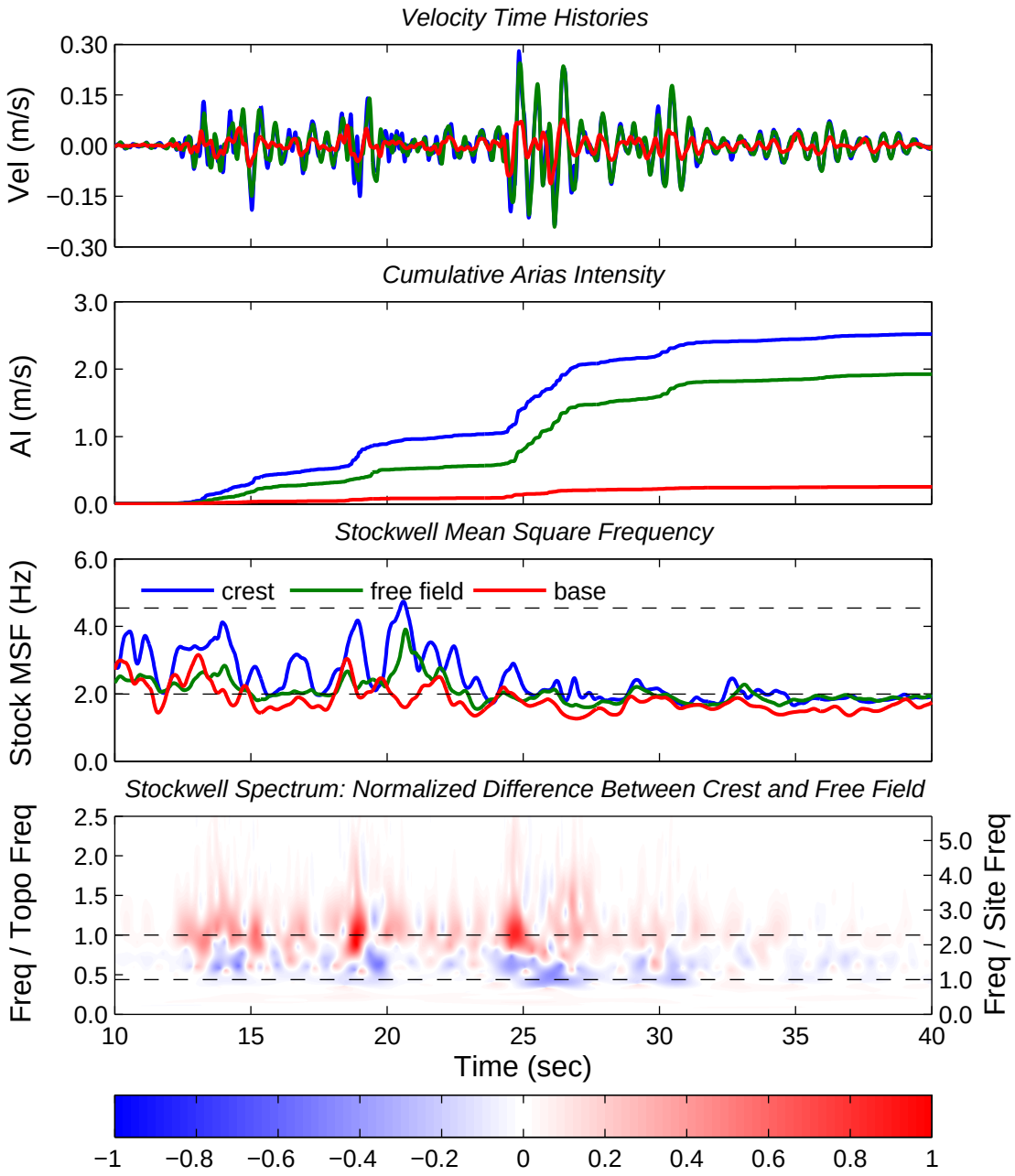

Figure 4.33: Velocity time history, cumulative Arias Intensity, and Stockwell MSF plots for the base, crest and free field; and the difference between the crest and free field Stockwell amplitude, normalized by the maximum difference, for the (h) Chi Chi earthquake of the 55g, 30 degree slope model.

of the motion. The ground response is complicated by the introduction of multiple frequency components at any given instance in time (which was not typically true of the idealized motions). To better understand this more complex behavior, the ground motion is divided into four time frames for discussion.

Velocity time histories at the crest, base and free field are provided for the four reference time frames in Figure 4.34. The first time frame, $tf1$, is from 12.5 to 16.5 seconds (top plot); $tf2$ is from 18 to 21 seconds (second plot); $tf3$ is from 23.5 to 28.5 seconds (third plot); and $tf4$ is from 29 to 33 seconds (fourth plot).

Towards the beginning of $tf1$, the base (input) motion is rich in frequencies near the topographic frequency. This is evidenced by the higher Stockwell MSF (see Figure 4.33) and by the normalized Stockwell plot of the base in Figure 4.35. This results in excitation and amplification of these frequencies at the crest (see the second plot in Figure 4.35). And, as was seen for other ground motions, this amplification is generally proportional to the base amplitude at these frequencies. The frequencies near the topographic frequency are generally not amplified in the free field.

Amplification of the base motion is also proportional to the base amplitude for ground motion near the site frequency. Site amplification occurs towards the beginning and end of $tf1$, with greater amplification towards the end. As previously seen, the level of amplification at the site frequency is similar at the crest and free field.

Closer inspection of Figures 4.33 and 4.35 reveals that competition between frequencies can control the ground response. For $tf1$, the level of topographic amplification for the crest over the free field is slightly greater towards the end of the time frame, when site amplification is also greater. This is true despite the input amplitude and level of amplification being similar (if not less) at the topographic frequency at this time than earlier in $tf1$. Because the free field has a tendency towards resonance at the site frequency, ground motion at that frequency dominates the response towards the end of $tf1$, reducing the influence of motion near the topographic frequency. Indeed, inspection of the bottom plot in Figure 4.35 reveals that the spectral amplitude at the topographic frequency is slightly deamplified at this time

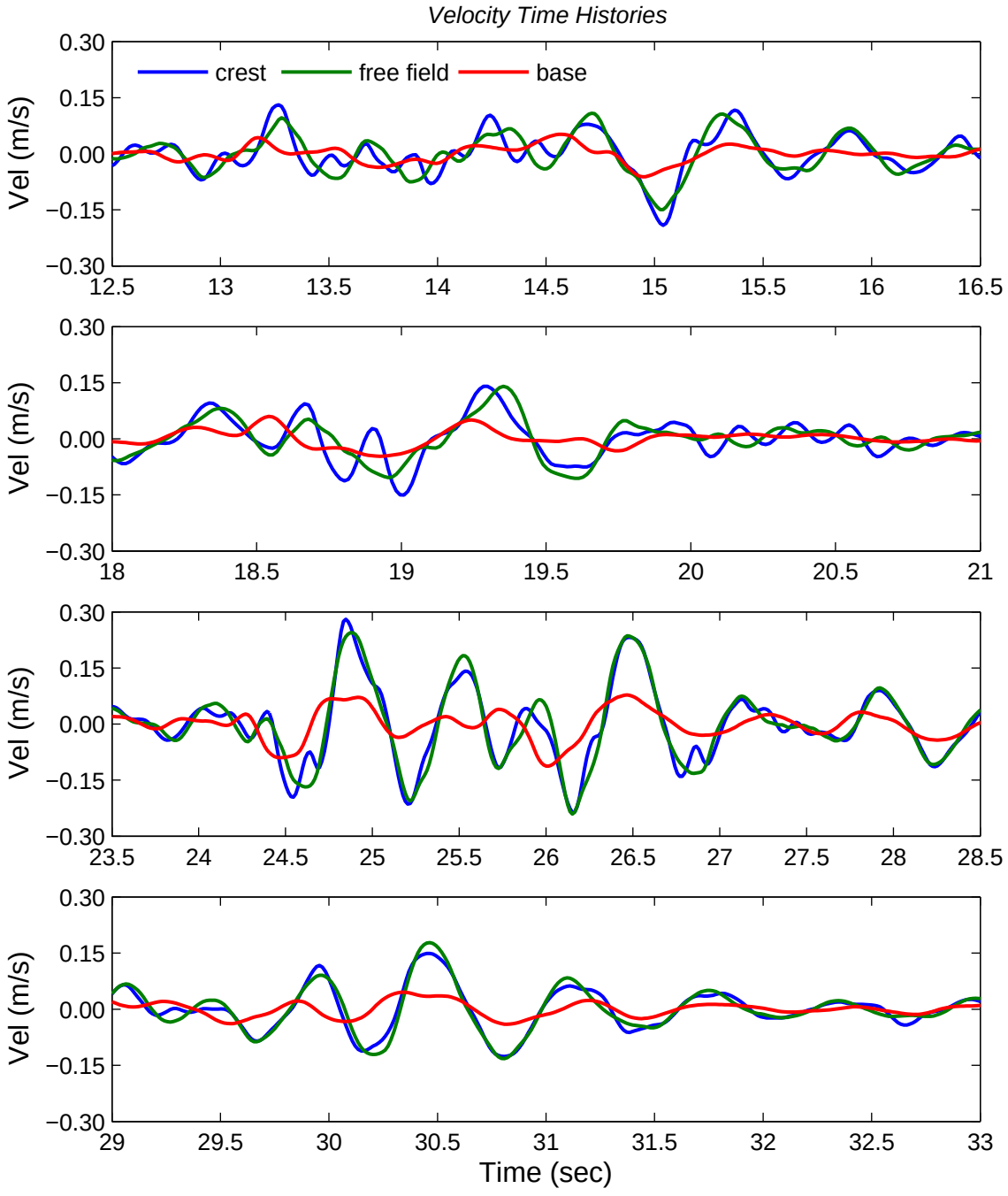

Figure 4.34: Velocity time histories for four times frames for the base, crest and free field for the (h) Chi Chi earthquake of the 55g, 30 degree slope model.

and slightly amplified earlier in $tf2$ (when site amplification is lower).

At the crest, excitation occurs at both the site and topographic frequencies. This controls the response and inhibits amplification at frequencies in between the site and topographic frequencies. Because frequencies near the topographic frequency are typically not amplified, these frequencies (between the site and topographic frequencies) *are* amplified in the free field. This results in the perceived deamplification at these frequencies when comparing the crest to the free field response.

One of the stronger components of motion of the incident wave for $tf1$ is at about half the site frequency (1Hz). However, amplification of this component is small compared to that at the site frequency for the crest and free field and topographic frequency at the crest. This behavior is the same as that observed for the (q) sine wave motion in Section 4.2.

Topographic amplification occurs throughout $tf1$, but is mainly concentrated between 12.5 and 15.2 seconds. This is evidenced by the normalized Stockwell plots (bottom plot of Figure 4.33, third plot in Figure 4.35), and is also illustrated by the contrast in the slope of the bottom plot of Figure 4.36. The difference in cumulative AI between the crest and free field increases by 0.18 between 12.5 and 15.2 seconds (a rate of 0.06 per second), but then only increases 0.04 between 15.2 and 18.6 seconds (a rate of 0.01 per second).

Even between 12.5 and 15.2 seconds, the increase in energy at the crest over the free field is gradual, and fluctuates. This reflects the gradual build-up of energy of the input (base) motion and the fluctuation in energy introduced near the topographic frequency. As a result, topographic effects are manifested as a series of smaller amplitude pulses, as shown in the top plot of Figure 4.34.

During $tf2$, a quicker increase in energy occurs between 18.6 and 19.4 seconds. The base motion is mainly comprised of frequencies near the topographic frequency and around 1Hz (see second plot of Figure 4.35). With little competition at the site frequency, this results in the greatest level of topographic amplification for the (h) Chi Chi motion (see bottom plot of Figures 4.33 and 4.35). The difference in cumulative AI between the crest and base increases by 0.26 (a rate of 0.33 per second), while the difference between the free field and

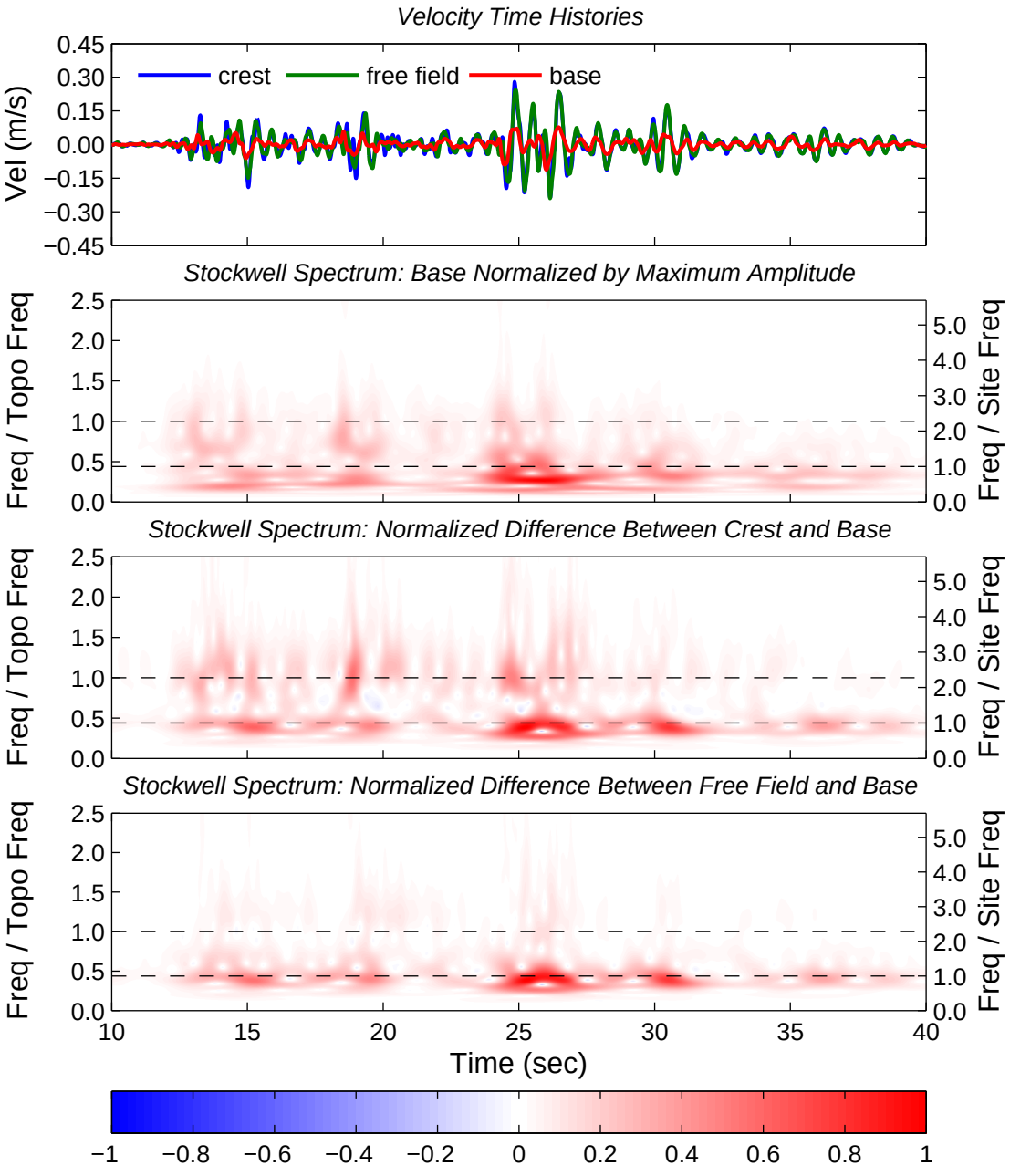

Figure 4.35: Velocity time histories, and normalized Stockwell plots of the base ground motion, the difference between the crest and base, and the difference between the free field and base, for the (h) Chi Chi earthquake of the 55g, 30 degree slope model.

crest only increases by 0.05 (a rate of 0.06 per second). The difference between the crest and free field increases at a rate of 0.28 per second.

Topographic amplification manifests as larger pulses at the crest between 18.6 and 19.4 seconds for the velocity time histories in Figure 4.34 (second plot). The underlying motion at 1Hz during this time interval results in a trending movement away from the slope face (negative values) and leads to a greater overall amplitude. This means that topographic amplification compounded with energy at other frequencies can lead to increases in the overall ground motion amplitude.

Beyond 19.4 seconds, energy at the topographic frequency dissipates and energy at the site frequency increases. The ground motion of the crest begins to match that of the free field, although is slightly lower in amplitude. Energy at the topographic frequency then increases again, but at a lower amplitude, with levels of topographic amplification similar to that of $tf1$.

The greatest overall amplitude for the entire ground motion occurs during $tf3$. This coincides with another sharp, although smaller, increase in topographic amplification between 24.3 and 25.3 seconds. The difference in cumulative AI between the crest and free field (see Figure 4.36) increases by 0.19 over this one second interval (compared to 0.33 per second in $tf2$).

The ground response during $tf3$, however, is mainly dominated by site amplification. The difference in cumulative AI between the free field and base is 0.25, while the difference between the crest and base is 0.44 between 24.3 and 25.3 seconds. This means that even when topographic amplification is strongest, more than half the ground motion energy can be attributed to the typical free field response. Between 25.3 and 26.8 seconds, the response is mainly controlled by site effects. The free field cumulative AI increases by 0.48 (an increase of 0.32 per second), while the difference between the crest and base increases by 0.41 (an increase of 0.27 per second). This behavior is reflected in Figure 4.33. The Stockwell MSF at the crest is close to half way between the site and topographic frequency (but closer to the site frequency) between 24.3 and 25.3 seconds, but then is near the site frequency afterwards.

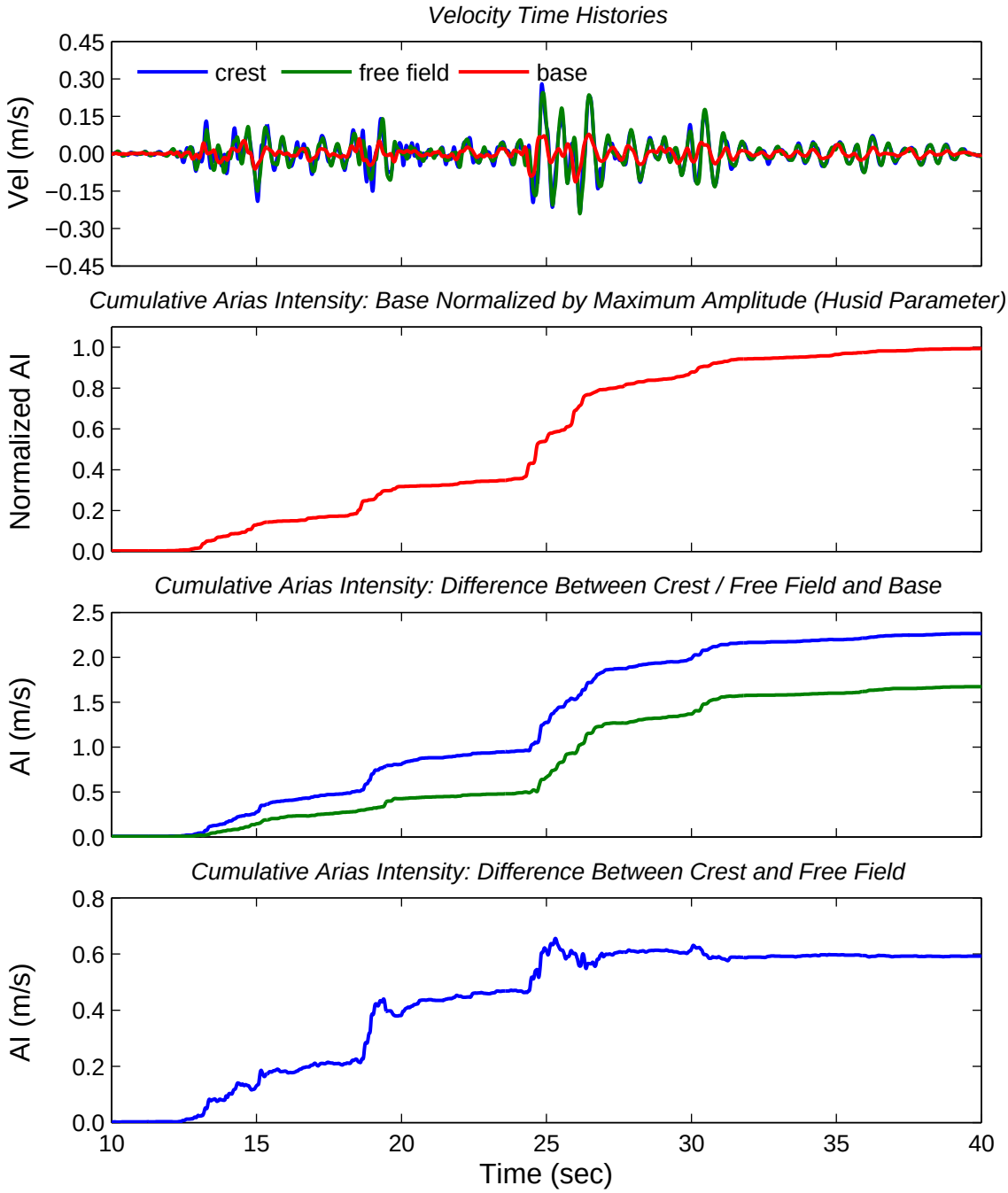

Figure 4.36: Velocity time histories, and cumulative Arias Intensity plots of the base ground normalized by the maximum, the crest and free field normalized by the base, and the crest normalized by the free field, for the (h) Chi Chi earthquake of the 55g, 30 degree slope model.

The amplification patterns for $tf3$ are also illustrated by the normalized Stockwell spectra in Figure 4.35. From the third plot, it can be seen that some components of motion near the topographic frequency are amplified after 25.3 seconds. However, inspection of the velocity time histories in Figure 4.34 reveals that the overall amplitude at the crest can be lower (particularly between 25.5 and 26 seconds) than that of the free field.

The behavior described above suggests that competing motion at the site and topographic frequencies can inhibit overall ground motion at the crest. There are also cases, such as earlier in $tf3$, or during $tf2$ and $tf1$, however, where the combined contribution at these (and other) frequencies leads to an increase in overall amplitude. This increase or decrease in overall amplitude can typically be tied to the relative amplitude at these frequencies and phasing between the crest and free field at a given instance in time.

During $tf2$, topographic amplification peaks for the ground motion between 18.6 and 19.4 seconds. While this amplification occurs, the crest moves in and out of phase with the free field due to differences in frequency content. This is illustrated by the second time history plot in Figure 4.34 and the phase difference plot in Figure 4.37. A reduction in ground motion can occur when the areas move out of phase. However, because the amplitude of ground motion at the topographic frequency is greater than that at other frequencies, the impact of this reduction is minimal. That is, the pulses at the topographic frequency remain similar in amplitude while moving in and out of phase. When the areas are in phase, the contributions at the different frequencies compound, and the overall amplitude of at the crest is greater.

During $tf3$, topographic amplification is strongest between 24.3 and 25.3 seconds, but is generally weaker than site amplification. The crest increases in velocity in the negative (moving away from the slope towards the free field) direction faster than the free field, and locally peaks at greater velocity than that of the free field. The velocity at the crest then reduces as the free field reaches a local maximum velocity. The crest, still excited at the topographic frequency, then attempts to increase in velocity back towards the free field, but is slowed by the free field landmass. Now in phase, the free field and crest increase in velocity

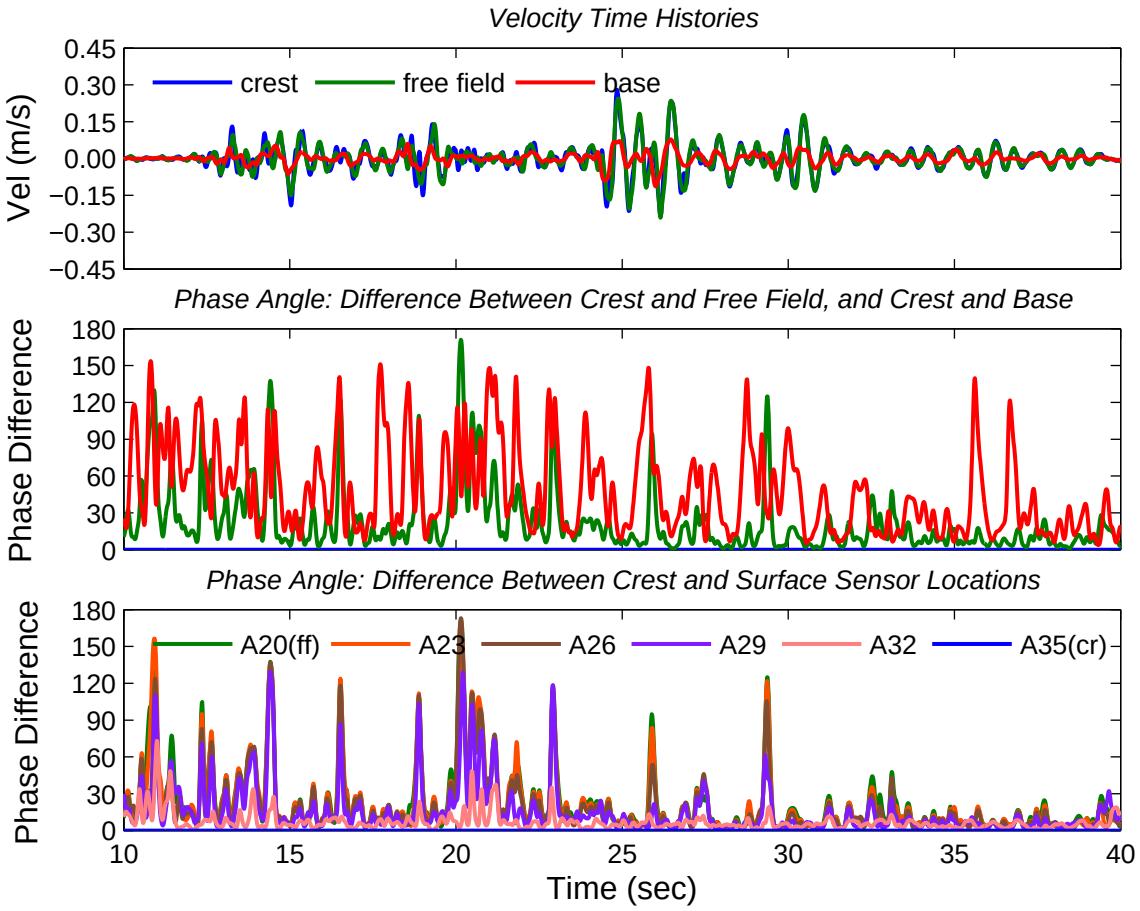

Figure 4.37: Velocity time histories, and plots of the difference in phase angle between the base, free field, other surface locations and the crest, for the (h) Chi Chi earthquake of the 55g, 30 degree slope model. In the bottom plot, legend designations represent near surface sensor locations ranging from the free field (A20) to the crest (A35).

towards the slope face, with the crest reaching a greater maximum velocity than the free field due to the combined energy from the site and topographic frequencies.

Excitation at the topographic frequency is dampened by the excitation at the site frequency when the crest and free field move out of phase and site amplification is greater than topographic amplification. And as a result, the level of topographic amplification decreases. This is evidenced by the bottom plot in Figure 4.36. The difference in cumulative AI between the crest and free field increases less quickly or even reduces when the crest and free field move out of phase (such as around 24.6 seconds).

This effect is more pronounced between 25.3 and 26.5 seconds, where the amplitude at the topographic frequency decreases further. The crest and free field again move out of phase, as the crest reaches a local maximum velocity around 25.9 seconds, moving towards the slope. The crest slows as the free field increases in velocity in the opposite direction reaching a local maximum velocity around 26.0 seconds. The opposing motion from the free field dampens excitation at the topographic frequency. This essentially causes movement at the crest to stall (reaching zero velocity) until the underlying motion at the site frequency again dictates movement. This behavior results in a lower overall amplitude at the crest.

It should be noted that while differential movement between the free field and crest landmasses does affect overall ground motion amplitude, the response at the crest is mainly dictated by the frequency content and amplitude of the incident wave. For example, a tendency towards excitation at both the site and topographic frequencies would still occur within the slope landmass regardless of the existence of the free field. Likewise, motion at both these frequencies (and/or other frequencies) would still occur simultaneously, and therefore some of the behavior described above would also occur regardless of phasing.

For the final time frame, $tf4$, the ground response is mainly controlled by site amplification. The base motion is mainly composed of frequency content near the site frequency and the level of site amplification is similar at the crest and free field (see Figure 4.35 and Figure 4.36). The velocity time histories also closely match (see Figure 4.34). Thus, without energy near the topographic frequency, typical site response is observed at the crest.

Chi Chi (za)

The Chi Chi motion discussed above was introduced to the 55g model, which is consistent with the rest of the ground motions introduced in this chapter. The Chi Chi motion presented below is the same motion with the time step cut in half, introduced to the 27.5g model. The prototype for the 27.5g model is half the size of the prototype for the 55g model, meaning that parameters of interest are different from that of the 55g prototype. Those parameters are as follows:

- Slope height (H) is 5.5 meters (m), (11m at 55g);
- Maximum soil thickness (Z) is 15.7m, (31.4m at 55g);
- Shear wave velocity (V_s) is 200 meters per second (m/s), (250 m/s at 55g);
- Site frequency is 3.2Hz (2.0Hz at 55g); and
- Topographic frequency is 7.3Hz (4.5Hz at 55g).

Topographic effects were clearly present for the Chi Chi motion at 55g. However, the majority of the motion consisted of low frequency components (the base ground motion MSF is 2.5Hz) and site amplification was typically greater than topographic amplification. By cutting the time step in half, the ground motion frequencies increased (the base ground motion MSF is 6.4Hz), resulting in an increase in the magnitude of topographic effects. Some of these effects are illustrated in Figure 4.38 for the Chi Chi motion at 27.5g.

Inspection of the Stockwell MSF plot (third plot) reveals that the base motion is richer in frequencies that are closer to the topographic frequency than that of the (h) Chi Chi motion. These higher frequency components again tend to be amplified at the crest, and the Stockwell MSF gravitates towards the topographic frequency. In the free field, the Stockwell MSF gravitates towards the site frequency as these components of motion are the most amplified.

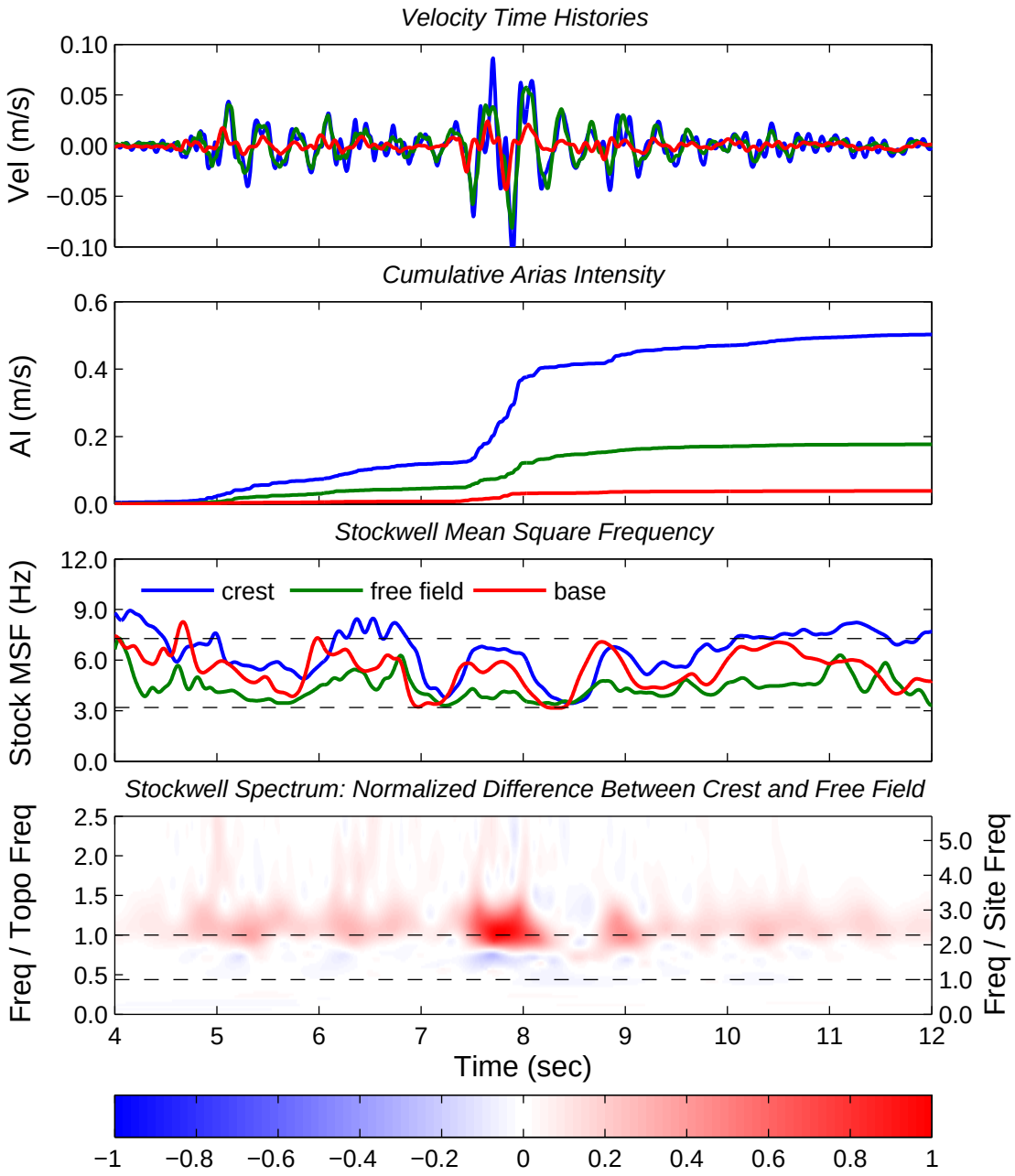

Figure 4.38: Velocity time history, cumulative Arias Intensity, and Stockwell MSF plots for the base, crest and free field; and the difference between the crest and free field Stockwell amplitude, normalized by the maximum difference, for the (za) Chi Chi earthquake of the 27.5g, 30 degree slope model.

Differences in amplitude between the crest and free field are illustrated by the cumulative AI plot (second plot) and normalized Stockwell plot (fourth plot). Components of ground motion near the topographic frequency are amplified at the crest. Frequencies between the site and topographic frequency are deamplified and the amplitude at the site frequency is nearly identical. This is consistent with behavior observed for other ground motions.

The greatest level of topographic amplification occurs between about 7.5 and 8.0 seconds. This coincides with the strongest portion of the motion (i.e., that at which the amplitude is greatest), which was dominated by site amplification for the (h) Chi Chi motion. Inspection of Figure 4.39 reveals that amplification (for the crest over the base) is greater near the topographic frequency than it is at the site frequency during this time frame. This is true despite the input (base) motion having a higher spectral amplitude near the site frequency (see second plot of 4.39).

Closer examination of the second plot of Figure 4.39, however, reveals that the base motion also has frequency components in between the site and topographic frequency. These frequencies are slightly amplified in the free field, but don't appear to be amplified at the crest. Thus, it is likely that the energy at these frequencies contributes to the stronger levels of amplification near the topographic frequency. That is, the frequency content shifts towards the topographic frequency as a result of the strong excitation at that frequency. This is supported by the Stockwell MSF plot in Figure 4.38 and is consistent with the behavior observed for the Ricker wavelets in Section 4.2.

The behavior described above indicates that topographic amplification can be greater than site amplification for a transient ground motion, depending on the frequency content and amplitudes at those frequencies. The combined effects of site and topographic amplification can lead to greater levels of overall amplification and ground motion amplitude. This is evidenced and quantified by the cumulative AI plots in Figure 4.40. The contribution of site amplification is captured by the difference between the free field and base, which is about 0.05 between 7.5 and 8.0 seconds (an increase of 0.10 per second). The difference between the crest and base is 0.22 over this time frame (an increase of 0.44 per second), again showing

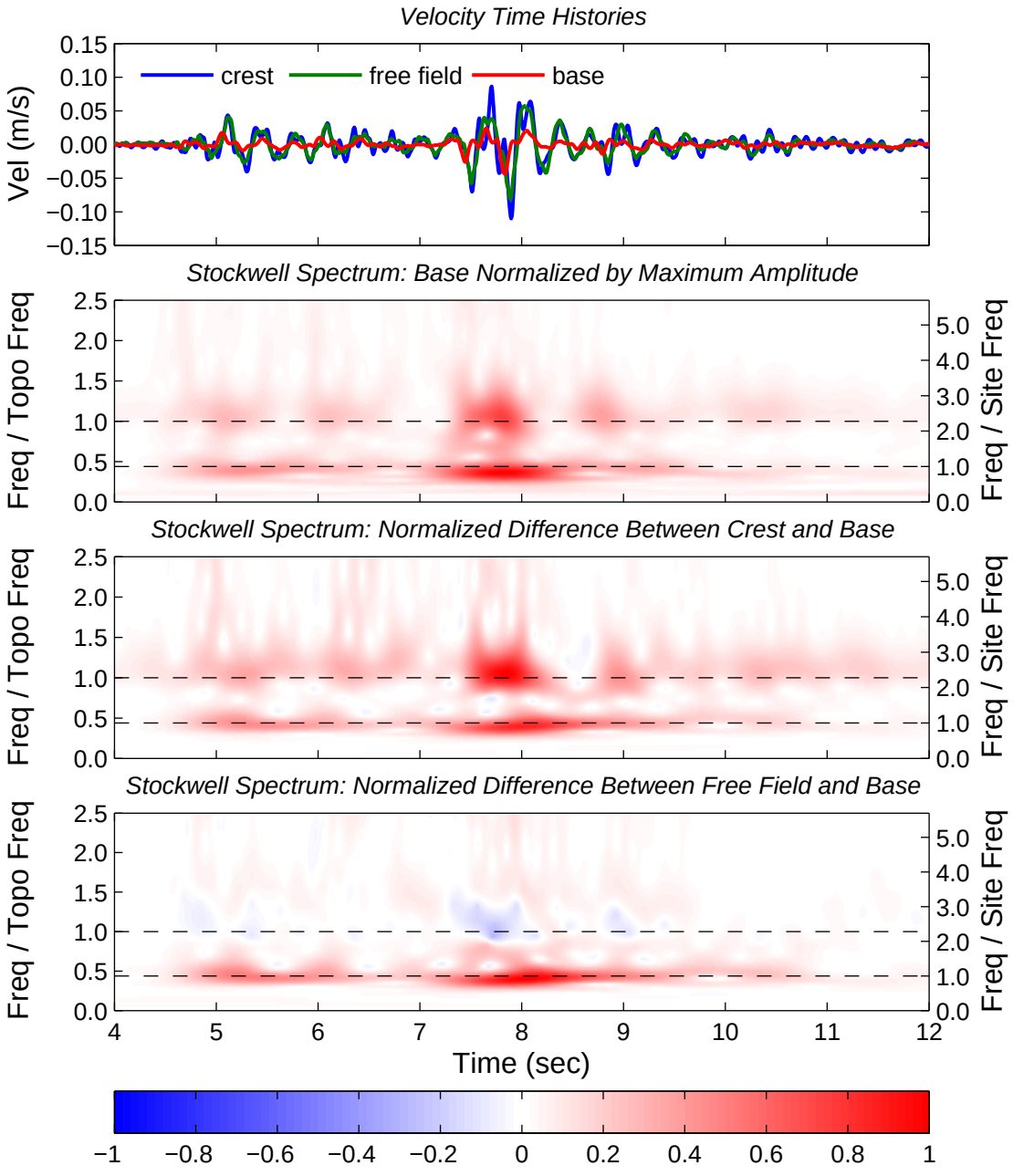

Figure 4.39: Velocity time histories, and normalized Stockwell plots of the base ground motion, the difference between the crest and base, and the difference between the free field and base, for the (za) Chi Chi earthquake of the 27.5g, 30 degree slope model.

topographic amplification to be more significant. The difference between the crest and free field increases at a rate of 0.34 per second.

Differences in the frequency content can lead to differences in phasing between the crest and free field areas. As was discussed for the (h) Chi Chi motion, the impact of phasing on the ground motion amplitude can vary depending on the relative amplitude at the competing frequencies; with the impact being greater the more out of balance these amplitudes are. When the amplitude at the site frequency was much greater than that at the topographic frequency, this led to decreases in the overall ground motion amplitude.

The effect of phasing for the (za) Chi Chi motion is illustrated in Figure 4.41. Cross sections with velocity contours are provided during the time frame bounded by dashed vertical black lines on the velocity time history and phase difference plots. The velocity contours represent snapshots at each of the local peaks for the ground motion at the crest.

At the first peak, the response is mainly dictated by amplification at the site. Some high frequency components of motion are amplified at the crest, which leads to a slight increase in overall amplitude. The free field and crest are in phase and the area amplified is confined to about the upper third of the slope.

At the second peak, the free field and crest are moving out of phase. The response at the crest is mainly controlled by topographic amplification. The free field is at a transition point from negative (away from the slope) to positive (towards the slope) motion. This results in an amplified response over the entire slope.

The crest then temporarily moves away from the slope face. However, the underlying motion at the site frequency, and the movement of the free field is increasing in velocity *towards* the slope face. This results in a lower amplitude at crest and differential movement within the slope, causing a reduction in the area amplified in this direction. Note that smoothing of the phase difference using a boxcar filter has likely decreased the phase difference; in reality the crest and free field are almost completely out of phase at this instance.

At the fourth peak, the motion of the crest and free field coincide, peaking nearly simultaneously. Underlying motion at the site frequency temporarily matches that at the

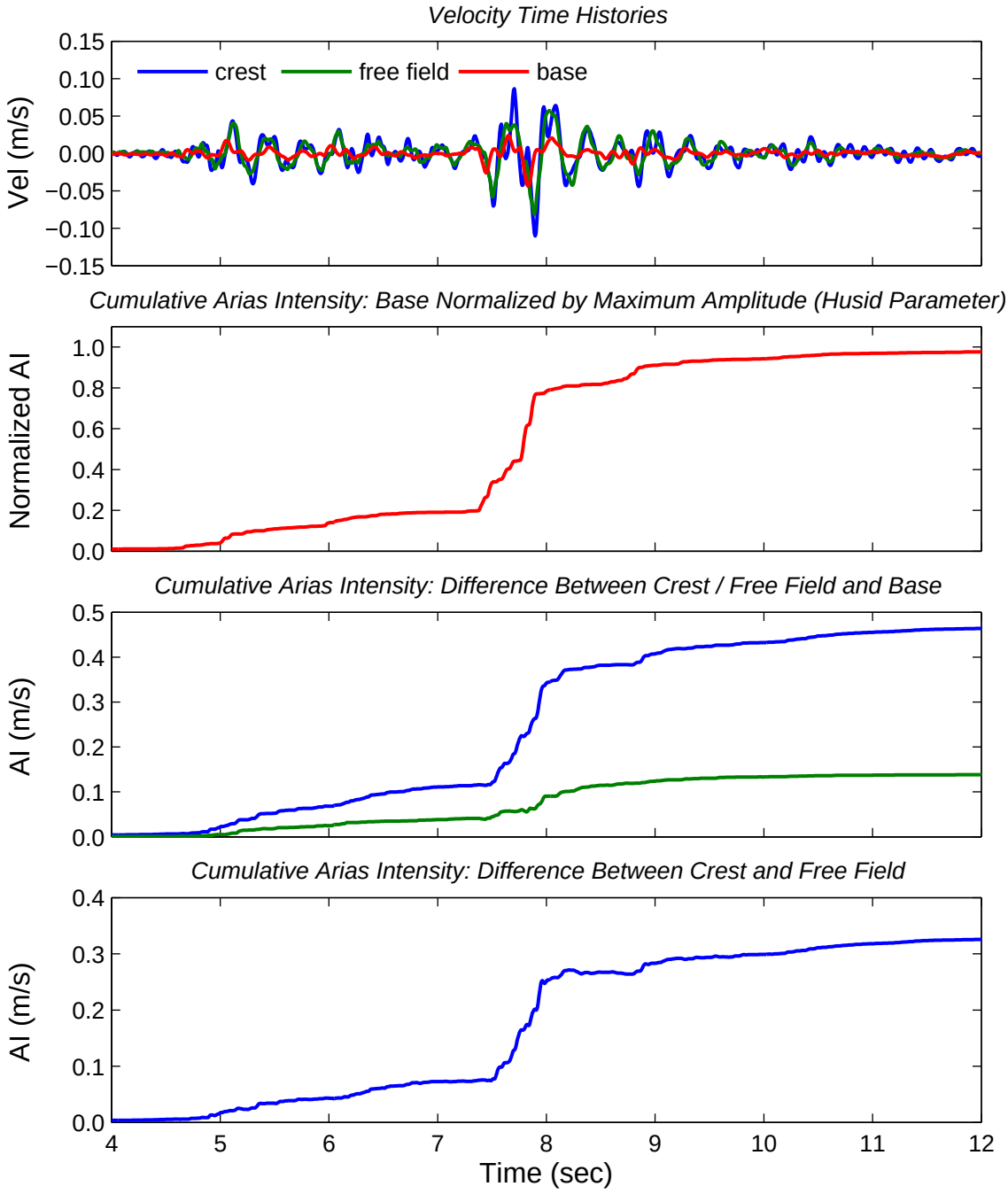

Figure 4.40: Velocity time histories, and cumulative Arias Intensity plots of the base ground normalized by the maximum, the crest and free field normalized by the base, and the crest normalized by the free field, for the (za) Chi Chi earthquake of the 27.5g, 30 degree slope model.

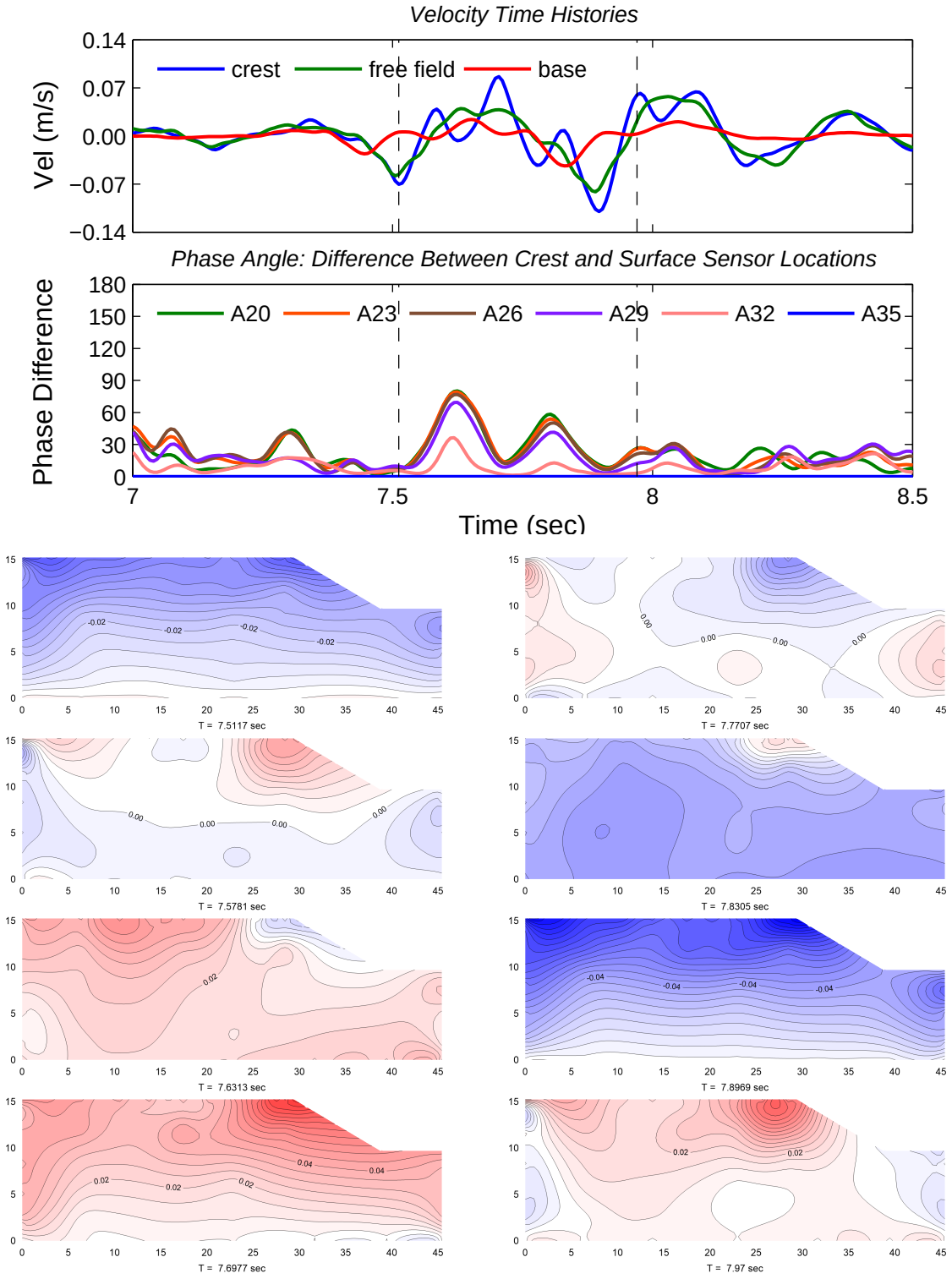

Figure 4.41: Time series of velocity contours for the (za) Chi Chi earthquake of the 27.5g, 30 degree slope model. The time series spans the vertical dashed lines shown in the velocity time history (top plot) and phase difference (second plot) plots.

topographic frequency leading to an increase in overall amplitude. The entire slope exhibits an amplified response.

The next three peaks exhibit similar behavior to the previous peak, but with the motion reversed. The behavior of the last peak is similar to the second and fifth peaks. The behavior of the sixth peak is similar to the third peak and the behavior of the seventh peak is similar to the first and fourth.

This demonstrates that competing motion at the site and topographic frequencies can have a significant impact on the overall ground response. During this time frame, site and topographic amplification were comparable, which resulted in a strong influence from both components of motion. When the free field and crest moved in opposing directions, not only the amplitude, but also the size of the area influenced by topographic effects is reduced.

4.3.2 Superstition Hills and Joshua Tree

The (h) Chi Chi, and particularly the (za) Chi Chi motion, were examples of transient ground motions for which topographic effects significantly impacted the ground response. Although more complex, the patterns and mechanisms identified were similar to those presented in Section 4.2 for the idealized motions. Additionally, the influence of compounding and competing frequencies was further explored. The (g) Superstition Hills and (w) Joshua Tree earthquake motions presented in this section represent ground motions for which the effect of topography on the ground response is minimal.

Figure 4.42 provides the normalized Stockwell difference between the crest and free field for the (g) Superstition Hills motion. As seen with other ground motions, components of motion at the topographic frequency are amplified at the crest compared to the free field. Components of motions between the site and topographic frequencies are deamplified. However, inspection of the velocity time histories and cumulative AI in Figure 4.42 reveal that differences in the ground response are minimal. The cumulative AI is a slightly higher, with increases above the free field coinciding with small levels of amplification at the topographic frequency. Differences in the Stockwell MSF are also minimal throughout the

ground motion, with small increases also occurring at the crest during times of topographic amplification.

The Stockwell MSF plot indicates a higher concentration of energy at low frequencies throughout the ground motion. This is also evidenced by the normalized base Stockwell plot in Figure 4.43. There are lower amplitude, high frequency, components of motion that exhibit amplification at the crest (see the third plot in Figure 4.43), but these are weak compared to the spectral amplitude near and below the site frequency. In the free field, amplification is mainly reserved to these lower frequency components of motion, and that amplification (over the base motion) is similar to that at the crest.

The effects of topography are even more muted for the (w) Joshua Tree motion presented in Figures 4.44 and 4.45. The cumulative AI at the crest and free field show little deviation throughout the motion. The same is true for the Stockwell MSF, which is mainly below the site frequency, with the exception of a few instances towards the beginning of the motion for the crest. The Stockwell MSF of both the crest and free field gravitate towards the site frequency, at which the majority of amplification occurs.

There are some higher frequency components of motion that are amplified at the crest. However, these are even smaller relative to the low frequency components than was observed for (g) Superstition Hills. The motion is again dominated by energy at lower frequencies, which dictate the response at both the crest and free field. Amplification of the base motion is mainly due to site amplification with a minimal contribution from topographic amplification.

It should be noted that differences in the Stockwell spectrum between the crest and free field appear extreme for the (g) Superstition Hills and (w) Joshua Tree motions (bottom plot of Figures 4.42 and 4.44). However, this is due to the fact that the plots are normalized by the maximum differences between the two. Inspection of the bottom two plots in Figures 4.43 and 4.45 reveals that the amplification over the base motion is similar at the crest and free field, meaning the differences in actual amplitude between the two locations is small.

The (g) Superstition Hills and (w) Joshua Tree motions highlight the importance of the incident ground motion frequency content. If strong components near the topographic

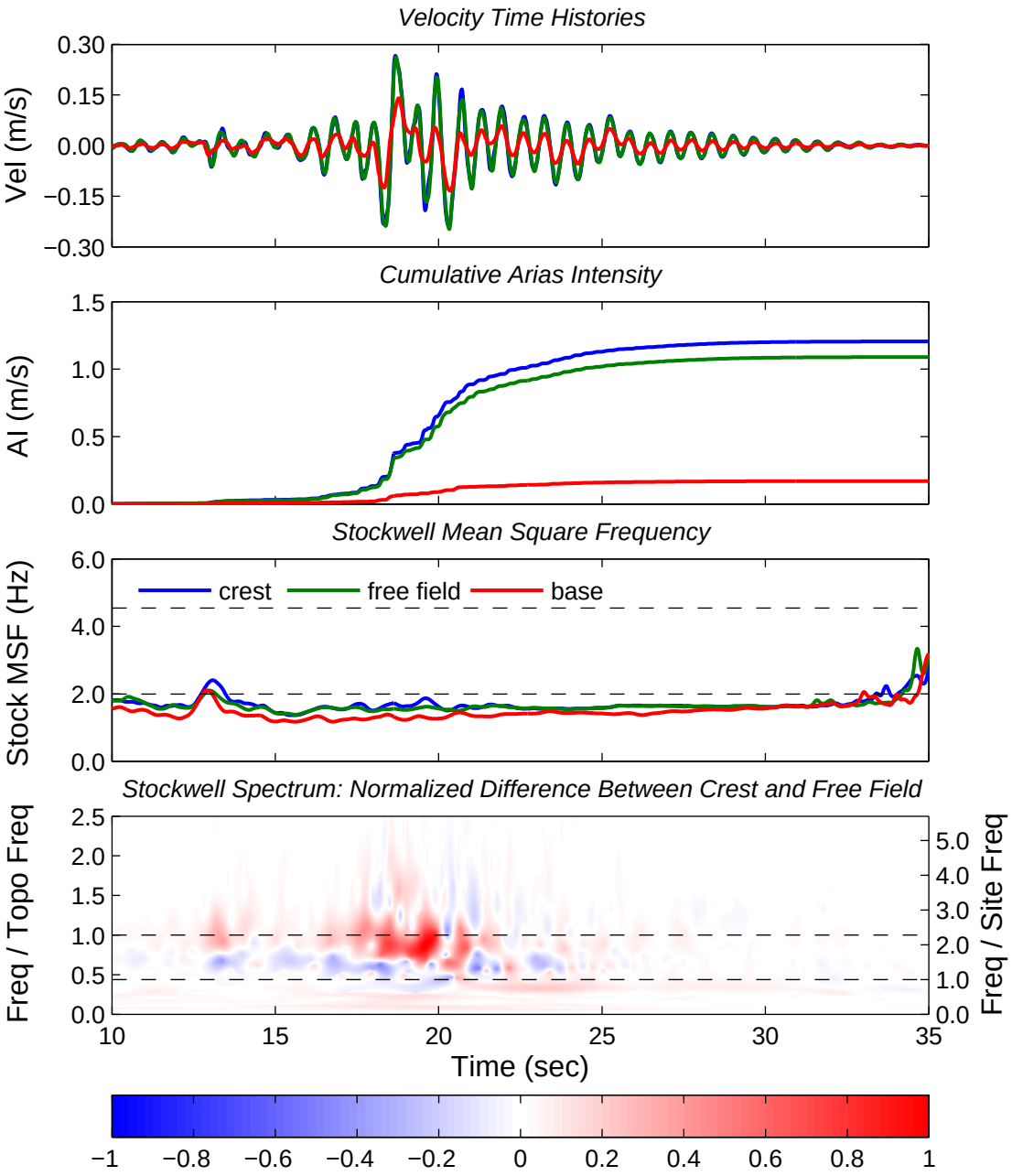

Figure 4.42: Velocity time history, cumulative Arias Intensity, and Stockwell MSF plots for the base, crest and free field; and the difference between the crest and free field Stockwell amplitude, normalized by the maximum difference, for the (g) Superstition Hills earthquake of the 55g, 30 degree slope model.

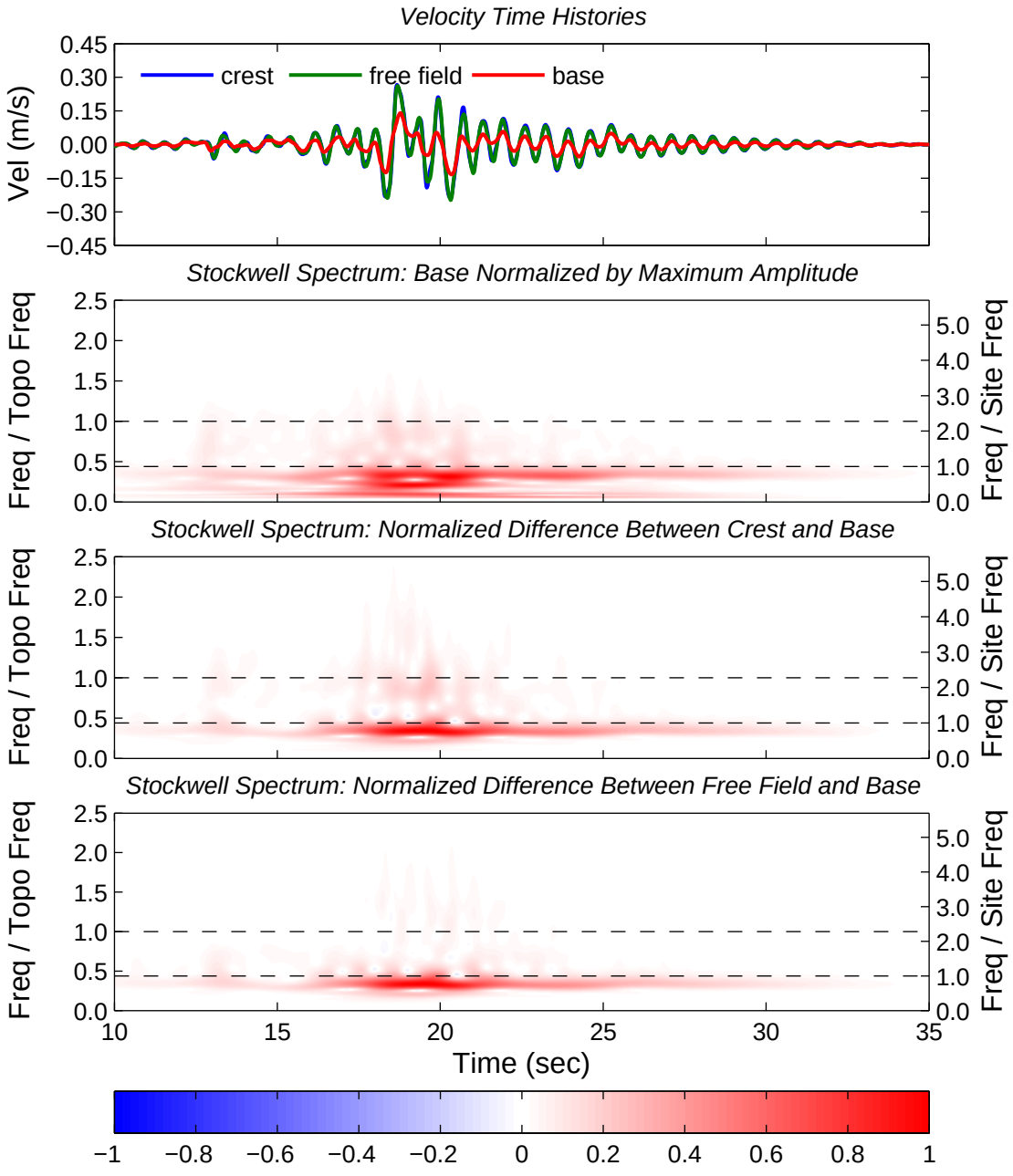

Figure 4.43: Velocity time histories, and normalized Stockwell plots of the base ground motion, the difference between the crest and base, and the difference between the free field and base, for the (g) Superstition Hills earthquake of the 55g, 30 degree slope model.

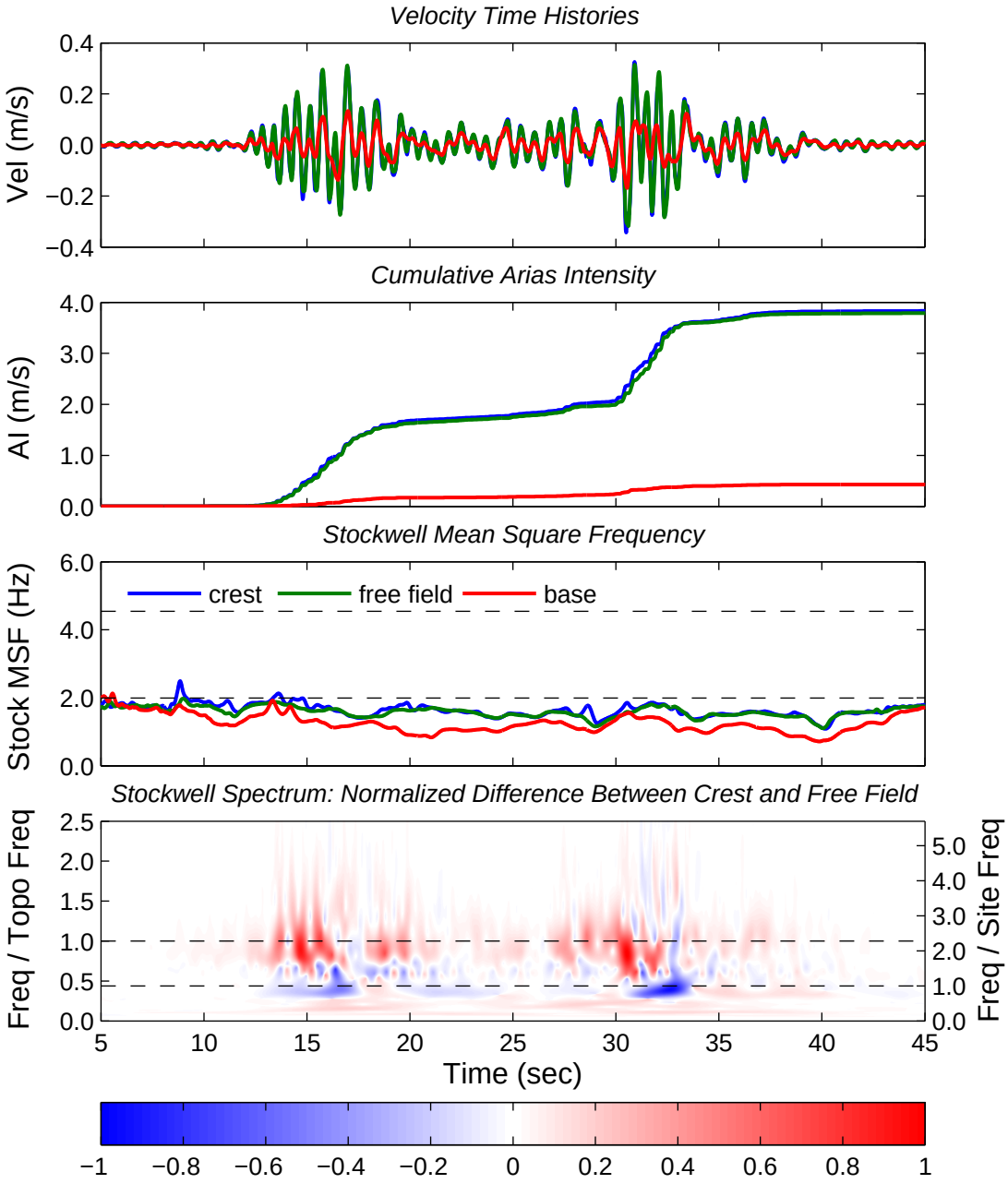

Figure 4.44: Velocity time history, cumulative Arias Intensity, and Stockwell MSF plots for the base, crest and free field; and the difference between the crest and free field Stockwell amplitude, normalized by the maximum difference, for the (w) Joshua Tree earthquake of the 55g, 30 degree slope model.

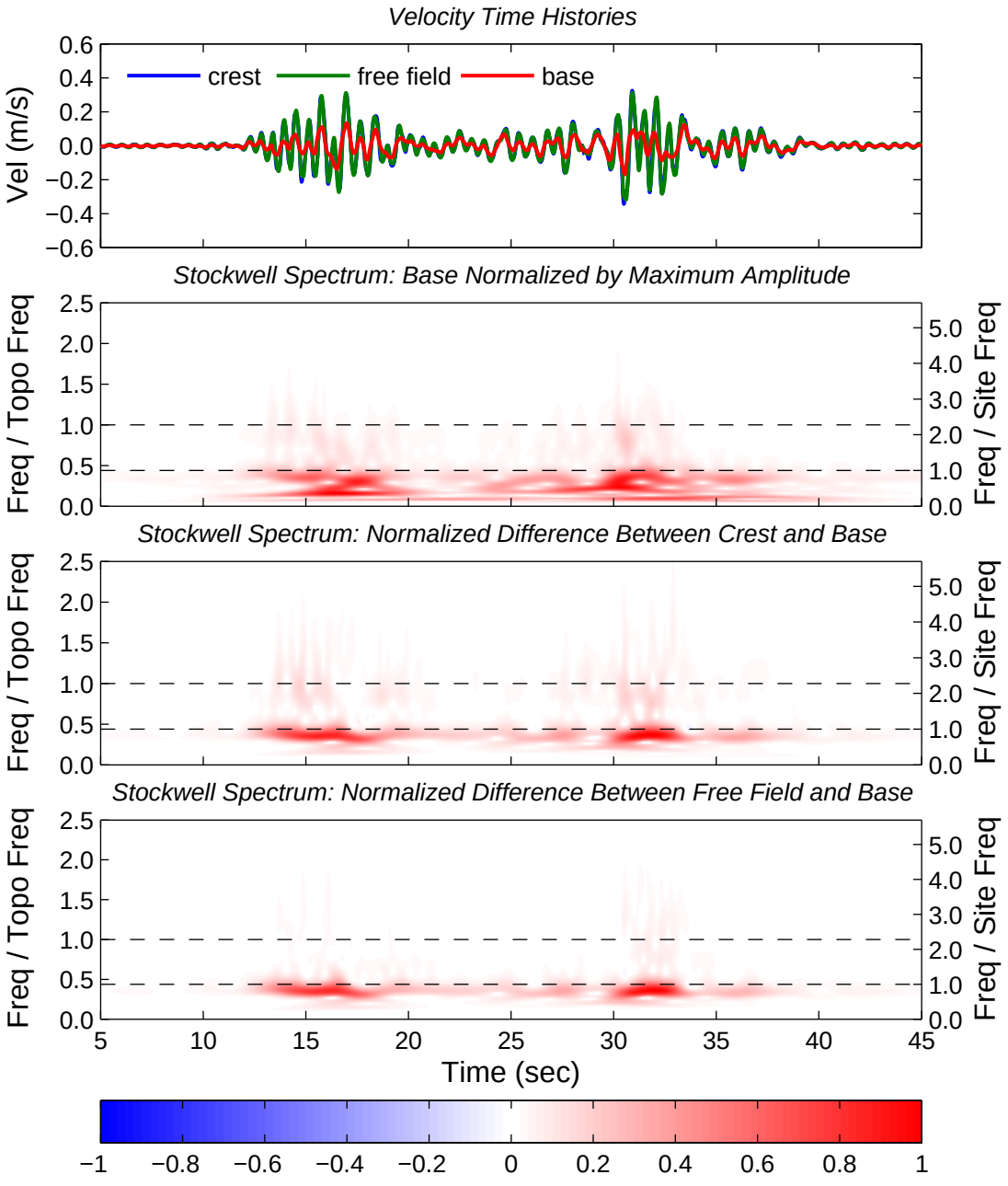

Figure 4.45: Velocity time histories, and normalized Stockwell plots of the base ground motion, the difference between the crest and base, and the difference between the free field and base, for the (w) Joshua Tree earthquake of the 55g, 30 degree slope model.

frequency are not present, then the effects of topography are minimized for the horizontal component of motion. This is particularly true when strong components of motion at the site frequency exist.

4.4 Vertical and Combined Ground Motion

The previous sections focused on horizontal ground motion for the 30 degree slope. This section considers vertical and combined (both horizontal and vertical) ground motion recorded on the 25 degree slope. Although it was shown that topographic effects are more muted, displacement time histories, and displacement based plots, are presented in this section to better understand the relationship between vertical and horizontal ground movement.

As was discussed in Chapter 3, and shown in Figure 4.3, vertically oriented accelerometers were placed in close proximity to near surface horizontally oriented sensors along the centerline of the models. Three vertically oriented sensors were also placed on the bottom of the container (below the sand deposit) and two were placed on top of the container boundaries (one on each side). No vertical sensors were placed between the near surface and bottom of the sand deposit.

Several of the vertical sensors experienced electronic failure or malfunctioned throughout the experiment. One of these sensors was at the crest of 30 degree slope, thus limiting the ability to properly interpret vertical and combined motion. Vertical ground motion was, however, captured at the crest of the 25 degree slope, and therefore is presented here. It should be noted that topographic effects are generally less pronounced for the 25 degree, than for the 30 degree slope (see Chapter 3).

The shaker used in the centrifuge experiments is designed to introduce only horizontal ground motion to the models. For the flat ground model, this means that theoretically only horizontal ground motion would be recorded. However, as seen in Figure 4.46, both horizontal and vertical ground motions are recorded at the near surface sensor locations.

Figure 4.46 presents displacement time histories for the (l3) Ricker wavelets introduced to the flat ground model. Horizontal (top plot) and vertical displacements (second plot)

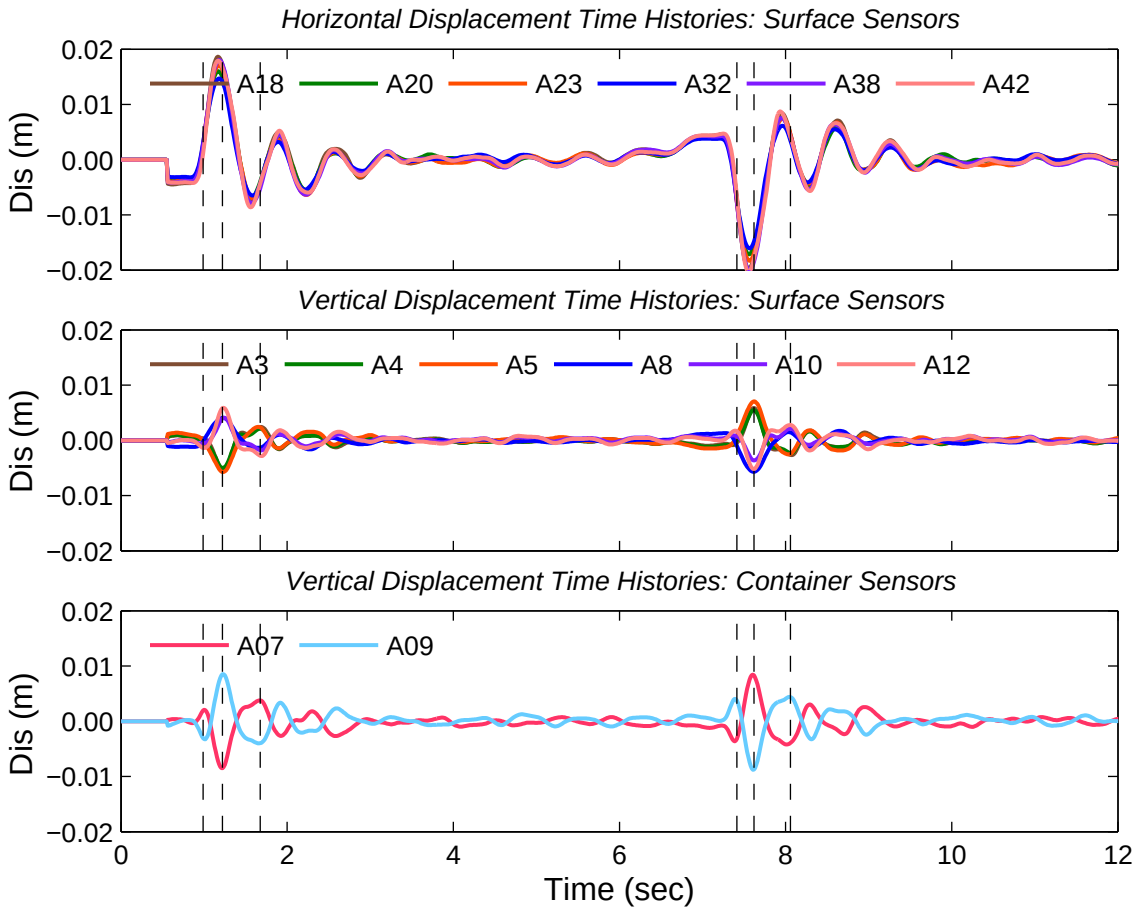

Figure 4.46: Horizontal and vertical displacement time histories for surface and container locations for the (l3) Ricker wavelets of the 55g, flat ground model. Legend designations represent sensor locations. Dashed vertical black lines correlate to snapshots in Figure 4.48.

are provided at near surface locations where both were recorded. Locations where either the vertical or horizontal sensor malfunctioned are not included (even if one of the two sensors at the location recorded data). The locations of the sensors is provided in Figure 4.3. Coupled vertical and horizontal sensors are plotted using the same color (i.e., sensor A18 and A3). Sensors A20 and A4 represent the reference free field sensors, and sensors A32 and A8 represent the sensors just behind the slope crest. Vertical sensors located on top of the container on the north (sensor A07) and south (sensor A09) side of the model are presented in the bottom plot (see 4.3 for direction - north to the left, south to the right).

The introduction of vertical ground motion to the flat ground model is mainly the result of the interaction between the shaker-container-soil mass system, 3-D effects, and container rocking. Rocking of the model container is evidenced by the bottom two plots in Figure 4.46. The sensors on opposite sides of the container are 180 degrees out of phase with each other; as one side of the containers moves upward (positive), the other side moves in the downward (negative) direction. Likewise, sensors within the model north of the center of mass (sensors A3, A4, and A5) are 180 degrees out of phase with sensors south of the center of mass (sensors A8, A10, and A12). Additionally, the amplitude of motion for the container, farther from the center mass, is greater than that in the model. This is consistent with a rocking motion.

Horizontal ground motion (top plot) is similar in amplitude and in phase for the near surface locations. This behavior is expected for the flat ground model. This behavior differs slightly from that of the 25 degree slope, as shown in Figure 4.47. Movement of the slope (sensor A32 is behind the crest, A38 on the slope, and A42 at the toe of the slope) is in phase with that of the free field (sensors A18, A20 and A23). However, the amplitude of displacement for the slope is less than that of the free field. This could be for reasons previously discussed in Sections 4.2 and 4.3. Namely, higher frequencies (that may be amplified at the crest) are filtered out by the integration process, the ground motion is dominated by low frequency motion, and competing motion at lower and higher frequencies may inhibit overall movement of at the crest. Additionally, these effects are likely more pronounced for

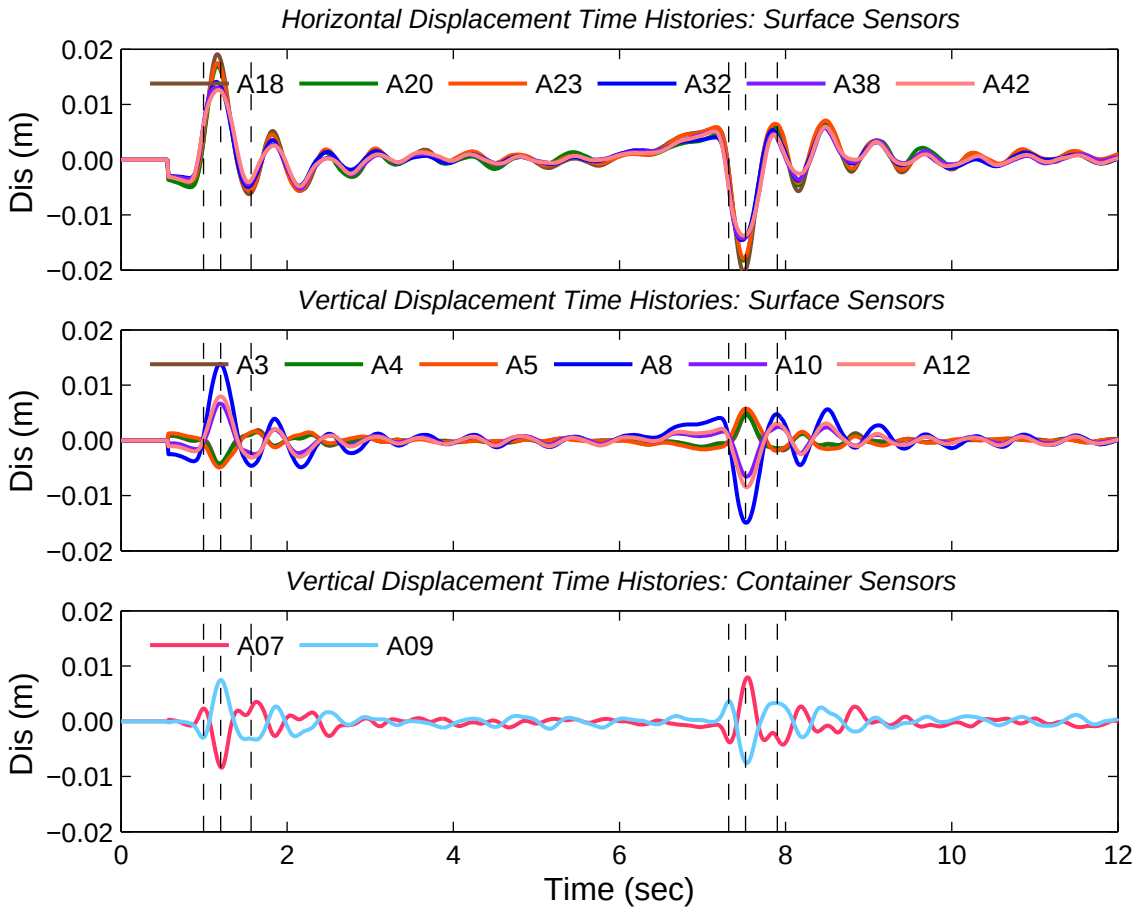

Figure 4.47: Horizontal and vertical displacement time histories for surface and container locations for the (l3) Ricker wavelets of the 55g, 30 degree slope model. Legend designations represent sensor locations. Dashed vertical black lines correlate to snapshots in Figure 4.48.

the 25 degree than the 30 degree slope. At the toe and on the slope, displacement may also be lower as a result of a shortened soil column.

Vertical motion for the 25 degree slope, however, exhibits behavior that more significantly differs from the flat ground model. Vertical displacement is greatest and is comparable to horizontal displacement at the crest. The amplitude of vertical displacement is also greater on the slope and at the toe than it is for the free field. The free field and slope, as well as the container boundaries, remain 180 degrees out of phase. This indicates that rocking still has some influence on the overall behavior. However, the increase in amplitude at the slope crest indicates an influence of topographic effects. It should be noted that vertical displacement is greater on the north side than the south side of the container (see bottom plot of Figure 4.47); likely a result of the shift in the center of mass towards that side of the container from the presence of the slope.

Comparison of the overall ground movement between the flat ground and 25 degree slope for the (l3) Ricker wavelet is provided in Figure 4.48. The displacement vectors and mesh are given at instances in time marked by the vertical dashed black lines in Figures 4.46 and 4.47. Displacements are exaggerated for illustrative purposes (by a factor of 250). It should be noted that vertical ground motion within the mesh is less constrained due to the lower density of vertical sensors in the model.

The pattern of ground motion is similar for the flat ground and 25 degree slope. The ground moves in the positive horizontal (towards the right) direction, and then begins to move in the positive vertical (upward) direction. Displacement peaks in the horizontal direction and begins to move towards the negative direction. This is followed shortly by a peak in vertical displacement in the upward direction. This same process then occurs in the opposite direction, creating an elliptical shape. Thus, the vertical motion mimics, but is lower in amplitude and lags slightly behind (i.e., peak displacements occurs at different times), that of the horizontal.

From Figure 4.48 it is clear that the vertical component of motion is amplified at the crest compared to other locations, and along the slope compared to the free field. The free field

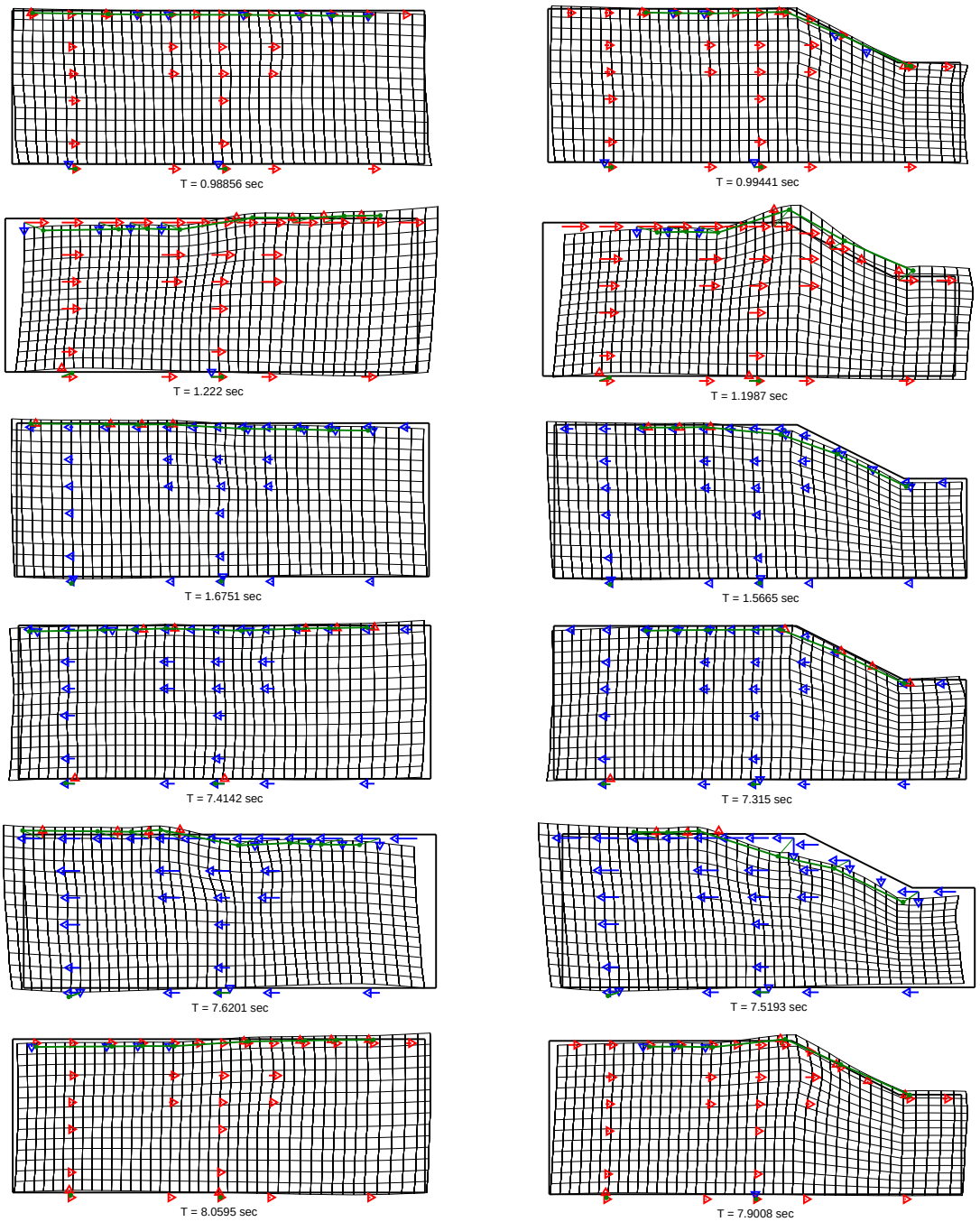

Figure 4.48: Time series of displacement vectors and mesh for the (l3) Ricker wavelets of the 55g, flat ground (left side) and 30 degree slope (right side) models. The snapshots are marked by vertical dashed black lines shown in Figures 4.46 and 4.47. Displacement is scaled by 250.

also has a comparable, but greater vertical component of motion for the 25 degree slope than it does for the flat ground. However, because the shape and spatial variation of movement is similar for the flat ground and 25 degree slope, it is difficult to completely separate the contribution of rocking and 3-D effects to the vertical component of ground motion.

It is possible that the introduction of the slope exacerbates the level of rocking. This could be a result of the uneven distribution of mass within the model container, which could lead to a greater vertical component of motion along the slope. However, it is likely there are other contributors to the strong component of vertical motion.

Other researchers have suggested the vertical component of motion results from the generation of surface waves (Assimaki et al., 2005b; Bard and Riepl-Thomas, 2000; Bouckovalas and Papadimitriou, 2005; Pedersen et al., 1994, among others). The surface waves form due to interactions with two-dimensional and three-dimensional geometry. These surface waves are typically believed to be Rayleigh waves, but Assimaki et al. (2005b) has also suggested that surface waves are generated at and propagate up the slope face at the compression (P) wave velocity. This resulted from the fact that the slope analyzed was near the critical angle of incidence. Therefore, the body wave would hit the slope face and propagate up the slope.

Either of the above explanations may be plausible for the given slope configuration. For a typical Poisson's ratio of sand around 0.3, the critical angle of incidence for a incoming wave at the shear wave velocity and leaving at the compression wave velocity is about 30 degrees. This is near the 25 degree slope face used in this example, and therefore could be a contributor to the vertical component of motion.

The other contributor, Rayleigh waves, move with a retrograde elliptical motion. This is consistent with the motion behind the crest, along the slope and at the toe if a Rayleigh wave formed at the crest and propagated down the slope. Likewise, the motion in the free field is consistent with a Rayleigh wave forming near the crest and propagating towards the free field.

It is likely that the strong vertical component of motion at the crest and along the slope face is the result of a combination of surface waves, rocking, and the inherent 3-D effects

mentioned above. The true contribution from surface topography would therefore be mainly attributed to the formation of surface waves. In particular, the ground motion is consistent with the formation of Rayleigh waves at the crest.

The (l3) Ricker wavelet depicted in Figures 4.47 and 4.48 focused on a single pulse at a single central frequency. Figures 4.49 through 4.51 highlight the combined motion at three different frequencies (1Hz, 2Hz, and 4Hz, respectively) for the (q) sine wave motion. The snapshots span the time frame bounded by the dashed vertical black lines in the horizontal (top plot) and vertical (second plot) displacement time histories. The ground motion at the near surface locations is traced in brown throughout the time snapshots.

Figures 4.49 through 4.51 illustrate that the elliptical motion previously described is consistent regardless of frequency. This is true whether below the site frequency, and not near the site or topographic frequency (1Hz), at the site frequency (2Hz), or near the topographic frequency (4Hz). The amplitude of horizontal motion at the crest varies in comparison to the free field at these three frequencies (in line with that discussed previously in this chapter). However, in all cases the amplitude and timing of the vertical motion closely follows that of the horizontal motion.

The pattern described above is consistent with all other ground motions explored in this chapter. This is illustrated in Figure 4.52, where the combined motion at the crest (blue), toe (pink), and free field (green) is plotted on a polar diagram. The shape of the ellipse changes some with frequency and overall amplitude, however, the overall ground behavior is fairly consistent. Motion at the crest is typically close to a 45 degree angle (measured from horizontal). This indicates the amplitude of the vertical component and horizontal component is similar. At the toe, the relative amplitude of the vertical ground motion is less, resulting in an angle slightly below 30 degrees. In the free field, the combined motion follows an overall angle closer to 15 degrees, meaning the vertical component is even smaller relative to the horizontal component.

Ground motion in the vertical direction occurs regardless of ground motion type or ground motion frequency content. Because it closely mimics the ground motion in the horizontal

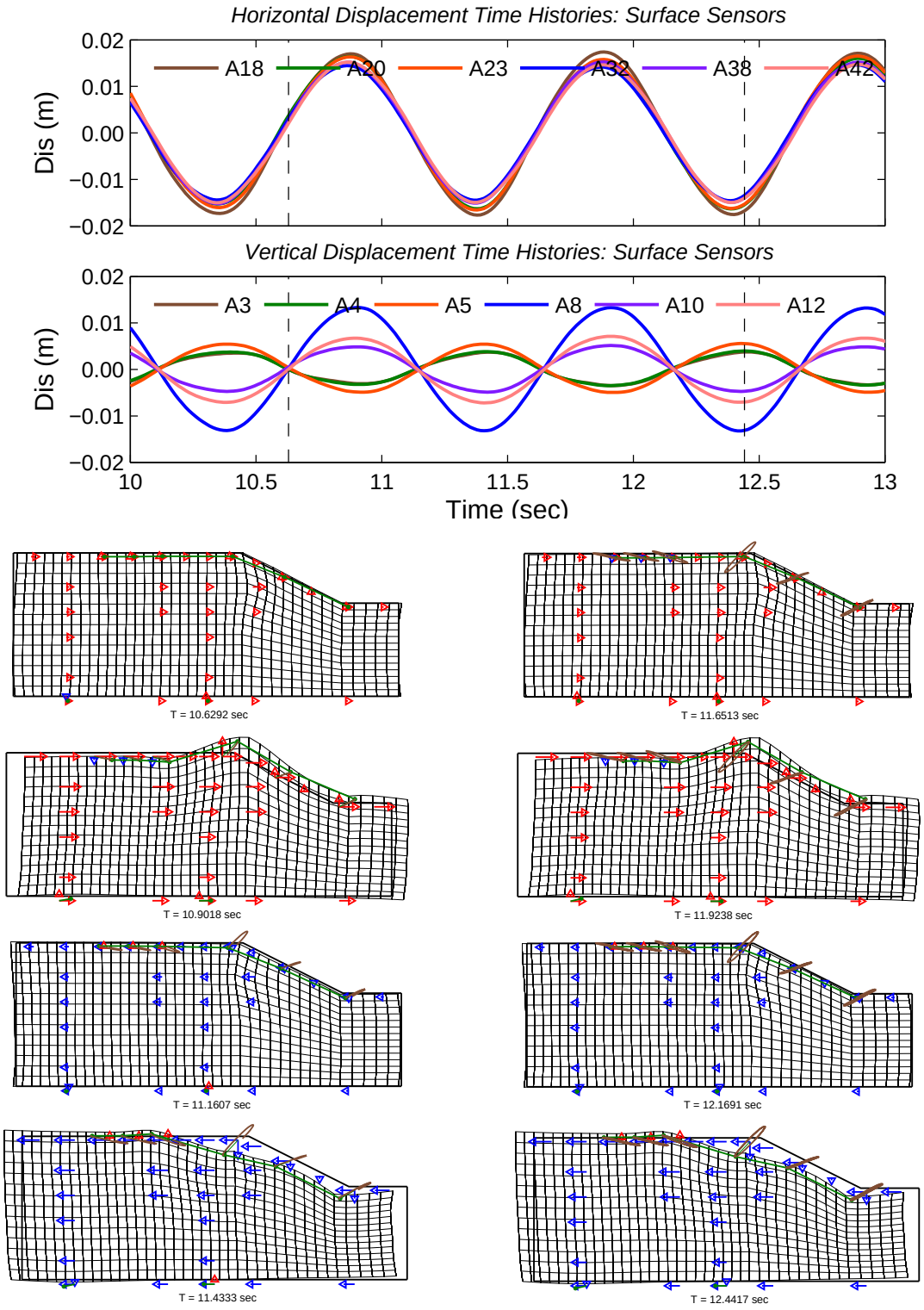

Figure 4.49: Time series of displacement vectors and mesh for 1Hz (q) sine wave motion of the 55g, 30 degree slope model. The time series spans the vertical dashed lines shown in the horizontal and vertical displacement time histories. Displacement is scaled by 250.

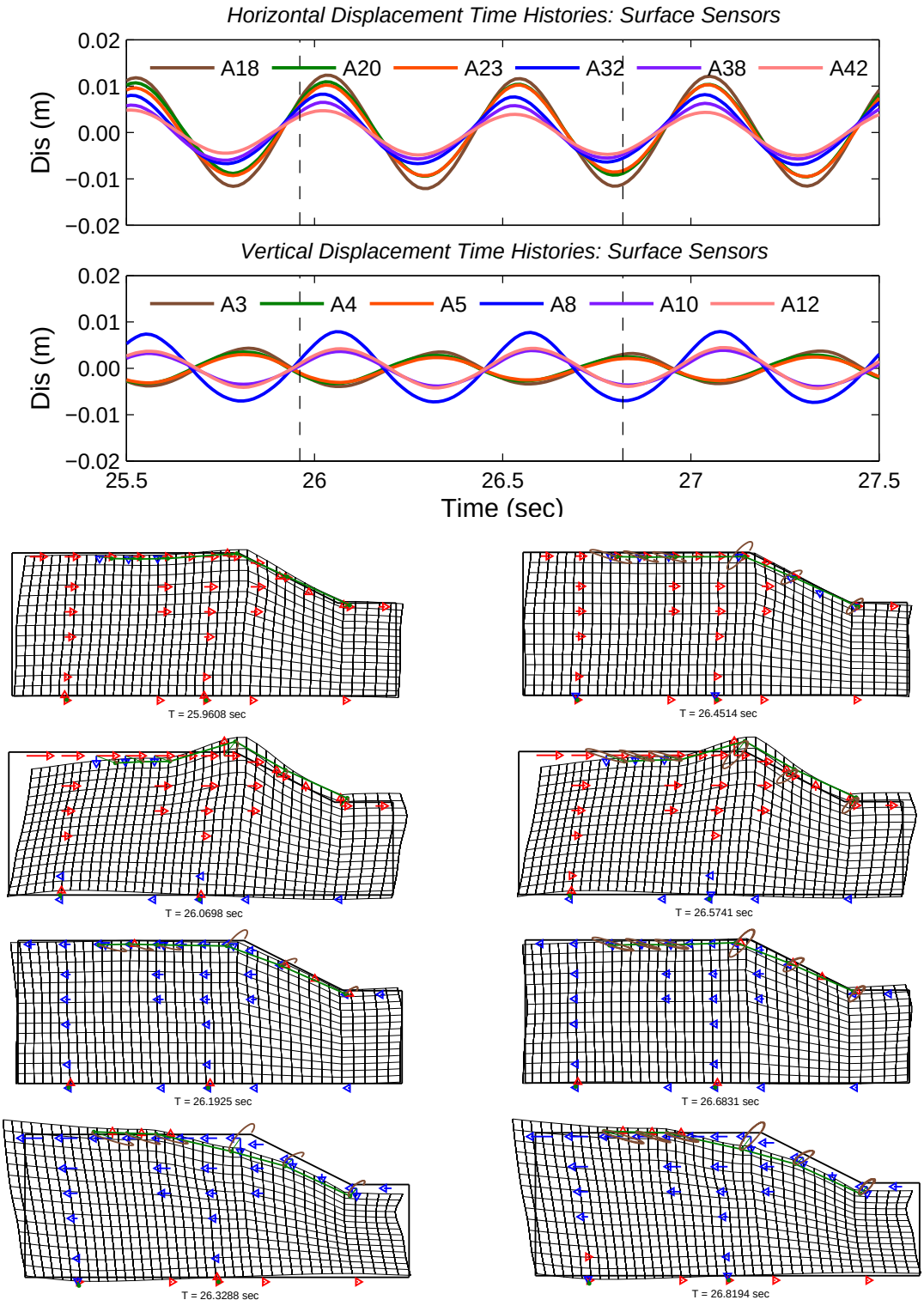

Figure 4.50: Time series of displacement vectors and mesh for 2Hz (q) sine wave motion of the 55g, 30 degree slope model. The time series spans the vertical dashed lines shown in the horizontal and vertical displacement time histories. Displacement is scaled by 400.

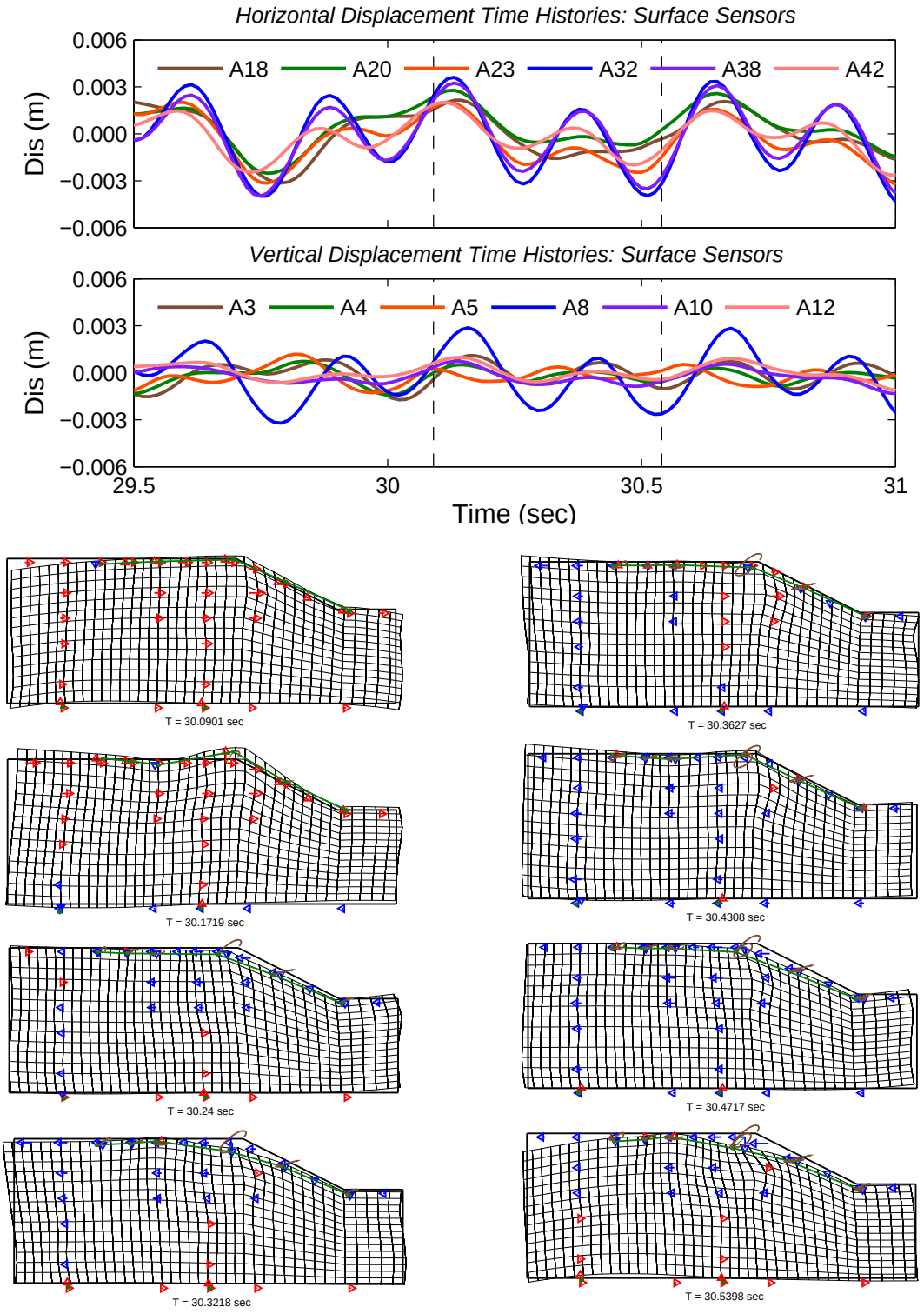

Figure 4.51: Time series of displacement vectors and mesh for 4Hz (q) sine wave motion of the 55g, 30 degree slope model. The time series spans the vertical dashed lines shown in the horizontal and vertical displacement time histories. Displacement is scaled by 900.

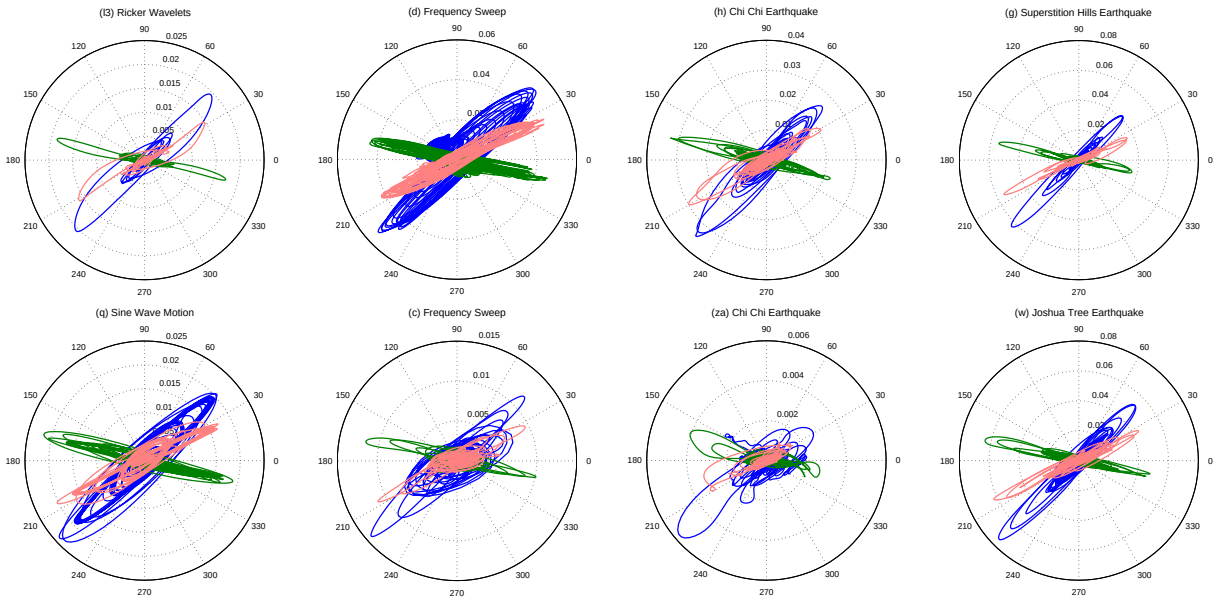

Figure 4.52: Vertical versus horizontal polar displacement plots for the ground motions listed above each plot. Plots include the slope crest (blue), free field behind the crest (green) and slope toe (pink). Vertical is represented by 90 degrees.

direction, the vertical component of motion at the crest would be greater for motions with significant frequency content near the site or topographic frequency. However, even for cases where the horizontal component of motion is not significantly amplified or topographic amplification of the horizontal ground component does not occur, the vertical component of motion is observed. Therefore, topographic effects must be considered for all ground motions regardless of frequency content, when considered for design.

4.5 Discussion

Based on the results of the parametric analysis performed in Chapter 3, eight ground motions were selected to analyze the causes and influences of topographic effects. Analysis methods and results have been presented for both idealized and non-idealized (earthquake) motions. The ground motions included examples that exhibited both strong and weak topographic effects, so that differences in behavior could be observed. The analysis focused on the response of a 30 degree slope for horizontal motion, but the response of the 25 degree slope

and flat ground models were used to analyze vertical and combined motion.

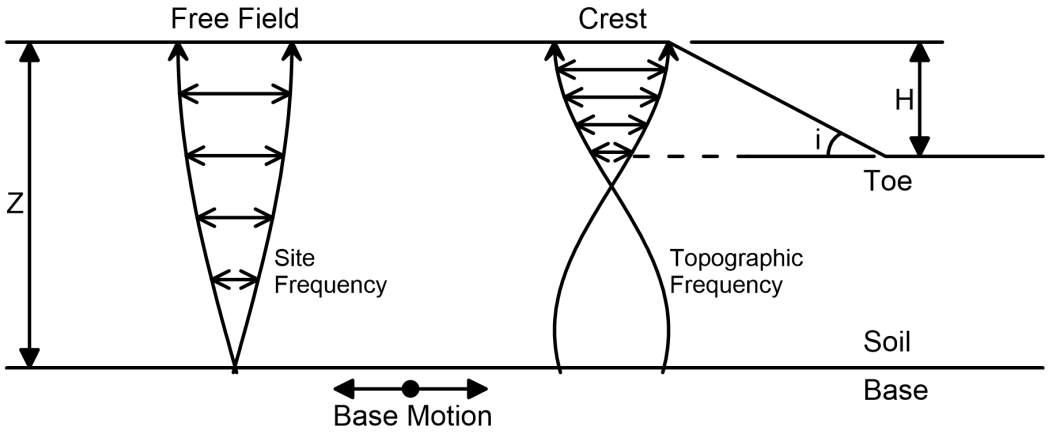

Figure 4.53: Simplified reference diagram highlighting important dimensions and the mode shapes of at the site and topographic frequencies, relative to the soil stratum and slope.

For discussion purposes, an idealized slope cross section is shown in Figure 4.53. Important parameters, such as the soil stratum thickness (Z), slope inclination (i), and slope height (H), are illustrated. Key features, such as the location of the crest, toe, free field, and base are also labeled. Additionally, the mode shapes for propagating waves at the site and topographic frequencies are shown.

A number of mechanisms that contribute to topographic effects were explored in this chapter and highlighted by the different ground motions introduced. Topographic amplification has been shown to occur for frequencies ranging from 0.7 to 1.3 times the topographic frequency (see for example Figure 4.19). The main cause of this amplification, for the horizontal component of motion, is resonance at and near the topographic frequency.

For a typical site with soil overlying bedrock, shear waves propagating from the bedrock will reflect off the soil ground surface, and travel back towards the bedrock. The constructive interference of the propagating and reflected wave can create a standing wave, which has a fixed shape with respect to depth. For certain wavelengths, and therefore frequencies, a site will have a tendency towards resonant conditions when these standing waves develop. The

first mode of resonance for a site occurs at the site frequency, when the wavelength is four times that of the thickness of the soil stratum. This is depicted for the soil stratum behind the crest in the reference diagram in Figure 4.53. The relationship of this mode shape to the soil stratum is similar to the relationship of the mode shape at the topographic frequency to the slope. That is, both represent a case for which ground motion is maximized and a tendency towards oscillation occurs. Note that the mode shapes are shown in both the positive in negative directions.

Compared to the free field behind the crest, the slope represents a reduction of mass and stiffness. This reduction in mass, or lack of confinement on the slope face, and stiffness allows the slope to move more freely. Based on this reasoning, if the slope were 90 degrees, the mass in front of the crest would be zero, allowing excitation at the topographic frequency to be maximized. As the slope inclination decreases, the mass in front of the crest increases, meaning a greater driving force is required for slope movement.

The introduction of a slope (less than 90 degrees) introduces additional complexities to ground response. Waves propagating upward will reach the toe and slope face prior to reaching the slope crest. This can lead to differential movement which may impede the movement of the soil mass behind the crest (or allow it to move more freely). This differential movement is illustrated in Figure 4.24. Additionally, these waves will reflect in different directions depending upon the angle of the slope face relative to the incident wave. For slopes 30 degrees or less, discussed here, reflected waves will travel away from the slope crest, back towards the base, which could create interference patterns with propagating waves. These interference patterns, however, were not observed in this study.

At the topographic frequency, the wavelength is such that the entire slope will generally move together, with maximum amplitude at the crest. As a result, an amplified response is typically observed over the entire slope, and the level of amplification decreases with depth. As the wavelength decreases, differential movement within the slope increases and the size of the area amplified around the slope crest reduces. Eventually the area becomes small enough that topographic effects are minimized. As the wavelength increases, the amplified area also

increases. Eventually the size of the slope becomes insignificant compared to the wavelength and typical site response again controls. This is demonstrated in Figures 4.24 and 4.30.

When topographic amplification occurs, a topographic zone of influence develops for which the depth is typically proportional to the width of the area affected. The overall shape of the amplified area is similar to that of a deep seated landslide slip surface (see for example Figure 4.15). The excitation of this landmass can lead to differential motion between it and the surrounding landmass. This differential movement can introduce softening at the base of the slope (likely as a slip surface begins to develop). Softening at the base of the slope can then lead to base isolation, where energy is impeded from propagating into the slope, thereby reducing the level of amplification (Figures 4.22 and 4.28).

Excitation of the slope landmass can also create differential motion between it and the free field landmass behind the crest. This differential motion, or difference in phasing, can impede movement, or inhibit excitation of the slope landmass. Thus, differences in phasing can lead to a reduction in amplitude at the crest and within the slope as well. This was illustrated in Figures 4.17 and 4.18.

Differences in phasing result from differences in the frequency content between the crest and free field areas. The crest is excited at frequencies encompassing the topographic frequency; the free field is not. Excitation of the free field does, however, occur at frequencies encompassing the site frequency. Because the column of soil beneath the crest is the same as that of the free field, excitation at the site frequency also occurs at the crest. Since energy is absorbed at both these frequencies at the crest, frequencies between the site and topographic frequency tend to appear deamplified compared to the free field (see Figures 4.31 and 4.33).

The level of amplification at the site and topographic frequencies can be tied to the amplitude of the input (base) motion at those frequencies. Amplification can occur at the site and topographic frequencies simultaneously at the crest. However, competition between these frequencies can inhibit overall ground motion. This typically occurs when ground motion at the topographic frequency is weak compared to that at the site frequency (i.e., site effects dominate the response). When topographic amplification is greater than site

amplification, it too can dominate the ground response at the crest. This is illustrated in Figures 4.34 and 4.35.

Ground motion with frequency components at the topographic and site (as well as other) frequencies can also lead to enhancements in overall ground motion amplitude. When peaks in ground motion at the respective frequencies occur simultaneously, and in the same direction, the overall amplitude can be significantly magnified. This can occur, for example, when higher frequency oscillations at the topographic frequency peak at the same time as a lower frequency pulse. This is again illustrated in Figures 4.34 and 4.35, as well as Figure 4.41.

These oscillations relative to underlying low frequency motion can also lead to differential motion within the slope landmass. When peaks occur simultaneously, the entire slope may exhibit amplification and move in phase. However, when ground motions at these frequencies are out of phase, the area around the crest that is responsive to this high frequency pulse is reduced. That is, the rest of the slope may continue to move in the direction of the underlying low frequency pulse. Therefore, competition at these frequencies can influence ground motion amplitude and the size of the area affected by topographic amplification (see Figure 4.41).

The discussion thus far has focused on horizontal ground motion. A strong vertical component of motion, comparable to that of the horizontal component, is also produced at the crest of the slope. The vertical movement typically mimics that of the horizontal component (Figure 4.47). The resultant combined motion forms an elliptical shape, which is consistent with the formation of a Rayleigh wave (Figure 4.52). Movement along the slope and in the free field is consistent with that of a Rayleigh wave forming and traveling from the slope crest towards those regions. Additionally, the amplitude of the vertical component is greatest, and therefore consistent with the formation of a surface wave, at the crest. This is true because the amplitude of the surface wave would likely reduce as it propagates along the surface, particularly if interference with incoming body waves occurs. The elliptical motion at the crest and along the slope is illustrated in Figures 4.49, 4.50, and 4.51.

The vertical component of motion is present regardless of frequency content (see Figures

4.49, 4.50, and 4.51). Because it generally mimics the horizontal motion, however, the vertical component may be greater when amplification of the horizontal motion occurs (such as at the site and topographic frequencies). This depends on the frequency content and amplitude of the incident waves.

The presence of a strong vertical component of motion can certainly be tied to topographic effects, and has been suggested by numerous other researchers (see Assimaki et al., 2005b; Bard and Riepl-Thomas, 2000; Bouckovalas and Papadimitriou, 2005; Pedersen et al., 1994; Tripe et al., 2013, among others). However, for this investigation, it is difficult to separate the contributions of container rocking and 3-D container effects to vertical ground motion. Container rocking was demonstrated in Figures 4.46, 4.47, and 4.48. Therefore, the portion of vertical motion attributed to topographic effects cannot be fully characterized.

4.6 Conclusions

Data from the centrifuge experiment proved useful for analyzing the causes and influences of topographic effects. The density of sensors within the model configurations allowed wave propagation and the separation of behavior between the slope and free field behind the slope to be observed. The suite of ground motions considered cases where topographic effects were and were not significant, allowing the influences of topographic effects to be more easily identified. Specific influences were isolated in time for idealized motions. These influences, as well as others, were then identified for transient earthquake motions. A summary of causes and influences of topographic effects is provided below.

- The main cause of topographic amplification for horizontal ground motion is excitation, due to a tendency towards resonance, at frequencies typically ranging from 0.7 to 1.3 times the topographic frequency.
- A slope represents a reduction in mass and stiffness compared to the free field behind the crest. It is for this reason that excitation can occur at the topographic frequency. This also helps explain the increase in amplification for steeper slopes.

- The level of topographic amplification is related to the input (base) amplitude at frequencies near the topographic frequency, such that an increase in the base amplitude leads to an increase in amplification.
- Ground softening at the base of the slope can impede energy from propagating up the slope, and thus reduce the level of amplification.
- Differential movement between the slope landmass and free field landmass can lead to a reduction in overall ground motion amplitude for the slope. The impact of this is dependent upon the relative amplitude of ground motion for each landmass.
- Absorption of energy at the at the topographic frequency, due to topographic amplification, and at the site frequency, due to site amplification, leads to an apparent deamplification of frequencies between the site and topographic frequencies at the crest compared to the free field.
- Site amplification and topographic amplification can occur simultaneously at the crest. Topographic amplification can also coincide with ground motion at other frequencies. Depending on the relative amplitude at these frequencies and phasing, this can either reduce or enhance overall ground motion amplitude.
- When topographic amplification occurs, the size of the area affected is dependent upon the ground motion wavelength, and the influence of phasing when multiple frequency components are present. The area affected increases with increasing wavelength and decreases when the crest moves out of phase with the surrounding landmass.
- A strong vertical component of motion, comparable to the horizontal component of motion develops at the slope crest due to the development of surface waves. These waves propagate outward and downward from the crest. This occurs regardless of ground motion frequency content.

Topographic effects can be significant given the right conditions. The (c) frequency

sweep presented in Section 4.2 provided an example of idealized conditions for topographic effects and topographic amplification to occur. The ground motion was rich in frequencies near the topographic frequency, with little energy at competing frequencies. Energy near the topographic frequency was introduced quickly, but gradually built up in amplitude (see Figures 4.25 and 4.26). This allowed excitation, and softening within the slope landmass to occur before softening at the base of the slope occurred (Figure 4.28). Because the amplitude at other frequencies, and therefore the free field, was minimal, differential motion with the free field land mass also had less of an impact on the movement of the slope (Figure 4.29).

With the exception of the vertical component of motion, topographic effects can also be minimal if site effects and site amplification dominate the response. The effect of the slope is minimized for wavelengths which are large compared to the height of the slope. And the area behind the crest experiences a tendency towards resonance at the site frequency.

The response becomes particularly complicated when energy at both the site and topographic frequencies is comparable. Ground motion can either be impeded or enhanced. This interaction between site and topographic effects suggests that, although the behavior can be separated, it can't necessarily be decoupled. That is, it would be difficult to predict topographic effects without also understanding site effects and site conditions. This is in agreement with Assimaki et al. (2005a); Graizer (2009) and Tripe et al. (2013).

In order to understand the complexities, it is important to explore new methods for analyzing topographic effects. The methods utilized in this study, and outlined in this chapter, have proven to be very useful for interpreting the mechanisms and causes of topographic effects. Several of the methods applied have not been used in other studies of topographic effects to the knowledge of the author. In particular, the Stockwell spectrum, and the Stockwell MSF (newly introduced) should be used to track ground motion frequency content in time; the cumulative AI should be used to track changes in energy; the Hilbert transform should be used to track phasing between the crest and free field areas; and the effects of non-linearity, such as within the slope landmass and at the base of the slope, should be considered.

Chapter 5

TOPOGRAPHIC EFFECTS: REDCLIFFS, NEW ZEALAND CASE STUDY

The previous chapters presented a centrifuge investigation of topographic modification of ground motion. Various topographic effects were identified based on trends in the centrifuge data and were presented in Chapter 3. The mechanisms and causes of topographic effects were then demonstrated in Chapter 4. The aim of this chapter is to determine if the trends from the previous chapters are observed in data recorded in the field. This is accomplished by applying similar analysis methods to a New Zealand case study.

The case study presented in this chapter focuses on the steep Redcliffs ridge located in the Port Hills suburb of Christchurch, New Zealand, located about 7.5 kilometers from the city center. The Redcliffs site is part of an area that suffered extensive damage during the 2010-2011 Canterbury earthquake sequence (Revell and Browne, 2013). This prompted geotechnical exploration and further study of the area, including the installation of a downhole accelerometer array in Redcliffs. GNS Science of New Zealand established this downhole array as station $RCBS$ on 29 January 2013. More details about the Redcliffs site and downhole array are provided in Section 5.1.

Field case studies of topographic effects have typically been limited to aftershock recordings with sparse instrumentation, and often lack geological or geotechnical information necessary for the separation of site and topographic effects. Numerous case studies, including in the Redcliffs and Port Hills area (Holden et al., 2014; Kaiser et al., 2013, 2014), have been performed based on temporary seismic arrays installed across the surface of a geologic feature (Barani et al., 2014; Buech et al., 2010; Davis and West, 1973; Hailemikael et al., 2016; Hartzell et al., 2014, 2017, 1994; LeBrun et al., 1999; Massa et al., 2010, 2014; Pischiutta

et al., 2010; Spudich et al., 1996; Stewart and Sholtis, 2005; Stolte et al., 2017; Wood and Cox, 2015). As a result, topographic effects are often quantified and qualitatively analyzed without a true free field reference site for comparison. Instead, the sensor with the weakest ground motion recording, or one that is located at the toe of a slope, hill, ridge, or cliff, is often used as a reference sensor for calculating spectral ratios and for making intensity measure comparisons. Alternatively, horizontal to vertical (H/V) spectral ratios are determined for single sensor locations to identify site resonance (Nakamura, 1989) and capture topographic effects (Cháves-García et al., 1996, 1997; Panzera et al., 2011).

Utilizing the downhole array, a new method for determining the free field response is established as part of this case study. Based on data provided by GNS Science and reported in Revell and Browne (2013) and Tonkin & Taylor (2012), a baseline shear wave velocity profile was determined for the Redcliffs site. This profile was stochastically varied to produce 50 shear wave velocity profiles that considered the full range of available data. Using the downhole recording at station RCBS, 50 free field simulations were performed using ProSHAKE (Edu, 1998-2017) for each ground motion. These free field simulations were then compared to the RCBS surface recordings to identify the effects of topography at the Redcliffs site. This process, and other analysis methods used in this study are described in more detail in Section 5.2.

5.1 Site and Data Description

5.1.1 Site Description

The Redcliffs site consists of a 15 to 50 meter high ridge, with cliff faces near the RCBS station ranging from 30 to 40 meters high (see Figures 5.1 and 5.2). For the various cross sections shown in Figure 5.2, the width at the base of the ridge (which may include build-up from rock fall) ranged from about 170 meters (S-N and NNW-SSE directions) to 480 meters (NE-SW direction). The crest-to-crest width (i.e., the distance from cliff crest to cliff crest) of the ridge ranges from 110-120 meters (S-N and NNW-SSE directions) to 380 meters (NE-

SW direction). The RCBS station is about 15 meters from the nearest cliff face, measured in the direction labeled perpendicular (NE-SW direction) in Figure 5.1, and about 40 meters from the nearest cliff face in the direction labeled parallel (SE-NW direction). The cliff faces at Redcliffs are generally have inclinations greater than 60 degrees.

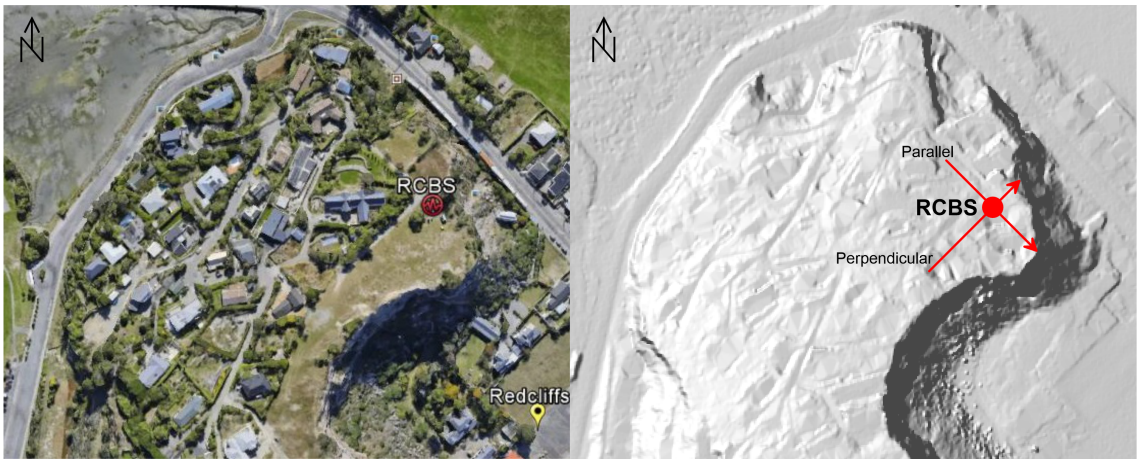

Figure 5.1: Google Earth (Google Earth, 2016) image (left) and hill shade (right) of the Redcliffs site. The approximate location of the RCBS station, representing the downhole accelerometer array, is marked on both maps. The perpendicular and parallel components of motion analyzed in this study are marked by red arrows (pointing in the positive direction) on the hill shade map.

The RCBS station is located at latitude, longitude, -43.557934, 172.73265, at an elevation of about 35 meters above sea level. The array consists of two Kinemetrics force balance accelerometers, with one installed at the ground surface and another installed at a depth of about 39.5 meters. Near the location of the array, the cliff is composed of about 3 meters of loess and colluvium, underlain by the Mount Pleasant Formation. The Mount Pleasant Formation consists of moderately weathered tuffaceous sandstone and lapilli tuff, moderately weathered lahar deposits, slightly to highly weathered basalt breccia and slightly to highly weathered basalt (Revell and Browne, 2013).

Redcliffs has experienced earthquake induced rockfalls, slides, slumps, debris avalanches and cliff-top cracking (Kaiser et al., 2013, 2014; Massey et al., 2016a,b). The rockfall and debris avalanches have led to the build up of talus at the base of the slopes (see Figures 5.3

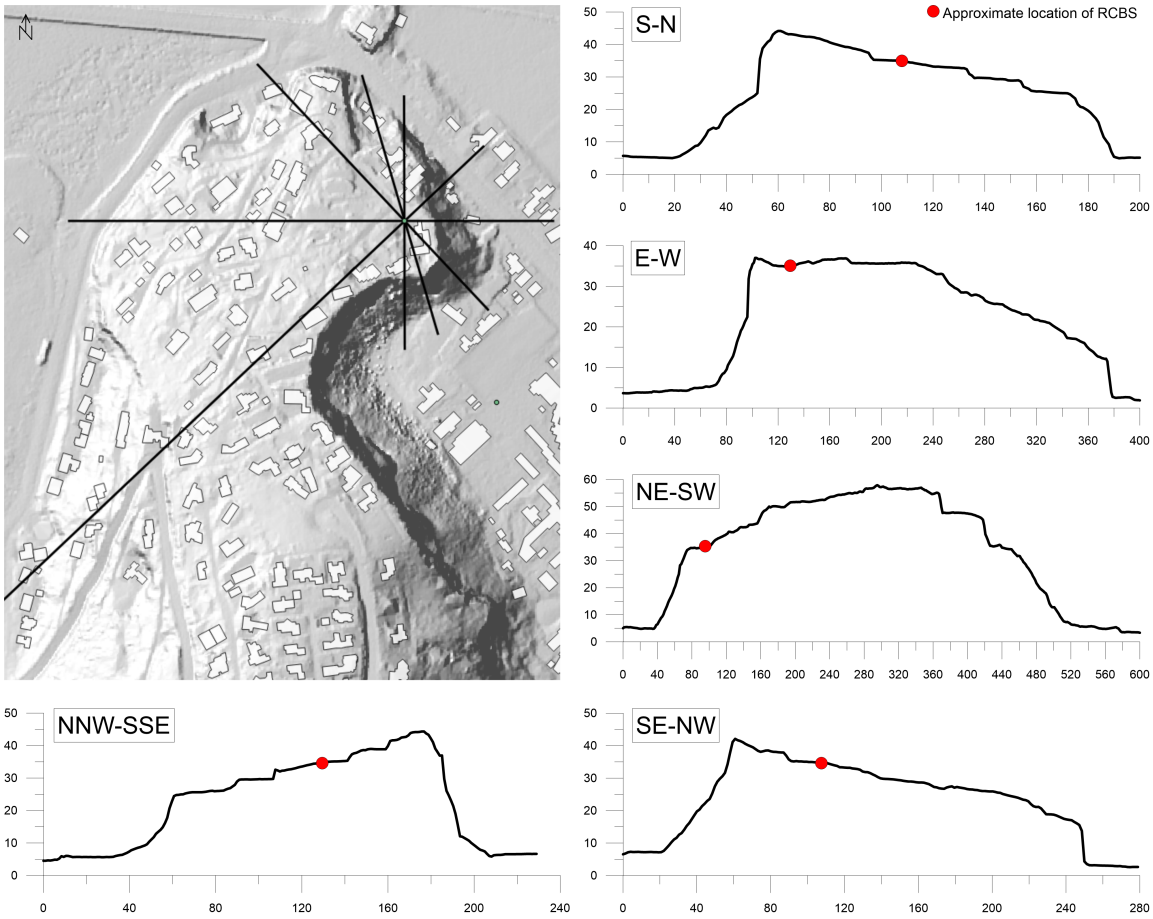

Figure 5.2: Hill shade image of Redcliffs (upper left corner) showing locations of cross sections plots. The RCBS station is at the intersecting location of the cross sections and is marked by a green dot on the hill shade image. The approximate location of the RCBS station is marked by a red dot on the cross sections. Dimensions are reported in meters.

and 5.4), but more importantly have also induced damage to structures near the base of the Redcliffs slopes. Structures on top of the ridge are also susceptible to stronger shaking as a result of site and topographic amplification. It is important to understand these phenomenon so that impacts on slope stability and structural demand can be assessed.

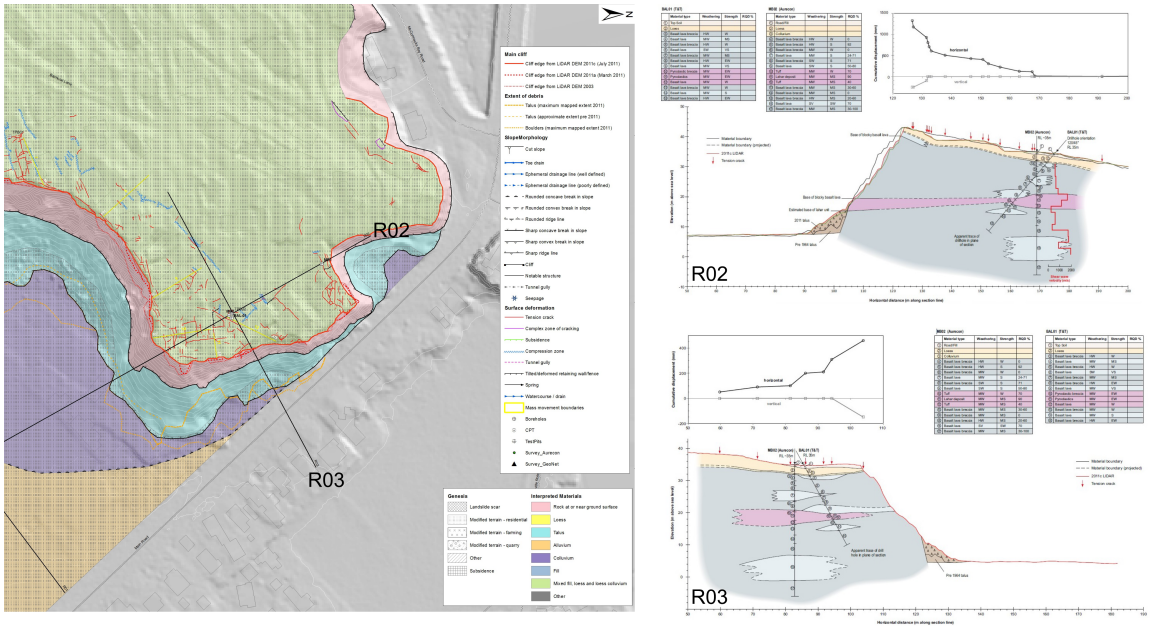

Figure 5.3: Plan view and cross sections provided by GNS Science. Cross sections are labeled according to the GNS Science labeling system. Redcliffs lithology is provided on the plan view and cross sections. Boring locations and shear wave velocity information is also provided on the cross sections.

5.1.2 Ground Motions

Data recorded at the RCBS station was obtained from the GNS Science and Earthquake Commission (EQC) website, GeoNet (GNS Science and EQC, 2017). Between the instrumentation installation date and April 2017, 17 seismic events were recorded, processed and made available for download. Of the 17 events, 5 were eliminated due to peculiarities with the data or a low signal to noise ratio (i.e., below 2). Information about the 12 remaining ground motions analyzed in this study is provided in Table 5.1. Three components of ground motion were recorded for each event, two horizontal and one vertical. After processing, the

Table 5.1: Ground motion parameters for the earthquake motions (Figure 5.5 and 5.6)

ID	Date	M	Depth (m)	R (m)	Bearing	V PGA (mm/s^2)	HT PGA (mm/s^2)	HL PGA (mm/s^2)	Location
1	20 Jul 2013	5.83	19.8	261	N32E	2.1	5.0	4.5	surface
						1.6	3.5	3.5	base
2	21 Jul 2013	6.54	16.8	253	N32E	5.8	11.7	9.9	surface
						5.0	6.7	5.5	base
3	29 Jul 2013	4.75	8.9	99	N04W	3.5	7.1	8.7	surface
						2.7	6.6	4.7	base
4	16 Aug 2013	6.64	8.2	234	N30E	23.2	48.5	40.3	surface
						19.3	25.3	39.1	base
5	16 Aug 2013	5.39	5.8	229	N30E	5.6	13.7	10.5	surface
						5.0	7.9	9.1	base
6	16 Aug 2013	5.55	8.5	229	N29E	13.9	29.7	30.7	surface
						11.2	20.2	19.5	base
7	16 Aug 2013	5.01	17.3	226	N29E	2.6	5.5	3.7	surface
						2.1	2.4	2.6	base
8	16 Aug 2013	5.59	19.4	238	N30E	3.3	6.1	4.6	surface
						1.6	2.3	2.3	base
9	16 Aug 2013	4.89	21.1	231	N29E	3.1	7.1	4.4	surface
						1.8	2.1	2.5	base
10	16 Aug 2013	5.96	14.3	245	N31E	11.3	23.2	24.8	surface
						10.9	17.9	21.1	base
11	16 Aug 2013	5.49	19.6	245	N32E	3.5	8.0	7.0	surface
						2.9	4.4	4.2	base
12	16 Aug 2013	4.67	26.6	223	N32E	2.5	4.4	3.5	surface
						0.8	1.6	1.7	base

M = earthquake magnitude; R = epicentral distance; PGA = peak ground acceleration; V = vertical; HT = horizontal transverse (north); HL = horizontal longitudinal (west)

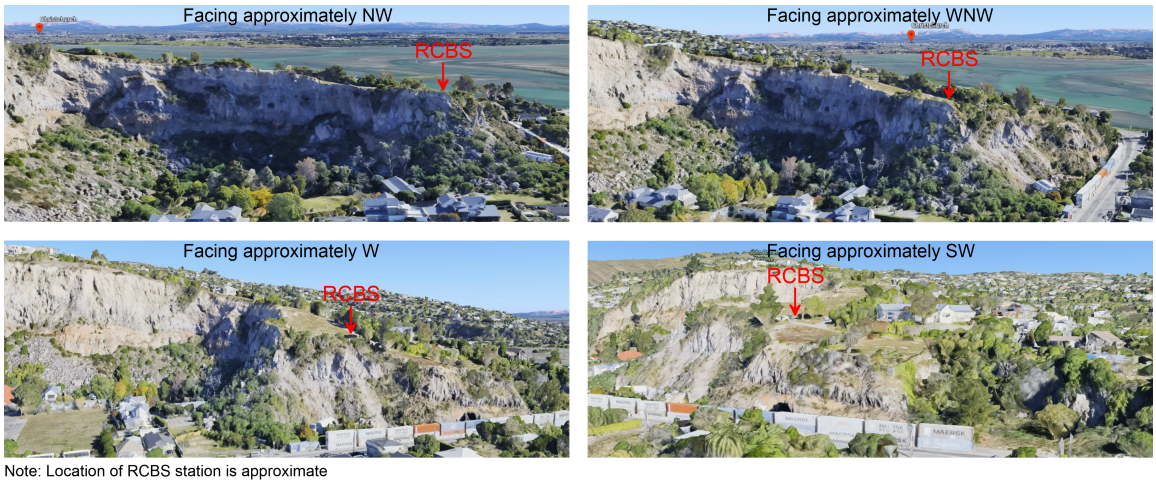

Figure 5.4: Four Google Earth (Google Earth, 2016) images of Redcliffs facing the approximate directions provided. The approximate location of the RCBS station is also given.

longitudinal component was oriented positive west and the transverse component was oriented positive north. For the purpose of analyzing the data in the framework of topographic effects, these components were rotated relative to the nearby cliff faces. The transverse component was rotated to be roughly parallel to the nearest cliff face (about 15 meters from the RCBS station, as mentioned above), and the longitudinal component was rotated to be roughly perpendicular to the nearest cliff face. This required a rotation of 225 degrees; 45 degrees to get the proper alignment and another 180 degrees so that positive was towards the nearest cliff faces (indicated by the arrows in Figure 5.1). It should be noted that the parallel component is indeed roughly parallel to the *nearest* cliff face, but it is also perpendicular to a different cliff face about 40 meters away. Plots of the base, and crest recordings, along with a representative simulated free field motion, for the perpendicular, parallel, and vertical components, is provided for the 12 ground motions in Figures 5.5 and 5.6.

The data set analyzed is limited to weak ground motions with peak ground accelerations ($PGAs$) ranging from 0.6 to 48.5 $mm/s/s$ (i.e., less than 0.005g) at the ground surface. The 12 seismic events occurred on six different dates between 17 February 2013 and 16 August 2013. It should be noted that a larger seismic event occurred in the region on 14 February 2016 (deemed the"Valentine's Day earthquak") and a PGA of 0.28g was recorded at the

surface sensor of the RCBS station (Massey et al., 2016a). This data was made available by GNS Science, but was not posted on the GeoNet website. It was discovered that the base sensor only recorded noise during the event. Attempts were made to use outcrop motions at other GeoNet stations, but differences in the ground motions were too significant for use in this case study. It is possible that the downhole sensor malfunctioned some years ago, which may explain why data for the RCBS station has not been posted since the 16 August 2013 events.

5.2 Analysis Methods

For this study, topographic effects and topographic amplification were analyzed in a manner similar to that presented in Chapter 3. Topographic effects are quantified and qualitatively analyzed by making comparisons between the crest and free field, and crest and base ground motions. However, definitions of the *topographic factor* (TF) and *apparent amplification* (AA), for example, will not be repeated here. The reader is referred to Section 3.2 in Chapter 3 and the Chapter 3 Glossary prior to reading Section 5.3.

In comparing the centrifuge experiments to the Redcliffs site, differences in the site conditions and available data must be acknowledged. The centrifuge experiments were set up to model slopes that could be analyzed in two dimensions. At Redcliffs, however, the influence of the 3-D structure must be considered. The slopes analyzed in the centrifuge experiments consist of soil slopes with inclinations of 30 degrees or less, while at Redcliffs, the nearby cliffs are typically greater than 60 degrees and mainly consist of weathered rock. Additionally, the data at the Redcliffs site is confined to two locations (one surface, one base), whereas the centrifuge experiment was densely instrumented. Therefore, although the inherent heterogeneity is greater for the Redcliffs site, the impact of that heterogeneity and the spatial variability of topographic effects cannot be explicitly considered.

Another difference between the centrifuge experiments and the Redcliffs site, is the availability of data recorded at a free field location. For the centrifuge experiments, data was recorded in the free field behind the slope crest. For Redcliffs, free field data does not exist.

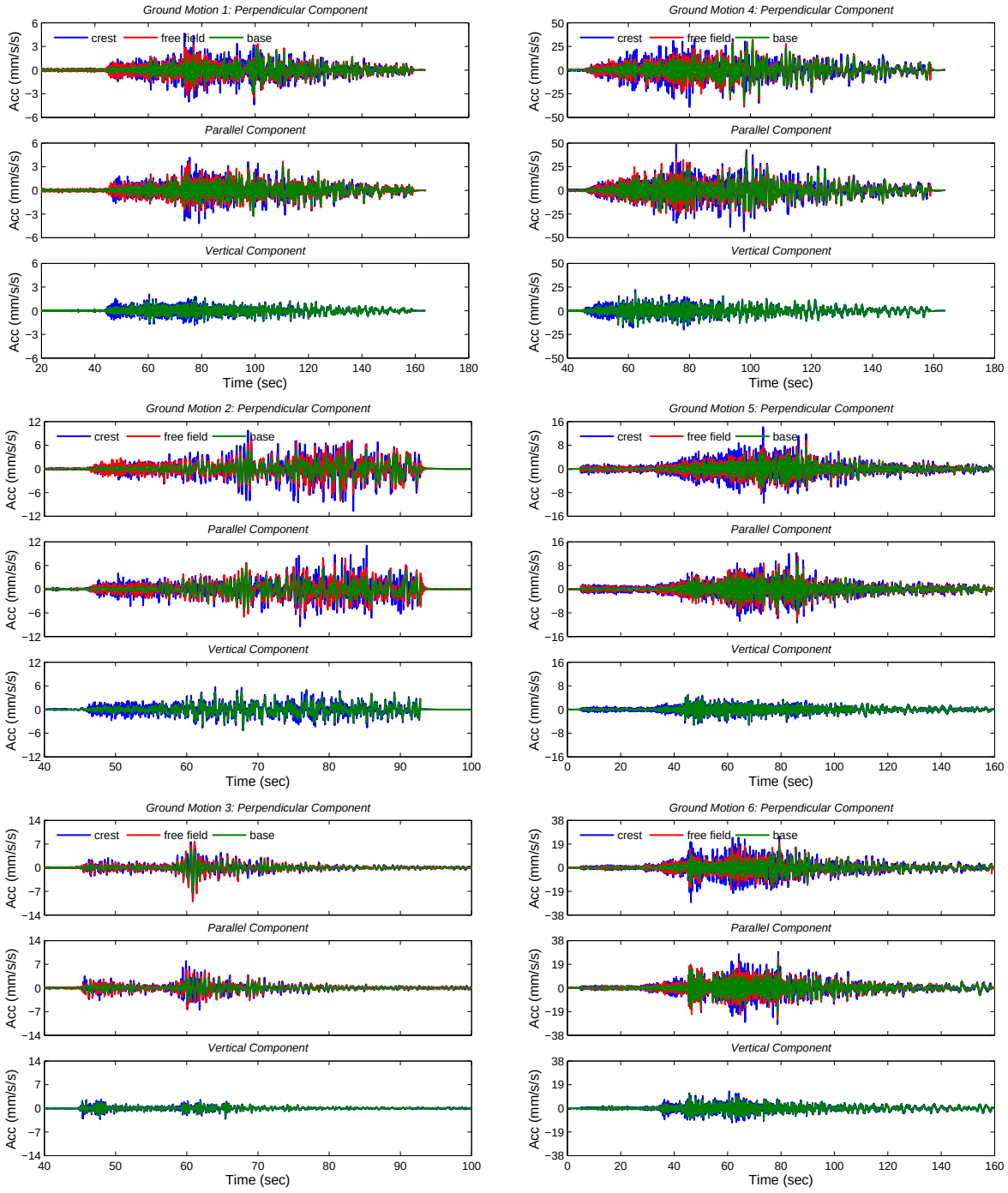

Figure 5.5: Ground motions 1 through 6 – acceleration time histories for the crest, free field, and base motions. The crest and base motions represent the surface and downhole recordings for the RCBS station, respectively. The free field consists of a representative surface motion based on 1-D analysis performed in SHAKE ((Edu, 1998-2017)). Perpendicular, parallel, and vertical components are provided.

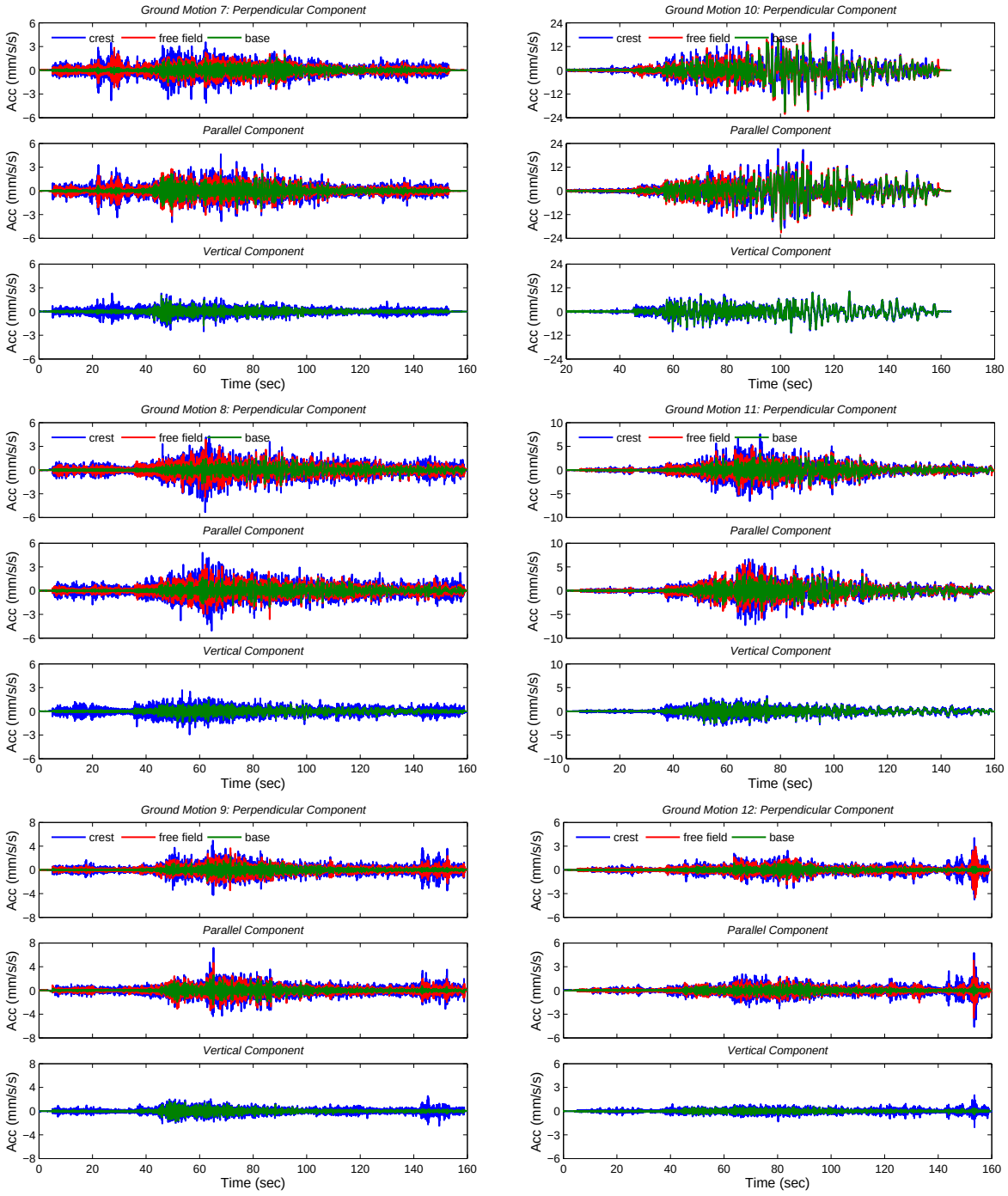

Figure 5.6: Ground motions 7 through 12 – acceleration time histories for the crest, free field, and base motions. The crest and base motions represent the surface and downhole recordings for the RCBS station, respectively. The free field consists of a representative surface motion based on 1-D analysis performed in SHAKE ((Edu, 1998-2017)). Perpendicular, parallel, and vertical components are provided.

To enable comparisons between the free field and crest, and thus identify topographic effects, the free field response was simulated. This is discussed in the subsection below. Differences between the analysis methods outlined in the previous chapters and those used for this case study are highlighted in the subsection that follows.

5.2.1 Free Field Analysis

Understanding the expected free field response is critical to understanding the effects of topography on ground motion. By comparing the free field response to that near or on a topographic feature, differences in behavior, and thus topographic effects can be observed. For a more direct comparison, the subsurface below the topographic feature should be consistent with that below the free field and the ground motions introduced to the sites should be similar. This was accomplished by using the downhole data recorded at the RCBS station and establishing a statistically robust range of shear wave velocity profiles for the site based on available data.

Shear Wave Velocity Profiles

Shear wave velocity uncertainty consists of both epistemic and aleatoric uncertainty. Epistemic uncertainty can be reduced by increasing knowledge of the shear wave velocity, such as by collecting more data or using better data collection methods. Aleatoric uncertainty cannot be reduced as it is related to the inherent variability within a soil or rock mass. One way to account for this uncertainty in the shear wave velocity, and subsequently in the free field response, is to stochastically vary the shear wave velocity and consider a number of profiles within an analysis. In other words, the shear wave velocity profile can be randomly varied based on a statistical distribution to develop a series of profiles, which can used to analyze site response.

The shear wave velocity profiles used in this study were developed using a stationary gaussian model outlined in Montalva (2010). The stationary model develops shear wave velocity profiles based on the log normal mean velocity profile, the coefficient of variation

(COV) for the profile, subsurface layering information and an auto-correlation factor between the subsurface layers (ρ). The first point in the shear wave velocity profiles is developed based on values determined through a randomly generated Gaussian process, and the log normal standard deviation of the initial profile (calculated based on the COV). The difference between these values and the log normal mean is then determined (ϵ). The ϵ and ρ values are then used, along with the log normal standard deviation, and randomly generated Gaussian values, to determine the shear wave velocities for the next subsurface layer. This process is repeated for the number of profiles, layers and depths desired.

Using the process outlined above requires the evaluation of a baseline shear wave velocity profile. The baseline profile was developed for this study based on data provided by GNS Science and reported in GNS Science (2013b); Revell and Browne (2013) and Tonkin & Taylor (2012) for the Redcliffs site. Subsurface data was obtained through rock coring in five borings, and seismic cone penetration tests in the loess and colluvium. Lab testing and downhole geophysics were used to determine rock mass properties (Revell and Browne, 2013; Tonkin & Taylor, 2012), including the rock unit weight and shear wave velocity. Shear wave velocity ranges provided by GNS Science for the loess and different rock types were used along with the geophysics data to establish a lower and upper bound shear wave velocity profile. The log normal mean shear wave velocity profile was computed based on these bounds. It should be noted that shear wave velocity data for rock was obtained in a boring adjacent to that drilled for installation of the RCBS accelerometer array.

A COV of 0.2 was adopted for this analysis based on the available data and previous studies. Assuming the shear wave velocity bounds computed for the Redcliffs site represent two standard deviations, a maximum and average COV of 0.23 and 0.12 were determined, respectively. This is slightly below the average for the Kiknet network in Japan of 0.27, and 0.26, for seismic site classes A and B, and site class C, respectively, (Montalva, 2010). The Kiknet database was found to be statistically consistent with strong-motion data from the Canterbury region (where Redcliffs is located), when considering ground motion prediction equations ($GMPEs$) for surface response (Chen and Faccioli, 2013). At the RCBS station,

the Redcliffs site was defined as site class B in Massey et al. (2016a), but the shear wave velocities in the upper 28 meters are more consistent with site class C.

Use of a lower COV than the average for these regions is justified in that geophysics data is available for the Redcliffs site. Considering variation in the shear wave velocity in the upper 30 meters of a site (V_{s30}), Moss (2008) found a COV ranging from 1% to 6% for data collected using geophysics, depending on the method used. He also found that COV ranged from 20% to 35% if the shear wave velocity was determined based on matching values to a geologic profile. Therefore, a value of 0.2 may be slightly conservative considering the available data. A value of 0.2 was used, however, for the Thyspunt nuclear facility, for which multichannel analysis of surface waves ($MASW$) and downhole PS suspension logging was performed at 6, and 29 locations, respectively (Rodriguez-Marek et al., 2014).

The subsurface was divided into layers according to the baseline shear wave velocity profile and lithology at the site. The shear wave velocity profiles were calculated between the ground surface and downhole instrument depth of approximately 40 meters. For the purposes of the calculation, the subsurface between 0 and 40 meters depth was divided into 1 meter layers. This allowed boundaries representing a strong impedance contrast to be respected, such that an auto-correlation factor of zero (i.e., $\rho = 0$) could be applied between layers above and below the contrast.

Strong impedance contrasts exist at depths of 3 and 28 meters below the ground surface at the location of the RCBS station. The contrast at 3 meters represents the soil-to-rock contact and the contrast at 28 meters represents a contact between weathered and more intact rock. The stationary model was set up such that the shear wave velocity of soil did not influence that of the weathered rock and that of the weathered rock did not influence the more intact rock. Within the soil and more intact rock layers, $\rho = 1$ was used, meaning a constant shear wave velocity was maintained through these layers for the each shear wave velocity profile (although the value varied from profile to profile). In between the strong impedance contrasts (i.e., between 3 and 28 meters), constant shear wave velocities were applied over 4 meter depth intervals, with a 1 meter thick interval between 27 and 28 meters. Between

these layers, $\rho = 0.75$ was used, which is in about in the middle of the ρ values identified for single-layer and two-layer correlations for the Kiknet data in Montalva (2010).

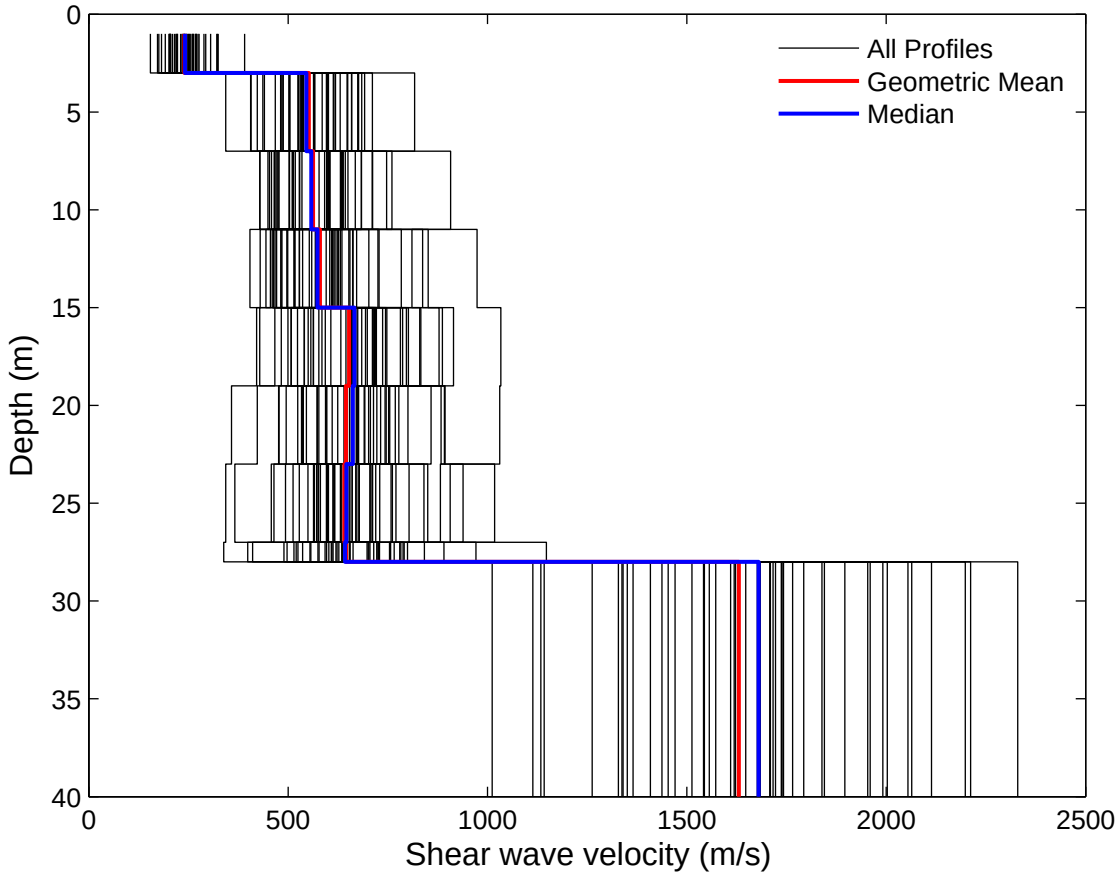

Figure 5.7: Stochastic variation of the site shear wave velocity profile based on data from (GNS Science, 2013b; Revell and Browne, 2013; Tonkin & Taylor, 2012). The 50 profiles were considered in evaluating the free field response at the site.

Using the parameters outlined above, 50 shear wave velocity profiles were developed to analyze an equivalent free field response for the Redcliffs site. The shear wave velocity profiles, along with the geometric mean and median of the 50 profiles are provided in Figure 5.7. The profiles span and exceed the upper and lower bounds identified through analysis of the available data for the site. Additionally, the median and geometric mean are similar to the log normal mean profile originally determined from the data. Therefore, 50 profiles is sufficient for considering the uncertainty in shear wave velocity at the site.

SHAKE Analysis

Free field simulations were performed using a Matlab (MATLAB, 2011) script designed to perform ProSHAKE (Edu, 1998-2017) analysis. The script allowed batch analysis, meaning a number of simulations could be performed sequentially without the burden of setting up new files in ProSHAKE (SHAKE). The calculations performed by the script and SHAKE, however, are identical.

SHAKE analysis was performed for the parallel and perpendicular components of motion (previously described) for each ground motion, for each of the 50 shear wave velocity profiles (Figure 5.7. The surface and base motions were retained for each simulation, and simulated ground motion at other subsurface locations was discarded. The simulated base and surface motions were then compared to the recorded base motion (i.e., that at the downhole accelerometer of the RCBS station) and recorded crest motion (i.e., that at the surface of the RCBS station). Note that a simulated vertical component of motion does not exist in the free field.

Typically SHAKE analysis is performed such that the base motion is initiated at the location of a strong impedance contrast, such as a soil-to-rock contact. At the RCBS station, this would correspond to a depth of about 28 meters. However, downhole data was recorded below, in this case, a transition from weaker to stronger rock, at a depth of about 40 meters. Therefore, to be consistent with the data, a site with a thickness of 40 meters was modeled. It should be noted, however, that the shear wave velocity used between 28 and 40 meters was also used for the infinite half space below 40 meters.

The recorded ground motions at RCBS represent "within" rather than "outcrop" motions. When ground motions are modeled as within motions in SHAKE, all energy in the system is reflected off the base layer. That is, no energy reflected off the surface is allowed to leave the system by propagating into the infinite half space below the modeled site. This is appropriate for modeling within motions as any energy that left the system would already be accounted for by the recorded within ground motion. Using the downhole data, and modeling the

Redcliffs site in this way, however, led to extreme resonance at the first and second modes of vibration. This produced ground motions much stronger than those actually recorded at the ground surface. This response can likely be tied to the damping curves used in the analysis.

The equivalent free field site for Redcliffs was modeled using built-in damping curves (as discussed below). These curves may not account for increases in damping, including radiation damping, associated with the presence of weathered zones or fracturing within the Redcliffs rock mass. Custom damping curves would have to be used for ground motions to be modeled as within motions. However, no data was available (including damping data or surface recordings free of topographic influence) to justify the development of these curves. Therefore, in order to obtain a more realistic response, the base ground motions were instead introduced as outcrop motions, which allowed energy to leave the system through the compliant base. This can be viewed as a limitation to adopting this approach for complex ground conditions. However, this could be remedied with additional site characterization.

Introducing the recorded base (within) motions as outcrop motions does have an additional limitation. Namely, because the shear wave velocity profile is varied, the base motion introduced to the modeled site also varies. However, as will be shown in Section 5.3, the various base motions introduced in SHAKE closely match that of the recorded base motion at the Redcliffs site (particularly at lower frequencies where amplification associated with the topographic frequencies calculated for the site are most pronounced). Additionally, by introducing the motions as outcrop motions, the influence of varying the shear wave velocity profile (i.e., that below the strong impedance contrast) is considered.

In addition to establishing a shear wave velocity and unit weight, modulus reduction and damping curves also had to be defined to simulate the free field response. Unit weights were obtained through data provided by GNS Secience (as previously mentioned). Modulus reduction and damping information, however, was not available for the site. Therefore, prior to performing the batch analysis, the effects of using various built-in modulus reduction and damping curves was explored. For this sensitivity analysis, the strongest ground motion (ground motion 4) was used for the following setups:

- Average Sand curves for entire profile, Rock curves for infinite half space;
- Darendeli curves for entire profile, Rock curves for infinite half space;
- Linear curves for entire profile, Rock curves for infinite half space;
- EPRI curves for entire profile, Rock curves for infinite half space;
- EPRI curves for loess, Rock curves for remaining profile and infinite half space;
- EPRI curves above strong impedance contrast (at 28 meters), Rock curves for remaining profile and infinite half space;
- Upper Bound Sand curves for loess, Rock curves for remaining profile and infinite half space; and
- Rock curves for entire profile and infinite half space.

Although some of these curves are likely not applicable to the site (i.e., the Darendeli and Average Sand curves), they were included as an extreme case to explore the potential influence of ground softening that may occur. However, it was concluded that the choice of modulus reduction and damping curves had a negligible effect on the surface response. In other words, the response was essentially linear elastic because the ground motion was not strong enough to induce significant strain levels within the ground mass. Because the strongest ground motion was used for this sensitivity analysis, it was assumed that the effects of using different curves would also be negligible for the remaining weaker ground motions. For the remainder of the analysis, the Upper Bound Sand curve was used for the 3 meter loess layer, and the Rock curves were used for the remaining profile and infinite half space.

5.2.2 Topographic Effects

With a reference free field station established, analysis of topographic effects was performed using the methods outlined in Chapter 3. However, the variation in the shear wave velocity profiles, and subsequently in the free field response had to be accounted for. In particular,

because the *topographic frequency* (defined by $f_t = \bar{V}_s/5H$, where $\bar{V}_s$ is the average shear wave velocity, and H is the slope height) and *site frequency* (defined by $f_s = \bar{V}_s/Z$, where Z is the site thickness) are dependent upon the site shear wave velocity, a range of values had to be established to account for the various shear wave velocity profiles. Additionally, the impact of changes in slope height at Redcliffs had to be considered in defining the topographic frequency.

The 3-D nature of the ridge at Redcliffs was considered by analyzing components parallel and perpendicular to the nearest cliff face to the RCBS station. Directional polar plots were also utilized to observe directional changes in spectral and intensity measure amplitudes. Lastly, horizontal to vertical (H/V) spectral ratios (sometimes written as $HVSR$) were considered as a means of analyzing the ground motion data without the use of a references free field station. The H/V method gained traction as a method for identifying site resonances after the Nakamura (1989) paper was introduced. These additional methods and considerations are outlined in more detail in the next section.

5.3 Analysis Results

This section presents results of the analysis of topographic effects for the Redcliffs site. The section first discusses the range of topographic and site frequencies to be considered for the site. Analysis results are then presented for a single ground motion, emphasizing comparison between the range of free field responses and the ground motion recordings. Analysis results for all the ground motions are then presented. The analysis results for the single ground motion concentrate on horizontal ground motion. The vertical component of motion, however, is considered in the presentation of all ground motions.

5.3.1 Topographic and Site Frequencies

Parameters for the site, such as slope height (H) and substratum thickness (Z), had to be defined in order to interpret the topographic and site frequencies for Redcliffs. A value of 28 meters, representing the depth to the strong impedance contrast between weaker and

stronger rock, at the RCBS station, was chosen as a value for Z. This depth also roughly coincided (within a couple meters) with the slope height of the nearest cliff face (i.e., in line with the perpendicular component of motion; Figure 5.2). Therefore a value of 28 meters was also chosen to represent H for one iteration of the topographic frequency. For a second iteration of the topographic frequency, $H = 35$ meters was selected based on the mid-range cliff height for the nearest cliffs in the perpendicular and parallel directions (cliff heights varied from roughly 30 to 40 meters).

The range of topographic and site frequencies defined for the 50 shear wave velocity profiles are plotted against each other in Figure 5.8 for the Z and H values given above. From this figure, it can be observed that the site frequency is greater than the topographic frequency for the profiles considered. For $\bar{V}_s$ values ranging from about 380 to 710 meters per second (m/s), the site frequency ranges from about 3.4 to 6.3Hz; and the topographic frequency ranges from about 2.2 to 5.1Hz (2.7 to 5.1Hz for the first iteration and about 2.2 to 4.0Hz for the second iteration). It should be noted that $\bar{V}_s = \sum d_i / \sum d_i / V_{si}$, where d is the layer thickness, and V_s the shear wave velocity for layer i.

The geometric mean $\bar{V}_s$ of the 50 shear wave velocity profiles is about 455 m/s. For this mean profile, the site frequency is about 4.1Hz, and the topographic frequency is about 3.2Hz and 2.6Hz for the first and second iteration, respectively. A mean topographic frequency of 3.2Hz was adopted for the analysis results presented below as it is more representative of the nearest cliff face to the RCBS station. Additional discussion of the variation in the topographic frequency based on varying ridge height is reserved for Section 5.3.2.

It should be reiterated here that the topographic frequency is based on the definition by Ashford et al. (1997) where $f_t = \bar{V}_s/5H$, and not the definition suggested by Geli et al. (1988) and later modified by Paolucci (2002) where $f_t = (0.7 - 1.0)\bar{V}_s/2L$, where $2L$ is equal to the width of the topographic feature. This is consistent with the definition used throughout this dissertation. However, it should be noted that numerous researchers have performed case studies using the Paolucci (2002) definition (see for example the summary in Pagliaroli et al., 2011). Use of each frequency is discussed further in the next subsection.

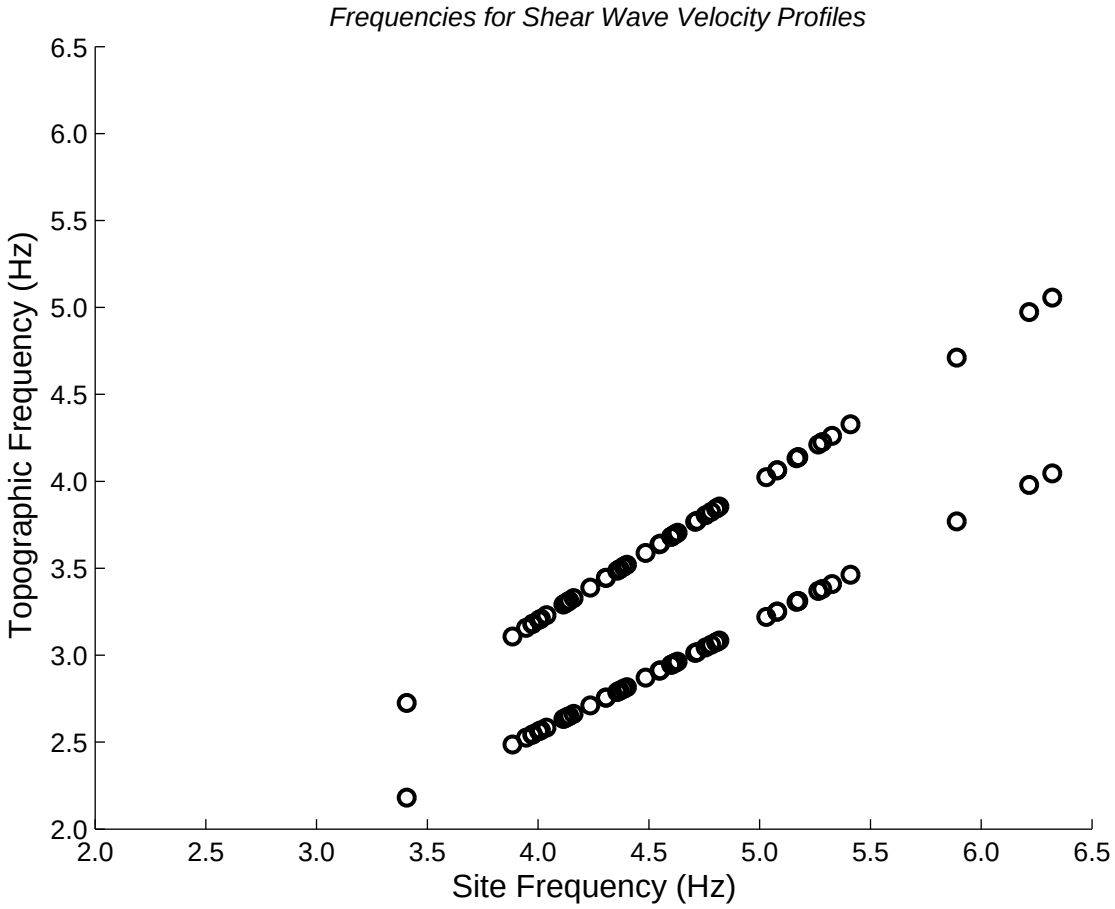

Figure 5.8: Topographic frequency versus site frequency based on the 50 shear wave velocity profiles. Two different ranges of topographic frequency are considering due to the variation in height between the slope face and the RCBS station.

5.3.2 Single Ground Motion

This section presents analysis results and data for ground motion 9 (see Table 5.1. These plots were produced and interpreted for all ground motions and the results were found to be consistent with those presented here. Ground motion 9 was selected, as it represented a ground motion for which topographic effects were more pronounced than some of the other motions.

Figure 5.9 provides acceleration time histories for the perpendicular (left) and parallel (right) components of motion. The data recorded downhole (i.e., the base motion) and at the surface (i.e., the crest motion) are plotted in green and blue, respectively. The middle plot

shows the 50 free field simulations in gray, and the data at the crest in blue. The bottom plot shows the 50 base (input) simulations in gray, and the data at the base in green. The figure demonstrates that the difference between the simulated input motions and recorded input motions is small. Differences between the surface motions, however, are more significant. The amplitude at the crest is greater than the range of free field simulations over short instances at various portions of the time history. For this ground motion, these differences are more pronounced for the perpendicular component of motion.

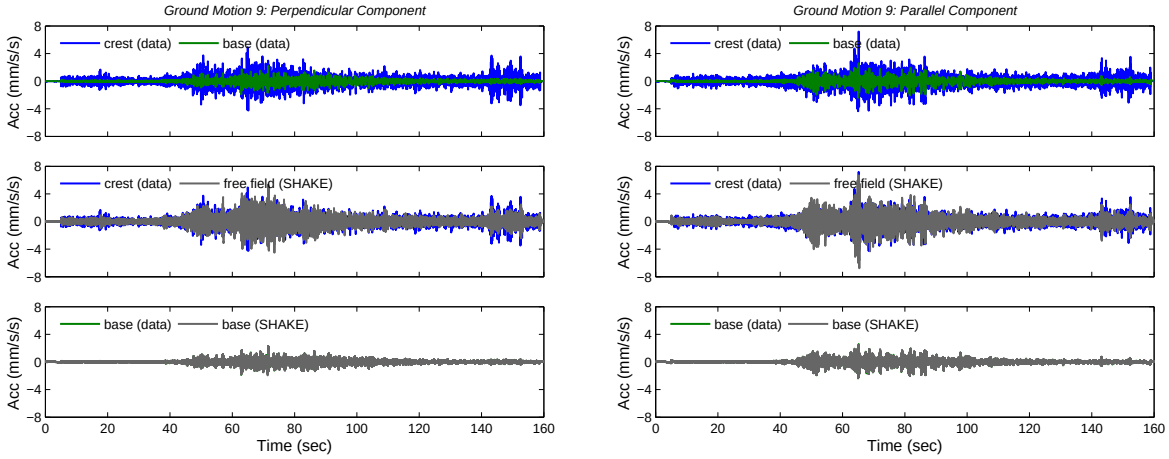

Figure 5.9: Ground motion 09 – acceleration time histories for the perpendicular component (left) and parallel component (right) of motion. The top plots consist of the downhole (base) and surface (crest) recordings. The middle plots compare the 50 free field simulations to the crest recording. The bottom plots compare the 50 base simulations to the base recording.

Differences between the ground motion simulations and RCBS data are more easily identified by inspecting the Fourier spectra of the ground motions. In particular, differences in the amplitude at various frequencies can be observed. Figures 5.10 and 5.11 show the Fourier spectra for the 50 ground motion simulations for the perpendicular (left) and parallel (right) components of motion as compared to data for the base, and ground surface, respectively. The geometric mean, and mean plus or minus a standard deviation, for the ground motion simulations are plotted using solid, and dashed red lines, respectively. Data is plotted in blue for both figures.

The Fourier spectra for the simulated base ground motions closely matches that of the

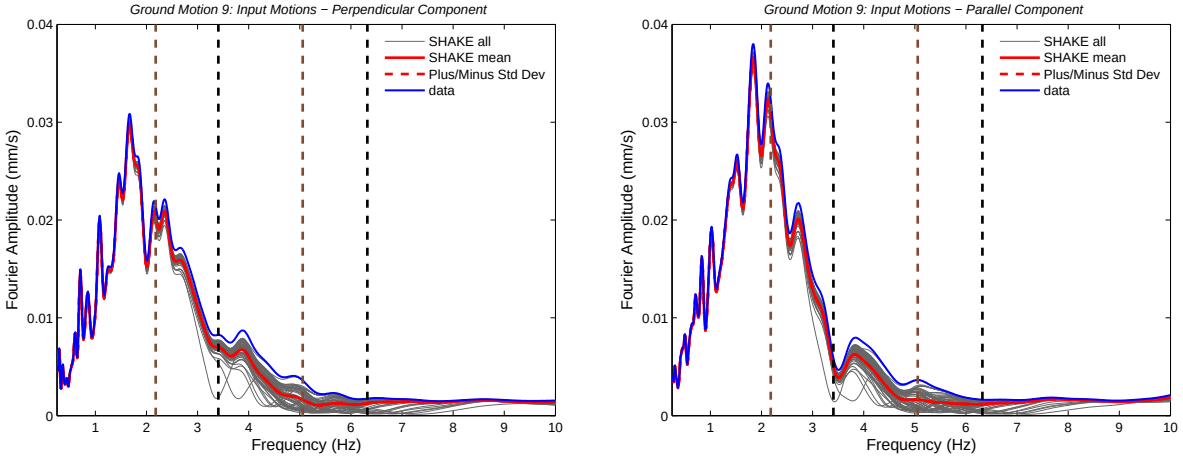

Figure 5.10: Ground motion 09 – Fourier spectra for the perpendicular component (left) and parallel component (right) of motion. The downhole (base) recording is compared to the 50 base simulations with geometric mean and mean plus/minus a standard deviation. Vertical dashed brown lines bound the range of topographic frequencies, and vertical dashed black lines bound the range of site frequencies, for the 50 shear wave velocity profiles.

data for both the perpendicular and parallel components of motion. However, some deviation does occur between about 3 and 8Hz. Through this frequency range, the amplitude of the data is greater than that of the simulations. This is likely a result of the data being introduced as an "outcrop" motion, as previously discussed. The outcrop motion is deconvolved to convert it from a surface outcrop motion to a "within" motion at some selected depth. Because ground motion is typically amplified at the surface compared to within the ground, the input motion is deamplified as a result of this process. It should be noted that the geometric standard deviation does not significantly deviate from the geometric mean, meaning the variation in simulated ground motion is not significant.

The reduction in the base ground motion amplitude between 3 and 8Hz likely results in a reduction in the modeled free field response in this frequency range. Amplification at the crest (compared to the free field) therefore may be enhanced for this frequency range. However, the frequencies at which amplification occurs, particularly at the mean topographic frequency (which is close to 3Hz and less affected), can still be clearly identified.

Figure 5.11 reveals that the free field motion simulations do match or encompass the

range of amplitudes recorded at the crest across most frequencies. Therefore, for the given range of possible profiles, it may be that the amplitude recorded at the surface can be explained by site effects alone. However, closer inspection of Figure 5.11 reveals that the majority of the simulated motions have frequency bands with lower Fourier amplitudes than the ground motion at the crest. The couple motions that do have greater amplitudes across most frequencies are likely outliers. This is evidenced by the geometric standard deviation, which again closely matches the geometric mean (which tends to give less weight to outliers than the arithmetic mean).

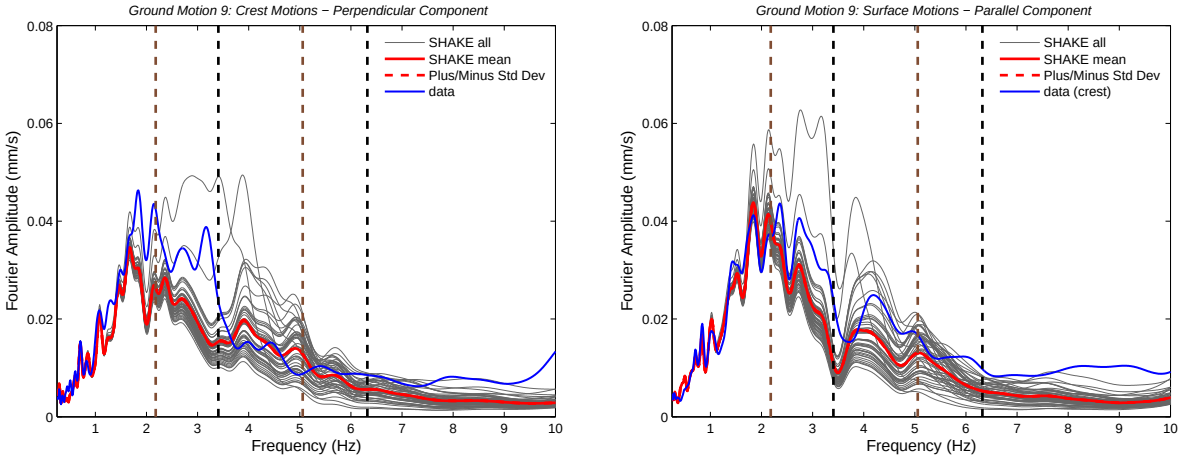

Figure 5.11: Ground motion 09 – Fourier spectra for the perpendicular component (left) and parallel component (right) of motion. The surface (crest) recording is compared to the 50 free field simulations with geometric mean and mean plus/minus a standard deviation. Vertical dashed brown lines bound the range of topographic frequencies, and vertical dashed black lines bound the range of site frequencies, for the 50 shear wave velocity profiles.

For the perpendicular component of motion, the response at the crest is amplified over the free field between about 1.7 and 3.7Hz. For the parallel component of motion, the amplified response of the crest over the free field is less pronounced and mainly occurs between 2.2 and 3.7Hz. However, the Fourier amplitude is also generally greater between about 4 and 5Hz for this component of motion. Note that the amplified response of the crest over the free field generally occurs within the bounds of the topographic frequencies previously discussed, marked by vertical dashed brown lines in Figures 5.10 and 5.11. It should also be noted

that the base motion is dominated by energy at low frequencies (in this case peaking around 1.7 Hz) for both components of motion. This is true of all motions in the data set used for this analysis. While these lower frequency components do exhibit some amplification at the surface, amplification is more pronounced at higher frequencies (such as those associated with the site and topographic frequencies). Thus, even though the input motion is rich in low frequency energy, the surface motion may have strong components of energy at higher frequencies as well.

While the raw Fourier spectra are informative, comparisons between the crest data and simulated free field response is more easily made using the *Fourier topographic factor* ($F\,TF$) spectrum. The $F\,TF$ spectra are provided for the perpendicular and parallel components of motion of ground motion 9 in Figure 5.12. As a reminder, a value below zero represents a deamplified response at the crest compared to the free field, and a value above zero represents amplification of the crest over the free field, or *topographic amplification*. Assuming the average shear wave velocity profile is the most representative of the site, the topographic frequency is about 3.2Hz for a cliff face of 28 meters. This frequency is marked by a vertical dashed black line spanning from the raw frequencies on the upper x-axis to the frequency normalized by the topographic frequency on the lower x-axis.

For frequencies below 7Hz, the maximum peak in the $F\,TF$ spectra, and thus maximum topographic amplification, consistently occurs at the mean topographic frequency for the perpendicular component of motion. For the parallel component of motion, maximum topographic amplification consistently occurs just above the mean topographic frequency at about 3.4Hz. This is evidenced by Figure 5.13 which plots the peak $F\,TF$ within the range of topographic frequencies calculated (see Section 5.3.1) versus the range of topographic frequencies calculated for the 50 shear wave velocity profiles. This shows that, with the exception of a couple simulations, maximum topographic amplification consistently occurs at the same frequency for the perpendicular (3.2Hz) and parallel (3.4Hz) components of motion. This provides confidence that amplification at these frequencies is, therefore, a result of topographic, and not site amplification.

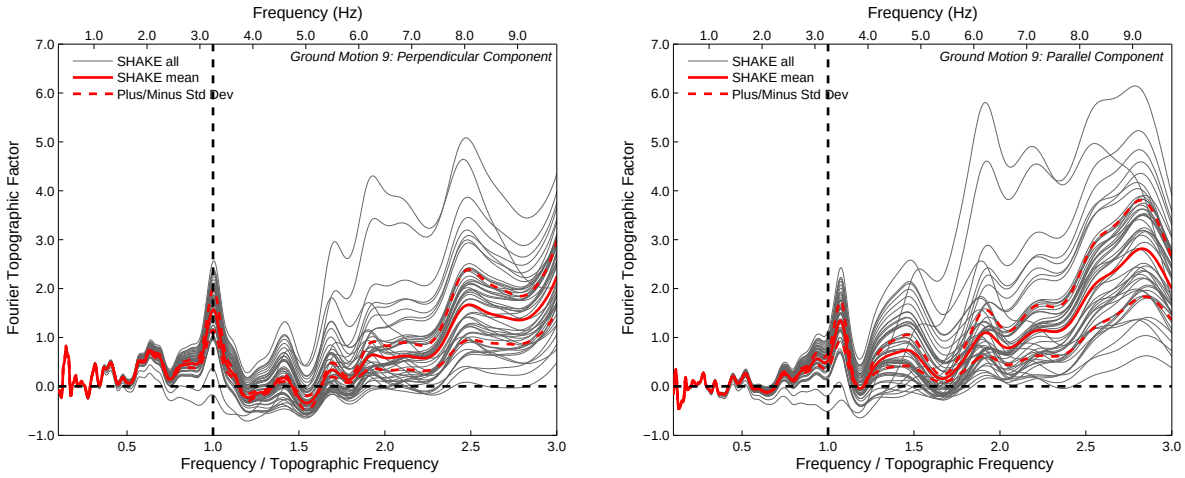

Figure 5.12: Ground motion 09 – $F\ TF$ versus frequency normalized by the mean topographic frequency for the perpendicular component (left) and parallel component (right) of motion. The $F\ TF$ is provided for the 50 simulations with geometric mean and mean plus/minus a standard deviation. The mean topographic frequency is based on the 50 shear wave velocity profiles and is marked by a vertical dashed black line. Raw frequency values are provided on the top x-axis.

The mean topographic frequency based on a 28 meter cliff height is shown on the plots in Figure 5.12. However, in reality the topographic frequency would change with slope height, even if only considering the mean shear wave velocity profile. This may help explain the small difference in frequency associated with the maximum $F\ TF$ (below 7Hz) between the perpendicular and parallel components of motion. This also provides insight into the other peaks in the $F\ TF$ spectra.

In the parallel direction (SE-NW), the top of the ridge slopes downward from SE to NW, such that the cliff face varies in height from about 35 meters to about 15 meters (see Figure 5.2). For these cliff heights, the mean topographic frequencies are about 2.6Hz for the 35 meter cliff and 6.0Hz for the 15 meter cliff. Peaks in the parallel $F\ TF$ spectrum exist near both these frequencies; the peak near 6.0Hz more pronounced.

The difference in elevation between the two slopes crests (42 and 17 meters for the taller and shorter cliffs, respectively) is about 25 meters, which also corresponds to the average cliff height. The mean topographic frequency is about 3.6Hz for a slope of this height, which closely matches the peak at 3.4Hz. Thus, it may be that the average cliff height or differential

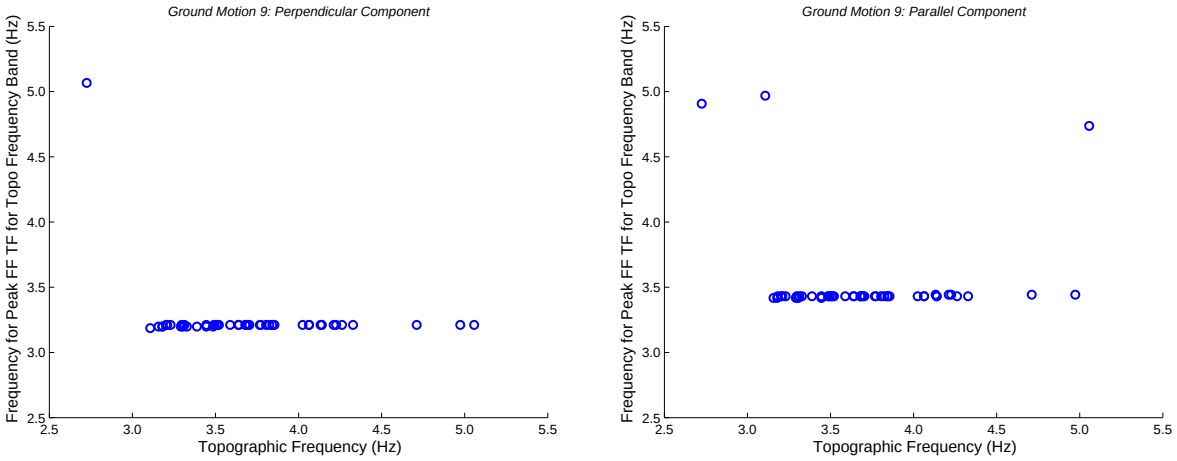

Figure 5.13: Ground Motion 09 – frequency at which the peak $F\ TF$ occurs within the range of topographic frequencies considered versus topographic frequency for the 50 free field simulations for the perpendicular and parallel components of motion.

cliff height should be considered when identifying topographic frequencies (depending on the shape of the ridge). The former may be more closely related to the overall movement of the ridge, while the latter may be related to differential movement, such as from oscillation of the ridge above the cliff crests.

The taller cliff face (35 meters) is about 40 meters from the RCBS station, while the shorter cliff face (15 meters) is roughly 140 meters away. Therefore, the expectation would be that the effects of the taller cliff would be more pronounced. However, the opposite appears to be true, in that topographic amplification near 6.0Hz is greater than at 2.6Hz. Although, it should be noted that the peak near 6.0Hz is not as well constrained (i.e., the standard deviation is greater) when considering the full breadth of free field simulations.

The shape of the ridge may explain the lack of strong amplification at 2.6Hz, in that the height of the ridge sharply decreases between the taller cliff face and the RCBS station. Therefore, a slope height of 35 meters may not be indicative of the behavior of the ground mass in the vicinity of the RCBS station. This also may be why the topographic frequency based on the slope height at the RCBS station better matches the peak in the $F\ TF$ spectrum.

The peak near 6.0Hz, and at higher frequencies, may be the result of other influences.

Aside from the shorter cliff face to the NW, the response at the RCBS station may be influenced by several smaller stepped slopes that exist along the ridge surface. The smaller slopes may oscillate at higher frequencies associated with their slope heights. The strong peak near 9Hz in the parallel FTF spectrum, for example, may be related to features that are about 10 meters in height, for which the mean topographic frequency would be 9.1Hz.

Another possible explanation for the strong peaks at higher frequencies is local site effects that are not captured by the 1-D free field simulations. The 1-D simulations do consider variation in the velocity structure, but do not consider changes in the substratum thickness above the strong impedance contrast (between weaker and stronger rock) or in the thickness of the upper loess/colluvium layer. Fracturing, and variation in the degree of weathering within the rock mass would also influence the surface response, but cannot be accounted for in the 1-D SHAKE simulations. In particular, rock blocks within the rock mass or highly weathered zones may oscillate at higher frequencies than the larger cliffs at Redcliffs.

As was discussed in Chapter 4, site and topographic effects cannot always be decoupled. This was recognized in relation to subsurface impedance contrasts in (Assimaki and Jeong, 2013; Assimaki et al., 2005a; Graizer, 2009; Hailemikael et al., 2016; Tripe et al., 2013). The interaction of topography with lateral heterogeneities (Imperatori and Mai, 2015; Takemura et al., 2015) and fracturing within a rock mass (Burjánek et al., 2012; Durante et al., 2017) has also been recognized to impact the surface response. Therefore, the amplified response at high frequencies is likely due to combined of site and topographic effects; partially explained by local site effects not captured in the free field simulations. This same logic can be applied for the amplification at higher frequencies in the perpendicular direction.

The peak between 4 and 5Hz may also be influenced by the factors explained above. However, this peak could also be explained by considering the narrower portion of the Redcliffs ridge oriented about NNW-SSE (5.2). For this cross section (which is close to the parallel direction), the shorter cliff face is about 18 meters in height and the difference in height between the shorter and taller cliff faces is about 20 meters. For these heights, the mean topographic frequency would be about 4.6 to 5.0Hz. In this case, the RCBS station is about

70 meters from the shorter cliff face. The average cliff height for this portion of the ridge is about 28 meters, which again aligns with the mean topographic frequency of 3.2Hz.

In the perpendicular direction (NE-SW), the cliff height is about 30 meters in height on both sides of the ridge (Figure 5.2). This corresponds to a mean topographic frequency around 3.0Hz (note that 28 meters, and 3.2Hz was used to be consistent with the height above the strong impedance contrast for the RCBS station). The ridge height increases gradually behind the RCBS station (i.e., moving away from the cliff face) on the NE side of the ridge and steps up on the SW side of the ridge to a height of about 50 meters. For a height of 50 meters, the mean topographic frequency would be about 1.8Hz. The perpendicular $F\ TF$ spectrum does have a smaller peak near this frequency.

Although not the focus of this study, the topographic frequency associated with the width of the feature should be considered (see Section 5.3.1). As with height, the width of a 3-D topographic feature can be difficult to define. Therefore, different frequencies can be considered depending upon the width chosen. If considering the base, or crest to crest width of Redcliffs, the mean topographic frequency would be below 2.6Hz for cross sections in the perpendicular and parallel directions. For the NNW-SSE, S-N and E-W sections (i.e., not in the parallel or perpendicular directions), the topographic frequency would be about 3.8 to 4.0Hz considering the crest to crest width. These frequencies do not correlate with strong peaks in the $F\ TF$ spectra for either component of motion. Widths associated with smaller features on the ridge (i.e., those at higher elevations), however, could be used to better match peaks in the data, as was proposed by Hartzell et al. (2017).

Both site and topographic amplification can be observed using the *Fourier apparent amplification* ($F\ AA$) provided in Figure 5.14 for the perpendicular and parallel components of ground motion 9. The free field simulations are again provided in gray with the geometric mean (solid line) and mean plus or minus a standard deviation (dashed line) in red. The free field simulations are normalized by the simulated base motions. Data is provided in blue, with the recorded crest response normalized by the recorded base motion. Values above and below zero represent amplification and deamplification, respectively of the surface over the

base.

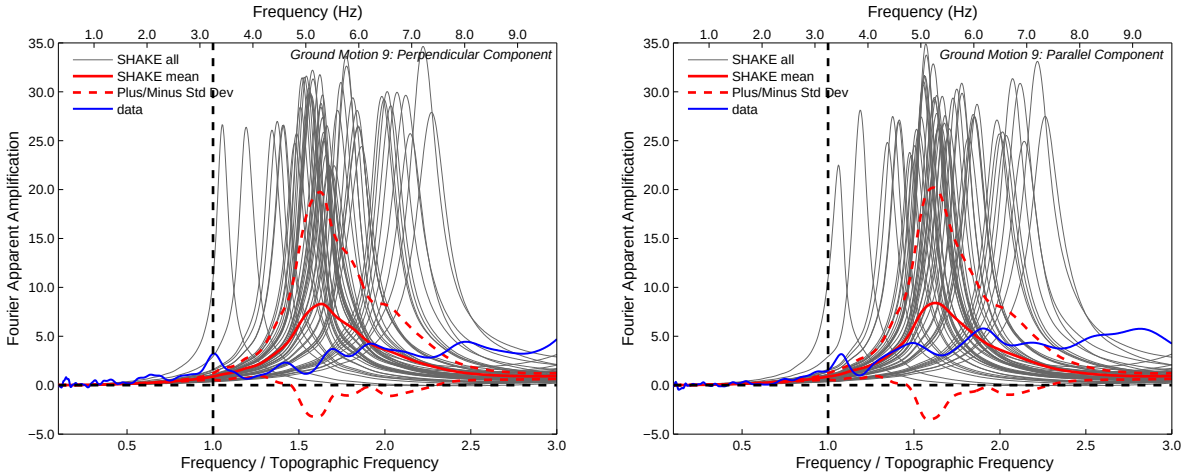

Figure 5.14: Ground motion 09 – $F\ AA$ versus frequency normalized by the mean topographic frequency for the perpendicular component (left) and parallel component (right) of motion. The $F\ AA$ is provided for the surface (crest) recording and the 50 free field simulations with geometric mean and mean plus/minus a standard deviation. The mean topographic frequency is based on the 50 shear wave velocity profiles and is marked by a vertical dashed black line. Raw frequency values are provided on the top x-axis.

As was previously noted, the simulated input motions were deamplified in comparison to the data at frequencies between 3 and 8Hz. These frequencies correspond to the first mode of resonance for the range of shear velocity profiles considered. This is illustrated in Figure 5.14, where peaks for the free field simulations range from roughly 3.5 to 7.5Hz, but are more concentrated in the range of 4.0 to 6.0Hz. The deamplification of the simulated input motions (in deconvolving from an outcrop motion) resulted in Fourier amplitudes near zero for the 3 to 8Hz frequency range. Consequently, the magnitude of AA is extreme for the free field case and dwarfs the AA calculated using the data. For this reason, the AA amplitude of the free field simulations should not be considered directly comparable to the AA amplitude of the data. Frequency content, however, is unaffected and thus the frequency at which peaks occur can be observed. It should be noted that the simulated free field amplitude (rather than amplification), however, is comparable to that recorded at the crest (see Figure 5.11).

A comparison of frequencies at which the peak AA occurred versus the site frequency

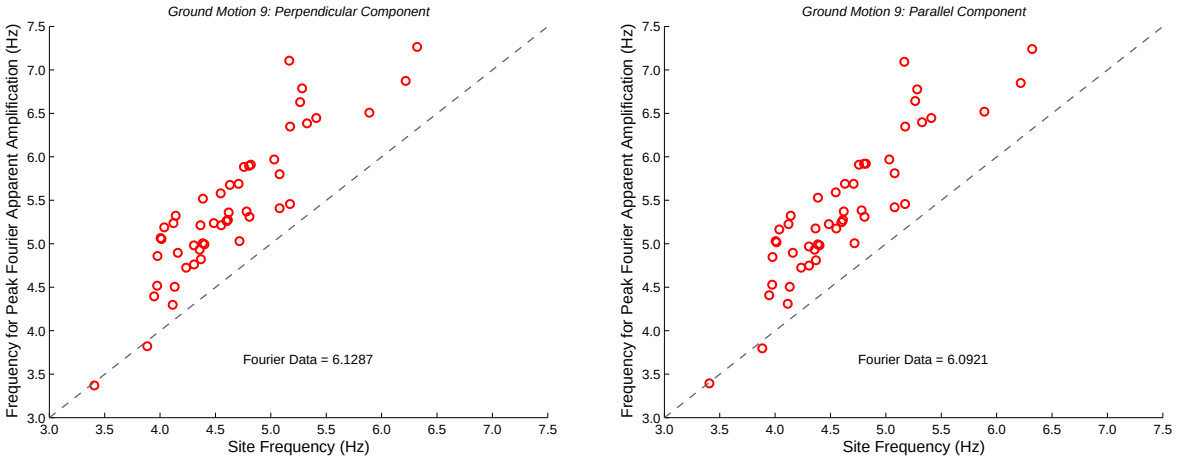

Figure 5.15: Ground Motion 09 – frequency at which the peak $F\ AA$ occurs versus site frequency for the 50 free field simulations, for the perpendicular and parallel components of motion. The peak $F\ AA$ value for the data is written on each plot. The dashed lines have a slope of 1:1.

calculated for each velocity profile is shown in Figure 5.15. The plots for the perpendicular and parallel components are the same, with the exception of the peak value reported for the data AA. This is expected as the material properties of the subsurface were maintained in simulating both components of motion. The frequencies associated with the peak AA tend to be slightly greater than the calculated site frequency. This could be due to the influence of the three-meter-thick loess/colluvium layer on the simulated free field response, which would not be accounted for by the equal weighting scheme used to determine the average shear wave velocity for the site frequency calculations.

Figure 5.16 reintroduces additional parameters from Chapter 3 as a final comparison of the data at the crest to the range of free field simulations for ground motion 9. The $PGA\ TF$, $PGV\ TF$, $AI\ TF$ and MSF for the perpendicular component of motion are plotted against the parallel component of motion. Considering both components of motion, the $PGA\ TF$ ranges from about -0.1 to 1.5, the $PGV\ TF$ ranges from about -0.25 to 0.5 and the $AI\ TF$ ranges from about -0.2 to 3.0. As was seen previously, the range of simulations encompasses the data at the crest, but for the majority of the simulations, the ground motion at the crest is stronger. Mean TF values for *each* ground motion are used for comparing *all* ground

motions in the next section. It should be noted that for this ground motion, $PGA\ TF$ tends to be greater for the parallel component of motion, and the $PGV\ TF$ and $AI\ TF$ tend to be greater for the perpendicular component of motion. This directional dependence is discussed in the next section.

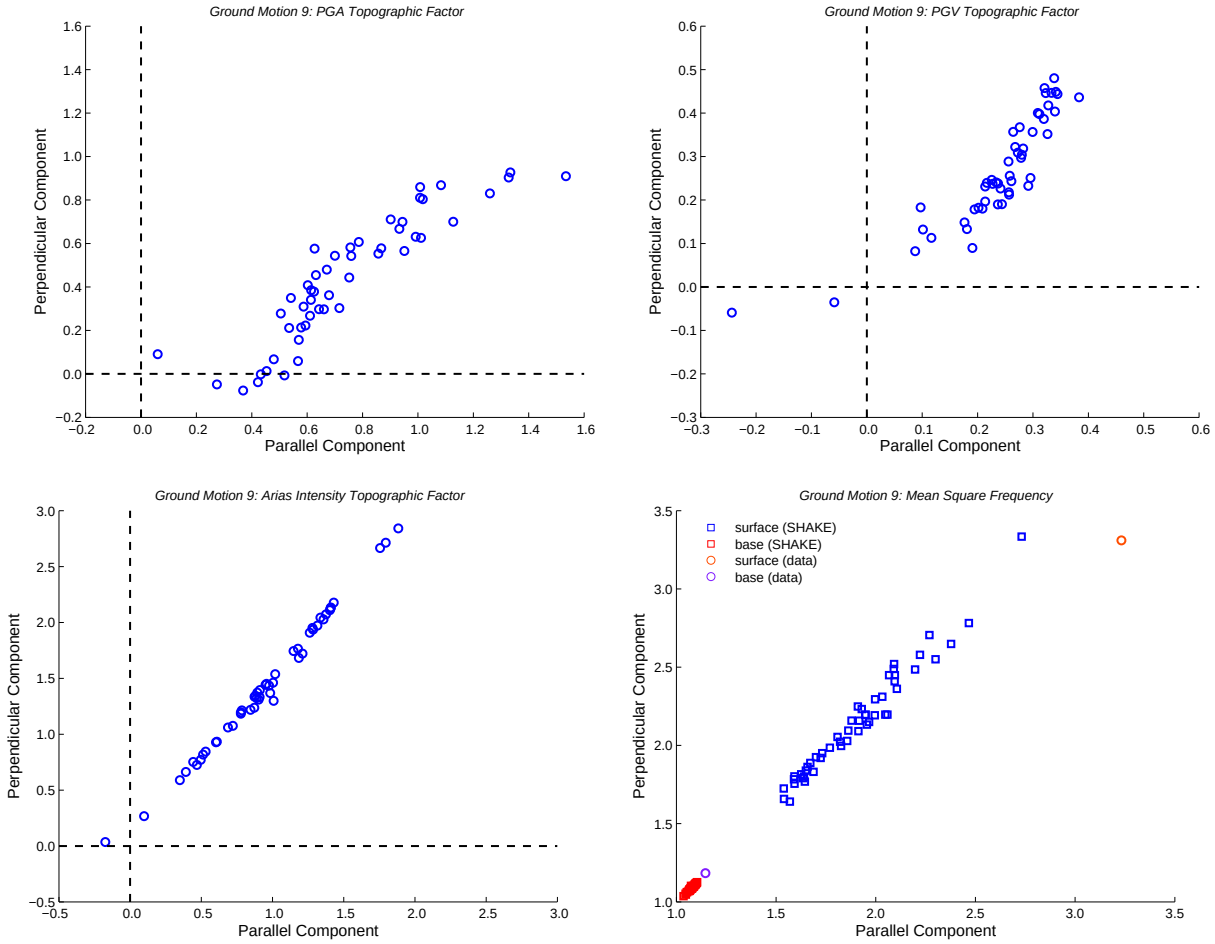

Figure 5.16: Ground motion 09 – perpendicular versus parallel component for the $PGA\ TF$, $PGV\ TF$, $AI\ TF$ and MSF for the 50 simulations. The MSF plot includes base and surface (crest) recordings as well as the base and free field simulations.

In general, the MSF of both the simulations and data is comparable for the perpendicular and parallel components of motion. The simulated MSF for the base motion is lower than the data, a result of the deamplification between 3 and 8Hz, previously discussed. The MSF of the free field simulations are also below the MSF for the crest recording. This is attributed

to topographic amplification. Mean MSF values for the simulated ground motions are used when considering all ground motions in the next section.

5.3.3 All Ground Motions: Horizontal

Analysis results presented in this section build off those in the previous section, but represent all 12 ground motions utilized in this study. The figures presented are similar to those presented in Chapter 3. Additional plots, such as those used to understand directional effects are also included. Mean values are presented for the spectra and intensity measures related to the free field simulations (i.e., raw values or TFs). In general, the commentary is limited to observations from the figures presented and comparisons to the results found in Chapter 3. Further discussion of the results is provided in Section 5.4

Figure 5.17 demonstrates the range of base PGA and *banded peak Fourier amplitude* ($bp\ FA$) values, and the corresponding crest and free field values for the perpendicular and parallel components of motion. For this case study, the $bp\ FA$ refers to the peak Fourier amplitude within the topographic frequency band. The topographic frequency band corresponds to the range of topographic frequencies defined by the various shear wave velocity profiles described in Section 5.3.1 (2.2 to 5.1Hz).

The ground motions are overall weak, with input PGA and $bp\ FA$ ranging from about 1 to 35 $mm/s/s$ and 0.01 to 0.21 mm/s, respectively. Overall, the input values for the perpendicular and parallel components are similar, although the parallel component is slightly higher for some ground motions.

The PGA in the free field is similar to that of the base, with values slightly above the 1:1 line for both components of motion. PGA is often associated with higher frequency components of motion. Therefore, this suggests that these components of motions are not strongly amplified in the free field.

At the crest, the PGA is generally twice that of the base for the lowest amplitude motions and is closer to 1.5 times greater for the higher amplitude motions. For the strongest motion, the PGA for the parallel component is greater; otherwise, PGA values are similar for the

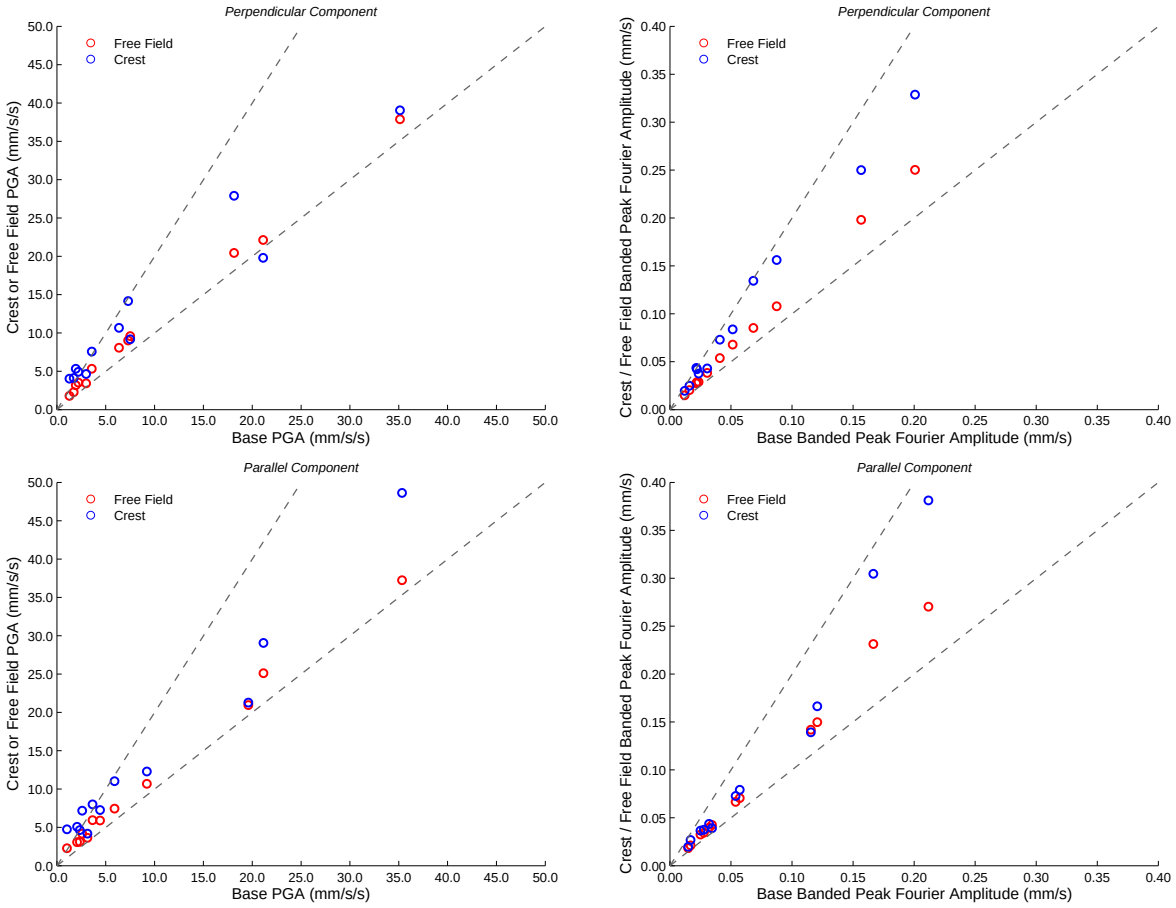

Figure 5.17: All motions – crest and free field PGA versus base PGA (left plots), and crest and free field $bp\ FA$ versus base $bp\ FA$ (right plots), for the perpendicular (top plots) and parallel (bottom plots) components of motions. The free field values represent mean values from the 50 free field simulations. The dashed lines have slopes of 2:1 and 1:1.

two components. This differs from the slopes in Chapter 3, where the free field and crest PGA were generally 1 to 2 times, and 2 to 3 times greater than the base PGA, respectively.

For the *bp* FA, the free field is generally about 1.5 times greater than the base, and the crest is generally 1.5 to 2 times greater. The ratio between the free field and base response is fairly consistent, and is within the range observed in Chapter 3. The ratio between the crest and base is again generally lower than the typical ratio of 2 to 3.5 for the slopes in Chapter 3. Interestingly, the trend in the crest to base ratio is reversed for the perpendicular and parallel components. For the perpendicular component, the ratio decreases from 2 to closer to 1.5 as the *bp* FA increases, while for the parallel component the opposite is true.

Comparison of the ground motion frequency content for the crest, free field and base are presented in Figure 5.18, using the MSF. The left plots compare the crest and free field MSF to the base MSF, with MSF normalized by the mean topographic frequency (3.2Hz). The right plots show the $MSF\,TF$ (representing the change in MSF between the crest and free field) versus the free field MSF normalized by the topographic frequency.

From the left plot in Figure 5.18, it can be inferred that the base motions are mainly dominated by energy at low frequencies, with values less than 40% of the mean topographic frequency (or less than 1.3Hz). The MSF for the free field and crest, however, strongly deviate from the base MSF, particularly once the base MSF is greater than about 30% of the topographic frequency. The free field MSF deviates as a result of site amplification at higher frequencies, while the crest MSF deviates as a result of both site and topographic amplification at higher frequencies. For this reason, the difference between the base and crest MSF is always greater than the difference between the base and free field.

The right plot in Figure 5.18 shows that the difference between the crest and free field MSF increases for free field $MSFs$ above 0.5 times the topographic frequency. This suggests that the pull towards the topographic frequency is greater for ground motions with stronger components of motion near the topographic frequency. In this case the free field is used as a proxy for the typical response expected absent the presence of topography.

Changes in frequency content are generally greater for the parallel than the perpendicular

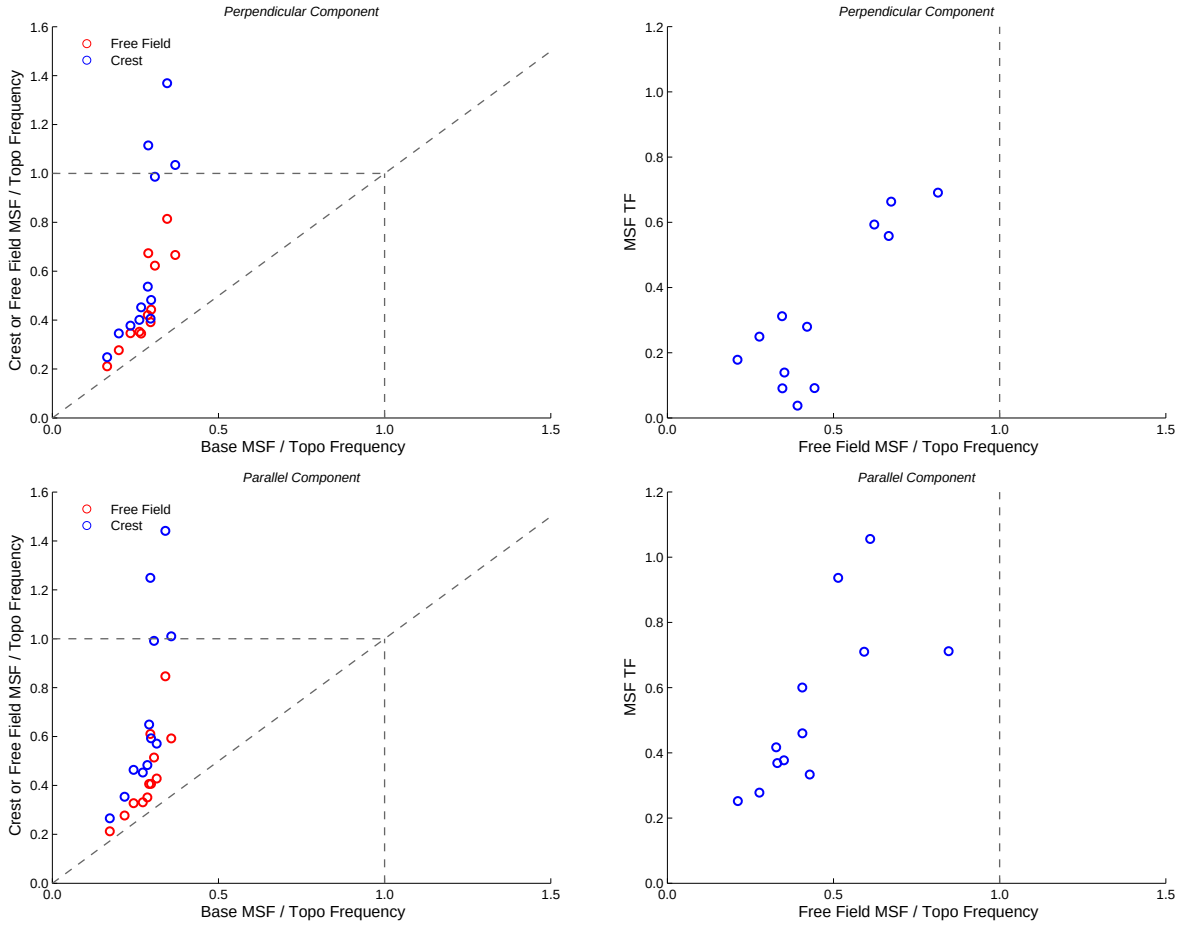

Figure 5.18: All motions – crest and free field MSF versus base MSF, all normalized by the mean topographic frequency (left plots), and $MSF\ TF$ versus free field MSF normalized by the mean topographic frequency (right plots), for the perpendicular (top plots) and parallel (bottom plots) components of motion. The free field and TF values represent mean values from the 50 free field simulations. The dashed lines mark the normalized frequencies of 1.0 in all plots. The other dashed line in the left plot has a slope of 1:1. The other dashed line in the right plots marks a TF of zero.

component of motion. This is likely a result of amplification at additional frequencies greater than the mean topographic frequency, at which the perpendicular component of motion was not amplified (i.e., around 4.5Hz). These additional frequencies were discussed in detail in the previous section.

The patterns described above are generally similar to those found in Chapter 3. However, the deviation of the free field MSF from the base and the $MSF\ TF$ values are both greater for Redcliffs than they were for the slopes tested in the centrifuge. This is likely due to the relationship between the frequency content of the base ground motions and the site and topographic frequencies. Namely the site frequency was more comparable to the base MSF values in the centrifuge experiments.

Redcliffs and the centrifuge slopes also differ in the $MSF\ TF$. For the centrifuge slopes, the $MSF\ TF$ did increase once the free field MSF was above 50% of the topographic frequency. However the $MSF\ TF$ then decreased as the free field MSF approached the topographic frequency, and negative $MSF\ TF$ values were found if the MSF of the free field was above the topographic frequency. In other words, the shift towards the topographic frequency was proportional to the difference between the typical free field MSF and the topographic frequency. This pattern is not observed for Redcliffs. However, this may be due to a lack of data with the MSF near the topographic frequency.

The previous figures highlighted relationships between the crest, free field and base considering amplitude and frequency content separately. Figure 5.19 plots the $PGA\ TF$ and $bpF\ TF$ versus the MSF at the crest normalized by the mean topographic frequency. For both the perpendicular and parallel components of motion, the $PGA\ TF$ increases as the MSF approaches the topographic frequency. The $PGA\ TF$ ranges from about -0.1 to 1.3, and 0.0 to 1.1 in the perpendicular and parallel directions, respectively. This is similar to the range found in Chapter 3 for most ground motions, but below the maximum of about 2.0. It should be noted that the $PGA\ TF$ is greatest for the ground motion which has a MSF about 1.4 to 1.5 times the crest MSF. The is likely the result of topographic amplification at frequencies greater than the mean topographic frequency (discussed previously) and the

fact that PGA is often associated with higher frequency ground motion.

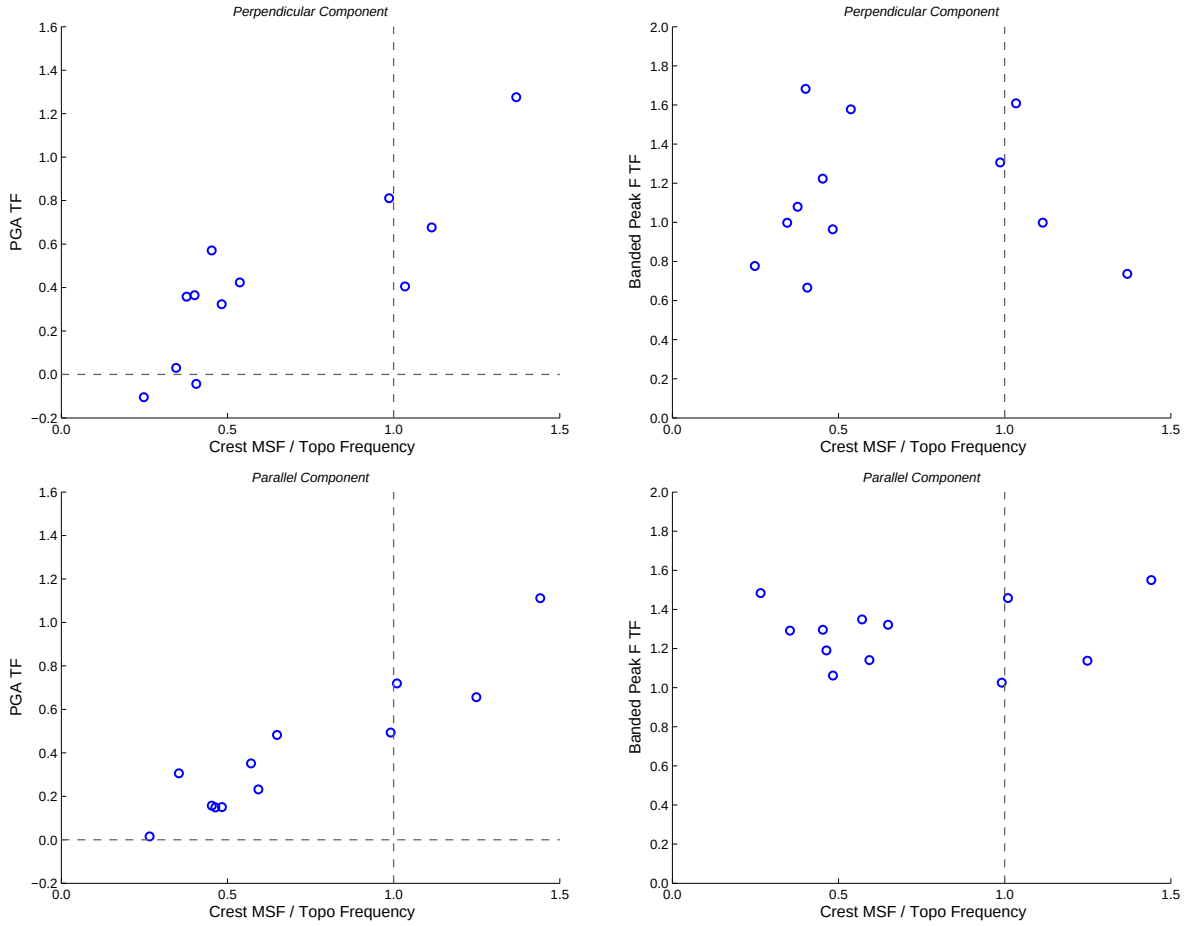

Figure 5.19: All motions – $PGA\ TF$ (left plots) and $bp\ F\ TF$ (right plots) versus MSF at the crest normalized by the mean topographic frequency for the perpendicular (top plots) and parallel (bottom plots) components of motion. The TF values represent mean values considering the 50 free field simulations. The dashed lines mark normalized frequencies of 1.0 and TF values of zero.

The $bpF\ TF$ values range from about 0.7 to 1.7, and 1.0 to 1.6 for the perpendicular and parallel components of motion, respectively. This differs significantly from the range of about -0.2 to 5.0 for the slopes in the centrifuge (using spectral acceleration instead of Fourier amplitude). However, most of the earthquake motions introduced to the slopes had a $bpF\ TF$ below 2.2. Greater TF values were typically associated with idealized frequency sweeps and sine wave motion.

The trend for the perpendicular component of motion more closely matches that illustrated in Chapter 3. The *bpF TF* increases as the MSF at the crest reaches the topographic frequency. The expected trend is also observed in that the *bpF TF* decreases for ground motions with a MSF above the topographic frequency. The ground motions in Chapter 3 did not have MSF values more than about 10% greater than the topographic frequency, and therefore, this expected trend was not observed.

For the parallel component of motion, a trend with the MSF at the crest does not exist. That is, the range of *bpF TF* values is fairly consistent regardless of MSF. Because the parallel component of motion exhibits strong topographic amplification at two frequencies within the topographic frequency band (i.e., 3.4 and 4.5Hz), the likelihood for a high *bpF TF* is greater for the parallel than the perpendicular component of motion. This is true even if strong components of motion exist at other frequencies, which influence the relationship between the MSF and the mean topographic frequency. Therefore, if topographic amplification is expected at multiple frequencies (i.e., for the Redcliffs site), the MSF may not correlate well to amplification within specific frequency bands.

In addition to the intensity measures considered above, comparisons between the crest and free field were also made for PGV and AI. The $PGV\ TF$ and $AI\ TF$ are plotted against the $PGA\ TF$ in Figure 5.20. The $PGV\ TF$ ranges from about -0.4 to 0.3, and about 0.2 to 0.7 for the perpendicular and parallel components, respectively. $AI\ TF$ ranges from about 0.2 to 1.5 for both components of motion.

While there is considerable scatter for both components of motion, there is a stronger correlation between $AI\ TF$ and $PGA\ TF$, than $PGV\ TF$ and $PGA\ TF$. The $AI\ TF$ ranges from greater than 1 to greater than 2 times the $PGA\ TF$ for the perpendicular component, and typically is between 1 and 2 times the $PGA\ TF$ for the parallel component of motion. The AI is a measure of the ground motion energy and accounts for amplitude, frequency content, and duration of the ground motion. Therefore, the amplification of the AI would be greater than that of the PGA if ground motion is amplified at more than one instance in the time history. The ranges of $PGA\ TF$ are similar for both components

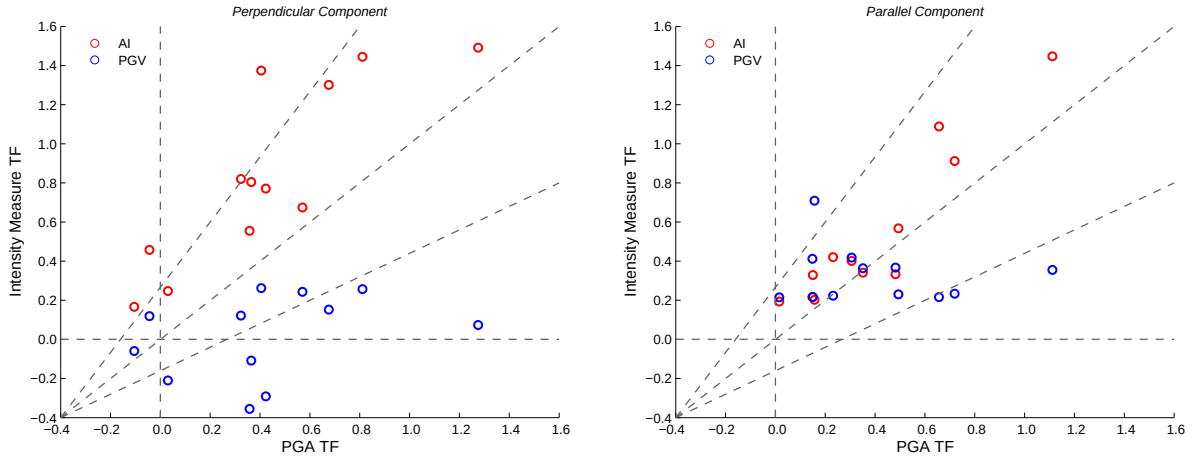

Figure 5.20: All motions - $PGV\ TF$ and $AI\ TF$ versus $PGA\ TF$ for the perpendicular (left plot) and parallel (right plot) components of motion. The TF values represent mean values considering the 50 free field simulations. The dashed lines have a slopes of 2:1, 1:1 and 0.5:1.

of motion, but $AI\ TF$ is consistently greater for the perpendicular component, indicating the overall amplification of the ground motion is greater in that direction. This emphasizes the importance of considering more than one intensity measure when analyzing topographic effects.

The $PGV\ TF$ is greater in the parallel, than the perpendicular direction. The PGV typically is associated with amplitude at intermediate frequencies. Therefore, this suggests that these frequencies are more strongly amplified in the parallel direction. This may be again be related to stronger topographic amplification at 4.5Hz in the parallel direction.

The values of $PGV\ TF$ and $AI\ TF$ are lower overall than those observed in Chapter 3. The $PGV\ TF$ values ranged from about -0.5 to 2.5; however, the majority were below about 0.8, which is more consistent with Redcliffs. The $AI\ TF$ values range from about -0.5 to 18.5, with the majority below about 3.6. The $AI\ TF$ also increased exponentially with the $PGA\ TF$ for the centrifuge slopes. These differences can likely be attributed to differences in the ground motion attributes. Frequency sweeps and sine wave motions with numerous cycles at the topographic frequency (and perhaps no motion at other frequencies) would have a PGA associated with that frequency, leading to high $PGA\ TF$ values; and for these same motions, the $AI\ TF$ would increase with each cycle of motion, resulting in very

high $AI\ TF$ values.

While the intensity measures and MSF provide insight into the level of topographic amplification and associated ground motion frequency content, the level of amplification at various frequencies is more readily observed using the $F\ TF$ spectrum. The $F\ TF$ spectrum is provided for the perpendicular and parallel components of all motions in Figure 5.21. The geometric mean and mean plus or minus a standard deviation is also shown. It should be noted that the gray lines represent the geometric mean spectrum, based 50 free field simulations, for each ground motion.

The frequencies at which topographic amplification occurs are similar to those previously identified in Figure 5.12 for ground motion 9. For the perpendicular component, there are peaks in the $F\ TF$ spectrum at 3.2, 4.5, between 5.5 and 6.5, and around 8.0Hz. For the parallel component, there are peaks at 3.4, 4.5, 6.0 and between about 8.5 to 9.0Hz.

Overall, the spectra are consistent for all ground motions, but more tightly constrained below about 5Hz. That is, above 5Hz, more deviation in the spectra is observed. Amplification at the various frequencies can be accounted for by considering the various ridge structure in the vicinity of the RCBS station. In particular, the variation in cliff height can explain the peaks at lower frequencies (below about 5Hz). The peaks at higher frequencies may be explained by smaller stepped slopes along the ridge, and the shorter cliff faces farther from the RCBS station, combined with local site effects which are not captured in the free field simulations. These include lateral heterogeneity, fracturing and weathering within the rock mass. This was discussed in more detail in the previous section.

A strong peak exists near the mean topographic frequency for both components of motion. For both components, the $F\ TF$ ranges from about 0.5 to 1.0; the mean values are 1.0 and 0.9 for the perpendicular and parallel components, respectively. This is similar to the geometric mean topographic amplification of about 0.9 found for all motions in Chapter 3. The level of amplification around 4.5Hz is similar to that at the mean topographic frequency for the parallel component, but is muted for the perpendicular component. The peaks around 6.0Hz are again similar in amplitude to those near the mean topographic frequency. The level of

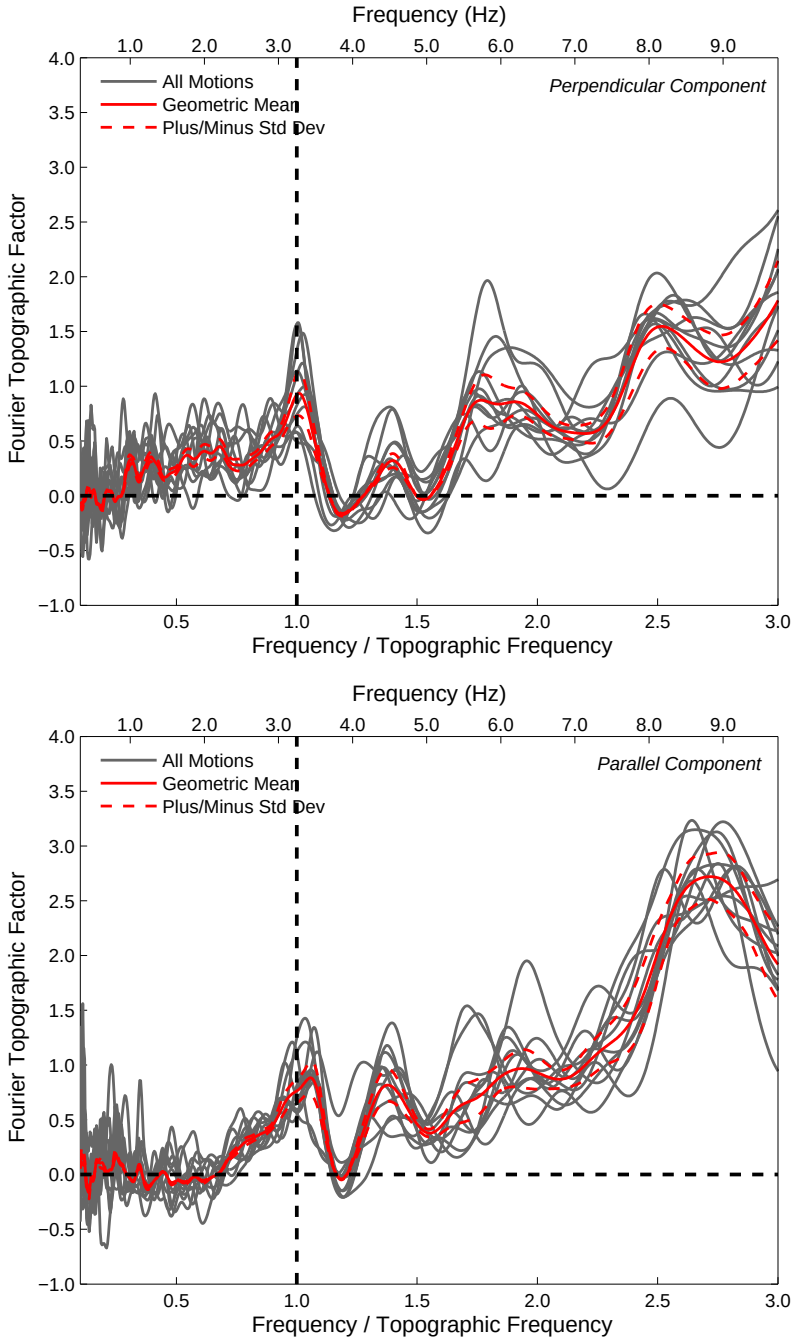

Figure 5.21: All motions - $F\ TF$ versus frequency normalized by the mean topographic frequency for the perpendicular (top plot) and parallel (bottom plot) components of motion. Raw frequencies are provided on the top x-axis. The spectra represent the mean values from the 50 simulations for each motion. The geometric mean and mean plus/minus a standard deviation is provided considering all motions. Motions are separated by those that have an MSF within and not within the topographic frequency band. Dashed lines mark a normalized frequency of 1.0 and a TF of zero.

amplification then increases at higher frequencies.

More insight into the level of amplification for the crest over the free field at the various frequencies can be gained by also considering the amplification of the crest over the base. This is shown in Figure 5.22, where the $F\ AA$ for all ground motions, with the geometric mean and mean plus or minus a standard deviation, is provided. It should be noted that this plot represents data from the RCBS station only. Thus, the gray lines are not mean values.

Peaks in the $F\ AA$ spectrum occur at the same frequencies as those found in the $F\ TF$ spectrum. This is logical, since the $F\ AA$ spectrum includes contributions from topographic amplification. However, the $F\ AA$ spectrum also includes contributions from site amplification. In Section 5.3.1, it was established that the range of site frequencies for the 50 free field simulations was between about 3.4 and 6.3Hz, with that associated with the geometric mean velocity profile equal to 4.1Hz. In Section 5.3.2, it was also shown that the site frequency determined using equally weighted mean shear wave velocity values slightly under-predicted the frequency at which the peak site amplification occurred. It was also pointed out, that for ground motion 9, the peak amplification of the crest over the base occurred around 6Hz (see Figure 5.15), which is consistent with most of the other ground motions shown in Figure 5.22.

Considering the discussion above, and both the $F\ TF$ and $F\ AA$ spectra, it is likely that site amplification contributes to the amplification at 4.5Hz. The peak at 4.5Hz corresponds to the mean site frequency for the site (particularly when considering a weighted shear wave velocity profile which would shift this to a slightly higher frequency). In the perpendicular direction, there is little topographic amplification at this frequency (mean $F\ TF$ of 0.25), as expected based on the Redcliffs topography. Therefore the mean AA of about 2.5 in the perpendicular direction can mainly be attributed to site amplification. In the parallel direction, the ridge topography promotes amplification at 4.5Hz, which is reflected in the $F\ TF$ and $F\ AA$ spectra. If the site amplification is comparable for the two components of motion, then about 37.5% (1.5/4.0) of the AA can attributed to topographic amplification for the parallel component.

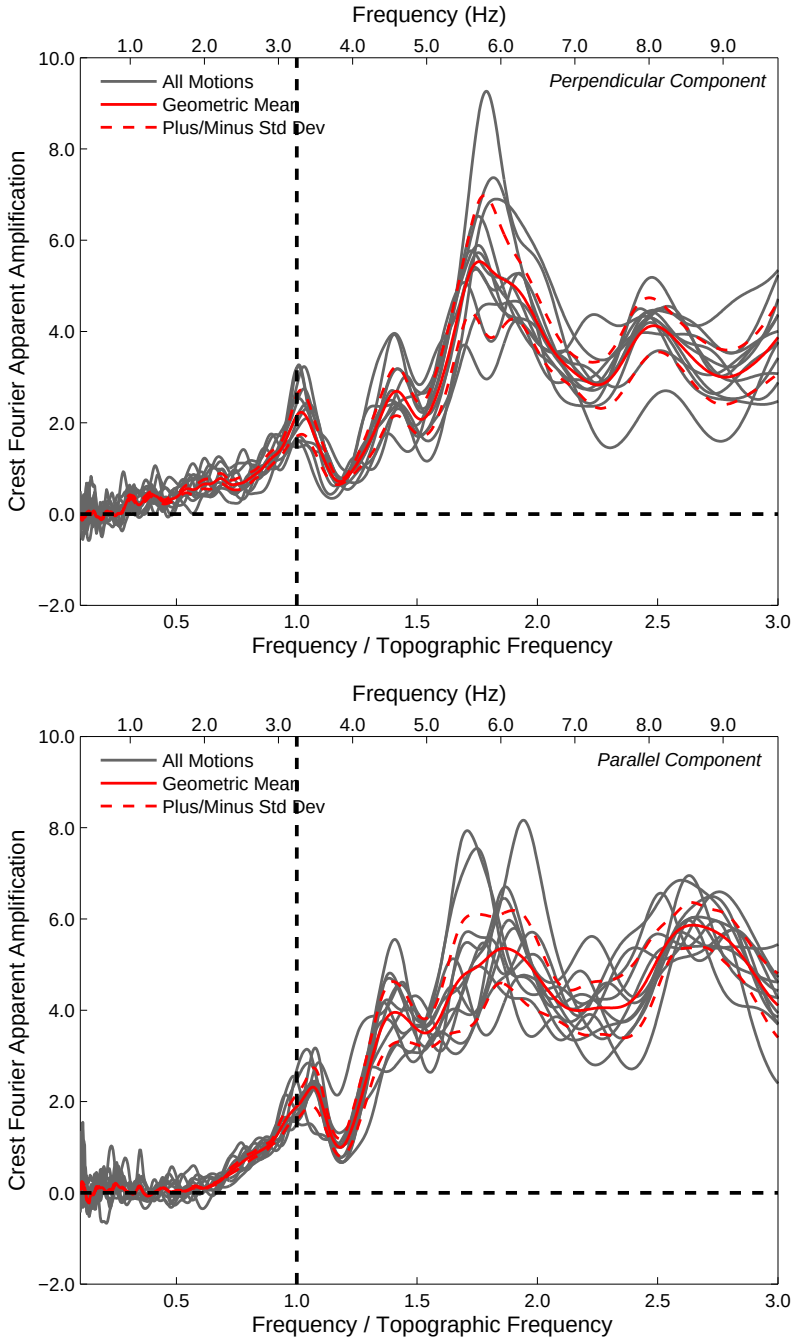

Figure 5.22: All motions - FAA for the crest versus frequency normalized by the mean topographic frequency for the perpendicular (top plot) and parallel (bottom plot) components of motion. Raw frequencies are provided on the top x-axis. The spectra represent the mean values from the 50 simulations for each motion. The geometric mean and mean plus/minus a standard deviation is provided considering all motions. Motions are separated by those that have an MSF within and not within the topographic frequency band. Dashed lines mark a normalized frequency of 1.0 and an AA of zero.

The peak in the $F\ AA$ spectrum around 5.5 to 6.5Hz is within the range of possible site frequencies for the shear wave velocity profile. However, for reasons previously discussed, the AA at these and higher frequencies is likely due to combined site and topographic amplification. In particular, the interaction between local site effects and the topography.

5.3.4 All Ground Motions: Vertical

Thus far, analysis results have focused on the horizontal components of motion. The vertical component of motion is considered in this section in relation to the horizontal ground motion at the crest, free field and base. The results are again compared to the findings in Chapter 3.

The amplitude and frequency content of vertical and horizontal ground motion are compared for the base and crest, and for the perpendicular and parallel components of motion in Figures 5.23 and 5.24. For both components of motion, and at both locations (i.e., crest and base), the vertical PGA is generally half that of the horizontal PGA. This is similar to the trends observed for the free field (note that there is no vertical free field component in this case) and base for the slopes in the centrifuge. However, at the crest, the vertical PGA was typically equal to (but ranged from 0.5 to 1.0 times) the horizontal PGA for the centrifuge slopes. A portion of this strong vertical component of motion has been attributed to centrifuge container rocking. However, in addition, the discrepancy between Redcliffs and the centrifuge slopes may be attributed to the disruption of Rayleigh waves resulting from the complex topography (Wang et al., 2015) at Redcliffs.

The vertical MSF is typically greater than the MSF for the horizontal components of motion, as shown in Figure 5.24. The vertical base MSF is typically about 1.5 times the horizontal base MSF. At the crest, the vertical MSF more closely follows that of the horizontal components of motion. This is consistent with the findings of Chapter 3.

For vertical ground motion, topographic effects have typically been analyzed by comparing spectral amplitudes at the crest to the horizontal ground motion in the free field (Ashford and Sitar, 1997; Assimaki et al., 2005a; Bouckovalas and Papadimitriou, 2005).

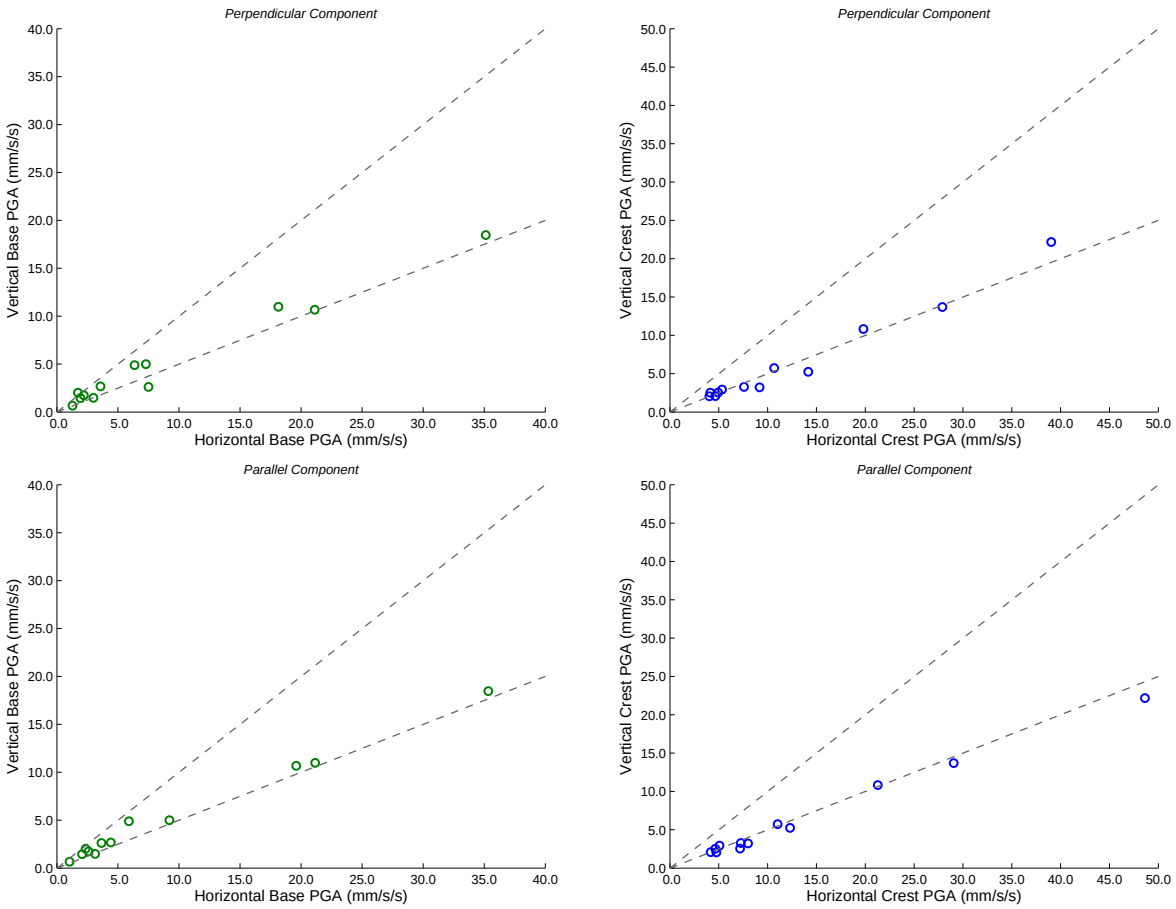

Figure 5.23: All motions – vertical PGA versus horizontal PGA for the base (left plots) and crest (right plots) surface recordings, for the perpendicular (top plots) and parallel (bottom plots) components of motion. Dashed lines have slopes of 1:1 and 0.5:1.

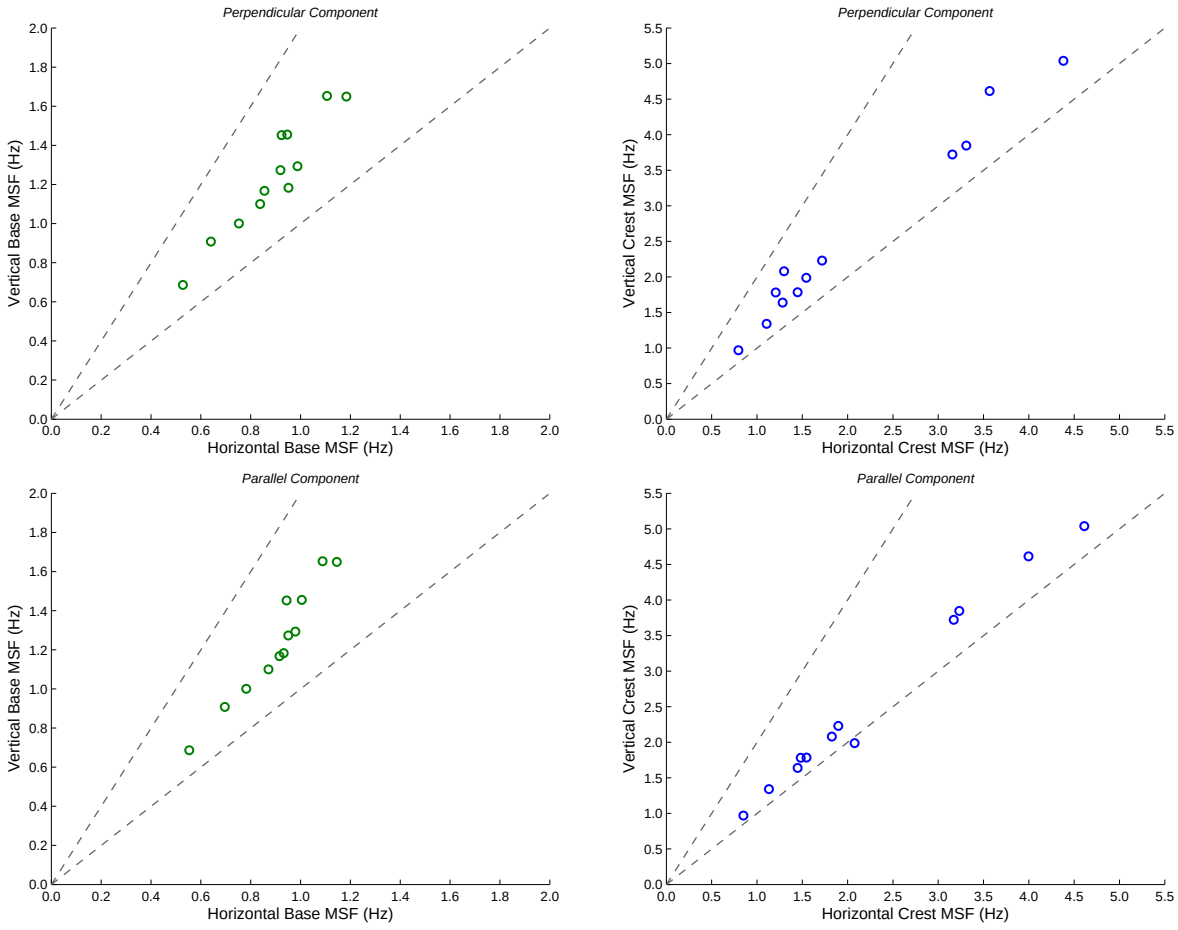

Figure 5.24: All Motions – vertical MSF versus horizontal MSF for the base (left plots) and crest (right plots) surface recordings, for the perpendicular (top plots) and parallel (bottom plots) components of motion. Dashed lines have slopes of 1:1 and 2:1.

this comparison is made using the vertical to horizontal $F\,TF$ spectrum in Figure 5.25. The gray lines represent geometric mean spectra, for the 50 free field simulations, for each ground motion. The geometric mean (solid line) of these spectra and mean plus or minus a standard deviation (dashed lines) are plotted in red.

The overall shape of the spectrum is similar to that observed in Chapter 3 in that the spectrum peaks at and near the (in this case mean) topographic frequency. Interestingly, amplification of the vertical over the perpendicular component is less than that of the vertical over the parallel component. The $F\,TF$ values range from 0 to 1.2, with a mean of 0.5 for the perpendicular component, and range from 0.5 to 2.4, with a mean of 1.1 for the parallel component. This comparable to and greater than the range of 0.2 to 0.5 observed for the mean spectra in Chapter 3.

Because the vertical component remains unchanged, this indicates that the Fourier amplitude at and near the mean topographic frequency is stronger for the perpendicular than the parallel component of motion in the free field. This component of motion is stronger as a result of the base motion also having more energy near the topographic frequency in the perpendicular direction. This is evidenced by the vertical to horizontal $F\,AA$ spectrum shown in Figure 5.26, where the same pattern is observed.

Vertical ground motion typically is not amplified by site resonance, which amplifies the horizontal component of motion. This is the theory behind using single station H/V spectral analysis to identify site resonance (Nakamura, 1989). Because the horizontal component is amplified as a result of site resonance, and the vertical is not, the H/V spectrum should peak at frequencies associated with site resonance. The H/V Fourier spectra for the crest are provided for all ground motions in Figure 5.27.

As previously discussed, the vertical component of motion is typically amplified at frequencies associated with topographic amplification. Therefore, it would be expected that peaks at the topographic frequency (or frequencies) would be suppressed in the H/V spectrum. It should be noted that application of the H/V spectrum to the analysis of site response is often debated (ATAKAN et al., 2004). Researchers have attempted to use H/V

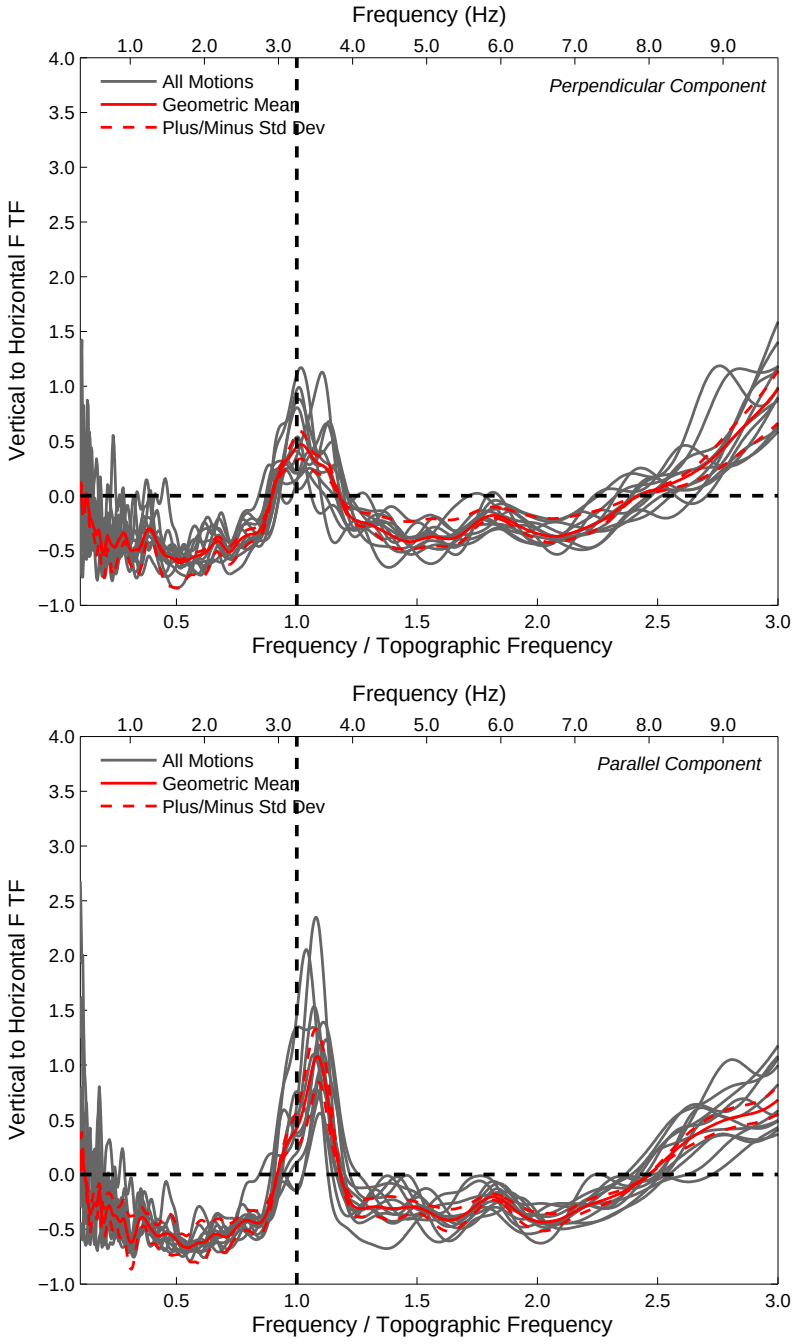

Figure 5.25: All motions - Vertical to horizontal $F\ TF$ versus frequency normalized by the mean topographic frequency for the perpendicular (top plot) and parallel (bottom plot) components of motion. Raw frequencies are provided on the top x-axis. The spectra represent the mean values from the 50 simulations for each motion. The geometric mean and mean plus/minus a standard deviation is provided considering all motions. Motions are separated by those that have an MSF within and not within the topographic frequency band. Dashed lines mark a normalized frequency of 1.0 and a TF of zero.

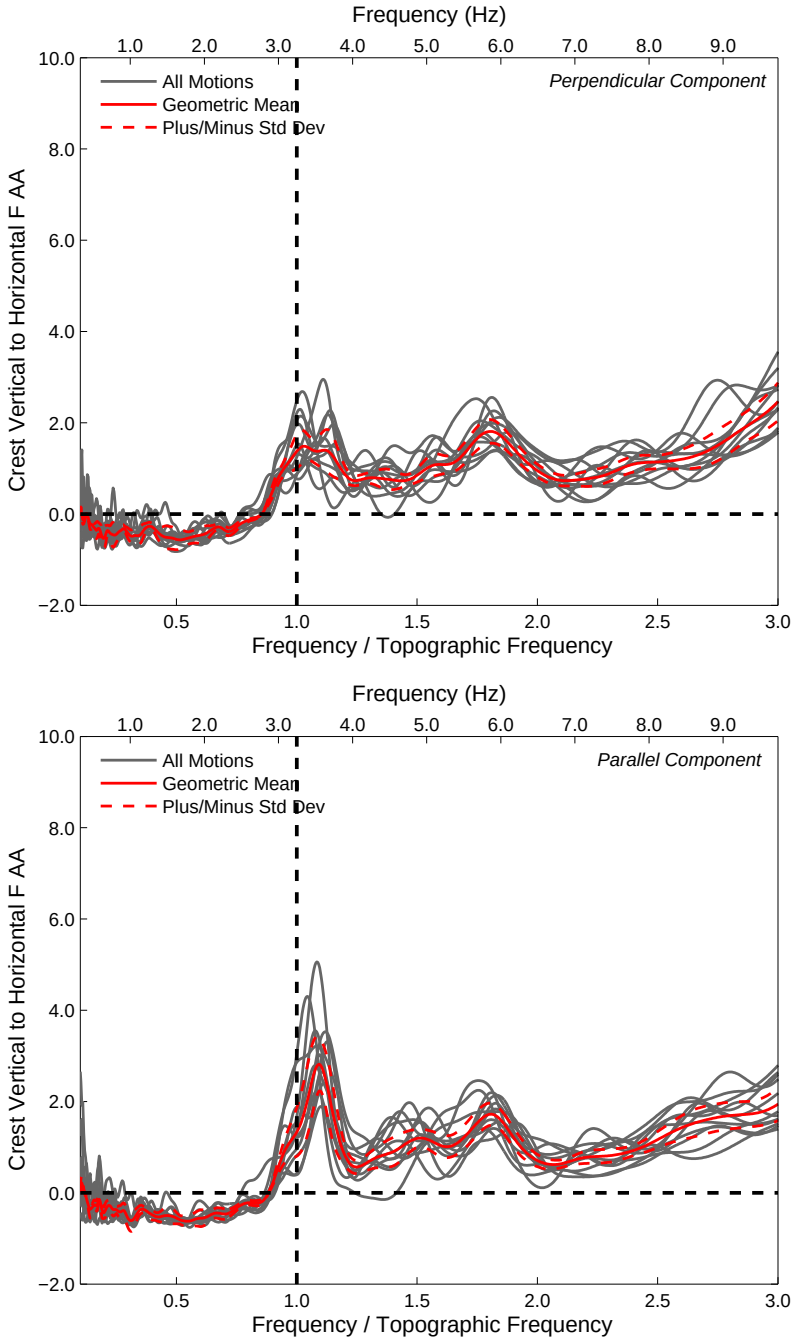

Figure 5.26: All motions - vertical to horizontal $F\ AA$ for the crest versus frequency normalized by the mean topographic frequency for the perpendicular (top plot) and parallel (bottom plot) components of motion. Raw frequencies are provided on the top x-axis. The spectra represent the mean values from the 50 simulations for each motion. The geometric mean and mean plus/minus a standard deviation is provided considering all motions. Motions are separated by those that have an MSF within and not within the topographic frequency band. Dashed lines mark a normalized frequency of 1.0 and an AA of zero.

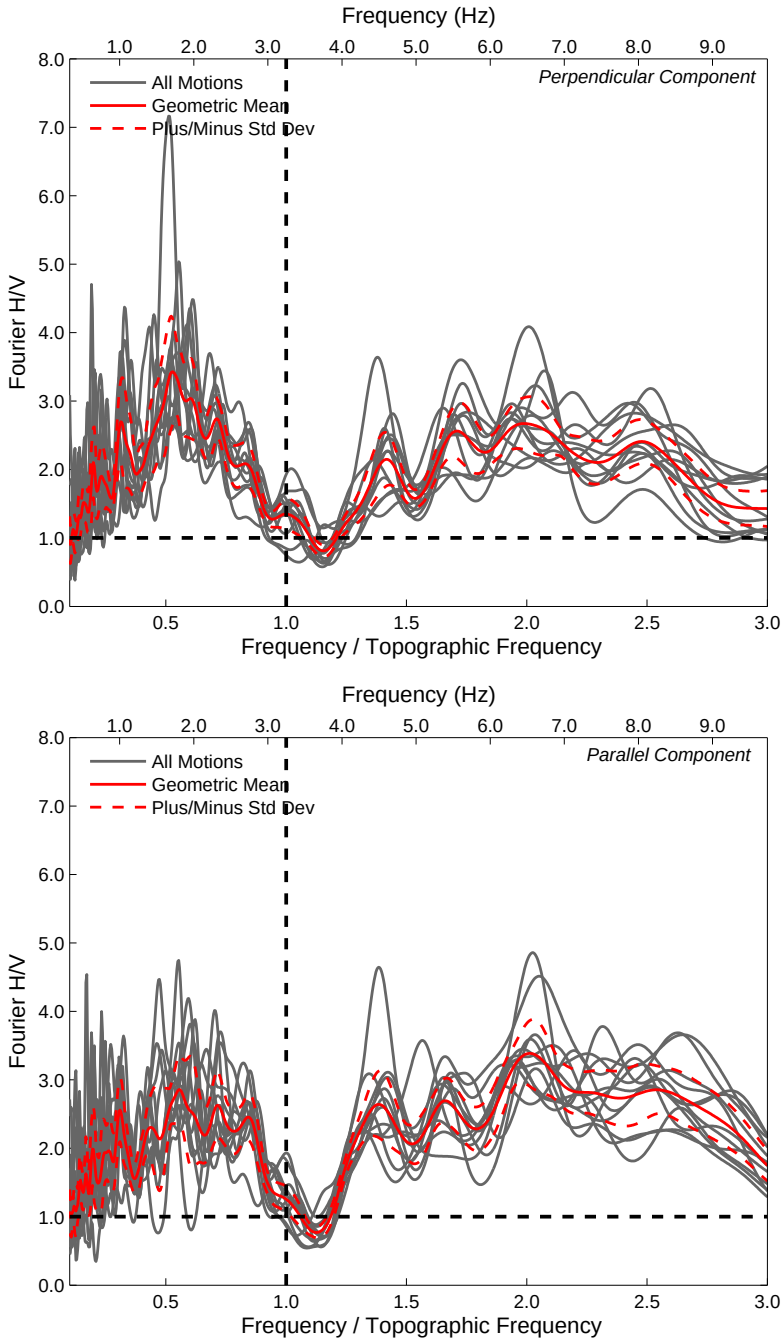

Figure 5.27: All motions - F H/V for the crest versus frequency normalized by the mean topographic frequency for the perpendicular (top plot) and parallel (bottom plot) components of motion. Raw frequencies are provided on the top x-axis. The spectra represent data from each motion. The geometric mean and mean plus/minus a standard deviation is provided considering all motions. Motions are separated by those that have an MSF within and not within the topographic frequency band. Dashed lines mark a normalized frequency of 1.0 and a H/V ratio of 1.0.

to identify topographic resonance (Cháves-García et al., 1996, 1997; Hailemikael et al., 2016; Panzera et al., 2011). However, the use of H/V for this purpose has recently been brought into question (Hartzell et al., 2014; Massa et al., 2014; Pagliaroli et al., 2015) and the application of H/V to rock sites remains controversial (Durante et al., 2017).

If the H/V spectrum can identify frequencies associated with site amplification, then it can be used in concert with the vertical to horizontal $F\ TF$ and $F\ AA$ to determine the frequencies associated with site and topographic amplification. Inspection of the H/V spectrum reveals that peaks at about 4.5, 5.5 to 6.5, and 8.5 to 9.0Hz can be associated with site amplification. Inspection of the $F\ TF$ and $F\ AA$ spectra reveals that peaks at these same frequencies can also be associated with topographic effects, with the peak at 4.5Hz present for the parallel component of motion only. This is consistent with the findings in the previous subsection, in that amplification at this frequencies is the result of combined site and topographic amplification. The peak at 3.2 and 3.4Hz for the perpendicular and parallel components, respectively, can be associated with topographic amplification only; also consistent with the previous subsection. Using this simple technique, it may be possible to identify topographic and site frequencies using only data from the downhole array.

It should be noted that a low frequency peak, between about 1 and 3Hz, exists in the H/V spectrum. This was said to be related to topographic amplification by Kaiser et al. (2014) and consistent with "ridge-scale" amplification in Massey et al. (2016b), for which the topographic frequency was calculated based on the width of the Redcliffs ridge. However, this is inconsistent with other observations outlined in this section. Other researchers have noted that the H/V method can identify "resonant" frequencies outside of those found using other methods (Massa et al., 2010; Wood and Cox, 2016).

5.3.5 Directional Effects

The effect of azimuth, or directional effects, on ground motion and topographic amplification have been highlighted in the previous sections by comparing the perpendicular and parallel components of motion. This section focuses on directional effects, but considers ground

motion in all horizontal directions (from 0 to 360 degrees). This is accomplished by utilizing polar plots for various intensity measures and spectra.

For reference, and to understand the frequency content and amplitude entering the site, polar plots of the base Fourier amplitude are provided for the 12 ground motions in Figures 5.28 and 5.29. The plots were created by calculating the Fourier amplitude in 10 degree intervals and contouring the data based on these points. Black concentric circles mark every 1Hz from 1 to 7Hz. Frequencies above 7Hz are not included in the plots. The mean topographic frequency is marked by a dashed black circle.

The base Fourier polar plots reveal that the input motions are dominated by energy at lower frequencies (below 3Hz). The polarization of ground motion does not follow a consistent pattern at frequencies within this range, despite a similar bearing for most ground motions (see Table 5.1). However, the plots clearly show the polarization of ground motion amplitude at various frequencies for the different ground motions. This is likely influenced by source to site effects, as the epicentral location, epicentral distance and depth vary from motion to motion.

The directional dependence of amplification of the crest over the base ground motion is provided in Figures 5.30 and 5.31. These figures show the $F\ AA$ spectra for all ground motions. For better comparison between ground motions, the $F\ AA$ spectra are normalized by the maximum $F\ AA$. Therefore a value of 1 represents maximum amplification.

Maximum amplification typically occurs between about 5.5 and 6.5Hz and can be attributed to both site and topographic amplification. Although amplification at these frequencies is strong in all directions, it is generally greatest in an E-W direction and spans between the NE-SW and SE-NW directions (i.e., the perpendicular and parallel components of motion). For some ground motions, the direction of strongest amplification shifts more towards the parallel or perpendicular directions.

Significant amplification also occurs around 4.5Hz and the mean topographic frequency of 3.2Hz. Amplification at 4.5Hz, however, is generally greater than that at 3.2Hz and less than that between 5.5 and 6.5Hz. At 4.5Hz, amplification is typically strongest in the SE-

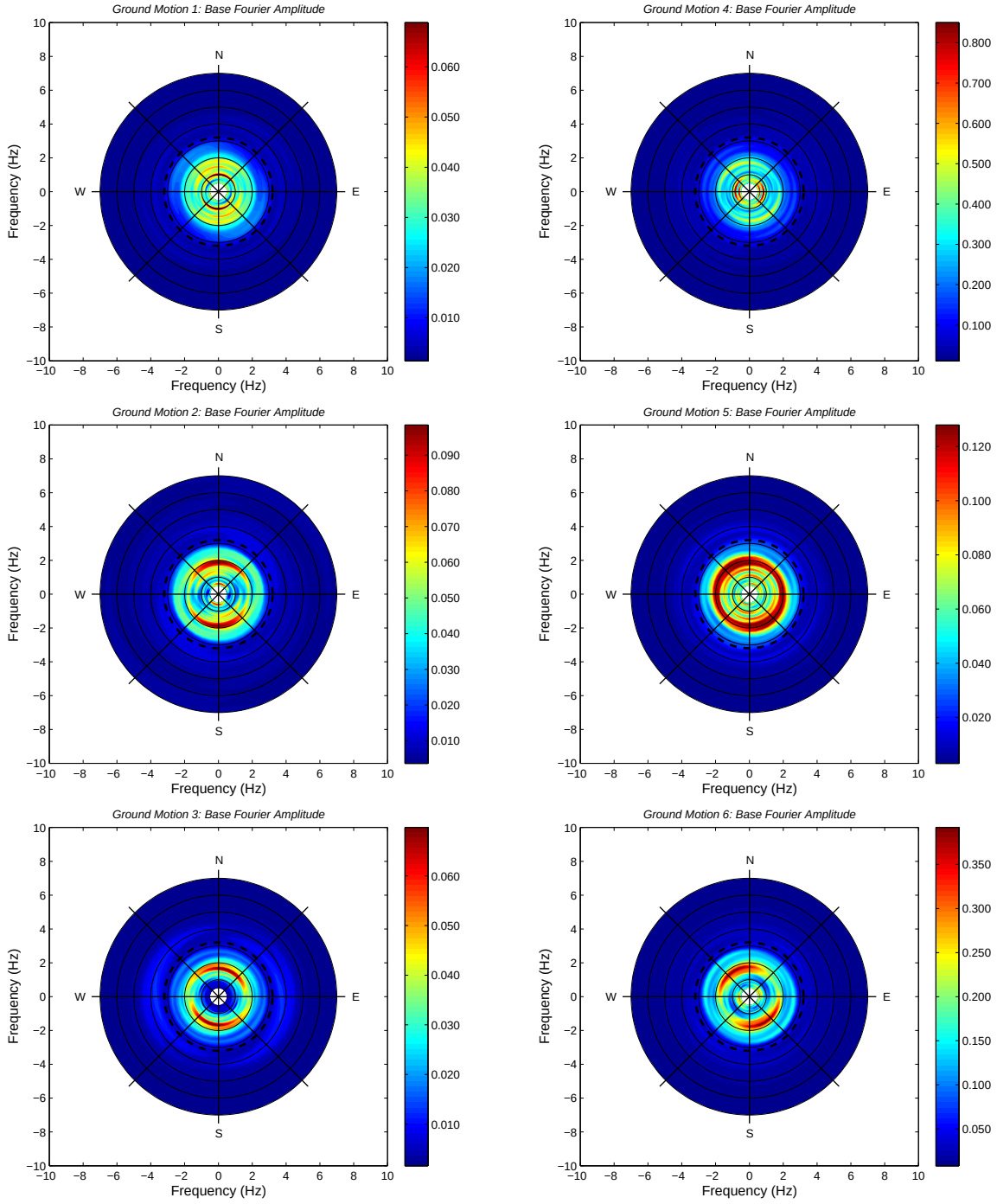

Figure 5.28: Ground motions 1 through 6 – contoured base Fourier amplitude versus frequency considering 10 degree directional intervals. Black circles mark every 1Hz for frequencies ranging from 1 to 7Hz. The mean topographic frequency is marked by a dashed black circle.

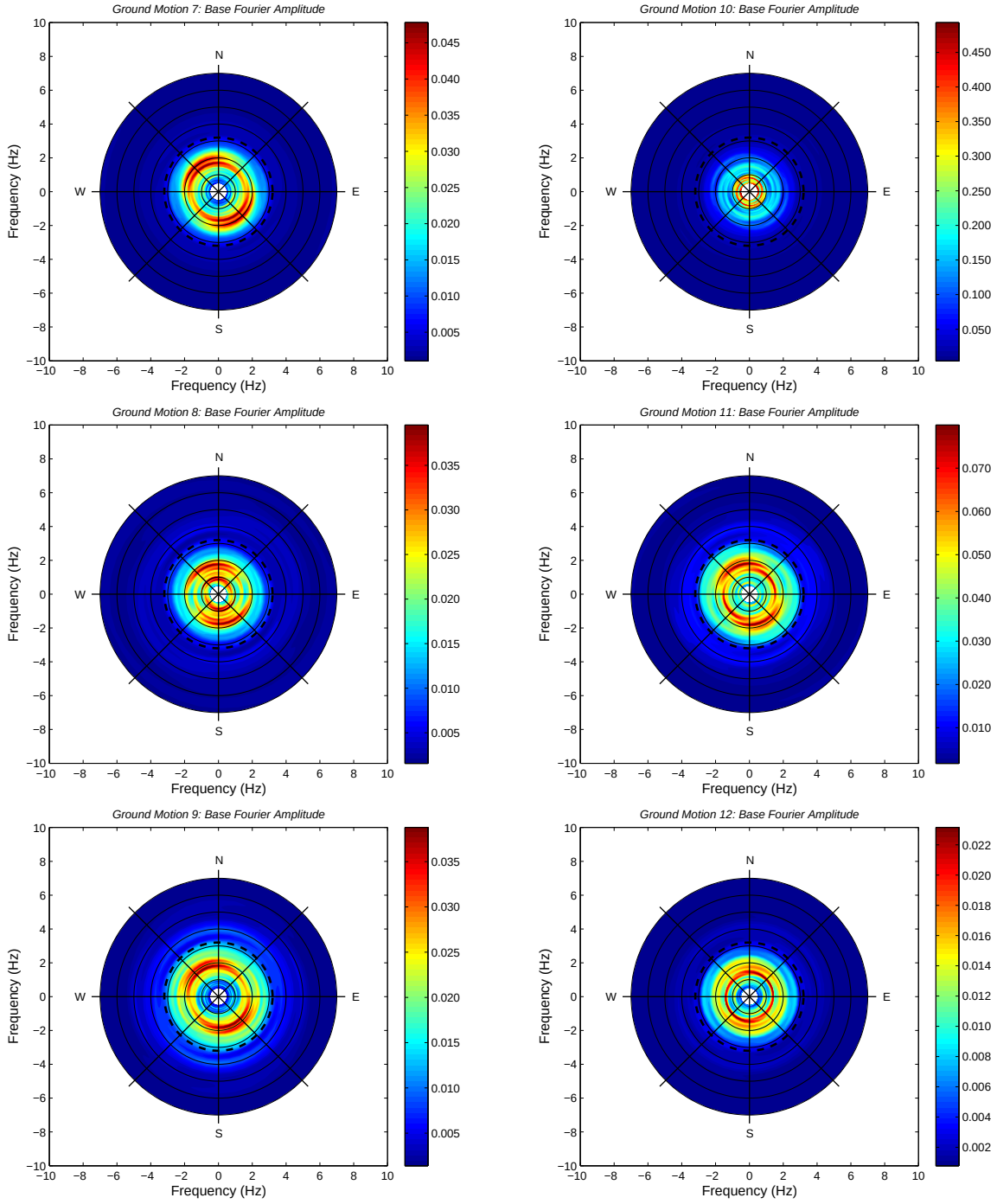

Figure 5.29: Ground motions 7 through 12 – contoured base Fourier amplitude versus frequency considering 10 degree directional intervals. Black circles mark every 1Hz for frequencies ranging from 1 to 7Hz. The mean topographic frequency is marked by a dashed black circle.

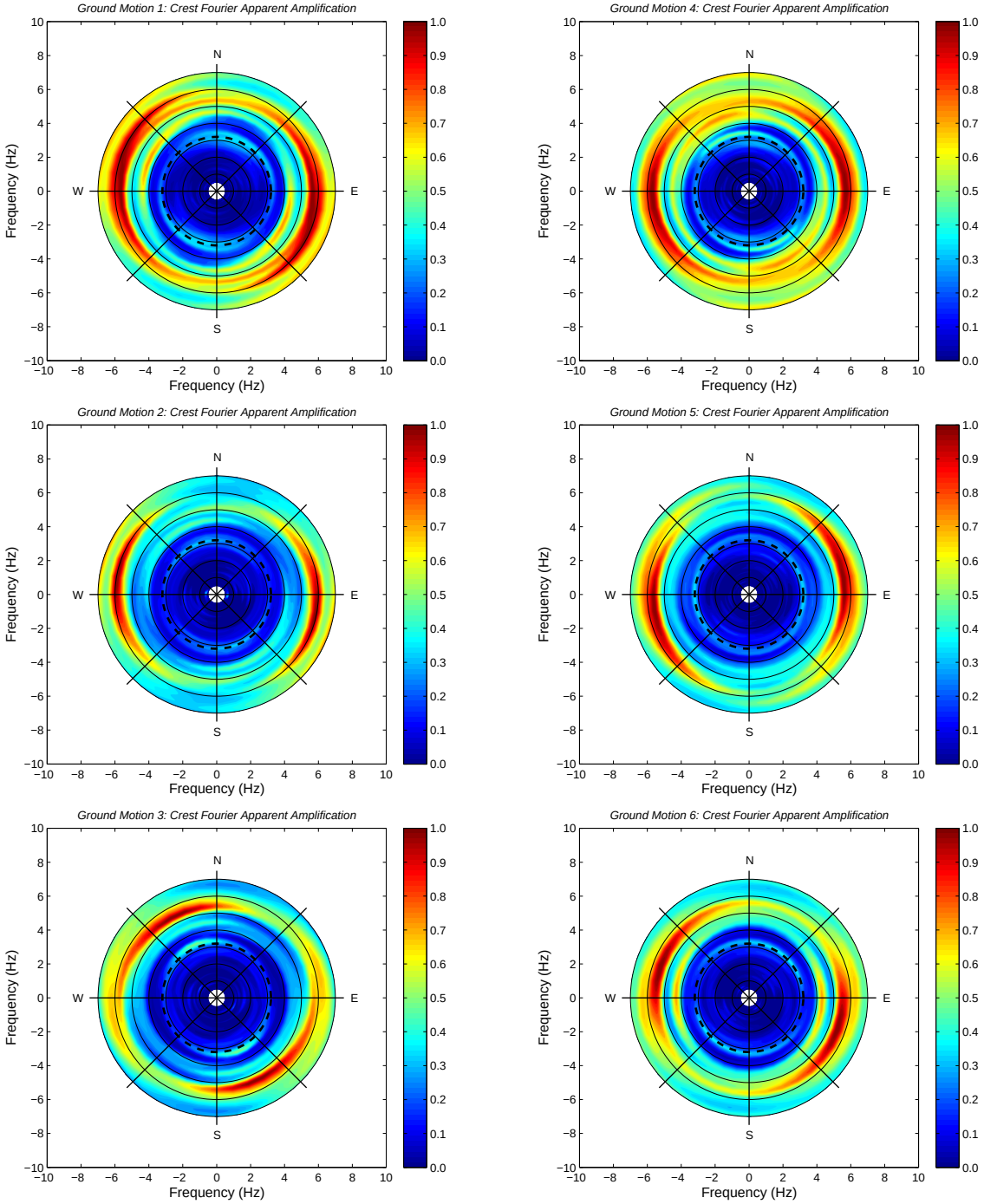

Figure 5.30: Ground motions 1 through 6 – contoured $F\ AA$ normalized by the maximum $F\ AA$ at the crest versus frequency considering 10 degree directional intervals. Black circles mark every 1Hz for frequencies ranging from 1 to 7Hz. The mean topographic frequency is marked by a dashed black circle.

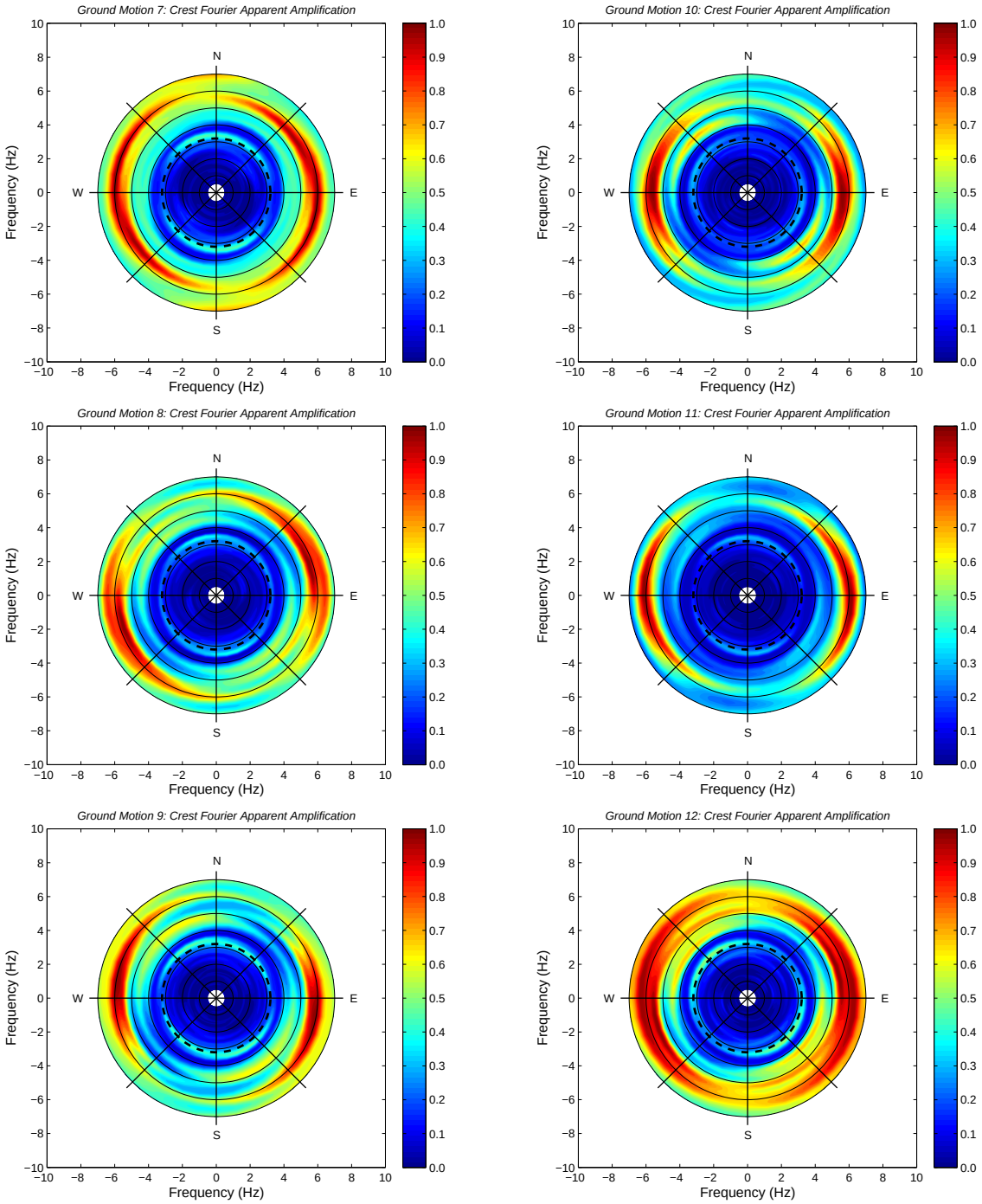

Figure 5.31: Ground motions 7 through 12 – contoured $F\,AA$ normalized by the maximum $F\,AA$ at the crest versus frequency considering 10 degree directional intervals. Black circles mark every 1Hz for frequencies ranging from 1 to 7Hz. The mean topographic frequency is marked by a dashed black circle.

NW, or parallel direction. This is consistent with the findings throughout the chapter. This amplification can be attributed to both site and topographic amplification. Amplification near 3.2Hz is associated with topographic amplification only. The direction of strongest amplification varies from the perpendicular to parallel direction, but often is oriented more N-S, spanning between the perpendicular and parallel directions. Below about 3Hz, amplification is comparatively low, with $F\ AA$ values less than 0.2 (or 20% of the maximum).

To better understand the contribution of topography to ground motion amplification, the $F\ TF$ spectrum is plotted for all ground motions in Figures 5.32 and 5.33. For comparative purposes, the spectra are again normalized by the maximum $F\ TF$ value. In this case, geometric mean spectra, considering normalization by the 50 free field simulations, are provided. The polarization patterns are similar to those found for the $F\ AA$ spectra, as expected. However, considering only the effects of topography, the level of amplification at the various frequencies (i.e., 3.2Hz, 4.5Hz and 5.5 to 6.5Hz) is more similar.

Directional, or directivity effects and ground motion polarization patterns are often complex and have been attributed to topography (Bouchon and Barker, 1996; Durante et al., 2017; Hartzell et al., 2014, 2017; Holden et al., 2014; Kaiser et al., 2013; Panzera et al., 2011; Spudich et al., 1996), local site effects and near surface geology (Bonamassa et al., 1991; Burjánek et al., 2014; Panzera et al., 2011), faults, folds or fractures within a rock mass (Burjánek et al., 2012; Durante et al., 2017; Holden et al., 2014; Kaiser et al., 2013; Panzera et al., 2011), or the presence of unstable landmasses (Burjánek et al., 2010; Kaiser et al., 2013; Panzera et al., 2011). Results of directional analysis have also been inclusive, such that no clear pattern emerges (Durante et al., 2017; LeBrun et al., 1999). When considering topographic effects, it has typically been observed that the strongest shaking occurs in the ridge perpendicular direction (that is perpendicular to the nearest cliff face, or for the case of a ridge line, transverse to the ridge). However, strong shaking has also been observed in the ridge parallel direction when frequency dependent polarization is considered. For fractured media, stronger shaking is again typically observed in the direction perpendicular to the fracture planes. However, it has also been observed in the parallel direction. For unstable

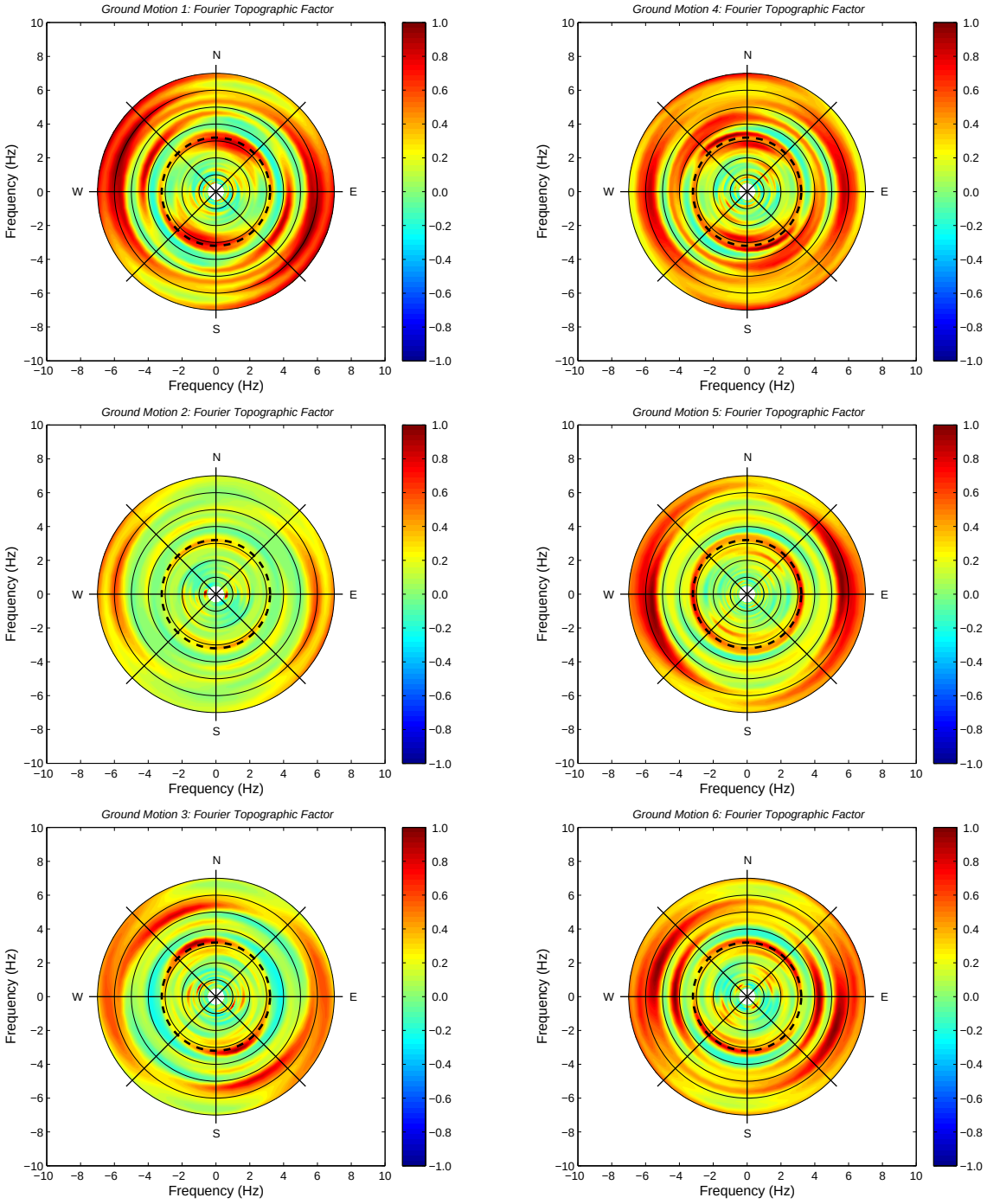

Figure 5.32: Ground motions 1 through 6 – contoured FTF normalized by the maximum FTF versus frequency considering 10 degree directional intervals. Black circles mark every 1Hz for frequencies ranging from 1 to 7Hz. The mean topographic frequency is marked by a dashed black circle.

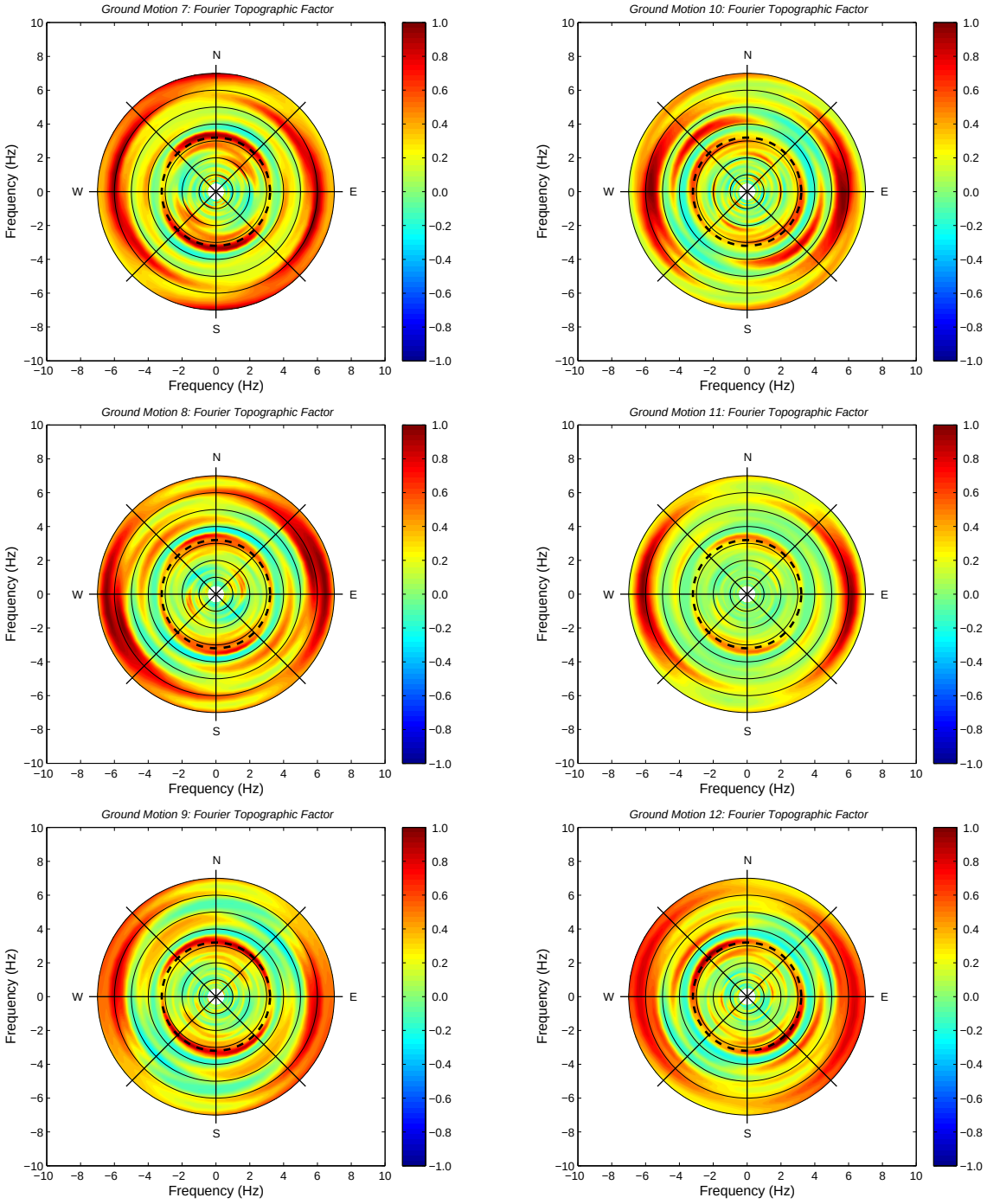

Figure 5.33: Ground motions 7 through 12 – contoured FTF normalized by the maximum FTF versus frequency considering 10 degree directional intervals. Black circles mark every 1Hz for frequencies ranging from 1 to 7Hz. The mean topographic frequency is marked by a dashed black circle.

landmasses, ground motion is typically polarized in the direction of previous deformation.

Given the site conditions at Redcliffs and history of rock fall and debris avalanches (Massey et al., 2016b), any of the above factors could contribute to ground motion polarization. In general, the directional variation of amplification at the various frequencies is consistent with the topography surrounding the RCBS station, in that amplification is strongest in directions perpendicular to the surrounding cliff faces. The parallel component of motion is farther from a cliff face, but also is oriented more favorably with the shorter width of the Redcliffs ridge (see Figure 5.2). It should be noted, however, that subsurface structure likely also contributes to the ground motion polarization; particularly at high frequencies that may be associated with the oscillation of rock blocks within the rock mass.

Reasons for greater shifts in the polarization of maximum amplification at the mean topographic frequency is unclear. The direction of greatest amplification occurs in the NE-SW, SE-NW and N-S directions, depending on the ground motion. This may, however, be influenced by the polarization of the ground motion entering the site, and the subsequent relationship between this polarization and the surface and subsurface geometry.

As a final spectral comparison, the H/V spectrum, normalized by the maximum H/V, is plotted for all ground motions in Figures 5.34 and 5.35. The amplification patterns are similar to those found for the $F\ TF$ and $F\ AA$ spectra at higher frequencies. Notably, the H/V amplitude is comparatively low in all directions (typically less than 10% of the maximum amplification) for frequencies encompassing the mean topographic frequency. This is consistent with the findings from the previous section.

The previous figures demonstrated directional effects using different Fourier based spectra. Figures 5.36 and 5.37 show directional effects for different intensity measures (i.e., PGA, PGV, PGD, and AI), as well Trifunac duration and MSF. Figures 5.36 and 5.37 show these six ground motion parameters for the crest normalized by the base and free field, respectively. The gray lines represent each ground motion; geometric mean values are plotted in red. Gray lines represent geometric mean values for the 50 free field simulations in Figure 5.37.

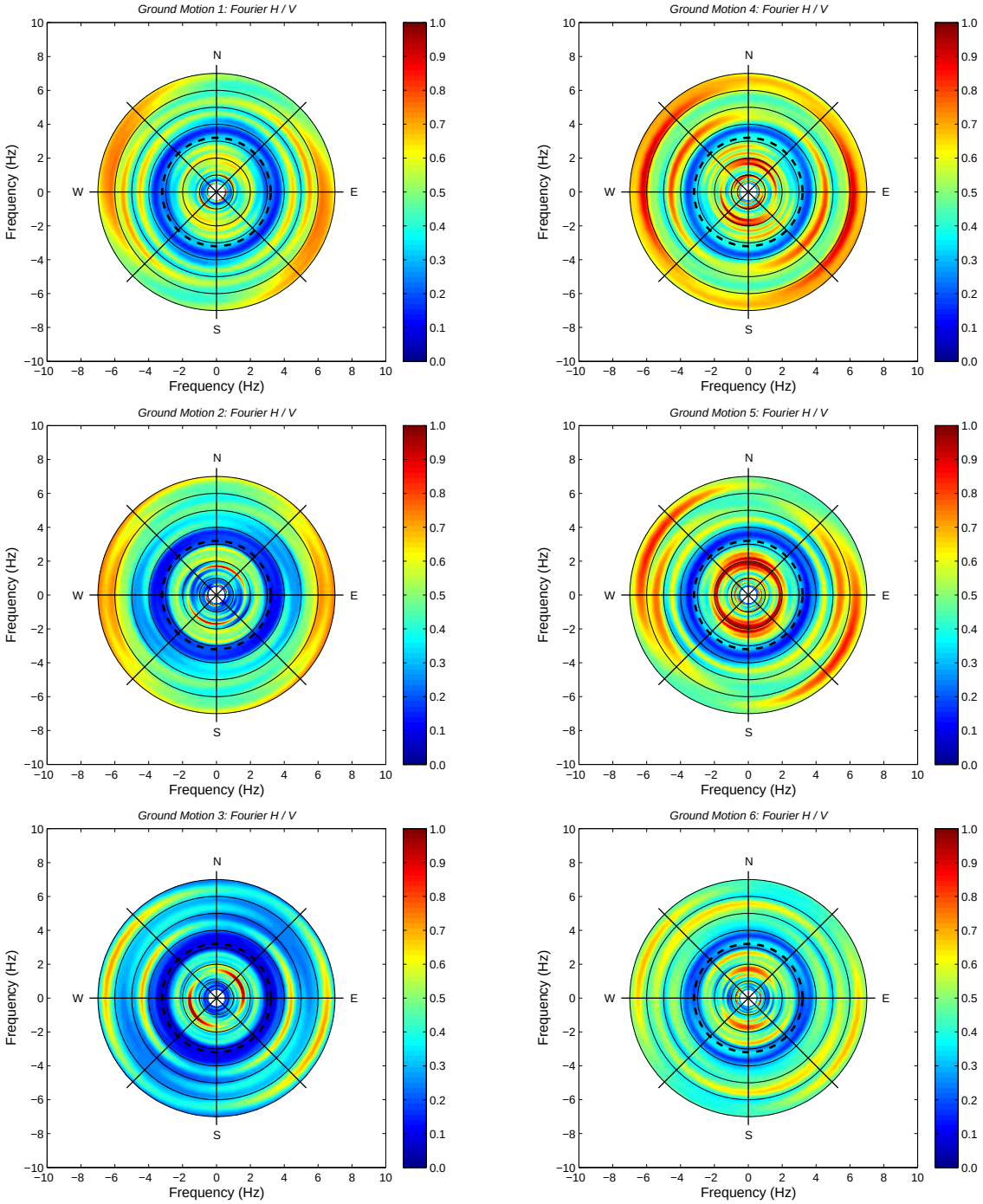

Figure 5.34: Ground motions 1 through 6 – contoured $F\ H/V$ normalized by the maximum $F\ H/V$ at the crest versus frequency considering 10 degree directional intervals. Black circles mark every 1Hz for frequencies ranging from 1 to 7Hz. The mean topographic frequency is marked by a dashed black circle.

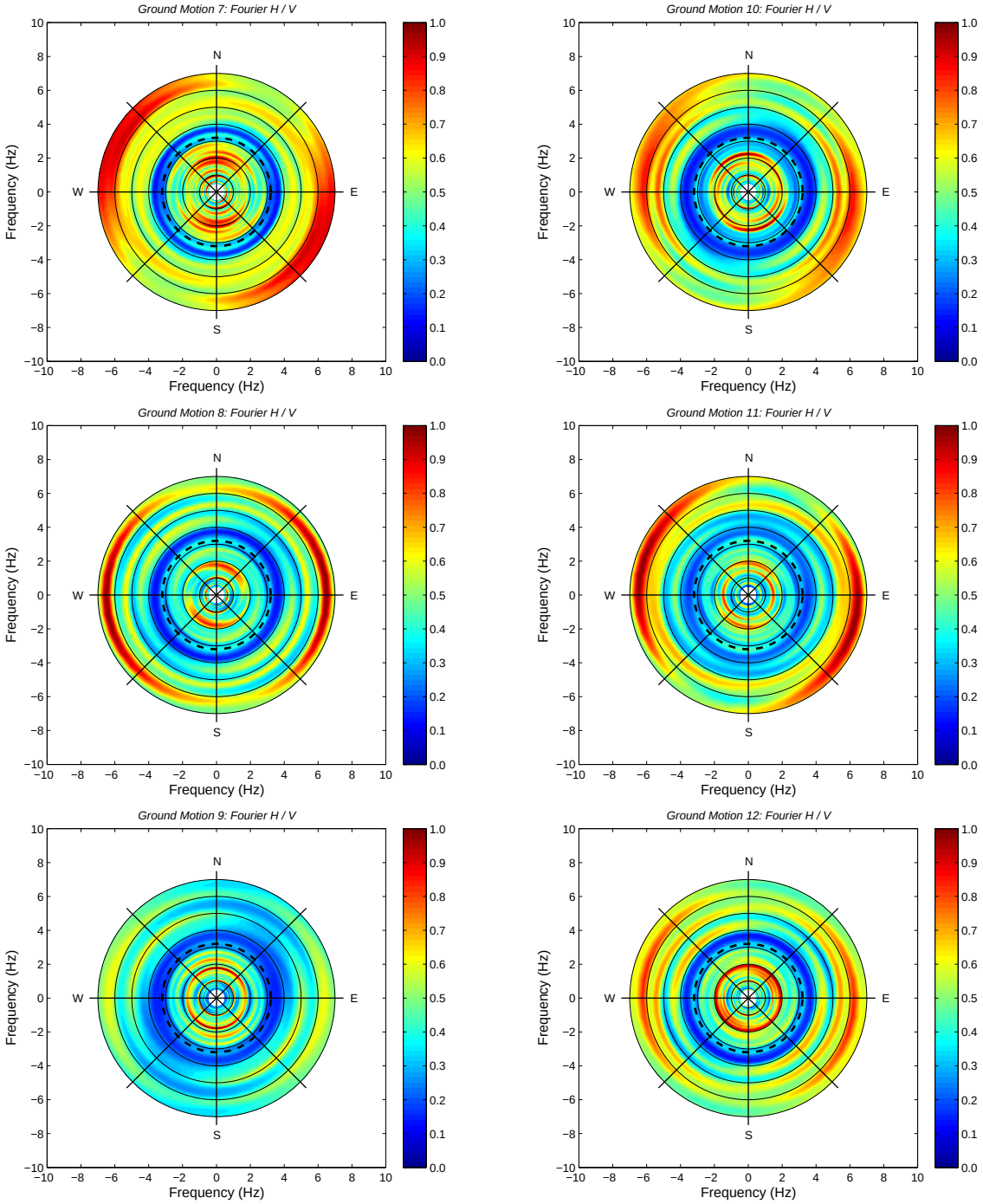

Figure 5.35: Ground motions 7 through 12 – contoured $F\ H/V$ normalized by the maximum $F\ H/V$ at the crest versus frequency considering 10 degree directional intervals. Black circles mark every 1Hz for frequencies ranging from 1 to 7Hz. The mean topographic frequency is marked by a dashed black circle.

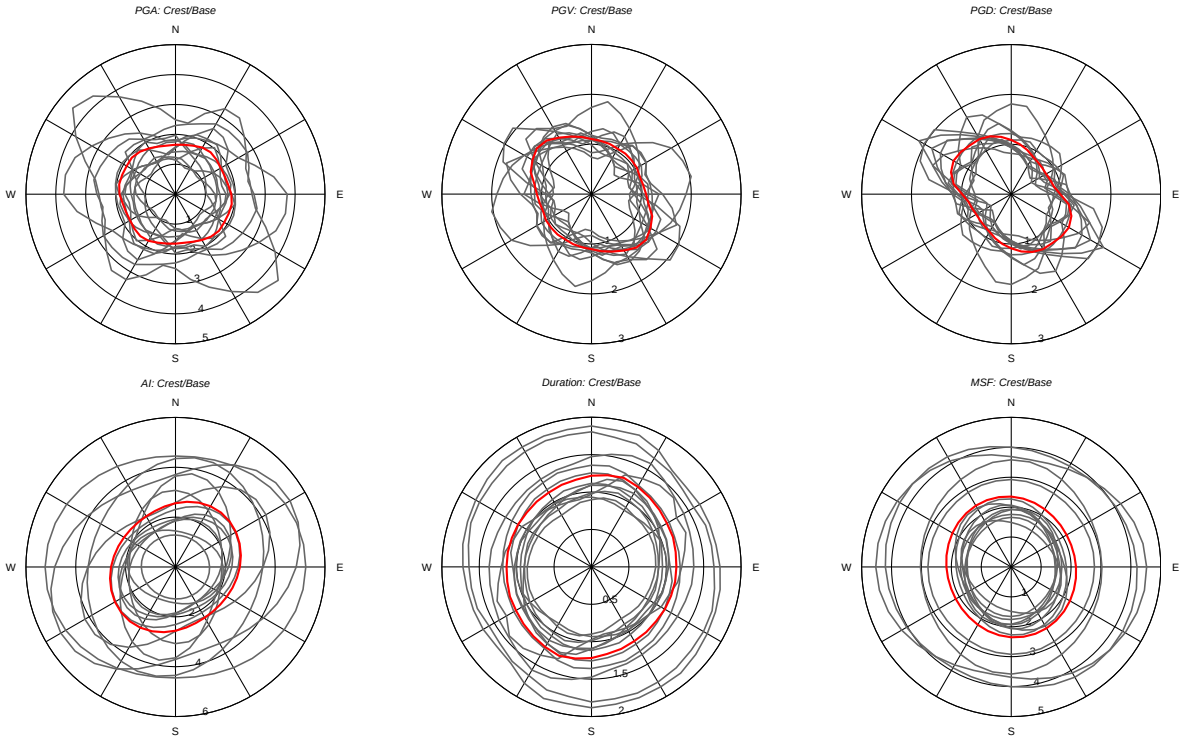

Figure 5.36: All motions – Ratio of surface (crest) recording to the base recording for the PGA, PGV, PGD, AI, $Duration$, and MSF. Motions are separated by those that have an MSF within (light blue) and not within (gray) the topographic frequency band. Mean values are provided for those within the topographic frequency band (orange) and for all motions (red). Values of 0, 90, 180 and 270 degrees represent north, east, south and west, respectively.

In general the amplification patterns are similar when comparing the crest to base or the crest to the free field. For all parameters, the amplification patterns vary from motion to motion. However, the individual ground motions, and mean values do exhibit directional trends.

Amplification of the PGA is stronger in both the parallel and perpendicular directions, but amplification in these directions are comparable to one another. PGV is also more strongly amplified in both the parallel and perpendicular directions, but the amplification is greater in parallel direction. Amplification of the PGD and increases in the MSF are greater in the parallel direction as well. Amplification of the AI, however, is stronger in the perpendicular direction. Increases in duration generally do not exhibit directional trends.

The duration of the free field is about equal to that of the crest in all directions.

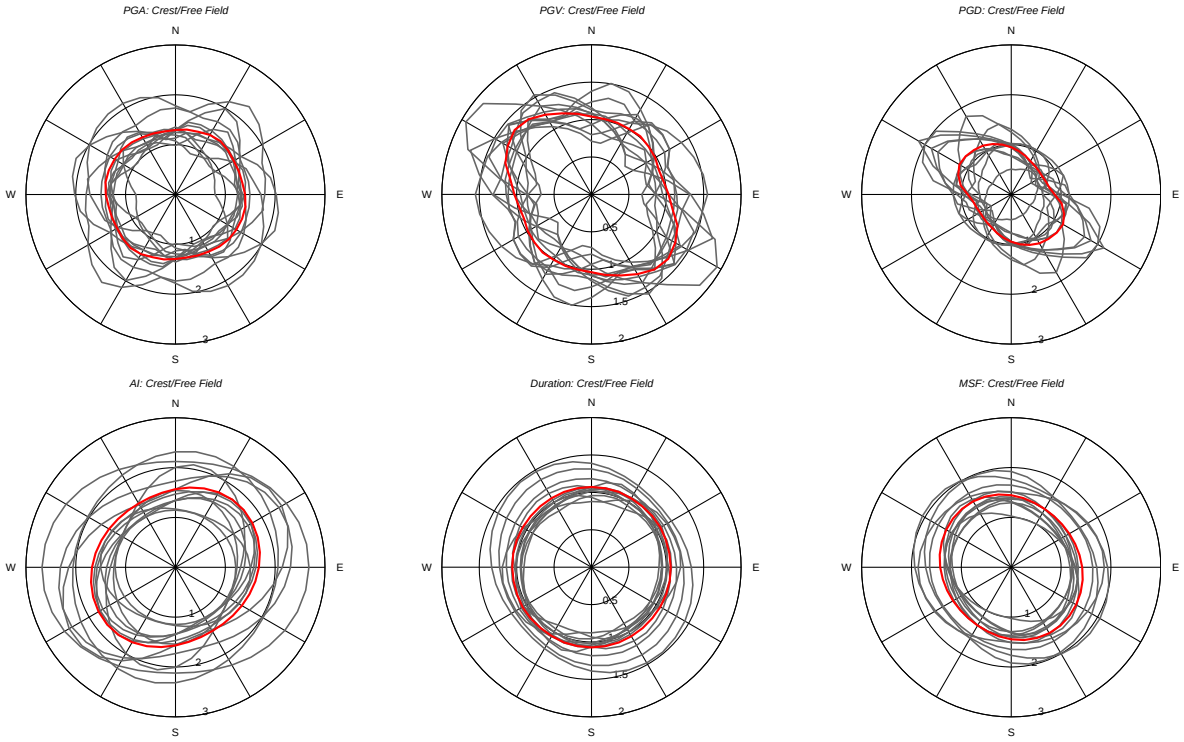

Figure 5.37: All motions – Ratio of surface (crest) recording to free field for the PGA, PGV, PGD, AI, $Duration$, and MSF. The free field values represent the mean values from the 50 simulations for each motion. Motions are separated by those that have an MSF within (light blue) and not within (gray) the topographic frequency band. Mean values are provided for those within the topographic frequency band (orange) and for all motions (red). Values of 0, 90, 180 and 270 degrees represent north, east, south and west, respectively.

The polarization of the various parameters is consistent with the amplification patterns illustrated throughout this chapter. Namely, observations from the $F\,TF$ and $F\,AA$ spectra in Figures 5.21 and 5.22. Amplification in the parallel direction tends to be greater than the perpendicular direction at higher frequencies, which explains the polarization of the MSF in the parallel direction. This is partially due to the stronger peak at 4.5Hz that does not exist (crest over free field) or is weaker (crest over base) in the perpendicular direction. This peak may also explain the polarization of the PGV which is typically associated with intermediate frequencies.

The polarization of PGD may be influenced by preexisting fracture patterns, instabilities

or weathering within the rock mass, which may promote movement in the parallel direction. Stronger amplification of the PGD could also be related to the ridge width, which is smaller in the parallel direction. However, it should be noted that PGD is based on the displacement time histories, which were calculated by integrating the acceleration time histories twice. This can lead to drift in the time history and be strongly influenced by low period noise. Therefore, this polarization may be artificial.

The polarization of amplification for the AI may be related to the proximity of the RCBS station to the cliff face in the perpendicular direction. As mentioned previously, AI is influenced by amplitude, frequency content and duration. Increases in duration are not directionally influenced. Therefore, the polarization of the AI is the result of greater overall ground motion amplification.

5.4 Discussion

Analysis results have been presented for a New Zealand case study of the Redcliffs ridge in the Port Hills suburb of Christchuch, New Zealand. Twelve weak ground motion recordings from a downhole array were used to interpret topographic effects utilizing the methods outlined in Chapter 3. The downhole array (station RCBS) is part of the strong-motion GeoNet network, and is located on a spur of the Redcliffs ridge about 15 meters from a NW striking cliff face, and about 40 meters from a NE striking cliff face. Ground motions were rotated into those perpendicular and parallel to the nearest cliff face (with the parallel component also perpendicular to the cliff face 40 meters away). Directional effects were additionally considered for the full range of compass directions using polarization plots.

The aim of this case study was to assess the effects of topography for the Redcliffs site and compare the results of this analysis to the findings from the previous chapters. Due to differences in the site conditions, site characterization and available data, different analysis techniques had to be utilized to make comparisons between Redcliffs and the slopes studied in the centrifuge experiments. The analysis techniques and findings from this case study are discussed in this section.

5.4.1 Analysis Techniques

One of the main issues with interpreting topographic effects in the field has been the lack of a proper reference free field station for comparison to ground motion on or near a topographic feature. This was also true for the Redcliffs site. Data was limited to a single surface and single base recording in close proximity to multiple cliff faces. However, it is likely that an equivalent free field site on the Redcliffs ridge could not be found even if additional accelerometers were installed.

In this study, a simplified approach was adopted to establish a reference free field station. A stochastic variation of the available shear wave velocity data was used, along with the base data recordings, to produce 50 free field simulations for each horizontal component of ground motion using a SHAKE-based batching program.

The development of the free field reference station was crucial for identifying topographic effects. Use of 50 free field simulations provided confidence that amplification around the mean topographic frequency at 3.2Hz, and additionally at 4.5Hz in the parallel direction, were indeed the result of topographic amplification. However, variation in the simulations did introduce additional complexities to the analysis.

In particular, with a varying shear wave velocity profile, a range of topographic and site frequencies had to be considered. For the case of Redcliffs, these frequency ranges overlapped, making the distinction between and site and topographic frequencies less clear. However, using the geometric mean shear wave velocity profile, the associated mean topographic frequency (3.2Hz) and mean site frequency (4.1Hz) matched frequencies associated with peak data amplification values (although the site frequency may have been slightly under-predicted). This was demonstrated for all ground motions using the $F\,TF$ and $F\,AA$ spectra in Figures 5.21 and 5.22.

The use of SHAKE for performing free field analysis had other limitations. Redcliffs mainly consists of rock with different degrees of weathering and fracturing throughout the rock mass (see Figures 5.3 and 5.4). These lateral heterogeneities can strongly influence the

ground response at the surface, but cannot be accounted for in the SHAKE analysis. Local site effects associated with the complex subsurface geometry and the interaction with local topography are likely responsible for strong amplification at higher frequencies (i.e around 6.0Hz and spanning 8.0 to 9.0Hz) observed at Redcliffs.

The limitations described above can mainly be attributed to site characterization. Establishing a characteristic shear wave velocity profile (or multiple profiles, or a 3-D velocity structure) would require additional geophysical testing across the site. Likewise, a more sophisticated 1-D analysis could be performed, but it would rely on capturing realistic variation in the material properties. Therefore, the importance of good site characterization for understanding the complex interaction between site and topographic effects should be emphasized.

Aside from variation in the shear wave velocity, variation in the topographic characteristics of the site had to be considered in evaluating topography frequencies. Three dimensional variation across the ridge made defining characteristic widths and heights difficult to define (see Figure 5.2). However, accounting for variation in slope height, it was found that the topographic frequency defined by Ashford et al. (1997) (based on a characteristic slope height) more closely matched the observed topographic amplification at various frequencies. The topographic frequency typically used for analysis in field case studies, that most recently modified by Paolucci (2002) (based on the characteristic width of the topographic feature), did not align well with the observed topographic amplification.

5.4.2 Topographic Effects

With a reference free field site, and topographic and site frequencies established, analysis of topographic effects was carried out in a manner similar to that in Chapter 3. However, two horizontal components of motions were considered, while for the centrifuge experiments only horizontal motion perpendicular to the slope was considered. In addition, directional effects at other compass directions were considered at the Redcliffs site.

Despite significant differences in the site conditions (weathered rock versus sand), slope

inclinations (greater than 60 degrees versus 30 degrees or less), overall topography (3-D ridge versus essentially 2-D slope), and ground motions (weak earthquake motions versus a wide range of motions), similar trends and levels of topographic amplification were observed for Redcliffs and the centrifuge experiments. Direct comparisons of all trends, however, could not be accomplished. In particular, spatial variability at Redcliffs could not be analyzed.

Topographic effects were mainly quantified by comparing the response near the crest of the topographic feature to an equivalent free field site of the same thickness and material properties as that below the crest. These comparisons were made using various intensity measures, spectra and frequency-based parameters, such as MSF. The analysis results presented for Redcliffs were then compared to those for the 30 degree slopes tested in the centrifuge experiments (note that 25 degrees slopes were used for vertical motions). The results are summarized below.

- For Redcliffs, crest PGA was typically 1 to 2 times the base, and crest *bp* FA was typically 1.5 to 2 times the base (Figure 5.17); the centrifuge, PGA was 2 to 3 times, and *bp* FA 2 to 3.5 times the base (Figure 3.9).

- For Redcliffs, deviations in MSF for the crest and free field versus the base were typically greater than that observed for the centrifuge slopes; this is attributed to the relationship between base MSF and the site and topographic frequencies. The $MSF\ TF$ was also greater for Redcliffs than for the centrifuge slopes (see Figures 5.18 and 3.10).

- For Redcliffs, $PGA\ TF$ ranged from -0.1 to 1.3, and 0.0 to 1.1 for the perpendicular and parallel components of motion; the centrifuge from -0.3 to 2.0, but below 0.8 for most motions. For Redcliffs, *bpF* TF ranged from 0.7 to 1.7, and 1.0 to 1.6 for perpendicular and parallel components of motion; the centrifuge *bpSA* TF from -0.2 to 5.0, but below 2.2 for most motions (see Figures 5.17 and 3.11).

- For Redcliffs, $PGV\ TF$ ranged from -0.4 to 0.3, and 0.2 to 0.7 for perpendicular and

parallel components; the centrifuge from -0.5 to 2.5, but below 0.8 for most motions. For Redcliffs, $AI\ TF$ ranged from 0.2 to 1.5; the centrifuge -0.5 to 18.5, but below 3.6 for most motions (see Figures 5.20 and 3.23).

- For Redcliffs, the peak in $F\ TF$ near the mean topographic frequency ranged from 0.5 to 1.5, with means of 1.0 and 0.9 for perpendicular and parallel components of motion (Figure 5.21); the centrifuge peak in mean $SA\ TF$ ranged from 0.6 to 2.0 depending on the grouping of ground motions, but was 0.9 for all motions (Figure 3.12).
- For Redcliffs, peak vertical to horizontal $F\ TF$ near mean topographic frequency ranged from 0.0 to 1.2, with a mean of 0.5, and from 0.5 to 2.4, with a mean of 1.1 for perpendicular and parallel components (Figure 5.25; the centrifuge peak mean vertical to horizontal $SA\ TF$ ranged from 0.1 to 0.5 depending on the grouping of ground motions, but was 0.2 for all motions (Figure 3.76).

Interestingly topographic amplification of the parallel component of motion is typically comparable to that of the perpendicular component despite the greater distance to a slope crest. Based on the findings from Chapter 3, ground motion in the parallel direction would be just outside the *topographic zone of influence*, defined, on average, to extend a distance of about H (i.e the cliff height) behind the crest. The perpendicular component of motion, however, is about $0.5H$ behind the nearest cliff face.

Comparable amplification for the two components may be related to the ridge width, which is smaller in the parallel direction. Alternatively, the zone of influence, and subsequently degree of amplification may be tied to the back slope angle behind the crest. In the parallel direction, the back slope angle is negative (i.e., it is angled downward) behind the crest and the elevation continues to decrease beyond the RCBS station. In the perpendicular direction, the back slope behind the RCBS station is positive. Either scenario requires movement of a larger landmass in the perpendicular direction. This may offset the proximity of the sensor to a cliff face. An additional consideration is that polarized amplification of the ground motion may be related to a combination of site and topographic effects, as

was discussed in the previous section. In other words, strong amplification in the parallel direction may be related to the combination of topographic and local site effects.

The relationship between ground motion MSF, the topographic frequency, and the level of topographic amplification defined in Chapter 3 was weaker for the Redcliffs case study. For the centrifuge slopes, the level of topographic amplification increased as the ground motion MSF approached the topographic frequency. This was found to be generally true considering $PGA\ TF$ for both components of motion and the $bpF\ TF$ for the perpendicular component. However, for the $bpF\ TF$ of the parallel component of motion, this trend did not exist. Because the parallel component of motion exhibited strong topographic amplification at two frequencies within the topographic frequency band (i.e., 3.4 and 4.5Hz), the likelihood for a high $bpF\ TF$ was greater for the parallel than the perpendicular component of motion. This is true even if strong components of motion exist at other frequencies, which influence the relationship between the MSF and the mean topographic frequency. Therefore, if topographic amplification is expected at multiple frequencies (i.e., for the Redcliffs site), the MSF may not correlate well to amplification within specific frequency bands.

5.5 Conclusions

Previous seismic events have led to rockfall, slides, and debris avalanches at the Redcliffs ridge, which have caused damage to numerous homes within the Redcliffs suburb (Massey et al., 2016b). To mitigate future hazards to people and structures, it is important to understand the factors that may contribute to those hazards. Hazards such as seismically induced landslides and damage to structures will depend upon the ground motion experienced during an earthquake. For a ridge, such as Redcliffs, this ground motion will be influenced by both site and topographic effects.

Analysis of site and topographic effects is limited by the ability to the properly characterize the site. To fully understand the complex interaction between the fractured, weathered, rock mass and highly variable surface topography found at Redcliffs would require extensive site investigation. In particular, the variation in the shear wave velocity profile and subsur-

face layering across the site must be understood. Additionally, an accurate survey of the surface topography would be required.

For this site, shear wave velocity data, material unit weights and lithologic information were available. This data combined with ground motion data from the downhole array at RCBS enabled use of a simplified procedure to establish a reference free field station for the site. Although not all complexities associated with the site response were captured, the method outlined in this chapter, along with the analysis techniques, could be easily applied to other sites to better understand the topographic modification of ground motion.

Frequencies associated with topographic resonance could potentially be identified using data from the downhole array without the use of a free field station. The H/V spectrum at the surface could be used to identify frequencies associated with site resonances, and the $F\ AA$ used to identify frequencies associated with both site and topographic amplification. Frequencies that peak on the $F\ AA$ spectrum, but not the H/V spectrum may be associated with topographic amplification. This method would be limited to cases where there are distinct differences in the site and topographic frequencies. However, given the ongoing debate on the use of H/V spectra, this method should be used with caution. It is therefore recommended that a reference free field station be established when possible.

Other significant findings from this case study include:

- Although field case studies often define the topographic frequency by the characteristic width of ridges or mountains, the topographic frequency defined by slope/cliff height should be considered, and was found to better align with topographic resonance for the Redcliffs site.

- The characteristic dimensions of a complex 3-D ridge can be difficult to define. Therefore, multiple ridge heights and widths should be considered when identifying topographic frequencies. This may include average or differential cliff heights along various cross sections of the ridge.

- For complex geology and surface topography the separation of site and topographic

effects is even more difficult to achieve. Extensive subsurface investigation may be required to fully understand the interaction between the two.

- Topographic and site amplification are directionally and frequency dependent for the Redcliffs site. Although overall topographic and site amplification levels were similar for the perpendicular and parallel components of motion, amplification varied according to frequency.

- Directional dependence can be partially tied to topographic influences (i.e., amplification was mainly concentrated at resonant frequencies associated with the ridge geometry). However, it is likely also influenced by local site effects.

- Topographic amplification can occur at multiple frequencies in a given direction. When this occurs, the relationship of the MSF to the level of amplification may not be well correlated.

- It is unclear why amplification at the mean topographic frequency varied directionally from ground motion to ground motion. This may be related to the polarization of the ground motion entering the site in relation to the subsurface and surface geometry.

- Frequencies associated with site resonance, or combined site and topographic amplification could be obtained using the H/V spectrum. However, those associated with topographic amplification only are muted on the H/V spectrum. Therefore, the H/V spectrum should not be used alone to identify or quantify topographic amplification.

- The vertical to horizontal $F\ TF$ was useful in separating the contributions of topographic and site amplification. Although the vertical component of motion was not as pronounced as that observed in the centrifuge experiments. This is partially due to container rocking in the experiments, and also likely partially due to the disruption of Rayleigh waves over the complex topography at Redcliffs.

- Levels of topographic amplification were similar to those found in the centrifuge ex-

periments discussed in Chapters 3 and 4.

Although the results were consistent for the ground motions analyzed, it would be interesting to see if the trends observed in this study are solidified when including additional motions. In particular, would the ground response be similar for strong ground motion? Additional subsurface characterization may also aid in better understanding the variation in the polarization of ground motion near the mean topographic, and other amplified frequencies.

Chapter 6

CONCLUSIONS AND FUTURE WORK

A list of research questions was provided at the beginning of this dissertation in Chapter 1. These questions were designed to accomplish the overarching goals of this research. The aim of this chapter is systematically address these questions based on the findings from Chapters 3, 4, and 5.

1. **What is the main cause of topographic amplification?**

   The main cause of topographic amplification of horizontal ground motion is excitation, due to a tendency towards resonance, at frequencies typically ranging from 0.7 to 1.3 times the *topographic frequency* (defined as $f_t = \bar{V}_s/5H$, where $\bar{V}_s$ is the average shear wave velocity, and H is the height of the slope). A slope represents a reduced mass and stiffness compared to the free field behind the crest. It is for this reason that excitation can occur at the topographic frequency. This also helps explain the increase in amplification for steeper slopes, for which the mass in front of crest is reduced further.

2. **What ground motion characteristics have the greatest influence on topographic effects?**

   The level of topographic amplification is related to the input (base) amplitude at frequencies near the topographic frequency, such that an increase in the base amplitude at these frequencies leads to an increase in amplification. Competition, or energy at other frequencies also impacts the level of amplification. Therefore, frequency content and energy content at specific frequencies have the greatest influence on topographic effects.

3. How are the amplitude, frequency content, and duration of ground motion affected by slopes?

Both the frequency content and amplitude are affected by topography. The most significant levels of topographic amplification are concentrated to a frequency band encompassing the topographic frequency (or frequencies in the case of Redcliffs). As a result of this amplification, ground motion frequency content shifts towards the topographic frequency. The ground motion duration is not influenced by topography.

For the slopes tested in the centrifuge, the amplitude and frequency content were affected as follows:

- *peak ground acceleration* (PGA) ranged from 50% less than to 200% greater than the free field behind the crest;
- for motions with a *mean square frequency* (MSF) within 30% of the topographic frequency (STR motions), at locations of peak amplification, mean PGA values are roughly 60%, 40%, and 40% greater (adjusted for natural fluctuations) than the free field for the 30, 25, and 20 degree slopes, respectively;
- peak spectral acceleration for a frequency band which ranged from about 0.6 to 1.1 times the topographic frequency, deemed *banded peak spectral acceleration* ($bp\ SA$) ranged from 50% less than to 500% greater than the free field;
- for STR motions, at locations of peak amplification, mean peak SA are roughly 190%, 120–140% and 120–140% greater (adjusted for natural fluctuations) than the free field for the 30, 25, and 20 degree slopes, respectively (the peak amplitude listed for the 20 degree slopes is reflective of the peak response, which occurred on the slope face; at the slope crest the mean peak values are roughly 60% greater than the free field);
- ground motion MSF shifts by as much as 55% for the 30 and 25 degree slopes and 30% for the 20 degree slopes in comparison to the free field;

- vertical SAs are on average 50% greater than that of the horizontal free field motion for STR motions for the 25 degree slopes.

For the Redcliffs case study, the amplitude and frequency content were affected as follows:

- PGA ranged from 10% less than to 140% greater than the free field, and from equal to, to 120% greater than the free field for the perpendicular and parallel components of motion, respectively;
- banded peak Fourier amplitude ($bp\ FA$) ranged from 70% to 170% greater than the free field, and from 110% to 160% greater than the free field for perpendicular and parallel components of motion, respectively;
- The mean peak FA near the mean topographic frequency ranged from 50% to 150% greater than the free field, with means of 100% greater and 90% greater for perpendicular and parallel components of motion, respectively;
- ground motion MSF shifts by as much as 70% and 110% in comparison to the free field for the perpendicular and parallel components of motion, respectively;
- Vertical FAs near the mean topographic frequency ranged from equal to, to 120% greater than the horizontal free field motion, with a mean of 50% greater, and from 50% to 240% greater than the free field, with a mean 110% greater, for perpendicular and parallel components of motion, respectively.

4. What is the spatial extent of the effects on the above parameters?

For slopes tested in the centrifuge, the spatial extent of topographic effects, defined as the *topographic zone of influence*, on average spanned a horizontal distance of the slope height, H, behind (towards the free field), and $2H$ in front of (towards the slope toe), the location where peak amplification occurred. It should be noted that $2H$ in front of the location of maximum amplification typically included the entire face of the

slope. The location of maximum amplification is typically at the slope crest, but can migrate to the face of shallower slopes.

The spatial extent of topographic effects could not analyzed at Redcliffs.

5. What factors influence the spatial extent of topographic effects?

The spatial extent of topographic effects was found to be related to the level of topographic amplification for static parameters, such as PGA or peak SAs. When topographic amplification occurs during an earthquake, the size of the area affected is dependent upon the ground motion wavelength. and the influence of phasing when multiple frequency components are present. The area increases with increasing wavelength and decreases when the crest moves out of phase with the surrounding land mass.

6. Do topographic effects lead to differential motion and how does this affect the ground response?

Differential movement between the slope landmass and free field landmass can lead to a reduction in overall ground motion amplitude for the slope. The impact of this is dependent upon the relative amplitude of ground motion for each landmass. This behavior can be observed by tracking the phasing between the crest and free field in time.

Differential movement between the slope and the ground below the slope can lead to softening, or induced non-linearity, at the base of a slope. This can impede energy from propagating up the slope, and thus reduce the level of amplification. Conversely, softening within the slope can lead to greater levels of amplification.

7. How does slope inclination affect the topographic modification of ground motion?

Topographic modification of ground motion was found to be greater for steeper slopes in the centrifuge experiments, with all else equal (i.e., similar site conditions, ground motions etc). Differences in the level of topographic amplification for the three slopes were presented in response to question 3. However, the level of topographic amplification for the 30 degree soil slopes tested in the centrifuge exceeded that of Redcliffs, which has slopes steeper than 60 degrees. This is likely related to the lack of energy near the topographic frequencies for ground motions entering the Redcliffs site, and the increased distance between recording locations and the slope crest.

8. What geometric feature has the greatest influence: height or length of the slope?

The topographic frequency defined by Ashford et al. (1997) was found to correlate best to topographic amplification for both the soil slopes in the centrifuge and the weathered rock slopes that are part of a larger ridge at Redcliffs. This topographic frequency is related to the height of the slope. Therefore, the height of the topographic feature has the greatest influence.

9. Does the type of ground motion (i.e., broadband versus narrow band) influence topographic effects?

The type of ground motion did not influence the magnitude of topographic effects captured in this study. Both broadband and narrow-band motions exhibited changes in frequency content and amplitude and typically followed the same trends. Because frequency content has a significant impact on topographic effects, in general, a broadband motion would be more susceptible to topographic effects, as the likelihood of the motion containing frequencies that would be amplified is greater. The amplification of these components of motion would also, subsequently, have a more profound effect on the ground motion MSF. However, a narrow-banded motion with energy concentrated at a frequency compatible with the topographic feature can still be significantly

modified. It should be noted that topographic effects were more pronounced for sine wave motion concentrated at the topographic frequency.

10. At the crest, do site effects or topographic effects dominate the ground response? Under what circumstances does one or the other control?

Site amplification and topographic amplification can occur simultaneously at the crest. Topographic amplification can also coincide with ground motion at other frequencies. Depending on the relative amplitude at these frequencies and phasing, this can either reduce or enhance overall ground motion amplitude.

In other words, site effects will control if the ground motion is rich in frequencies near the site frequency. Likewise, topographic effects can control if the ground motion is rich in frequencies near the topographic frequency. If the components are roughly equal, this can lead to a complex interaction. Additionally, absorption of energy at the topographic frequency, due to topographic amplification, and at the site frequency, due to site amplification, leads to an apparent deamplification of frequencies between the site and topographic frequencies at the crest compared to the free field.

11. Can site effects be separated from topographic effects or do they influence each other?

For the slopes in the centrifuge and those at Redcliffs, there is a strong interaction between site and topographic effects. The complexity of this interaction was touched upon in answering the previous question. Topographic effects in some way depend on site conditions in that the topographic frequency is related to the shear wave velocity of the subsurface material. Topographic effects, however, can be more easily isolated for idealized ground motions (i.e., frequency sweeps).

12. Under what circumstances do topographic effects exist or not exist?

Topographic effects can be strongly muted if ground motion energy is concentrated at the site frequency or if little to no energy is concentrated at the topographic frequency. However, even for these conditions, Rayleigh waves may still develop. Therefore, topographic effects cannot be eliminated.

13. How does horizontal ground motion compare to vertical ground motion?

Vertical ground motion can be similar in amplitude and frequency content to horizontal ground motion at the slope crest. This was the case for the centrifuge experiments. However, this was partially due to the presence of container rocking. Typically, the vertical component of motion is weaker than the horizontal component of motion at the crest. This was the case for Redcliffs, where the PGA was closer to 50% of the horizontal PGA. For both the centrifuge experiments and Redcliffs, however, the vertical component of motion was amplified compared to the horizontal free field motion at frequencies encompassing the topographic frequency. The presence of a strong vertical component of motion is likely due to the development of Rayleigh waves.

14. Can single station methods, such as H/V spectral analysis be used to analyze topographic effects?

For the Redcliffs site, it was found that frequencies associated with site resonance, or combined site and topographic amplification could be obtained using the H/V spectrum. However, those associated with topographic amplification only were muted on the H/V spectrum. Therefore, the H/V spectrum should not be used alone to identify or quantify topographic amplification.

15. For complex topographies, what influence does the polarization of ground motion have on topographic effects?

Topographic and site amplification were directionally and frequency dependent for the Redcliffs site. Although overall topographic and site amplification levels were similar for

the perpendicular and parallel components of motion (i.e., perpendicular and parallel to the nearest cliff face at Redcliffs), amplification varied according to frequency. At Redcliffs, directional dependence could be partially tied to topographic influences (i.e., amplification was mainly concentrated at resonant frequencies associated with the ridge geometry). However, it was likely also influenced by local site effects.

16. How useful is a centrifuge investigation for understanding topographic effects? How do findings from this investigation compare to a field case study? Can the same analysis methods be applied?

Physical modeling in the centrifuge proved to be a powerful tool for collecting data used for analyzing topographic effects in a systematic and practical manner. Data from the centrifuge experiment also proved useful for analyzing the causes and influences of topographic effects. The density of sensors within the model configurations allowed wave propagation and the separation of behavior between the slope and free field behind the slope to be observed. Additionally, a large suite of ground motions was used, which included those that did and did not exhibit significant topographic effects. This allowed the influences of topographic effects to be more easily identified. The main limitations were boundary effects and container rocking. Boundary effects did affect the ability to quantify the spatial extent of topographic effects. Container rocking influenced the vertical component of motion.

Findings from centrifuge experiment were comparable to those of the Redcliffs case study, despite significant differences in the site conditions and topographic settings. A free field station was established for Redcliffs using a simplified procedure. This allowed analysis methods similar to those used for the centrifuge analysis to be employed.

17. How do trends discovered in this study compare to past work?

A number of qualitative findings from this study align with those of previous researchers. Quantitatively, topographic amplification ranges exceed previous numerical

investigations and span the lower range of field studies. However, some new findings from this study include:

- Ground motion MSF correlates well with topographic amplification, such that amplification increases as the MSF approaches the topographic frequency. This is true for one-sided slopes, but may not be valid for complex ridge-like geometries where more than one topographic frequency may exist.
- Topographic amplification can exceed site amplification for the right ground motion and ground conditions.
- A Stockwell MSF can be used to identify resonant conditions at different instances in time and can be correlated to differences in the Stockwell spectrum, and cumulative AI between the crest and free field.
- The Hilbert transform can be used to track phasing between the free field and crest. Differential motion between the slope landmass and free field landmass can influence the ground response of the slope.
- A reference free field station can be established using a simplified procedure to aid in the analysis of topographic effects for sites with complex subsurface and surface geometry.
- *Apparent Amplification* (AA) can be used in concert with surface H/V spectra to help identify topographic frequencies at locations where downhole and surface data is available.

18. How easily can topographic effects be predicted?

Due to the complex interaction between topographic and site effects, it would be difficult to consistently predict the contribution of topographic effects on ground motion. However, for well characterized sites, the influence of topographic effects could be more easily identified. For instance, if a topographic frequency (or frequencies) can be calculated, predictions of the amplification at those frequencies could at least be empirically

quantified. Additionally, numerical models which are well calibrated to the site and topographic conditions have performed better in predicting the recorded ground motion on topographic features (Assimaki and Jeong, 2013; Hartzell et al., 2017).

19. Do these effects occur within the frequency band of interest for engineering applications?

Topographic frequencies were found at 3.2Hz and 4.5Hz at Redcliffs, and 4.5Hz for the slopes tested in the centrifuge at 55g. These frequencies would coincide with resonant frequencies of 2 to 5 story buildings, and therefore are within the frequency band of interest for engineering applications. Buildings built on slopes similar to those analyzed in this study could be exposed to extreme shaking, resulting in damage or destruction of the building.

20. What impact could these effects have on the triggering of landslides?

Although not the focus of this study, the impact of topographic effects on the triggering of landslides should be considered. As was discussed in Chapter 4, differential movement between a landmass encompassing the slope and the surrounding soil can lead to softening near the base of the slope. The landmass encompassing the slope typically took on the shape of a deep-seated landslide. Therefore, differential movement associated with resonant conditions of the slope could lead to the development of shear planes, and result in a landslide failure.

6.1 Future Work

There are numerous avenues for further study of topographic effects. Those that more immediately build off the research presented in this dissertation are provided below.

- Two other slope configurations were tested as part of the centrifuge investigation presented in this dissertation. One consists of a dam-like structure with a 30 degree slope

on one side a 20 degree slope on the other. The other configuration consists of a dam-like structure with a 30 degree slope on one side and a 70 degree slope on the other. For the latter configuration, the model material was changed to cemented sand and the slope was brought to failure. Data from these slope configurations could be analyzed in the framework presented in this dissertation.

- Centrifuge experiments could be performed for a wide variety of soil and topographic conditions. It would be interesting to attempt to model a specific topographic feature, such as the Redcliffs ridge. This particular ridge would be difficult to accurately model, but perhaps a more simple structure could be found. Alternatively, features present at Redcliffs could be explored, such as the effects of systematically changing the back slope angle behind the crest.

- Additional analysis could be performed with the Redcliffs data. Namely, the time and time frequency domain analysis utilized in Chapter 4 could be applied. This process has already been started and, although not included in this dissertation, may be used for a future journal paper.

- Assuming the RCBS station is still recording down hole data, more ground motions, particularly strong ground motions, could be analyzed using the methods outlined in Chapter 5. Additionally, it would be interesting to employ a temporary horizontal array directly adjacent to the RCBS station, running in the perpendicular and parallel directions. In this way, spatial variability of topographic effects could be assessed.

- Temporary arrays could be installed at sites where the arrays could be extended from the crest of a slope to a free field location. A site with relatively homogeneous subsurface would be most ideal for a study of this nature.

REFERENCES

Carlos Acosta. Progress report draft: Static properties of lightly cemented nevada sands for centrifuge test models for nees Topo Project. For preliminary discussion only, January 2011a.

Carlos Acosta. Progress report draft: Summary of first set of resonant column (RC) tests on cemented sands. For preliminary discussion only, February 2011b.

Manager Adrian Rodriguez-Marek. Project: Topographic effects in strong ground motion - from physical and numerical modeling to design, 2010. URL `https://nees.org/warehouse/project/977`.

Timothy D. Ancheta, Jonathan P. Stewart, Norman A. Abrahamson, and Robert L. Nigbor. Preliminary estimation of seismically induced ground strains from spatially variable ground motions. *Geotechnical Earthquake Engineering and Soil Dynamics IV*, 181, May 2008. ASCE special publication.

Scott A. Ashford and Nicholas Sitar. Seismic response of steep natural slopes. Technical Report UCB/EERC-94/05, Earthquake Engineering Research Center, University of California Berkeley, May 1994.

Scott A. Ashford and Nicholas Sitar. Analysis of topographic amplification of inclined shear waves in a steep coastal bluff. *Bulletin of the Seismological Society of America*, 87(3): 692–700, June 1997.

Scott A. Ashford, Nicholas Sitar, John Lysmer, and Nan Deng. Topographic effects on the seismic response of steep slopes. *Bulletin of the Seismological Society of America*, 87(3): 701–709, June 1997.

D. Assimaki and S. Jeong. Ground-motion observations at hotel montana during the m 7.0 2010 haiti earthquake: Topography or soil amplification? *Bulletin of the Seismological Society of America*, 103(5):2577–2590, October 2013.

Dominic Assimaki, George Gazetas, and Eduardo Kausel. Effects of local soil conditions on the topographic aggravation of seismic motion: Parametric investigation and recorded field evidence from the 1999 Athens earthquake. *Bulletin of the Seismological Society of America*, 95(3):1059–1089, June 2005a.

Dominic Assimaki, Eduardo Kausel, and George Gazetas. Soil-dependent topographic effects: A case study from the 1999 Athens earthquake. *Earthquake Spectra*, 21(4):929–966, November 2005b.

Kuvvet ATAKAN, Anne-Marie DUVAL, Nikos THEODULIDIS, Bertrand GUILLIER, Jean-Luc CHATELAIN, Pierre-Yves BARD, and the SESAME-Team. The h/v spectral ratio technique: Experimental conditions, data processing and empirical reliability assessment. In *13th World Conference on Earthquake Engineering*, August 2004. Paper No. 2268.

G.A. Athanasopoulos and C.S. Zervas. Effects of ridge-like surface topography on seismic site response. *Transactions on the Built Environment*, 3, 1993.

Simone Barani, Marco Massa, Sara Lovati, and Daniele Spallarossa. Effects of surface topography on ground shaking prediction: implications for seismic hazard analysis and recommendations for seismic design. *Geophysical Journal International*, 197:1551–1565, April 2014.

P.-Y. Bard and J Riepl-Thomas. *Wave propagation in complex geological structures and their effects on strong ground motion*, chapter 2, pages 37–95. WIT Press, Southhampton, UK, 2000.

Julian J. Bommer and Carlos E. Rodríguez. Earthquake-induced landslides in Central America. *Engineering Geology*, 63:189–220, 2002.

Ornella Bonamassa, John E . Vidale, Heidi Houston, and Susan Y. Schwartz. Directional site resonances and the influence of near-surface geology on ground motion. *Geophysical Research Letters*, 18(5):901–904, May 1991.

David M. Boore. The effect of simple topography on seismic waves: Implications for the accelerations at the Pacoima Dam, San Fernando Valley, California. *Bulletin of the Seismological Society of America*, 63(5):1603–1609, October 1973.

David M. Boore and Julian J. Bommer. Processing of strong-motion accelerograms: needs, options and consequences. *Soil Dynamics and Earthquake Engineering*, 25:93–115, 2005.

Michel Bouchon. Effect of topography on surface motion. *Bulletin of the Seismological Society of America*, 63(3):615–632, April 1973.

Michel Bouchon and Jeffrey S. Barker. Seismic response of a hill: The example of Tarzana, California. *Bulletin of the Seismological Society of America*, 86(1A):66–72, February 1996.

Michel Bouchon, Craig A. Schultz, and M. Nafi Toksoz. Effect of three-dimensional topography on seismic motion. *Journal of Geophysical Research*, 101(B3):5835–5846, March 1996.

George D. Bouckovalas and Achilleas G. Papadimitriou. Numerical evaluation of slope topography effects on seismic ground motion. *Soil Dynamics and Earthquake Engineering*, 25:547–558, 2005.

F. Bozzano, L. Lenti, S. Martino, A. Paciello, and G. Scarascia Mugnozza. Self-excitation process due to loacl seismic amplification responsible for the reactivation of the Salcito landslide (Italy) on 31 October 2002. *Journal of Geophysical Research*, 113, 2008.

F. Bozzano, L. Lenti, Salvatore Martino, A. Paciello, and G. Scarascia Mugnozza. Evidences of landslide earthquake triggering due to self-excitation process. *International Journal of Earth Science*, February 2010. Published online - Springer-Verlag.

P. Brabhaharan, D. Mason, and E. Gkeli. Research into seismic design and performance of high cut slopes in new zealand. In *6th International Conference on Earthquake Geotechnical Engineering*, November 2015.

P. Brabhaharan, D. Mason, and E. Gkeli. Seismic design and performance of high cut slopes. Technical Report Research report 613, NZ Transport Agency, February 2017. research performed by Opus International Consultants Ltd.

S.J. Brandenberg, S. Choi, B.L. Kutter, D.W. Wilson, and J.C. Santamarina. A bender element system for measuring shear wave velocities in centrifuge models. In *6th International Conference on Physical Modeling in Geotechnics*, 2006.

A.J. Brennan and S.P.G. Madabhushi. Amplification of seismic accelerations at slopes crests. *Can. Geotech. J.*, 46:585–594, 2009.

A.J. Brennan, N.I. Thusyanthan, and S.P.G. Madabhushi. Evaluation of shear modulus and damping in dynamic centrifuge tests. *Journal of Geotechnical and Geoenvironmental Engineering*, 131(12):1488–1497, December 2005.

Ian C. Briggs. Machine contouring using minimum curvature. *Geophysics*, 39(1):39–48, 1974.

F. Buech, T.R. Davies, and J.R. Pettinga. The Little Red Hill experimental study: Topographic effects on ground motion at a bedrock-dominated mountain edifice. *Bulletin of the Seismological Society of America*, 100(5A):2219–2229, October 2010.

Jan Burjánek, Gabriela Gassner-Stamm, Valerio Poggi, Jeffrey R. Moore, and Donat Fäh. Ambient vibration analysis of an unstable mountain slope. *Geophysical Journal International*, 180:820–828, 2010.

Jan Burjánek, Jeffrey R. Moore, Freddy X. Yugsi Molina, and Donat Fäh. Instrumental evidence of normal mode rock slope vibration. *Geophysical Journal International*, 188: 559–569, 2012.

Jan Burjánek, Benjamin Edwards, and Donat Fäh. Empirical evidence of local seismic effects at sites with pronounced topography: a systematic approach. *Geophysical Journal International*, 197:608–619, 2014.

M. Celebi. Topographical and geological amplification: Case studies and engineering implications. *Structural Safety*, 10:199–217, 1991.

Francisco J. Cháves-García, Luis R. Sánchez, and D. Hatzfeld. Topographic site effects and hvsr. a comparison between observations and theory. *Bulletin of the Seismological Society of America*, 86(5):1559–1573, October 1996.

Francisco J. Cháves-García, Miguel Rodríguez, Edward H. Field, and Denis Hatzfeld. Topographic site effects. a comparison of two nonreference methods. *Bulletin of the Seismological Society of America*, 87(6):1667–1673, December 1997.

Longwei Chen and Ezio Faccioli. Single-station standard deviation analysis of 20102012 strong-motion data from the canterbury region, new zealand. *Bulletin of Earthquake Engineering*, 11:1617–1632, April 2013.

Seokhyeon Choi. Implementation of bender element testing on centrifuge at UC Davis. Technical report, Department of Civil and Environmental Engineering, UC Davis, December 2004.

J. Dafni and J. Wartman. Centrifuge modeling of dyanmic response in slopes. In *8th International Conference on Physical Modeling in Geotechnics*, January 2014.

Lawrence T. Davis and Lewis R. West. Observed effecst of topography on ground motion. *Bulletin of the Seismological Society of America*, 63(1):283–298, February 1973.

Ross Boulanger (Director) and Dan Wilson (Associate Director). Signal processing and filtering of raw accelerometer records, 1998. URL `http://nees.ucdavis.edu/signalprocessing.php`.

Ross Boulanger (Director) and Dan Wilson (Associate Director). NEES @ UC Davis Center for Geotechnical Modeling, 2013. URL `http://nees.ucdavis.edu/index.php`.

F. Durante, G. Di Giulio, M. Tallini, G. Milana, and L. Macerola. A multidisciplinary approach to the seismic characterization of a mountain top (Monteluco, central Italy). *Physics and Chemistry of the Earth*, 98:119–935, 2017.

ProShake: Ground Response Analysis Program User's Manual. EduPro Civil Systems Inc., 1998-2017.

Ahmed Elgamal, Zhaohui Yang, Tao Lai, Bruce L. Kutter, and Daniel W. Wilson. Dynamic response of saturated dense sand in laminated centrifuge container. *Journal of Geotechnical and Geoenvironmental Engineering*, 131(5):598–609, May 2005.

Eurocode 8: Design of structures for earthquake resistance Part 5: Foundations, retaining structures and geotechnical aspects. European Committee for Standardization, CEN, 2004. Annex A.

Yufeng Gao, Ning Zhang, Dayong Li, Hanlong Liu, Yuanqiang Cai, and Yongxin Wu. Effects of topographic amplification induced by a u-shaped canyon on seismic waves. *Bulletin of the Seismological Society of America*, 102:1748–1763, August 2012.

J. Garnier, C. Gaudin, S.M. Springman, P.J. Culligan, D. Goodings, D. Konig, B. Kuttervii, R. Phillips, M.F. Randolph, and L. Thorel. Catalogue of scaling laws and similitude questions in geotechnical centrifuge modeling. *International Journal of Physical Modelling in Geotechnics*, 3:01–23, 2007.

G. Gazetas, P.V. Kallou, and P.N. Psarropoulos. Topography and soil effects in the M_s 5.9 Parnitha (Athens) earthquake: The case of Adámes. *Natural Hazards*, 27:133–169, 2002.

Louis Geli, Pierre-Yves Bard, and Bẽatrice Jullien. The effect of topography on earthquake ground motion: A review and new results. *Bulletin of the Seismological Society of America*, 78(1):42–63, February 1988.

T.L. Gipprich, R.K. Snieder, R.W. Jibson, and W. Kimman. The role of shear and tensile failures in dynamically triggered landslides. *Geophys. J. Int.*, 172:770–778, 2007.

GNS Science. Engineering geology cross section r01. Preliminary figure – Redcliffs cross section, July 2013a.

GNS Science. Engineering geology cross section r02. Preliminary figure – Redcliffs cross section, July 2013b.

GNS Science. Engineering geology cross section r03. Preliminary figure – Redcliffs cross section, July 2013c.

GNS Science and EQC. Geonet, 2017. URL `https://www.geonet.org.nz/`.

Golden Software Inc. *Grapher 9 Full User's Guide*, May 2011. URL `www.GoldenSoftware.com`.

Golden Software Inc. *Surfer 11 Full User's Guide*, July 2012. URL `www.GoldenSoftware.com`.

Google Earth. Redcliffs, new zealand, 2016. -43.557934, 172.73265.

Vladimir Graizer. Low-velocity zone and topography as a source of site amplification effect on Tarzana hill, California. *Soil Dynamics and Earthquake Engineering*, 29:324–332, 2009.

S. Hailemikael, L. Lenti, S. Martino, A. Paciello, D. Rossi, and G. Scarascia Mugnozza. Ground-motion amplification at the colle di roio ridge, central italy: a combined effect of stratigraphy and topography. *Geophysical Journal International*, 206:1–18, 2016.

Stephen Hartzell, Mark Meremonte, Leonardo Ramírez-Guzmán, and Daniel McNamara. Ground motion in the presence of complex topography: Earthquake and ambient noise sources. *Bulletin of the Seismological Society of America*, 104(1), February 2014.

Stephen Hartzell, Leonardo Ramírez-Guzmán, Mark Meremonte, and Alena Leeds. Ground motion in the presence of complex topography ii: Earthquake sources and 3d simulations. *Bulletin of the Seismological Society of America*, 107(1):344–358, February 2017.

Stephen H. Hartzell, David L. Carver, and Kenneth W. King. Initial investigation of site and topographic effects at robinwood ridge, california. *Bulletin of the Seismological Society of America*, 84(5):1336–1349, October 1994.

H.-B. Havenith, M. Vanini, D. Jongmans, and E. Faccioli. Initiation of earthquake-induced slope failure: influence of topographical and other site specific amplification effects. *Journal of Seismology*, 7:397–412, 2003.

C. Holden, A. Kaiser, and C. Massey. Observations and analysis of topographic effects in the seismic response of the port hills following the 2011 christchurch earthquake. In *Tenth U.S. National Conference on Earthquake Engineering*, July 2014.

Susan E. Hough, Jean Robert Altidor, Dieusuel Anglade, Doug Given, M. Guillard Janvier, J. Zebulon Maharrey, Mark Meremonte, Bernard Saint-Louis Mildor, Claude Prepetit, and Alan Yong. Localized damage caused by topographic amplification during the 2010 M 7.0 Haiti earthquake. *Nature Geoscience*, 3:778–782, November 2010.

L.R. Husid. Características de terremotos, análisis general. *Revista del IDIEM 8, Santiago del Chile*, pages 21–42, 1969.

Mahadevan Ilankatharan. Numerical simulation of a soil model-model container-centrifuge shaking table system. *Geotechnical Earthquake Engineering and Soil Dynamics IV*, 181, 2008. ASCE special publication.

Mahadevan Ilankatharan and Bruce Kutter. Modeling input motion boundary conditions for simulations of geotechnical shaking table tests. *Earthquake Spectra*, 26(2):349–369, May 2010.

W. Imperatori and P.M. Mai. The role of topography and lateral velocity heterogeneities on near-source scattering and ground-motion variability. *Geophysical Journal International*, 202:2163–2181, 2015.

A. Kaiser, C. Holden, and C. Massey. Determination of site amplification, polarization and topographic effects in the seismic response of the port hills following the 2011 christchurch earthquake. In *NZSEE Conference*, 2013.

A.E. Kaiser, C.I. Massey, and C. Holden. Site amplification, polarity and topographic effects in the port hills during the canterbury earthquake sequence. Technical report, GNS Science, June 2014. Consultancy Report 2014/121.

Hiroshi Kawase and Keiiti Aki. Topographic effect at the critical *sv*-wave incidence: Possible explanation of damage pattern by the Whittier Narrows, California earthquake of 1 October 1987. *Bulletin of the Seismological Society of America*, 80(1):1–22, February 1990.

David K. Keefer. Landslides caused by earthquakes. *Geological Society of America Bulletin*, 95(4):406–421, April 1984.

Katsuaki Konno and Tatsuo Ohmachi. Ground-motion characteristics estimated from spectral ratio between horizontal and vertical components of microtremor. *Bulletin of Seismological Society of America*, 88(1):228–241, February 1998.

Steven L. Kramer. *Geotechnical Earthquake Engineering*. Prentice-Hall Inc., Upper Saddle River, NJ, 1996.

T. Lai, A. Elgamal, B.L. Kutter, and D.W. Wilson. Three-dimensional modeling for site seismic response in laminated and rigid centrifuge containers. In *6th International Conference on Physical Modeling in Geotechnics*, 2002.

T. Lai, A. Elgamal, Z. Zang, B.L. Kutter, and D.W. Wilson. Numerical modeling of dynamic centrifuge experiments on a saturated dense sand stratum. In *11th International Conference on Soil Dynamics and Earthquake Engineering and 3rd International Conference on Earthquake Geotechnical Engineering*, January 2004.

Benoît LeBrun, D. Hatzfeld, P.Y. Bard, and M. Bouchon. Experimental study of the ground motion on a large scale topographic hill at Kitherion (Greece). *Journal of Seismology*, 3: 1–15, 1999.

S.T. Lee, T.T. Yu, W.F. Peng, and C.L. Wang. Incorporating the effects of topographic amplification in the analysis of earthquake-induced landslide hazards using logistic regression. *Natural Hazards and Earth Science Systems*, 10:2475–2488, 2010.

L. Lenti and S. Martino. The interaction of seismic waves with step-like slopes and its influence on landslide movements. *Engineering Geology*, 126:19–36, 2012.

L. Lenti and S. Martino. A parametric numerical study of the interaction between seismic waves and landslides for the evaluation of the susceptibility to seismically induced displacements. *Bulletin of the Seismological Society of America*, 103(1):33–56, February 2013.

Casper T. Leth, Anette Krogsboll, and Ole Hededal. Centrifuge Facilities at Technical University of Denmark. In *Proceedings Nordisk Geoteknikermote nr. 15*, pages 335–342, 2008.

C. Lévy, L. Baillet, D. Jongmans, P. Mourot, and D. Hantz. Dynamic response of the Chamousset rock column. *Journal of Geophysical Research*, 115, 2010.

Yangguang Liu. DRAFT: shear wave velocity estimates from bender elements used during nees topo centrifuge tests by jake dafni. Internal project document, August 2012a.

Yi-Wen Liu. *Hilbert Transform and Applications*, chapter 12, pages 291–300. InTech, April 2012b.

S. Marzorati, C. Ladina, E. Falcucci, S. Gori, M. Saroli, G. Ameri, and F. Galadini. Site effects on the rock: the case of castelvecchio subequo (laquila, central italy). *Bull Earthquake Eng*, 9:841–868, April 2011.

H.B. Mason, J.D. Bray, B.L. Kutter, D.W. Wilson, and B.Y. Choy. Earthquake motion selection and calibration for use in a geotechnical centrifuge. *Physical Modeling in Geotechnics – Springman, Laue & Seward (eds)*, 2010.

M. Massa, S. Lovati, E. D'Alema, G. Ferretti, and M. Bakavoli. An experimental approach for estimating seismic amplification effects at the top of a ridge, and the implication for ground-motion predictions: The case of narni, central italy. *Bulletin of the Seismological Society of America*, 100(6):3020–3034, December 2010.

Marco Massa, Simone Barani, and Sara Lovati. Overview of topographic effects based on experimental observations: meaning, causes and possibile interpretations. *Geophysical Journal International*, 197:1537–1550, May 2014.

C. Massey, G. Archibald, B. Lukovic, M. Yetton, N. Horspool, W. Ries, J. Thomson, K. Jones, and C. Mangos. Geonet landslide response to the mw5.7 14 february 2016 (valentine's day) earthquake, christchurch, new zealand. Technical report, GNS Science, November 2016a. Report 2016/035.

C. Massey, F. Della Pasqua, C. Holden, A. Kaiser, L. Richards, J. Wartman, M. J. McSaveney, G. Archibald, M. Yetton, and L. Janku. Rock slope response to strong earthquake shaking. *Landslides*, February 2016b.

MATLAB. *version 7.13.0 (R2011b)*. The MathWorks Inc., Natick, Massachusetts, 2011.

Emeline Maufroy, Victor M. Cruz-Atienza, and Stéphane Gaffet. A robust method for assessing 3-D topographic site effects: A case study at the LSBB Underground Laboratory, France. *Earthquake Spectra*, 28(3):1097–1115, August 2012.

Partick Meunier, Niels Hovius, and John Allan Haines. Topographic site effects and the location of earthquake induced landslides. *Earth and Planetary Science Letters*, 275:221–232, 2008.

Roozbeh Geraili Mikola and Nicholas Sitar. Seismic earth pressures on retaining structures in cohesionless soils. Technical Report UCB GT 13-01, California Department of Transportation (Caltrans), March 2013.

Gonzalo Andres Montalva. *Site-specific seismic hazard analyses*. PhD thesis, Washington State University, August 2010.

Brina M. Montoya, Ray Gerhard, Jason T. DeJong, Daniel W. Wilson, Matthew H. Weil, Brian C. Martinez, and Lars Pederson. Fabrication, operation and health monitoring of bender elements for aggressive environments. *Geotechnical Testing Journal*, 35(5), 2012.

Robb Eric S. Moss. Quantifying measurement uncertainty of thirty-meter shear-wave velocity. *Bulletin of the Seismological Society of America*, 98(3):1399–1411, June 2008.

W. Murphy. The role of topographic amplification on the initiation of rock slopes failures during earthquakes. *S.G. Evans et al. (eds.), Landslides from Massive Rock Slope Failure*, pages 139–154, 2006.

Yutaka Nakamura. A method for dynamic characteristics estimation of subsurface using microtremor on the ground surface. *Quarterly Report of RTRI*, 30(1), January 1989.

Fatma Ozkahriman, Abu Nasim, and Joseph Wartman. Topographic effects in a centrifuge model experiment. In *4th International Conference on Earthquake Geotechnical Engineering*, June 2007. paper 1262.

Alessandro Pagliaroli, Giuseppe Lanzo, and Beniamino D'Elia. Numerical evaluation of topographic effects at the Nicastro Ridge in Southern Italy. *Journal of Earthquake Engineering*, 15:404–432, 2011.

Alessandro Pagliaroli, Alessandra Avalle, Emanuela Falcucci, Stefano Gori, and Fabrizio Galadini. Numerical and experimental evaluation of site effects at ridges characterized by complex geological setting. *Bull Earthquake Eng*, 13:2841–2865, 2015.

F. Panzera, G. Lombardo, and R. Rigano. Evidence of topographic effects through the analysis of ambient noise measurements. *Seismological Research Letters*, 82(3):413–419, June 2011.

Roberto Paolucci. Amplification of earthquake ground motion by steep topographic irregularities. *Earthquake Engineering and Structural Dynamics*, 31:1831–1853, 2002.

Achilleas Papadimitriou. Topographic aggravation of the peak seismic acceleration near two dimensional hills and slopes. In *5th International Conference on Earthquake Geotechnical Engineering*, January 2011. paper TAOPA.

H. Pedersen, B. Le Brun, D. Hatzfield, M. Campillo, and P.-Y. Bard. Ground-motion amplitude across ridges. *Bulletin of the Seismological Society of America*, 84(6):1786–1800, 1994.

Wen-Fei Peng, Chein-Lee Wang, Shih-Tsu Chen, and Shing-Tsz Lee. Incorporating the effects of topographic amplification and sliding areas in hte modeling of earthquake-induced landslide hazards, using the cumulative displacement method. *Computers & Geosciences*, 35:946–966, 2009.

Marta Pischiutta, Giovanna Cultrera, Arrigo Caserta, Lucia Luzi, and Antonio Rovelli. Topographic effects on the hill of Nocera Umbra, central Italy. *Geophysical Journal International*, 2010.

Manisha Rai, Adrian Rodriguez-Marek, , and Brian S. Chioub. Empirical terrain-based topographic modification factors for use in ground motion prediction. *Earthquake Spectra*, 33(1):157–177, 2017.

Ellen M. Rathje, Norman A. Abrahamson, and Johnathon D. Bray. Simplified frequency content estimates of earthquake ground motions. *Journal of Geotechnical and Environmental Engineering*, 1998. Single page note.

Tom Revell and Tim Browne. Moa bone point: Ground investigation report. Technical Report 218782-011-06-01, Aurecon New Zealand Limited, September 2013. for Christchurch City Council.

Samuela Rizzitano, Ernesto Cascone, and GiovanniBiondi. Coupling of topographic and stratigraphic effects on seismic response of slopes through 2d linear and equivalent linear analyses. *Soil Dynamics and Earthquake Engineering*, 67:66–84, 2014.

A. Rodriguez-Marek, E.M. Rathje, J.J. Bommer, F. Scherbaum, and P.J. Stafford. Application of single-station sigma site-response characterization in a probabilistic seismic-hazard analysis for a new nuclear site. *Bulletin of the Seismological Society of America*, 104(4), August 2014.

Roberto Romeo. Seismically induced landslide displacements: a predictive model. *Engineering Geology*, 58:337–351, 2000.

Harold Ryan. Ricker, Ormbsy, Klauder, Butterworth – a choice of wavelets, September 1994. Hi-Res Geoconsulting.

Francisco J. Sánchez-Sesma. Elementary solutions for response of a wedge-shaped medium to incident SH and SV waves. *Bulletin of the Seismological Society of America*, 80:737–742, June 1990.

Francisco J. Sánchez-Sesma and Michel Campillo. Topographic effects for incident P, SV and Rayleigh waves. *Tectonophysics*, 218:113–125, 1993.

S.A. Sepúlveda, W. Murphy, and D.N. Petley. Topographic controls on coseismic rock slides during the 1999 Chi-Chi earthquake, Taiwan. *Quarterly Journal of Engineering Geology and Hydrogeology*, 38:189–196, 2005a.

Sergio A. Sepúlveda, William Murphy, Randall W. Jibson, and David N. Petley. Seismically induced rock slope failures resulting from topographic amplification of strong ground motions: The case of the Pacoima Canyon, California. *Engineering Geology*, 80:336–348, 2005b.

W.H.F. Smith and P. Wessel. Gridding with continuous curvature splines in tension. *Geophysics*, 55(3):293–305, March 1990.

S.M. Springman. Modelling in geotechnics. Technical report, Institute of Geotechnical Engineering, ETH Zurich, 1997. Only have Chapters 4-6.

Paul Spudich, Margaret Hellweg, and W.H.K. Lee. Directional topographic site response at tarzana observed in aftershocks of the 1994 Northridge, California, earthquake: Implications for mainshock motions. *Bulletin of the Seismological Society of America*, 86(1B): S193–S208, February 1996.

D.K. Stevens, B.-I. Kim, D.W. Wilson, and B.L. Kutter. Comprehensive invesitgation of nonlinear site response - centrifuge data report for dks02. Technical Report UCD/CGMDR-99/02, Center For Geotechnical Modeling at UC Davis, August 1999.

Jonathan P. Stewart and Shawn E. Sholtis. Case study of strong ground motion variations across cut slope. *Soil Dynamics and Earthquake Engineering*, 25:539–545, 2005.

Jonathon P. Stewart, Jonation D. Bray, David J. McMahon, Patrick M. Smith, and Alan L. Kropp. Seismic performance of hillside fills. *Journal of Geotechnical and Geoenvironmental Engineering*, 127(11):905–919, November 2001.

R.G. Stockwell, L. Mansinha, and R.P. Lowe. Localization of the complex spectrum: The S transform. *IEEE Transactions on Signal Processing*, 44(4):998–1001, April 1996.

Andrew C. Stolte, Brady R. Cox, and Richard C. Lee. An experimental topographic amplification study at los alamos national laboratory using ambient vibrations. *Bulletin of the Seismological Society of America*, 107(3), June 2017.

Shunsuke Takemura, Takashi Furumura, and Takuto Maeda. Scattering of high-frequency seismic waves caused by irregular surface topography and small-scale velocity inhomogeneity. *Geophysical Journal International*, 201:459–474, 2015.

R.N. Taylor, editor. *Geotechnical Centrifuge Technology*. Blackie Academic and Professional, an imprint of Chapman & Hall, Bishopbriggs, Glasgow, 1995.

Tonkin & Taylor. Christchurch earthquake recovery geotechnical factual report: Balmoral/glendevere. Technical report, Tonkin & Taylor LTD, May 2012. Draft.

R. Tripe, S. Kontoe, and T.K.C. Wong. Slope topography effects on ground motion in the presence of deep soil layers. *Soil Dynamics and Earthquake Engineering*, 50:72–84, 2013.

Richard Tripe and Stavroula Kontoe. A numerical investigation into the interaction between topographic amplification and soil layer amplification of earthquake motion. In *5th International Conference on Earthquake Geotechnical Engineering*, January 2011. paper ANITR.

Nicholas Trombetta, Josh Zupan, Katherine Jones, Hamilton Puangnak, and Chandrakanth Bolisetti. Centrifuge Test Plan: NEESR-SG: City Block Test-4, Code Name: NWT01. NEES Centrifuge Test Plan for the City Block Team, March 2011.

Deng-How Tsaur. Scattering and focusing of SH waves by lower semielliptical convex topography. *Bulletin of the Seismological Society of America*, 101:2212–2219, October 2011.

Koji Uenishi. On a possible role of Rayleigh surface waves in dynamic slope failures. *International Journal of Geomechanics ASCE*, July/August 2010.

Limin Wang, Yixian Xua, Jianghai Xia, and Yinhe Luo. Effect of near-surface topography on high-frequency rayleigh-wave propagation. *Journal of Applied Geophysics*, 166:93–103, 2015.

Robert V. Whitman and Philip C. Lambe. Effect of boundary conditions upon centrifuge experiments using ground motion simulation. *The American Society for Testing and Materials (ASTM)*, 1986.

Daniel W. Wilson, Ross W. Boulanger, Bruce L. Kutter, and Abbas Abghari. Aspects of dynamic centrifuge testing of soil-pile-superstructure interaction. In *Observation and Modeling in Numerical Analysis and Model Tests in Dynamic Soil-Structure Interaction Problems*, July 1997. Geotechnical Special Publication No. 64.

Clinton M. Wood and Brady R. Cox. Experimental data set of mining-induced seismicity for studies of full-scale topographic effects. *Earthquake Spectra*, 31(1):541564, February 2015.

Clinton M. Wood and Brady R. Cox. Comparison of field data processing methods for the evaluation of topographic effects. *Earthquake Spectra*, 32(4):21272147, November 2016.

Chin-Shung Yang, Szu-Pyng Kao, Fen-Bin Lee, and Pen-Shan Hung. Twelve different interpolation methods: A case study of Surfer 8.0. In *Proceedings of the XXth ISPRS Congress*, pages 778–785, 2004.

Yuzhen Yu, Lijun Deng, Xun Sun, and He Lu. Centrifuge modeling of a dry sandy slope response to earthquake loading. *Bull Earthquake Eng*, 6:447–461, 2007.

M. Zeghal, A.-W. Elgamal, H.T. Tang, and J.C. Stepp. Lotung downhole array. ii: Evaluation of soil nonlinear properties. *Journal of Geotechnical Engineering*, 121(4), April 1995.